

2008

Development of a micromechanics based failure criteria for transversely loaded composite materials

Dean C. Foster
University of Dayton

Follow this and additional works at: https://ecommons.udayton.edu/graduate_theses

Recommended Citation

Foster, Dean C., "Development of a micromechanics based failure criteria for transversely loaded composite materials" (2008). *Graduate Theses and Dissertations*. 2720.
https://ecommons.udayton.edu/graduate_theses/2720

This Dissertation is brought to you for free and open access by the Theses and Dissertations at eCommons. It has been accepted for inclusion in Graduate Theses and Dissertations by an authorized administrator of eCommons. For more information, please contact mschlange1@udayton.edu, ecommons@udayton.edu.

DEVELOPMENT OF A MICROMECHANICS BASED FAILURE CRITERIA FOR
TRANSVERSELY LOADED COMPOSITE MATERIALS

Dissertation

Submitted to

The School of Engineering of the

UNIVERSITY OF DAYTON

In Partial Fulfillment of the Requirements for

The Degree

Doctor of Philosophy in Materials Engineering

by

Dean Curtis Foster, P.E., P.S.

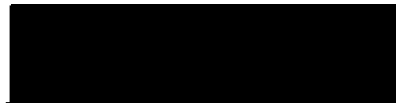
UNIVERSITY OF DAYTON

Dayton, Ohio

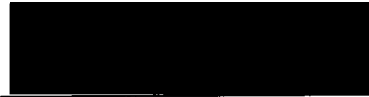
December 2008

DEVELOPMENT OF A MICROMECHANICS - BASED FAILURE CRITERIA FOR
TRANSVERSELY LOADED COMPOSITE MATERIALS

APPROVED BY:



Mandochehr Zoghi, Ph.D., P.E.
Professor and Chair, Civil and
Environment Engineering
Idaho State University
Committee Chairman



G. P. Tandon, Ph.D.
Distinguished Research Scientist
University of Dayton Research
Institute
Technical Chairman and
Committee Member



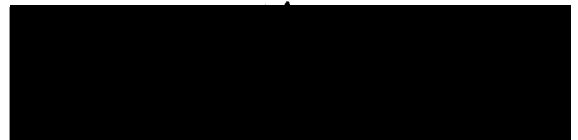
James M. Whitney, Ph.D.
Professor Emeritus, Civil and
Environmental
Engineering and Engineering
Mechanics
Committee Member



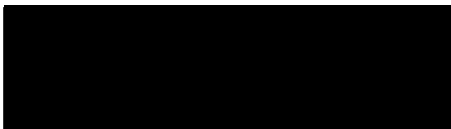
Steven L. Donaldson, Ph.D.
Assistant Professor, Civil and
Environmental
Engineering and Engineering
Mechanics
Committee Member



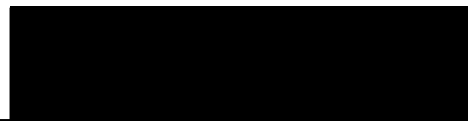
James A. Snide, Ph.D.
Professor Emeritus, Materials
Engineering
Committee Member



Gerald J. Shaughnessy, M.S.
Associate Professor,
Department of Mathematics
Committee Member



Malcom W. Daniels, Ph.D.
Associate Dean
School of Engineering



Joseph Z. Saliba, Ph.D., P.E.
Dean, School of Engineering

ABSTRACT

DEVELOPMENT OF A MICROMECHANICS BASED FAILURE CRITERIA FOR TRANSVERSELY LOADED COMPOSITE MATERIALS

Name: Dean Curtis Foster, P.E., P.S.
University of Dayton, 2008

Advisor: Dr. Manoochehr Zoghi, Ph.D., P.E.

The present work has identified two competing failure initiation mechanisms occurring in a unidirectional model composite system when loaded transverse to the direction of the fibers. Matrix cavitation and fiber-matrix debonding are the failure modes that have manifested themselves as a function of fiber spacing in multi-fiber cruciform specimens. The model composite system used two transparent epoxy systems, a linear room temperature cured 828/D-230 system and a nonlinear high temperature cured 862/W system, with five 0.36 mm diameter stainless steel wires as fibers. The fibers were arranged such that a single fiber was placed at the intersection of the face diagonals of four fibers located at the corners of a square. Seven different fiber spacing groups were tested ranging in volume fraction from 64% to 4%. Failure initiation was optically detected in-situ via the reflected light method using multiple high resolution, high magnification microscope video cameras. Three dimensional (3-D) finite element models (FEM) for all fiber spacing groups tested were used to analyze the stress state in the cruciform specimen at failure initiation. Residual stresses of both epoxy systems were measured by photoelasticity methods for incorporation into the micromechanical FEM. Analytical results of the individual cruciform 3-D FEMs in conjunction with the experimental observations were used to evaluate fiber-matrix debond and matrix failure criteria. A linear interaction debond criterion expressed as the sum of the ratios of the interfacial normal stress to tensile strength and interfacial shear stress to shear strength best validated the observed debond limits at the fiber spacing exhibiting fiber-matrix debonding as failure initiation. For the matrix failure criterion, analytical results indicated

that the Mohr-Coulomb criterion validated the fiber spacing exhibiting cavitation. This work has developed failure criteria that correctly identified the two competing failure initiation modes that occurred as a result of the varying internal stress state as a function of fiber spacing. The criteria accurately predicted the observed debonding limits and matrix cavitation of both matrix systems. The detailed understanding and findings of this work will assist the materials engineer by increasing the fidelity of composite solutions to meet the increasing aerospace structural demands.

To

My Mother, Diane C. Foster. She was one extraordinary person. I know you are smiling down upon me. God bless you, Mom, rest in peace.

ACKNOWLEDGMENTS

First and foremost without the support and love of my family, my wife Lisa and children Trevor and Alex, this would not have been possible. They have been extremely patient and have forgone my company many times during this endeavor and I am eternally grateful. They deserve this more than I do. To my parents William R. and Diane C. Foster for the many status updates we've had while I studied, researched and wrote the findings of this work. They know me best and have a calming influence when things didn't go quite right.

There are quite a number of people to whom I would like to express my sincerest gratitude for their assistance during this effort. Dr. Vernon Bechel for the impromptu discussions on every aspect of this work, his expertise in all facets of the cruciform specimen and experimental methods and for reviewing the draft manuscript are very truly appreciated. Dr. G. P. Tandon, my technical advisor, for his never ending patience, for teaching me the fine points of performing sound research and successfully guiding me through the myriad of obstacles encountered. My research committee, Dr. James Whitney, Dr. Steven Donaldson, Dr James Snide and Professor Gerald Shaughnessy for their patience and understanding allowing me the time to get it right. Dr. Manoochehr Zoghi, my academic advisor, for his insight on how things work in the academic arena and reminiscing about our prior research collaborations and working together at LJB. A special thanks to Mr. John Camping of UDRI who kept me straight every time I came into his lab wanting to do something. Plus for all his experimental insight and knowledge watching over my shoulder making sure I was carrying out the experiments correctly and safely. I truly appreciate Ms. Rae Parks help with the Photoshop program, analog-to-digital video converter and great cookie recipes. A big thanks to Mr. Jay Blair for getting me started with using the ANSYS finite element program. A huge thank you to Mr. Terry McClurg for providing the greatest ANSYS finite element support possible and answering all possible questions on why my models did run. Although Terry and I were both learning ANSYS at the same time, we did have lots of fun.

I also want to thank Dr Charles Browning for providing me the opportunity to work in a world class research facility. His advice and counsel has led me down this path to completion and will steer my future development. Finally, I owe a debt of gratitude to Dr. Nicholas Pagano for getting me started in this research area. His sage advice will guide me in future ventures.

TABLE OF CONTENTS

ABSTRACT.....	iii
ACKNOWLEDGMENTS.....	vi
LIST OF FIGURES.....	xvi
LIST OF TABLES.....	xxxi
LIST OF SYMBOLS.....	xxxvi
CHAPTER	
I. INTRODUCTION.....	1
Problem Statement.....	3
Overview of Research.....	5
Technical Significance	8
References.....	9
II. TRANSVERSE FAILURE EXPERIMENTAL TECHNIQUE	
AND RESULTS.....	13
Cruciform Specimen Geometry.....	16
Specimen Fabrication.....	18
Reflected Light Test Method.....	25
Photomicrograph Image Analysis.....	31
Fracture Surface Image Analysis.....	32
First Damage Mechanism Description.....	33
Fiber-Matrix Debonding.....	33
Fiber-Matrix Debond Measurements.....	35
Matrix Cavitation.....	35
Experimental Cruciform Specimen Results.....	37
828/D-230 Matrix System.....	39
Steel/828/D-230 Single Fiber Cruciform Results.....	39

Steel/828/D-230 6.0d _f Multi-Fiber Cruciform Results.....	43
Steel/828/D-230 2.5d _f Multi-Fiber Cruciform Results.....	47
Steel/828/D-230 2.0d _f Multi-Fiber Cruciform Results.....	51
Steel/828/D-230 1.9d _f Multi-Fiber Cruciform Results.....	57
Steel/828/D-230 1.84d _f Multi-Fiber Cruciform Results.....	61
Steel/828/D-230 1.75d _f Multi-Fiber Cruciform Results.....	70
Steel/828/D-230 1.57d _f Multi-Fiber Cruciform Results.....	75
Steel/828/D-230 Cruciform Experimental Results Summary.....	79
862/W Matrix System.....	82
Steel/862/W Single Fiber Cruciform Results.....	82
Steel/862/W 6.0d _f Multi-Fiber Cruciform Results.....	85
Steel/862/W 2.5d _f Multi-Fiber Cruciform Results.....	92
Steel/862/W 2.0d _f Multi-Fiber Cruciform Results.....	96
Steel/862/W 1.9d _f Multi-Fiber Cruciform Results.....	106
Steel/862/W 1.75d _f Multi-Fiber Cruciform Results.....	111
Steel/862/W 1.57d _f Multi-Fiber Cruciform Results.....	116
Steel/862/W Cruciform Experimental Results Summary.....	120
References.....	122

III ANALYTICAL MODEL DEVELOPMENT, RESULTS AND

DISCUSSION.....	125
Introduction.....	125
Review of Failure Criteria.....	126
Fiber-Matrix Debond Criterion.....	128
Matrix Failure Criterion.....	129
3-D Finite Element Model (FEM).....	136
Boundary Conditions.....	141
Mesh Sensitivity Study.....	142

Parametric Study.....	144
Analytical Results.....	145
828/D-230 Matrix System.....	145
Fiber-Matrix Interface Analytical Results.....	145
Center Fiber Interface Results.....	145
Corner Fiber Interface Results.....	148
Analysis of the $1.9d_f$ and $2.0d_f$ Fiber Spacing	
Group Behavior	151
Fiber-Matrix Interface Analytical Results-Conclusions.....	152
Fiber-Matrix Interface Debond Criterion.....	154
Matrix Failure Analytical Results.....	156
Matrix Failure Analytical Results Summary.....	163
862/W Matrix System.....	164
Fiber-Matrix Interface Analytical Results.....	164
Center Fiber Interface Results.....	165
Corner Fiber Interface Results.....	167
Fiber-Matrix Interface Analytical Results-Conclusions.....	169
Fiber-Matrix Interface Debond Criterion.....	171
Matrix Failure Analytical Results.....	172
Matrix Failure Analytical Results Summary.....	175
Summary.....	176
References.....	176
 IV RESULTS AND DISCUSSION.....	 181
Introduction.....	181
828/D-230 Matrix System.....	189
Fiber-Matrix Debond Initiation Criterion.....	189

	Quadratic Debond Initiation Criterion in the Field of View.....	190
	Linear Debond Initiation Criterion in the Field of View.....	195
	Quadratic vs. Linear Debond Criterion Evaluation.....	199
	Fiber-Matrix Debond Initiation Criterion – Summary.....	201
	Residual Stress Impact to Fiber-Matrix Debond Initiation Criterion.....	203
	Matrix Failure Initiation Criterion.....	207
	Matrix Failure Initiation Criterion Evaluation in the Field of View.....	211
	Matrix Failure Initiation Criterion – Summary.....	220
	Residual Stress Impact to the Matrix Failure Initiation Criterion.....	222
	862/W Matrix System.....	224
	Fiber-Matrix Debond Initiation Criterion.....	224
	Quadratic Debond Initiation Criterion in the Field of View.....	224
	Linear Debond Criterion in the Field of View.....	226
	Quadratic vs. Linear Debond Criterion Evaluation.....	230
	Fiber-Matrix Debond Initiation Criterion – Summary.....	231
	Residual Stress Impact to Fiber-Matrix Debond Initiation Criterion.....	232
	Matrix Failure Initiation Criterion	236
	Matrix Failure Initiation Criterion – Summary.....	242
	Residual Stress Impact to the Matrix Failure Initiation Criterion.....	243
	Constants A and B of the Fiber-Matrix Debond Criterion.....	244
	Summary.....	250
	References.....	251
V	CONCLUSIONS AND RECOMMENDATIONS.....	252
	Summary.....	252

Conclusions.....	254
Future Work Recommendations.....	256
Varying Fiber Diameters and Size Effects.....	257
Interfacial Adhesion Strength Determination.....	257
Fiber Arrangement Change.....	258
Realistic Composite Fibers.....	258
Additional Camera to Cover Fifth Fiber and Opposite Side of Specimen.....	258
Polarized Light.....	259
Failure Initiation Surface Investigation.....	259
Increase FEM Mesh Density.....	260
Final Recommendation.....	260

APPENDICES

A.	MATERIALS CHARACTERIZATION.....	261
	Room Temperature Cured 828/D-230 Epoxy System.....	261
	High Temperature Cured 862/W Epoxy System.....	275
	Materials Characterization Summary.....	287
	References.....	288
B.	RESIDUAL STRESS DETERMINATION.....	289
	Introduction.....	289
	Experimental Technique.....	290
	Specimen Geometry.....	290
	Materials.....	291
	Specimen Fabrication.....	292
	Testing.....	294
	Experimental/Analytical Results.....	295

	Material Fringe Constant.....	297
	828/D-230 Cure Induced Residual Stress Results.....	299
	862/W Cure Induced Residual Stress Results.....	301
	Analytical Results.....	302
	Conclusions.....	304
	References.....	305
C.	FINITE ELEMENT MODEL DETAILS.....	306
	862/W Finite Element Model Unit Displacement Determination.....	306
	Mesh Sensitivity Study.....	308
	Mesh Sensitivity Study – Summary.....	317
	Parametric Study.....	318
	Fiber Spacing Effects.....	319
	Fiber Spacing Effects – Summary.....	332
	Cruciform Thickness Effects.....	333
	Parametric Study – Summary.....	334
	ANSYS Parametric Design Language.....	335
	The Cruciform Model FEM Macro APDL Code.....	336
	The Key Point Generation APDL Code.....	337
	The Line Generation APDL Code.....	340
	The Volume Generation APDL Code.....	352
	The Applied Loading APDL Code.....	360
	The FEM Mesh Generation APDL Code.....	361
	The FEM Material APDL Code.....	362
	The APDL Code for the Residual Stress Models.....	364
	The 828/D-230 Shrinkage Stress Analysis APDL Code.....	364
	The 862/W Residual Stress Analysis APDL Code.....	366

D. INTERFACIAL ANALYTICAL RESULTS.....	371
828/D-230 System Fiber-Interface Analytical Results.....	371
Center Fiber Interface Results – Radial Stress.....	371
Center Fiber Interface Results – Shear Stress.....	377
Center Fiber Interface Results – Summary.....	382
Corner Fiber Interface Results – Radial Stress.....	382
Corner Fiber Interface Results – Shear Stress.....	394
Corner Fiber Interface Results – Summary.....	407
828/D-230 Fiber-Matrix Interface Debond Criterion Evaluation.....	408
862/W System Fiber-Interface Analytical Results.....	417
Center Fiber Interface Results – Radial Stress.....	417
Center Fiber Interface Results – Shear Stress.....	423
Center Fiber Interface Results – Summary.....	429
Corner Fiber Interface Results – Radial Stress.....	429
Corner Fiber Interface Results – Shear Stress.....	443
Corner Fiber Interface Results – Summary.....	455
862/W Fiber-Matrix Interface Debond Criterion Evaluation.....	455
Analysis of the 828/D-230 1.9d _f and 2.0d _f Fiber Spacing Group Behavior.....	463
Nanoindentation Study.....	463
Additional Cruciform Specimen Testing at the 1.9d _f and 2.0d _f Fiber Spacing.....	465
Failure Initiation Stress State Analysis.....	466
Cruciform Specimen Thickness Parametric Study.....	468
Summary.....	468
828/D-230 Matrix System Interfacial Stress Results.....	468
862/W Matrix System Interfacial Stress Results.....	469
Fiber-Matrix Debond Criterion Evaluation Results.....	470
Analysis of the 828/D-230 1.9d _f and 2.0d _f Fiber Spacing Group Behavior Results.....	470

E.	Fiber-Matrix Debond and Matrix Failure Criteria Evaluation.....	472
	828/D-230 Fiber-Matrix Debond Criterion Evaluation.....	472
	Quadratic Debond Criterion.....	472
	Linear Debond Criterion	473
	Quadratic vs. Linear Debond Criterion Evaluation in the 2 nd and 3 rd Quadrants of the Corner Fiber.....	474
	Fiber-Matrix Debond Initiation Criterion – Summary.....	479
	828/D-230 Matrix Failure Criterion Evaluation.....	482
	Matrix Failure Initiation Criterion – Summary.....	495
	862/W Fiber-Matrix Debond Criterion Evaluation.....	498
	Quadratic Debond Criterion.....	498
	Fiber-Matrix Debond Initiation Criterion – Summary.....	507
	Summary.....	510

LIST OF FIGURES

Figure 1: Schematic and nomenclature for cruciform specimen geometry.....	17
Figure 2: SCF as function of normalized distance from center of sample.....	18
Figure 3: Schematic of cross section of model cruciform specimen wing end for multi-fiber arrangement.....	19
Figure 4: Schematic of cross section of model cruciform specimen wing end for single fiber arrangement.....	20
Figure 5: Typical cruciform specimen milling to uniform thickness	22
Figure 6: Thin cruciform specimen milling to uniform thickness.....	23
Figure 7: Cruciform polishing operation.....	24
Figure 8: Schematic of the experimental set-up for the reflective light test method	27
Figure 9: Photomicrograph of single fiber cruciform specimen showing a debond at the north and south poles.....	28
Figure 10: Photograph showing camera position during testing.....	29
Figure 11: Photograph showing new and improved position during testing.....	30
Figure 12: Fiber group schematic delineating interior and exterior regions of fiber grouping.....	34
Figure 13: Fiber-matrix debond measurement schematic.....	35
Figure 14: Photomicrograph of steel/828 single-fiber cruciform debond.....	41
Figure 15: Photomicrograph showing the typical fracture surface of the single fiber cruciform specimen.....	41
Figure 16: SEM image of fracture initiation location showing the volcano feature.....	42
Figure 17: SEM image of fiber imprint area on fracture surface of single fiber cruciform specimen.....	42
Figure 18: Photomicrograph of steel/6.0d _f cruciform specimen debond.....	44
Figure 19: Subtracted image of interfacial debonding in a steel/6.0d _f cruciform specimen..	45
Figure 20: Debond failure of a steel/6.0d _f cruciform specimen.....	45
Figure 21: SEM image of fracture surface of steel/6.0d _f cruciform specimen.....	47

Figure 22: Photomicrograph of steel/2.5d _f cruciform specimen debond.....	49
Figure 23: Subtracted image of interfacial debonding in a steel/2.5d _f cruciform specimen.....	49
Figure 24: Debond failure of a steel/2.5d _f cruciform specimen with the inset showing a close-up of the fiber ends.....	50
Figure 25: SEM image of fracture surface of steel/2.5d _f cruciform specimen.....	51
Figure 26: Photomicrograph of steel/2.0d _f cruciform debond on the top, center and bottom fiber.....	53
Figure 27: Subtracted image of interfacial debonds on the top, center and bottom fiber in a steel/2.0d _f cruciform specimen.....	54
Figure 28: Photomicrograph showing fiber-matrix debonds and cracking after debond initiation in a steel/2.0d _f cruciform specimen.....	54
Figure 29: Photomicrograph showing fiber-matrix debonds prior to cracking shown in Figure 28.....	55
Figure 30: SEM image of fracture surface of steel/2.0d _f cruciform specimen.....	57
Figure 31: Subtracted image of interfacial debonds on the bottom and center fiber in the steel/1.90d _f cruciform specimen.....	59
Figure 32: SEM image of fracture surface of steel/1.9d _f cruciform specimen.....	61
Figure 33: Photomicrograph of steel/1.84d _f cruciform specimen showing no damage under a far-field stress of 0.62 MPa.....	62
Figure 34: Photomicrograph of steel/1.84d _f cruciform specimen showing matrix cavitation under a far-field stress of 2.87 MPa.....	63
Figure 35: Photomicrograph of steel/1.84d _f cruciform specimen showing matrix cavitation under a far-field stress of 8.17 MPa.....	63
Figure 36: Photomicrograph of steel/1.84d _f cruciform specimen showing matrix cavitation and fiber-matrix debonding under a far-field stress of 12.65 MPa.....	64
Figure 37: Subtracted image showing matrix cavitation in steel/1.84d _f cruciform specimen under a far-field stress of 2.87 MPa.....	65
Figure 38: Subtracted image showing matrix cavitation in steel/1.84d _f cruciform specimen under a far-field stress of 8.17 MPa.....	66
Figure 39: Subtracted image showing matrix cavitation in steel/1.84d _f cruciform specimen under a far-field stress of 12.65 MPa.....	66
Figure 40: Resultant final failure of steel/1.84d _f cruciform specimen.....	67
Figure 41: SEM image of fracture surface of steel/1.84d _f cruciform specimen.....	68
Figure 42: SEM image of failure initiation steel/1.84d _f cruciform at 230 times magnification.....	69

Figure 43: SEM image of mating failure initiation steel/1.84d _f cruciform at 230 times magnification.....	70
Figure 44: Subtracted image showing matrix cavitation in a steel/1.75d _f cruciform specimen at a far-field stress of 7.58 MPa.....	71
Figure 45: Subtracted image showing additional matrix cavitation and cavitation growth in a steel/1.75d _f cruciform specimen at a far-field stress of 9.77 MPa.....	72
Figure 46: Subtracted image showing additional matrix cavitation, fiber-matrix debonding and cavitation growth in a steel/1.75d _f cruciform specimen at a far-field stress of 11.13 MPa.....	72
Figure 47: SEM image of failure initiation site for the steel/1.75d _f cruciform specimen at 230 times magnification.....	73
Figure 48: SEM image of the mating failure initiation site for the steel/1.75d _f cruciform specimen at 230 times magnification.....	74
Figure 49: Subtracted image showing fiber-matrix debonds in steel/1.57d _f cruciform specimen.....	77
Figure 50: Subtracted image showing multiple fiber-matrix debond and debond growth in a steel/1.57d _f cruciform specimen.....	77
Figure 51: SEM image of fracture surface of steel/1.57d _f cruciform specimen.....	79
Figure 52: Photomicrograph of the steel/862 single-fiber cruciform debond at both the north and south pole.....	83
Figure 53: SEM image showing single fiber fracture surface and multiple fracture initiation locations.....	84
Figure 54: SEM image of single fiber imprint showing possible shear force interaction at the fiber-matrix interface.....	85
Figure 55: Photomicrograph of steel/6.0d _f 862 cruciform showing debond at the north pole of center fiber.....	87
Figure 56: Photomicrograph of steel/6.0d _f 862 cruciform showing two different debond characteristics, a thin fiber-matrix debond on bottom fiber and spot fiber-matrix debond at north pole of top fiber.....	89
Figure 57: SEM image of the fracture surface of steel/6.0d _f 862 cruciform specimen.....	91
Figure 58: SEM image of the fracture surface of steel/6.0d _f 862 cruciform specimen at 300 times magnification showing fiber imprint area.....	92
Figure 59: Subtracted image showing multiple debonds in steel/2.5d _f 862 cruciform specimen.....	94
Figure 60: SEM image of the fracture surface of the steel/2.5d _f 862 cruciform specimen.....	95

Figure 61: Photomicrograph of steel/2.0d _f 862 cruciform specimen showing matrix cavitation under a far-field stress of 10.2 MPa.....	97
Figure 62: Subtracted image showing matrix cavitation in steel/2.0d _f 862 cruciform specimen under a far-field stress of 10.20 MPa.....	98
Figure 63: Subtracted image showing additional matrix cavitation in steel/2.0d _f 862 cruciform specimen at a far-field stress of 25.90 MPa.....	99
Figure 64: Subtracted image showing additional matrix cavitation in steel/2.0d _f 862 cruciform specimen at a far-field stress of 35.85 MPa.....	99
Figure 65: Photomicrograph of steel/2.0d _f 862 cruciform specimen before light intensity and fiber group expansion.....	101
Figure 66: Photomicrograph of steel/2.0d _f 862 cruciform specimen after light intensity and fiber group expansion.....	102
Figure 67: Variational image between Figure 65 and 66 showing the change in light intensity and fiber grouping expansion.....	103
Figure 68: SEM image of fracture surface of steel/2.0d _f 862 cruciform specimen.....	105
Figure 69: SEM image of same failure initiation feature shown in Figure 68 at 95X magnification.....	105
Figure 70: SEM image of failure initiation features on different steel/2.0d _f 862 cruciform specimen than shown in Figure 68 and 69.....	106
Figure 71: Variational photomicrograph of the steel/1.90d _f 862 cruciform specimen showing the light intensity and fiber group expansion changes characteristic of internal debonds.....	108
Figure 72: Subtracted image showing bottom corner fiber thin fiber-matrix debond in steel/1.9d _f 862 cruciform specimen.....	109
Figure 73: SEM image of steel/1.90d _f 862 cruciform specimen fracture surface.....	110
Figure 74: SEM image at 250X magnification showing failure initiation site encircled by the white ellipsoid of steel/1.9d _f 862 cruciform specimen.....	111
Figure 75: Subtracted image showing thin fiber-matrix debonds in steel/1.75d _f 862 cruciform specimen.....	113
Figure 76: SEM of fracture surface of steel/1.75d _f 862 cruciform specimen.....	115
Figure 77: SEM of fracture surface of steel/1.75d _f 862 cruciform specimen at 200X magnification showing possible failure initiation feature.....	115
Figure 78: Subtracted photomicrograph of the steel/1.57d _f fiber 862 specimen showing a fiber-matrix debond at the south pole of the top corner fiber.....	117
Figure 79: SEM image of fracture surface of steel/1.57d _f 862 cruciform specimen.....	119
Figure 80: Mohr Circle plot of the 828/D-230 tensile and compression yield stress test results for the determination of the bulk friction parameter μ	136

Figure 81: 3D FEM of model cruciform specimen (Inset is planar view of the whole cruciform specimen).....	138
Figure 82: 3D FEM of model cruciform specimen showing mesh density in and around fibers.....	139
Figure 83: Final mesh configuration showing mesh refinement over mesh density results beyond outer band around fibers.....	143
Figure 84: Radial stress distributions at the fiber-matrix interface due to the combination of mechanical loading and chemical shrinkage.....	147
Figure 85: Shear stress distributions at the fiber-matrix interface due to the combination of mechanical loading and matrix chemical shrinkage.....	147
Figure 86: Radial stress distributions at the fiber-matrix interface due to the combination of mechanical loading and matrix chemical shrinkage from $\theta = 180^\circ$ to 270°	149
Figure 87: Shear stress distributions at the fiber-matrix interface due to the combination of mechanical loading and matrix chemical shrinkage from $\theta = 90^\circ$ to 180°	150
Figure 88: Finite Element Model plot showing the partitioning of the matrix volumes.....	158
Figure 89: Exterior Matrix and Upper Exterior Matrix volumes of the Finite Element Model.....	160
Figure 90: The Modified Tresca criterion YZ plane distribution in the Exterior-Matrix and Upper-Exterior-Matrix region for all fiber spacing groups tested.....	162
Figure 91: The Mohr-Coulomb criterion distribution acting in the YZ plane in the Exterior-Matrix and Upper-Exterior-matrix region for all fiber spacing groups tested	163
Figure 92: Radial stress distributions at the fiber-matrix interface due to the combination of mechanical loading and matrix residual stresses from cure cycle	166
Figure 93: Shear stress distributions at the fiber-matrix interface due to the combination of mechanical loading and matrix residual stresses from cure cycle	166
Figure 96: Exterior Matrix volume of the Finite Element Model for the 862/W cruciform specimen.....	173
Figure 97: The Modified-Tresca criterion YZ plane distribution in the Exterior-Matrix region for all fiber spacing groups tested	174
Figure 98: The Mohr-Coulomb criterion distribution acting in the YZ plane in the Exterior-Matrix region for all fiber spacing groups tested.....	175
Figure 99: Typical video tape view of the cruciform specimen testing at low magnification.	184
Figure 100: Typical fiber-matrix debonds at the north and south pole of a single fiber specimen.....	185
Figure 101: Fiber-matrix debond measurement schematic.....	185
Figure 102: Cruciform specimen finite element model showing model Cartesian directions and fiber interface angular orientation.....	187

Figure 103: The multi-fiber cruciform FEM matrix volumes for the center and corner fiber in the experimental field of view.....	187
Figure 104: The multi-fiber cruciform FEM volumes for the EM, UEM, UM, UBTF and CNB in the experimental field of view.....	188
Figure 105: Quadratic Debond Criterion evaluated at the fiber matrix interface of the corner fiber in the field of view from $\theta = 0^\circ$ to 90° at $Z = 0$ with A and B equal to 1.0	191
Figure 106: Quadratic Debond Criterion evaluated at the fiber matrix interface of the corner fiber in the field of view from $\theta = 270^\circ$ to 360° at $Z = 0$ with A and B equal to 1.0 ...	192
Figure 107: Quadratic Debond Criterion evaluated at the fiber matrix interface of the corner fiber in the field of view from $\theta = 0^\circ$ to 90° at $Z = 0$ with A = 15.0 and B = 1.0	193
Figure 108: Quadratic Debond Criterion evaluated at the fiber matrix interface of the corner fiber in the field of view from $\theta = 270^\circ$ to 360° at $Z = 0$ with A = 15.0 and B = 1.0 ...	194
Figure 109: Linear Debond Criterion evaluated at the fiber matrix interface of the corner fiber in the field of view from $\theta = 0^\circ$ to 90° at $Z = 0$ with A and B equal to 1.0	195
Figure 110: Linear Debond Criterion evaluated at the fiber matrix interface of the corner fiber in the field of view from $\theta = 270^\circ$ to 360° at $Z = 0$ with A and B equal to 1.0 ...	196
Figure 111: Linear Debond Criterion evaluated at the fiber matrix interface of the corner fiber in the field of view from $\theta = 0^\circ$ to 90° at $Z = 0$ with A = 11/3 and B = 4/3	197
Figure 112: Linear Debond Criterion evaluated at the fiber matrix interface of the corner fiber in the field of view from $\theta = 270^\circ$ to 360° at $Z = 0$ with A = 11/3 and B = 4/3 ...	198
Figure 113: Effects of the matrix cure shrinkage residual stress on the Linear Debond Criterion in the 1st quadrant of the corner fiber	206
Figure 114: Effects of the matrix cure shrinkage residual stress on the Linear Debond Criterion in the 4th quadrant of the corner fiber	207
Figure 115: Mohr-Coulomb Criterion distribution in the YZ plane of the EM and UEM regions of the FEM	213
Figure 116: Mohr-Coulomb Criterion plot in the YZ plane along the vertical direction, Y, at $Z=0$ in the EM and UEM regions of the FEM.....	215
Figure 117: Mohr-Coulomb Criterion plot in the XZ plane along the specimen thickness, X, at $Z=0$ in the EM and UEM regions of the FEM.....	215
Figure 118: Mohr-Coulomb Criterion distribution in the YZ plane of the UM region of the FEM.....	217
Figure 119: Mohr-Coulomb Criterion plot in the YZ plane along the vertical direction, Y, at $Z=0$ in the UM region of the FEM.....	217
Figure 120: Mohr-Coulomb Criterion plot in the XZ plane along the specimen thickness, X, at $Z=0$ in the UM region of the FEM.....	218

Figure 121: Mohr-Coulomb Criterion distribution in the YZ plane of the EM and UEM regions of the FEM showing the critical value plane at 36.35 MPa and cavitation locations.....	220
Figure 122: Matrix cure shrinkage residual stress effect on the Mohr-Coulomb matrix failure criterion showing results from the mechanical load only.....	223
Figure 123: Quadratic Debond Criterion evaluated at the fiber matrix interface of the corner fiber in field of view from $\theta = 0^\circ$ to 90° at $Z = 0$ with $A = 21.0$ and $B = 14.0$	225
Figure 124: Quadratic Debond Criterion evaluated at the fiber matrix interface of the corner fiber in field of view from $\theta = 270^\circ$ to 360° at $Z = 0$ with $A = 21.0$ and $B = 14.0$	225
Figure 125: Linear Debond Criterion evaluated at the fiber matrix interface of the corner fiber in field of view from $\theta = 0^\circ$ to 90° at $Z = 0$ with $A = 4.62$ and $B = 1.95$	228
Figure 126: Linear Debond Criterion evaluated at the fiber matrix interface of the corner fiber in field of view from $\theta = 270^\circ$ to 360° at $Z = 0$ with $A = 4.62$ and $B = 1.95$	228
Figure 127: Effects of the matrix cure shrinkage residual stress on the Linear Debond Criterion in the 1st quadrant of the corner fiber.....	237
Figure 128: Effects of the matrix cure shrinkage residual stress on the Linear Debond Criterion in the 4th quadrant of the corner fiber.....	237
Figure 129: Mohr-Coulomb Criterion distribution in the YZ plane of the EM region of the FEM with each specimen's cavitation location.....	240
Figure 130: Mohr-Coulomb Criterion distribution in the YZ plane at $Z = 0$ of the EM region of the FEM.....	240
Figure 131: Mohr-Coulomb Criterion distribution in the XZ plane along the specimen thickness at $Z = 0$ of the EM region of the FEM.....	241
Figure 132: Mohr-Coulomb Criterion distribution in the YZ plane at $Z = 0.45$ of the EM region of the FEM.....	241
Figure 133: Mohr-Coulomb Criterion distribution in the XZ plane along the specimen thickness at $Z = 0.45$ of the EM region of the FEM.....	242
Figure 134: Matrix cure shrinkage residual stress effect on the Mohr-Coulomb matrix failure criterion showing results from the mechanical load only.....	244
Figure 135: 828/D-230 typical neat resin dog bone specimen	263
Figure 136: 828/D-230 Stress vs. Strain curve.....	265
Figure 137: 828/D-230 Compression Stress vs. Displacement curve.....	269
Figure 138: 828/D-230 Poisson's Ration vs. load curve.....	270
Figure 139: 828/D-230 strain vs. temperature plot with trend lines determining the CTE....	272
Figure 140: 828/D-230 moisture measurement diagram.....	273
Figure 141: 828/D-230 Percent moisture gain.....	274

Figure 142: 828/D-230 Average Length and Width moisture strain.....	274
Figure 143: 862/W typical neat resin dog bone specimen	276
Figure 144: 862/W Stress vs. Strain curve.....	277
Figure 145: 862/W representative stress strain curve utilized for the finite element program.....	279
Figure 146: 862/W Compression stress vs. displacement curve.....	281
Figure 147: 862/W Poisson's Ration vs. load curve.....	283
Figure 148: 862/W strain vs. temperature plot with trend lines determining the CTE.....	284
Figure 149: 862/W percent moisture gain.....	285
Figure 150: 862/W average length and width moisture strain.....	286
Figure 151: Photographs of an (a) 828 photoelastic specimen and (b) 862 photoelastic specimen.....	291
Figure 152: Stress-Strain response for both the 828/D-230 and the 862/W epoxy systems.....	292
Figure 153: A typical silicon rubber mold used to cast the epoxy disk specimens.....	293
Figure 154: The polariscope set-up used for all experimentation. Not shown are the focusing lens and camera.....	295
Figure 155: 828/D-230 and 862/W matrix system calibration curves used for experimentation.....	298
Figure 156: A bright field photoelastic image of an 828/D-230 disk specimen.....	299
Figure 157: Bright and Dark Field Fringe order verses radial distance of 828/D-230 Specimen S201.....	300
Figure 158: A bright field photoelastic image of an 862/W disk specimen.....	301
Figure 159: Bright Field Fringe order verses radial distance of 862/W Specimen A.....	302
Figure 160: Finite element plot for the 828/D-230 and 862/W matrix systems residual stress models.....	303
Figure 161: FEM applied displacement vs. FEM Far-field Stress results.....	307
Figure 162: Element plots of the mesh density study models for the 190d _{RT} -LDM model.....	309
Figure 163: Element plots of the mesh density study models for the 190d _{RT} model.....	310
Figure 164: Element plots of the mesh density study models for the 190d _{RT} -MDM model.....	311

Figure 165: Center Fiber interface mesh density results for the Radial SCF.....	312
Figure 166: Center Fiber interface mesh density results for the Hoop SCF.....	313
Figure 167: Center Fiber interface mesh density results for the Shear SCF.....	313
Figure 168: Corner Fiber mesh density results for the Radial SCF.....	315
Figure 169: Corner Fiber mesh density results for the Hoop SCF.....	315
Figure 170: Corner Fiber mesh density results for the Shear SCF	316
Figure 171: Final mesh configuration showing mesh refinement over mesh density results beyond outer band around fibers.....	318
Figure 172: Variation of radial stress due to chemical shrinkage at the interface of the center fiber as a function of fiber spacing.....	320
Figure 173: Variation of radial stress due to chemical shrinkage at the interface of the corner fiber as a function of fiber spacing.....	321
Figure 174: Variation of hoop stress due to chemical shrinkage at the interface of the center fiber as a function of fiber spacing.....	321
Figure 175: Variation of hoop stress due to chemical shrinkage at the interface of the corner fiber as a function of fiber spacing.....	322
Figure 176: Variation of shear stress due to chemical shrinkage at the interface of the center fiber as a function of fiber spacing.....	322
Figure 177: Variation of shear stress due to chemical shrinkage at the interface of the corner fiber as a function of fiber spacing.....	323
Figure 178: Variation of radial stress due to mechanical loading at the interface of the center fiber as a function of fiber spacing.....	325
Figure 179: Variation of radial stress due to mechanical loading at the interface of the corner fiber as a function of fiber spacing.....	326
Figure 180: Variation of hoop stress due to mechanical loading at the interface of the center fiber as a function of fiber spacing.....	327
Figure 181: Variation of hoop stress due to mechanical loading at the interface of the corner fiber as a function of fiber spacing.....	327
Figure 182: Variation of shear stress due to mechanical loading at the interface of the center fiber as a function of fiber spacing.....	329
Figure 183: Variation of shear stress due to mechanical loading at the interface of the corner fiber as a function of fiber spacing.....	329
Figure 184: Variation of axial stress due to mechanical loading at the interface of the center fiber at $\theta = 90^\circ$ as a function of fiber spacing.....	331

Figure 185: Variation of axial stress due to mechanical loading at the interface of the corner fiber at $\theta = 270^\circ$ as a function of fiber spacing.....	331
Figure 186: Radial SCF as a function of cover thickness.....	334
Figure 187: Radial stress distributions at the fiber-matrix interface due to the combination of mechanical loading and chemical shrinkage.....	372
Figure 188: Radial stress distributions at the fiber-matrix interface due to the matrix chemical shrinkage.....	374
Figure 189: Radial stress distributions at the fiber-matrix interface due to the mechanical loading.....	375
Figure 190: Shear stress distributions at the fiber-matrix interface due to the combination of mechanical loading and matrix chemical shrinkage.....	378
Figure 191: Shear stress distributions at the fiber-matrix interface due to the matrix chemical shrinkage.....	379
Figure 192: Shear stress distributions at the fiber-matrix interface due to the mechanical loading.....	380
Figure 193: Radial stress distributions at the fiber-matrix interface due to the combination of mechanical loading and matrix chemical shrinkage from $\theta = 0^\circ$ to 90°	384
Figure 194: Radial stress distributions at the fiber-matrix interface due to the combination of mechanical loading and matrix chemical shrinkage from $\theta = 90^\circ$ to 180°	384
Figure 195: Radial stress distributions at the fiber-matrix interface due to the combination of mechanical loading and matrix chemical shrinkage from $\theta = 180^\circ$ to 270°	385
Figure 196: Radial stress distributions at the fiber-matrix interface due to the combination of mechanical loading and matrix chemical shrinkage from $\theta = 270^\circ$ to 360°	385
Figure 197: Radial stress distributions at the fiber-matrix interface due to the matrix chemical shrinkage from $\theta = 0^\circ$ to 90°	387
Figure 198: Radial stress distributions at the fiber-matrix interface due to the matrix chemical shrinkage from $\theta = 90^\circ$ to 180°	387
Figure 199: Radial stress distributions at the fiber-matrix interface due to the matrix chemical shrinkage from $\theta = 180^\circ$ to 270°	388
Figure 200: Radial stress distributions at the fiber-matrix interface due to the matrix chemical shrinkage from $\theta = 270^\circ$ to 360°	388
Figure 201: Radial stress distributions at the fiber-matrix interface due to the mechanical loading from $\theta = 0^\circ$ to 90°	391
Figure 202: Radial stress distributions at the fiber-matrix interface due to the mechanical loading from $\theta = 90^\circ$ to 180°	391

Figure 203: Radial stress distributions at the fiber-matrix interface due to the mechanical loading from $\theta = 180^\circ$ to 270°	392
Figure 204: Radial stress distributions at the fiber-matrix interface due to the mechanical loading from $\theta = 270^\circ$ to 360°	392
Figure 205: Shear stress distributions at the fiber-matrix interface due to the combination of mechanical loading and matrix chemical shrinkage from $\theta = 0^\circ$ to 90°	395
Figure 206: Shear stress distributions at the fiber-matrix interface due to the combination of mechanical loading and matrix chemical shrinkage from $\theta = 90^\circ$ to 180°	396
Figure 207: Shear stress distributions at the fiber-matrix interface due to the combination of mechanical loading and matrix chemical shrinkage from $\theta = 180^\circ$ to 270°	397
Figure 208: Shear stress distributions at the fiber-matrix interface due to the combination of mechanical loading and matrix chemical shrinkage from $\theta = 270^\circ$ to 360°	397
Figure 209: Shear stress distributions at the fiber-matrix interface due to the matrix chemical shrinkage from $\theta = 0^\circ$ to 90°	399
Figure 210: Shear stress distributions at the fiber-matrix interface due to the matrix chemical shrinkage from $\theta = 90^\circ$ to 180°	399
Figure 211: Shear stress distributions at the fiber-matrix interface due to the matrix chemical shrinkage from $\theta = 180^\circ$ to 270°	400
Figure 212: Shear stress distributions at the fiber-matrix interface due to the matrix chemical shrinkage from $\theta = 270^\circ$ to 360°	400
Figure 213: Shear stress distributions at the fiber-matrix interface due to the mechanical loading from $\theta = 0^\circ$ to 90°	402
Figure 214: Shear stress distributions at the fiber-matrix interface due to the mechanical loading from $\theta = 90^\circ$ to 180°	403
Figure 215: Shear stress distributions at the fiber-matrix interface due to the mechanical loading from $\theta = 180^\circ$ to 270°	404
Figure 216: Shear stress distributions at the fiber-matrix interface due to the mechanical loading from $\theta = 270^\circ$ to 360°	404
Figure 217: Radial stress distributions along the corner fiber-matrix interface from $\theta = 0^\circ$ to 90° at $Z = 0$ due to the combination of mechanical loading and matrix chemical shrinkage.....	412
Figure 218: Shear stress distributions along the corner fiber-matrix interface from $\theta = 0^\circ$ to 90° at $Z = 0$ due to the combination of mechanical loading and matrix chemical shrinkage.....	412

Figure 219: Radial stress distributions at the fiber-matrix interface due to the combination of mechanical loading and matrix residual stresses from cure cycle.....	418
Figure 220: Radial stress distributions at the fiber-matrix interface due to the matrix residual stresses from cure cycle.....	419
Figure 221: Radial stress distributions at the fiber-matrix interface due to the mechanical loading.....	421
Figure 222: Shear stress distributions at the fiber-matrix interface due to the combination of mechanical loading and matrix residual stresses from cure cycle.....	424
Figure 223: Shear stress distributions at the fiber-matrix interface due to the matrix residual stresses from cure cycle.....	426
Figure 224: Shear stress distributions at the fiber-matrix interface due to the mechanical loading.....	427
Figure 225: Radial stress distributions at the fiber-matrix interface due to the combination of mechanical loading and matrix cure residual stresses from $\theta = 0^\circ$ to 90°	430
Figure 226: Radial stress distributions at the fiber-matrix interface due to the combination of mechanical loading and matrix cure residual stresses from $\theta = 90^\circ$ to 180°	431
Figure 227: Radial stress distributions at the fiber-matrix interface due to the combination of mechanical loading and matrix cure residual stresses from $\theta = 180^\circ$ to 270°	431
Figure 228: Radial stress distributions at the fiber-matrix interface due to the combination of mechanical loading and matrix cure residual stresses from $\theta = 270^\circ$ to 360°	432
Figure 229: Radial stress distributions at the fiber-matrix interface due to the matrix cure residual stress from $\theta = 0^\circ$ to 90°	434
Figure 230: Radial stress distributions at the fiber-matrix interface due to the matrix cure residual stress from $\theta = 90^\circ$ to 180°	434
Figure 231: Radial stress distributions at the fiber-matrix interface due to the matrix cure residual stress from $\theta = 180^\circ$ to 270°	435
Figure 232: Radial stress distributions at the fiber-matrix interface due to the matrix cure residual stress from $\theta = 270^\circ$ to 360°	435
Figure 232: Radial stress distributions at the fiber-matrix interface due to the mechanical loading from $\theta = 0^\circ$ to 90°	437
Figure 234: Radial stress distributions at the fiber-matrix interface due to the mechanical loading from $\theta = 90^\circ$ to 180°	438
Figure 235: Radial stress distributions at the fiber-matrix interface due to the mechanical loading from $\theta = 180^\circ$ to 270°	438

Figure 236: Radial stress distributions at the fiber-matrix interface due to the mechanical loading from $\theta = 270^\circ$ to 360°	439
Figure 237: Shear stress distributions at the fiber-matrix interface due to the combination of mechanical loading and matrix cure residual stresses from $\theta = 0^\circ$ to 90°	443
Figure 238: Shear stress distributions at the fiber-matrix interface due to the combination of mechanical loading and matrix cure residual stresses from $\theta = 90^\circ$ to 180°	444
Figure 239: Shear stress distributions at the fiber-matrix interface due to the combination of mechanical loading and matrix cure residual stresses from $\theta = 180^\circ$ to 270°	444
Figure 240: Shear stress distributions at the fiber-matrix interface due to the combination of mechanical loading and matrix cure residual stresses from $\theta = 270^\circ$ to 360°	445
Figure 241: Shear stress distributions at the fiber-matrix interface due to the matrix cure residual stress from $\theta = 0^\circ$ to 90°	447
Figure 242: Shear stress distributions at the fiber-matrix interface due to the matrix cure residual stress from $\theta = 90^\circ$ to 180°	447
Figure 243: Shear stress distributions at the fiber-matrix interface due to the matrix cure residual stress from $\theta = 180^\circ$ to 270°	448
Figure 244: Shear stress distributions at the fiber-matrix interface due to the matrix cure residual stress from $\theta = 270^\circ$ to 360°	448
Figure 245: Shear stress distributions at the fiber-matrix interface due to the mechanical loading from $\theta = 0^\circ$ to 90°	450
Figure 246: Shear stress distributions at the fiber-matrix interface due to the mechanical loading from $\theta = 90^\circ$ to 180°	451
Figure 247: Shear stress distributions at the fiber-matrix interface due to the mechanical loading from $\theta = 180^\circ$ to 270°	451
Figure 248: Shear stress distributions at the fiber-matrix interface due to the mechanical loading from $\theta = 270^\circ$ to 360°	452
Figure 249: Radial stress distributions along the corner fiber-matrix interface from $\theta = 0^\circ$ to 90° at $Z = 0$ due to the combination of mechanical loading and matrix residual stresses.....	458
Figure 250: Shear stress distributions along the corner fiber-matrix interface from $\theta = 0^\circ$ to 90° at $Z = 0$ due to the combination of mechanical loading and matrix residual stresses.....	459
Figure 251: Photomicrograph of nanoindentation pattern for the 1.9d _f fiber spacing cruciform specimen.....	465
Figure 252: Quadratic Debond Criterion evaluated at the debond locations in the 2 nd quadrant of the corner fiber with $A = 15.0$ and $B = 1.0$	475

Figure 253: Linear Debond Criterion evaluated at the debond locations in the 2 nd quadrant of the corner fiber with $A = 11/3$ and $B = 4/3$	476
Figure 254: Quadratic Debond Criterion evaluated at the debond locations in the 3 rd quadrant of the corner fiber with $A = 15.0$ and $B = 1.0$	478
Figure 255: Linear Debond Criterion evaluated at the debond locations in the 3 rd quadrant of the corner fiber with $A = 11/3$ and $B = 4/3$	478
Figure 256: Linear Debond Criterion at the fiber-matrix interface of the center fiber.....	481
Figure 257: Mohr-Coulomb Criterion distribution in the YZ plane of the BTF and UBTF regions of the FEM.....	483
Figure 258: Mohr-Coulomb Criterion plot in the YZ plane along the vertical direction, Y_1 at $Z=0$ in the BTF and UBTF region of the FEM.....	483
Figure 259: Mohr-Coulomb Criterion plot in the XZ plane along the specimen thickness, X_1 at $Z=0$ in the BTF and UBTF region of the FEM.....	484
Figure 260: Mohr-Coulomb Criterion distribution in the center fiber matrix band at the fiber matrix interface.....	486
Figure 261: Mohr-Coulomb Criterion distribution in the center fiber matrix band at the mid-plane of the matrix band, $R = 0.1978$ mm.....	486
Figure 262: Mohr-Coulomb Criterion distribution in the center fiber matrix band at the outer band limits, $R = 0.2178$ mm.....	487
Figure 263: Mohr-Coulomb Criterion distribution in the corner fiber $0^\circ - 90^\circ$ matrix band at the fiber matrix interface.....	488
Figure 264: Mohr-Coulomb Criterion distribution in the corner fiber $0^\circ - 90^\circ$ matrix band at the mid-plane of the matrix band, $R=0.1978$ mm.....	488
Figure 265: Mohr-Coulomb Criterion distribution in the corner fiber $0^\circ - 90^\circ$ matrix band at the outer band limits, $R=0.2178$ mm.....	489
Figure 266: Mohr-Coulomb Criterion distribution in the corner fiber $270^\circ - 360^\circ$ matrix band at the fiber matrix interface.....	490
Figure 267: Mohr-Coulomb Criterion distribution in the corner fiber $270^\circ - 360^\circ$ matrix band at the mid-plane of the matrix band, $R=0.1978$ mm.....	490
Figure 268: Mohr-Coulomb Criterion distribution in the corner fiber $270^\circ - 360^\circ$ matrix band at the outer band limits, $R=0.2178$ mm.....	491
Figure 269: Mohr-Coulomb Criterion distribution in the corner fiber $90^\circ - 180^\circ$ matrix band at the fiber matrix interface.....	492
Figure 270: Mohr-Coulomb Criterion distribution in the corner fiber $90^\circ - 180^\circ$ matrix band at the mid-plane of the matrix band, $R=0.1978$ mm.....	492
Figure 271: Mohr-Coulomb Criterion distribution in the corner fiber $90^\circ - 180^\circ$ matrix band at the outer band limits, $R=0.2178$ mm.....	493

Figure 272: Mohr-Coulomb Criterion distribution in the corner fiber 180° – 270° matrix band at the fiber matrix interface.....	493
Figure 273: Mohr-Coulomb Criterion distribution in the corner fiber 180° – 270° matrix band at the mid-plane of the matrix band, $R=0.1978$ mm.....	494
Figure 274: Mohr-Coulomb Criterion distribution in the corner fiber 180° – 270° matrix band at the outer band limits, $R=0.2178$ mm.....	494
Figure 275: Mohr-Coulomb Criterion distribution in the YZ plane of the EM and UEM regions of the FEM showing the critical value plane at 36.35 MPa and cavitation locations.....	496
Figure 276: Mohr-Coulomb Criterion distribution in the YZ plane of the UM regions of the FEM showing the critical value plane at 36.35 MPa and cavitation locations.....	497
Figure 277: Mohr-Coulomb Criterion distribution in the YZ plane of the UBTF regions of the FEM showing the critical value plane at 36.35 MPa and cavitation locations.....	497
Figure 278: Quadratic Debond Criterion evaluated at the fiber matrix interface of the corner fiber at debond locations in field of view from $\theta = 0^\circ$ to 90° with $A = 21$ and $B = 14$	499
Figure 279: Quadratic Debond Criterion evaluated at the fiber matrix interface of the corner fiber at debond locations in field of view from $\theta = 270^\circ$ to 360° with $A = 21$ and $B = 14$	500
Figure 280: Linear Debond Criterion evaluated at the fiber matrix interface of the corner fiber at debond locations in field of view from $\theta = 0^\circ$ to 90° with $A = 4.62$ and $B = 1.95$	500
Figure 281: Linear Debond Criterion evaluated at the fiber matrix interface of the corner fiber at debond locations in field of view from $\theta = 270^\circ$ to 360° with $A = 4.62$ and $B = 1.95$	501
Figure 282: Linear Debond Criterion evaluated at the fiber matrix interface of the corner fiber in field of view from $\theta = 90^\circ$ to 180° at $Z = 0$ with $A = 4.62$ and $B = 1.95$	503
Figure 283: Linear Debond Criterion evaluated at the fiber matrix interface of the corner fiber in field of view from $\theta = 180^\circ$ to 270° at $Z = 0$ with $A = 4.62$ and $B = 1.95$	504
Figure 284: Linear Debond Criterion at the fiber-matrix interface of the center fiber.....	509

LIST OF TABLES

Table 1: Final average cruciform specimen dimensions including the silicon rubber mold utilized for all 828/D-230 specimens and the Teflon mold for all 862/W specimens.....	20
Table 2: Field of view limits for 1.57d _f , 1.75d _f , 1.84d _f and 1.90d _f cruciform specimens.....	29
Table 3: Single fiber cruciform specimen test results where IAS indicates Instantaneously Across Screen (IAS) meaning it is greater than 4 mm.....	40
Table 4: Far-field applied stress at debond initiation in multi-fiber specimens having 6.0d _f fiber spacing.....	43
Table 5: Steel/828 6.0d _f cruciform specimen debond measurements, where CA = central angle.....	46
Table 6: Far-field applied stress at debond initiation in multi-fiber specimens having 2.5d _f fiber spacing.....	48
Table 7: Steel/828 2.5d _f cruciform specimen debond measurements where CA = central angle.....	50
Table 8: Far-field applied stress at debond initiation in multi-fiber specimens having a 2.0d _f fiber spacing where * indicates vertical cracking after debond initiation.....	52
Table 9: Steel/828 2.0d _f cruciform debond measurements, where CA = central angle.....	56
Table 10: Far-field applied stress at debond initiation in multi-fiber specimens having 1.9d _f fiber spacing.....	58
Table 11: Steel/828 1.9d _f cruciform specimen debond measurements.....	60
Table 12: Far-field applied stress at matrix cavitation and debond initiation in multi-fiber specimens having 1.84d _f fiber spacing.....	67
Table 13: Far-field applied stress at matrix cavitation and debond initiation in multi-fiber specimens having 1.75d _f fiber spacing.....	71
Table 14: Far-field applied stress at debond initiation in multi-fiber specimens having 1.57d _f fiber spacing.....	76
Table 15: 828 1.57d _f cruciform specimen debond measurements.....	78
Table 16: Summary of 828 cruciform test results.....	82
Table 17: Steel/862 Single fiber cruciform specimen test results.....	83
Table 18: Far-field applied stress at matrix cavitation and debond initiation in specimens having 6.0d _f fiber spacing	86

Table 19: Steel/862 6.0d _f cruciform specimen debond measurements.....	90
Table 20: Far-field applied stress at debond initiation in multi-fiber specimens having 2.5d _f fiber spacing.....	93
Table 21: Steel/862 2.5d _f cruciform specimen debond measurements.....	94
Table 22: Far-field applied stress at matrix cavitation and debond initiation in multi-fiber specimens having 2.0d _f fiber spacing.....	96
Table 23: Far-field applied stress at debond initiation in multi-fiber specimens having 1.9d _f fiber spacing where the superscript indicates approximate location.....	107
Table 24: Far-field applied stress at debond initiation in multi-fiber specimens having 1.75d _f fiber spacing where the superscript indicates approximate location.....	112
Table 25: Steel/862 1.75d _f cruciform specimen debond measurements.....	113
Table 26: Far-field applied stress at debond initiation in multi-fiber specimens having 1.57d _f fiber spacing where the superscript NH and SH designate Northern Hemisphere, and Southern Hemisphere respectively.....	117
Table 27: Steel/862 1.57d _f cruciform specimen debond measurements.....	118
Table 28: Summary of 862 cruciform test results.....	120
Table 29: Material properties for the finite element model analysis.....	140
Table 30: Comparing Experimental far-field stress to 862 mechanical FEM far-field stress.....	142
Table 31: Mesh density study statistics.....	143
Table 32: Experimental fiber matrix debond measurements.....	156
Table 33: Limits of the Exterior-Matrix and Upper-Exterior-Matrix regions and locations of the bottom and top corner fiber matrix band.....	159
Table 34: Experimental fiber matrix debond measurements.....	171
Table 35: Representative volume fraction of the multi-fiber cruciform specimen spacing groups.....	182
Table 36: Cruciform Specimen Experimental Results for both Matrix Systems showing first failure mechanisms and corresponding far-field stress at first failure.....	183
Table 37: The center fiber viewable area in multi-fiber cruciform specimens.....	185
Table 38: Fiber matrix debond limits for the corner fiber 1st and 4th quadrant determined by quadratic debond criterion evaluated from the cruciform FEM results.....	194
Table 39: Fiber matrix debond limits for the corner fiber 1st and 4th quadrant determined by linear debond criterion evaluated from the cruciform FEM results.....	198
Table 40: Comparison of the fiber matrix debond limits predicted by the Quadratic and Linear Debond Criterion for the 1st quadrant of the corner fiber at the location	

of the debonds along the fiber.....	199
Table 41: Comparison of the fiber matrix debond limits predicted by the Quadratic and Linear Debond Criterion for the 4th quadrant of the corner fiber.....	200
Table 42: Criteria comparison using neat resin tests.....	210
Table 43: Cavitation locations for 1.75d _f and 1.84d _f fiber spacing groups and average apparent critical Mohr-Coulomb Criterion value.....	212
Table 44: Fiber matrix debond limits for the corner fiber 1st and 4th quadrant determined by quadratic debond criterion evaluated from the cruciform FEM results.....	226
Table 45: Fiber matrix debond limits for the corner fiber 1st and 4th quadrant determined by the linear debond criterion evaluated from the cruciform FEM results.....	229
Table 46: Comparison of the fiber matrix debond limits predicted by the Quadratic and Linear Debond Criterion for the 1st quadrant of the corner fiber at Z = 0.....	230
Table 47: Comparison of the fiber matrix debond limits predicted by the Quadratic and Linear Debond Criterion for the 4th quadrant of the corner fiber at Z = 0.....	231
Table 48: Criteria comparison using neat resin tests.....	237
Table 49: Cavitation locations for 2.0d _f fiber spacing group and average apparent critical Mohr-Coulomb Criterion value.....	238
Table 50: Literature Search Summary of Interfacial Adhesive Normal and Shear Stress Results for Various Two-Part Epoxy Systems.....	248
Table 51: 828/D-230 specimen maximum stress and strain, ultimate stress and strain, and linear modulus.....	266
Table 52: Compression specimen dimensions, maximum load and maximum strength.....	269
Table 53: 828/D-230 Poisson's ratio specimen results.....	271
Table 54: 828/D-230 measured average length and width percent moisture strain.....	275
Table 55: 862/W specimen maximum stress and strain, ultimate stress and strain, and linear modulus.....	278
Table 56: 862/W Compression specimen dimension, maximum load and maximum strength.....	281
Table 57: 862/W Poisson's ratio specimen results.....	283
Table 58: 862/W measured average length and width percent moisture strain.....	287
Table 59: Summary of matrix material properties used for this work.....	288
Table 60: Cure induced radial stresses for the 828/D-230 resin system at the interface.....	300
Table 61: Cure induced radial stresses for the 862/W resin system at the interface.....	302

Table 62: Final FEM applied displacements.....	307
Table 63: Comparing Experimental far-field stress to 862 mechanical FEM far-field stress.....	308
Table 64: Mesh density study statistics.....	308
Table 65: Center Fiber interface SCF mesh density results for the 190d _r TR-LDM, 190d _r RT and 190d _r RT-MDM FEM models.....	314
Table 66: Corner Fiber interface SCF mesh density results.....	317
Table 67: Material properties for the finite element model analysis.....	336
Table 68: The percent reduction of the radial stress over the mechanical load due to the matrix chemical shrinkage.....	377
Table 69: Maximum shear stress variation due to matrix shrinkage and percent reduction of the maximum shear stress due to the mechanical load.....	381
Table 70: The percent reduction of the radial stress over the mechanical load due to the matrix chemical shrinkage for quadrants 1, 2, and 4 of the corner fiber.....	393
Table 71: The percent reduction of the radial stress over the mechanical load due to the matrix chemical shrinkage for quadrant 3 of the corner fiber.....	393
Table 72: Maximum Shear Stress variation in all four quadrants of the Corner Fiber.....	401
Table 73: Maximum shear stress variation due to matrix shrinkage and percent reduction of the maximum mechanical load shear stress for all four quadrants of the corner fiber.....	406
Table 74: Experimental fiber matrix debond measurements.....	417
Table 75: The percent reduction of the radial stress over the mechanical load due to the residual stress from the high temperature matrix cure.....	422
Table 76: Maximum shear stress variation due to matrix cure and percent reduction of the maximum shear stress due to mechanical load.....	428
Table 77: Third quadrant percent reduction of the radial stress over the mechanical load due to the residual stress from the high temperature matrix cure	441
Table 78: Percent reduction of the radial stress of the mechanical load by the residual stress due to the matrix cure at the location of maximum mechanical radial stress	442
Table 79: Maximum Shear Stress variation in all four quadrants of the Corner Fiber.....	449
Table 80: Percent reduction of maximum shear stress due to residual stress from matrix cure at the location of maximum shear due to mechanical loading.....	453
Table 81: Experimental fiber matrix debond measurements.....	463
Table 82: Nanoindentation Modulus Results	464

Table 83: Average far-field applied stress for the additional specimens and the original specimens at the 1.9d _f and 2.0d _f fiber spacing.....	466
Table 84: Center fiber radial and shear SCF for all fiber spacing groups tested where FF is defined as Far-Field.....	467
Table 85: Corner fiber radial and shear SCF for all fiber spacing groups tested.....	467
Table 86: Comparison of the fiber matrix debond limits predicted by the Quadratic and Linear Debond Criterion for the 2 nd quadrant of the corner fiber.....	475
Table 87: Comparison of the fiber matrix debond limits predicted by the Quadratic and Linear Debond Criterion for the 3 rd quadrant of the corner fiber.....	477
Table 88: Experimental standard deviation debond limits with debond limits determined by the Quadratic and Linear Debond Criteria	479
Table 89: Comparison of the fiber matrix debond limits predicted by the Quadratic and Linear Debond Criterion for the 1 st quadrant of the corner fiber at debond locations on the corner fiber	501
Table 90: Comparison of the fiber matrix debond limits predicted by the Quadratic and Linear Debond Criterion for the 4 th quadrant of the corner fiber at debond locations on the corner fiber.....	502
Table 91: Comparison of the fiber matrix debond limits predicted by the Linear Debond Criterion for the 2 nd and 3 rd quadrant of the corner fiber at Z = 0.....	505
Table 92: Experimental standard deviation debond limits with debond limits determined by the Linear Debond Criteria.....	507

LIST OF SYMBOLS

RVE	Representative Volume Element
FEM	Finite Element Model
APDL	ANSYS Parametric Design Language
t	Cruciform specimen thickness
$2h$	Cruciform specimen wing height
$2l$	Cruciform specimen fiber arm length
$2a$	Cruciform specimen loading arm width
$2tb$	Cruciform specimen distance between tabs
d_f	Diameter of fiber
θ	Angle of orientation along fiber-matrix interface
C/C	Center-to-center distance
FEA	Finite Element Analysis
SEM	Scanning Electron Microscope
NP	North Pole
SP	South Pole
α	Central debond angle
IAS	Instantaneously Across Screen
L	Debond length along fiber
db	Fiber-matrix debond
Loc	Location
CA	Central Angle
CF	Center fiber
TF	Top fiber
BF	Bottom fiber
SF	Single fiber specimen

AVG FF	Average Far-field
NH	Northern Hemisphere
SH	Southern Hemisphere
σ_r	Interfacial Radial stress
σ_{yt}	Tensile strength
$\tau_{r\theta}$	Interfacial Shear stress
τ_y	Shear strength
$\sigma_1, \sigma_2, \sigma_3$	Principle stresses
ν	Poisson's ratio
E	Modulus of Elasticity
U_v	Dilatation Energy Density
J_1	Stress invariant
σ_{yc}	Compressive strength
τ_{oct}, τ_o	Octahedral shear stress
σ_m	Octahedral normal stress
τ_s^0	Shear stress in absence of any pressure
μ	Bulk friction parameter
BTF	Between-the-fiber FEM region of volume
UBTF	Upper Between-the-fiber FEM region of volume
EM	Exterior Matrix FEM region of volume
UEM	Upper Exterior Matrix FEM region of volume
UM	Upper Matrix FEM region of volume
CNB	Center Band of matrix volume in FEM
CRB090	Corner Band of matrix volume in FEM from $\theta = 0^\circ$ to 90°
CRB90180	Corner Band of matrix volume in FEM from $\theta = 90^\circ$ to 180°

CRB180270 Corner Band of matrix volume in FEM from $\theta = 180^\circ$ to 270°
CRB270360 Corner Band of matrix volume in FEM from $\theta = 270^\circ$ to 360°

CHAPTER I

INTRODUCTION

Transverse failure initiation of composite materials, i.e. failure occurring when load is applied normal to the direction of the fiber, is one of the oldest problems in composite mechanics. Transverse failure initiation is not a simple problem and also one of the least understood. Designing a specimen shape replicating a real composite, but free of stress singularities plaguing typical sample geometry, while duplicating the failure mechanisms, is quite challenging. Crack initiation usually occurs at a much lower stress state or failure strain than expected due to the stress concentrations from the relatively stiffer fibers. A review of the literature reveals that competing failure mechanisms, namely fiber-matrix debonding and matrix cavitation, exist within the same area of a composite part. There is no comprehensive study in the literature of this phenomenon as each failure mechanism is dealt with individually while recognizing that the other possibility exists. Although attempts to predict the failure have had limited success on the individual basis; no attempt has been made to develop failure criteria describing the competing failure mechanisms.

The goal of this research is to develop a micromechanics based failure criteria for realistic composite materials loaded in tension transverse to the fiber direction. The micromechanics approach considers the constituent material properties and investigates the stresses at the fiber-matrix interface and in and around the surrounding matrix volume. Past work [1-9] has identified two competing mechanisms namely, matrix failure and fiber-matrix debonding, causing the transverse failure of unidirectional composite materials. Furthermore, it is obvious that interface quality, i.e., a strong or a weak interface, can cause a shift in the failure mode. The literature review, investigating matrix failure as the first damage mechanism, indicates that a hydrostatic tensile state of stress exists in the matrix constrained by high transverse stiffness fibers. The hydrostatic tensile stress state is typically located near the fiber-matrix interface in line

with the direction of the applied load [1]. A hydrostatic tensile state of stress implies that the principal stresses are equal in magnitude. However, in all cases a bias exists with the largest principal stress usually initiating the failure [2]. Therefore, instead of using the hydrostatic term under a false pretense, the state of stress will be referred as a tensile tri-axial state of stress. Several investigators have suggested that the matrix cavitates under these conditions. Matrix cavitation is the formation of micro-voids away from the fiber-matrix interface and that it is a precursor to crazing in polymer materials. The cavitation phenomenon has never been actually observed. Rather, through fracture surface analysis, initiation sites have been located. The cavitation initiation site has the form of a star which seems to correlate with the postulated mechanism of formation [2]. These previous studies indicate that the critical dilatational energy density, a modified von Mises failure criterion, a parabolic stress criterion, a modified Tresca criterion and Mohr-Coulomb criterion are candidates to describe failure under the tensile tri-axial stress state of the matrix constrained by the fibers.

Several types of test specimens have been investigated in past research to study the competing failure mode, namely, fiber-matrix debonding that can lead to transverse failure. Most specimens are straight sided and rely on fracture surface examination to determine if the matrix debonds from the fiber. However, fiber-matrix debonding has been observed, in situ, utilizing the cruciform shaped test specimen for single fibers in a transparent matrix by the reflected light test method [10]. It is clear that the nature of interfacial debonding depends upon the magnitude of the tractions on the interfacial surface, i.e., the radial normal stress, σ_r , the radial shear stress, $\tau_{r\theta}$, and the axial shear stress, τ_{rz} . In this research, a test sample with multiple fibers is used in order to produce stress states in the interior similar to those found in a typical composite. Previous works using multiple fibers in a cruciform shaped specimen have been limited to metal matrix composite. Thus, observation of the debond initiation is impossible due to the opacity of the material [5, 8, 11-21]. All other tests not involving the cruciform shape are typically straight sided specimens cut from filament wound tubes or flat plates although thick curved beams have also been used. Consequently it is not known if debonding actually occurs. In addition, weak analytical models characterize the existing studies. Composite plies are often modeled by homogenization

theory with a further assumption neglecting edge effects. Additional simplifying assumptions include the treatment of the microstructure by a representative volume element (RVE) or an average volume fraction and the analysis assuming a single fiber embedded in a matrix material [2, 3, 5-9, 11].

Testing approaches have not shed much light on the transverse failure problems either. Testing of commercial unidirectional and laminated composites and/or resin tests of dubious quality have led to speculative results. The potentially prominent effect of specimen edges, producing elastic singularities, has led to more confusing conclusions. Detailed observations of the failure initiation process have not been fruitful, either at the micro- or macro-scale, due to the fact that most of the tests are done with specimens having opaque matrix materials.

In addition to the testing approaches, the basic constitutive properties of the resin material, which include non-linear load response behavior, shrinkage, thermal effects, and moisture swelling and their influence on residual stress, have not been adequately incorporated in the numerical analysis. The most commonly used fiber in structural composites is the carbon fiber, which is highly anisotropic. This anisotropy has never been conclusively defined. Interphases have been postulated but never completely characterized. A coating or a sizing is a material layer placed on the surface of the fiber to aid in bonding to the matrix material used in advanced composites. Quite often, an interphase rejoin develops between the fiber and matrix as a product of the processing conditions involved in the manufacture of the composite. Usually the interphase region has different properties than the bulk matrix material, typically being more compliant. Fiber-matrix interface strength properties as well as interphase properties also have not been satisfactorily addressed in the micromechanical analyses.

Problem Statement

In light of the preceding discussion, we reconsider the problem of transverse crack initiation in polymeric matrix composites. We will attempt to establish a consistent program of experiment and theory, with controlled material and geometric parameters, such that the work is grounded in fundamentals and well-characterized materials. As mentioned earlier, the work to

date depends on analysis of the fracture surface *after* the damage event has occurred to determine the location and mechanism of failure initiation [2-4, 22-24]. Critical to determining transverse failure initiation is the *direct* observation and recording of first damage. In addition, previous test methods have used specimen geometries fraught with edge effects that compound the determination of failure initiation. Also test methods have been used that claim to mimic the stress state in the composite under a tensile tri-axial state of stress. These tests required bonding neat materials to substrates via a more compliant adhesive than the material being tested. For example, Lindsey, et al. [25], bonded circular disk specimens or poker chip to rigid substrates and tested them in tension [1, 4, 25]. In poker chip experiments, specimen and substrate alignment is critical as bending will be introduced if not perfectly aligned. Thus, the actual failure load of the neat material is unknown due to the different strain rates occurring in the sample and adhesive and the loading at failure initiation is also suspect due to the criticality of alignment. Consequently the disk test does not mimic the stress state in the composite under a tensile tri-axial state of stress because the neat resin disk test mentioned above cannot replicate the stress concentrations due to the constraining influence of the stiff fibers. Moreover, free edges still exist and the failure surface has to be carefully scrutinized to determine if it was adhesive or cohesive failure. Well characterized constituent materials is also a contention in previous work as well as the use of carbon fiber.

Simplifying numerical analysis has been used to determine the stress state at failure initiation in all test specimens investigated to date. Most common has been the use of homogenization theory along with the modeling of a unit cell and/or a regular repeating array of fibers for representation of the composite material, as previously mentioned [2, 4-8, 11, 26-32]. In addition, the use of 2-D analysis [2-4, 32] for a 3-D stress state has been used. To fully investigate the interaction between the matrix and the fibers, an explicit 3-D micromechanical model of the test specimen is extremely important. Equally important in the analytical model are constituent material properties and the precise location of the fibers in the matrix.

This work will address many of the above noted deficiencies and will establish a clear definition and a rigorous understanding of transverse failure. The best features of the existing

research, the most rigorous analysis formulation, the best established failure models that have been colloquial in the fields of polymer science, mechanics, and material science, and the experiments at an appropriate micro-scale will be employed to offer the best chance to enhance the state of the art in this area of research.

The term "failure initiation" often leads to confusion. For the purposes of this paper failure initiation will be defined as the first detectable damage event. As mentioned above, two damage mechanisms are possible for realistic composite materials loaded transverse to the fiber direction. Furthermore, the debonding mechanism may form directly or emanate from the coalescence of micro-voids due to cavitation at or near the interface. The objective of this proposed research is to develop a micromechanics based failure criterion for realistic composite materials loaded in tension transverse to the fiber direction. This criterion will provide a foundation for a comprehensive transverse failure mechanics model being developed under the 3-D failure mechanics umbrella.

Overview of Research

The emphasis on this research is to establish a micromechanical based failure criterion for composite materials when loaded transverse to the direction of the fiber. To accomplish this objective a model composite system was employed consisting of two transparent epoxy systems and rigid fibers. The variables for the proposed work, critical to the development of the micromechanical based failure criteria are; the spatial distribution of fibers, the fiber-matrix interface properties, the properties of the interphase region in the vicinity of the fiber surface, the residual stress from matrix shrinkage and thermal effects, and moisture uptake for each matrix system. To evaluate these variables, numerous laboratory experiments are performed in addition to the standard material characterization experiments needed for the typical material properties. For example, photoelasticity tests were conducted for measuring the residual stresses due to the resin systems individual cure kinetics at the fiber-matrix interface. Also, multi-fiber cruciform tests were run at various fiber spacing's for the investigation of the internal stress distribution due to changes in the spatial distribution of the fibers. To achieve this objective, a model composite

system consisting of two transparent isotropic resin systems and small diameter stainless steel wires as the fibers was used. Cruciform specimen geometry was utilized to conduct transverse tension experiments because the specimen's shape virtually eliminates the stress concentration at the specimen's edges typical of straight sided specimen geometry. Single fiber cruciform specimens and multi-fiber cruciform specimens were tested in tension using the reflected light method for direct observation and determination of the failure initiation mechanism. All cruciform experiments were videotaped to capture the in-situ failure and determine the loading at the time of failure initiation.

This project focused on a brittle room temperature cured matrix material and a ductile high temperature cured matrix material. The brittle matrix is the Epon 828 epoxy using 35% by weight Jeffamine D-230 curing agent. It cures in approximately seven days at room temperature. The ductile matrix is the Epon 862 epoxy using an EPI-CURE W curing agent at a ratio of 79.4% 862 to 20.6% W. The 862 epoxy has a curing cycle of two hours at 250° F and two hours at 350°F. The residual stresses of each resin system were thoroughly investigated for proper input parameters in the analytical efforts. These two matrix systems cover a wide range of the mechanical response of commonly used commercial epoxy systems. The 828/D-230 system has a linear elastic behavior, thus the number of variables affecting the micromechanical models are minimal and can easily be experimentally controlled. The non-linear 862/W system increases the complexity of the analysis and possibly changes the failure mechanism. Furthermore, the 862/W system closely resembles the complex resin systems used in today's aerospace applications.

The fibers of the model composite system were stainless steel wires having a diameter of 0.36 mm. The stainless steel wires are large enough for ease of handling that allow precise placement in the mold to represent resin rich/fiber rich areas common to commercially produced composites. They also allow specimens to be made with specific fiber spacing in order to validate the proposed failure criteria by providing multiple points on the proposed failure surface. The wires are isotropic materials with their material properties well documented and understood, thus eliminating some variability in the experiments and in the analysis. The stainless steel wires are known to bond to the resins being used in this investigation without the use of any surface

treatments or sizing. Consequently, no interphase region around the fiber is considered in the cruciform specimen.

A three dimensional finite element model (FEM) was made of the photoelasticity experiments to determine an effective coefficient of thermal expansion by matching the interfacial residual radial stress for each matrix system. A parametric study was conducted using a constant width three dimensional cruciform specimen and varying the fiber spacing to investigate the fiber-matrix interfacial stress distributions for optimum camera placement during experimentation and to guide the multi-fiber cruciform test matrix. Three dimensional FEM were developed to analyze the internal stresses in the cruciform specimens due to the matrix curing and from the applied load. Individual FEMs were developed at all cruciform specimen fiber spacing tested for the matrix system residual stress effects and mechanical loading effects. The effective coefficient of thermal expansion for each matrix system, derived through experimentation and analysis mentioned above was used in their respective residual stress cruciform model. Post processing the cruciform specimen analytical results included combining the model results to arrive at the internal stresses due to the combination of residual stress and mechanical load stresses at the instance of first damage. Once the combined analytical results were obtained from the cruciform models, several failure criteria explaining the fiber-matrix debond and matrix failure were investigated to determine if they adequately predicted the observed failure initiation. It should be noted that for all FEMs the fiber and matrix were explicitly modeled using material properties derived by the neat resin testing mentioned earlier and that the average specimen dimensions were used for all models unless otherwise specifically stated.

Chapter 2 discusses the experimental technique used for this research. In this chapter a review of prior testing methods is given. Moreover, the importance of the cruciform specimen geometry is thoroughly reviewed. The emphasis is on failure initiation and its location relative to the fibers within the specimen. In addition, the cruciform specimen fabrication details as well as the testing details are explained. Chapter 3 details the analytical efforts for this work and a comprehensive review of past work is given. The focus is on developing the numerical solution of the stress state within the specimen at failure initiation. Details of the stress state at the fiber-

matrix interface as well as within the matrix surrounding the fiber grouping are thoroughly interrogated. Chapter 4 will discuss the experimental and analytical results. This chapter details the development of the transverse failure criterion from the results of chapters 2 and 3. The summary of this research effort and recommendations for future research work are given in Chapter 5.

The appendices define much of the supportive research. Appendix A describes the neat resin characterization to obtain material properties used for analysis. Appendix B describes the residual stress determination for each resin system from their respective curing cycle. Appendix C describes several FEM details including the 862/W non-linear response modeling, mesh sensitivity results, parametric study results and the ANSYS Parametric Design Language (ADPL) methodology utilized to construct the three dimensional FEM used thorough out this work.

Technical Significance

As advanced composite materials are increasingly being used throughout industry, the need to understand the failure mechanics and to develop a failure criterion ensuring robust designs becomes progressively more important. Although prior experimental and analytical work have laid a good foundation for the understanding of this phenomenon, this work corrects many of the short comings and sorts out the competing failure mechanisms issue. The specimen geometry utilized in this investigation is not dominated by free edge stress singularities and concentrates the loading at the center of the specimen. Failure initiation has been observed in-situ, consequently, the failure mechanism is known. Analytical models used in this work incorporate actual composite specimen fiber spacing and specimen dimensions.

In addition to advancing the state of the art for understanding the failure mechanics and corresponding internal stress state, this research supports many other efforts that are investigating composite materials from the complex chemical interaction of the constituent materials to complex 3-D fiber architecture level mechanical analysis. One goal of these other programs is to develop mechanics based failure models at the fiber matrix level. These models will provide the composite material designer with tools to predict life of a particular material

system. The current dissertation is the start of developing a comprehensive transverse failure mechanics model that will ultimately reduce the time, effort, and cost it takes for material systems to be used in aerospace applications.

The current research expands a novel experimental technique to identify the failure initiation mechanism when composites are loaded normal to the direction of the fiber. As will be shown in Chapter 2, most existing experimental techniques utilized to investigate this phenomenon either suffer from free edge stress singularities or incorrect loading to induce the required stress state for failure. Stress concentrations at the free edge of typical straight sided specimens dominate the failure. Consequently, determining the stress at failure initiation due to the positive triaxial state of stress within the center of the specimen is very difficult. Failure initiation is also usually determined from examination of the fracture surface mostly because of the opaque materials used for experimentation. Sometimes test specimens are cut from manufactured unidirectional composite parts; typically a filament wound vessel or a flat plate. Therefore, in-situ failure of the specimen cannot be observed. Since competing failure mechanisms have been previously identified, the failure mechanism occurring first is unknown. In addition to the problems associated with the experimental methods used to date, analytical models usually ignore the free edge stress singularities. Most analytical models developed only use a 2-D analysis for the 3-D problem. These models also use a repeating array or a representative volume element (RVE) to calculate the stress state in the matrix due to the transverse loading. Using a perfect array when calculating the internal stress state of an actual composite specimen can lead to erroneous results because of fiber and resin rich areas, fiber misalignment, and variations in fiber diameters within the actual composite that are not accounted for in the analysis.

References

1. Asp, L.E. and L.A. Berglund, *Effects of a composite-like stress state on the fracture of epoxies*. Composites Science and Technology, 1995. **53**: p. 27-37.
2. Asp, L.E., L.A. Berglund, and R. Talreja, *Prediction of a matrix-initiated transverse failure in polymer composites*. Composites Science and Technology, 1996. **56**: p. 1089-1097.

3. Asp, L.E., L.A. Berglund, and R. Talreja, *A criterion for crack initiation in glassy polymers subjected to a composite-like stress state*. Composites Science and Technology, 1996. **56**: p. 1291-1301.
4. Asp, L.E., L.A. Berglund, and R. Talreja, *Effects of fiber and interphase on matrix-initiated transverse failure in polymer composites*. Composites Science and Technology, 1996. **56**: p. 657-665.
5. Busschen, A.T., *Micromechanical modeling of the transverse strength of unidirectional glass fiber reinforced polyester*, in *Engineering*. 1996, Delft Technical University: Delft, the Netherlands. p. 246.
6. Fiedler, B., et al., *Finite-element modeling of initial matrix failure in CFRP under transverse tensile load*. Composites Science and Technology, 2001. **61**: p. 95-105.
7. Kim, P. and S. Toll, *Stress spectra and the effective elastic and viscoelastic properties of unidirectional composites under transverse loading*. Journal of Composite Materials, 2000. **34**(17): p. 1418-1436.
8. Kok, J.M.M.d., *Deformation, yield and fracture of unidirectional composites in transverse loading*, in *Engineering*. 1995, Eindhoven University of technology: Eindhoven, the Netherlands. p. 141.
9. Kok, J.M.M.d. and H.E.H. Meijer, *Deformation, yield and fracture of unidirectional composites in transverse loading 1. Influence of fiber volume fraction and test-temperature*. Composites Part A, 1999. **30**: p. 905-916.
10. Bechel, V.T. and G.P. Tandon, *Characterization of interfacial failure using a reflected light technique*. Experimental Mechanics, 2002. **42**(2): p. 200-205.
11. Akser, E.O. and K.L. Choy, *Finite element analysis of the stress distribution in a thermally and transversely loaded Ti-6Al-4V/SiC fiber composite*. Composites Part A, 2001. **32**: p. 243-251.
12. Gundel, D.B., B.S. Majumdar, and D.B. Miracle, *Evaluation of the transverse response of fiber-reinforced composites using a cross-shaped sample geometry*. Scripta Metallurgica et Materialia, 1995. **33**(12): p. 2057-2065.
13. Gundel, D.B. and D.B. Miracle, *Transverse tensile behavior of SiC-fiber/Ti-6Al-4V composites 1: Experimental results*. Composites Science and Technology, 1998. **58**: p. 1571-1581.

14. Gundel, D.B., S.G. Warrier, and D.B. Miracle, *The interface debond stress in single and multiple SiC fiber/Ti-6Al-4V composites under transverse tension*. Acta mater., 1997. **45**(3): p. 1275-1284.
15. Gundel, D.B., S.G. Warrier, and D.B. Miracle, *The transverse tensile behavior of SiC-fiber/Ti-6Al-4V composites 2: Stress distribution and interface failure*. Composites Science and Technology, 1999. **59**: p. 1087-1096.
16. Nimmer, R.P., et al., *Micromechanical modeling of fiber/matrix interface effects in transversely loaded SiC/Ti-6-4 metal matrix composites*. Journal of Composites Technology and Research, 1991. **13**(1): p. 3-13.
17. Varna, J., L.A. Berglund, and M.L. Ericson, *Transverse single-fiber test for interfacial debonding in composites 2: Modeling*. Composites Part A, 1997. **28**: p. 317-326.
18. Warrier, S.G., et al., *Interface effects on the micromechanical response of a transversely loaded single fiber SCS-6/Ti-6Al-4V composite*. Metallurgical and Materials Transactions A, 1996. **27A**: p. 2035-2043.
19. Warrier, S.G., et al., *Stress distribution in a transversely loaded cross-shaped single fiber SCS-6/Ti-6Al-4V composite*. Scripta Metallurgica et Materialia, 1996. **34**(2): p. 293-299.
20. Warrier, S.G., et al., *Implications of tangential shear stress induced failure during transverse loading of SiC/Ti-6Al-4V composites*. Acta mater., 1997. **45**(8): p. 3469-3480.
21. Warrier, S.G., B.S. Majumdar, and D.B. Miracle, *Determination of the interface failure mechanism during transverse loading of single fiber SiC/Ti-6Al-4V composites from torsion tests*. Acta mater., 1997. **45**(1): p. 309-320.
22. Bauwens, J.C., *Yield Condition and Propagation of Luders' Lines in Tension-Torsion Experiments on Poly(vinyl Chloride)*. Journal of Polymer Science: Part A-2, 1970. **8**: p. 893 - 901.
23. Fiedler, B., A. Klishch, and K. Schulte, *Stress concentrations in multiple fiber model composites*. Composites Part A, 1998. **29A**: p. 1013-1019.
24. Piggott, M.R., *A new model for interface failure in fiber-reinforced polymers*. Composites Science and Technology, 1995. **55**: p. 269-276.
25. Lindsey, G.H., et al., *The Triaxial Tension Failure of Viscoelastic Materials*, in ARL Technical Documentary Reports, A.R. Laboratories, Editor. 1963, Aerospace Research Laboratories: Wright-Patterson Air Force Base.

26. Benzarti, K., L. Cangemi, and F.D. Maso, *Transverse properties of unidirectional glass/epoxy composites: Influence of fiber surface treatments*. Composites Part A, 2001. **32**: p. 197-206.
27. Bulsara, V.N., R. Talreja, and J. Qu, *Damage initiation under transverse loading of unidirectional composites with arbitrary distributed fibers*. Composites Science and Technology, 1999. **59**: p. 673-682.
28. Ghosh, S., et al., *Interfacial debonding analysis in multiple fiber reinforced composites*. Mechanics of Materials, 2000. **32**: p. 561-591.
29. Nimmer, R.P., P.A. Siemers, and M.R. Eggleston, *Fiber array geometry effects upon composite transverse tensile behavior*. 1991, GE Corporate Research and Development Center: Schenectady, NY. p. 369-370.
30. Schuller, T., et al., *Single-fiber transverse debonding: tensile test of a necked specimen*. Composites Science and Technology, 2000. **60**: p. 2077-2082.
31. Wisnom, M.R., *Micromechanical modeling of the transverse tensile ductility of unidirectional silicon carbide/6061 aluminum*. Journal of Composites Technology and Research, 1992. **14**(2): p. 61-69.
32. Zhu, H. and J.D. Achenbach, *Radial matrix cracking and interphase failure in transversely loaded fiber composites*. Mechanics of Materials, 1991. **11**: p. 347-356.

CHAPTER II

TRANSVERSE FAILURE EXPERIMENTAL TECHNIQUE AND RESULTS

Introduction

Prior experimental work investigating initial matrix failure in a fiber reinforced polymer used a combination of techniques. Primarily composite specimens were made via the filament winding manufacturing method in various volume fractions and in various configurations ranging from flat plates to tubes [1-4]. Rectangular tensile and dogbone specimens as well as flexural specimens and curved beam specimens were cut from the filament wound composites. Biaxial testing specimens have also been used in which a composite plate is cut into a cross shape and tested in tension in both the directions [5-7]. In most cases the specimen edges were polished to reduce any influence from surface flaws. The fiber volume fraction of the composite materials used for these specimens typically ranged from 40% to 60% with the fiber being either carbon or glass. Tensile, three point bending tests, bending of thick curved beams and the biaxial tests were done to determine the transverse strength used as the experimental bases for comparison to predicted analytical strengths [1-4, 6, 7]. In some cases a thermostatically controlled tensile testing machine was used to study the effect of temperature [3]. Neat resin specimens were also used for matrix failure initiation work. These specimens ranged from the typical dogbone flat tensile specimens, rectangular compression specimens; to dogbone shaped hollow tubes and circular disks. Some neat resin tests imparted a biaxial stress state by combined tensile and torsion loading or through flat-wise tension tests [3, 8-10]. Neat resin cubes were also used typically for compression strength determination [11]. In most cases the fracture surface of both the neat resin and composite material tests was examined to determine matrix failure initiation and failure was not observed in-situ during the experiment.

Sample shapes used to investigate fiber-matrix debonding initiation in fiber reinforced polymers play a huge role in how the stress state at the fiber-matrix interface develops under loading. Past specimen shapes have consisted of single fibers in cross or cruciform shaped specimens, in hourglass shaped specimens and rectangular shaped specimens all tested in tension [12-17]. The cross or cruciform shape specimen offers the best shape for studying the fiber-matrix debond since specimen free edge effects are virtually eliminated and that the load is concentrated at the specimen center away from the free edge. The hour glass shaped specimen in which a single fiber is positioned in the direction of loading through the center of the necked specimen still suffers from free edge effects. Since the fiber is in the direction of the loading the tensile stress in the gage length of the specimen is parallel to the fiber thus it acts as a shear stress at the fiber-matrix interface. However, due to the specimen shape the maximum magnitude is still at the specimen edge. Special care must be taken at the edges to remove all imperfections because these will initiate failure away from the fiber-matrix interface. Straight sided specimens suffer from dominating free edge stress effects masking any true fiber-matrix debond initiation occurring internally to the specimen. In some cases [18], the fibers were fragmented and the debond initiated away from the fiber fracture site. Fracture mechanic techniques were used to determine the energy release rate at the crack tip as a measure of interface strength that translated to transverse strength gains. In most tests using the fiber fragmentation technique the fiber is glass and the matrix is transparent whereby in-situ observation is performed as the debond is initiated. While, a few researchers [3, 4, 19, 20] have used specimens consisting of single and multiple composite plies in cruciform shaped specimens to investigate multiple fibers; most experimentation has used rectangular specimens and curved beams cut from actual composite plates or tubes manufactured via the filament winding method. In these cases the fibers are usually carbon and the composites are manufactured having the volume fraction mentioned above. In most cases the fiber-matrix debond is determined by analysis of the fracture surface of the specimen and not directly observed.

Results for the multi-fiber cruciform sample, where debond initiation was inferred by the initial point of nonlinearity of the far-field stress vs. strain curve, indicate an increase in the stress

concentration in the matrix and at the fiber-matrix interface decreasing fiber spacing [19, 21]. This would suggest a much lower debond initiation load compared to single fiber tests. However, far-field stress at debond initiation on the multi-ply multi-fiber cruciform specimens were nearly the same for the single fiber specimens [19]. Due to this experimental observation, the stress concentration factor is dependent on the spatial distribution of the fibers in the composite. It is also believed that the residual stresses are influenced by the fiber distribution [19]. Several different mechanisms of failure initiation have been proposed, normal stress failure and shear stress failure, but in each multi-fiber test case the failure has not been observed due to the opaque matrix [3, 4, 19, 21]. Acoustic emission, scanning electron microscopy of the failure surface, transverse strength comparisons, and stress-strain plots of experimental runs have been used to indicate debond initiation in all of the previous multi-fiber specimen tests [3, 4, 19, 21].

In the experiments using real composite specimens the corresponding results suffer from free edge effects as well as effects due to cut fibers, fiber misalignment, resin rich areas, and fiber rich areas. These issues play a big role in the stress state in and around the fibers contributing to the failure initiation stress and its location. One of the reasons for this work is to investigate the effect of fiber spatial distribution on the stress state at failure initiation. The various fiber distributions used during the course of this work provide multiple points on a failure surface to validate the proposed failure criteria. The cruciform specimen geometry, developed in the last 11 years, concentrates the load in the center of the specimen away from the free edge [22]. Due to continued refinement and subsequent optimization of the cruciform shape [15] the free edge singularity is practically nullified. For this reason the cruciform specimen shape was used for the proposed work in evaluating the failure initiation.

Critical to determining the load at failure initiation and consequently the stress state is the observation of the failure initiation mechanism. With the exception of the work by Tandon, Bechel, and Kim [12, 15, 23] the failure mechanisms from all the previous work could not be directly observed. Various techniques mentioned above have been utilized to determine the failure initiation mechanism and its location. Tandon, Bechel and Kim [15, 23] have used transparent epoxy systems to observe the in-situ initiation and location of fiber-matrix debonding. This

method, known as the reflected light method, uses light reflected off the surface of the fiber to observe the initiation and growth of the fiber-matrix debond. It has been successfully used on single fiber cruciform specimens having steel fibers, silicon carbide fibers, and Nicalon fibers [23]. Since this work employs a model composite system consisting of two transparent epoxies, the reflected light method was used in this work exclusively for all experimentation investigating the transverse failure.

Cruciform Specimen Geometry

The cruciform-shaped specimen, as shown in Figure 1, nullifies free edge effects that typically dominate the failure of straight-sided specimens under transverse loading, by concentrating the applied load in the center of the specimen. Figure 2 shows the stress concentration factor (normal stress on the interface in the loading direction normalized by the external applied stress) as a function of distance measured from the center of the specimen for a single fiber Al-epoxy composite [24]. The maximum stress concentration factor for the cruciform shape occurs in the interior region of the specimen rendering the free edge singularity ineffective because the wings of the specimen carry very little load. Therefore, failure initiates in the central region of the specimen devoid of the influence of the free edge stresses at the fiber ends.

The cruciform-shaped specimen dimensions and nomenclature are also presented in Figure 1. In this study the model composite system consists of single and multi-fiber cruciform specimens. The fibers are located in the cruciform specimen wings and centered with respect to the specimen thickness (t) while extending the full width of the specimen ($2l$). The distance between the apexes of the tabs is ($2tb$) and the fiber wing height is designated ($2h$). The fiber arrangement in the multi-fiber cruciform specimens entails four fibers located at the corners of a square and the fifth fiber, i.e., the center fiber, is placed at the intersection of face diagonals of the four corner fibers. Figure 3 shows a schematic diagram of the cross section of the fiber wing for a multiple fiber specimen. For the single fiber cruciform specimens the fiber is centered within the specimen thickness and extends the full width of the wing. Figure 4 shows a schematic diagram of the cross section of the single fiber specimen wing. Fiber spacing (Xd_f) is defined as the

center-to-center distance of the corner fibers and is expressed as a multiple of the fiber diameter. In this study multi-fiber cruciform specimens having a fiber spacing of $6d_f$, $2.5d_f$, $2.0d_f$, $1.9d_f$, $1.84d_f$, $1.75d_f$ and $1.57d_f$ are considered, where d_f is the fiber diameter. Single-fiber cruciform specimens were also tested. The average dimensions for all the cruciform specimens tested for this work are presented in Table 1.

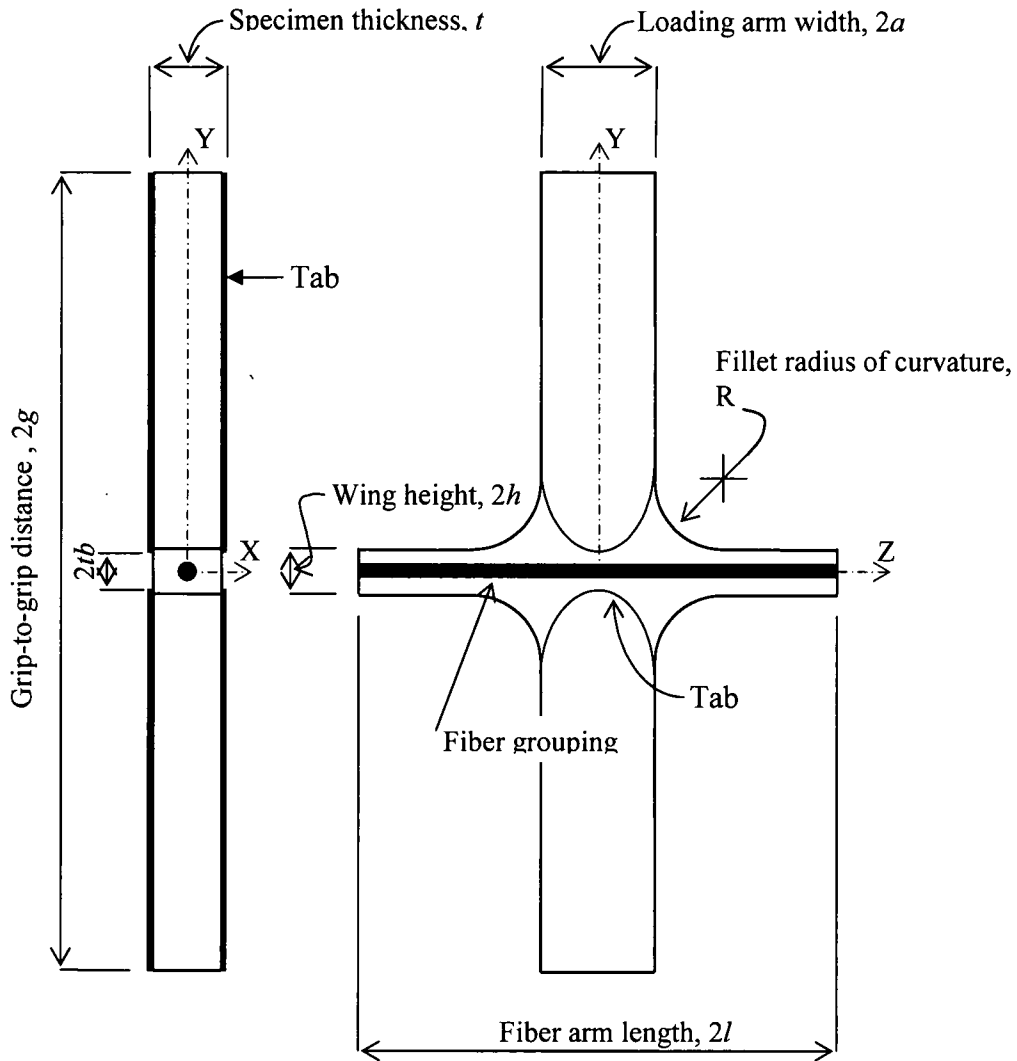


Figure 1: Schematic and nomenclature for cruciform specimen geometry

Specimen Fabrication

Silicon rubber molds conforming to the cruciform shape as shown in Figure 1 with the dimensions listed in Table 1 were fabricated from aluminum patterns and used to make the room temperature cured 828/D-230 specimens. Due to the high temperature curing cycle of the 862/W specimens Teflon molds were made to the dimensions shown in Table 1. Fiber template slots were located at the end of the wings to precisely position the fibers within both molds. Prior to the placement of fibers into the wings of the molds, they were thoroughly cleaned, first, by blowing dust from the molds using compressed air and second, by vigorously washing with acetone using cotton swabs. After the acetone wash had dried the molds were again blown out with compressed air removing any cotton swab hairs and other foreign object debris.

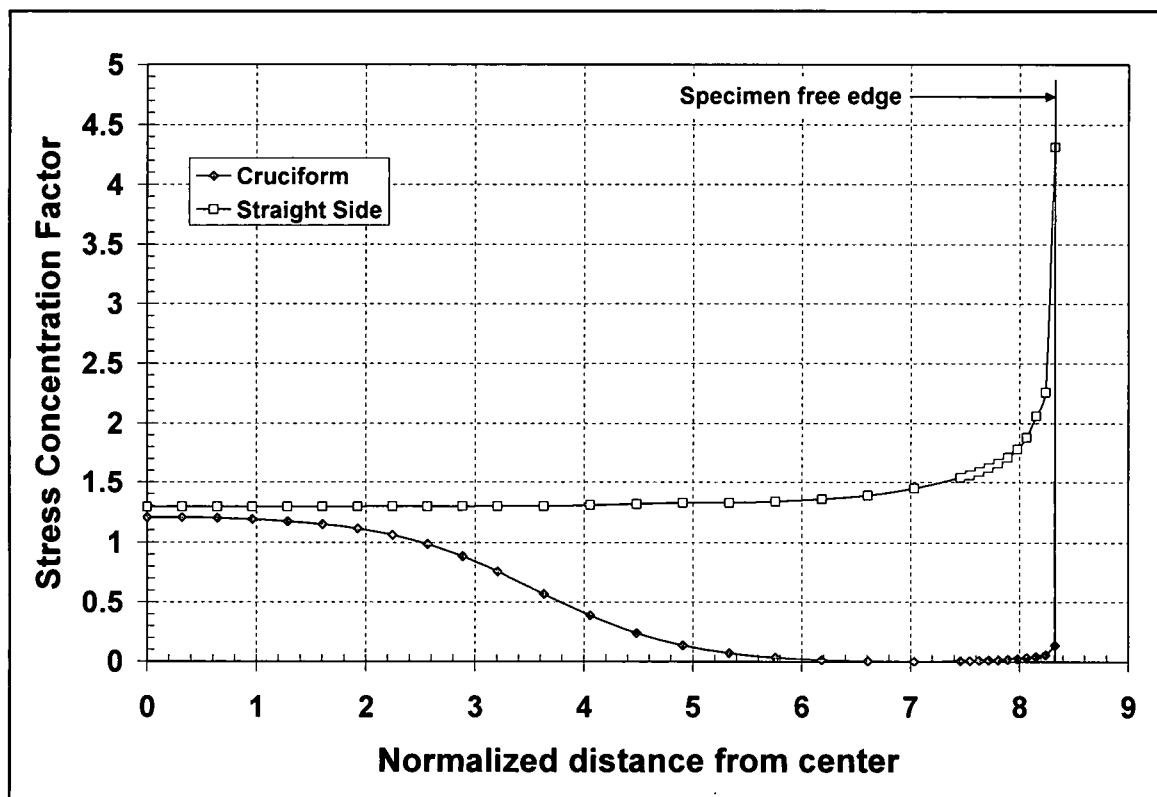


Figure 2: SCF as function of normalized distance from center of specimen

Fiber templates, having the five-fiber configuration at the spacing described above as well as the single fiber configuration, were C-N-C drilled using a #80 bit in 0.127 mm thick

aluminum sheet. Alignment holes were also drilled so that the fiber templates when cut from the sheet measured 13 mm by 4 mm and fitted into slots of the cruciform molds. The stainless steel wires were cut to lengths of approximately 50 mm. Each fiber was cleaned with an acetone wash and threaded through two fiber templates. The templates were then separated and placed into the fiber slots in the mold. Prior to placing the epoxy matrix in the mold, the fibers were again washed thoroughly with acetone along with the specimen wings and loading arms of the mold.

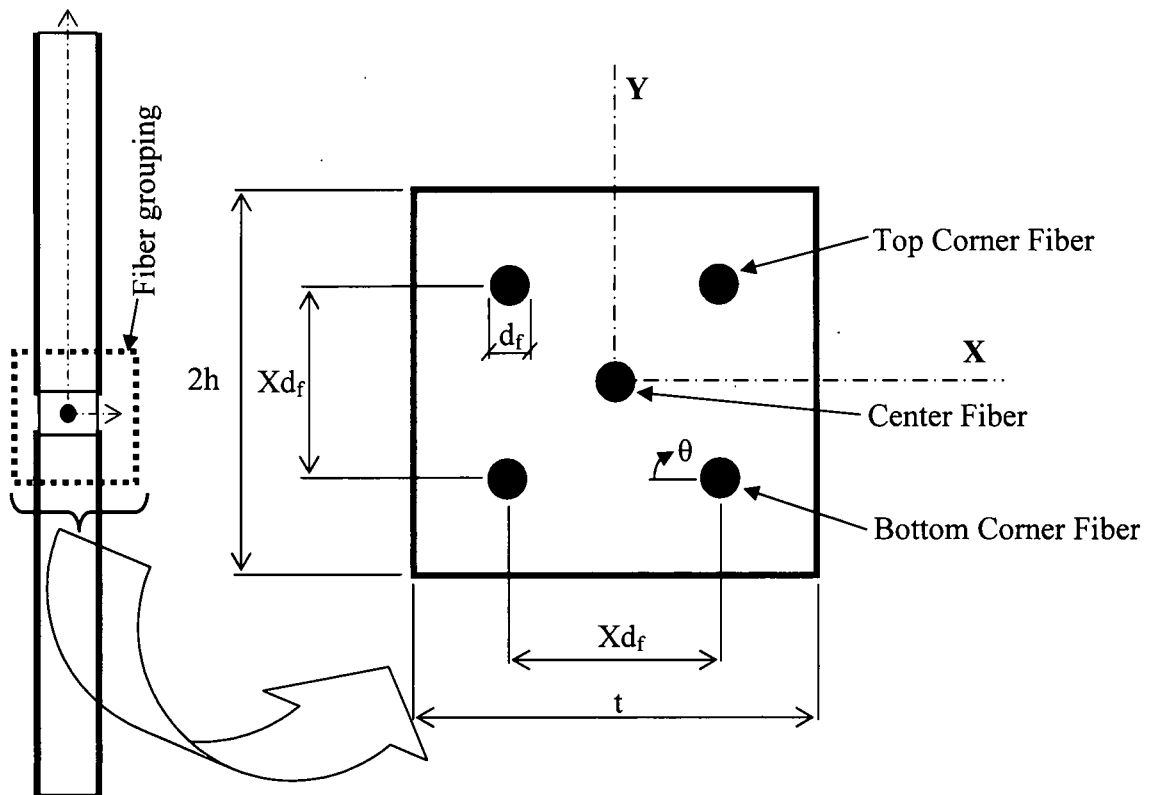


Figure 3: Schematic cross section of model cruciform fiber wing for multi-fiber arrangement

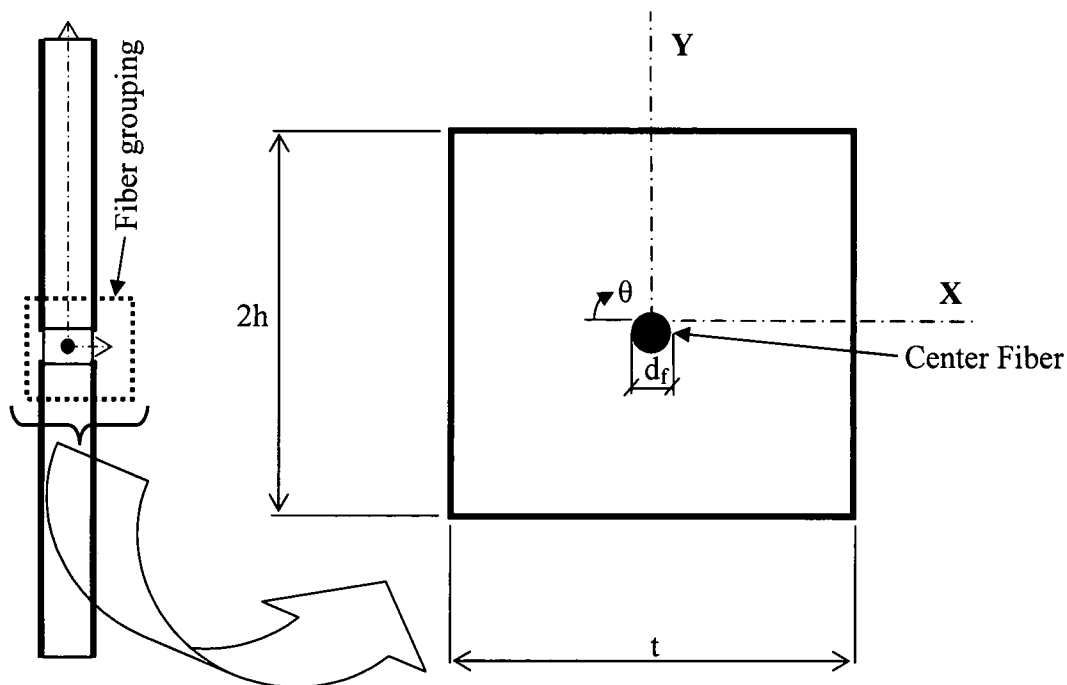


Figure 4: Schematic cross section of model cruciform specimen fiber wing for single-fiber arrangement

Table 1: Final average cruciform specimen dimensions including the silicon rubber mold utilized for all 828/D-230 specimens and the Teflon mold for all 862/W specimens

828/D-230 Specimen	t , (mm)	$2h$, (mm)	$2l$, (mm)	$2a$, (mm)	$2g$, (mm)	$2tb$, (mm)
$1.57d_f$	1.86	5.06	41.41	13.13	106.09	4.28
$1.75d_f$	1.81	5.06	39.98	13.01	105.90	3.53
$1.84d_f$	1.71	4.88	25.58	12.76	107.26	5.02
$1.9d_f$	1.87	5.02	39.99	12.85	106.36	3.41
$2.0d_f$	1.81	5.03	40.10	12.78	106.11	3.43
$2.5d_f$	2.4	5.05	36.21	13.37	107.14	5.69
$6.0d_f$	3.23	5.05	42.75	12.91	107.47	5.34
Single	2.30	5.05	41.05	13.46	107.56	5.32
862/W Specimen	t , (mm)	$2h$, (mm)	$2l$, (mm)	$2a$, (mm)	$2g$, (mm)	$2tb$, (mm)
$1.57d_f$	1.81	5.04	35.47	12.99	106.93	3.86
$1.75d_f$	1.87	5.06	39.44	12.62	107.09	4.60
$1.9d_f$	1.77	5.05	35.90	12.61	107.10	5.00
$2.0d_f$	2.04	5.07	35.29	12.62	107.13	5.44
$2.5d_f$	2.27	5.01	41.72	13.66	108.05	5.40
$6.0d_f$	3.38	5.03	43.66	12.73	107.10	6.20
Single	2.86	5.06	44.06	12.92	108.63	4.57
Silicon Rubber Specimen mold	4.0	5.09	51.75	12.47	106.8	N/A
Teflon Specimen mold	3.90	4.90	54.20	12.70	106.6	N/A

Each epoxy system was properly measured and thoroughly mixed by hand for approximately 5 minutes. Next it was de-bulked to remove any entrained air for approximately 30 minutes or when air bubbles no longer rose to the surface. Once de-bulked the epoxy was carefully placed into the mold such that no air bubbles were created. If air bubbles formed in the mold, they were brought to the surface by using a piece of stainless steel wire to move the bubble to the surface. Prior to placing the epoxy, the molds were blown out with compressed air to remove any dust or foreign particles that may have accumulated in the mold since cleaning. Once the matrix system had been placed in the mold and no bubbles observed to have been created the individual specimen molds were placed into aluminum pans and covered. This prevented dust or foreign objects to enter the specimens during their respective cure cycles. The room temperature 828/D-230 specimens were left to cure in their molds a minimum of three days. The 862/W specimens were then placed into an oven and cycled through their curing cycle. After removing from the molds they were stored in a sealed plastic bag until prepared for testing.

Specimen preparation for testing was a four step process. The first step was removing the fiber template from the cruciform specimen. This was done by using a diamond cutting saw carefully cutting the fiber template from the specimen fiber wing at the inside of the template. Care was taken by cutting slowly and with low pressure so that the ends of the stainless steel fibers did not debond from the matrix. In some cases, bubbles formed during the matrix cure cycle near the fiber wing ends. In those instances, the cut to remove the fiber templates was made at the location along the fiber wing length that removed the bubble but could maintain a constant fiber wing length for that particular batch of specimens.

Step two involved machining the specimens to where the central fiber in multi-fiber specimens was centered within the specimen thickness. For the single fiber specimens the specimens are machined to where the fiber is centered and the batch of specimens were a uniform thickness. Care was taken in the multi-fiber specimens such that the fibers at outside corners of the square in the five fiber pattern have the same epoxy thickness from the side faces, i.e. in the X direction as shown in Figure 3. The milling was done with a fly cutter at 1800 revolutions per second. The depth of cut was precisely controlled by a digital measuring system

attached to the milling machine. The specimens were machined flat, as shown in Figure 5, and once the top of the specimen was located the digital gage in the vertical direction is set to 0.0. Cuts ranged in depth between 0.010 and 0.005 inches were made until the desired specimen cross section, as described above, was achieved. Milling was done on both sides of the specimens.

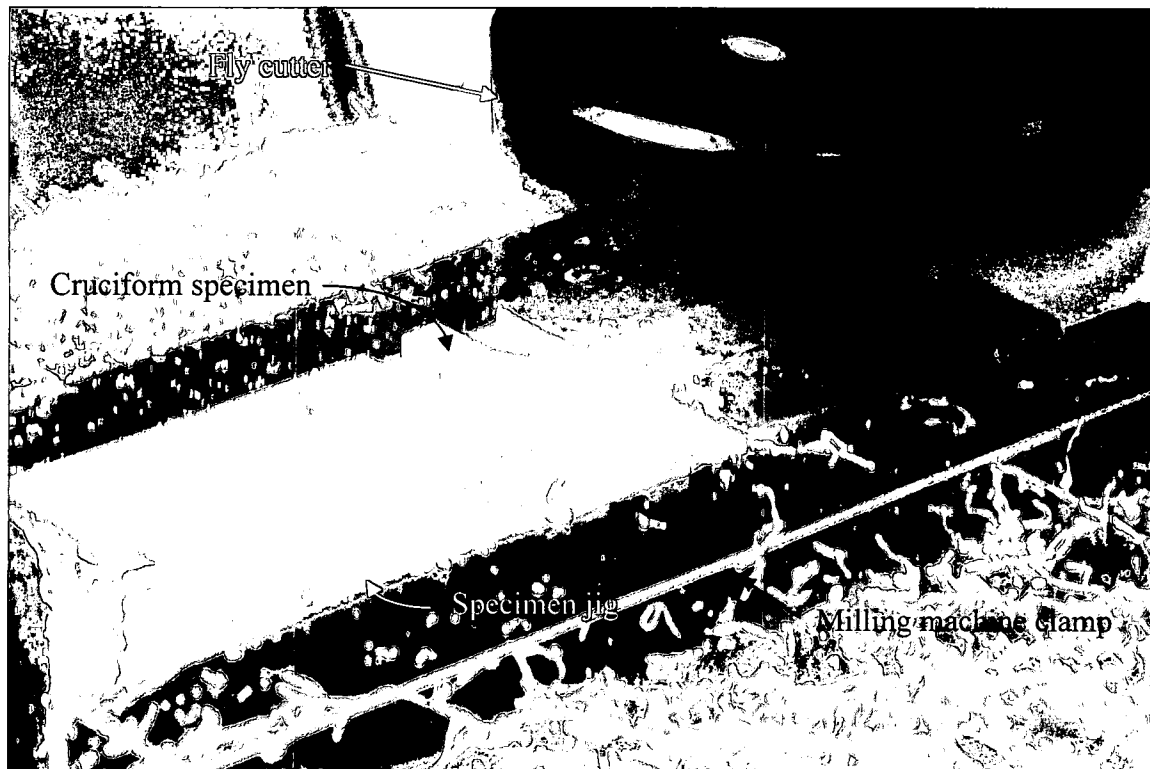


Figure 5: Typical cruciform specimen milling to uniform thickness

The speed that the specimens were feed into the fly cutter was such that one complete pass took approximately 45 seconds to complete. The specimens were held in place by a vise and centered with respect to the fly cutter. A jig was used to secure the specimens in the vise, as shown in Figure 5. Each specimen was held in place by recesses cut into the jig for the loading arm and fiber wing. Thin rectangular strips of rubber were placed between the jig blocks under the specimen for uniform clamping pressure in the vise. Clamping pressure in the vise was such that the specimen did not bow upward. Occasionally the thinner cruciform specimens, namely the

1.57d_r specimens, were double sided taped to the vise for machining. In those instances two rectangular pieces of thick tab material were use to support the cruciform specimen in the direction of the fly cutter. The support tabs were made such that two sides were parallel and the width was greater than the fiber wing length. The parallel sides are positioned such that one edge was against the vise back stop and the other supported the specimen loading arm. The specimen was taped down against the support tabs, as shown in Figure 6, and machined as described above. The machining process produced cruciform specimens that had parallel faces and uniform thickness within the gage area, i.e. the area bounded by the radius returns on the fiber wing and the loading arm width.



Figure 6: Thin cruciform specimen milling to uniform thickness

Step three involved polishing the specimens using 0.3 μm alumina powder on a polishing wheel. Matrix transparency was achieved by polishing the specimen on both sides to a glassy surface in the area bounded by the fiber wing and loading arm. The specimen was placed into a jig specifically made for polishing cruciform specimens. The jig had machined recesses the width

of the loading arm and fiber wing, as shown in Figure 7. The jig ensured that uniform pressure was applied in the fiber area to maintain the parallel faces of the cruciform specimen within the gage area and produce a glassy polished surface.



Figure 7: Cruciform polishing operation

The fourth and final step was to bond tabs to each side of the loading arms. The tabs were 0.57 mm thick equal bi-directional, 0°- 90° plain weave, glass fiber/epoxy composite. They were cut into strips having the same width, 12.7 mm, as the loading arm and approximately 50 mm in length. The fiber direction of the tab material must align with the loading direction of the cruciform specimen to ensure proper load transfer into the specimen. They were rounded in pairs at one end to ensure the tabs have the same configuration. The use of rounded tabs further concentrated the load into the center of the specimen. This optimized the cruciform shape reducing the free edge stress singularity even more than square end tabs. One side of each tab was lightly sanded with a rotary tool for proper bond to the specimen. Cellophane tape is applied to the cruciform specimen over the fiber wing to protect the highly polished area. The loading

arms of the cruciform specimens were also lightly sanded to the cellophane tape protecting the fiber wing. The adhesive, a room temperature cured equal parts Epon 828 epoxy and Epon V40 curing agent, was applied to both sides of the specimen's loading arm and the sanded side of the tab. The paired tabs were placed on the loading arms and positioned so the rounded tip was at the edge of the cellophane tape. The tabs were then clamped in place with binder clips. This process was repeated for the other loading arm. A minimum of three medium sized binder clips for each loading arm were used to clamp the tabs. The binder clips were arranged such that two were opposite each other located as close as possible to the rounded end of the tabs and the third at the very end of the load arm. Once all specimens had their tabs bonded and clamped in place the cellophane tape protecting the fiber wing area was removed before the adhesive cured. The clamps remained in place a minimum of 24 hours for the adhesive to properly cure.

In all cases excessive adhesive from between the tab and specimen collected on the specimen edge when positioning the tabs. This was carefully removed by a spatula prior to clamping. Due to the clamping force, additional adhesive was squeezed onto the specimen edges and could not be removed due to the clamps. After the clamps were removed the excess adhesive was sanded down either to the original specimen edge or as close as possible to the original specimen edge. This maintained a uniform width.

The last procedure prior to testing was labeling the specimen. Labels were made at a #4 font and cut with an exacto knife and glued to the specimen at the rounded tip of the tab. In some cases where room existed between the tab tip and the outside fibers the label was placed there. The glue was a non-toxic, washable, and acid free adhesive used for bonding paper, cardboard, and photos. It did not provide additional strength or create a stiffened area on the specimen.

Reflected Light Test Method

The reflected light method used the change in light reflected off the surface of the fiber, in the case of fiber-matrix debond, or off the surface of a micro-crack or cavitation, in the case of matrix failure, for damage detection. Prior to the start of the test the cruciform-shaped specimen was illuminated by high intensity fiber optic lights, as shown schematically in Figure 8, until either

a thin bright white line appears at the center line of the stainless steel fibers or a series of bright white spots appear at the centerline of the fibers. Previous experience with single fiber cruciform specimens had shown that the fiber-matrix debond was hard to detect with lower intensity lighting. The fiber optic lights were positioned at an approximate angle of 45° to the specimen surface. One light was located slightly above the fiber grouping illuminating downward while the other light was located slightly below the fiber grouping illuminating upward. It was critical that no shadows appear in the image that could make first damage detection difficult. The fiber optic lights were adjusted accordingly to eliminate any shadows prior to each test. The background lighting was also very important. Due to the high reflectivity of the stainless steel wires coupled with the high intensity lighting needed for debond detection the background had to be light absorbing to a certain degree. A nonreflective but illuminating background was needed to detect the slightest failure initiation. Trial and error determined that about a 40 mm manila file folder strip approximately 150mm to 180mm long taped to the upper specimen grip provided a medium grey background. The background strip could be adjusted based upon individual specimens needs by crimping the strip causing it to hang closer to or farther from the specimen.

Mechanical testing was conducted to detect damage initiation and subsequent growth within the cruciform specimen under a uniaxial tensile stress. The wedge grips were spaced to optimize loading into the specimen. Specimens were centered within the grips and the distance between the grips were measured for every test. Due to the way the wedge grips were manufactured the distance between grips varied slightly depending upon the specimen's thickness. Course sand paper cut into 13mm by 100mm strips was used between the wedge grips and the specimen loading arms to prevent grip slippage. The specimens were loaded monotonically between $5.1 \mu\text{m/s}$ and $8.5 \mu\text{m/s}$ in tension along the Y axis (as shown in Figure 1) to final failure.

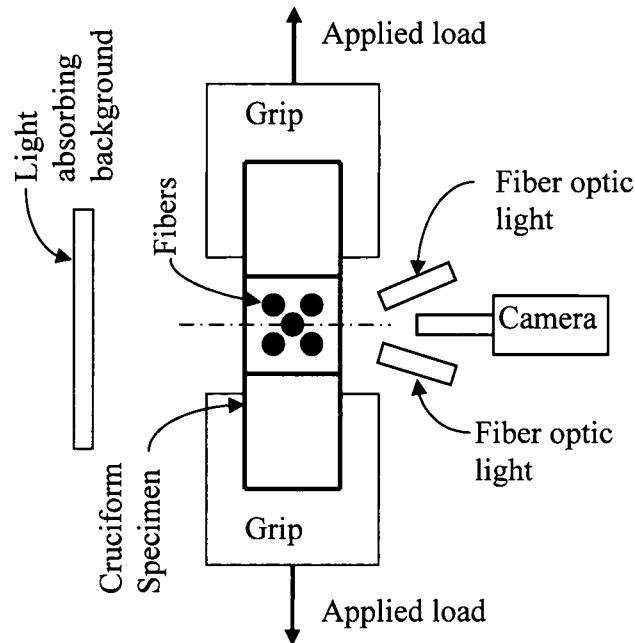


Figure 8: Schematic of the experimental set-up for the reflective light test method

Failure initiation was directly observed in the model composite specimen via the reflected light method as described above. Figure 9 shows a debond on a single fiber utilizing the reflected light method. The fiber centerline is clearly demonstrated by the white dots in the center of the fiber and delineated by the red line in the Figure 9. Debonds occur in the northern and southern hemisphere of the fiber and are clearly brighter than the rest of the fiber. The debond width is also shown. Note that the term pole refers to the angular position of $\theta = 90^\circ$ or $\theta = 270^\circ$ as shown in Figure 3. For simplicity $\theta = 90^\circ$ will be referred to as the north pole (NP) and $\theta = 270^\circ$ will be referred to as the south pole (SP). Likewise, the fiber equator will be defined as $\theta = 0^\circ$ and 180° . The northern hemisphere is defined as that section of fiber from $\theta = 0^\circ$ to 180° while the southern hemisphere is defined as that section of fiber from $\theta = 180^\circ$ to 270° .

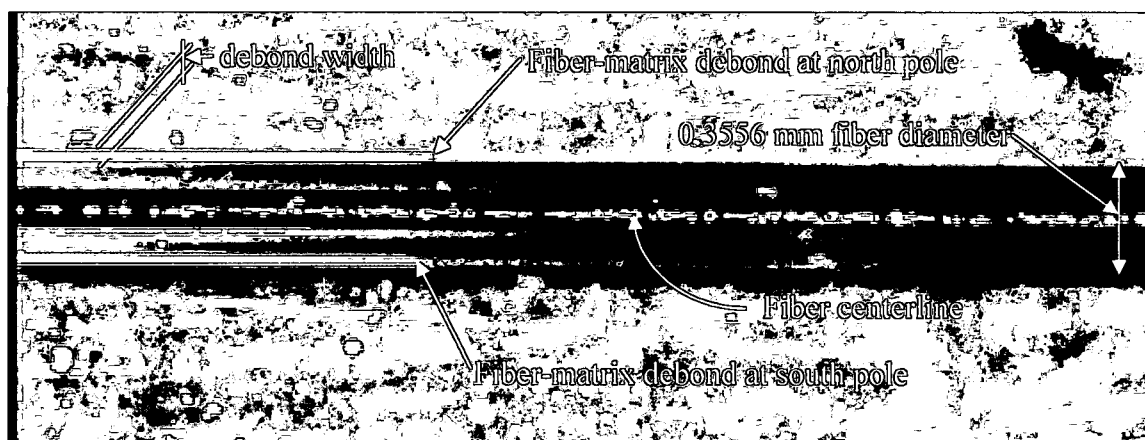


Figure 9: Photomicrograph of single fiber cruciform specimen showing a debond at the north and south poles.

All specimen tests were videotaped capturing the failure initiation and subsequent damage growth. The videotaped experiments allowed the damage events to be measured at a resolution of 1/30 of a second while correlating the load-displacement data to the damage event at a resolution of 2.54 μm of displacement. Since the rounded tabs concentrated the applied load in approximately the center third of the load arm, changes in the fiber spacing, as indicated by the parametric study results (see Appendix C), and interface and or material non-uniformity could alter the failure initiation location. For this reason a second camera was used to capture failure initiation outside of the high stress areas. Consequently, multiple video cameras were used to view different areas of the specimen and captured the entire load history of each specimen. Both video cameras were Sony monochromatic CCD cameras. The first or primary video camera used a high resolution and high magnification zoom lens focused at the intersection of the center of the loading arm and center of the fiber wing. This camera was positioned at the apex of the rounded tab normal to the front side of the specimen, as shown in Figure 10, to capture all events that occurred in the center of the specimen. The field of view was approximately 1/8 the width of the loading arm in the horizontal direction. The vertical direction field of view ranged between one fiber diameter above and below the fiber grouping for the large fiber spacing to three fiber diameters above and below the fiber grouping for the close fiber spacing. However, for the $1.57d_f$, $1.75d_f$, $1.84d_f$, and $1.9d_f$ fiber spacing groups the center fiber was partially obstructed from view.

Table 2 lists the field of view limits for these cruciform specimens having the aforementioned fiber spacing.

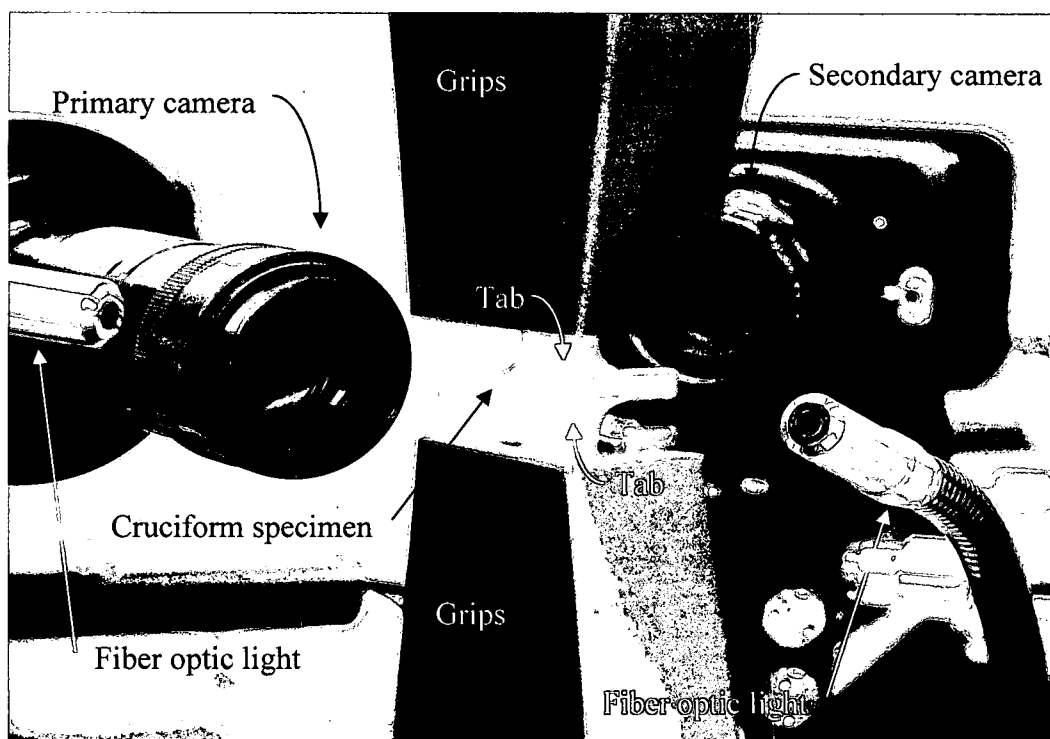


Figure 10: Photograph showing camera position during testing

Table 2: Field of view limits for 1.57d_f, 1.75d_f, 1.84d_f and 1.90d_f cruciform specimens

Fiber Spacing	C/C Dist between corner fibers (mm)	Angular sweep along Center fiber interface (deg)
1.57d _f	0.565	0° to 35° and 360° to 325°
1.75d _f	0.630	0° to 49° and 360° to 311°
1.84d _f	0.662	0° to 58° and 360° to 302°
1.9d _f	0.684	0° to 66° and 360° to 294°

Each fiber is sub-divided into four quadrants. The first quadrant is from $\theta = 0^\circ$ to 90° , the second quadrant is from $\theta = 90^\circ$ to 180° , the third quadrant being $\theta = 180^\circ$ to 270° and the fourth quadrant is $\theta = 270^\circ$ to 360° . Thus the field of view encompasses the first and fourth quadrant of the top and bottom corner fiber respectively and the first and fourth quadrant of the center fiber.

The second camera position evolved over the course of testing multi-fiber cruciform specimens. As mentioned above, changing fiber spacing changed the failure initiation location. In

addition, due to experience from the initial testing of multi-fiber cruciform specimens the location of the origin of some fiber-matrix debonds could not be determined. In some cases the fiber-matrix debond occurred instantaneously flashing across the entire field of view occurring in one frame in the video, i.e. 1/30 of a second. In other cases the fiber-matrix debond propagated across the field of view. Consequently, one camera position, shown in Figure 10, was at approximately a 45° angle to the front of the specimen in a horizontal plane with the primary camera. Its field of view covered most of the fiber wing. However, since it was on the same horizontal plane as the primary camera its field of view did not capture any additional fibers already observed by the primary camera. Therefore a second position, utilized for most of the testing, as shown in Figure 11, was employed to observe 4 of the 5 fibers in the multi-fiber cruciform specimens. This secondary camera used a high resolution (albeit a lower magnification) zoom lens than the primary camera for a wider field of view. It was focused on the fibers and its field of view was centered on the sample and captured a width equal to the width of the loading arm. Thus, the second camera would capture failure events occurring outside the field of view of the primary camera.

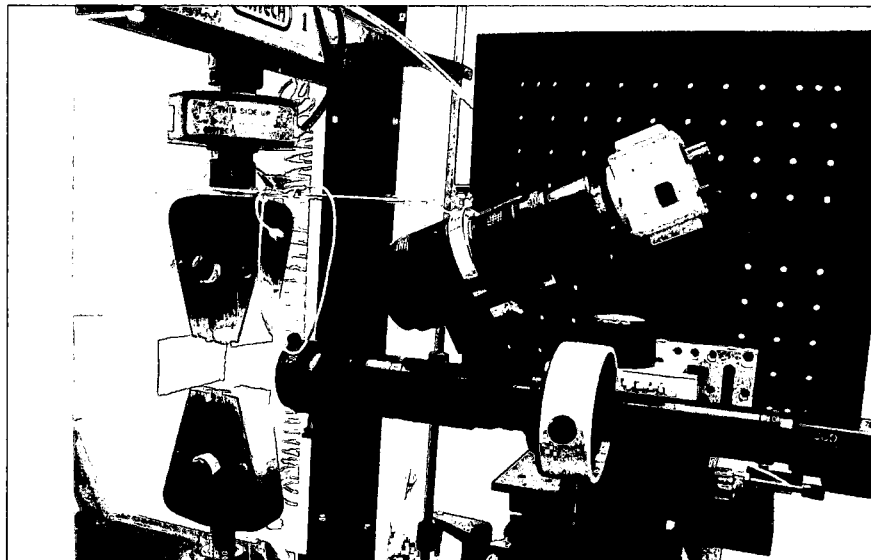


Figure 11: Photograph showing new and improved camera position during cruciform testing

With the two camera test setup, the probability of capturing the failure initiation increases. Provided the failure initiates in the field of view the failure mechanism can be determine. Failure initiation occurring outside the area of greatest load induction is further scrutinized to determine if caused by internal flaws.

A thorough frame-by-frame review of the video with respect to time relates the failure initiation to loading. As mentioned above, all tests were videotaped until failure is achieved while the testing equipment captures the load and time histories. Consequently the complete load history of each specimen was known. From the instant of complete specimen fracture, the time is measured back to the instant of failure initiation detection. Thus, the load at failure initiation was determined. From the specimen dimensions the far-field stress at failure initiation was calculated. This stress state was then used in the finite element analysis (FEA) to determine the internal stresses in the specimen at failure initiation.

Photomicrograph Image Analysis

At the magnification level used in this work light noise caused by surface imperfections imperceptible to the eye can hinder the detection of the first damage. Consequently, the cruciform specimens have to have a mirror-like surface. The imperfections can be either on the surface of the fiber or the cruciform surface. Thus a photomicrograph image analysis technique was used to clarify the observed damage initiation in all cruciform specimens. By converting the analog VCR video tapes to digital video, individual images can be captured one video frame at a time or at 1/30 of a second. This technique was used to determine the first failure for each cruciform specimen tested. In reviewing the videotape to determine the time at first failure, the sequence of frames before, at and after the first failure was captured. The individual still images were then stacked on each other in sequence to confirm the videotape time at failure initiation. In addition, frames from the start of the tests were also captured from the digital video and incorporated into the sequenced still images at the appropriate time step. This base image was taken at the very beginning of the experiment when the specimen was under no load. The image with the first failure was thus superimposed over the base image via the stacking sequence and features

common to both images were subtracted. The subtraction technique resulted in an image only showing the effects of the mechanical load on the specimen over that timeline and clearly highlights the damage mechanism in the specimen being either a fiber-matrix debond or matrix cavitation. Since all features common to the base image and the image capturing the failure initiation were subtracted the fiber edges needed to be marked on the resulting image for clarity otherwise they were not visible in the final image. This technique was accomplished using Photoshop software.

Fracture Surface Image Analysis

The fracture surface of two specimens of each fiber spacing group was examined under the scanning electron microscope (SEM) to determine any features leading to the first damage mechanism. It is important to note that features on the fracture surface reflect the fracture initiation and do not necessarily reveal the failure initiation. For example, some cruciform specimen's videotaped experiments showed failure initiated as a fiber-matrix debond in the vicinity of the fiber poles. It also showed the debond propagating along the fiber axis while wrapping around the fiber circumference as load is continually applied. However, the fracture surface analysis may indicate that the final specimen fracture initiated at the fiber equator. Thus, the videotaped experiments showed failure initiation while the fracture surface analysis indicated fracture initiation. Analyzing the fractured surface of the cruciform specimens gives clues to the state of stress present at the time of final failure. However, the videotaped experiments show the failure initiation mode. Thus, for all fiber-matrix debond initiation cases, the fiber imprint area of the fracture surface was thoroughly examined. Correspondingly, in all matrix cavitation cases, the cavitation occurring in the fracture plane of the specimen was found and photographed. Analyzing the failure initiation surfaces observed experimentally along with the fractured specimen surfaces suggest possible stress states present at failure initiation. Comparing the fracture surface features with the videotaped experiments is not a 1:1 correlation. However, features on the fractured surface of the specimen can infer stresses present at the time of failure initiation. These findings will be used along with the analytical results and most importantly the observed failure

initiation mechanism to arrive at the most logical stress state that created the first damage mode. This in turn will guide the development of the failure criteria for transversely loaded composite materials.

First Damage Mechanism Description

As indicated in the literature, composite materials when subjected to loads normal to the direction of the fiber exhibit either fiber-matrix debonding or matrix cavitation as their first failure mechanism. These two competing damage mechanisms appear to be dependent on fiber spacing. In this work fiber-matrix debonding and matrix cavitation were observed in cruciform specimens at specific fiber spacing in both matrix system used. A description and specific characteristics of the fiber-matrix debonding and matrix cavitation damage mechanism follows.

Fiber-Matrix Debonding

The fiber-matrix debond is characterized as separation of the matrix from the fiber by the stress field existing at the fiber-matrix interface. Using the reflected light method, it is typically observed as a very light grey almost white spot, usually at the fiber pole, that spreads or propagates along the fiber almost instantaneously once initiated. As it propagates along the fiber, the debond front forms a tip at or near the fiber pole. As the debond propagates along the fiber length, its front forms a tip at or near either fiber pole. As the debond front continues to advance, the edge of the debond wraps around the circumference of the fiber and is seen as a very light grey/white region of the fiber while the bonded region is dark grey. In some cases the fiber-matrix debond does not advance instantaneously but propagates either moderately, very slowly or not at all, as load is continuously applied. In these situations it can be difficult to discern between a spot debond or matrix cavitation (which is described later). Note that the spot debond almost always occurs at or near the fiber pole and has a shape very similar to a typical debond but has a very small length. In such cases, a thorough photomicrograph image analysis was completed.

It is important to note that for the multi-fiber specimens there exist multiple interfaces associated with the 5 different fibers. These can either debond simultaneously or separately with

increasing load although only the first and fourth quadrants of 3 of the 5 fibers are visually observed in the near field high magnification view. Four of the 5 fibers are visible in the far-field low magnification view as described earlier. In addition, the location of the debond initiation can be exterior or interior to the fiber group. Figure 12 is a schematic delineating the interior and exterior regions of the fiber grouping. The fiber-matrix interface stresses are expected to be higher along the interior quadrants of the fibers than along the exterior quadrants. By definition, exterior to the fiber groups occurs when the debond initiates at either the NP of the top corner fiber or the SP of the bottom corner fiber. Likewise, interior to the fiber group is when the debond initiates at either the SP of the top corner fiber, at the NP of the bottom corner fiber or on the center fiber.

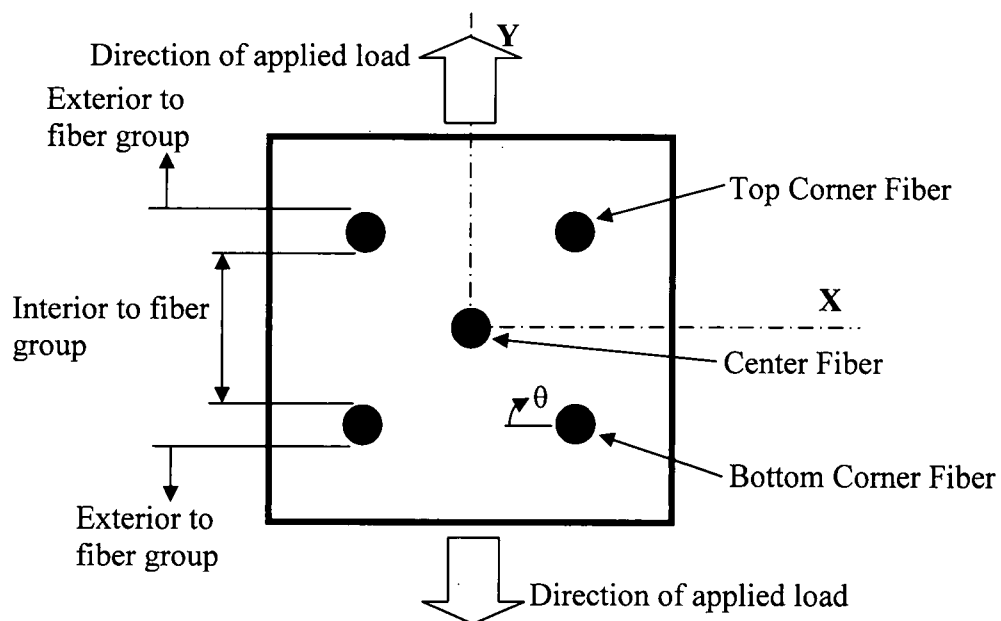


Figure 12: Fiber group schematic delineating interior and exterior regions of fiber grouping

Fiber-Matrix Debond Measurements

Once the photomicrograph images are constructed capturing the failure initiation, the fiber-matrix debond widths can be measured. Since the diameter of the fiber is known, the width of the debond can be determined to the correct scale. Through simple geometry, the central angle of the debond can be calculated, as shown in Figure 13, assuming that the debond is symmetric. In the cases where the fiber-matrix debond propagated slowly or occurred as a spot debond, the length can also be determined. For each cruciform specimen in which debonds were directly observed, the length, width and central angle were all determined (with the caveat that some of it may be hidden behind the other fibers when measuring it on the central fiber).

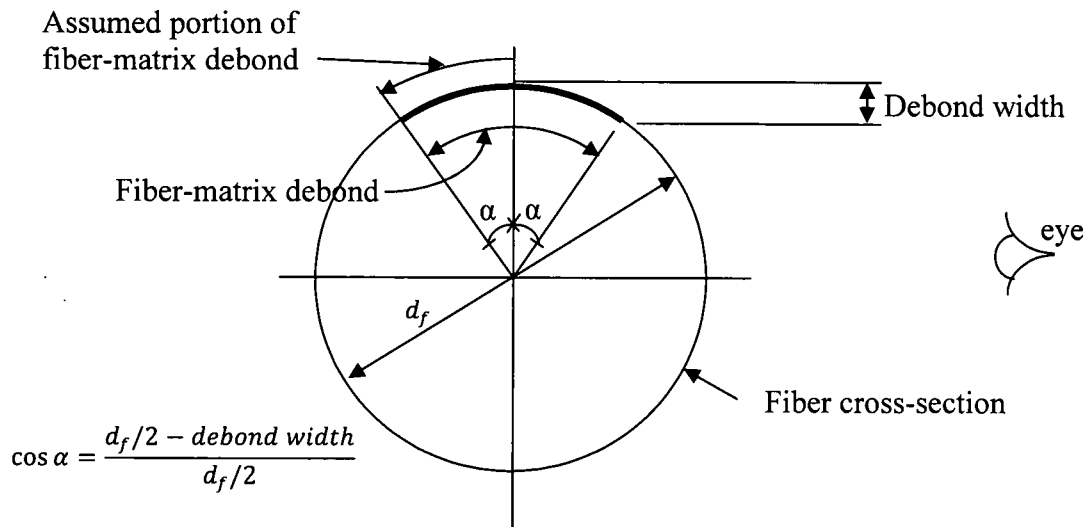


Figure 13: Fiber-matrix debond measurement schematic

Matrix Cavitation

The matrix cavitation failure initiation is characterized as non-uniform or irregular shaped micro-voids developing in the matrix under loading due to the triaxial stress state resulting from the constraining influence of the relatively stiff fibers. The light grey or white spots often occurred within the matrix area bounded by at least one fiber diameter beyond the volume contained by the corner fibers. They typically happened randomly prior to fiber-matrix debonding. The shape of the

spots was random and varied from a smooth edge circular spot, to a jagged edge oblong shape, to rectangular in shape. The size of the micro-voids varied as well usually being a few hundredths of the fiber diameter. Some of the spots often occurred at the fiber-matrix interface as evidence by their relative brighter intensity than did those clearly forming away from the interface. However, the cavitation spots did not propagate if it appeared they occurred at the fiber-matrix interface. In addition, they differed in relative intensity at different locations throughout the cruciform specimen. Furthermore, in most of the specimens exhibiting cavitation, multiple cavitations formed prior to final specimen failure. As mentioned above the reflected light method used the change in light reflected off the surface of the fiber, in the case of fiber-matrix debond, or off the surface of a micro-crack or cavitation, in the case of matrix failure, for damage detection. When damage occurred in the specimen, light reflected differently from the damaged surface and usually made the existing surrounding features brighter. The reflected light method, unfortunately, did not discriminate between reflections from the surface defects, pits and scratches from specimen preparation present in the unloaded specimen and cavitations or micro voids created from the triaxial state of stress induced by mechanical loading. Typically those features present throughout the test did not change light intensity very much, if at all, however, new features, i.e. the reflections due to damage, did change light intensity. It had been observed that the cavitations can grow by a combined change in their light intensity and size. To clarify the cavitations occurring in the specimen during loading, the image subtraction technique described above was used.

It was mentioned earlier in the specimen preparation section that extreme care was taken to keep the fiber surface clean before casting epoxy around the fiber arrangement in the silicone mold. Moreover, prior to loading, the specimen viewing area comprised of the loading arm width and area between the tabs, was cleaned with distilled water and dried with compressed air. The average time of the transverse loading test was approximately two minutes and it is therefore highly unlikely that during this short time interval, external dust from the environment could settle on the specimen. Further to eliminate the possibility of observed white spots during loading being reflections of any embedded or surface dust particles, laboratory dust was placed on the sides of

a polished untested cruciform specimen. Using the primary video camera utilized for the experimental testing images were taken of the specimen. The dusted specimen was examined at different lighting angles and at different light intensities using the same fiber-optic lights used in the cruciform tests. The lab dust on the viewing surface of the specimen appeared as white circular spots more uniform in shape and intensity than the cavitations. On the opposite side of the specimen the lab dust had the same uniform circular shape and intensity but was light grey in color. The lab dust also contained fibers that appeared as white lines on the viewing side or light grey lines on the opposite side of the specimen. The color, shape, and intensity of the dust did not change when the primary camera was moved vertically simulating a specimen test. We even simulated dust landing on the specimen by sprinkling dust collected by a sheet of paper on the specimen. There were no spots observed by sprinkling dust on the specimen. In fact the dust drifted up toward the vacuum hood located approximately 3 feet behind the test setup. Since the image subtraction technique was used, if the specimen had dust on its surface it would be common to both images and thus subtracted out. Consequently, the white spots observed to form during loading were not reflections of embedded or external dust particles.

It was further noted that all specimens at the 1.84d_r fiber spacing were tested using screw-action type grips. The screw-action grip clamps the specimen between two serrated square plates (38 mm wide and 6.5 mm thick) by the action of 12 set screws (6 on each side of the grip). This type of grip prevents specimen slippage during the tests and thereby eliminates the possibility of existing specimen features such as micro voids or surface defects to move into favorable positions (due to slippage) relative to the fiber optic light and cause reflections that could seem to appear as spots. The discussion presented in the previous paragraphs therefore leads us to firmly believe that the observed white spots during loading are manifestations of light reflected from the newly initiated micro damage, namely, matrix cavitation.

Experimental Cruciform Specimen Results

At the start of this work the cruciform specimen geometry using the reflected light testing method for single fibers had been successfully utilized for interface failure purposes [12, 15, 23].

However, multi-fiber cruciform specimens having a specific fiber spacing using the reflected light test method had not. For an experimental trial, fiber templates were made with spacing small enough to partially hide the center fiber and tested to observe the failure mechanism. The templates were designed having a $1.90d_f$ fiber spacing and were made on a jeweler's drill press with a horizontal stage having micrometer adjustment capability. The overall templates were designed to have 20 individual specimen templates thus making 10 cruciform specimens. In addition, cut holes were placed away from the individual patterns at dimensions making the individual cruciform specimen templates. Once the overall template was created the individual templates were cut from the aluminum sheet by an exacto knife cutting between the cut holes. Very thin, 0.127mm, aluminum sheet stock was cut into small rectangular shapes large enough to fit the overall template. Beneath the aluminum sheet was placed a similar sized plate of Plexiglas material to drill into. A #80 drill bit was used to make the template holes. Because this process did not utilize a C-N-C machine to create the fiber patterns there was variation in the fiber spacing. It was also observed that the #80 drill "danced" around the aluminum sheet while drilling the fiber patterns. This was due to the length of drill bit extending from the chuck and was a characteristic of this process minimized through several unsuccessful trials. Therefore once the cruciform specimens were cast and prepared for testing, the coordinates of the center of the fiber ends in each multi-fiber cruciform specimen wing were determined by setting one corner of the wing cross section as the origin. Thus the actual distance of the fiber spacing can be determined. For the initial batch of multi-fiber cruciform specimens to test the reflected light method for capturing failure initiation, the actual average fiber spacing was $1.84d_f$. Seven specimens are made and tested with this fiber spacing in the 828 matrix.

The $1.84d_f$ fiber spacing specimens exhibited multiple fiber-matrix debonds thus the current cruciform specimen geometry is considered optimized for this work. In addition, two different tab end shapes were used in the trial, rounded tabs and straight tabs. The reasoning behind the two different tab end shapes was to see if there were any differences in failure mechanisms by how the load was introduced into the specimen. For the straight sided or straight end tab, the load is introduced over the width of the loading arm but using the rounded tab

concentrates the load further in the center of the specimen. Prior cruciform geometry optimization study indicated stress concentrations at the radius return to the loading arm [15]. The rounded tab ends were a way to minimize this stress concentration while optimizing the loading of the specimen. Four of the seven cruciform specimens used the rounded tabs while the other three used straight tabs. This experimental trial was very successful in demonstrating the failure mechanism of multi-fiber cruciform specimens and deciding the tab shape for all future cruciform experimentation and is described below. Furthermore, due to the dancing of the #80 drill bit it was decided that the fiber templates would be C-N-C machined to ensure accurate fiber spacing geometry.

828/D-230 Matrix System

Steel/828/D-230 Single Fiber Cruciform Results. A total of 21 828/D-230 single-fiber cruciform specimens were tested. Table 3 lists the applied far-field stress at failure initiation, the debond width and corresponding central angle at failure initiation and the debond type. As mentioned earlier, the debonds can occur instantaneously across the screen or as a spot where propagation is either moderate or very slow to nonexistent. In all cases the observed first damage mechanism is fiber-matrix debonding initiating in the vicinity of the fiber pole. Figure 14 shows a photomicrograph of a single-fiber cruciform debonding in the southern hemisphere of the fiber in the vicinity of the fiber pole. The debond tip is clearly shown and designated by point A and A' in Figure 14. Between the debond tips the change in light intensity on the fiber is indicative of the debond wrapping around the fiber circumference as load is continually applied. The light area of the fiber is where the fiber-matrix interface has debonded, whereas the darker area is where the fiber-matrix interface is still intact. Also shown in Figure 14 are the debond length and width. The average far-field stress at failure initiation for the 828/D-230 matrix system is 19.82 MPa.

Figure 15 shows a photomicrograph of the fracture surface of a typical single fiber specimen. The black arrow delineates the fracture initiation location where it appears like a map symbol of a volcano. The location is away from the fiber edge. Figure 16 is an SEM image of the same location at 550 times magnification. The center of the volcano feature is smooth indicating a

tensile stress failure mode where the stress is in the direction of the applied load. From a thorough analysis of the fracture surface no other failure mechanisms are present. Since the single fiber failure initiation was experimentally observed as a fiber-matrix debond and no indication of other possible failure mechanisms are present on the fracture surface, it can be concluded that the damage initiation mechanism is interfacial fiber-matrix debonding. Figure 17 is an SEM image of the fiber imprint area of the fractured surface. The imprint is smooth also indicating a tensile dominated failure at the fiber-matrix interface.

Table 3: 828 Single fiber cruciform specimen test results where IAS indicates Instantaneously Across Screen (IAS) meaning it is greater than 4 mm.

Specimen	Far-Field Stress at debond initiation (MPa)	Debond width (mm)	Debond Central Angle, 2α (deg)	Debond Type & Debond length
SFR1-A	26.01	0.130	150°	IAS
SFR1-B	26.33	0.122	144°	IAS
SFR1-C	26.27	0.050	88°	IAS
SFR1-J	19.98	0.034	72°	Spot~0.02 mm
SFR1-K	17.09	0.119	142°	IAS
SFR1-L	22.58	0.144	158°	IAS
SFR1-M	29.78	0.040	78°	IAS
SFR1-N	19.01	0.050	88°	IAS
SFR1-O	17.06	0.043	82°	IAS
SFR1-P	16.85	0.083	116°	IAS
SFR1-Q	17.95	0.047	86°	IAS
SFR1-R	18.55	0.043	82°	IAS
SFR1-X	19.97	0.040	78°	IAS
SFR1-Y	21.12	0.064	100°	IAS
SFR1-AA	19.49	0.062	98°	IAS
SFR1-BB	17.48	0.052	90°	Spot~1.75 mm
SFR1-CC	16.13	0.040	78°	Spot~0.025 mm
SFR1-DD	8.23	0.048	86°	Spot~0.13 mm
SFR1-EE	18.26	0.100	128°	IAS
SFR1-FF	16.24	0.090	122°	IAS
SFR1-GG	21.80	0.070	106°	IAS
AVG	19.82	0.070	106°	
Std-dev	4.54	0.033	37° to 143° NP 217° to 323° SP	

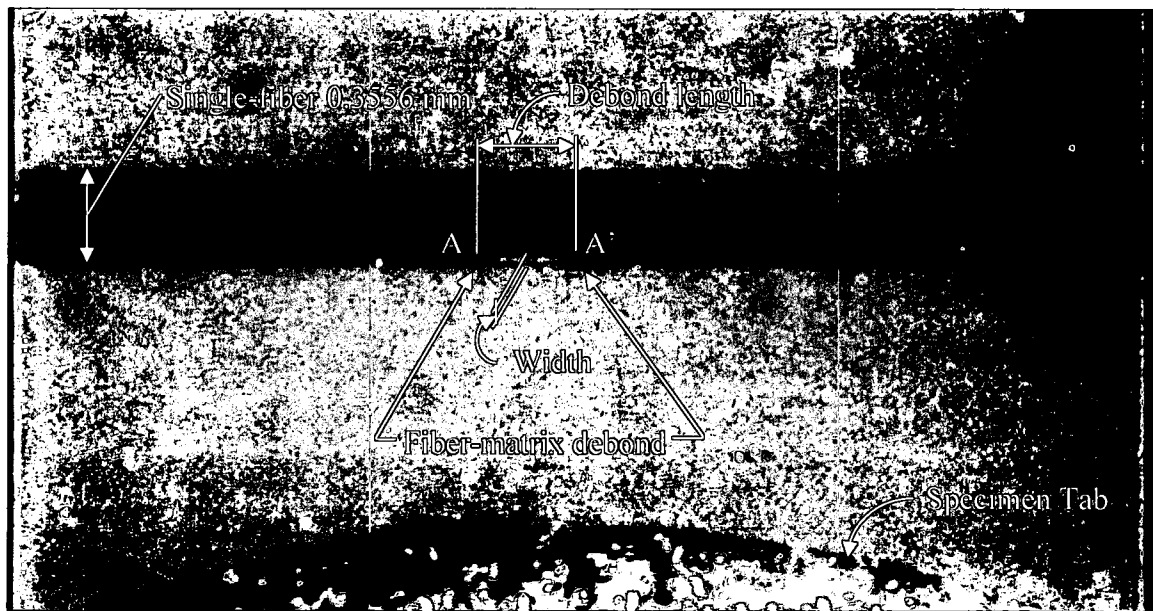


Figure 14: Photomicrograph of steel/828 single-fiber cruciform debond

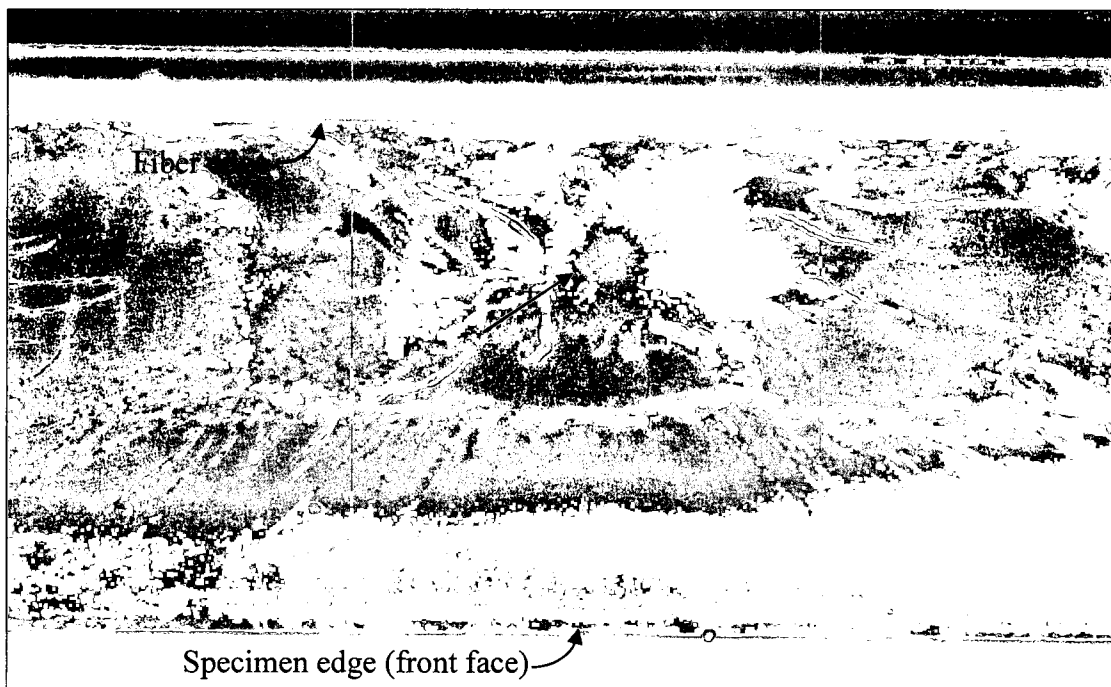


Figure 15: Photomicrograph showing the typical fracture surface of the single fiber cruciform specimen



Figure 16: SEM image of fracture initiation location showing the volcano feature

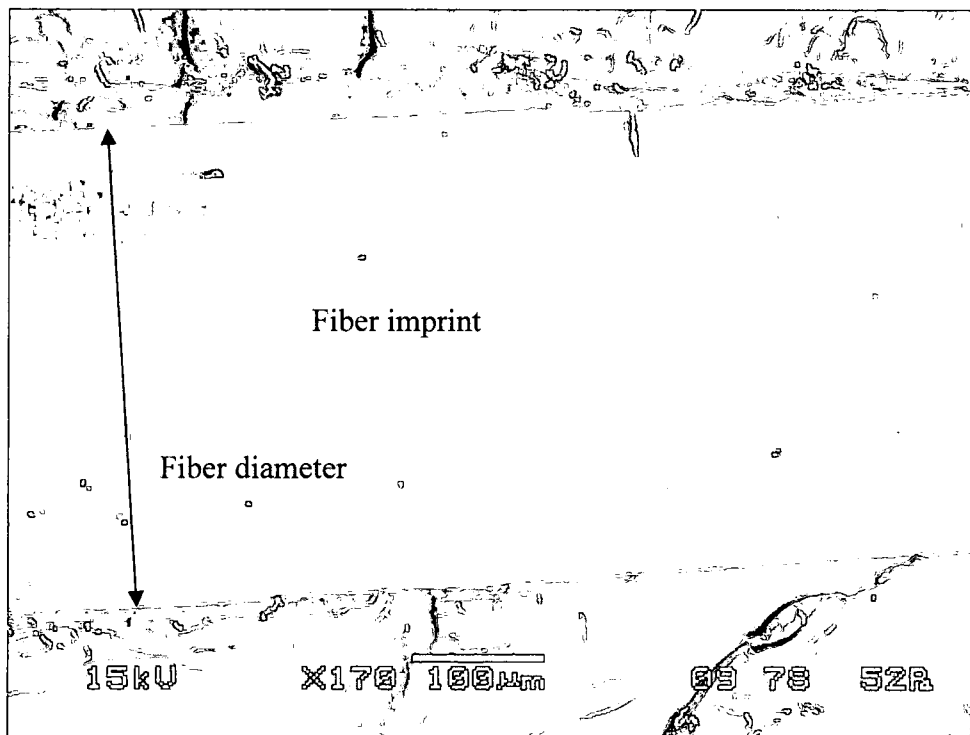


Figure 17: SEM image of fiber imprint area on fracture surface of single fiber cruciform specimen

Steel/828/D-230 6.0d_f Multi-Fiber Cruciform Results. Eight multi-fiber cruciform specimens having a fiber spacing of 6.0d_f were tested and Table 4 lists the far-field applied stress at failure initiation for the top, center, and bottom fiber. In each case, the observed failure initiation is fiber matrix debonding.

The bold italicized values in Table 4 are the smallest far-field stress values at which debonding first occurred for that specimen and the corresponding fiber identifies the location of damage initiation. Table 4 also indicates the location of the debond initiation referring to which fiber pole the debond initiated in the vicinity of and whether it was interior or exterior to the fiber group. Specimen S600R1C1-A experienced grip slippage thus the far-field stress could not be determined and specimen S600R1C1-I was defective due to the fibers being exposed during specimen preparation for testing.

In 7 of the 8 specimens tested, debonding initiated at a point on the interface in the loading direction in either the top or bottom fiber. In 5 of the 8 specimens either the top or bottom corner fiber debonded first followed by the center fiber and the other corner fiber. For 5 of 8 specimens the debond initiated interior to the fiber group. The average far-field stress at debond initiation for the 828/D-230 matrix system is 10.70 MPa.

Table 4: Far-field applied stress at debond initiation in multi-fiber specimens having 6.0d_f fiber spacing

828 Matrix	Far-field stress at debond initiation (MPa)			Location w/r/t Fiber group
Specimen	Top Fiber	Center Fiber	Bottom Fiber	
S600R1C1-B	-	18.46^{NP}	-	Interior
S600R1C1-C	10.32^{NP}	14.24 ^{SP}	12.85 ^{SP}	Exterior
S600R1C1-D	19.49 ^{NP}	15.39 ^{SP}	5.24^{NP}	Interior
S600R1C1-E	12.71 ^{SP}	12.48 ^{SP}	10.42^{NP}	Interior
S600R1C1-F	15.90 ^{SP}	15.20 ^{SP}	15.16^{NP}	Interior
S600R1C1-G	4.98^{NP}	20.27 ^{SP}	19.72 ^{SP}	Exterior
S600R1C1-H	17.49 ^{SP}	16.60 ^{NP}	10.68^{SP}	Exterior
S600R1C1-J	10.34^{SP}	14.01 ^{NP}	16.07 ^{SP}	Interior

Figure 18 shows a photomicrograph of a fiber-matrix interface debond on the center fiber in a cruciform specimen having a fiber spacing of 6d_f. The debond tips can be seen at point A and A' at the fiber pole. As the debond has propagated over the length L, the front has wrapped

approximately 180° around the fiber circumference. Figure 19 shows the same photomicrograph using the image subtraction technique described above. The subtracted image clearly illustrates the fiber-matrix debond in the vicinity of the north pole of the center fiber. It also shows that a second debond has formed in the vicinity of the north pole of the top corner fiber that is very difficult to see in the photomicrograph of Figure 18 but easily seen in the video tape. The fiber edges have been superimposed in Figure 19 for clarity and orientation. By subtracting current and base images the damage events occurring due to the loading are easily differentiated from existing features allowing a detailed interrogation of the damage phenomenon. Thus, Figure 19 clearly shows that the fiber-matrix debond is the only failure initiating event at this particular fiber spacing. In all cases the final failure is fiber matrix debonding with the failure occurring either at the corner fibers as shown in Figure 20 or at the center fiber in a similar manner.

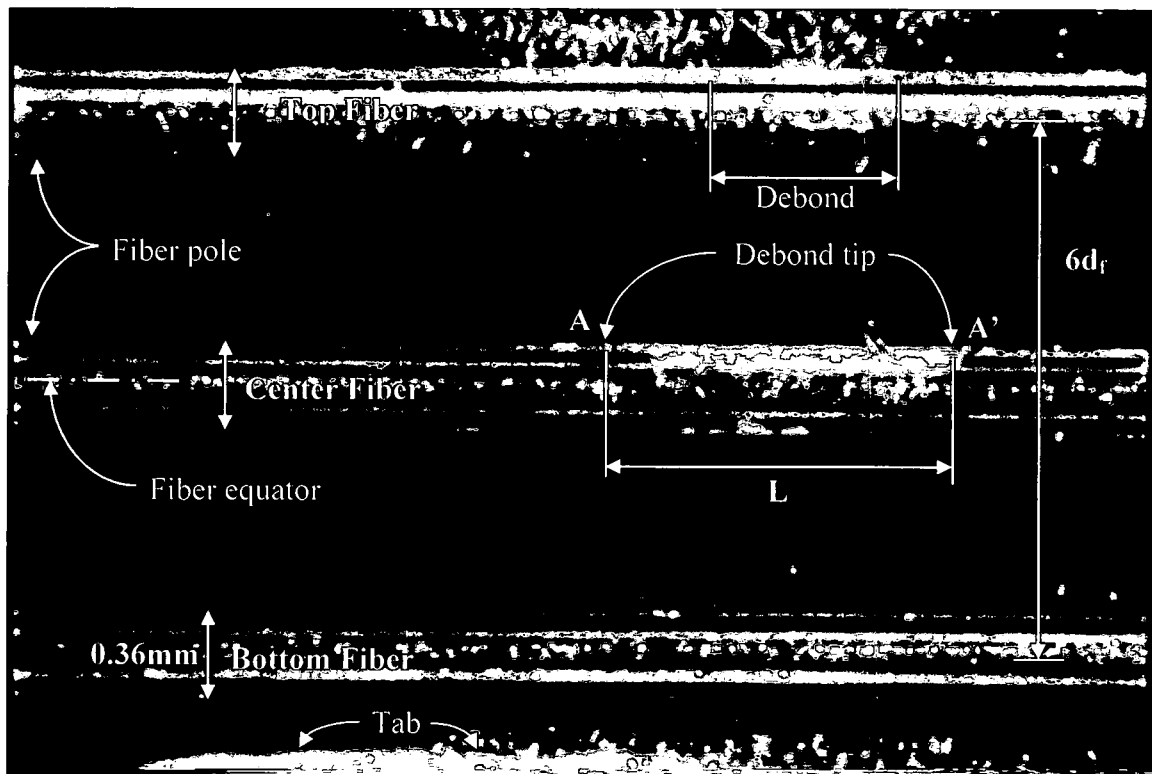


Figure 18: Photomicrograph of steel/ $6.0d_f$ cruciform specimen debond

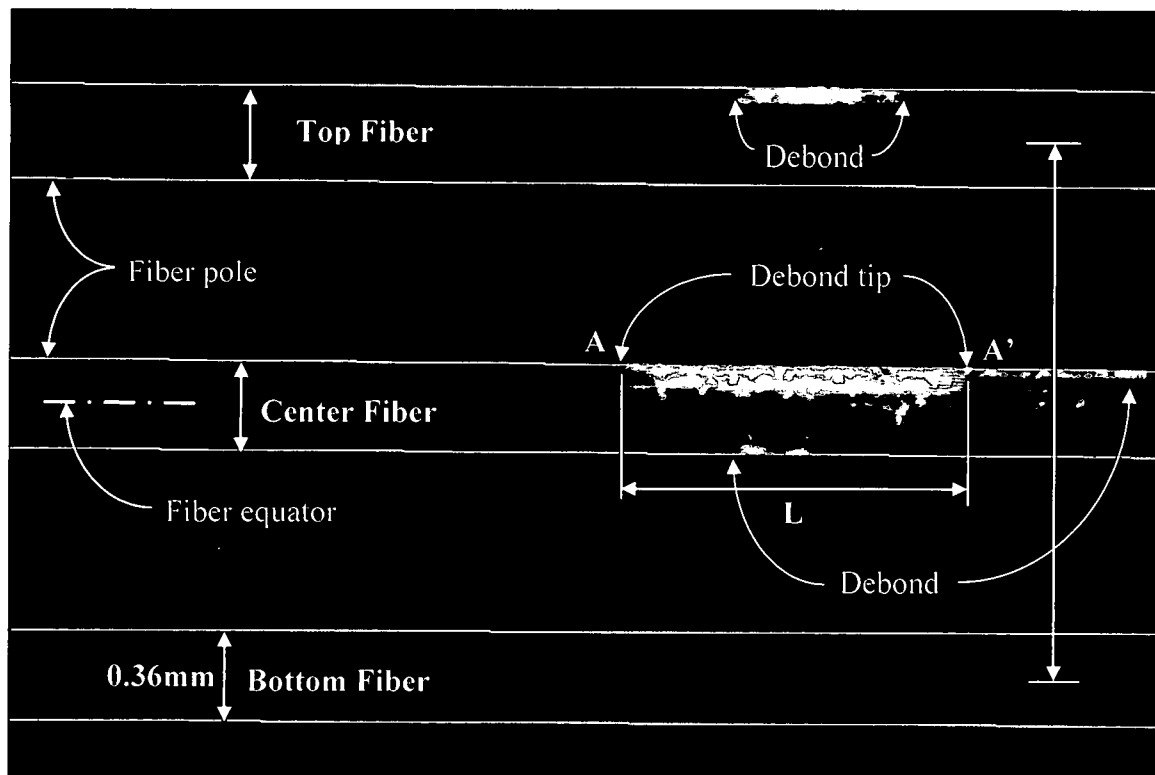


Figure 19: Subtracted image of interfacial debonding in a steel/6d_f cruciform specimen

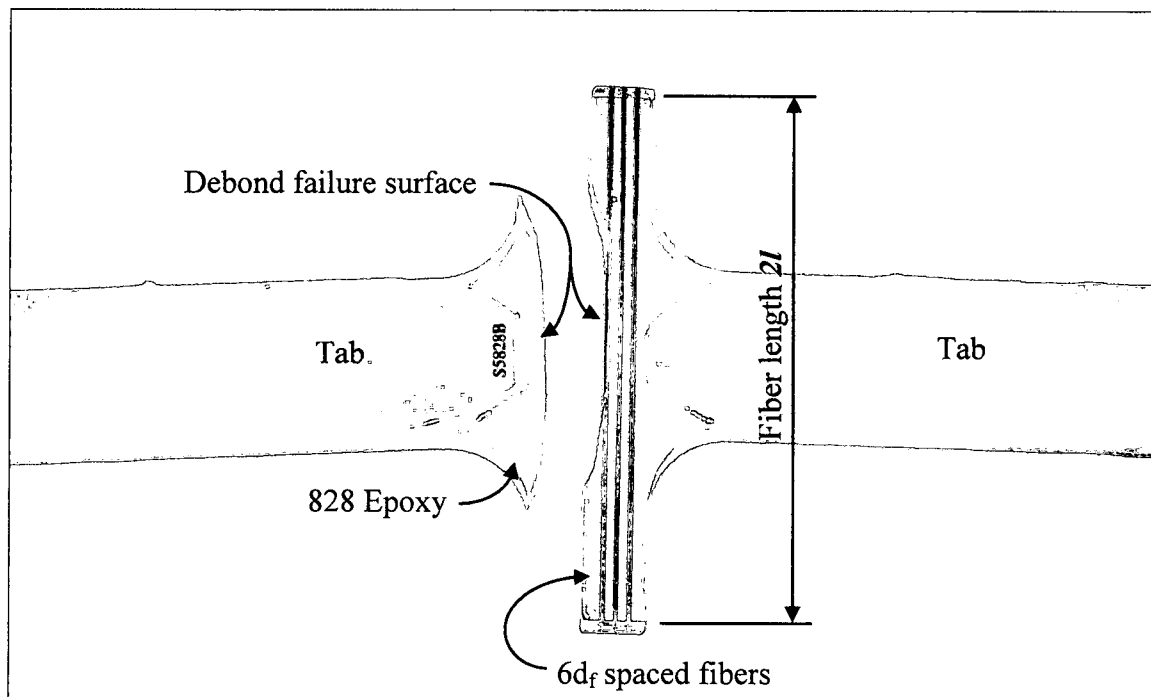


Figure 20: Debond failure of a steel/6d_f cruciform specimen

Table 5 lists the debond initiation measurements consisting of debond width, central angle, location, corresponding FEM location, and debond type. The center fiber has been abbreviated as CF and likewise the top fiber is TF and the bottom fiber is BF. Due to symmetry of the multi-fiber cruciform in the XY and YZ planes, the FEM is only 1/8 of the actual specimen. Therefore, if a debond initiates at the SP-BF it translates to the NP-TF for FEM purposes. The central angle of 48° determined by the average debond width is only 2° off the median of the range of the individual specimen central debond angles of 36° to 64°. Furthermore, it is only 1.125° from the average of the individually calculated central debond angles as shown in Table 5. In all but one case the debond initiated as a spot having a small length as indicated in Table 5.

Table 5: Steel/828 6.0d_r cruciform specimen debond measurements, where CA = central angle

Specimen	db width (mm)	db Central Angle	Loc	FEM Loc	db Type
600R1C1-B	0.010	48°	NP-CF	NP-CF	IAS
600R1C1-C	0.011	40°	NP-TF	NP-TF	Spot ~ 0.15 mm
600R1C1-D	0.015	47°	NP-BF	SP-TF	Spot ~ 0.2 mm
600R1C1-E	0.009	36°	NP-BF	SP-TF	Spot ~ 0.34 mm
600R1C1-F	0.017	50°	NP-BF	SP-TF	Spot ~ 0.08 mm
600R1C1-G	0.010	48°	NP-BF	NP-TF	Spot ~ 0.08 mm
600R1C1-H	0.020	64°	SP-BF	NP-TF	Spot ~ 1.07 mm
600R1C1-J	0.012	42°	SP-TF	SP-TF	Spot ~ 3.23 mm
AVG	0.0153	48° Avg CA => 66° to 114° NP & 246° to 294° SP			
Std-dev	0.0051				

The fracture surface analysis indicated that final fracture occurred in the matrix area away from the fiber-matrix interface as shown in Figure 21 by the white arrow. The fracture surface indicated that a tensile force in the loading direction caused the fracture of the specimen. The fractured surface gave no indication of any other stresses present at the initiation point of final fracture. No other failure initiation sites are present on the cruciform failure surface. Consequently, the failure initiated as a fiber-matrix debond as observed during the cruciform test. The lines contained within the fiber imprint area as pointed out by the black arrows are a characteristic of the fiber manufacturing process. The imprint of the fiber is smooth indicating a tensile dominating force acting at the interface creating the debond.

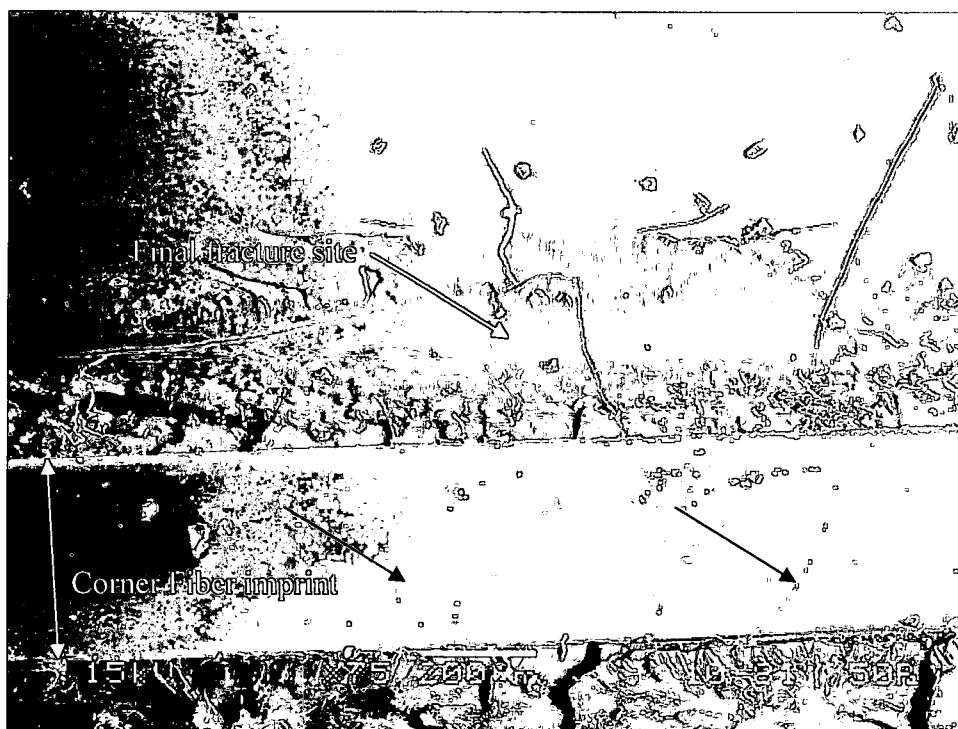


Figure 21: SEM image of fracture surface of steel/6.0d_f cruciform specimen

Steel/828/D-230 2.5d_f Multi-Fiber Cruciform Results. Five multi-fiber specimens having a fiber spacing of 2.5d_f were also tested and in every specimen, failure initiated as a fiber-matrix debond. Table 6 lists the far-field applied stress at failure initiation for the top, center, and bottom fibers as well as the location with respect to the fiber grouping. All specimens had their debonds initiate in the vicinity of the fiber pole. In 4 of the 5 specimens that exhibited multiple debonds, either the top or bottom corner fiber debonded first. In 3 of the 5 specimens, the debond occurred exterior to the fiber group. The average far-field stress at debond initiation for the 2.5d_f fiber spacing is 6.58 MPa.

Figure 22 is a photomicrograph that shows a fiber-matrix interface debond on the top fiber or corner fiber in a cruciform specimen having a fiber spacing of 2.5d_f. The debond tips can be seen at points A and A'. L is the debond length and the debond has wrapped approximately 90° around the fiber circumference. Figure 23 is the photomicrograph obtained by subtracting the base image from the micrograph in Figure 22 and clearly shows the debond in the vicinity of the south pole of the top corner fiber. The fiber edges have been superimposed in Figure 23 for

clarity and orientation. No other damage from the applied load is seen in Figure 23 giving clear indication that the fiber-matrix debond is the only failure initiating event at this fiber spacing.

Table 6: Far-field applied stress at debond initiation in multi-fiber specimens having 2.5d_f fiber spacing

828 Matrix Specimen	Far-field stress at debond initiation (MPa)			Location w/r/t Fiber group
	Top Fiber	Center Fiber	Bottom Fiber	
S250R1C1-E	10.37 ^{SP}	-	6.16 ^{SP}	Exterior
S250R1C1-F	6.70 ^{NP}	6.55 ^{SP}	-	Interior
S250R1C1-G	5.85 ^{NP}		7.83 ^{SP}	Exterior
S250R1C1-H	10.68 ^{NP}	11.96 ^{SP}	11.09 ^{NP}	Exterior
S250R1C1-I	8.90 ^{SP}	9.71 ^{NP}	3.67 ^{NP}	Interior

Table 7 list the specimen's debond initiation measurements, consisting of the width, the central angle, location and debond type. The average debond width results in a central angle of 47° which is one degree off the median of the range of the individual specimen central debond angles of 38° to 54°. All debonds initiated as a spot with a very small length at the fiber pole and grew slowly before specimen final failure as indicated in Table 7. The final failure in all specimens was by fiber-matrix debonding either failing at the center fiber as shown in Figure 24 or at the corner fibers in a similar manner.

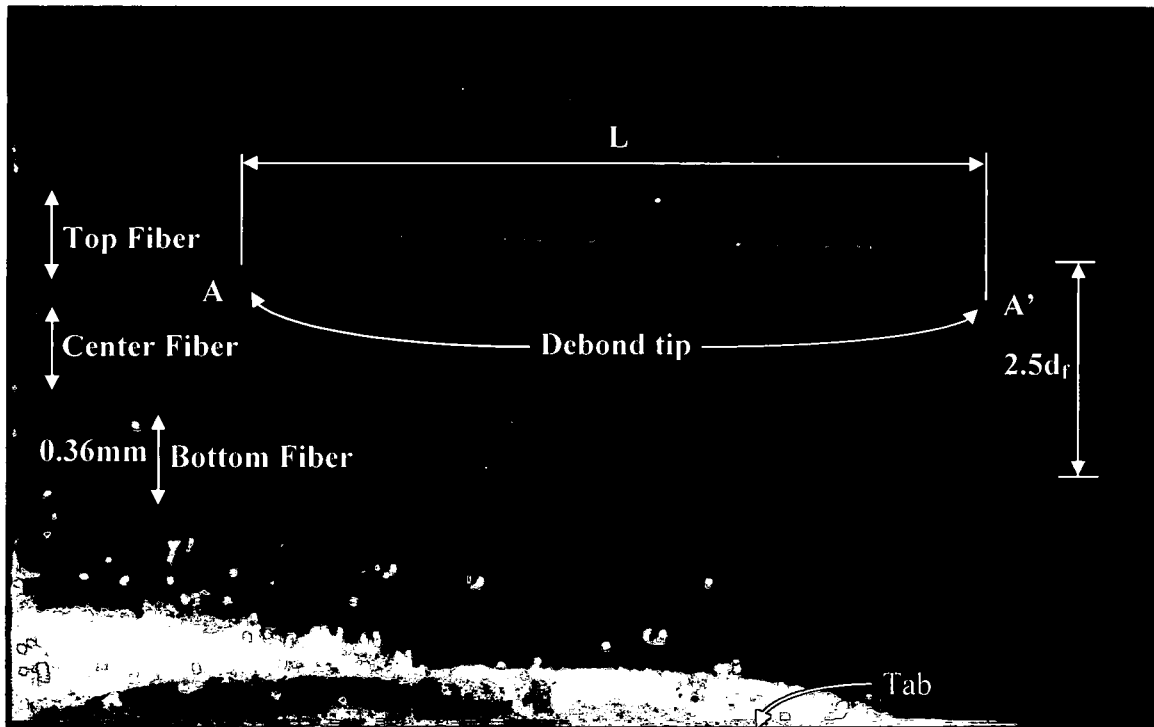


Figure 22: Photomicrograph of steel/2.5d_f cruciform specimen debond

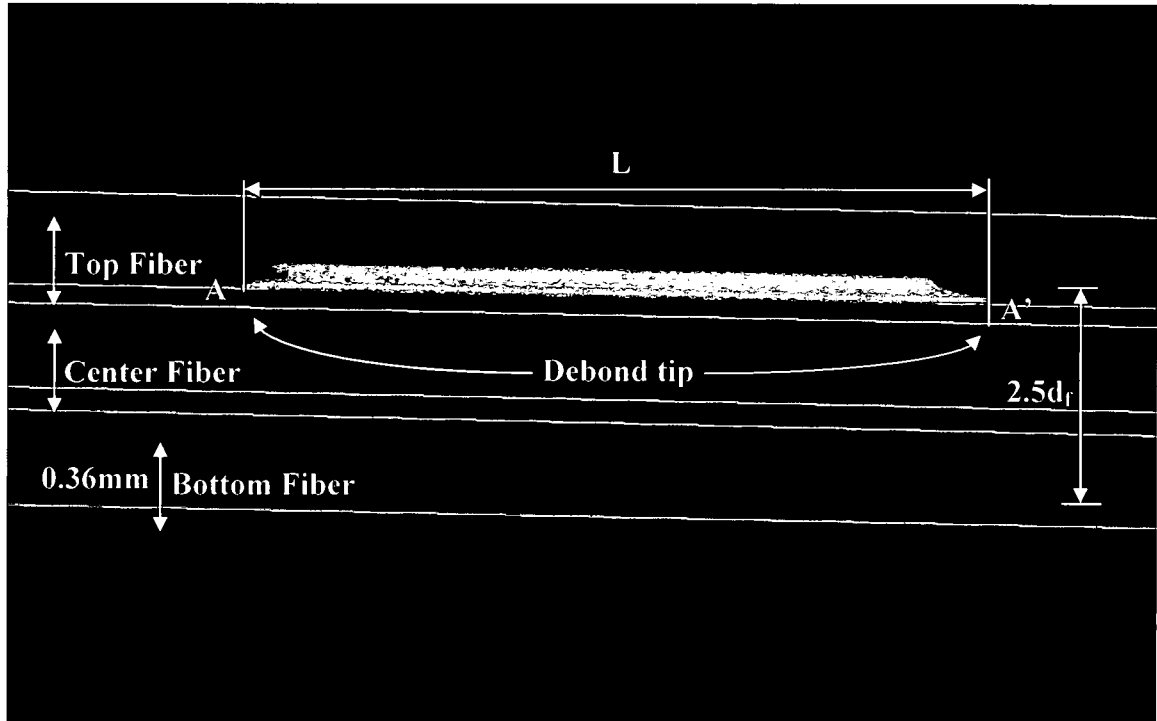


Figure 23: Subtracted image of interfacial debonding in a steel/2.5d_f cruciform specimen

Table 7: Steel/828 2.5d_r cruciform specimen debond measurements where CA = central angle

Specimen	db width (mm)	db Central Angle	Loc	FEM Loc	Type
250R1C1-E	0.019	54°	SP-BF	NP-TF	Spot ~ 0.22 mm
250R1C1-F	0.0189	53°	SP-CF	NP-CF	Spot ~ 0.16 mm
250R1C1-G	0.0099	38°	NP-TF	NP-TF	Spot ~ 0.35 mm
250R1C1-H	Top Back	-	NP-TF	NP-TF	-
250R1C1-I	0.014	46°	NP-BF	SP-TF	Spot ~ 0.04 mm
AVG	0.015	47° Avg CA => 66.5° to 113.5° NP & 246.5° to 293.5° SP			
Std-dev	0.004				

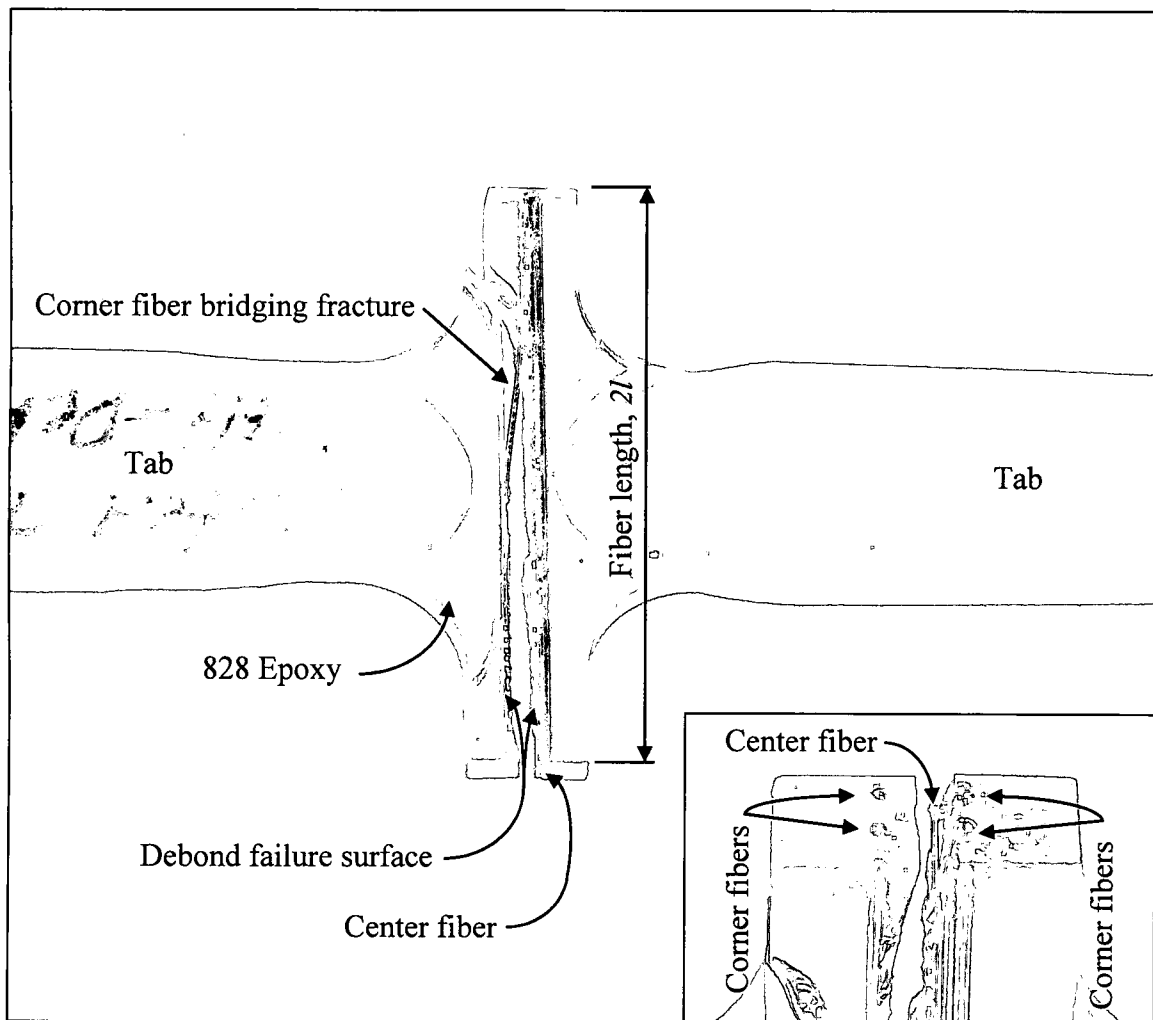


Figure 24: Debond failure of a steel/2.5d_r cruciform specimen with the inset showing a close-up of the fiber ends

Figure 25 shows the fracture surface of a $2.5d_f$ fiber spacing cruciform specimen. The fracture surface analysis was inconclusive as to the location of the fracture initiation. However, the jagged features emitting from the fiber imprint indicate possible shear stress interaction with the normal stress component at final failure. No other failure initiation sites are present on the cruciform failure surface. The fiber imprint surface is smooth indicating a tensile dominated force acting at the interface creating the debond initiation observed experimentally as the first damage mechanism. Consequently, the failure initiated as a fiber-matrix debond as observed during the cruciform test.



Figure 25: SEM image of fracture surface of steel/ $2.5d_f$ cruciform specimen

Steel/828/D-230 $2.0d_f$ Multi-Fiber Cruciform Results. Nine multi-fiber specimens having a fiber spacing of $2.0d_f$ were tested and in every specimen the first failure initiated as a fiber-matrix debond. Table 8 lists the far-field applied stress at failure initiation for the top, center, and bottom fibers. All but one specimen debonded on multiple fibers and in six specimens all three fibers visible in the near field view debonded. Four fibers experienced multiple debonds in that they

initiated in the vicinity of the north pole and south pole of the fiber. Also, the far-field view revealed four fibers debonding in several specimens. In 7 of the 9 specimens the debond initiated on the interior of the fiber group. The average far-field stress at debond initiation is 15.66 MPa.

Table 8: Far-field applied stress at debond initiation in multi-fiber specimens having a 2.0d_f fiber spacing where * indicates vertical cracking after debond initiation

Specimen	Far-Field Stress at debond initiation (MPa)			Location w/r/t Fiber Group
	Top Fiber	Center Fiber	Bottom Fiber	
S200R1C1-A	-	19.28 ^{SP}	18.19^{SP}	Exterior
S200R1C1-B	12.88 ^{NP}	12.48^{NP}	17.52 ^{NP}	Interior
S200R1C1-C*	16.80^{SP}	16.95 ^{SP}	16.95 ^{NP}	Interior
S200R1C1-D	18.96 ^{NP}	19.14 ^{NP}	18.32^{NP}	Interior
S200R1C1-E	19.16 ^{NP}	19.40 ^{SP}	12.14^{NP}	Interior
S200R1C1-F*	13.53 ^{SP}	18.79 ^{NP}	13.21^{SP}	Exterior
S200R1C1-G*	-	13.24 ^{SP}	13.12^{NP}	Interior
S200R1C1-H*	25.77 ^{NP}	14.85^{NP}	16.10 ^{SP}	Interior
S200R1C1-J	-	-	21.86^{NP}	Interior

Similar to the 6.0d_f and 2.5d_f specimens, the 2.0d_f debond initiates in the vicinity of the fiber pole. At this fiber spacing the debond forms almost instantaneously across the field of view instead of more gradually as observed in the 6.0d_f and 2.5d_f specimens. Figure 26 is a photomicrograph showing typical fiber-matrix debonds at this fiber spacing. The debonds shown in the vicinity of the north pole of the top and center fibers extend the full width of view, whereas the debond in the vicinity of the north pole of the bottom fiber only extends to the center of the field of view. Figure 27 is a photomicrograph showing the subtracted images which clearly delineate the limits of the fiber matrix debonds. The fiber edges are superimposed for clarity.

Particular to this fiber spacing, four of the specimens formed vertical or transverse cracks i.e. in the direction of the applied load, after debond initiation but before final failure. Figure 28 is a photomicrograph showing the vertical cracks forming after the top fiber has debonded in the vicinity of the south pole, the center fiber has debonded in the vicinity of both poles and the bottom fiber has debonded in the vicinity of the north pole. Note the angle of the cracks with respect to the fiber horizontal axis, indicates a shear stress component present in the cruciform specimen. Figure 29 is a photomicrograph before formation of the vertical cracks and also shows the top fiber debond at its south pole, the center fiber debond at its south pole and bottom fiber

debond at its north pole. The elapsed time between the images is 10 seconds. In all cases the cracks formed across the fiber group and extended very little into the surrounding matrix. In the four specimens where cracks appeared, they appear to be concentrated within the fiber group, specifically between the top and center fibers. Furthermore for these specimens, the final failure was at the center fiber either at its north hemisphere or at its south hemisphere. In three of the four, the debond initiation was internal to the fiber group at the location of the final failure. It must be noted that at the $2.0d_f$ spacing the south pole of the top fiber is located in the same horizontal plane as the north pole of the center fiber and likewise for the south pole of the center fiber and the north pole of the bottom fiber. Therefore it is conceivable that once the debond initiated and wrapped around the fiber to the fiber equator the debond branched out into the matrix. As load is continually applied the cracks internal to the fiber group link together first then continue rapidly to the exterior of the specimen.

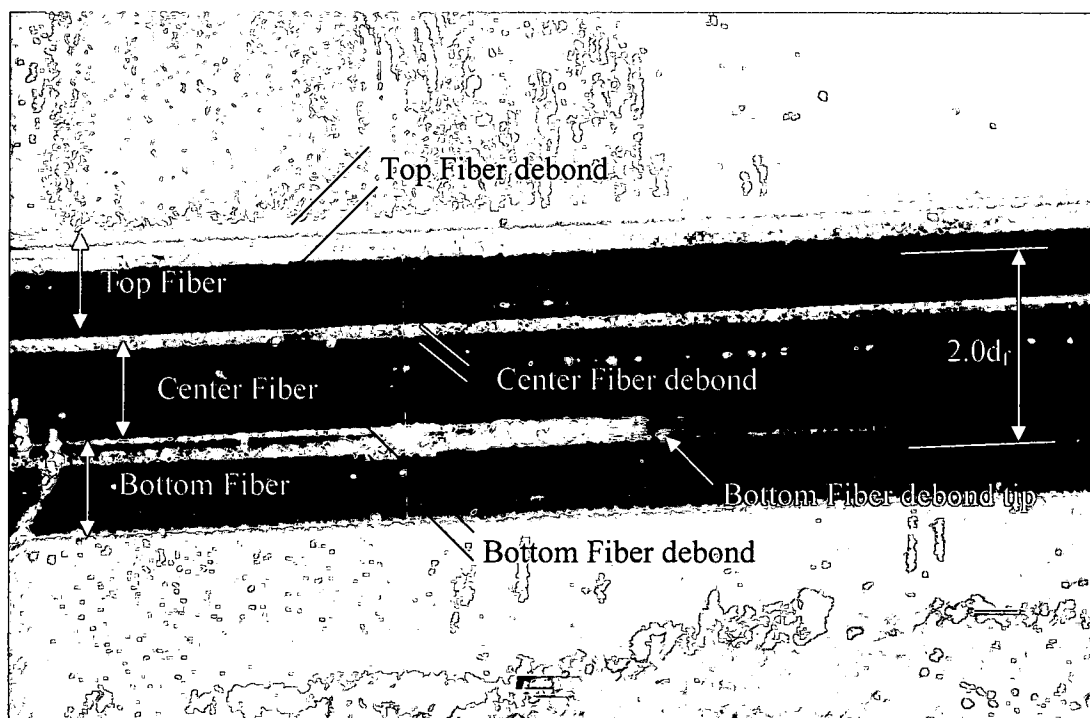


Figure 26: Photomicrograph of steel/ $2.0d_f$ cruciform debond on the top, center and bottom fiber

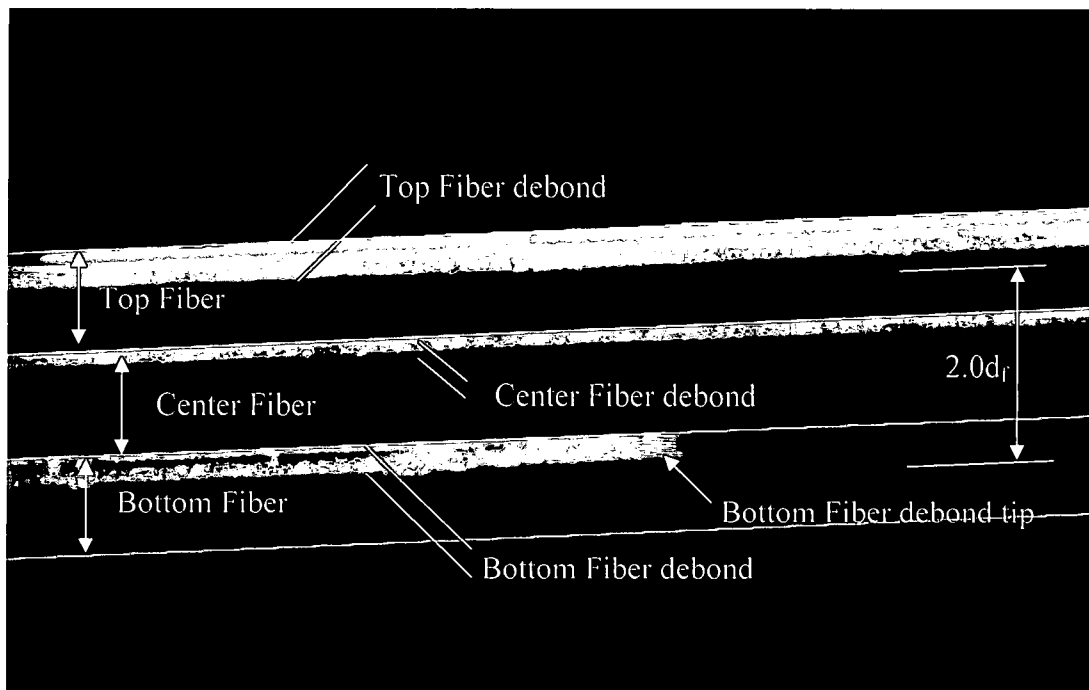


Figure 27: Subtracted image of interfacial debonds on the top, center and bottom fiber in a steel/ $2.0d_f$ cruciform specimen

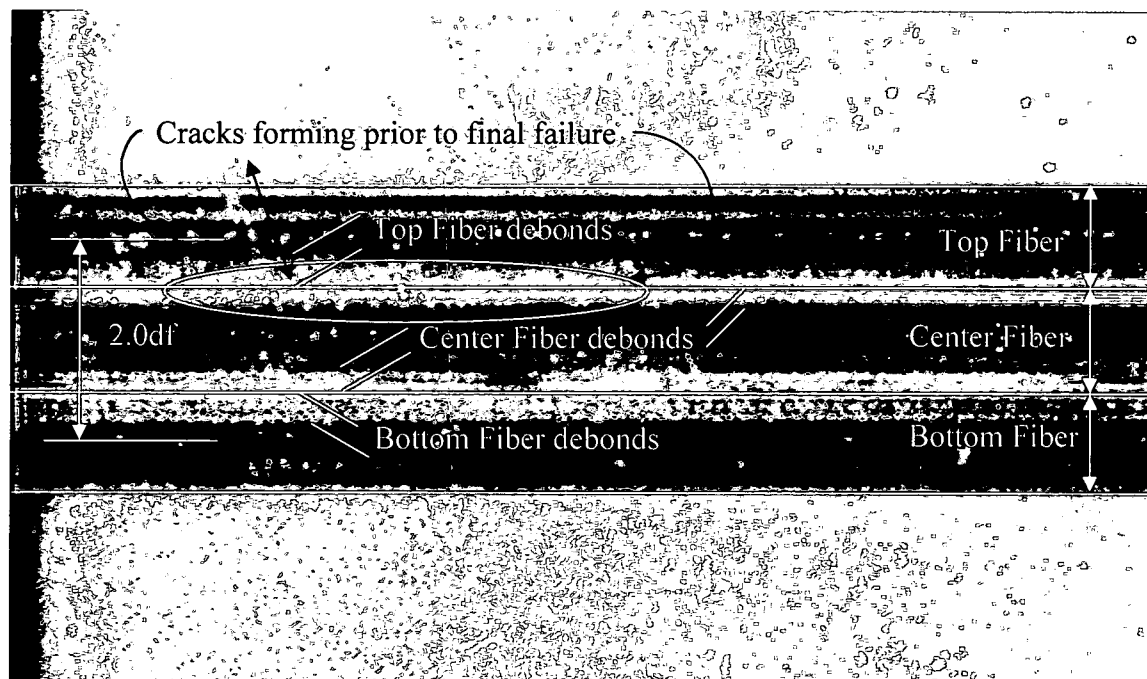


Figure 28: Photomicrograph showing fiber-matrix debonds and cracking after debond initiation in a steel/ $2.0d_f$ cruciform specimen

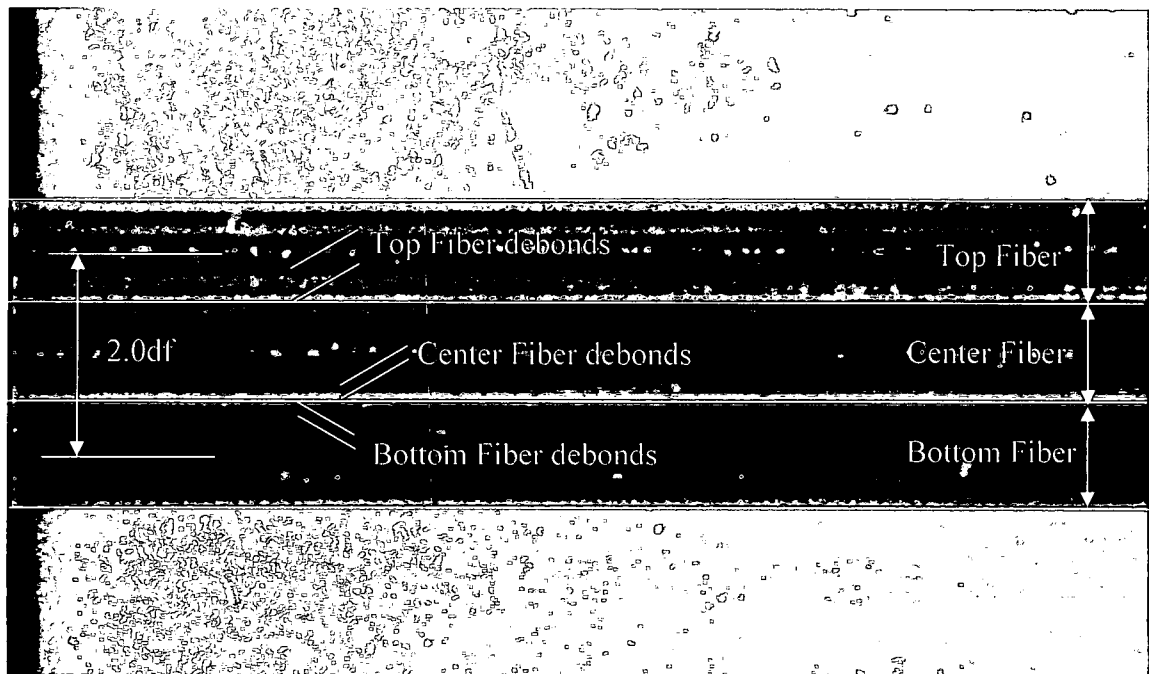


Figure 29: Photomicrograph showing fiber-matrix debonds prior to cracking shown in Figure 28

Each specimen's debond initiation width, central angle, location and debond type is listed in Table 9. For specimen S200R1C1-J the image quality due to the specimen preparation was such that the debond limits could not be measured with any accuracy. The average debond width results in a central angle of 110° which is 3° off the median of the range of the individual specimen central debond angles of 68° to 146° and 3.5° from the average of the individual central angles. Of the specimens where measurements were clearly observed, half the specimens instantaneously debonded across the screen while the other half initiated as a spot and either propagated very slowly or initiated at a finite length as indicated in Table 9.

Table 9: Steel/828 2.0d_f cruciform debond measurements, where CA = central angle

Specimen	db width (mm)	db Central Angle	Loc	FEM Loc	Type
S200R1C1-A	0.039	76°	SP-BF	NP-TF	Spot ~ slow prop
S200R1C1-B	0.069	105°	NP-CF	NP-CF	IAS
S200R1C1-C	0.113	137°	SP-TF	SP-TF	IAS
S200R1C1-D	0.031	68°	NP-BF	NP-BF	Spot ~ slow prop
S200R1C1-E	0.035	74°	NP-BF	SP-TF	Spot ~ 0.2 mm
S200R1C1-F	0.125	146°	SP-BF	NP-TF	IAS
S200R1C1-G	0.110	136°	NP-BF	SP-TF	IAS
S200R1C1-H	0.077	110°	NP-CF	NP-CF	Spot ~ 0.4 mm
AVG	0.075	110° Avg CA => 35° to 145° NP & 215° to 325° SP			
Std-dev	0.04				

Figure 30 shows an SEM image of the fractured surface of a cruciform specimen magnified 200 times indicating that the final failure, delineated by the white arrow, occurred away from the fiber edge. The volcano appearance of the fracture initiation site indicated only tensile forces acting in the loading direction that caused the final failure of the cruciform specimen. The fracture initiation location occurred approximately 0.076 mm from the fiber imprint edge. Analysis of the fracture initiation location surface gave no indication that any shear stress contributed to the final failure. The smooth imprint area of the fiber indicated that a dominating radial or normal force acting at the fiber-matrix interface created the observed fiber-matrix debond initiation. No other failure initiation sites were found on the fracture surface. As with the 6.0d_f and 2.5d_f fiber spacing groups, the failure initiated as a fiber-matrix debond for the cruciform specimens having the 2.0d_f fiber spacing.

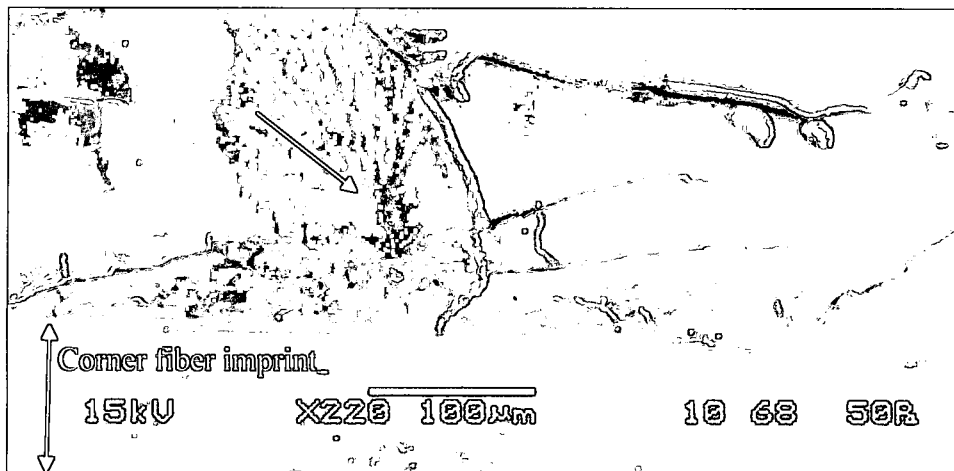


Figure 30: SEM image of fracture surface of steel/2.0d, cruciform specimen

Steel/828/D-230 1.9d, Multi-Fiber Cruciform Results. Continuing to observe the failure initiation as the fiber spacing decreases, ten specimens were tested having a fiber spacing of 1.9d, in the 828/D-230 matrix system. In all cases the failures initiated as a fiber matrix debond. Table 10 lists the far-field applied stress at failure initiation for the top, center, and bottom fibers. All specimens exhibited debonds on multiple fibers, however, only one specimen exhibited a multiple debond on a single fiber. In six of the ten specimens the fiber-matrix debond initiated external to the fiber group, i.e. either in the vicinity of the north pole of the top fiber or in the vicinity of the south pole of the bottom fiber. However, in eight of the ten specimens the final failure occurred internal to the fiber group generally happening around the center fiber either in the vicinity of the south pole of the top fiber or the north pole of the bottom fiber. It is noted that at this fiber spacing the poles of the center fiber are hidden from view by the top and bottom fiber. The average far-field stress at debond initiation is 16.38 MPa.

Table 10: Far-field applied stress at debond initiation in multi-fiber specimens having 1.9d_f fiber spacing

Specimen	Far-field stress and debond initiation (MPa)			Location w/r/t Fiber group
	Top Fiber	Center Fiber	Bottom Fiber	
S190R1C1-G	13.24^{NP}	15.42 ^{SP}	15.41 ^{SP}	Exterior
S190R1C1-H	14.47^{SP}	16.18 ^{NP}	16.29 ^{NP}	Interior
S190R1C1-I	14.97^{SP}	17.38 ^{SP}	17.22 ^{SP}	Interior
S190R1C1-J	16.89^{NP}	17.84 ^{NP}	-	Exterior
S190R1C1-K	16.57^{NP}	16.80 ^{NP}	16.80 ^{NP}	Exterior
S190R1C1-L	-	18.31 ^{SP}	18.25^{SP}	Exterior
S190R1C1-M	-	18.81^{NP}	18.97 ^{NP}	Interior
S190R1C1-N	-	15.51^{SP}	15.51^{NP}	Interior
S190R1C1-O	-	18.44 ^{SP}	16.60^{SP}	Exterior
S190R1C1-P	18.62 ^{NP}	18.62 ^{NP}	18.48^{SP}	Exterior

Figure 31 is a photomicrograph showing the subtracted images clearly illustrating the fiber-matrix debond in the vicinity of the south pole of both the bottom and center fiber. Similar to the 2.0d_f spacing, the debonds occur instantaneously across the field of view. It is also quite obvious that the bottom fiber debond extends almost to the equator of the fiber. The fiber edges have been superimposed for clarity. No other damage from the applied load is seen in Figure 31 giving clear indication that the fiber-matrix debond is the only failure initiating event at this fiber spacing. It should be noted that debonds initiating on the center fiber form as a thin debond occurring almost instantaneously across the field of view, as shown in Figure 31. The far-field view captures the fiber-matrix debond occurring almost instantaneously over a width equal to ¾ of the width of the loading arm. It also confirms that the debonds of the top corner fibers form near the north pole. Therefore it can be assumed that the center fiber debond initiates around the fiber poles. This assumption has a high confidence level since the observed portion of the center fiber behaves as a fiber having debonds forming near the fiber poles.

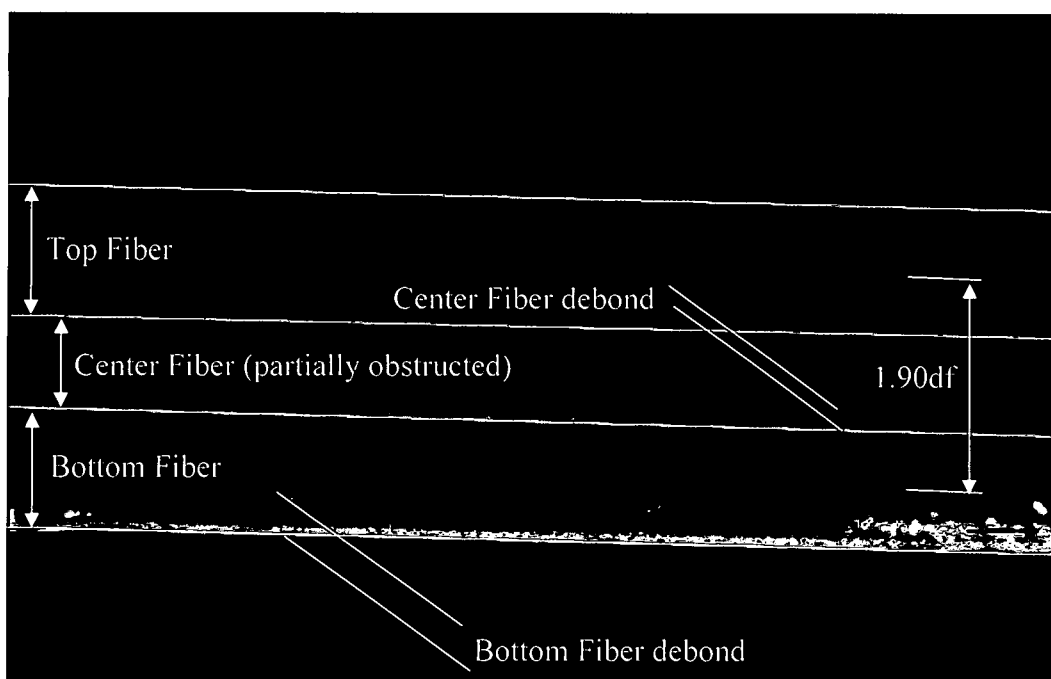


Figure 31: Subtracted image of interfacial debonds on the bottom and center fiber in the steel/1.90d, cruciform specimen

The debond initiation width, central angle, location and debond type of each specimen is listed in Table 11. In three of the ten specimens tested, the debond was obstructed from the view of the primary camera used for the debond measurements. The average debond width results in a central angle of 116° . Since four of the specimens had their debond partially obstructed the standard deviation is rather large for this sample set. Only two specimens instantaneously debonded across the screen while the rest initiated as a spot and either propagated very slowly or initiated at a finite length as indicated in Table 11.

The debond for specimens S190R1C1-J and K initiated around the north pole of the top back fiber, captured by the secondary camera, hence their debond measurements were obstructed from the view of the primary camera. Likewise, specimen S190R1C1-M debond initiated on the center fiber. However, slight fiber misalignment allowed specimen S190R1C1-P debond occurring in the vicinity of the south pole of the bottom back fiber to be caught by the primary camera.

Table 11: Steel/828 1.9d_f cruciform specimen debond measurements

Specimen	db width (mm)	db Central Angle	Loc	FEM Loc	Type
S190R1C1-G	0.140	155°	NP-TF	NP-TF	IAS
S190R1C1-H	0.080	113°	SP-TF	SP-TF	Spot ~ 0.2 mm
S190R1C1-I	0.016	49°	SP-TF	SP-TF	Spot ~ slow prop
S190R1C1-J	NP-TF Back obstructed		NP-TF	NP-TF	
S190R1C1-K	NP-TF Back obstructed		NP-TF	NP-TF	
S190R1C1-L	0.127	147°	SP-BF	NP-TF	IAS
S190R1C1-M	NP-CF obstructed		NP-CF	NP-CF	
S190R1C1-N	0.036	74°	NP-BF	SP-TF	Spot ~ 2.0 mm
S190R1C1-O	0.099	127°	SP-BF	NP-TF	Spot ~ 0.2 mm
S190R1C1-P	SP-BF Back obstructed		SP-BF	NP-TF	
AVG Std-dev	0.083 0.045	116° AVG CA => 32° to 148° NP & 212° to 328° SP			

Similar to the 2.5d_f fiber spacing, analysis of the fracture surface, shown in Figure 32, was inconclusive to the location of the fracture initiation. Figure 32 also shows the same jagged features emitting normal to the fiber, as seen in the 2.5d_f fracture surface. These indicate a possible shear stress interaction with the normal stress acting at final failure. Although, the fiber imprint is relatively smooth the spotty features shown also occur in the 6.0d_f, 2.5d_f and 2.0d_f fiber spacing groups. In all of those cases the failure initiation is fiber-matrix debonding. No other failure mechanisms features were seen in the fracture surface analysis. Therefore, failure initiates as a fiber-matrix debond as was experimentally observed.

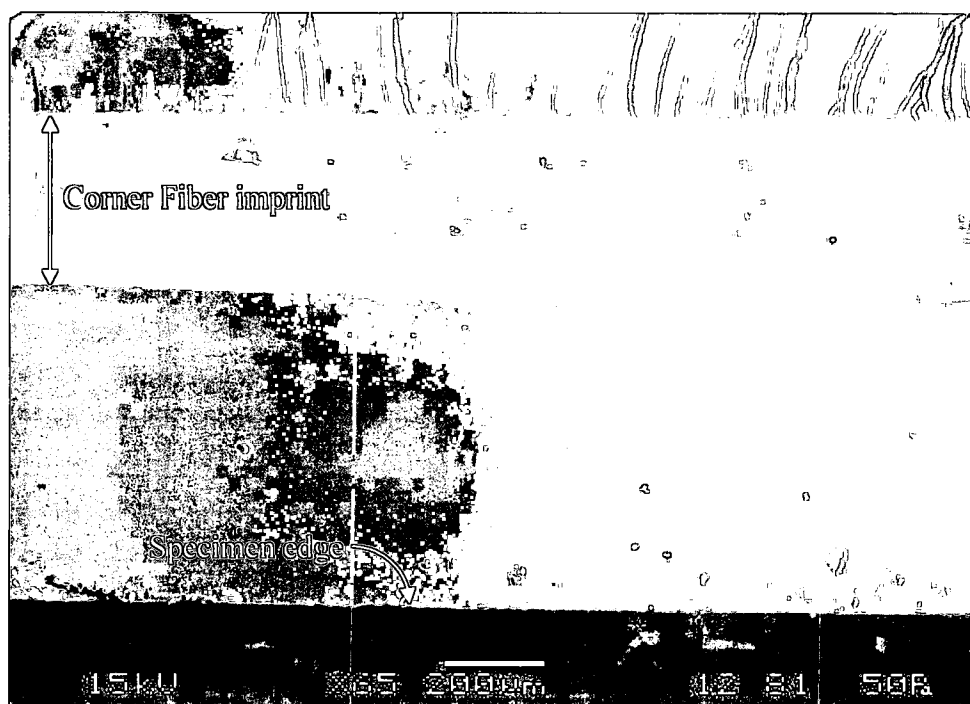


Figure 32: SEM image of fracture surface of steel/1.9d_f cruciform specimen

Steel/828/D-230 1.84d_f Multi-Fiber Cruciform Results. Unlike the 6d_f, 2.5d_f, 2.0d_f and 1.9d_f fiber spacing, the fiber-matrix interface in specimens at the 1.84d_f spacing generally did not debond first. Instead, damage initiated mostly in the form of matrix cavitation and appeared as light grey or white spots in the matrix.

Figure 33 exhibits photomicrographs of a multi-fiber composite with 1.84d_f fiber spacing when (a) under a far-field stress of 0.62 MPa, (b) under a far-field stress of 2.87 MPa, (c) under a far-field stress 8.17 MPa and (d) under a far-field stress of 12.65 MPa. The fiber edges have been highlighted in these figures by a white line to clarify the fiber spacing. The top and bottom corner fibers are clearly seen whereas the center fiber is partially blocked due to the fiber spacing. The development of white spots in the matrix due to cavitation is seen, as marked in Figure 34, by the white ellipsoids. As the load increases, the number of cavitations also increase as shown in Figure 35 with the new cavitations shown in white and the previously developed cavitations shown in black. Note the variations in the size and intensity of the cavitations as some seem to be growing with increasing load. Subsequently, the fiber-matrix interface also debonds as the

applied load is further increased as shown in Figure 36. In addition, cavitations continue to form as shown by the white ellipsoids in Figure 36. Cavitation growth can be seen by inspecting the cavitations on both sides of a point marked **X** shown in Figure 34, 35 and 36.

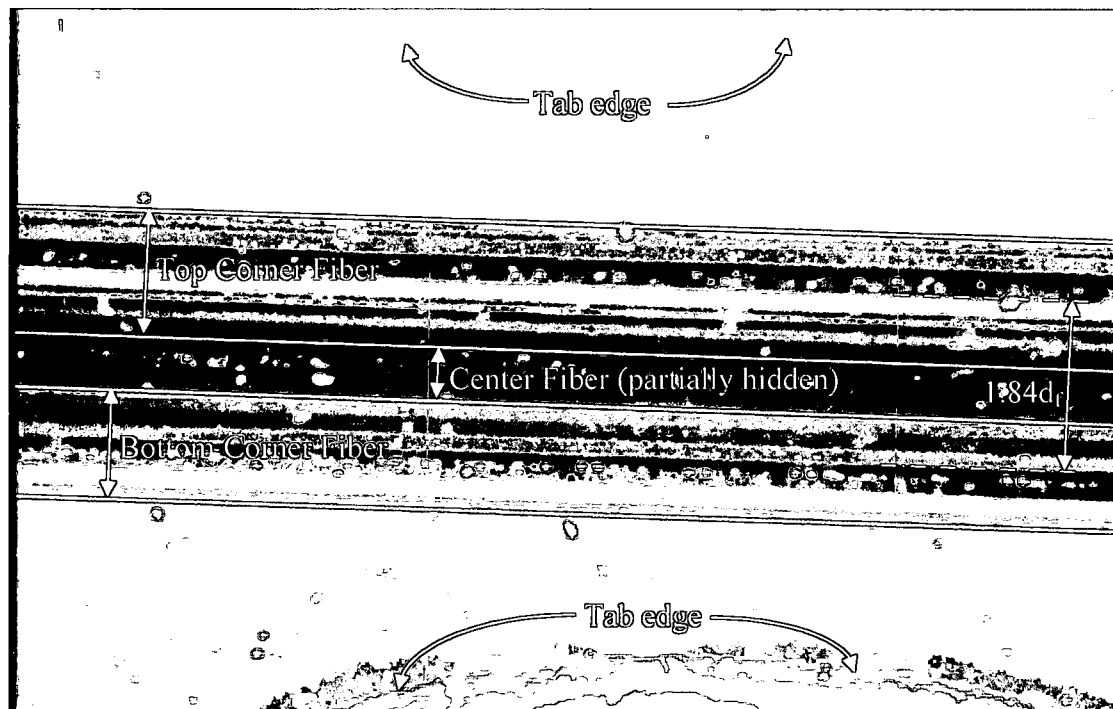


Figure 33: Photomicrograph of steel/1.84d_r cruciform specimen showing no damage under a far-field stress of 0.62 MPa

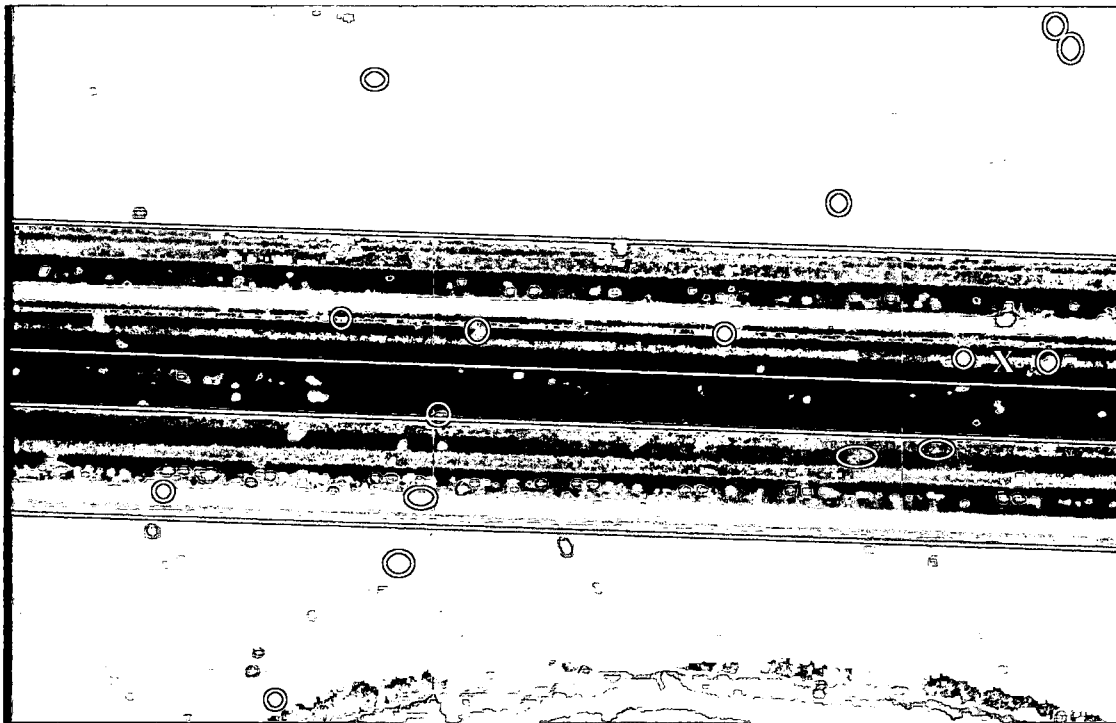


Figure 34: Photomicrograph of steel/1.84d, cruciform specimen showing matrix cavitation under a far-field stress of 2.87 MPa

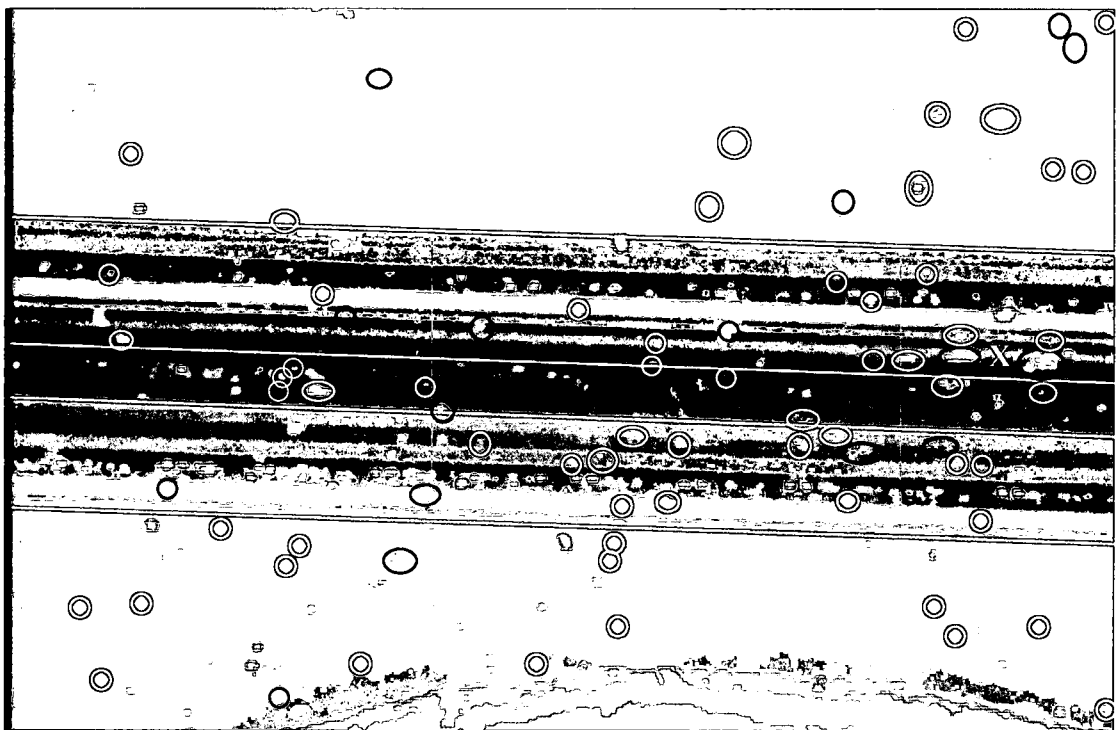


Figure 35: Photomicrograph of steel/1.84d, cruciform specimen showing matrix cavitation under a far-field stress of 8.17 MPa

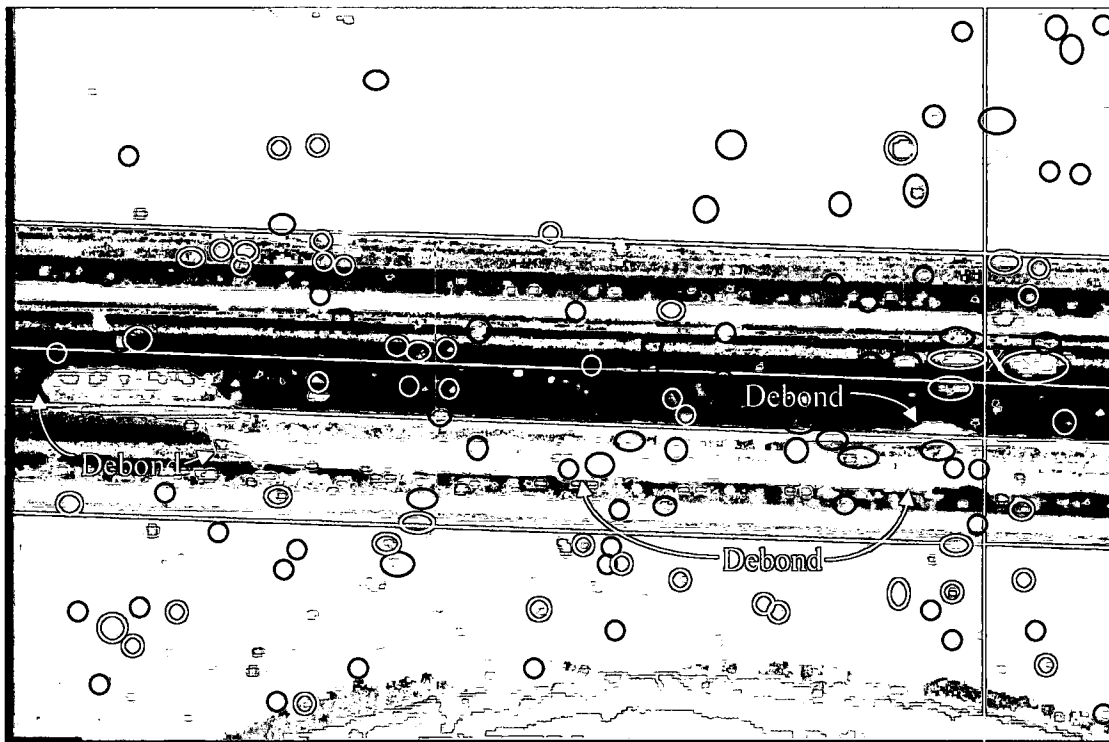


Figure 36: Photomicrograph of steel/1.84d, cruciform specimen showing matrix cavitation and fiber-matrix debonding under a far-field stress of 12.65 MPa

The image subtraction technique was used to clarify the cavitation occurring in the specimen during loading. Figure 37 shows the resulting image subtracting Figure 34 from the base image and the cavitations are clearly identifiable and vary in intensity and shape. The matrix cavitations occur within the fiber grouping, i.e. the area bounded by the north pole of the top corner fiber and the south pole of the bottom corner fiber and around the surrounding area. Figure 38 shows the resulting image obtained by subtracting Figure 35 from the base image. As the far-field stress increased from 2.87 MPa in Figure 37 to 8.17 MPa in Figure 38, more cavitations appear and grow in size. More cavitations appeared within the fiber grouping than outside of the fiber grouping. Once cavitation occurred, the stress at that point is relieved; however, as load is continuously applied the surrounding area becomes further stressed forming additional cavitations. The cavitation growth can be attributed to coalescence of individual cavitation events into micro cracks or micro crack growth. This is different than a fiber-matrix debond in that the debond occurs at the fiber-matrix interface and for the most part propagates

along the fiber length and circumference exhibiting a distinct change in length and area. On the other hand, the cavitation growth is observed as a larger spot independent of fiber direction occurring instantaneously several seconds after initiation, and is not continuous like the fiber-matrix debond. The time difference shown in Figure 37 is 19 seconds whereas the time difference shown in Figure 38 is 59 seconds. The cavitations appear instantaneously and independently over the time range while several seconds may lapse between individual cavitation formations. In some cases, however, they occur between frames of the videotaped test. Figure 39 is the subtracted image between Figure 36 and the base image and shows the fiber-matrix debond, additional cavitations and cavitation growth.

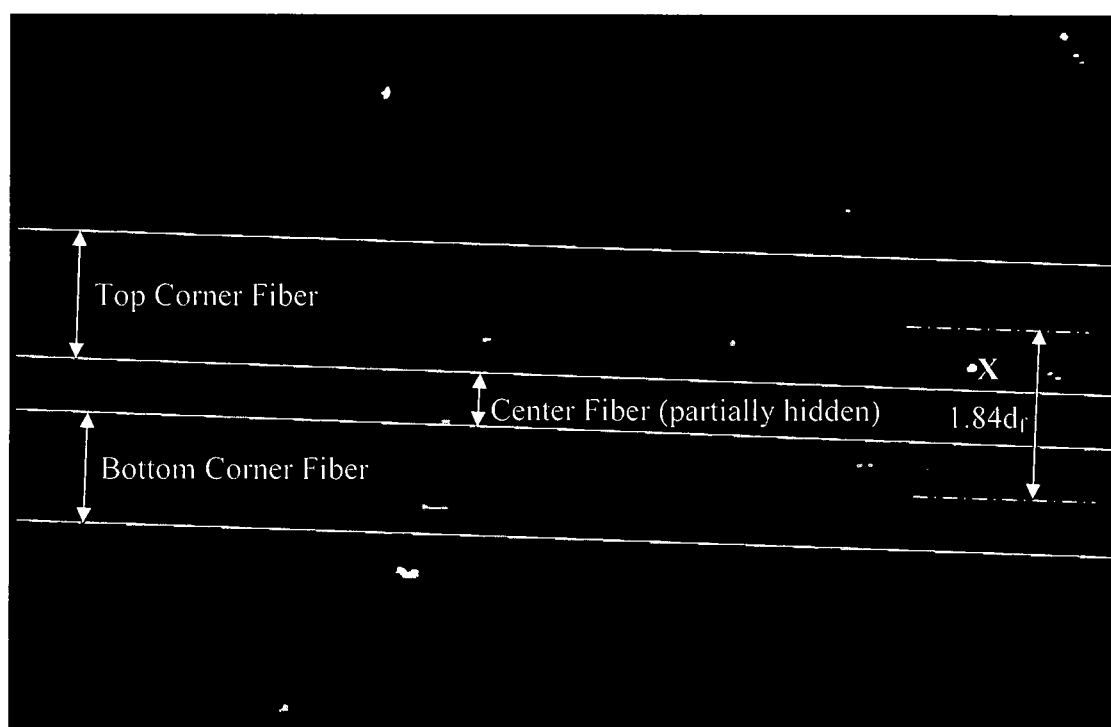


Figure 37: Subtracted image showing matrix cavitation in steel/ $1.84d_f$ cruciform specimen under a far-field stress of 2.87 MPa

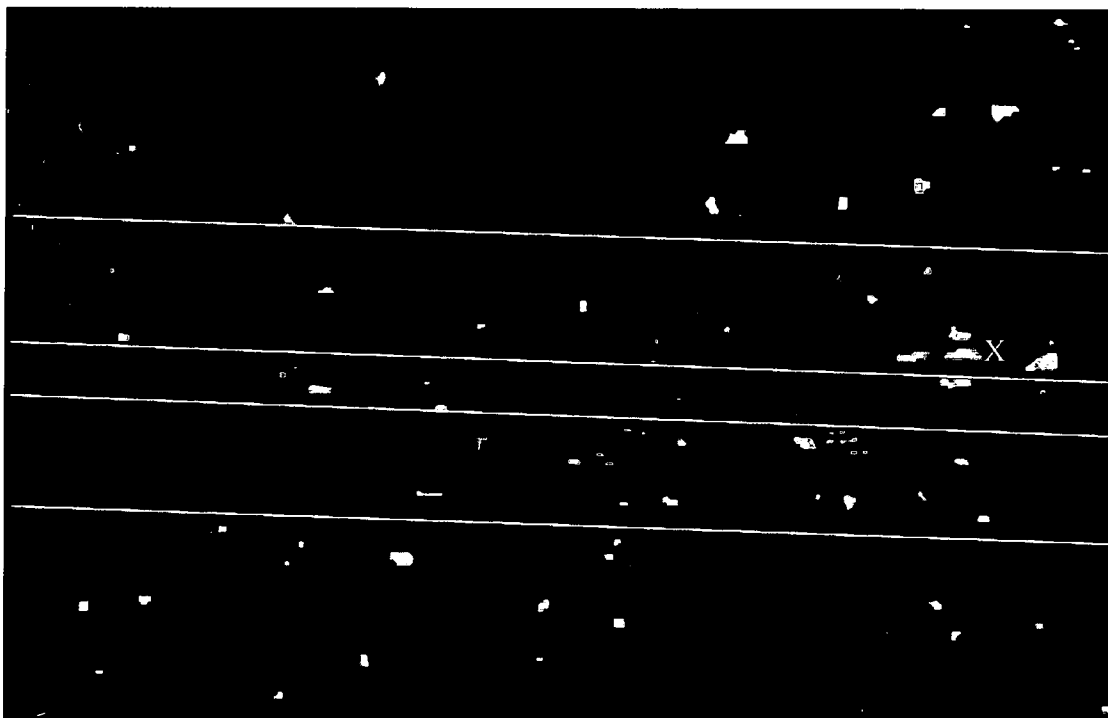


Figure 38: Subtracted image showing matrix cavitation in steel/1.84d_f cruciform specimen under a far-field stress of 8.17 MPa

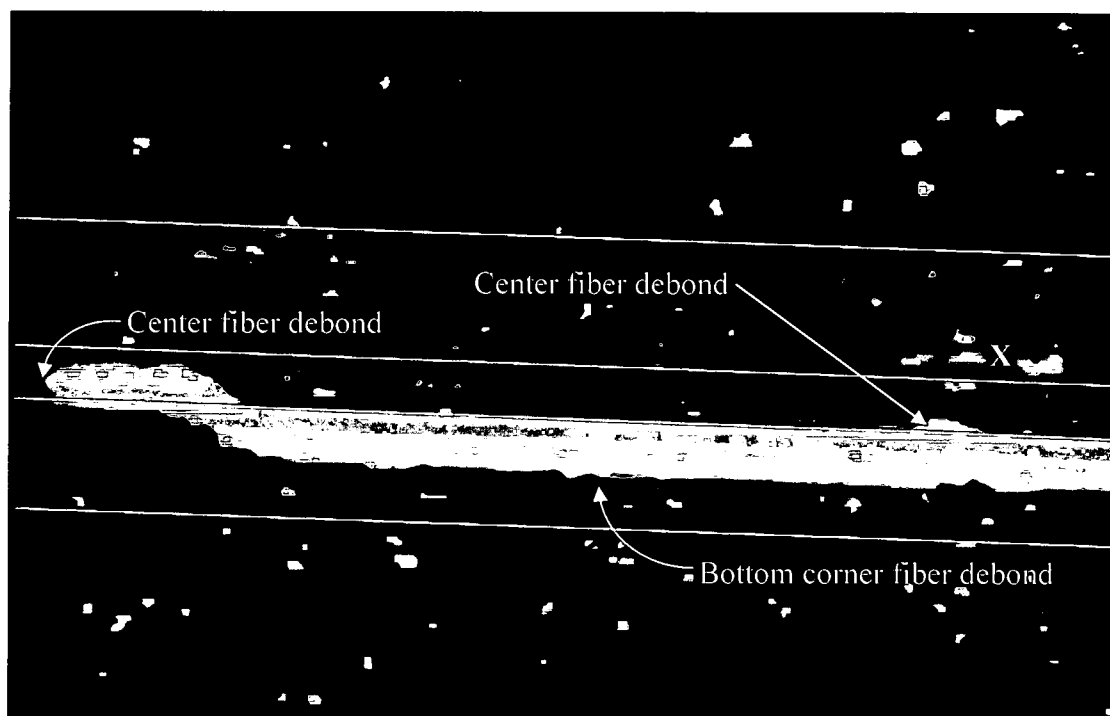


Figure 39: Subtracted image showing matrix cavitation in steel/1.84d_f cruciform specimen under a far-field stress of 12.65 MPa

Table 12 lists the far-field stress at which damage initiated as matrix cavitation and the far-field stress levels at which the fiber-matrix interface debonded in composites with $1.84d_f$ fiber spacing. It is observed that failure initiated as matrix cavitation for all but one sample tested. The average stress values for the initial cavitation and subsequent initial fiber-matrix debonding for the $1.84d_f$ fiber spacing specimens were 3.97 MPa and 12.11 MPa, respectively. It should be noted that specimen D does not figure in the calculation of the average cavitation initiation far-field stress since it debonded first. All specimens failed at the center fiber as shown in Figure 40.

Table 12: Far-field applied stress at matrix cavitation and debond initiation in multi-fiber specimens having $1.84d_f$ fiber spacing

828 Matrix Specimen	Far-field stress at cavitation (MPa)	Far-field stress at debond initiation (MPa)		
		Top Fiber	Center Fiber	Bottom Fiber
S184R1C1-D	3.90	2.90 ^{NP}	-	8.79 ^{SP}
S184R1C1-E	1.31	-	12.76 ^{SP}	12.61 ^{NP}
S184R1C1-F	4.93	18.59 ^{NP}	-	18.63 ^{NP}
S184R1C1-G	5.67	14.34 ^{NP}	14.46 ^{NP}	14.80 ^{SP}

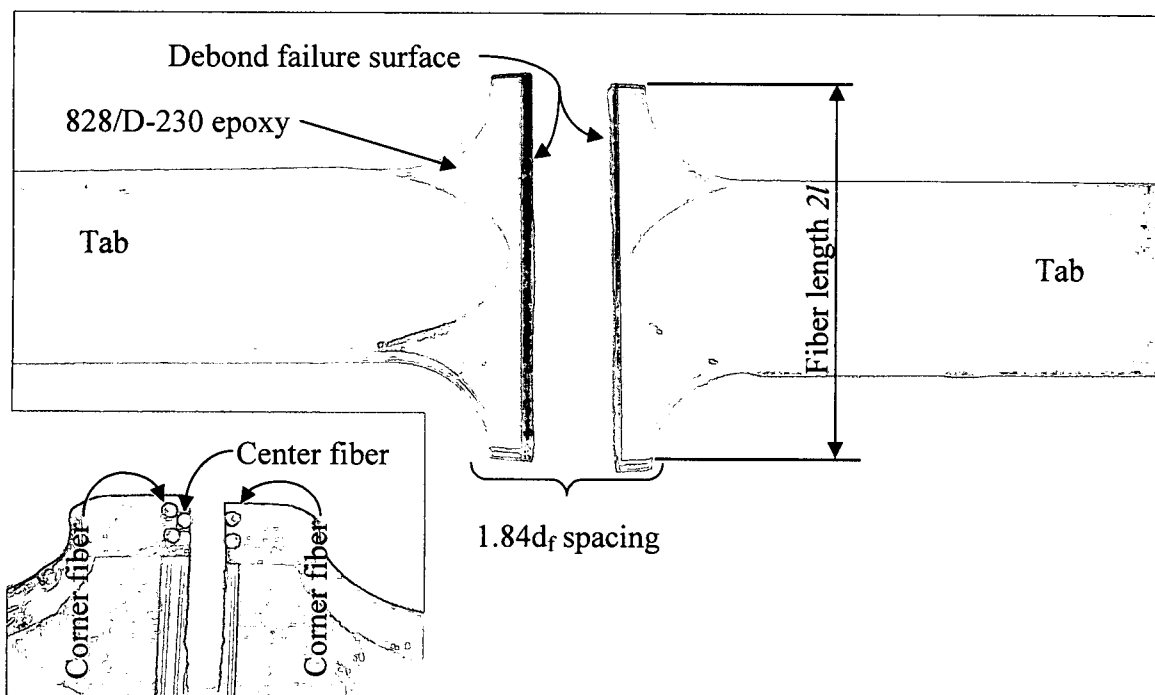


Figure 40: Resultant final failure of steel/1.84d_f cruciform specimen

Figure 41 shows an SEM image of the fracture surface of the 1.84d_f fiber spacing cruciform specimen. Typical with the 6.0d_f, 2.5d_f, 2.0d_f and the 1.9d_f fiber spacing groups are the jagged features emitting almost normal to the fiber imprint, however, the white arrow points to a failure initiation site in the matrix area away from the fiber-matrix interface. This feature appears as a spiral “U” shaped hole not present in the fracture surface analysis of the aforementioned fiber spacing groups. Figure 42 is an SEM image of the spiral U shaped hole at a magnification of 230 times and Figure 43 is an SEM image of the mating side of the of the spiral U shaped hole at the same magnification.

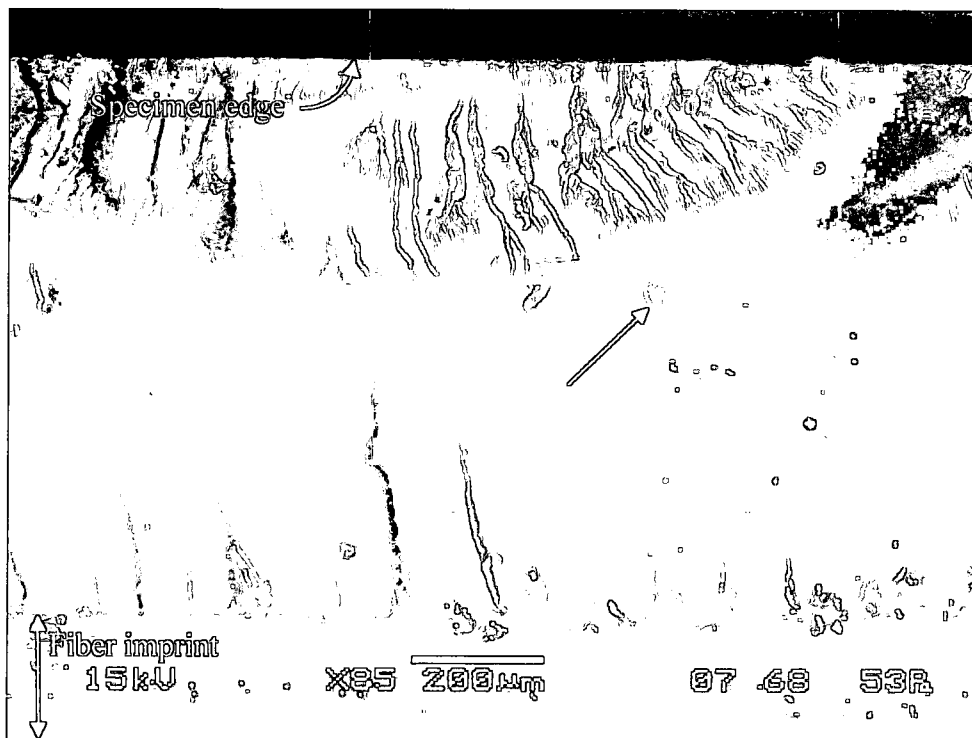


Figure 41: SEM image of fracture surface of steel/1.84d_f cruciform specimen

At the tip of the arrow in Figures 42 and 43 there appears to be a semi-circle shape in the feature. Specifically in Figure 43 the arrow points at the bottom of the spiral U shaped plane. This point would seem to be the location of the damage initiation since it appears to be at the deepest point in the spiral shaped “U” shown in Figure 42 and correspondingly at the peak of the spiral shaped “U” shown in Figure 43. It is possible that the featured captured on the fracture surface

could be created in the follow manner: the dominating or first principal stress would be normal to the plane the arrows are pointing to in Figures 42 and 43. The second and third principal stress, orthogonal to the first principal stress, would create the rounded spiral U shape of the feature. Imagine rolling a lump of clay into a log then twisting it while pulling it apart. This creates very similar features as those shown on the fracture surface of the 1.84d_f cruciform specimen. Since failure initiation at this fiber spacing was experimentally observed as matrix cavitation and no other failure mechanisms appear to be present on the fracture surface; this feature was most likely created by cavitation of the matrix under a triaxial state of stress. In addition, the cavitation measures approximately 0.031 mm in width parallel to the fiber direction. This size would be clearly visible with the high magnification camera used for all cruciform experiments.

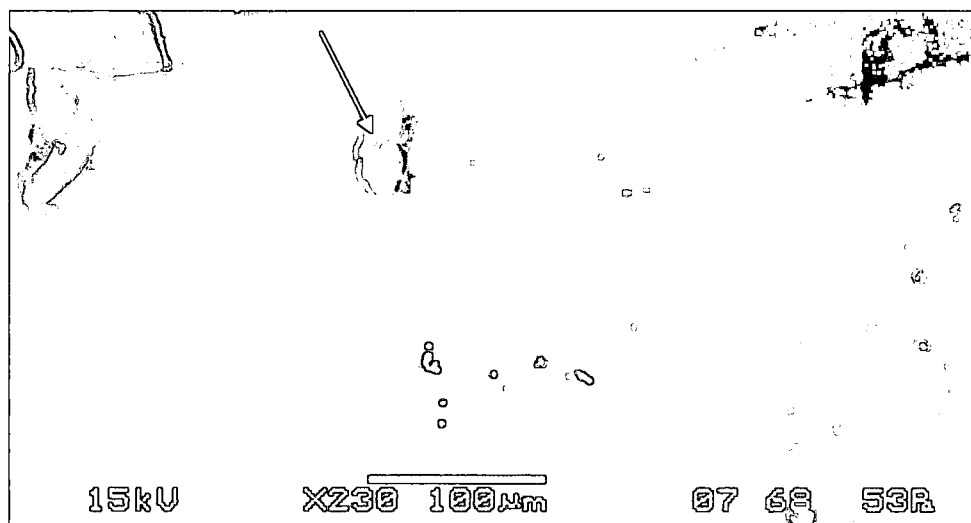


Figure 42: SEM image of failure initiation steel/1.84d_f cruciform at 230 times magnification



Figure 43: SEM image of mating failure initiation steel/1.84d_f cruciform at 230 times magnification

Steel/828/D-230 1.75d_f Multi-Fiber Cruciform Results. Seven model cruciform specimens were tested having fiber spacing of 1.75d_f and like the 1.84d_f spacing specimens in the 828/D-230 matrix system the failure initiated as matrix cavitation for all specimens. Subsequent to matrix cavitation all specimens exhibited fiber-matrix debonding. Table 13 lists the far-field stress at which damage initiated as matrix cavitation and the far-field stress at which the fiber-matrix interface debonded. The average far-field stress at failure initiation is 4.67 MPa where the average far-field stress at first fiber-matrix debonds is 7.88 MPa. Like the 1.84d_f 828/D-230 specimens, the cavitation is characterized by light grey almost white spots occurring instantaneously as the specimens is loaded. Employing the image subtraction technique, Figure 44 shows the typical development of matrix cavitations in the 1.75d_f specimens at a far-field stress of 7.58 MPa. The fiber edges have been superimposed for clarity. After continued loading, Figure 45 shows continuous matrix cavitation development in and around the fiber group under a far-field stress of 9.77 MPa. Cavitation growth is evidenced by comparing the size and shape of the cavitation marked by the letter X in Figure 44 with that in Figure 45. Figure 46 shows additional cavitations occurring in and around the fiber group and a fiber-matrix debond on the south pole of the bottom fiber at a far-field stress of 11.13 MPa. Comparing Figure 45 and 46 in the fiber-matrix debond area reveals additional matrix cavitations after the debond. This indicates

that the cavitations form away from the fiber-matrix interface in addition to forming at the fiber-matrix interface. The cavitation light intensity is also an indicator of possible cavitation location where the brighter cavitations would form at or very close to the fiber interface or on the outside surface of the specimen.

Table 13: Far-field applied stress at matrix cavitation and debond initiation in multi-fiber specimens having $1.75d_f$ fiber spacing

Specimen	Far-field stress at cavitation (MPa)	Far-field stress at debond initiation (MPa)		
		Top Fiber	Center Fiber	Bottom Fiber
S175R1C1-A	6.11	12.38 ^{SP}	-	10.20 ^{SP}
S175R1C1-B	2.66	10.58 ^{NP}	13.01 ^{SP}	7.82 ^{SP}
S175R1C1-C	3.79	8.80 ^{SP}	5.29 ^{SP}	5.29 ^{NP}
S175R1C1-D	6.01	11.51 ^{337.5°}	11.19 ^{SP}	15.04 ^{SP}
S175R1C1-E	5.31	8.30 ^{SP}	11.77 ^{NP}	5.46 ^{NP}
S175R1C1-F	4.33	9.48 ^{NP}	6.14 ^{NP}	6.79 ^{NP}
S175R1C1-G	4.46	9.03 ^{NP}	-	12.19 ^{NP}

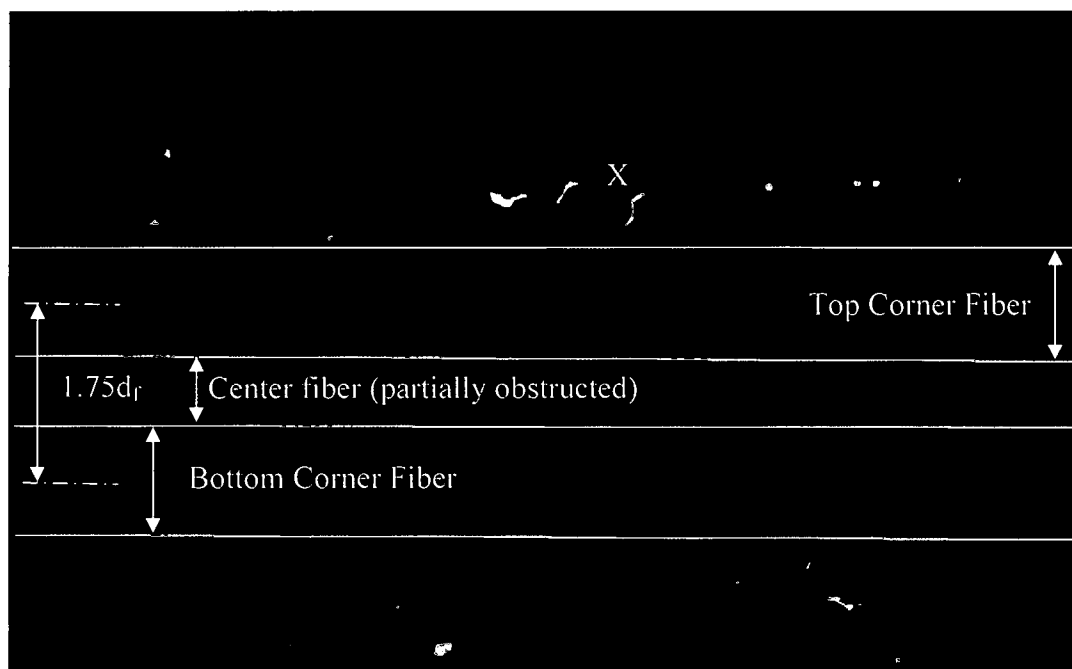


Figure 44: Subtracted image showing matrix cavitation in a steel/ $1.75d_f$ cruciform specimen at a far-field stress of 7.58 MPa

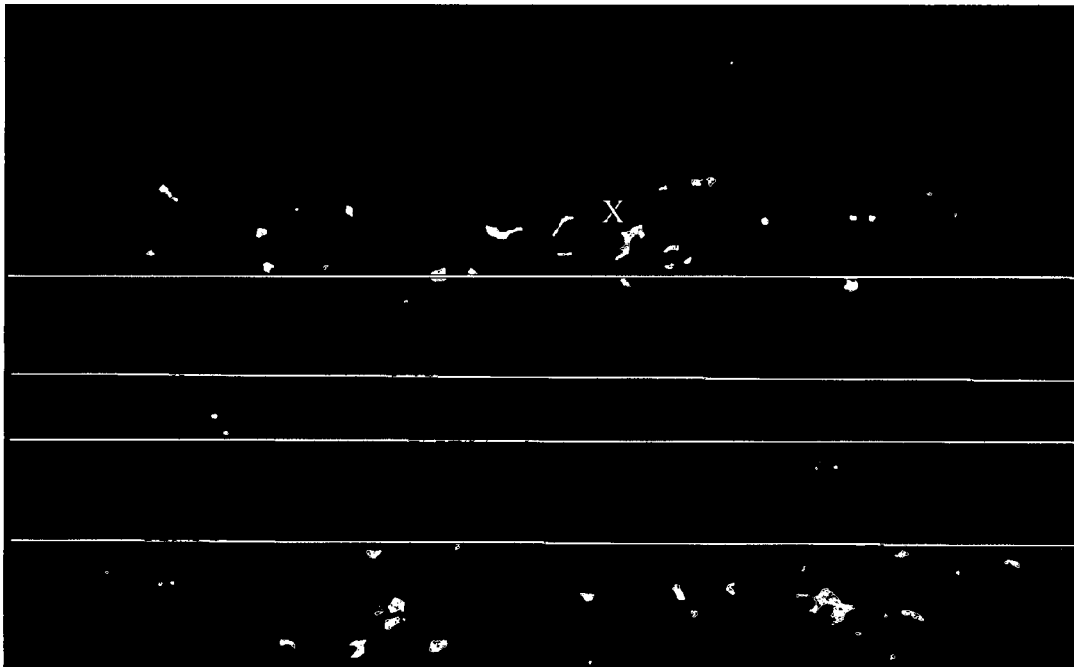


Figure 45: Subtracted image showing additional matrix cavitation and cavitation growth in a steel/1.75d, cruciform specimen at a far-field stress of 9.77 MPa

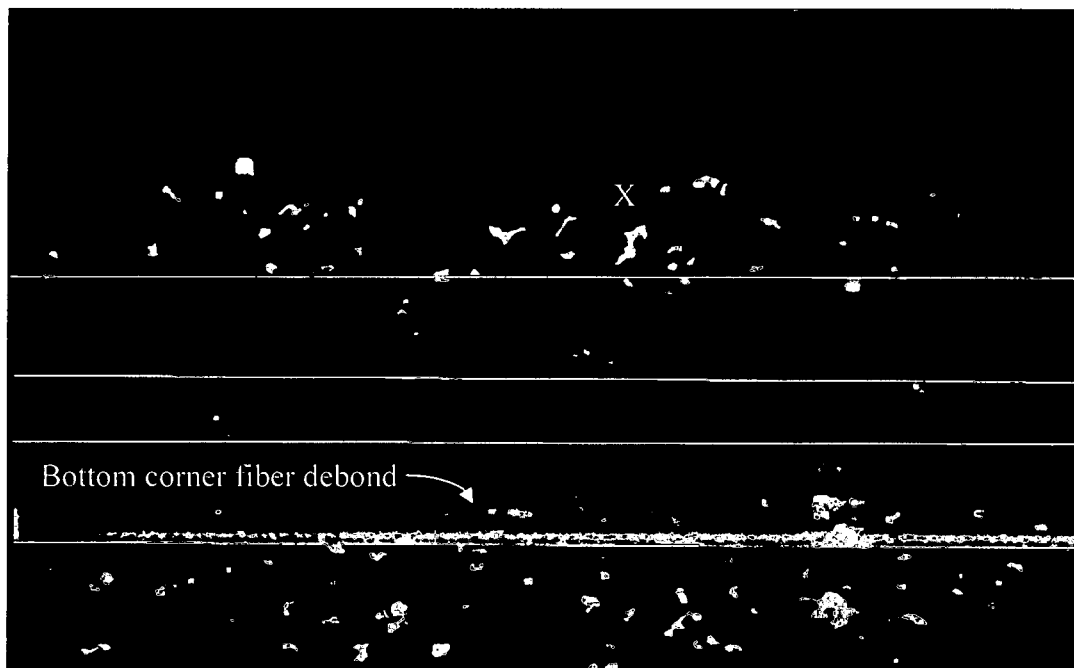


Figure 46: Subtracted image showing additional matrix cavitation, fiber-matrix debonding and cavitation growth in a steel/1.75d, cruciform specimen at a far-field stress of 11.13 MPa

Figure 47 shows an SEM image of the fracture surface of the 1.75d_f fiber spacing cruciform specimen. The feature pointed out by the white arrow is potentially the failure initiation site in the matrix away from the fiber-matrix interface. It is also very similar to the cavitation feature shown in Figure 43 on the fracture surface of the 1.84d_f fiber spacing cruciform specimen. Although, the feature shown in Figure 47 is more circular than that shown in Figure 43, both have a spiral pattern to the cleavage delineating the different horizontal planes of the feature. Also shown in Figure 47 are two chevron shaped features to the south and west of the white arrow. These features indicate a shear component of the failure stress.

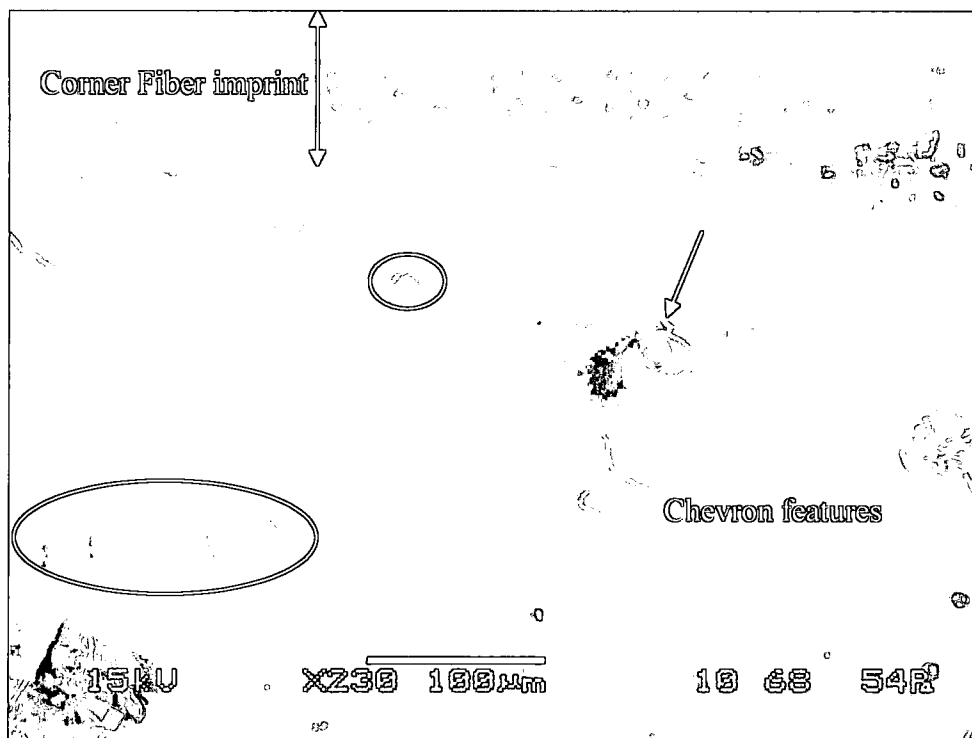


Figure 47: SEM image of failure initiation site for the steel/1.75d_f cruciform specimen at 230 times magnification

Figure 48 is an SEM image of the mating surface to Figure 47. The white arrow points to the mating feature shown in Figure 47. Quite apparent is the spiral pattern to the cleavage lines delineating the different stratifications of the failure initiation site shown in Figure 48. Encircled by the white ellipsoids in Figure 47 and 48 are more possible failure initiation sites having a similar

appearance as the top plateau of the feature pointed out by the white arrow in Figure 47. The encircled features shown in Figure 47 clearly have a flat horizontal plane depressed in the surrounding matrix surface. Those features encircled in Figure 48 are the relief patterns thus they are plateaus relative to the surrounding matrix surface. Since the encircled features and the feature pointed out by the white arrow are very similar it is highly likely that they were formed in the same manner. Thus, in this case the initiation point appears to be the small almost square plane pointed out by the white arrow in Figure 47. Consequently, the first principal stress acts normal to this plane while the second and third principal stresses, orthogonal to the first principal stress, create the spiral cleavage pattern. Like the $1.84d_f$ fiber spacing, since the first damage mechanism at this fiber spacing is experimentally observed as matrix cavitation and no other failure mode appear on the fracture surface; it can be concluded that this feature is a direct result of cavitation of the matrix due to a triaxial state of stress. This cavitation feature measures approximately 0.04 mm parallel to the fiber direction and would be clearly observed by the high magnification cameras used for all cruciform experimentation.

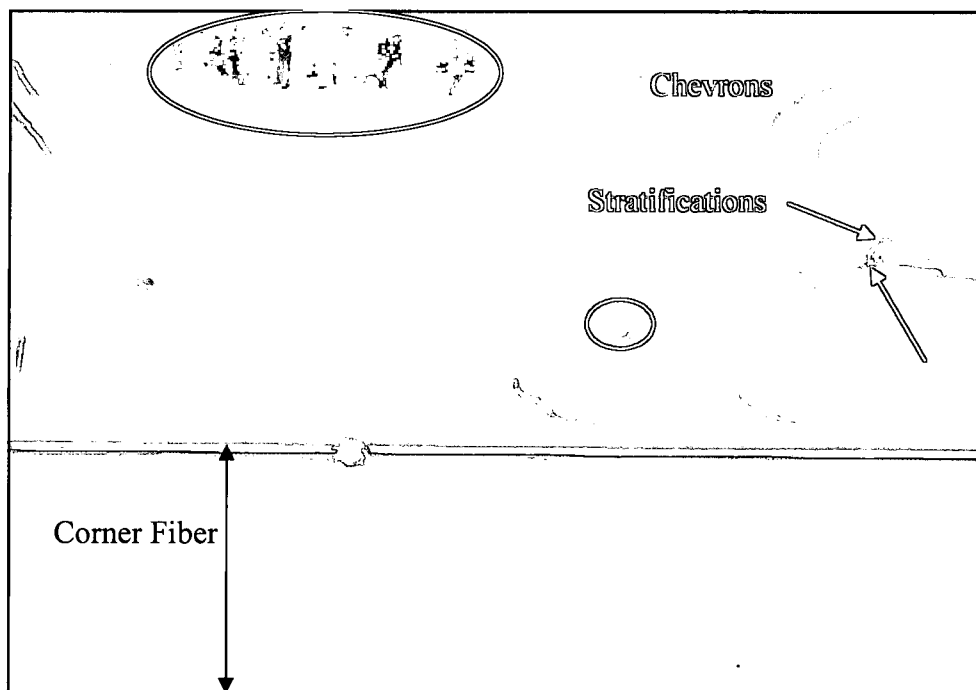


Figure 48: SEM image of the mating failure initiation site for the steel/ $1.75d_f$ cruciform specimen at 230 times magnification

It should be noted that porosity features are shown in the fiber imprint area of Figure 47. These are due to microscopic bubbles forming at the fiber-matrix interface while pouring the matrix into the cruciform molds. The largest bubbles range in diameter between approximately 0.01 mm to 0.006 mm. these were undetected prior to testing and were viewed as existing surface defects as described in the Photomicrograph Image Analysis section. These micro-bubbles did not affect the experimental results since matrix cavitation was observed, and confirmed by the image analysis technique, as the first failure mode for all specimens away from the fiber-matrix interface.

Steel/828/D-230 1.57d_f Multi-Fiber Cruciform Results. Finally 12 specimens having the smallest fiber spacing equivalent to 1.57d_f in the 828/D-230 matrix system were tested. The damage initiation mode in all specimens was fiber-matrix debonding. Table 14 lists the far-field applied stress at failure initiation for the top, center and bottom fibers. In seven of the twelve specimens the failure initiated internal to the fiber group and resulted in a final failure either at the south pole of the top fiber or the north pole of the bottom fiber. In addition, five of the twelve specimens initiated failure other than in the vicinity of the fiber poles. All but two specimens exhibited debonds on multiple fibers. In specimen S157R1C1-P the fibers were misaligned such that the center fiber was bowed out to the front specimen in the loading arm region of the cruciform. Thus, it was in full view but the proper fiber configuration was maintained at fiber arm ends. Therefore, in specimen S157R1C1-P the south pole of the top corner fiber and the north pole of the bottom corner fiber were obstructed. The average far-field stress at fiber-matrix debond initiation for the 1.57d_f fiber spacing was 8.29 MPa.

**Table 14: Far-field applied stress at debond initiation in multi-fiber specimens having
1.57d_f fiber spacing**

Specimens	Far-field stress at debond initiation (MPa)			Location w/r/t Fiber Group
	Top Fiber	Center Fiber	Bottom Fiber	
S157R1C1-A	12.54 ^{NP}	-	11.65 ^{NP}	Interior
S157R1C1-B	9.09 ^{SP}	8.99 ^{NP}	-	Interior
S157R1C1-C	-	9.37 ^{330°}	11.16 ^{NP}	Interior
S157R1C1-D	-	-	17.43 ^{SP}	Exterior
S157R1C1-E	-	-	14.26 ^{SP}	Exterior
S157R1C1-J	6.35 ^{330°}	-	5.85 ^{43°}	Interior
S157R1C1-K	3.83 ^{NP}	-	2.80 ^{347°}	Exterior
S157R1C1-L	4.66 ^{NP}	-	5.08 ^{SP}	Exterior
S157R1C1-M	4.97 ^{SP}	-	5.67 ^{NP}	Interior
S157R1C1-N	7.32 ^{13°}	-	7.05 ^{38°}	Interior
S157R1C1-O	8.40 ^{NP}	-	9.76 ^{SP}	Exterior
S157R1C1-P	7.27 ^{NP}	4.04 ^{59°}	6.41 ^{323°}	Interior

Figure 49 shows the subtracted image of a typical fiber-matrix debond formation at the 1.57d_f fiber spacing in the 828/D-230 matrix system. In all but two cases the debond initiated as a spot debond described earlier. The small or spot debond depicted in Figure 49 forms over a small length instantaneously, in this case in the vicinity of the north pole of the top front corner fiber. Also shown in Figure 49 is the top back corner fiber. At this fiber spacing the material between the holes of the CNC machined fiber templates broke quite often while inserting the fibers through the templates. This caused minor fiber misalignment shown in Figure 49 as the top back corner fiber is visible in the near field view and the space between the corner fibers showing the center fiber is smaller than the calculated distance of 0.21 mm. Figure 50 is a photomicrograph of fiber-matrix interface debonding prior to final fracture. Multiple debonds exist in four of the five fibers visible. As Table 14 shows, ten of the twelve specimens exhibit multiple debonds prior to final failure. The top half of the top front corner fiber and the bottom half of the bottom corner fiber have almost completely debonded. It appears that the center fiber has debonded along its equator. However, at this fiber spacing just over half of the center fiber, 0.21mm, is visible but due to fiber misalignment previously mentioned this distance is smaller. Since the center fiber debond was within the visible area it can be assumed that the debond extends upward toward the north pole since intuitively the stress state would be highest in the pole area.

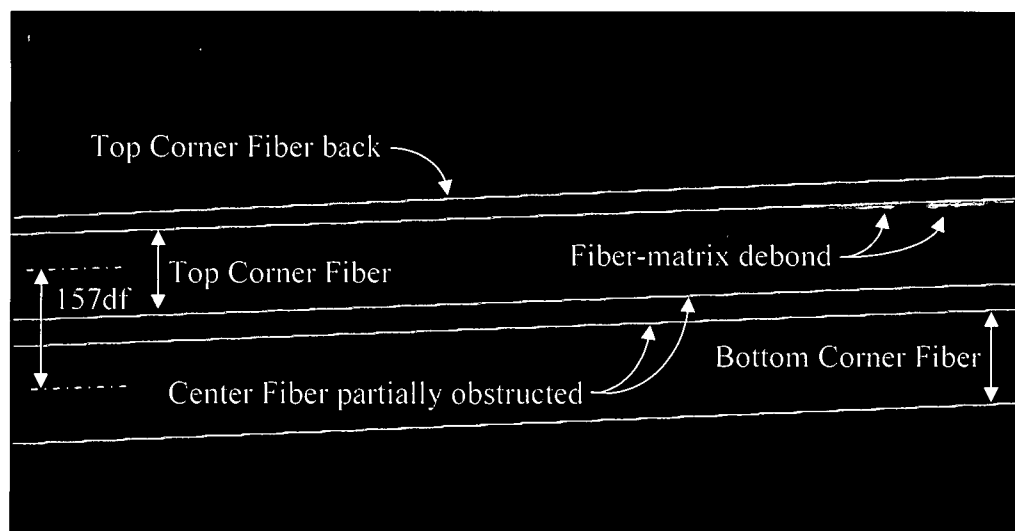


Figure 49: Subtracted image showing fiber-matrix debonds in steel/1.57d_f cruciform specimen

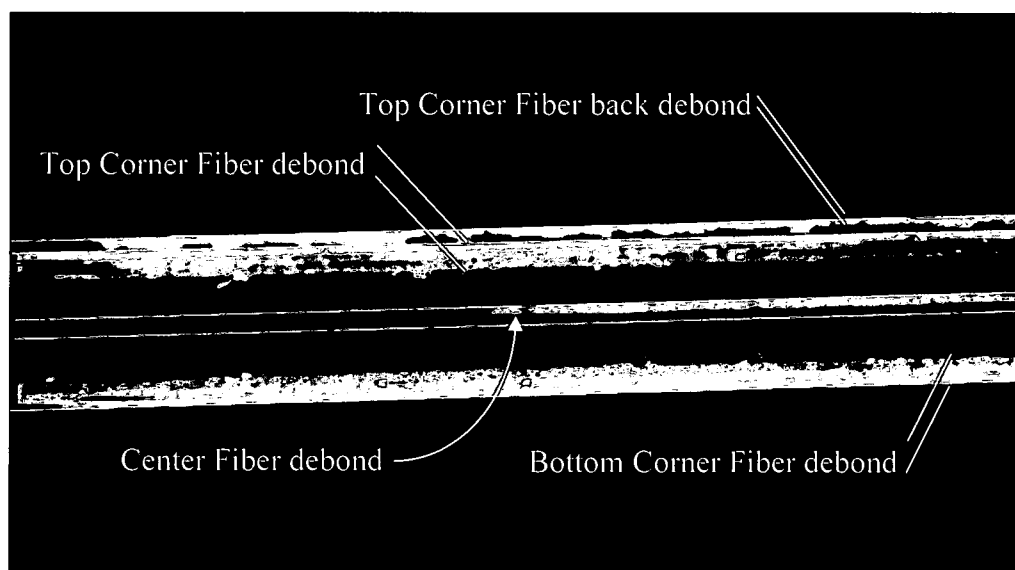


Figure 50: Subtracted image showing multiple fiber-matrix debond and debond growth in a steel/1.57d_f cruciform specimen

Table 15 lists the specimen's debond initiation measurements, consisting of the width, the central angle, location and debond type. Six of the twelve specimens debonded in the vicinity of the fiber poles and those were used to calculate the average debond width and central angle.

Three of the twelve debonded either in the northern hemisphere or southern hemisphere of the bottom fiber. The debond initiation of four specimens was obstructed from the view for obtaining accurate debond measurements as three of the four initiated on the center fiber and the other on the top back corner fiber. The average debond width results in a central angle of 91° which is one degree off the median of the range of the individual specimen central debond angles of 67° to 117° and 2° from the average of the individual central angles. All debonds initiated as a spot with a very small length at the fiber pole and grew slowly before specimen final failure as indicated in Table 15.

Table 15: 828 1.57d_f cruciform specimen debond measurements

Specimen	db Width (mm)	db Central Angle (deg)	Loc	FEM Loc	Type
S157R1C1-A	0.051	89°	NP-BF	SP-TF	IAS
S157R1C1-B	CF – obstructed	CF – obstructed	CF	CF	-
S157R1C1-C			CF	CF	-
S157R1C1-D	0.085	117°	SP-BF	NP-TF	Spot ~ 3.28 mm
S157R1C1-E	0.057	94°	SP-BF	NP-TF	IAS
S157R1C1-J	0.012	@ 43° BF	43° BF	317° TF	Spot ~ 0.32 mm
S157R1C1-K	Very Thin	@ 347° BF	347° BF	13° TF	Spot ~ 0.1 mm
S157R1C1-L	NP-TF Back – obstructed		NP-TF	NP-TF	Spot ~ 0.1 mm
S157R1C1-M	0.030	67°	SP-TF	SP-TF	Spot ~ 0.48 mm
S157R1C1-N	0.018	@ 38° BF	38° BF	322° TF	Spot ~ 0.48 mm
S157R1C1-O	0.040	78°	NP-TF	NP-TF	Spot ~ 0.72 mm
S157R1C1-P	CF – obstructed		CF	CF	-
AVG	0.053	91° AVG CA => 44.5° to 135.5° NP & 224.5° to 315.5° SP			
Std-dev	0.019				

The fracture surface of the 1.57d_f fiber spacing cruciform specimen is shown via the SEM image of Figure 51. The white arrow indicates the area of fracture initiation. Having features similar to the SF and 6.0d_f fiber spacing, the fracture surface indicates the final failure was initiated by a tensile stress normal to the fracture surface in the direction of the applied loading. No other failure initiation mechanisms features were observed on the fracture surface. The fiber imprint exhibits the porosity features seen in the 1.75d_f fracture surface fiber imprint. These micro-bubbles are a result of matrix being poured into the cruciform mold entrapping very small amounts of air. Unseen prior to testing and not observed in the field of view of the high magnification camera used for the cruciform testing, the largest diameters measures range

between approximately 0.017 mm to 0.027 mm. Through the image subtraction technique previously described and from the bubble size it is inconclusive what impact the bubbles had on the observed failure mechanism. However, it appears that the failure initiated as a fiber-matrix debond as observed during the cruciform testing of the $1.57d_f$ fiber spacing group. Other than the present micro-bubbles, the surface of the fiber imprint is smooth indicating a radial stress normal to the surface of the fiber as the dominating stress acting at the fiber-matrix interface causing the debond.

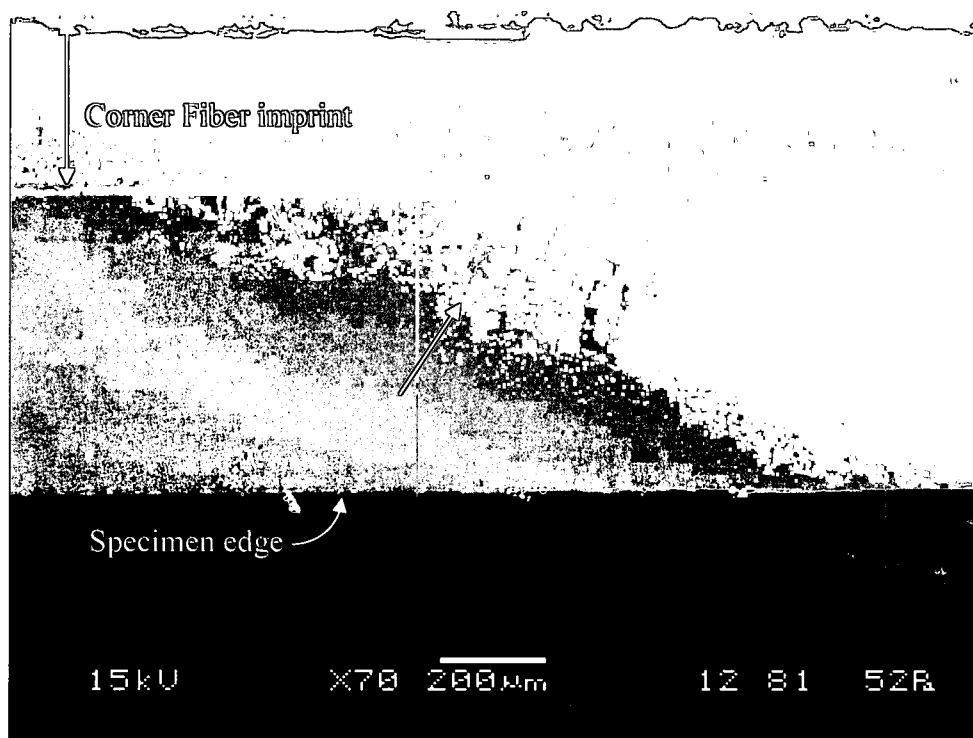


Figure 51: SEM image of fracture surface of steel/ $1.57d_f$ cruciform specimen

Steel/828/D-230 Cruciform Experimental Results Summary

In the 828/D-230 matrix system, seven different multi-fiber spacing groups, namely the $6.0d_f$, $2.5d_f$, $2.0d_f$, $1.9d_f$, $1.84d_f$, $1.75d_f$, and $1.57d_f$, of the cruciform specimen were tested along with the single fiber (SF) cruciform configuration. For the SF, $6.0d_f$, $2.5d_f$, $2.0d_f$, $1.9d_f$ and the $1.57d_f$ fiber spacing groups the failure initiated as a fiber-matrix debond. The location of the

debond initiation is, for the majority of the specimens, in the vicinity of the pole of either top or bottom corner fiber. For the $1.84d_f$ and $1.75d_f$ fiber spacing groups the failure initiation was observed as matrix cavitation. For these two fiber spacing groups, the failure initiation location was in the matrix away from the fiber-matrix interface. Table 16 lists the summary of test results for each fiber spacing group including the far-field stress at damage initiation, the failure initiation mechanism, the average debond initiation width and the average debond initiation central angle.

In general it appears that the debond initiation load increases as the fiber spacing decreases. The exceptions being the $2.5d_f$ and $1.57d_f$ fiber spacing groups although the latter group had microscopic bubbles at the fiber-matrix interface that could have contributed to its lower far-field debond initiation stress. Corresponding to this trend is the debond central angle increasing as fiber spacing decreases. It is plausible that as load increases stress redistribution occurs within the specimen to the fibers due to the shorter path through the matrix as fiber spacing decreases. Thus, the load redistribution, i.e. as the spacing decreases the failure initiation load increases, more load is carried by the fibers resulting in increased load carrying capacity. It also appears that the debond initiation has no preference to location above the fiber spacing that exhibited cavitation. The majority of specimens at the $2.5d_f$ and $1.9d_f$ fiber spacing initiate exterior to the fiber group while the $6.0d_f$ and $2.0d_f$ initiate interior to the fiber group. At the spacing below those that cavitated, i.e. the $1.57d_f$, the preference is interior to the fiber group. Although their initiation was matrix cavitation the majority of the $1.84d_f$ spacing debonded exterior while for the $1.75d_f$ spacing group the majority debonded interior to the fiber group. Including the cavitation specimens into the debond trend, it appears as if there is a spacing around the $1.8d_f$ such that no debond location preference exists for fiber spacing greater while at fiber spacing smaller the preference is interior to the fiber group. The location and position is important to note as the next sections introduce the analytical results to developing a debond criterion.

Although the interface stress results indicate that at the $6.0d_f$ spacing the fibers show no nearest neighbor effects, the far field stress is almost half of the SF. As mentioned previously, the thickness of each specimen was set such that all multiple fiber specimens had approximately the same amount of matrix cover over the corner fiber. The single fiber specimens were all made to a

constant thickness and thus, have a much thicker matrix cover. The thicker cover coupled with the multiple fibers of the $6.0d_f$ specimen creating multiple failure initiation sites explain the lower far field failure initiation stress of the $6.0d_f$ spacing.

For the two specimens that exhibited matrix cavitation, it appears that the majority of the cavitation occurs in an area bounded by one fiber diameter beyond the fiber grouping. The $1.84d_f$ and $1.75d_f$ fiber spacing groups exhibited both failure mechanisms as they debonded after exhibiting cavitation. From these observations it appears that the mechanisms are dependent upon the fiber spacing. More cavitations are developed at the $1.75d_f$ spacing than at the $1.84d_f$ spacing and the $1.84d_f$ spacing has a higher average debond far-field stress. The difference in fiber spacing between $1.9d_f$ and $1.84d_f$ specimens from the center fiber to the corner fiber along the diagonal is $0.04d_f$ or 0.014 mm, which is the smallest distance between all fiber spacing groups. It stands to reason that the $1.84d_f$ spacing may be the upper bound for matrix cavitation to occur. Primarily because this is the smallest fiber spacing between specimens that exhibited different failure modes coupled with the fact that the $1.84d_f$ has a significantly higher debond far-field stress than the $1.75d_f$ spacing. The difference in distance from the center fiber to the corner fiber along the diagonal between the specimens that cavitated is $0.06d_f$ or 0.021 mm. The difference in distance from the center fiber to the corner fiber along the diagonal between the $1.75d_f$ and $1.57d_f$ groups is $0.13d_f$ or 0.046 mm which is larger than between the $1.9d_f$ and $1.84d_f$ specimens. This suggests that a lower bound for matrix cavitation to occur may exist at a smaller spacing than the $1.75d_f$. Applying the diagonal distances from the center fiber to the corner fiber between the $1.84d_f$ and $1.90d_f$ groups as well as between the $1.84d_f$ and $1.75d_f$ groups to the $1.75d_f$ and $1.57d_f$ group give a possible fiber spacing of $1.66d_f$ as a lower bound for matrix cavitation.

Fracture surface analysis was performed on two representative samples from each cruciform fiber spacing group. The results of this analysis indicate that the failure initiation for the fiber spacing groups exhibiting fiber-matrix debond as their first damage mode have a dominating tensile stress that caused the specimen to fracture. However, for some fiber spacing groups that debonded first the fracture surface analysis showed features indicating that a shear component

coupled with the dominating tensile stress to create the fractured surface of the specimen. This suggests that it is possible for the debond to be a result of a combination of tensile and shear stresses acting at the fiber-matrix interface. For the fiber spacing groups exhibiting matrix cavitation, features specific to these fiber spacing groups were located on the fractured surface. These features show a shear bias to their failure initiation stress state and are most likely a direct result of matrix cavitation.

Table 16: Summary of 828 cruciform test results

Fiber Spacing Group	AVG Far-field stress at damage initiation (MPa)		Failure initiation mechanism	AVG db width (mm)	AVG db Central Angle (deg)
	debond	cavitation			
SF	19.82	N/A	debond	0.070	106°
6.0d _f	10.70	N/A	debond	0.015	48°
2.5d _f	6.58	N/A	debond	0.015	47°
2.0d _f	15.66	N/A	debond	0.075	110°
1.9d _f	16.38	N/A	debond	0.083	116°
1.84d _f	12.11	3.97	cavitation	N/A	N/A
1.75d _f	7.88	4.67	cavitation	N/A	N/A
1.57d _f	8.29	N/A	debond	0.053	91°

862/W Matrix System

Steel/862/W Single Fiber Cruciform Results. A total of 6 single-fiber cruciform specimens were tested and used for debond initiation measurements. Only 5 specimens yielded far-field stress at failure initiation data due to a test system crash. Table 17 lists the applied stress at failure initiation, the debond initiation width and corresponding central angle as well as the debond type. Half of the specimens debonded in the vicinity of the fiber poles and where used in calculating the debond initiation central angle. In all cases the observed first damage mechanism is fiber-matrix debonding initiating in the region near the fiber pole. Figure 52 shows a photomicrograph of a single-fiber cruciform debonding at both poles. The light or bright white area of the fiber is where the fiber-matrix interface has debonded, whereas the darker area is where the fiber-matrix

interface is still intact. The debond tip is clearly shown and designated by point A and A' in Figure 52 and the fiber centerline is delineated by the bright white spots running axially with the fiber at its center. The change in light intensity to the left of the debond tips, on the fiber, is indicative of the debond wrapping around the fiber circumference as load is continually applied. The average far-field stress at failure initiation is 14.46 MPa.

Table 17: Steel/862 Single fiber cruciform specimen test results

Specimen	FF Stress @ db initiation (MPa)	db width (mm)	db Central Angle (deg)	Type and length
S0862-A	13.49	0.038	@ 13°	Spot ~ 0.113 mm
S0862-B	25.85	0.024	60°	IAS
S0862-H	System crash	0.032	70°	IAS
S0862-I	12.29	0.041	@ 15°	Spot ~ 0.211 mm
S0862-J	8.28	0.015	48°	Spot ~ 0.045 mm
S0862-K	12.41	0.035	@ 13°	Spot ~ 0.09 mm
AVG	14.46	0.023	54° AVG CA => 63° to 117° NP & 243° to 297° SP	
Std-dev	5.96	0.007		

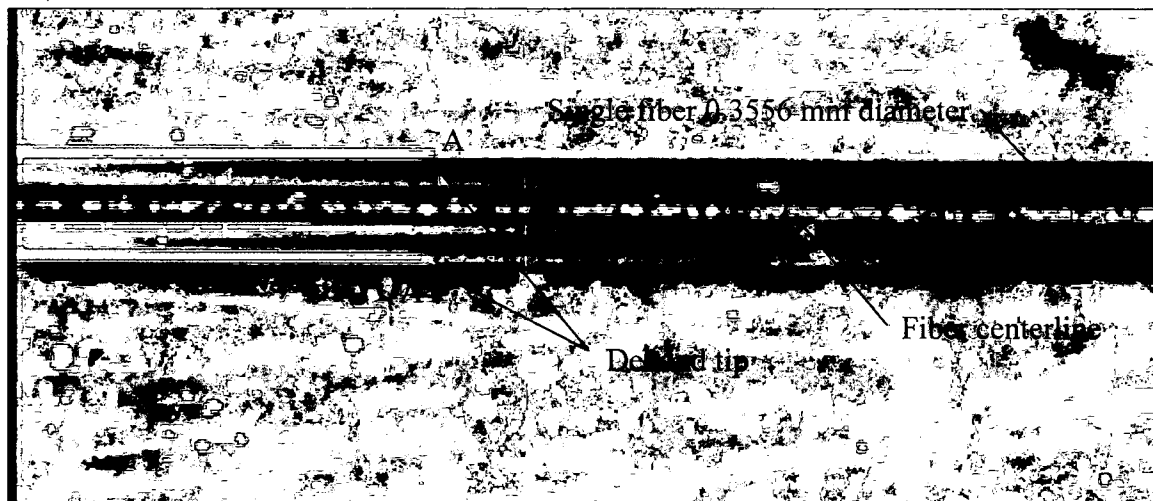


Figure 52: Photomicrograph of the steel/862 single-fiber cruciform debond at both the north and south pole

Figure 53 shows an SEM image of the single fiber fracture surface indicating multiple fracture initiation locations at the edge of the fiber imprint and beyond the imprint edge pointed

out by the black arrows. The failure initiation was experimentally observed in all cases as fiber-matrix debonding. It is also observed that once the debond wraps around the fiber circumference and propagates along the fiber length to a critical location the crack branches out into the matrix. The multiple locations could be undetected inclusions or micro-voids due to dust or air entrapped in the matrix during pouring into the cruciform molds. It is possible that once the debond traversed to the undetected inclusion location the final fracture of the specimen occurred.

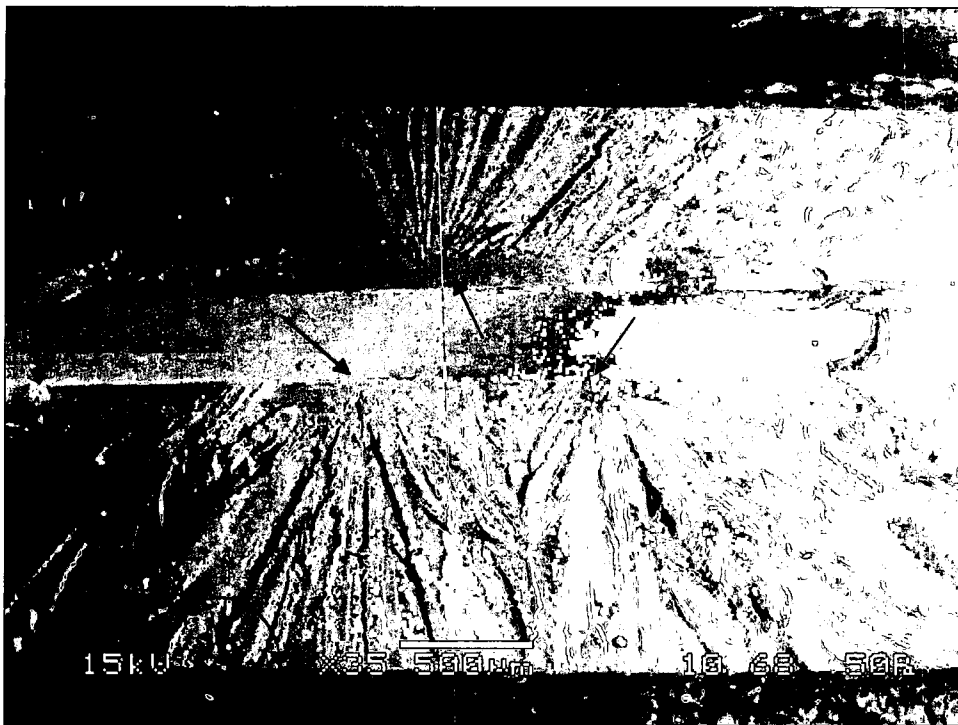


Figure 53: SEM image showing single fiber fracture surface and multiple fracture initiation locations

Figure 54 is an SEM image at a high magnification of the fracture surface of the single fiber specimen. These features in the fiber imprint at an angle with the longitudinal axis of the fiber, pointed out by the black arrows, indicate possible shear force interaction with the applied tensile force creating the observed debond. Also shown in the top left corner of the image is what appears to be another indication of shear interaction due to its shape and angle with the longitudinal axis of the fiber. This feature appears as a trench and is the mating portion of matrix

material still bonded to the fiber. Based upon the fracture surface analysis and the cruciform experimental observations; it is highly likely that the single fiber has a shear component coupled with a tensile component acting at the fiber-matrix interface creating the debond initiation.

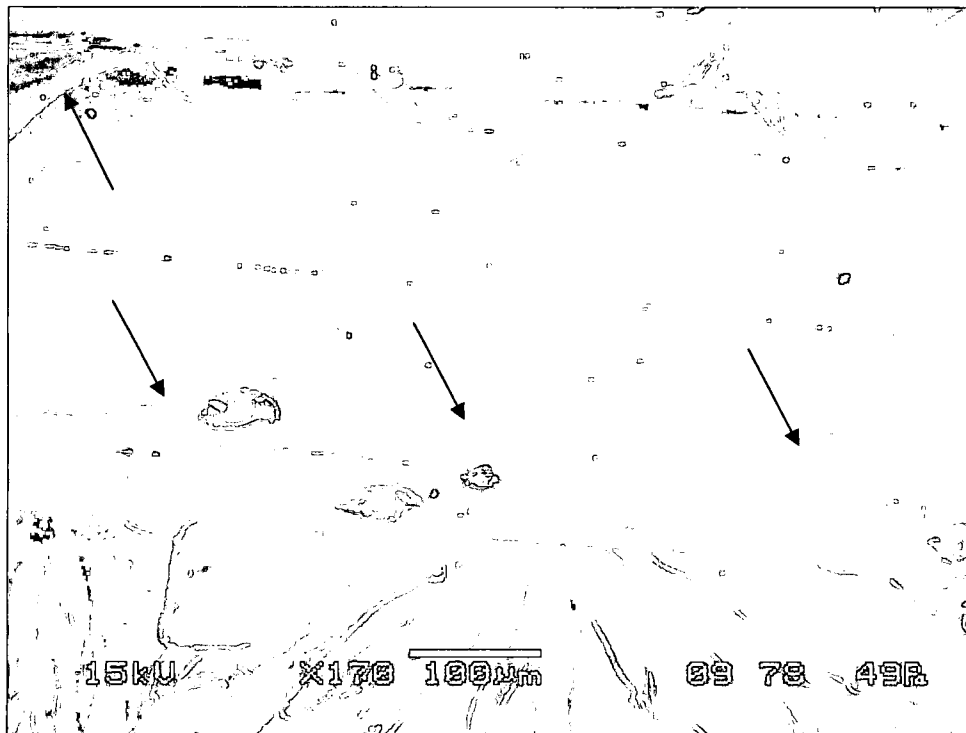


Figure 54: SEM image of single fiber imprint showing possible shear force interaction at the fiber-matrix interface

Steel/862/W 6.0d_f Multi-Fiber Cruciform Results. For the 862/W matrix system 8 specimens were tested at a fiber spacing equal to 6.0d_f. Table 18 lists the far-field applied stress at failure initiation for the top, center, and bottom fiber of 6.0d_f multi-fiber cruciform specimens. In five of the eight specimens, the failure occurs exterior to the fiber group. Half of the specimen exhibit debonds either exterior or interior to the fiber group, thus it appears the debonds occur independently. From Table 18, it appears that several specimens, namely S600R2C1-A, S600R2C1-B, S600R2C1-E and S600R2C1-L, initiated a fiber-matrix debond at a fairly low far-field stress level. Also characteristic of these specimens is that the location of the debond initiation is not in the vicinity of a fiber pole. Rather these specimens exhibited a debond along a

narrow strip closer to the fiber equator and debonded over a small finite length of fiber as shown in Table 19 below. Although the manufacturing of all cruciform specimens followed careful procedures, it is quite possible that the fiber surface did not get adequately cleaned prior to placement of the matrix into the cruciform mold. An argument for this case is made when investigating the far-field stress at fracture. The average far-field stress for all specimens at fracture is 31.33 ± 2.17 MPa while those exhibiting the thin debonds near the fiber equator is 32.12 ± 2.37 MPa. The average far-field stress at fracture of the specimens exhibiting debonds near the fiber poles is 30.14 ± 0.99 MPa. A difference of less than 2.5% exists between the whole sample and those exhibiting the thin debond while a difference of 6.16% exists between the thin debond group and those debonding near the fiber pole. Since very little difference exists between the sample groups exhibiting thin debonds and those debonding near the fiber poles. A plausible reason for the low far-field stress thin debond behavior for specimens S600R2C1-A, S600R2C1-B, S600R2C1-E and S600R2C1-L could be surface unseen porosity or microscopy flaws at the fiber-matrix interface affecting the matrix bond. However, another explanation for the thin debond observed behavior could be due to the residual stresses built up within the specimen by the high temperature cure cycle. Since the matrix has vitrified with the fibers at full expansion due to the high temperature post cure, it would be reasonable to suggest that during cool down the fiber shrinks weakening the interface by pulling away from the bulk matrix material.

Table 18: Far-field applied stress at matrix cavitation and debond initiation in specimens having 6.0d_f fiber spacing

Specimen	Far-field stress at debond initiation (MPa)			Location w/r/t Fiber Group
	Top Fiber	Center Fiber	Bottom Fiber	
S600R2C1-A	-	3.96 ^{323°-332°}	-	Interior
S600R2C1-B	6.01 ^{48°-61°}	-	6.71 ^{SP}	Exterior
S600R2C1-C	-	27.88 ^{NP}	29.32 ^{SP}	Interior
S600R2C1-E	-	4.31 ^{26°-37°}	27.81 ^{NP}	Interior
S600R2C1-F	21.71 ^{NP}	-	-	Exterior
S600R2C1-G	24.33 ^{NP}	-	26.22 ^{SP}	Exterior
S600R2C1-H	23.00 ^{NP}	-	-	Exterior
S600R2C1-L	-	-	10.30 ^{21°-34°}	Interior

Figure 55 shows a typical fiber-matrix debond at the north pole of the center fiber. The primary camera is zoomed in enough that the top fiber showing in Figure 55 is the center fiber of the specimen and the bottom fiber shown is the actual bottom fiber of the specimen. The bright white spots on the center of each fiber designate the fiber centerline and there exists a slight misalignment of the two bottom fibers. Debond initiation at this fiber spacing grows quicker under increasing load than that of the 828/D-230 matrix system. Consequently the 862/W debonds a far greater portion of the fiber interface in a much quicker time than that of the 828/D-230 matrix system. The average far-field applied stress at debond initiation for the 862/W matrix system having a 6.0d_f fiber spacing is 15.19 MPa.

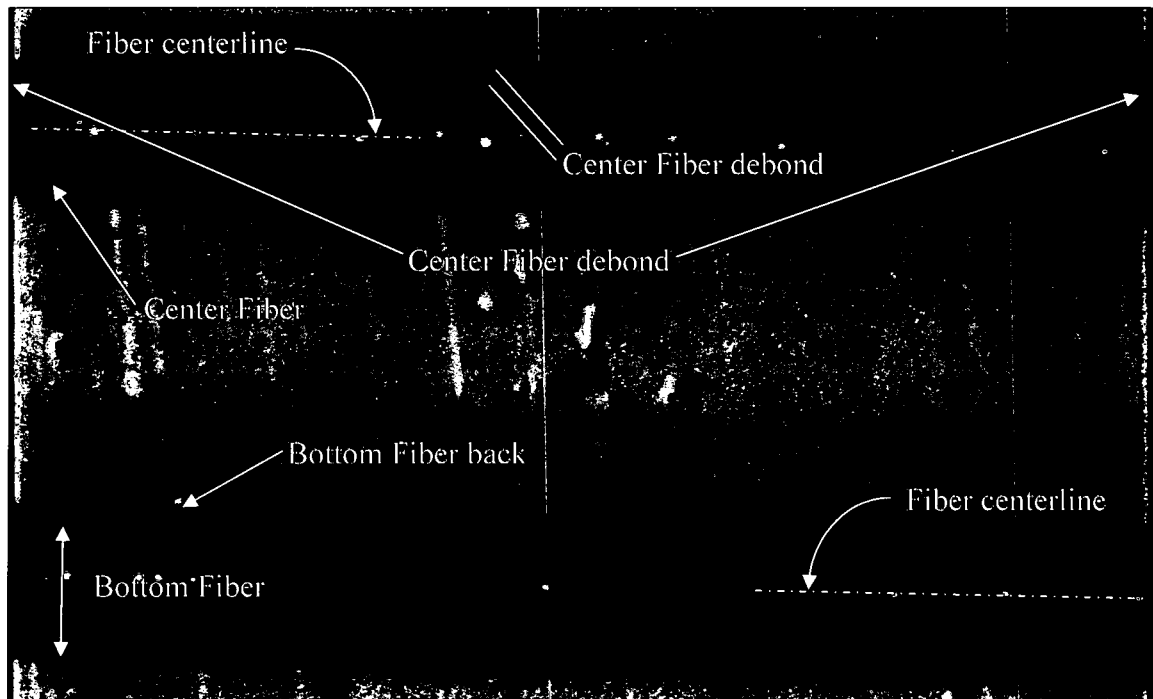


Figure 55: Photomicrograph of steel/6.0d_f 862 cruciform showing debond at the north pole of center fiber

For half of the specimens, the fiber-matrix debond occurs other than in the vicinity of the fiber pole. In these cases, the fiber-matrix debond is characterized by a very thin strip forming either in the northern or southern hemisphere of the fiber and propagates across the fiber length.

In some cases the specimen will exhibit the debond at both locations, near the fiber pole and at some angular location along its circumference. Figure 56 is a photomicrograph showing the thin debond formation on the bottom fiber and a spot debond at the north pole of the top fiber. A thin white debond is observed forming inside the white oval on the bottom fiber. While a spot debond forms near the north pole of the top fiber delineated in the white oval on the top fiber. Again, the line of bright white spots signifies the fiber centerline. For this specimen the top fibers and the bottom fibers are in perfect alignment. This type of very thin debond not located at the fiber pole does not debond a large circumferential area of the fiber that is typical of the other specimens that develop fiber-matrix debonds in this particular fiber spacing group and those described previous in the 828/D-230 matrix system. Furthermore, the single fiber cruciform specimens discussed earlier exhibited the same behavior in half of the specimens tested. Only one specimen at the 1.9d_f fiber spacing and a few at the 1.57d_f fiber spacing debond other than at the fiber poles in the 828/D-230 matrix system. Consequently, it appears that the 862/W matrix system exhibits quite different interfacial fiber-matrix debond failure characteristics at this fiber spacing than the 828/D-230 matrix system.

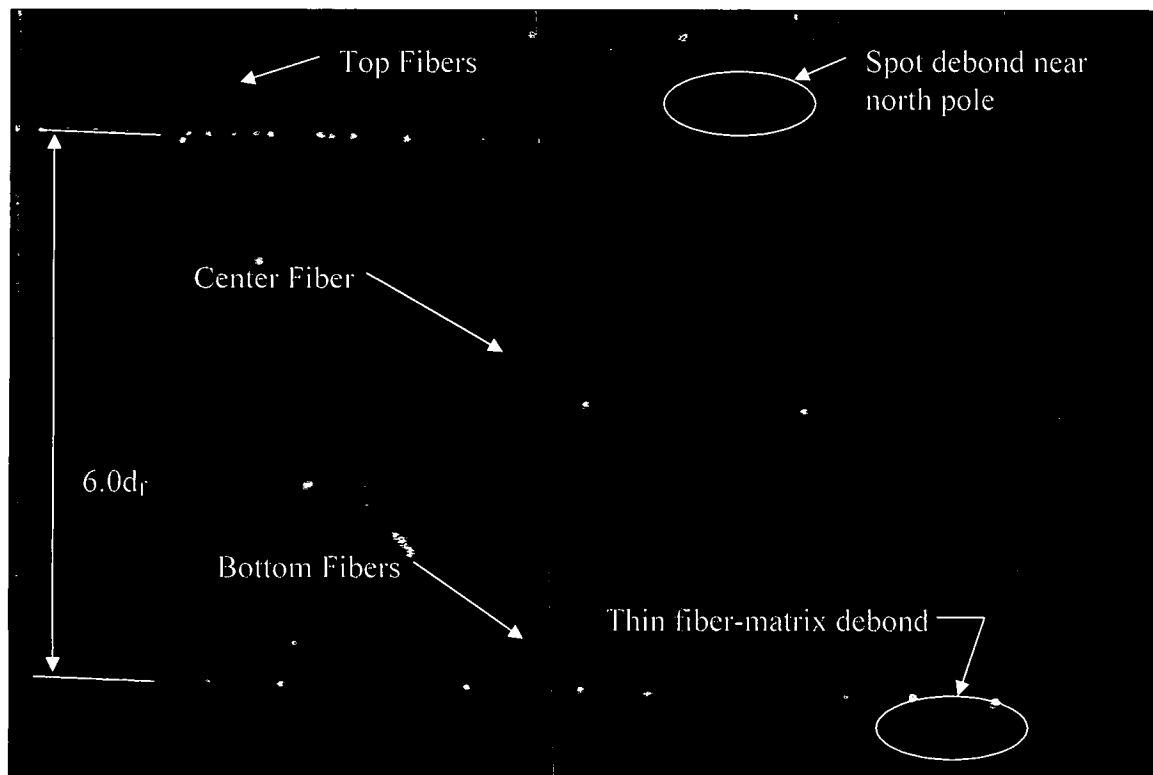


Figure 56: Photomicrograph of steel/6.0d_f 862 cruciform showing two different debond characteristics, a thin fiber-matrix debond on bottom fiber and spot fiber-matrix debond at north pole of top fiber

Table 19 lists the debond initiation measurements of width, central angle, location, FEM location and debond type. For specimen S600R2C1-F the debond occurred just outside the field of view of the primary camera but was captured by the secondary far-field view camera. At the magnification level of the secondary camera, the accuracy of the debond measurements is very poor therefore, they were not performed for this specimen. Furthermore, of the remaining seven specimens capable of obtaining the debond width only three debonded near the fiber poles. The average debond width of these three specimens were used to calculate the central debond angle. The average debond central angle calculated by the average of the measured debond width is less than one degree from the average of the individual specimen calculated central angles. However, the debond limits set by the central angle only encompasses one specimen that debonded other than at the fiber pole, S600R2C1-B. The other three specimens, S600R2C1-A

S600R2C1-E and S600R2C1-L, debond limits lie outside the limits set by the central angle. In all cases of the specimens exhibiting the thin debond not occurring in the vicinity of the pole, the debond initiation length is relatively small considering the other specimens debonded the majority of the loading arm length, which is approximately 12.73 mm listed in Table 1. Consequently, the 862/W matrix system may be more susceptible to fiber surface flaws or interface porosity, although stringent efforts were employed to ensure a clean fiber surface as described above.

Table 19: Steel/862 6.0d_f cruciform specimen debond measurements

Specimen	Db Width (mm)	Db Central Angle (deg)	Loc	FEM Loc	Type
S600R2C1-A	0.022	323°-332°	SH-CF	NH-CF	Spot ~ 0.092 mm
S600R2C1-B	0.044	48°-61°	NH-TF	NH-TF	Spot ~ 0.09 mm
S600R2C1-C	0.039	78°	NP-CF	NP-CF	IAS
S600R2C1-E	0.028	26°-37°	NH-CF	NH-CF	Spot ~ 0.15 mm
S600R2C1-F	Observed w/far-field camera		NP-TF	NP-TF	-
S600R2C1-G	0.037	76°	NP-TF	NP-TF	IAS
S600R2C1-H	0.04	78°	NP-TF	NP-TF	IAS
S600R2C1-L	0.037	326°-339°	SH-BF	NH-TF	Spot ~ 2.46 mm
AVG	0.039	78° Avg CA => 51° to 129° NP & 231° to 309° SP			
Std-dev	0.0012				

Figure 57 is an SEM image of the fracture surface of the 6.0d_f fiber spacing cruciform specimen. There exists multiple fracture initiation sites interior to the fiber grouping as delineated by the brackets shown in Figure 57. Due to the formation of the features angled to the fiber imprint, it appears there is a shear stress component coupled to the tensile stress component creating the cruciform fracture. However, the fiber imprint appears relatively smooth as shown in Figure 57 and at a much higher magnification shown in Figure 58. The higher magnification SEM image of Figure 58 reveals porosity in the fiber imprint area. These microscopic pores could be due to matrix impurities, fiber surface contaminants, or dust or air entrapped while pouring the matrix into the cruciform molds. Nevertheless, the microscopic pores most likely contribute to the thin debond observed in the single fiber and 6.0d_f spacing multi-fiber cruciform tests. No other failure initiation mechanisms are present on the fractured surface of the 6.0d_f cruciform specimen. Since the experimentally observed failure initiation is fiber-matrix debonding and no other failure

mechanisms exist; it can be concluded that the failure initiation mechanism for the 6.0d_r cruciform specimens is by the observed interfacial fiber-matrix debonding. Although, the fiber imprint does not reflect a shear stress component contribution to the fiber-matrix debond failure initiation mechanism, the features on the fractured surface indicate a shear stress component is present for fracture initiation. This evidence suggests that there is a possibility that the debonding mechanism has a shear stress component coupled with a more dominating tensile stress component that may be causing the fiber-matrix debonds.

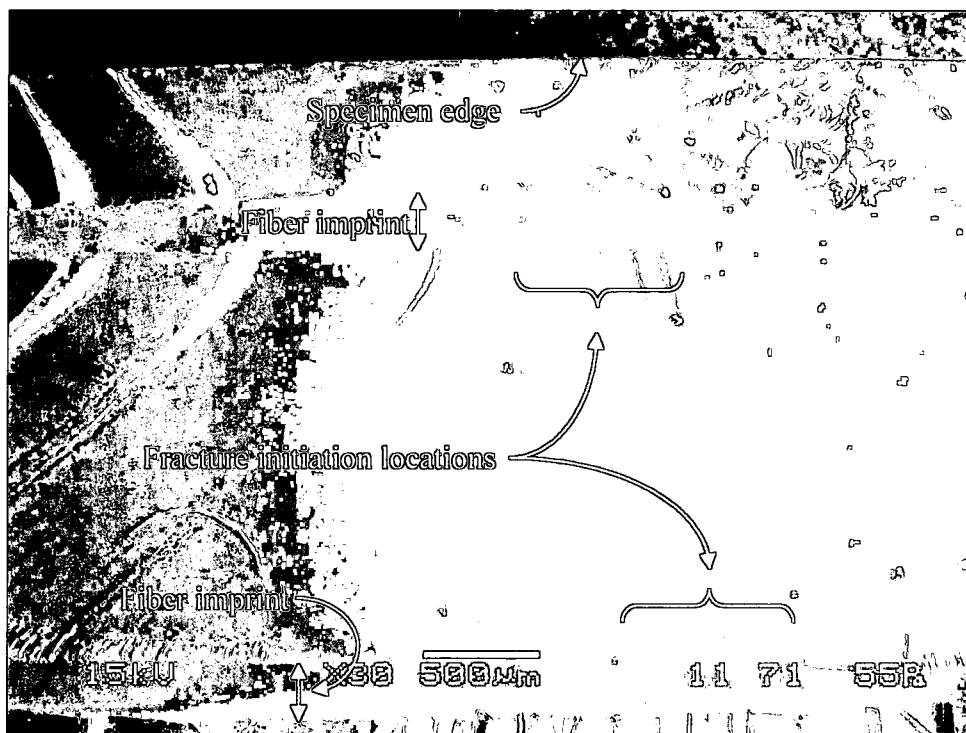


Figure 57: SEM image of the fracture surface of steel/6.0d, 862 cruciform specimen

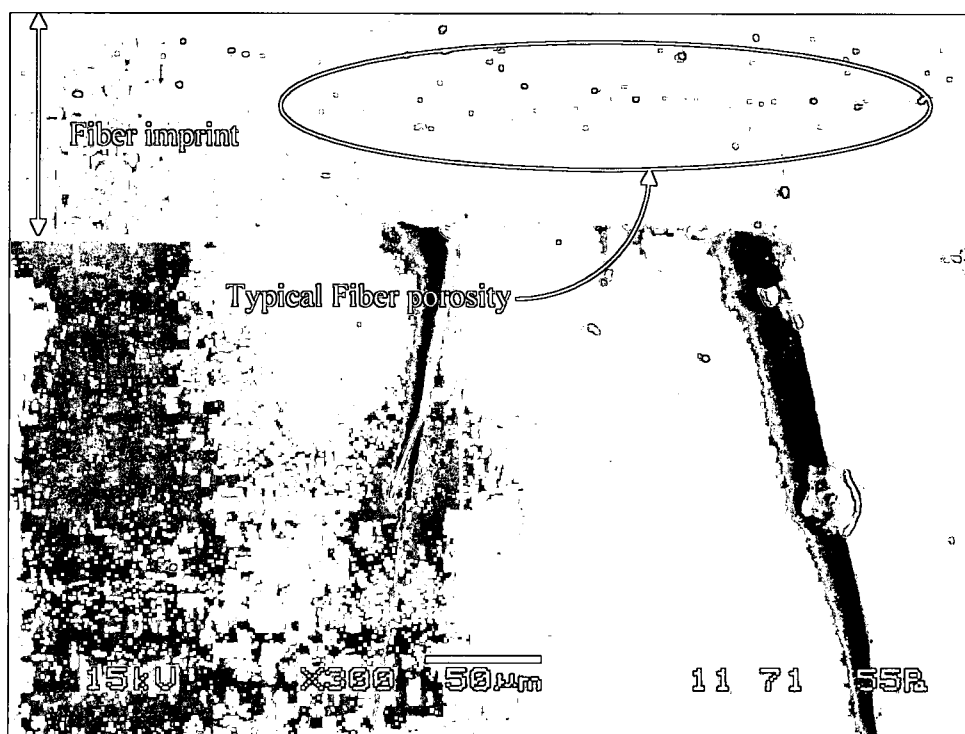


Figure 58: SEM image of the fracture surface of steel/6.0d, 862 cruciform specimen at 300 times magnification showing fiber imprint area

Steel/862/W 2.5d, Multi-Fiber Cruciform Results. A total of nine specimens were tested at the 2.5d, fiber spacing and all experienced fiber-matrix debonding as their first failure mechanism. Table 20 lists the far-field applied stress at which failure initiated as a fiber-matrix debond for the top, center and bottom fibers. In 5 of the 9 specimens the fiber-matrix debond initiated interior to the fiber group, although 7 of the 9 specimens exhibited the debond at the corner fiber. For all specimens, the fiber-matrix debond initiated in the vicinity of a fiber pole and only one did not have multiple debonds.

Table 20: Far-field applied stress at debond initiation in multi-fiber specimens having 2.5d_f fiber spacing

862/W	Far-Field Stress at debond initiation (MPa)			Location w/r/t Fiber Group
Specimen	Top Fiber	Center Fiber	Bottom Fiber	
S250R2C1-N	19.44 ^{NP}	19.97 ^{SP}	4.72^{SP}	Exterior
S250R2C1-O	12.81^{300°}	-	17.9 ^{SP}	Exterior
S250R2C1-P	15.79 ^{NP}	17.26 ^{NP}	10.78^{SP}	Interior
S250R2C1-Q	20.71 ^{NP}	14.82^{NP}	-	Interior
S250R2C1-R	16.47 ^{NP}	5.27^{SP}	8.94 ^{NP}	Interior
S250R2C1-T	18.02^{NP}	-	22.59 ^{SP}	Exterior
S250R2C1-U	13.63^{SP}	-	-	Interior
S250R2C1-V	17.78 ^{NP}	-	9.40^{SP}	Exterior
S250R2C1-AX	24.15 ^{SP}	24.64 ^{SP}	23.63^{SP}	Exterior

Much like the 6.0d_f 862/W specimens, the 2.5d_f specimen debond formation occurs very rapidly in fractions of a second. In 5 of the 9 cases, the debond formed instantaneously over the field of view. Figure 59 is a photomicrograph using the subtraction image technique of an 862/W 2.5d_f specimen showing debonds near the north pole of the top and center fiber. The debond initiated as a spot near the north pole of the center fiber then propagated in both directions. Subsequent to the center fiber debond, one forms in the vicinity of the north pole of the top fiber as shown in Figure 59. The debond is propagating along the fiber length very near the north pole of the center fiber, where the debond tip is designated as A. Only one tip is captured in this photomicrograph due to the speed of the debond formation as most propagate within one frame of the videotaped experiment, i.e. they propagate in 1/30 of a second. The debond near the north pole of the top fiber in Figure 59 clearly shows how most of the debond forms within this fiber spacing group. The fiber edges have been superimposed on the image for clarity. The average far-field stress for fiber-matrix debonding initiation is 12.56 ± 5.64 MPa.

Each specimen's debond initiation width, central angle, location and debond type is listed in Table 21. For specimen S250R2C1-T the debond occurred very near the north pole on the top back corner fiber, consequently the debond limits were obstructed. Thus, debond width could not be measured. The average debond angle is therefore calculated from the remaining specimens. Seven of the eight specimens whose debonds were measureable occurring within the field of view initiated as a spot debond instantaneously debonding a finite length indicated in Table 21.

The average debond width creates a central angle of 74° which, is equal to the median of the individual specimen's central debond angle range.

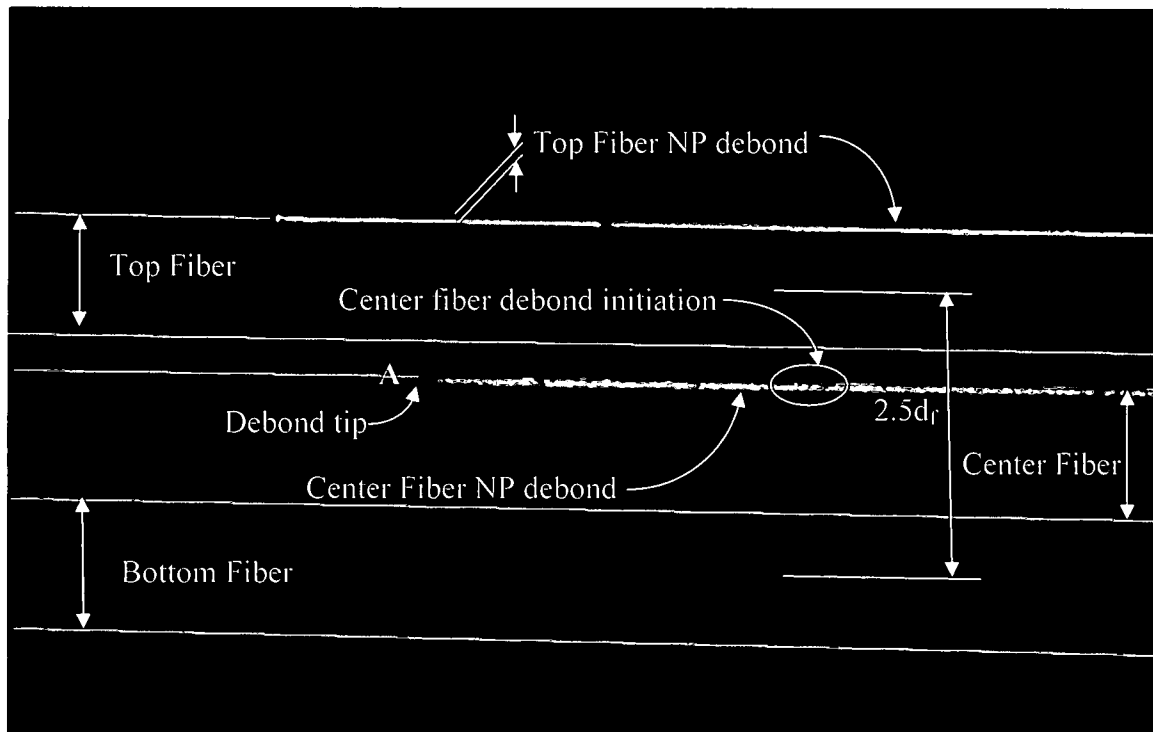


Figure 59: Subtracted image showing multiple debonds in steel/2.5d_r 862 cruciform specimen

Table 21: Steel/862 2.5d_r cruciform specimen debond measurements

Specimen	Db Width (mm)	Db Central Angle(deg)	Loc	FEM Loc	Type
S250R2C1-N	0.032	70°	SP-BF	NP-TF	IAS
S250R2C1-O	0.025	62°	SP-BF	NP-TF	Spot ~ 2.47 mm
S250R2C1-P	0.028	72°	SP-BF	NP-TF	Spot ~ 1.81 mm
S250R2C1-Q	0.029	66°	NP-CF	NP-CF	Spot ~ 0.029 mm
S250R2C1-R	0.084	116°	SP-CF	NP-CF	Spot ~ 0.36 mm
S250R2C1-T	NP-TF Back		NP-TF	NP-TF	-
S250R2C1-U	0.007	32°	SP-TF	SP-TF	Spot ~ 0.17 mm
S250R2C1-V	0.043	82°	SP-BF	NP-TF	Spot ~ 0.04
S250R2C1-AX	0.03	68°	SP-BF	NP-TF	Spot ~ 0.036
AVG	0.035	74° Avg CA => 53° to 127° NP & 233° to 307° SP			
Std-dev	0.021				

Figure 60 is an SEM image of the fracture surface of the 2.5d_r cruciform specimen showing the imprint of a corner fiber and the center fiber. Analysis of the failure surface reveals that there exist several fracture initiation points at the fiber imprint edge as indicated by the white brackets and arrows. Furthermore, the analysis suggests that the failure stress has a large component of tensile stress and due to the ridges or striations emitting from the fiber imprint edge at an angle to the fiber longitudinal axis that a shear component of the failure stress is also possibly present. No other failure initiation sites exist on the fracture surface. The experimentally observed failure initiation is fiber-matrix debonding. Since no other failure mechanism evidence exists, it can be concluded that the 2.5d_r cruciform specimen's failure initiation is by interfacial fiber-matrix debonding. The fiber imprint area is relatively smooth indicating a dominate tensile stress present causing the fiber-matrix debonds. However, since features exist on the fracture surface that indicates a possible shear component to the fracture stress; it is possible that the fiber-matrix debonding also has a shear component coupled with the dominate tensile component to create the interfacial fiber-matrix debond.

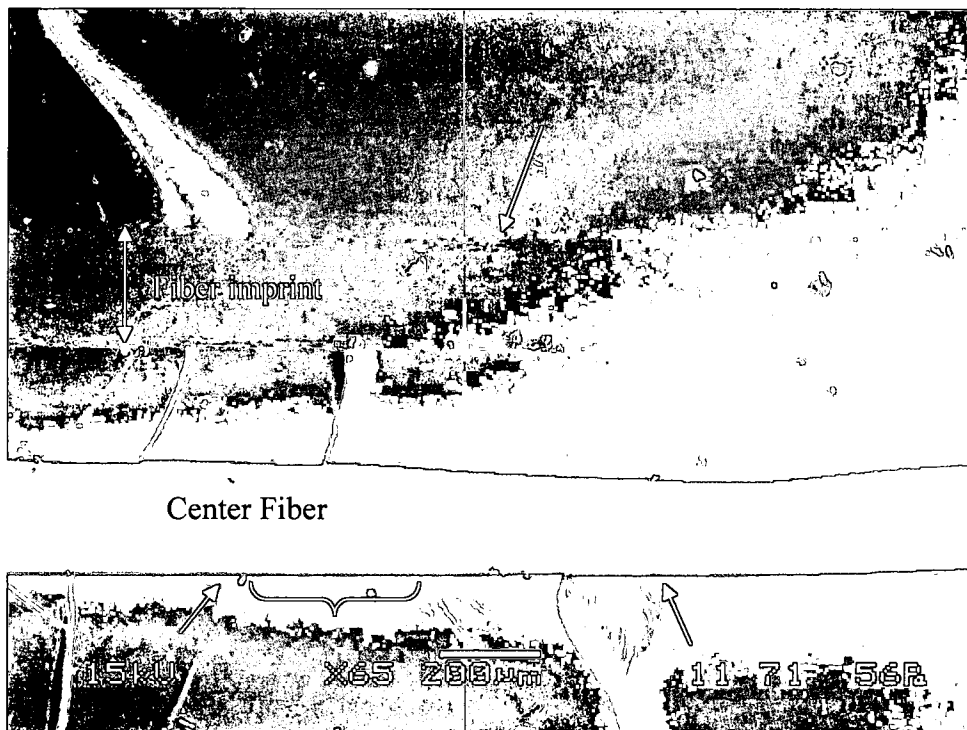


Figure 60: SEM image of the fracture surface of the steel/2.5d_r 862 cruciform specimen

Steel/862/W 2.0d_f Multi-Fiber Cruciform Results. A total of ten specimens having a fiber spacing of 2.0d_f in the 862/W matrix system were tested with Table 22 giving the individual specimen results. In 9 of the 10 specimens tested, matrix cavitation was the first damage initiation mechanism. Peculiar to this fiber spacing in the 862/W matrix system is the observation of what is believed to be an internal fiber-matrix debond failure which, will be described in detail below. The far-field stress at the first instance of this behavior is also listed in Table 22. The average far field applied stress for the initial cavitation and subsequent fiber matrix debond is 7.65 MPa and 10.69 MPa respectively.

Figure 61 is a photomicrograph of a multi-fiber composite with 2.0d_f fiber spacing, under a far-field stress of 10.20 MPa, showing several matrix cavitations encircled by the white ellipsoids. One cavitation formed just below the fiber group; one between the bottom fiber and center fiber; one between the corner fibers right in front of the center fiber and one just above the fiber group. The fiber edges have been superimposed for clarity. Due to the existing specimen features and since the 862/W resin system is amber in color the developing matrix cavitations are difficult to observe and appear as faint white or grey spots. Employing the image subtraction technique, Figure 62 is the subtracted image of Figure 61 and shows the matrix cavitations more clearly.

Table 22: Far-field applied stress at matrix cavitation and debond initiation in multi-fiber specimens having 2.0d_f fiber spacing

Specimen	FF stress at matrix cavitation (MPa)	FF stress at internal debond (MPa)	FF Stress at debond initiation (MPa)		
			Top Fiber	Center Fiber	Bottom Fiber
S200R2C1-A	3.09	-	-	-	7.82 ^{SP}
S200R2C1-B	7.78	12.35	-	-	-
S200R2C1-C	8.54	25.62	-	-	-
S200R2C1-D	10.12	24.24	-	-	28.45 ^{NP}
S200R2C1-E	7.93	27.51	-	-	-
S200R2C1-F	17.49	-	-	-	21.77 ^{SP}
S200R2C1-G	5.37	3.39	-	-	-
S200R2C1-H	-	20.36	-	-	-
S200R2C1-I	1.72	-	-	-	-
S200R2C1-J	-	8.32	-	-	-

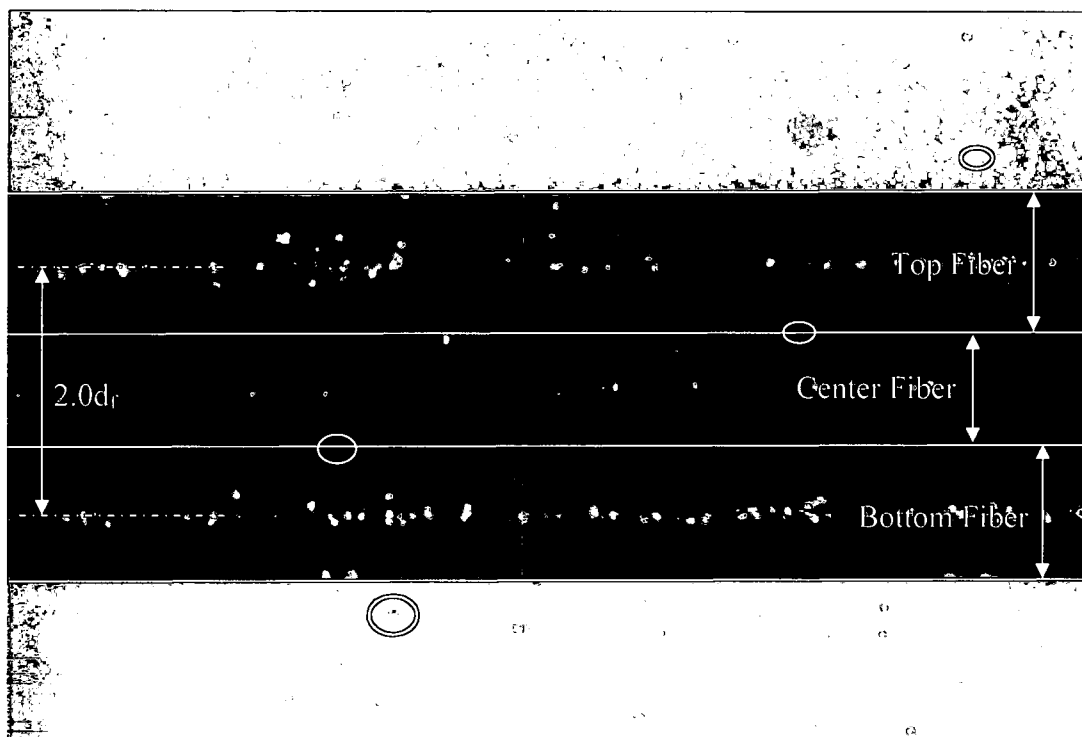


Figure 61: Photomicrograph of steel/2.0d_f 862 cruciform specimen showing matrix cavitation under a far-field stress of 10.2 MPa

Figure 63 shows the matrix cavitation accumulating as load increased from 10.20 MPa to 25.90 MPa. The white ellipsoids in Figure 63 were the cavitation sites shown in Figure 62. Also visible are the different cavitation sizes and light intensity levels. Figure 64 is the subtracted image at the far-field stress of 35.85 MPa and shows continued matrix cavitation accumulation as well as cavitation growth as evidenced by comparing the cavitation size at location "A" in Figure 63 to "A" in Figure 64. Also shown by the white ellipsoids are the original cavitation sites shown in Figure 62. As described above, once cavitation occurs, the stress at that point is relieved. However, as load is continuously applied the surrounding area becomes further stressed forming additional cavitations. The cavitation growth can be attributed to coalescence of individual cavitation events into micro cracks. The cavitations appear instantaneously, although very faintly, and independently over the time range while several seconds may lapse between individual cavitation formations. The time difference shown in Figure 63 is 143 seconds and time difference shown in Figure 64 is 198 seconds. Furthermore, the rate of matrix cavitation increases as the

specimen load increases to the final failure. Additionally, Figure 63 and 64 show changes in the cavitation light intensity. Changes in light intensity are attributed to additional micro cracks propagating toward the surface of the fiber matrix cavitation formation. The light intensity is an indication of the cavitation location and size. Bright cavitations most likely form either at the fiber-matrix interface or very close to the interface or even at the outer surface of the specimen and are most likely relatively large. Whereas, faint cavitations likely develop between the fiber-matrix interface and the outside surface of the specimen and are relatively small. It is also quite evident that most of the cavitations occur within the fiber group as indicated in Figures 62 through 64; where it is expected that this area experiences the highest stresses from the applied load due to the constraining influence of the fibers.

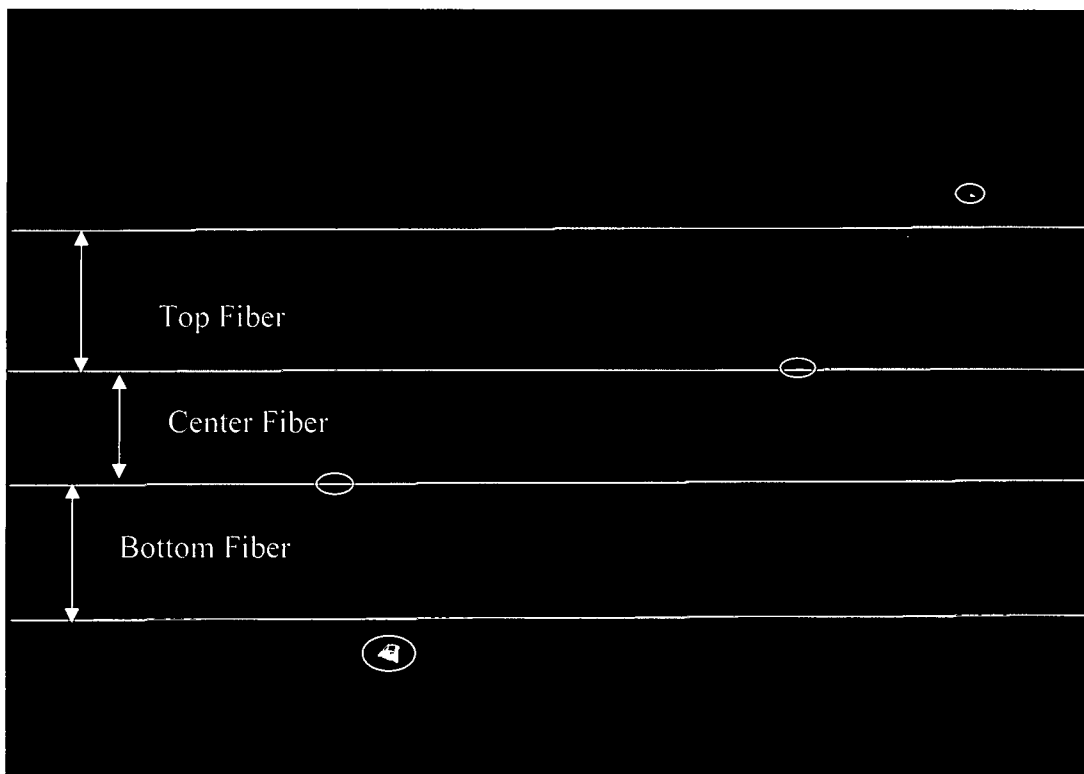


Figure 62: Subtracted image showing matrix cavitation in steel/2.0d, 862 cruciform specimen under a far-field stress of 10.20 MPa

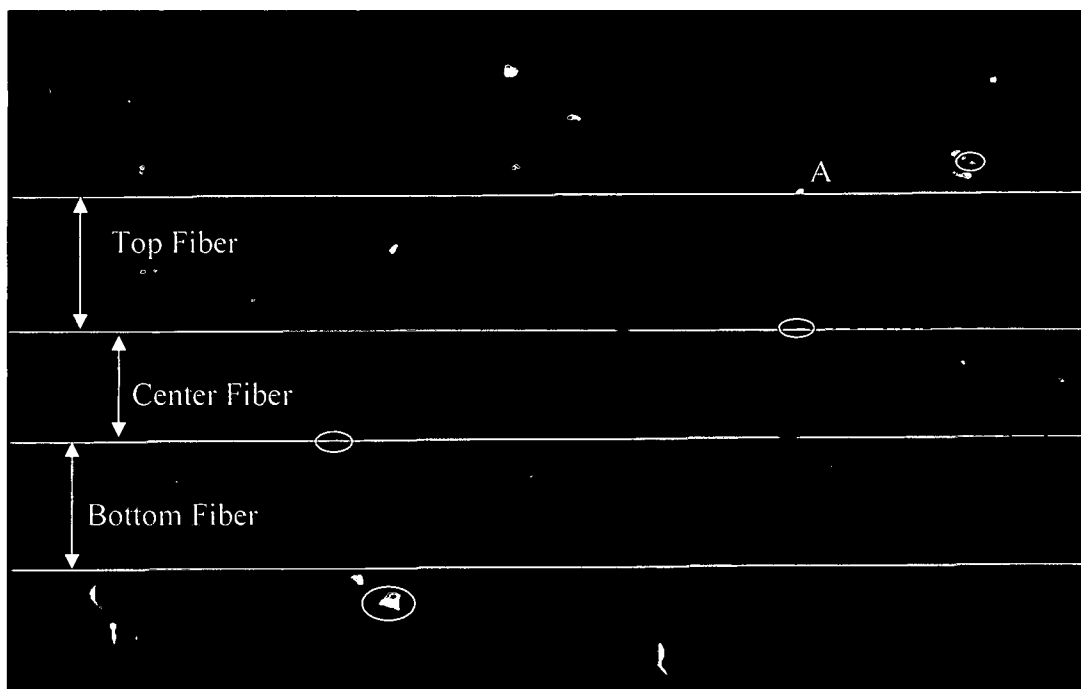


Figure 63: Subtracted image showing additional matrix cavitation in steel/2.0d, 862 cruciform specimen at a far-field stress of 25.90 MPa

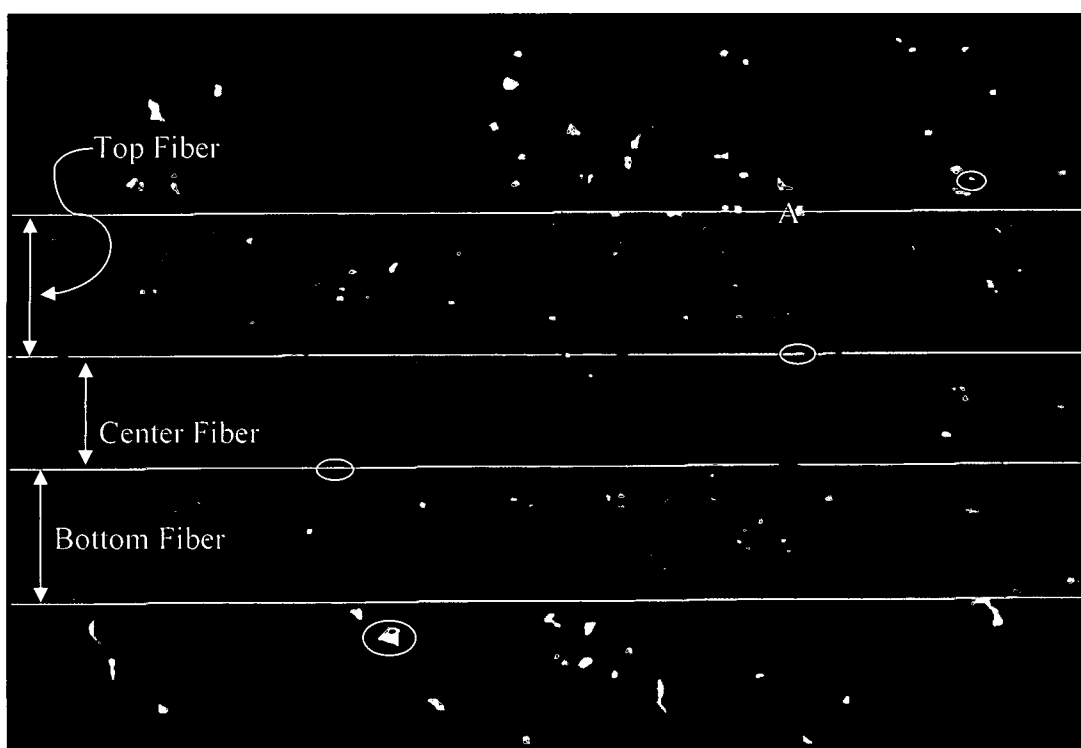


Figure 64: Subtracted image showing additional matrix cavitation in steel/2.0d, 862 cruciform specimen at a far-field stress of 35.85 MPa

Table 22 also reveals a rather large variance in the far-field stresses at matrix cavitation. The test setup videotaped only one side of the specimen and from Figures 63 and 64, the majority of cavitation occurs bounded by the corner fiber outside poles, i.e. the top corner fiber north pole and the bottom corner fiber south pole. Thus, it is very possible that cavitations occurred within the fiber grouping on the far side of the specimen not under observation.

Unlike the 6.0d_f and 2.5d_f specimens of both matrix systems and its counterpart in 828/D-230 resin system 8 of 10 specimens exhibit an internal failure characterized by an expansion of the fiber group and changes in light intensity other than those created by the matrix cavitations. The observed fiber group expansion is likely the result of the unseen fiber-matrix debond crack opening displacement causing the shifting of the fiber edges. Of the 8 experiencing the internal failure 6 experienced cavitations as well and in 5 of the 6 the cavitation preceded the internal failure. Only through detailed image analysis where images are extracted from the videotaped experiments is an internal failure realized. A characteristic of the 862/W matrix system mentioned above is that changes in light intensity are very gradual when damage occurs. In some cases a direct observation of a fiber-matrix debond is difficult to ascertain and can be completely missed unless detailed image analysis is performed. As described earlier, a fiber-matrix debond is identifiable by the distinct change in light intensity, from dark grey to a light grey almost white region, occurring along the fiber primarily at the fiber poles but not encompassing the entire fiber width. The light intensity change from the debond also creates an overall change in lighting within the field of view making the entire image brighter. Accompanying the light intensity change on the fiber is a small fiber group expansion where the top corner fiber moves up and the bottom corner fiber moves down, i.e. in the direction of the applied loading. The overall change in image lighting and the fiber group expansion exists in specimens exhibiting an internal debond not directly observed. These fiber-matrix debonds occur on the back corner top and bottom fibers hidden by the front top and bottom corner fibers seen in the field of view. The fiber group expansion and light intensity changes are determined by examining individual images extracted from the videotaped experiments. In most cases the images are extracted every 1/30 of a second, the video frame rate. Once aligned and stacked in ascending order of time, clicking between images

reveals changes that are usually missed when viewing the video tape due to the subtlety of the damage manifestation occurring in the specimen characteristic of this particular matrix system. Figure 65 and Figure 66 are photomicrographs of before and after fiber group expansion and light intensity changes. Close inspection between Figure 65 and 66 show slight changes in light intensity occurring between the top and center fibers, between the center and bottom fiber and along the bottom fiber. These changes are captured in the white ellipsoids of Figures 65 and 66. The fiber edges have been superimposed for clarity.

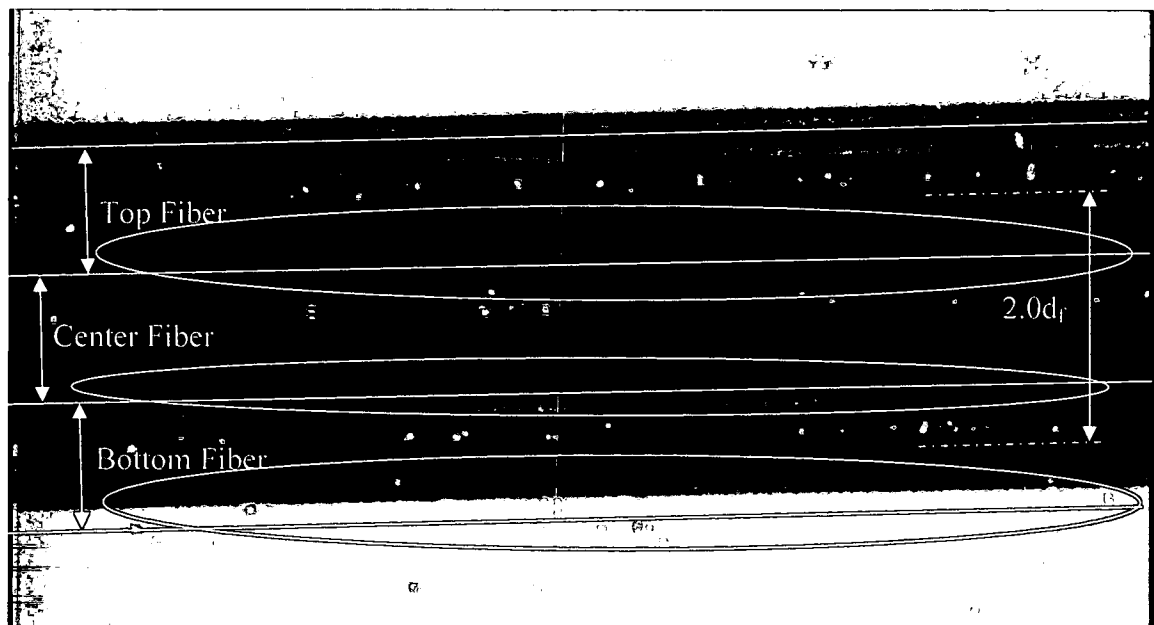


Figure 65: Photomicrograph of steel/2.0d_f 862 cruciform specimen before light intensity and fiber group expansion

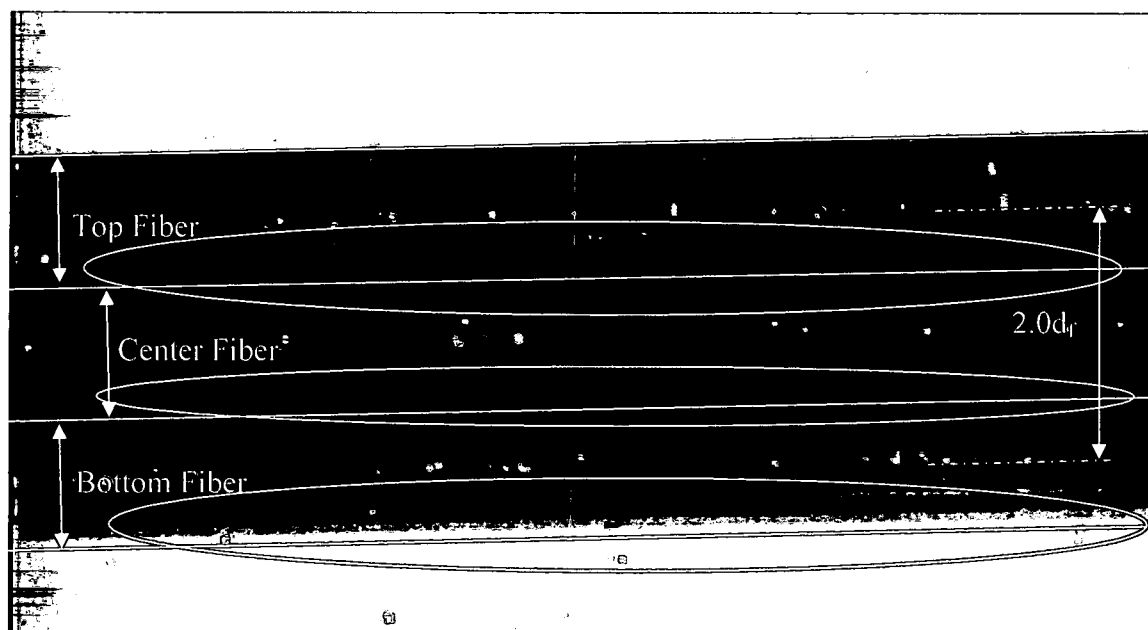


Figure 66: Photomicrograph of steel/2.0d, 862 cruciform specimen after light intensity and fiber group expansion

Viewing actual images side-by-side to observe the subtle changes is very difficult especially to determine if the fiber group expanded. A variation of the image technique similar to the image subtraction technique previously described is employed here to show the difference in light intensity and fiber group expansion. Figure 67 is a photomicrograph showing the difference between Figure 65 and Figure 66. However, in this case the differences between the images are of importance instead of subtracting features common to both images. The difference in the changes in light intensity is highlighted as shown in Figure 67 by the light streaks occurring at the 45° and 315° position on the bottom fiber and at the 45° position on the top fiber. In addition, other features common to both images is an increase in light intensity. The fiber edges are superimposed on the image before and after the fiber group expansion showing the relative movement. Figure 64 illustrates the fiber group expansion by the two lines at the north pole and south pole of the bottom fiber. The far field view, as described above, views the specimen fiber group from above the primary high magnification camera. Thus the top corner fibers, the center fiber and bottom front corner fiber are visible. The far field image analysis revealed no damage initiation at the time the changes in light intensity and fiber expansion occur. Based upon the

differences in the images described above, as well as the behavior illustrated in 6.0d, 862/W of a debond occurring at the approximate 315° position on the bottom fiber. The observations of this particular fiber group that the changes in light intensity and fiber group expansion occur instantaneously. It can be concluded that this behavior is the result of fiber matrix debonds occurring within the interior of the fiber group unseen due to the fiber spacing and camera positions. Further evidence that indicates these are interior fiber matrix debonds are that this behavior manifests itself with an observable fiber matrix debond as mentioned earlier. In addition, all specimens fail in the center of the specimen, 6 specimens at the south pole of the top fiber and 4 specimens at the north pole of the bottom fiber.

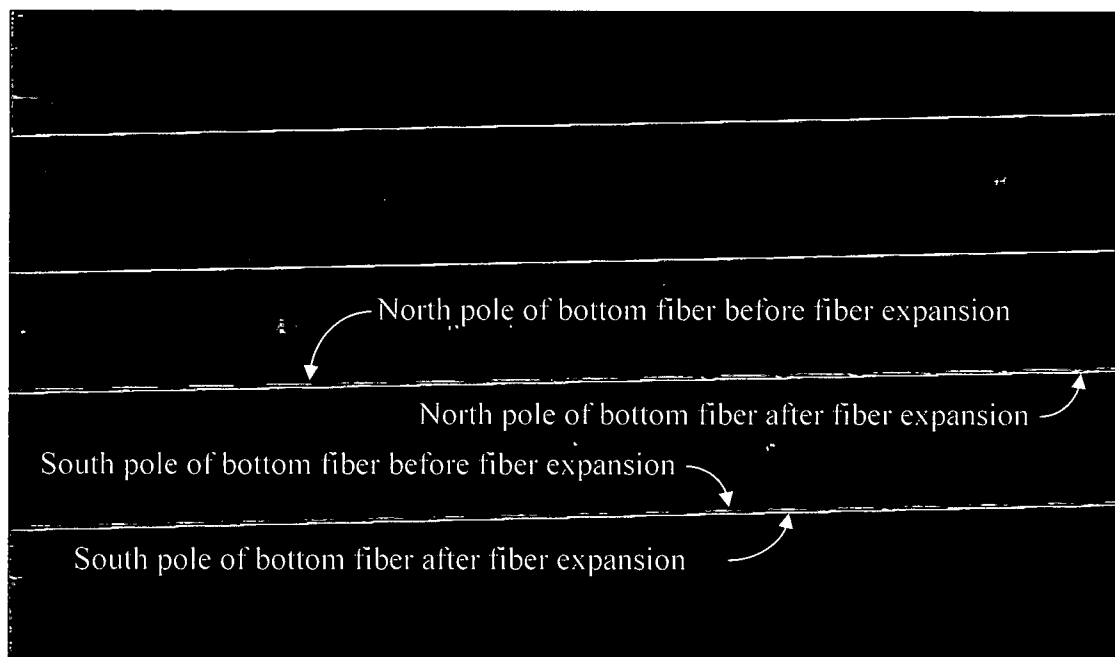


Figure 67: Variational image between Figure 65 and 66 showing the change in light intensity and fiber grouping expansion

The fracture surface SEM image is shown in Figure 68 where the center fiber is still intact and the imprints of the corner fibers are visible. The fracture initiation appears to be the flat smooth surface having a clam shell shape in the north central part of the image. The unlabeled white arrow in the center of the fracture surface points to a feature common at this fiber spacing

near the specimen edge that appears to be the failure initiation location inside the fracture initiation site. Figure 69 is a SEM image of the feature at a higher 95X magnification. Figure 69 reveals six other similar features within the same fracture initiation site. All have a similar shape although varying in size and have chevrons emitting from the bottom of their "U" shape. The chevron features indicate a shear component in the failure mechanism. Comparing these images to those occurring on the fracture surface of the 828/D-230 1.84d_f and 1.75d_f fiber spacing groups, they have similar characteristics; both have a "U" shape, are indented into the fracture surface having multiple horizontal planes at decreasing elevations from the fracture surface and appear to have a shear component accompanying the tensile component of the failure mechanism. Figure 70 is practically the same feature on another 2.0d_f fiber spacing fracture surface at 350X magnification. In all cases the failure features are very similar in shape but differing sizes and have the same chevrons features emitting from the bottom of their "U" shape. Through a thorough fracture analysis, no other failure or fracture initiation mechanisms are evident on the fractured surface of the cruciform specimens. The first damage mechanism at the 2.0d_f fiber spacing is by matrix cavitation and the fracture surface features pointed out by the white arrows in Figures 68 through 70 are similar to the features found in the 828/D-230 1.84d_f and 1.75d_f fiber spacing cruciform specimens that also exhibited matrix cavitation as their first damage mechanism. It is most likely that these features are examples of matrix cavitation in the 862/W matrix system. The largest cavitation feature in both Figures 68 and 69 measured approximately 0.038 mm and 0.086 mm respectively which is easily seen by the high magnification camera recording the cruciform experiments. In addition, the locations of the cavitation features are away from the fiber imprint edge, closer to the specimen edge.

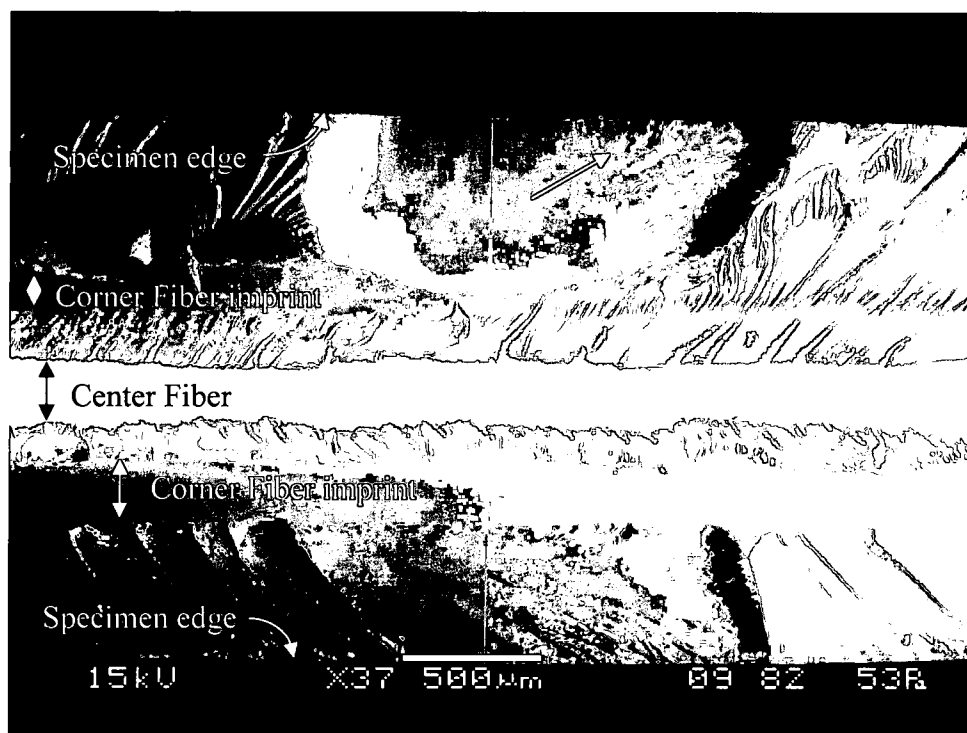


Figure 68: SEM image of fracture surface of steel/2.0d, 862 cruciform specimen

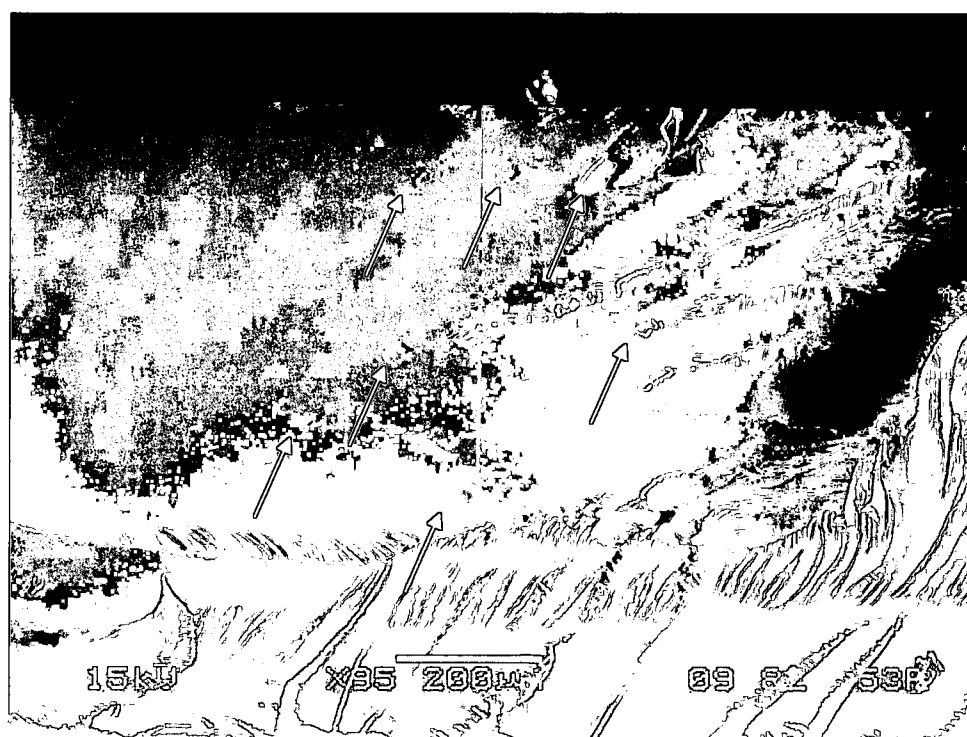


Figure 69: SEM image of same failure initiation feature shown in Figure 68 at 95X magnification

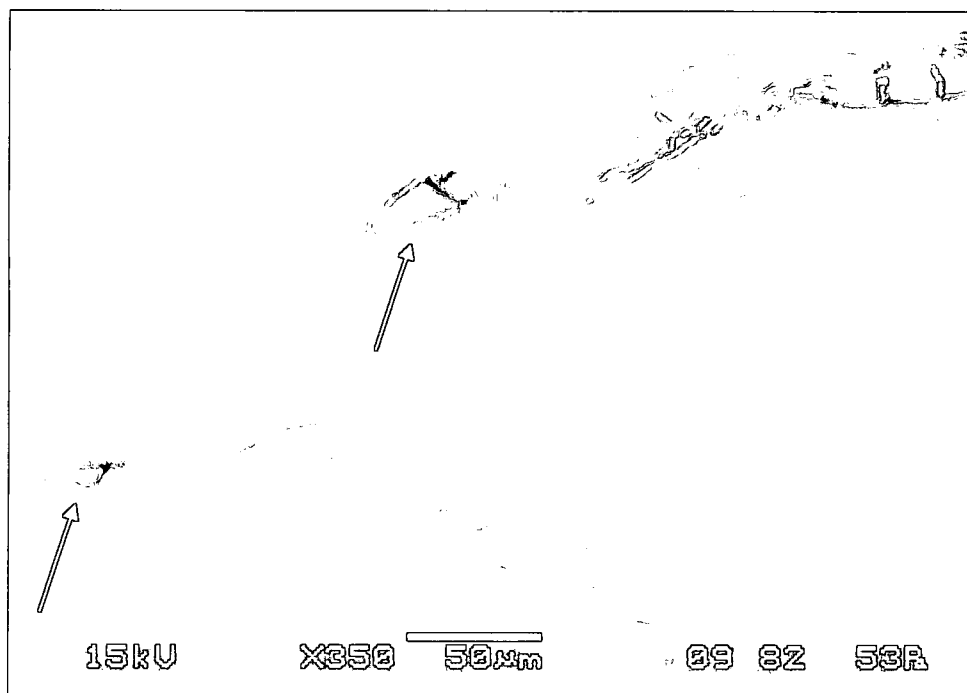


Figure 70: SEM image of failure initiation features on different steel/2.0d, 862 cruciform specimen than shown in Figure 68 and 69

Steel/862/W 1.9d_f Multi-Fiber Cruciform Results. Nine specimens were tested in the 862/W matrix system having the fiber spacing of 1.9d_f. Table 23 lists the far-field applied stress at failure initiation for the top, center and bottom fibers. One specimen did not exhibit an internal damage mechanism prior to final failure that occurred in the top loading arm. In 5 of the 9 specimens the failure was attributed to internal debonds in the same manner as the majority of the 2.0d_f 862/W specimens debonded. In 3 of the 9 specimens the failure initiation was directly observed as fiber-matrix debonding and occurred in the vicinity of the fiber pole in 2 of the 3 specimens. No multiple debonds occurred in any specimens or on any single fiber in any specimen at this particular fiber spacing in the 862/W matrix system.

Table 23: Far-field applied stress at debond initiation in multi-fiber specimens having 1.9d_r fiber spacing where the superscript indicates approximate location

Specimen	Far-field stress at internal debond initiation (MPa)	Far-field stress at debond initiation (MPa)		
		Top Fiber	Center Fiber	Bottom Fiber
S190R2C1-A	11.93	-	-	-
S190R2C1-B	-	-	-	17.44 ^{317°-335°}
S190R2C1-C	20.30	-	-	-
S190R2C1-D	21.55	-	-	-
S190R2C1-E	-	19.27 ^{NP}	-	-
S190R2C1-F	19.23	-	-	-
S190R2C1-G	-	-	-	-
S190R2C1-H	-	-	-	14.72 ^{NP}
S190R2C1-I	13.43	-	-	-

Figure 71 is a photomicrograph showing the difference between images before and after internal debonds. Recall that the difference between images show only the change in features after an event whereas subtracting images shows different features after an event by removing those common to both images. Figure 71 illustrates the fiber group displacement and light intensity changes typically observed for the 5 specimens that exhibited internal failure at this fiber spacing. The fiber edges of the top and bottom fibers have been superimposed for clarity and show the expansion that the fiber group experiences due to the internal debond. The top and bottom lines of both fibers are the location of the fiber poles after the expansion of the fiber group has taken place. Although not called out in Figure 71, the double lines at the south pole of the top fiber and north pole of the bottom fiber are the before and after fiber group expansion locations of the respective fiber poles. The light grey lines at the 305° position on the top fiber and between 22.5° to 90° and 270° and 337.5° position on the bottom fiber show the changes in light intensity typically observed that indicate an internal debond. As observed when other specimens experience fiber-matrix debonds, the existing features in the specimen also experience a change in light intensity. When not within the debond the existing features become brighter as shown in Figure 71 by the existing spots on the top and bottom fibers as well as the spots along the centerline of the center fiber. The streaks on the left side of the image are a result of the image extraction software used to capture images from the videotaped experiments and are not a result of the experiment.

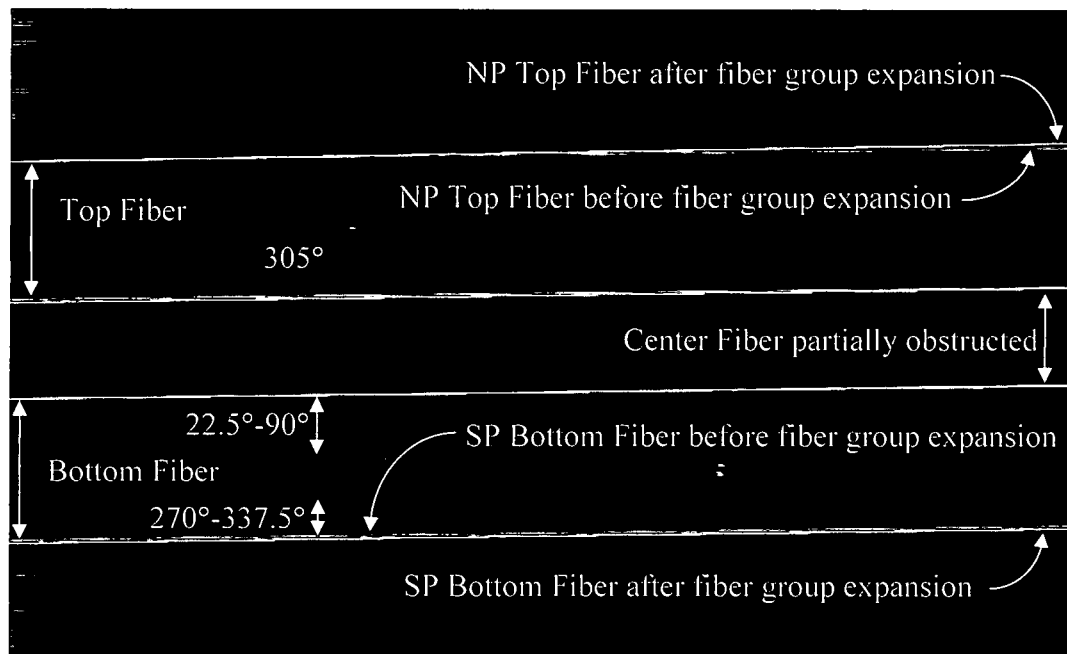


Figure 71: Variational photomicrograph of the steel/1.90d_f 862 cruciform specimen showing the light intensity and fiber group expansion changes characteristic of internal debonds

Of the three specimens where the fiber-matrix debond is directly observed two of the three formed thin debonds, one near the fiber north pole and the other as shown in the subtracted image of Figure 72. Between approximately the 317° to 327° position on the bottom fiber, two separate debonds formed as indicated by the light grey almost white strip on the bottom fiber. At approximately the center of the white strip the debond expanded along the fiber circumference to about the 335° position. Typical formations occur as small individual faint light grey-white bands formed on the fiber then connect as load is continually applied. The fiber edges have been superimposed in Figure 72 for clarity. No other damage from the applied load is seen in Figure 72 giving a clear indication that this is the specimen's only failure initiating event. The average far-field applied stress at debond initiation for the 1.90d_f fiber spacing in the 862/W matrix system is 17.23 MPa.

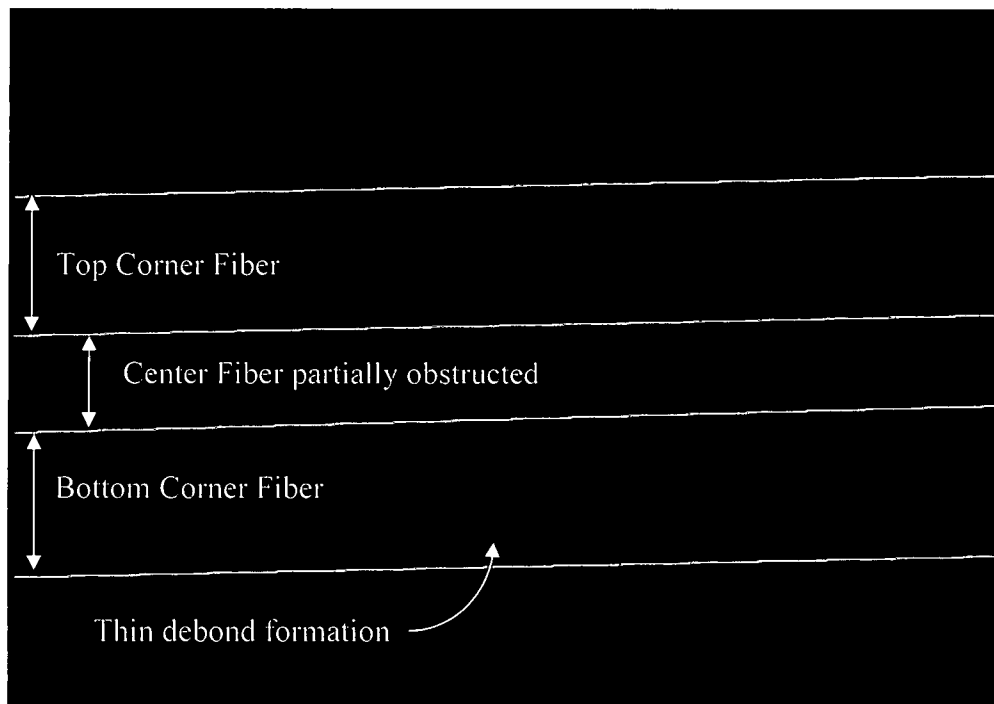


Figure 72: Subtracted image showing bottom corner fiber thin fiber-matrix debond in steel/1.9d, 862 cruciform specimen

In only 3 of the 9 specimens fiber-matrix debonds were actually observed, debond initiation measurements could only be made for two because the debond was on the back top corner fiber of specimen S190R2C1-E where the debond limits were obstructed. Of the 2 that were visible only one debonded in the vicinity of the fiber pole while the other debonded as shown in Figure 72. The specimen debonding at the fiber pole measured a debond width of about 0.041 mm creating a debond central angle of 80° . Thus, its debond limits at the north pole are from 50° to 130° and at the south pole from 230° to 310° .

The fracture surface typical of the 1.90d_f fiber spacing cruciform specimens is shown in Figure 73. Here one corner fiber is still attached while the imprint of the other corner fiber is visible. The fracture initiation appears to be between the corner fibers, internal to the fiber group, and between the two features emanating from the corner fiber imprint at opposite angles near the edge of the image. Directly in the center of the image encircled by the white ellipsoid at the fiber imprint edge is a possible failure initiation feature. Figure 74 is an SEM image of the failure

initiation feature, encircled by the white ellipsoid, at a 250X magnification. This feature has similar characteristics of matrix cavitation shown in the 2.0d_f fiber spacing group but no cavitation was observed anywhere at the 1.90d_f fiber spacing. There appears to be a ridge or possibly a crack protruding in a radial direction from the fiber imprint between the two half circles as evidenced by the thin dark line in the center of the white ellipsoid. It is possible that this could be a debond initiation since a combination of radial, shear and perhaps axial stress components could have created this feature. The two features defining the limits of the fracture initiation surface jutting from the fiber imprint at equivalent but opposite angles to the fiber longitudinal axis do indicate a shear component to the fracture stress.

No other failure or fracture initiation mechanisms are evident on the fractured surface of the cruciform specimen. From the cruciform experimental observations and the fracture surface analyses it can be concluded that the likely failure initiation mechanism at this fiber spacing is by fiber-matrix debond.

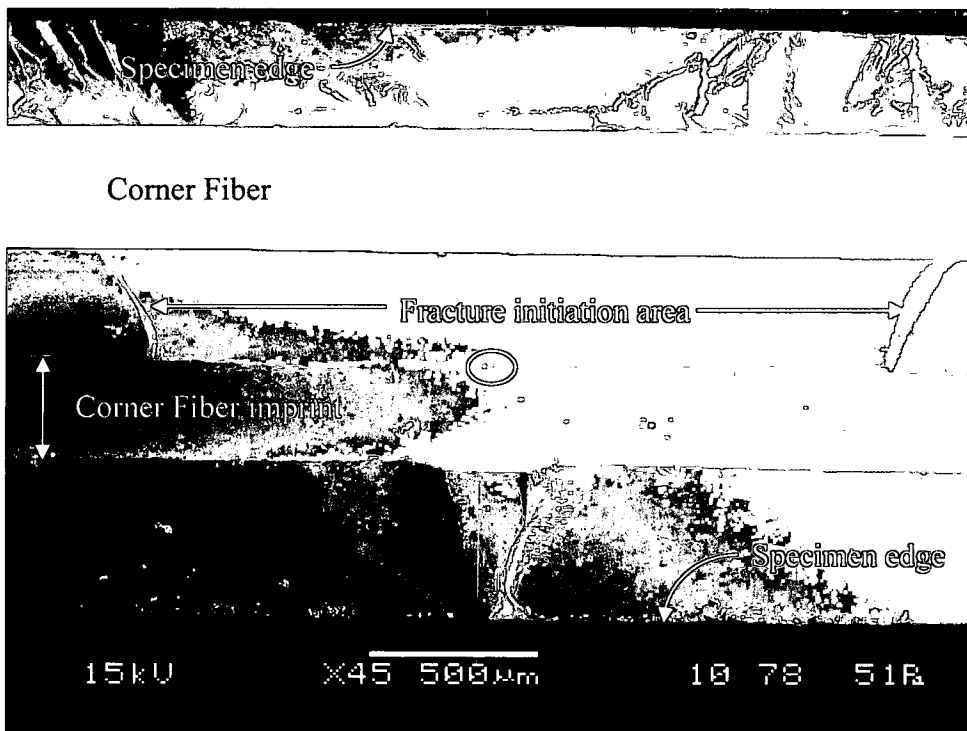


Figure 73: SEM image of steel/1.90d, 862 cruciform specimen fracture surface

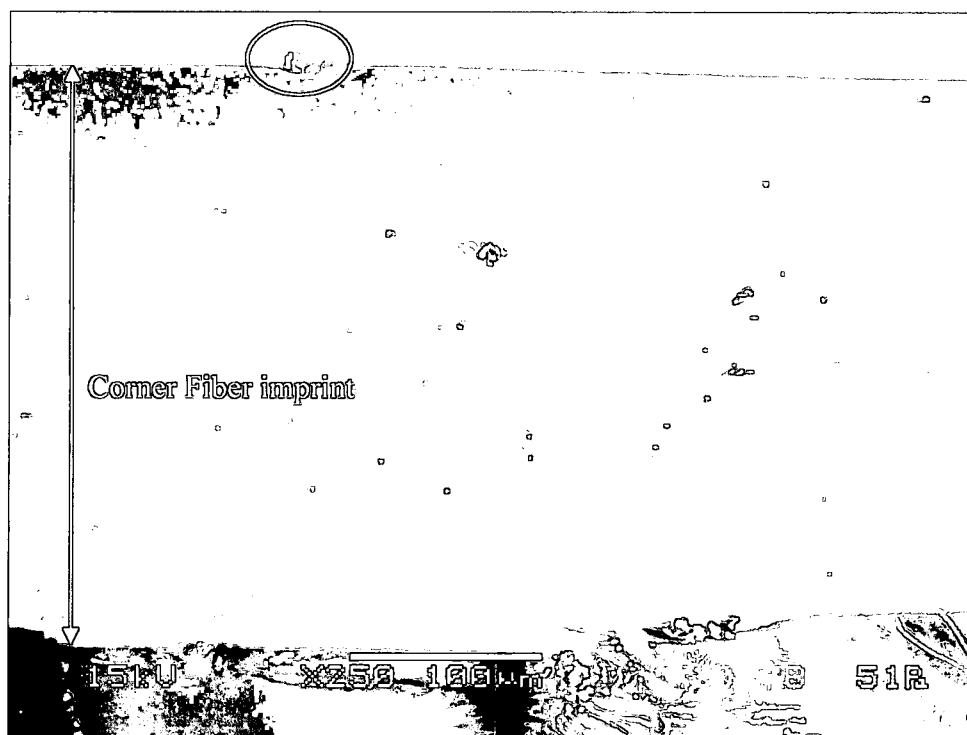


Figure 74: SEM image at 250X magnification showing failure initiation site encircled by the white ellipsoid of steel/1.9d, 862 cruciform specimen

Steel/862/W 1.75d, Multi-Fiber Cruciform Results. A total of 11 specimens at the 1.75d_f fiber spacing in the 862/W matrix system were tested. The first failure mechanism for all specimens was fiber-matrix debonding. Table 24 lists the average applied far-field stress at which damage initiates as a fiber-matrix debond for the top, center and bottom fibers. Seven of the eleven specimens initiate failure interior to the fiber group. For two of these, the internal debond was determined by the expansion of the fiber group and light intensity changes as observed for the 2.0d_f and 1.90d_f specimens in the 862/W matrix system. Of the nine specimens whose fiber-matrix debonds were directly observed, four specimens' debonds form as a thin band in the southern hemisphere of the fiber as indicated in Table 24. Figure 75 shows a subtracted image of the thin debonds occurring on the center fiber, typical of these four specimens. The fiber edges have been superimposed for clarity. These occurred on the top and center fibers usually starting as small non-uniform thin debonds. Several occurred within one second, determined by the

frame-by-frame analysis of the videotaped experiments, growing along the fiber axis coalescing as load was continually applied. In every instance that the debond formed in this manner it never completely connected across the entire fiber length prior to final failure. The average applied stress at fiber-matrix debond initiation was 17.41 MPa.

Table 24: Far-field applied stress at debond initiation in multi-fiber specimens having 1.75d_f fiber spacing where the superscript indicates approximate location

Specimen	FF Stress at internal debond (MPa)	FF stress at debond initiation (MPa)			Loc w/r/t Fiber group
		Top Fiber	Center Fiber	Bottom Fiber	
S175R2C1-A	-	18.52 ^{SP}	-	-	Interior
S175R2C1-E	-	-	8.43 ^{328°-338°}	12.43 ^{NP}	Interior
S175R2C1-F	-	19.81 ^{325°-332°}	-	-	Interior
S175R2C1-G	-	-	23.27 ^{SP}	15.71 ^{SP}	Exterior
S175R2C1-I	-	-	-	17.52 ^{SP}	Exterior
S175R2C1-J	-	-	-	14.84 ^{SP}	Exterior
S175R2C1-K	-	-	-	23.54 ^{SP}	Exterior
S175R2C1-L	27.3	-	15.49 ^{355°-359°}	-	Interior
S175R2C1-M	19.92	-	-	-	Interior
S175R2C1-N	21.75	-	-	-	Interior
S175R2C1-O	-	15.94 ^{318°-324°}	-	-	Interior

Table 25 lists each specimen's debond initiation measurements consisting of the debond width, central angle, location, FEM location and debond type. Five of the nine observed debonds occurred in the vicinity of the fiber pole; while the rest occurred in the southern hemisphere of the debonded fiber as previously mentioned. The average central angle calculated from the average debond width is 104° for the 1.75d_f fiber spacing group and only 5° from the median of the range of the individual specimen debond central angles. For the specimens were their debond initiation occurred other than the fiber pole; the angular location falls within the standard deviation of the average debond central angle.

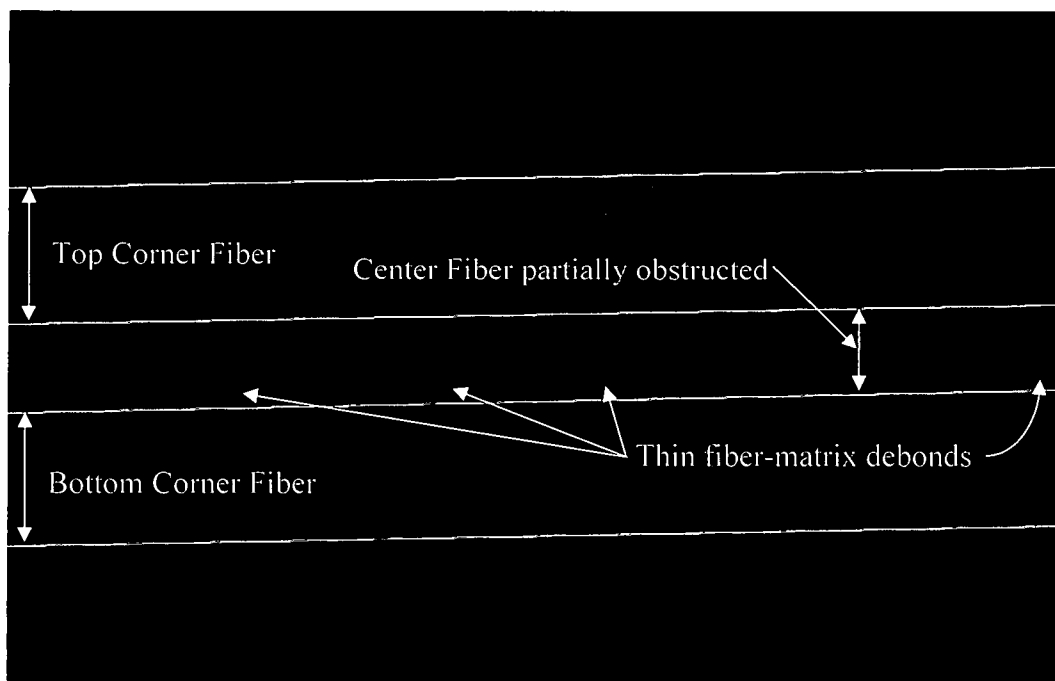


Figure 75: Subtracted image showing thin fiber-matrix debonds in steel/1.75d, 862 cruciform specimen

Table 25: Steel/862 1.75d_f cruciform specimen debond measurements

Specimen	Db Width (mm)	Db Central Angle (deg)	Loc	FEM Loc	Type
S175R2C1-A	0.135	152°	SP-TF	SP-TF	IAS
S175R2C1-E		@ 326° - 338°	SH-CF	NH-CF	Spot ~ 0.328 mm
S175R2C1-F		@ 325° - 332°	SH-TF	SH-TF	Spot ~ 0.43 mm
S175R2C1-G	0.095	124°	SP-BF	NP-TF	IAS
S175R2C1-I	0.045	84°	SP-BF	NP-BF	IAS
S175R2C1-J	0.037	76°	SP-BF	NP-TF	IAS
S175R2C1-K	0.028	66°	SP-BF	NP-TF	Spot ~ 0.053 mm
S175R2C1-L		@ 355° - 359°	SH-CF	NH-CF	Spot ~ 0.072mm
S175R2C1-M	Internal debond - obstructed		-	-	-
S175R2C1-N	Internal debond - obstructed		-	-	-
S175R2C1-O		@ 318° - 324°	SH-TF	SH-TF	Spot ~ 0.06 mm
AVG	0.068	104° AVG CA => 38° to 142° NP & 218° to 322° SP			
Std-dev	0.041				

Figure 76 is an SEM image of the typical fracture surface of the 1.75d_f cruciform specimen. Both corner fiber and the center fiber imprint are shown in the SEM image. The fracture initiation locations appear to occur at the exterior edge of both corner fibers between the features protruding from the edge of the fiber at similar but opposite angles as noted in Figure 76. There also appears to be a failure initiation site at the edge of the corner fiber pointed out by the black arrow. Figure 77 is an SEM image of that fracture initiation site at a 200X magnification showing features very similar to that shown on the fracture surface on the 1.90d_f fiber spacing cruciform specimen. Here the feature is a semicircle at the fibers edge pointed out by the white arrow. Parallel to the fiber are what appears to be cracks as pointed out by the black arrow. These cracks suggest that the semicircle feature could be caused by combination of radial and shear stress acting at the interface. This stress combination in all likely hood would create a fiber-matrix debond which would propagate along the fiber axis while wrapping around the fiber circumference. Several specimens at this fiber spacing initiate their debond other than the fiber pole as listed in Table 24 above. Also shown in Figure 77, are chevrons on the protruding or ridge like features marking the fracture initiation area limits. These features jutting from the fiber edge are more like ridges with the point of the chevron being the apex of the ridge. The shape of the ridge along with the chevrons indicates a shear stress presence along with the tensile component of fracture stress initiating the fracture of the 1.75d_f cruciform specimens. No other fracture or failure mechanisms were observed on the fracture surface in the analysis. The experimentally observed failure initiation mechanism at this fiber spacing is fiber-matrix debonding and the fracture surface analysis indicates a shear and tensile stress interaction causing the final failure. Since no other failure mechanisms were seen on the fractured surface, it can be concluded that the failure initiation is by fiber-matrix debonding. It is highly likely that the fiber-matrix debond was created by an interaction between the tensile stress and shear stress components.

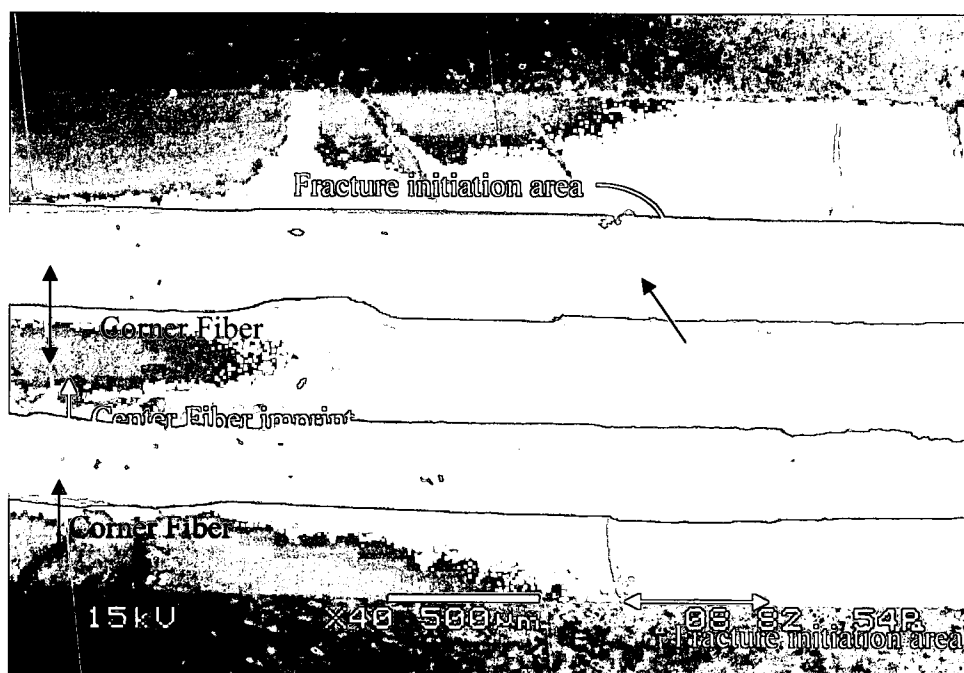


Figure 76: SEM of fracture surface of steel/1.75d, 862 cruciform specimen

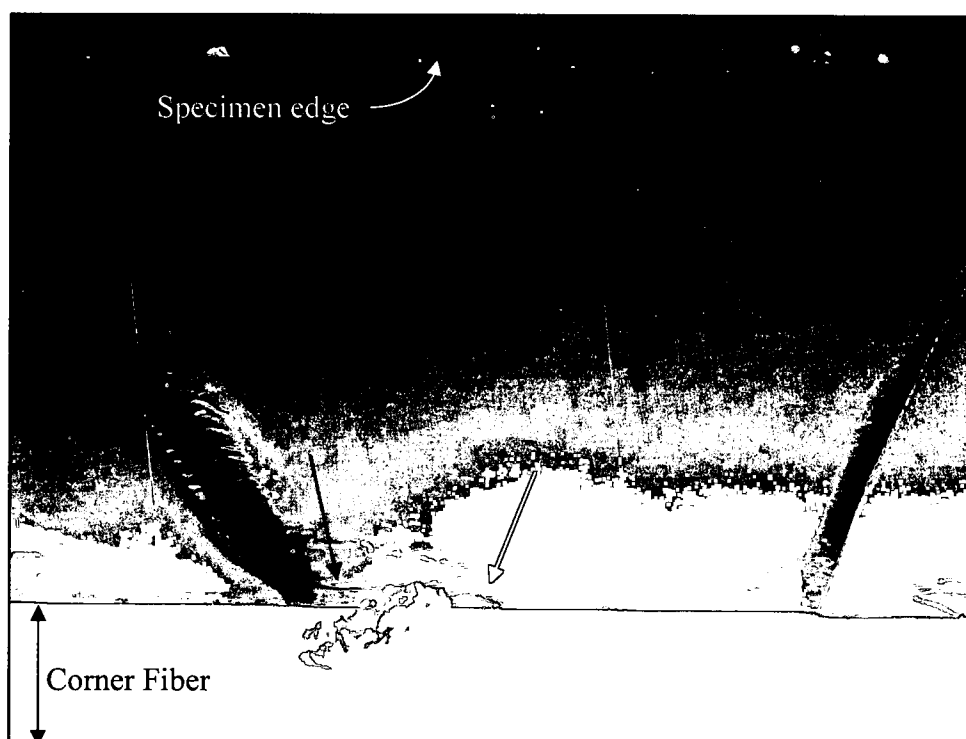


Figure 77: SEM of fracture surface of steel/1.75d, 862 cruciform specimen at 200X magnification showing possible failure initiation feature

Steel/862/W 1.57d_f Multi-Fiber Cruciform Results. A total of 16 specimens were tested having the fiber spacing of 1.57d_f and for all specimens the first damage mechanism is fiber-matrix debonding. Table 26 lists the applied far-field stress at debond initiation for the top, center and bottom fibers. In 9 of the 16 specimens the debond initiated interior to the fiber group. All but five specimens debonded on multiple fibers and, with the exception of when the center fiber debonded, all debonds initiated in the vicinity of a fiber pole. At this fiber spacing the center fiber's north and south pole is obstructed from view by the top and bottom corner fibers. Only 0.21 mm of the 0.36 mm fiber diameter is showing or a little over 58% of the fiber is visible. Consequently when the center fiber debonds the exact location is not observed, however, from detailed image analysis it can be determined in which hemisphere of the fiber that the debond initiates.

Figure 78 is a photomicrograph showing the subtracted images of a typical fiber-matrix debond at the 1.57d_f fiber spacing. In this case the debond initiated interior to the fiber group very near the south pole of the top fiber. The debond tip can be seen travelling from left to right in Figure 78. The fiber edges have been superimposed for clarity. In most cases, at this fiber spacing, the debond initiated instantaneously over a small length of fiber. Furthermore, the debond tip does not propagate around the fiber circumference thus forming a very thin debond having a small central debond angle. The average far-field applied stress at fiber-matrix debond initiation is 12.04 MPa.

Table 26: Far-field applied stress at debond initiation in multi-fiber specimens having 1.57d_r fiber spacing where the superscript NH and SH designate Northern Hemisphere, and Southern Hemisphere respectively

Specimen	Far-field applied stress at debond initiation (MPa)			Location w/r/t Fiber Group
	Top Fiber	Center Fiber	Bottom Fiber	
S157R2C1-F	6.67^{SP}	-	-	Interior
S157R2C1-G	7.80^{SP}	-	10.52 ^{SP}	Interior
S157R2C1-H	16.35 ^{SP}	16.61 ^{SH}	14.47^{SP}	Exterior
S157R2C1-I	8.61^{NP}	31.20 ^{NH}	15.07 ^{SP}	Exterior
S157R2C1-J	13.11 ^{NP}	27.62 ^{NH}	8.94^{NP}	Interior
S157R2C1-K	11.21^{SP}	-	23.0 ^{SP}	Interior
S157R2C1-L	11.95^{SP}	-	-	Interior
S157R2C1-M	16.44^{NP}	-	17.83 ^{SP}	Exterior
S157R2C1-N	19.44 ^{SP}	-	17.43^{SP}	Exterior
S157R2C1-O	16.02^{NP}	-	17.61 ^{NP}	Exterior
S157R2C1-P	11.40^{NP}	-	-	Exterior
S157R2C1-Q	14.16 ^{NP}	-	13.05^{SP}	Exterior
S157R2C1-R	14.34^{SP}	-	19.39 ^{SP}	Interior
S157R2C1-S	9.25^{SP}	-	12.49 ^{NP}	Interior
S157R2C1-U	-	14.28^{SH}	-	Interior
S157R2C1-V	-	10.72^{SH}	-	Interior

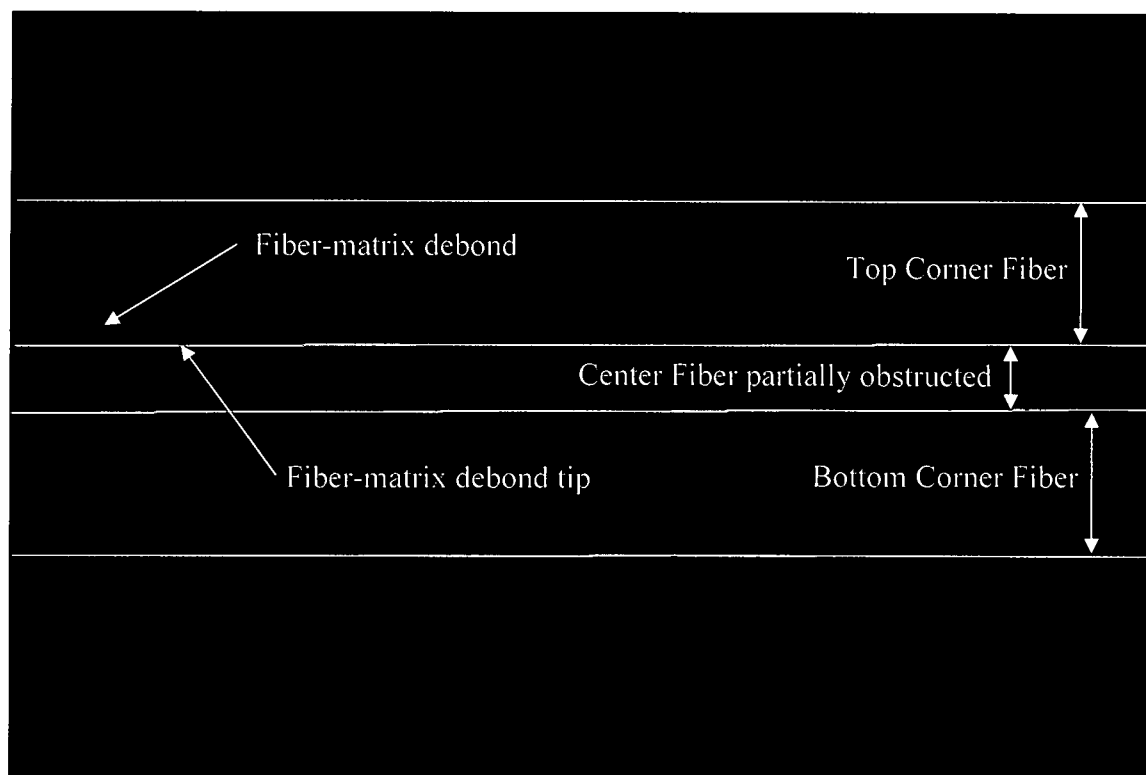


Figure 78: Subtracted photomicrograph of the steel/1.57d_r fiber 862 specimen showing a fiber-matrix debond at the south pole of the top corner fiber

Table 27 lists the debond initiation measurements of debond width, central angle, location, FEM location and debond type. Three specimens, namely S157R2C1-P debonded on the top back corner fiber, while S157R2C1-U and S157R2C1-V debonded on the center fiber. Thus in these cases the debond limits were obstructed from view consequently the width measurements could not be made. The average debond central angle calculated from the average width of the debonds is 88°, which is 9° less than the median of the range of the individual specimens' central angles.

Table 27: Steel/862 1.57d, cruciform specimen debond measurements

Specimen	Db Width (mm)	Db Central Angle (deg)	Loc	FEM Loc	Type
S157R2C1-F	0.034	72°	SP-TF	SP-TF	Spot ~ 0.39 mm
S157R2C1-G	0.032	70°	SP-TF	SP-TF	Spot ~ 0.43 mm
S157R2C1-H	0.047	86°	SP-BF	NP-TF	IAS
S157R2C1-I	0.040	78°	NP-TF	NP-TF	Spot ~ 0.055 mm
S157R2C1-J	0.073	108°	NP-BF	SP-TF	Spot ~ 0.52 mm
S157R2C1-K	0.024	60°	SP-TF	SP-TF	Spot ~ 1.27 mm
S157R2C1-L	0.049	88°	SP-TF	SP-TF	Spot ~ 1.71 mm
S157R2C1-M	0.109	134°	NP-TF	NP-TF	IAS
S157R2C1-N	0.026	62°	SP-BF	NP-TF	Spot ~ 0.16 mm
S157R2C1-O	0.086	118°	NP-TF	NP-TF	Spot ~ 2.57 mm
S157R2C1-P	NP-TF Back		NP-TF	NP-TF	-
S157R2C1-Q	0.046	84°	SP-BF	NP-TF	Spot ~ 0.992 mm
S157R2C1-R	0.033	70°	SP-BF	NP-TF	Spot ~ 0.455 mm
S157R2C1-S	0.042	80°	SP-TF	SP-TF	Spot ~ 0.16 mm
S157R2C1- U	Center fiber debond		SH-CF	NH-CF	-
S157R2C1-V	Center fiber debond		SH-CF	NH-CF	-
AVG	0.049	88° AVG CA => 46° to 134° NP & 226° to 314° SP			
Std-dev	0.024				

Figure 79 is an SEM image of a typical fracture surface of the 1.57d_f fiber spacing cruciform specimen. In this particular image the center fiber is still intact between the corner fiber imprints. There appears to be multiple fracture initiation sites at the exterior edge of the southern corner fiber imprint and at the southern center fiber edge indicating initiation at both interior and exterior to the fiber group. These sites are characterized by the "V" shaped feature at the fiber edge that juts out at a slight angle to the longitudinal fiber axis. The fracture initiation site at the northern corner fiber is pointed out by the white arrow. The features on exterior side of the

northern corner fiber imprint are more at an angle to the longitudinal fiber axis. In both cases, these features, due to the angle they make with the fiber, indicate a shear component present with the tensile component causing the fracture stress. The primary or largest fracture stress component appears to be a tensile stress due to the smooth surface between the features protruding from the fiber edges. The fiber imprints appear to be smooth indicating a dominate tensile stress, although there exists some porosity in the southern corner fiber imprint. No other fracture or failure initiation sites were indentified on the fractured surface. Based on the fractured surface analysis, it can be concluded that the observed fiber-matrix debond is in fact the failure initiation mechanism for this fiber spacing. Furthermore, it is highly likely that the fiber-matrix debond mechanism has a shear component to the dominate tensile stress component creating the debond.

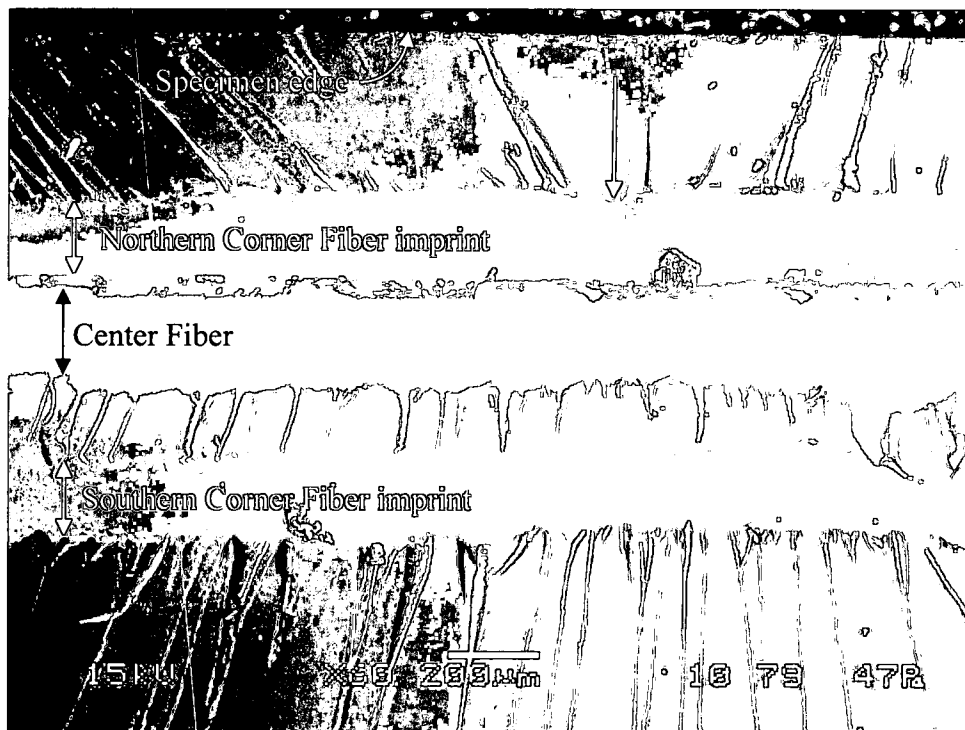


Figure 79: SEM image of fracture surface of steel/1.57d, 862 cruciform specimen

Steel/862/W Cruciform Experimental Summary

Multi-fiber cruciform specimens of six different fiber spacing groups, $6.0d_f$, $2.5d_f$, $2.0d_f$, $1.9d_f$, $1.75d_f$ and $1.57d_f$, along with a single fiber (SF) configuration were tested in the 862/W matrix system. The first damage mode for the SF, $6.0d_f$, $2.5d_f$, $1.9d_f$, $1.75d_f$ and $1.57d_f$ groups was fiber-matrix debonding. For the $2.0d_f$ fiber spacing group, matrix cavitation was observed as the first damage mode. Table 28 summarizes the average far-field applied stress at first failure, the first damage mode, the average debond initiation width and the corresponding average debond central angle for each fiber spacing group.

Table 28: Summary of 862 cruciform test results

Fiber Spacing Group	AVG Far-field stress at damage initiation (MPa)		Failure initiation mechanism	AVG db width (mm)	AVG db Central Angle (deg)
	debond	Cavitation			
SF	14.46	N/A	debond	0.023	54°
$6.0d_f$	15.19	N/A	debond	0.039	78°
$2.5d_f$	12.56	N/A	debond	0.035	74°
$2.0d_f$	16.82	7.65	cavitation	N/A	N/A
$1.9d_f$	17.23	N/A	debond	0.041	80°
$1.75d_f$	17.41	N/A	debond	0.068	104°
$1.57d_f$	12.04	N/A	debond	0.049	88°

Peculiar to the 862/W matrix system is the formation of interior debonds. This behavior was exhibited in specimens having the $2.0d_f$, $1.9d_f$, and the $1.75d_f$ fiber spacing. The behavior is characterized by the fiber group expansion and light intensity changes detectable only through detailed image analysis. Because the same behavior is exhibited when a fiber-matrix debond is directly observed, it can be concluded that a debond forms in the interior of the fiber group undetectable due to the corner fibers and camera position relative to the fiber group. The S190R2C1 cruciform specimen group exhibited the majority of their failure initiation in this manner with only three specimens have the initiation directly observed. Of the three observed failure initiations, one was partially obstructed, one debonded in the southern hemisphere of the bottom corner fiber and the last one debonded in the vicinity of the fiber pole.

Unlike in the 828/D-230 system, the 862/W single fiber far-field debond initiation stress did not have the largest magnitude but it was very close to that of the $6.0d_f$ fiber spacing group. One explanation for the single fiber behavior in contrast to the 828/D-230 system, could be that the wide fiber spacing in the 862/W matrix system acts as isolated fibers in the more compliant resin system. Although, the ultimate strength is greater in the 862/W matrix system than in the 828/D-230 system, it has a lower modulus and is a very ductile system exhibiting over 8% strain as seen in the neat resin tests described in Appendix A. Thus, due to the greater stiffness of the 828/D-230 matrix; the 828/D-230 SF cruciform can achieve a higher far-field stress at debond initiation. Whereas, the 862/W SF cruciform does not achieve a greater debond initiation far-field stress due to its lower modulus and more compliant system. However, as additional fibers are introduced in the multi-fiber configuration, loading is redistributed by the additional fibers while the more compliant matrix allows more strain enabling greater load carrying capacity.

In general, it appears that as the fiber spacing decreases the far-field stress at debond initiation increases for the multi-fiber cruciform specimens. The exceptions being the $1.57d_f$ and the $2.5d_f$ fiber spacing groups where their far-field stress at debond initiation is practically equal. It also appears that the $2.5d_f$ is influenced by three specimens that have relatively very low debond initiation far-field stresses. Removing these outliers yield a average debond initiation far-field stress for the remaining 6 specimens at the $2.5d_f$ fiber spacing of 15.61 MPa that falls directly in line with the general trend. Although the range of the far-field stress at debond initiation for the $1.57d_f$ fiber spacing is fairly large being 6.67 MPa to 17.43 MPa, there are no obvious outliers. In addition, the specimens exhibiting relatively low debond initiation stress preferably fail interior to the fiber group. It is conceivable that at the $1.57d_f$ spacing the volume of matrix between the fibers is so small that the inherent compliant characteristic of the matrix is not developed. Thus, the constraining influence of the fiber generates high stress concentration factors causing it to fail sooner than those at a wider spacing.

There appears to be a preference for debonding interior to the fiber group below the spacing that cavitation was observed to occur, i.e. below the $2.0d_f$ spacing. Even including the cavitated fiber spacing group, the vast majority of debonds initiate interior to the fiber group. For

the fiber spacing groups greater than the $2.0d_f$ spacing, no preference appears to exist. The majority of samples at the $2.5d_f$ spacing initiate exterior to the fiber group while at the $6.0d_f$ spacing equal numbers initiate exterior and interior to the fiber group.

Matrix cavitation is the first damage mechanism observed in the majority of specimens at the $2.0d_f$ fiber spacing in the 862/W matrix system. The bulk of the cavitations formed within the fiber group and appears to extend a fiber diameter beyond the corner fibers. Internal debonds were observed as the first failure mechanism for two of the 10 specimens that did not cavitated. The wider fiber spacing groups and small fiber spacing groups exhibit fiber-matrix debonding as their first damage mode. Therefore, it appears that the cavitations are dependent on the fiber spacing. In addition, the fiber spacing groups surrounding the $2.0d_f$ is $0.5d_f$ wider, i.e. the $2.5d_f$ spacing, and $1.0d_f$ smaller, i.e. the $1.9d_f$ spacing, and they debond initially. Furthermore, as spacing decreases the difference between the spacing groups decrease and all exhibit fiber-matrix debonds as initial failure. The converse is also true. Consequently, it appears that the $2.0d_f$ spacing may be the optimum spacing to develop matrix cavitations in the 862/W matrix.

Fracture surface analysis was performed on two representative samples from each cruciform fiber spacing group. For the specimens exhibiting fiber-matrix debonding as their first failure mechanism the analysis indicated that a shear component is present with the dominate tensile stress component at the final failure stress state. For the specimen group that exhibited matrix cavitation as its failure initiation mechanism, unique features on the fracture surface were found only at this fiber spacing. These features indicated that the failure possibly initiated at these locations. Furthermore, the distinctive features indicated that a shear component of the failure initiation stress is present.

References

1. Asp, L.E., L.A. Berglund, and R. Talreja, *Prediction of a matrix-initiated transverse failure in polymer composites*. Composites Science and Technology, 1996. **56**: p. 1089-1097.

2. Asp, L.E., L.A. Berglund, and R. Talreja, *A criterion for crack initiation in glassy polymers subjected to a composite-like stress state*. Composites Science and Technology, 1996. **56**: p. 1291-1301.
3. Busschen, A.T., *Micromechanical modeling of the transverse strength of unidirectional glass fiber reinforced polyester*, in *Engineering*. 1996, Delft Technical University: Delft, the Netherlands. p. 246.
4. Kok, J.M.M.d., *Deformation, yield and fracture of unidirectional composites in transverse loading*, in *Engineering*. 1995, Eindhoven University of technology: Eindhoven, the Netherlands. p. 141.
5. Makinde, A., L. Thibodeau, and K.W. Neal, *development of an apparatus for biaxial testing using cruciform specimens*. Experimental Mechanics, 1992. **32**: p. 138-144.
6. Makinde, A., et al., *Design of a biaxial extensometer for measuring strains in cruciform specimens*. Experimental Mechanics, 1992. **32**(132-137).
7. Welsh, J.S. and D.F. Adams, *Biaxial and triaxial failure strengths of 6061-T6 aluminum and AS4/3501-6 carbon/epoxy laminates obtained by testing thickness-tapered cruciform specimens*. Journal of Composites Technology and Research, 2001. **23**(2): p. 111-121.
8. Asp, L.E. and L.A. Berglund, *Effects of a composite-like stress state on the fracture of epoxies*. Composites Science and Technology, 1995. **53**: p. 27-37.
9. Bauwens, J.C., *Yield Condition and Propagation of Luders' Lines in Tension-Torsion Experiments on Poly(vinyl Chloride)*. Journal of Polymer Science: Part A-2, 1970. **8**: p. 893 - 901.
10. Sterstein, S.S. and L. Ohgchin, *Yield Criteria for Plastic Deformation of Glassy High Polymers in General Stress Fields*. American Chemical Society Polymer Preprints, 1969. **10**(2): p. 1117 - 1124.
11. Fiedler, B., et al., *Failure behavior of an epoxy matrix under different kinds of static loading*. Composites Science and Technology, 2001. **61**: p. 1615 - 1624.
12. Bechel, V.T. and G.P. Tandon. *Interfacial toughness measurement for a model SiC/epoxy composite*. in *SEM Annual Conference*. 2001. Portland, Oregon: SEM.
13. Bechel, V.T. and G.P. Tandon, *Modified cruciform test for application to graphite/epoxy composites*. Mechanics of Advanced Materials and Structures, 2002. **9**: p. 1-17.

14. Schuller, T., et al., *Single-fiber transverse debonding: tensile test of a necked specimen*. Composites Science and Technology, 2000. **60**: p. 2077-2082.
15. Tandon, G.P., R.Y. Kim, and V.T. Bechel, *Evaluation of interfacial normal strength in a SCS-0/epoxy composite with cruciform specimens*. Composites Science and Technology, 2000. **60**: p. 2281-2295.
16. Tandon, G.P., R.Y. Kim, and R.E. Dutton, *Failure modes in unidirectional composites under transverse loading*. Journal of Reinforced Plastics and Composites, 1997. **16**(1): p. 33-49.
17. Tandon, G.P., et al., *influence of free edge and corner singularities on interfacial normal strength: application in model unidirectional composites*. Composites Part B, 1999. **30**: p. 115-134.
18. Zhang, H., et al., *Transverse single-fiber test for interfacial debonding in composites 1: Experimental observations*. Composites Part A, 1997. **28**: p. 309-315.
19. Gundel, D.B., S.G. Warrior, and D.B. Miracle, *The interface debond stress in single and multiple SiC fiber/Ti-6Al-4V composites under transverse tension*. Acta mater., 1997. **45**(3): p. 1275-1284.
20. Nimmer, R.P., et al., *Micromechanical modeling of fiber/matrix interface effects in transversely loaded SiC/Ti-6-4 metal matrix composites*. Journal of Composites Technology and Research, 1991. **13**(1): p. 3-13.
21. Gundel, D.B., S.G. Warrior, and D.B. Miracle, *The transverse tensile behavior of SiC-fiber/Ti-6Al-4V composites 2: Stress distribution and interface failure*. Composites Science and Technology, 1999. **59**: p. 1087-1096.
22. Warrior, S.G., et al., *Stress distribution in a transversely loaded cross-shaped single fiber SCS-6/Ti-6Al-4V composite*. Scripta Metallurgica et Materialia, 1996. **34**(2): p. 293-299.
23. Bechel, V.T. and G.P. Tandon, *Characterization of interfacial failure using a reflected light technique*. Experimental Mechanics, 2002. **42**(2): p. 200-205.
24. Kim, P. and S. Toll, *Stress spectra and the effective elastic and viscoelastic properties of unidirectional composites under transverse loading*. Journal of Composite Materials, 2000. **34**(17): p. 1418-1436.

CHAPTER III

ANALYTICAL MODEL DEVELOPMENT, RESULTS AND DISCUSSION

Introduction

Predicting the failure initiation of composite materials loaded transverse to the direction of the fiber involves a thorough characterization of the constituent materials, a methodical analysis of the experimental results and parameters, and the proper use of the appropriate criterion. A good reliable failure criterion relies on the careful handling of the experimental measurements of the failure, identification of the experimentally observed failure mechanism, the use of an analytical model that accurately calculates all of the relevant stress components to be used in the criterion and accurate measurements of the constituent material properties for analytical model inputs. In this chapter each of these issues will be discussed briefly as an introduction to the topic. A section on fiber-matrix debonding criterion is next followed by a discussion and down selection of an appropriate criterion to be used for matrix failure. This discussion is based on observations from the experiments presented in Chapter 2 and the observed trends in properties measured for the matrix. Next is the major part of the chapter which details the solid model development for calculating stresses. The next section discusses the interfacial stresses calculated with the model for each fiber spacing group and how these stresses should be used when choosing a failure criterion and using it to predict interfacial failure. Finally, for each material an approach to separating the matrix into manageable sections for evaluating the matrix failure criterion is described followed by plots of the calculated values of the down selected matrix failure criteria.

Review of Failure Criteria

As stated, one of the difficulties in getting an accurate prediction of transverse failure is obtaining correct internal stresses of the experimental specimen used in the investigation. As discussed in Chapter 2, most specimen geometry was rectangular shaped and used two-dimensional (2D) models to calculate the internal stresses [1-11]. The simplifying assumptions of the 2D analytical models do not capture the internal stress state dominated by free edge stress singularities occurring with straight sided samples. For example, deKok [5] used samples cut from filament wound tubes in rectangular and dumbbell shapes, with polished edges, tested in tension and three point bending. His 2D models then tried to predict the transverse strength based on the experimental results using a periodic array for modeling the fibers. The problem with this is that the experimental results are influenced by the singularity where the fiber interface meets the free surface that the model completely ignores. Furthermore, using a periodic array to model the fibers within the specimen ignores fiber alignment issues, resin and fiber rich areas of the composite and fiber-matrix debonding due to cutting of the samples from the filament wound tubes. These issues further affect the experimental results and can never be captured by a periodic array 2D model. Another problem using a periodic array is the constraining influence from neighboring fibers on the surrounding matrix that will affect the interfacial stress as well as matrix stresses is not adequately captured. Another model used with straight sided experimental specimens for the calculation of internal stresses is a 2D concentric cylinder model [4]. Questions concerning the validity of this model are the appropriate diameter of the matrix material around the constant diameter fiber to capture the stresses influenced by neighboring fibers as well as the other problems pointed out earlier.

An improvement to the hour glass specimen shape introduced by Broutman tests a single fiber in tension to determine the adhesion strength between the fiber and matrix [12]. Two dimensional analytical models are used to calculate the internal stresses in the specimen gage length. Although a fairly significant shear stress is developed in the gage length free of stress singularities at the specimen boundary, the larger tensile stress still has a dominating free edge effect.

Parametric studies were also used to study transverse failure of composite materials. In all cases a periodic array of fibers was employed in the 2D analytical model [13-19]. The periodic array varied from a square diagonal to a hexagonal packing arrangement for various fiber volume packing ratios. The problem with these studies is that the models are representing a perfect composite material having uniform fiber spacing not realistic in real composite materials.

Previous attempts to develop criteria explaining the observed competing failure initiation mechanisms of unidirectional composite materials loaded transverse to the fiber direction are separated and fall naturally into addressing only the fiber-matrix debonding and only the matrix failure. In fact, both mechanisms may be present in the particular composite part subjected to loading normal to the direction of fibers. In the body of work encompassing either fiber-matrix debonding or matrix failure concessions are made that the other failure mechanism may precede the one under discussion. In this chapter a historical synopsis will be given on each criterion. Conclusions will be drawn pointing the direction for developing a failure initiation criterion based upon the observed experimental results presented in Chapter 2. In addition, details of the analytical models used to determine the stress state in the cruciform specimens will be presented.

Residual stresses play an important role in calculating the transverse strength of a composite material. Previous work in this area was based on the thermoelastic response of the fiber and matrix [1, 3, 5, 6, 20-23] using 2-D FEM to calculate residual stresses. Others either did not include the calculation of residual stresses, completely ignored them or it was unclear how these were incorporated into their work [9, 19, 24, 25]. Results indicated that the matrix residual stresses were affected by the fiber volume fraction. It should be noted that the fiber also experiences these residual stresses but it is unclear how they are incorporated into the analysis. In addition these studies indicate that the residual stress components acting on the fiber interface can be either compressive, tensile, both [1, 6, 20, 23]. Consequently the interaction of residual stresses with respect to fiber spacing, especially varying spatial distribution, will have impact on the failure initiation of a composite material.

In the current work these issues were overcome by using a cross shaped specimen originally developed by Grundel et al [26-28] for metal matrix composites and improved upon by Tandon and Bechel et al [29, 30] for polymer matrix composites. The cross shape or cruciform shape of the specimen dramatically reduces, practically eliminating, the free edge stress singularity. A three dimensional (3D) FEM was used to calculate the stresses only in the area of the specimen away from the singularity where stresses were finite and the failure is known to have occurred. This builds on work by Bechel and Tandon [31-36] utilizing the cruciform specimen shape and full 3D FEM but goes beyond it by using multiple fibers to more closely simulate the failure that occurs in a real composite. Furthermore, it also advances the past work by carefully searching through available failure criteria and making a logical argument for which criteria is most appropriate for predicting the observed types of failure.

Fiber-Matrix Debonding Criterion

The majority of previous work investigating the fiber-matrix debonding damage mechanism has been centered on improving the transverse strength of the composite material. To model these effects interface spring models and fracture mechanics methods have primarily been employed. The models try to capture the damage growth to gauge the effects of interface improvements. Through these efforts it has been recognized that fiber-matrix debonding is largely caused by an interaction between the stress acting normal to the fiber surface and the interfacial shear stress [5, 9, 17]. To that end only one criterion has been proposed that attempted to predict the occurrence of a fiber-matrix debond for calculating the transverse tensile strength of composite materials. It is a quadratic interaction involving the interfacial normal and shear stresses [17]. In addition, it has also been shown how strongly the residual stresses and fiber spacing can affect the transverse strength properties of the composite. Only recently in the past 7 years has there been a body of work focused on the fiber-matrix debond mechanism solely at the failure initiation point in polymer matrix composites [29, 30, 32-35, 37]. Although this work has focused only on the stress state of a single fiber it uses the cruciform shape specimen to impart a tensile stress normal to the fiber direction that eliminates free edge effects characteristic of

straight sided specimens commonly used. A quadratic failure criterion involving the interfacial normal and shear stresses have also been developed for the single fiber cruciform work [34, 35].

As a starting point in the analysis of the debond initiation, the point on the interface where maximum interfacial normal stress or radial stress, σ_r , occurs will be investigated. However, as additional fibers are introduced into the model composite the stress state along the fiber-matrix interface will change. Effects from fiber spacing, fiber distribution and residual stress from the matrix curing process will create a complex stress state in the area immediately surrounding the fibers. Consequently the stress that creates the debond will be a function of the combined effects. As pointed out above the likely combination of fiber-matrix interface stresses to cause a fiber-matrix debond are the interfacial normal and shear stresses. As suggested in the literature [5, 17] a quadratic interaction between the normal and shear stress at the fiber-matrix interface works well for predicting the failure of composites. One particular criterion [17] is the squared ratio of the normal and shear stresses at the interface to their respective failure stresses under tension and shear alone expressed as equation (1);

$$\left(\frac{\sigma_r}{\sigma_{yt}} \right)^2 + \left(\frac{\tau_{r\theta}}{\tau_y} \right)^2 = 1 \quad (1)$$

where, σ_r and $\tau_{r\theta}$ are the interfacial normal and shear stress respectively and σ_{yt} and τ_y are the tensile strength and shear strength respectively. The quadratic debond criterion as expressed in equation (1) will be the starting point in the development of a debond criterion explaining the observed experimental results presented in Chapter 2.

Matrix Failure Criterion

The experimentally observed matrix failure is cavitation of the matrix system due to the tensile tri-axial stress state induced by the constraining effects of the fiber spacing from the applied stress [1, 3, 5, 23, 38]. The stiff fibers act as stress magnifiers creating localized stress concentrations within the surrounding matrix material [39]. Due to the fact that both the 828/D-230

and 862/W matrix system exhibit a sensitivity to a hydrostatic component of applied stress since for both materials their compressive strength is greater than their tensile strength; the hydrostatic component will influence the yield process of both resin systems [40]. Consequently material subjected to a hydrostatic compressive state of stress will attain a much higher yield stress than in the absence of any hydrostatic compressive stress state. Conversely the yield stress will be lower when subjected to a tensile hydrostatic stress state. Matrix cavitation manifests itself through the formation of micro-voids or micro-cracks in the region of matrix subject to a tensile tri-axial stress state. It is a precursor to crazing in the polymer and induces a volume change within the material as the tensile tri-axial causes a dilatation of the material. Cavitation has been observed to occur at the interface of second-phase particle inclusions used to enhance impact resistance in glass polymers [41, 42].

Several failure criteria have been proposed in the investigation of matrix failure, specifically cavitation, and are based on the following [1, 3, 5, 6, 15, 21-23, 38, 43-47]:

- A dilatational-energy based criterion
- A distortional-energy based criterion leading to modifications of the von Misses failure criterion
- Eyring's Theory of non-Newtonian flow based criterion
- A modified Tresca failure criterion
- Mohr-Coulomb criterion

Local matrix failure may occur sooner than matrix yielding because failure of polymers is significantly influenced by a hydrostatic state of stress. Under these conditions some researchers have postulated that the matrix failure manifests itself as cavitation induced brittle failure and where this occurs the stress state in the surrounding material is below that required for yielding [1, 38]. They propose that the dilatational energy density expressed as equation (2),

$$U_v = \frac{1-2\nu}{6E} (\sigma_1 + \sigma_2 + \sigma_3)^2 = U_v^{crit} \quad (2)$$

where ν is Poisson's ratio, E is the modulus and σ_1 , σ_2 and σ_3 are the principal stresses; will reach a critical value at the location in the matrix approaching a tensile hydrostatic state of stress. The stress invariant is sign independent consequently the dilatational energy density will be the same for either a tensile or compressive hydrostatic state of stress while the failure is completely different. It should be noted that cavitation will not form while under a compressive hydrostatic or tri-axial state of stress. Crack propagation caused by cavitation-induced voids does not occur instantaneously and the crack may be arrested since the surrounding area is at a lower stress [1]. Propagation may occur once higher stress levels are applied. The crack tip induces high local stresses causing matrix yielding and further growth. Through the finite element analysis a strong dependency on the fiber volume fraction was seen on the predicted transverse failure initiation [1, 23].

A variation on the Dilatational Energy Density criterion is stress invariant, J_1 , expressed as equation (3);

$$J_1 = (\sigma_1 + \sigma_2 + \sigma_3) \quad (3)$$

where σ_1 , σ_2 and σ_3 are the principal stresses. The J_1 criterion is analogous to the strain invariant failure theory (SIFT) being proposed to predict matrix cavitation approaching a tensile hydrostatic state of stress [48].

Another failure criterion that has been proposed to describe the onset of matrix cavitation under conditions approaching a tensile hydrostatic state of stress is based on the distortion energy criterion. However, modifications must be made to account for effects of the hydrostatic dependency of polymers [1, 38, 40, 44]. The modified form of von Mises criterion can be expressed as equation (4),

$$A(\sigma_1 + \sigma_2 + \sigma_3) + B[(\sigma_1 - \sigma_2)^2 + (\sigma_2 - \sigma_3)^2 + (\sigma_3 - \sigma_1)^2] = 1 \quad (4)$$

where it has been previously proposed [38, 40] that the constants A and B can be expressed as shown in equation (5);

$$A = \frac{(\sigma_{yc} - \sigma_{yt})}{\sigma_{yc}\sigma_{yt}} \quad \text{and} \quad B = \frac{1}{(2\sigma_{yc}\sigma_{yt})} \quad (5)$$

where σ_{yc} and σ_{yt} are the uniaxial compression and tension yield stresses, respectively, and σ_1 , σ_2 , and σ_3 are the principle stresses. Equation (4) reduces to the classical von Mises criterion when A is equal to zero. The classical von Mises criterion also does not distinguish between the compressive and tensile state of stress under which the failure is vastly different.

While the term hydrostatic implies that the stresses in either all three Cartesian coordinates or all three principal stresses are equal, very rarely is it the case. Several researchers have introduced using the octahedral shear or the shear strength as a basis for yielding of polymer materials.

Eyring's theory of non-Newtonian flow at a given temperature and strain rate is expressed in equation (6) [1, 38, 43];

$$\tau_0 + Ap = C \quad (6)$$

where τ_0 is the octahedral shear stress, p is the hydrostatic state of stress taken to be the mean of the principal stresses and A and C are constants expressed in equation (7);

$$A = \frac{\sqrt{2}(\sigma_{yc} - \sigma_{yt})}{(\sigma_{yc} + \sigma_{yt})} \quad C = \frac{2\sqrt{2}(\sigma_{yc}\sigma_{yt})}{3(\sigma_{yc} + \sigma_{yt})} \quad (7)$$

The Tresca criterion states that the material yields when the shear stress reaches a critical value. To account for a polymer's dependency on the hydrostatic pressure, the Tresca

criterion can be modified by making the critical shear stress a function of the hydrostatic pressure as expressed by equation (8) [1, 38, 40]

$$\tau_s = \tau_s^0 - \mu \sigma_{on} \quad (8)$$

where τ_s is the critical shear stress, τ_s^0 is the shear stress in the absence of any pressure, σ_{on} is the octahedral normal stress and μ is a material constant that can be defined in terms of the tensile and compressive yield stresses as shown in equation (9) [40];

$$\mu = \frac{3}{2} \left[\frac{(\sigma_{yc} - \sigma_{yt})}{(\sigma_{yc} + \sigma_{yt})} \right] \quad (9)$$

Finally, several researchers have proposed a three-dimensional analogue to the Mohr-Coulomb failure criterion to describe the onset of matrix cavitation [41, 45, 47, 49]. This criterion is expressed in equation (10);

$$\tau_{oct} = \tau_s - \mu \sigma_m \quad (10)$$

where τ_{oct} is the octahedral shear stress under a tensile hydrostatic pressure; τ_s is the octahedral shear stress in the absence of any pressure; μ is a bulk friction parameter and σ_m is the octahedral normal stress. The bulk friction parameter, μ , is determined by the angle of a line tangent to the Mohr circle plots of the compression and tensile yield stresses with the horizontal and is expressed in equation (11) [47];

$$\mu = \tan \phi \quad (11)$$

as shown in Figure 80 for the 828/D-230 matrix system.

As a starting point for determining the criterion that best describes the observed matrix cavitation occurring in both resin systems the applicability of each failure criterion to the experimental results will be given. The fractured surface analysis of the specimens exhibiting matrix cavitation indicates a shear presence at both the cavitation sites and generally across the fracture surface. Consequently, it appears that an interaction between the shear and tensile forces is working to create the matrix cavitation. Cavitation causes the formation of micro-voids which in turn creates a volume increase or dilatation and thus changes the way the material behaves. It has been shown that a tensile tri-axial stress causes yielding of an epoxy much sooner compared to uniaxial tension tests [1, 21, 23, 38, 45]. The converse shows that under a hydrostatic pressure the strength increases [40, 47, 50]. In the case where cavitation was observed in the cruciform specimen as the first failure mechanism, the matrix cavitated under a large principal stress bias that created the cavitation features indicating a shear stress presence. The large principal stress bias, the ratios of the first principal stress to the second and third principal stress, indicate that the internal stress state is dominated by a shearing stress. Thus, the stress state in the cruciform specimen would suggest cavitation initiation at a critical shear strength below the matrix shear strength due to the tensile tri-axial stress presence. Cavitation forming under the stress state developed in the cruciform specimen would suggest that either the octahedral shear strength or the shear strength in pure shear is the upper limit. Due to the tri-axial stresses present causing dilatation of the material the limiting shear strength will be reduced at the onset of cavitation. This precludes the Dilatational Energy Density criterion and the stress invariant J_1 criterion given by equations (2) and (3) above as they predict that failure occurs under a tensile hydrostatic state of stress [1, 38]. The term hydrostatic implies that the magnitudes of the stress in all three principal directions are the same. In the work that applies the Dilatational Energy Density criterion it was found that the ratio of the stress components along the Cartesian coordinate system of $x:y:z$ was 1:1:2 [21]. Although not purely hydrostatic a large difference in principal stresses does not exist and no shear terms are present in the criterion. Furthermore, the authors of this body of work recognize that the competing fiber-matrix debonding type of failure may also be present [1]. The same can be said for the J_1 criterion; it describes a criterion

applicable only under a more hydrostatic state of stress. For the modified von Mises failure criterion expressed in equation (4), although it has a distortional basis and includes a term to account for the hydrostatic dependency of polymers; it does not properly reflect the physics creating the matrix cavitation initiation occurring within the cruciform specimen. As previously stated, the cavitation is caused by the tensile tri-axial stress state. Whether the tensile tri-axial stresses in the matrix approach a hydrostatic condition or not the dilatational effects cause yielding to initiate below the material property strength determined absent of the tri-axial stress state thus, creating an upper limiting case. However, in this case where the stress state is dominated by a shear stress due to the large bias on the principal stress ratios, the modified von Mises criterion has no upper limiting shear term. Bauwens' criterion based upon Eyring's theory of non-Newtonian flow at a given temperature and strain rate as expressed in equation (6) also does not adequately explain the failure initiation mechanism, observed in the cruciform specimens exhibiting matrix cavitation, as discussed earlier. In equation (6) the pressure is expressed as the positive sum of the principal stresses suppressing the flow of the polymer causing an increase in its yield strength. Application of the correct sign for the compressive and tensile yield stresses in equation (7) is not specifically stated in his paper and leads to conflicting results. Consequently, the modified Tresca criterion, expressed in equation (8), and the Mohr-Coulomb criterion, expressed in equation (10), having limiting shear strength terms in their respective criterion properly reflect the presence of the tri-axial stress at the onset of matrix cavitation. Through the results of the FEA, these two matrix failure criteria will be discussed in further detail for each fiber spacing group in both material systems.

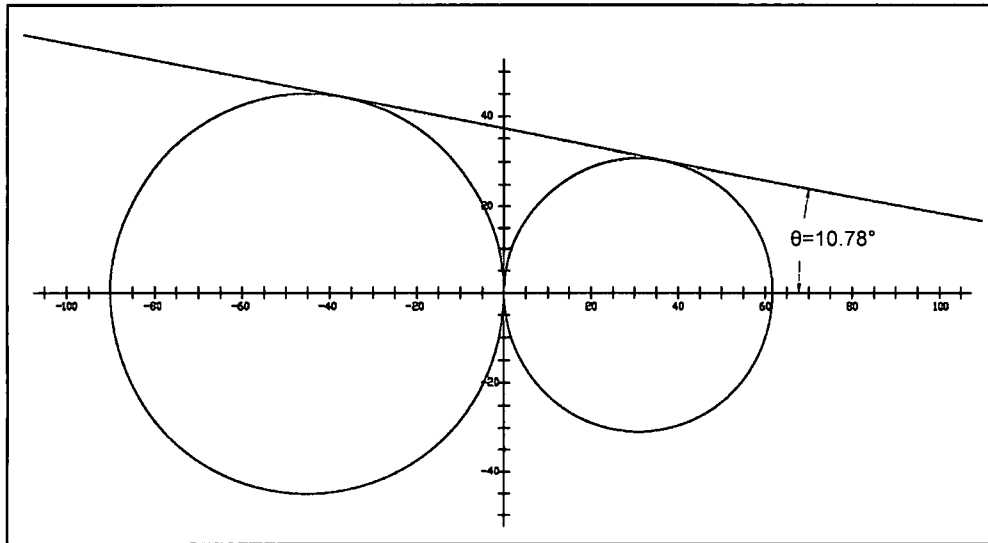


Figure 80: Mohr Circle plot of the 828/D-230 tensile and compression yield stress test results for the determination of the bulk friction parameter μ

3-D Finite Element Model (FEM)

All previous numerical analysis has been done through two-dimensional finite element analysis (FEA). The analysis has been based on plane strain condition with various assumed uniformed fiber-packing geometries. The two primary fiber-packing arrangements used in the analysis are the square (or "square-diagonal") and hexagonal fiber distributions. Two important points need to be brought to attention. First, the previous work determines the three-dimensional state of stress through a two dimensional analysis. Therefore analyzing the problem in a 2-D state can lead to erroneous results from the simplifying assumptions of the plane strain condition. The second point is that by assuming a periodic fiber array in the finite element model (FEM) the effect of varying spatial fiber distribution cannot be recognized. Important to the proposed work is the state of stress of the matrix and the effects that fiber spacing has on that stress state. As previously mentioned, both failure mechanisms may be present in the same composite material depending upon the spatial arrangement of the fibers.

In this section the development of the 3D FEM of the cruciform test specimen is detailed. The model was used for the following tasks:

1. To study the locations on the fiber-matrix interface and in the matrix surrounding the fibers of greatest stress in the test specimens
2. To study the relative magnitude of the stress components at these high stress locations in order to help understand which failure criteria might be most effective in predicting failure (a full failure criterion discussion is in the next chapter).
3. To study certain parameters of the cruciform specimen serving as a guide through the experimental portion of the work directing the choice of further fiber spacings to be tested experimentally as well as camera positioning to capture damage events most likely to occur in the high stresses volumes of the samples.

Due to the symmetrical fiber arrangement only 1/8 of the total cruciform specimen was modeled, as shown in Figure 81. Mesh refinement occurs at the fiber-matrix interface where the stress intensity was high. Figure 82 shows a portion of the 3-D FEM focusing on the mesh density around the fiber-matrix interface. Also shown, in Figure 82, is the angular orientation, θ , describing the locations for interface stress variations around the fiber circumference. The first quadrant of the fiber is defined as $\theta = 0^\circ$ to 90° , the second quadrant is defined as $\theta = 90^\circ$ to 180° , the third quadrant is $\theta = 180^\circ$ to 270° and the fourth quadrant is $\theta = 270^\circ$ to 360° . Additional notation used in this work will refer to the fiber north pole and south pole which are at $\theta = 90^\circ$ to 270° respectively. Also the fiber equator will be defined at $\theta = 0^\circ$ to 180° .

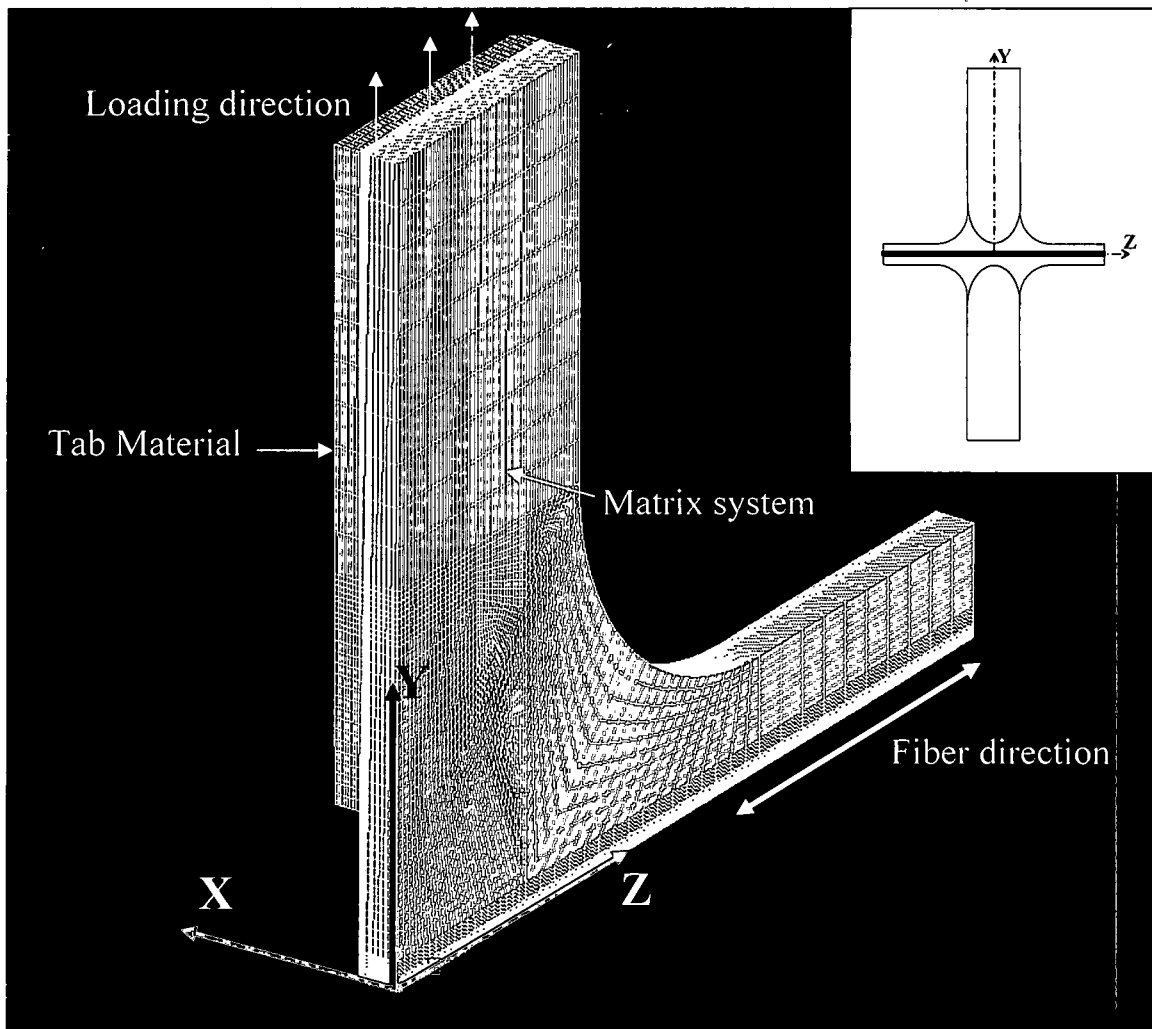


Figure 81: 3D FEM of model cruciform specimen (Inset is planar view of the whole cruciform specimen)

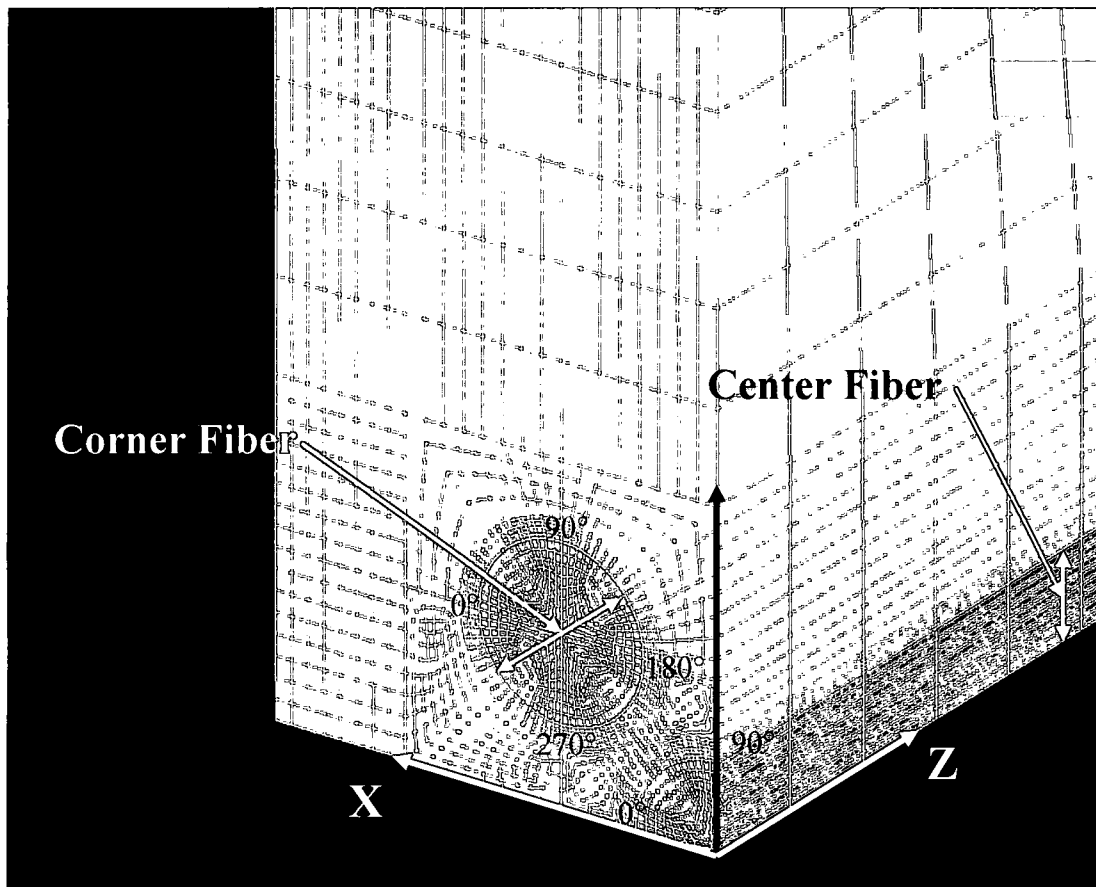


Figure 82: 3D FEM of model cruciform specimen showing mesh density in and around fibers

For both matrix systems the solid95 20-noded brick element was utilized. This element is capable of modeling curved boundaries as well as large deflection and large strain for nonlinear analysis. It can also handle both orthotropic and linear elastic material properties. The ANSYS Parametric Design Language (APDL) was utilized for all finite element models. Details of the FEM are discussed in Appendix C. Material properties for the matrix; the fiber and the tab material for the FEM are shown in Table 29. It should be noted that the modulus for the 862/W matrix shown in Table 29 is taken from one specimen representing the median of the sample set and not the average magnitude shown in Appendix A. The details of the data selection are contained in Appendix A.

Table 29: Material properties for the finite element model analysis

Constituent Materials	E (GPa)	ν	Effective Residual Cure Constant				
828/D-230	3.44	0.337	$741.8 \times 10^{-6}/^{\circ}\text{C}$				
862/W	2.496	0.346	$67.4 \times 10^{-6}/^{\circ}\text{C}$				
Stainless Steel	207	0.3	$16 \times 10^{-6}/^{\circ}\text{C}$				
	E_y, E_z (GPa)	E_x (GPa)	ν_{xy}	ν_{yz}	ν_{xz}	G_{xy}, G_{xz} (GPa)	G_{zy} (GPa)
Glass/epoxy Tab	24.7	10.1	0.14	0.11	0.34	3.3	3.1

A mechanical loading model and a residual stress model were developed for each cruciform fiber spacing group tested in each matrix system. The mechanical loading model analyzes the internal stresses due to the applied load at first damage observation. The residual stress model evaluated the internal stress due to the matrix curing process for both the room temperature cured 828/D-230 system and the high temperature cured 862/W system. The mechanical model applies a displacement loading to simulate the grips for the tensile test machine used for all cruciform experiments. The model's height is taken as half the distance between the grips of the test machine. The displacement load is then applied to the top of the loading arm. Details are explained in the Boundary Conditions Section below. The model also assumed that the matrix was perfectly bonded to the fibers.

Due to the issues outlined earlier regarding the modeling of the residual stresses in the previous work, the effects of the residual stresses for both matrix system used in this work are incorporated into the FEM. The residual stress models were made to measure the internal stresses due the effects of the matrix cure. For each matrix system an effective coefficient of thermal expansion was used to account for the internal stresses developed by the curing process of each epoxy system, the details of which can be found in Appendix B. This effective thermal expansion coefficient called the effective residual cure constant (ERCC) is $741.8 \times 10^{-6}/^{\circ}\text{C}$ for the 828 system and is $67.4 \times 10^{-6}/^{\circ}\text{C}$ for the 862 system. For both epoxy systems the residual stresses cause a compressive pre-stress around the fibers prior to mechanical loading. For the 828 room temperature system the residual stresses are caused from the chemical shrinkage during cure. To model this behavior the difference in temperature is taken to be -1°C in order to impart the compressive shrinkage stress around the fibers. However, for the 862 high

temperature epoxy system calculating its residual stresses requires a more involved approach. The temperature difference in this case is -99°C representing the temperature difference between room temperature, 22°C, and the temperature at which the epoxy system vitrifies at 121°C. The model captures the final state of the cruciform specimen after its cure cycle. The stainless steel fibers are modeled using a coefficient of thermal expansion of $16 \times 10^{-6} / ^\circ\text{C}$. The tab material is not included in the residual stress models since these are bonded to the specimens prior to testing having no impact on the residual stresses. The fiber-matrix interface, as well as, the tab-matrix interface is assumed to be perfectly bonded in the finite element analysis.

Boundary Conditions

Due to the symmetrical shape of the test specimen, the planes of symmetry, namely at $X = 0$, $Y = 0$, and $Z = 0$ are constrained by symmetry boundary conditions, whereas the outer surface is traction free. The center of the model is constrained to prevent rigid body translation (@ $x = y = z = 0$). The mechanical load is simulated in the FEM by applying tension perpendicular to the fiber axis, in the Y direction, by means of a constant displacement. For the linear 828 material system the load applied to the FEM is a unit displacement. The results are then scaled by the ratio of the far-field stress at first damage observed in the cruciform experiments to the FEM far-field stress when the results are post-processed.

Due to the nonlinear response of the 862 matrix system each model was run at 3 or 4 different displacement values. The far-field stress versus displacement was plotted and the equation of the line was obtained to calculate the displacement required to achieve the far-field stress at first damage observed in the 862 cruciform experiments. Details of this approach for matching the far-field experimental stress can be found in Appendix C. Table 30 is a comparison of the experimentally observed far-field stress to the resultant FEM far-field stress for all of the 862 cruciform model runs. The finite element analysis (FEA) technique uses energy principles to calculate stresses and strains from applied loads to arrive at an approximate solution of a structural mechanics problem. The degree of accuracy is dependent upon the density of the model's element mesh and for simple mechanics problems having a closed form solution the FEA

can match the exact solution. Due to the specimen's geometry and the nonlinear material, the FEA far-field stress solution will converge to be very close to the experimental far-field stress with increasing mesh density. However, a FEM mesh sensitivity study was conducted, and is discussed below; setting the mesh density based on interfacial stress components. Each calculated displacement input for the far-field stress analysis was carried out to 1×10^{-5} mm. Thus the worst case solution of the FEA for the far-field stress will be 96.5% of the experimental far-field stress and the best case solution is 100.7% of the experimental far-field stress. Consequently, the process of calculating the displacement necessary to match the experimental observation is very accurate and will introduce very little error into the analysis.

Table 30: Comparing Experimental far-field stress to 862 mechanical FEM far-field stress

862 Mechanical FEM	Experimental FF Stress (MPa)	FEM FF Stress (MPa)	% Δ
1.57d _f	12.04	11.88	1.3
1.75d _f	18.04	17.40	3.5
1.9d _f	17.23	16.75	2.8
2.0d _f	7.76	7.71	0.6
2.5d _f	13.66	12.63	0.6
6.0d _f	21.44	21.55	0.5
SF	14.46	14.56	0.7

Mesh Sensitivity Study

A study was conducted to measure the effects of the finite element mesh density on the calculated results. The linear 828 1.9d_f spacing FEM was used to gage these effects and the fiber matrix interface was investigated to see the effect of varying mesh density on the results. Three 3-D models were created, 190dfRT-LDM, 190dfRT, 190dfRT-MDM, where the mesh densities varied as shown in Table 31. This resulted in meshes along the fiber matrix interface of the center fiber varying from 8, to 16, to 32 subdivisions and for the corner fiber from 32, to 64 to 128 subdivisions as shown in Figure 83. The elements were also increased in the radial direction from the center of each fiber to the fiber-matrix interface and further concentrated in a band around both fibers. From the outer limits of the band the elements fan outward in a uniform manner

covering the rest of the matrix areas of the 3-D cruciform specimen model. Results of the study are detailed in Appendix C with the resultant mesh density shown in Figure 83.

Table 31: Mesh density study statistics

Model	Elements	Nodes	Degrees of Freedom
190dfRT-LDM	22,112	95,760	287,280
190dfRT	138,048	576,800	1,730,400
190dfRT-MDM	1,104,384	4,515,321	13,545,963

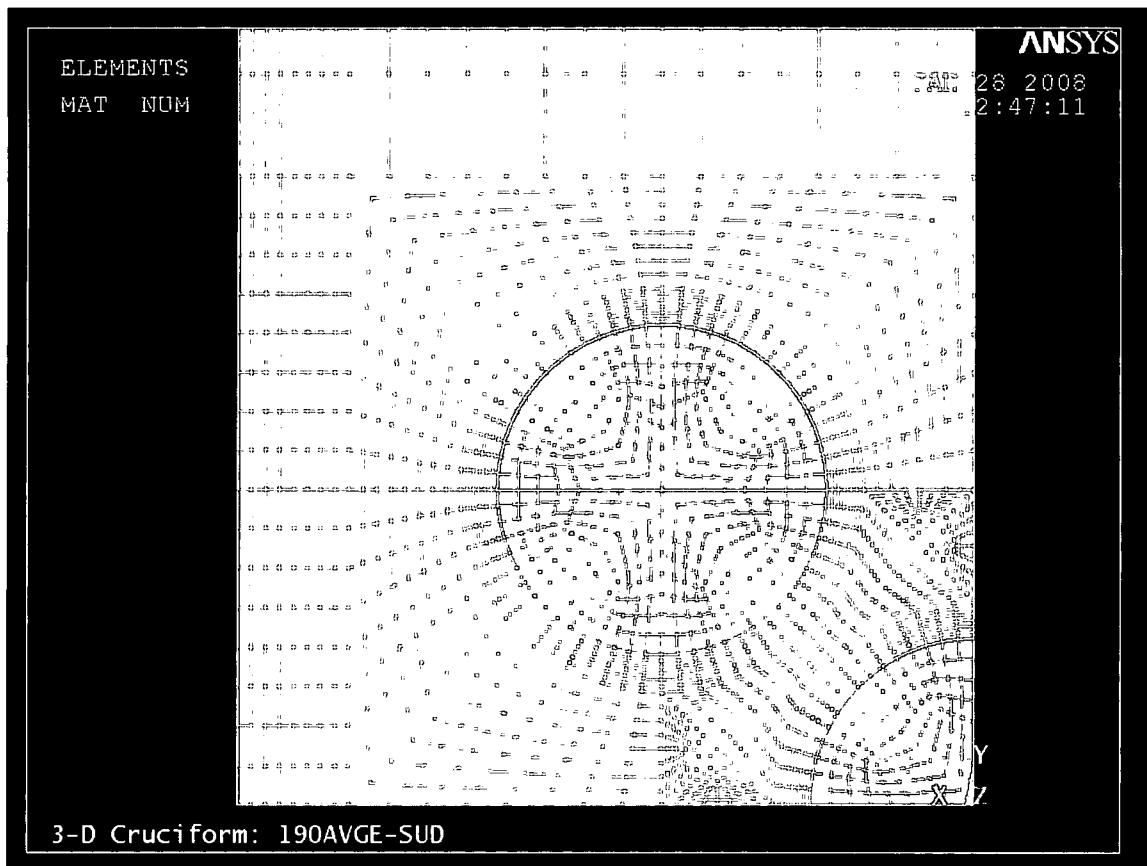


Figure 83: Final mesh configuration showing mesh refinement over mesh density results beyond outer band around fibers

Parametric Study

This section briefly summarizes results from modeling conducted a third through the test program to determine the best choice for the remaining fiber spacing groups to be tested. More details can be found in Appendix C. A parametric study was performed to examine the effects of fiber spacing on the stress and strain distributions as the fiber spacing is changed. The cruciform thickness in the 3D FEM is held constant at 4.75 mm while the center-to-center spacing between the central fiber and the corner fiber is varied. The study modeled multi-fiber model composites having a fiber spacing of $1.57d_f$, $1.75d_f$, $1.9d_f$, $2.5d_f$, $6.0d_f$ and $12d_f$. The $1.57d_f$, $1.75d_f$, and $1.9d_f$ spacing represent varying degrees of densely packed fibers while the $2.5d_f$ spacing represents closely packed fibers and the $6d_f$ and $12d_f$ fiber spacing represent varying degrees of isolated fibers. For comparison with larger fiber spacing solutions, the limiting case of a single-fiber (SF) was also simulated.

The smallest spacing model was the $1.57d_f$ fiber spacing as this was the smallest multi-fiber cruciform spacing that could be made. After already testing the $1.84d_f$, $2.5d_f$, and $6.0d_f$ fiber spacing groups and observing two different failure initiation mechanisms; the parametric study results gave insight for optimum positioning of the secondary camera for the multi-fiber cruciform experiments. The camera position to best capture damage initiation over the width of the loading arm and be focused on the high stressed areas within the sample was determined to be vertically above the primary camera instead of on the same horizontal plane as shown in Figure 11. They were also used as a guide for determining the fiber spacing for the remaining multi-fiber cruciform specimen's experimental matrix. The study showed that the $1.57d_f$, $1.75d_f$ and $1.9d_f$ fiber spacing groups covered a fairly wide interfacial stress component response. The $2.0d_f$ spacing was added to capture the onset of nearest neighboring fiber effects since the $2.5d_f$ showed virtually no interaction with neighboring fibers. The radial and shear interfacial stress distributions of the corner fiber at $6.0d_f$ and $12.0d_f$ spacing were virtually the same as the SF. This behavior indicates that they behave as isolated fibers having no nearest neighbor fiber effects.

Analytical Results

828/D-230 Matrix System

Fiber-Matrix Interface Analytical Results. The experimental results show that for the fiber groups having the $1.57d_f$, $1.90d_f$, $2.0d_f$, $2.50d_f$ and $6.0d_f$ fiber spacing and the single fiber specimens the first failure is fiber matrix debonding. However, for the $1.75d_f$ and $1.84d_f$ fiber spacing specimens, experimental results show that the first failure mechanism is matrix cavitation. As described above a mechanical FEM and residual FEM were constructed for each fiber spacing group using the average of the specimen dimensions and analyzed. The results were then extracted from each model and post processed into a spreadsheet for each fiber grouping. The post processing consisted of scaling the mechanical model results by the ratio of experimental far-field stress at failure initiation to the FEM far-field stress. The residual stresses were not scaled since these captured the internal stress state due to the resin system curing process that is present in the specimen during the test. The scaled mechanical load results are then added to the residual stresses for the combined effect to reflect the stress state in the specimen during the experimental test.

The center and corner fiber interfacial radial and shear stress results are discussed in detail in Appendix D. Presented below are the summary discussions for center fiber and corner fiber followed by conclusions based on the interfacial analysis. The next section discusses how these stresses should be used when choosing a failure criterion to predict interfacial failure.

Center Fiber Interface Results. The interfacial radial and shear analysis for the center fiber discussed in detail in Appendix D is summarized in the following discussion. The center fiber at the $6.0d_f$ fiber spacing group behaves as if the fibers were isolated from each other showing no interaction to the corner fibers due to the applied mechanical loads and the matrix cure shrinkage effects. Although nearest neighbor effects begin to manifest themselves at the $2.5d_f$ fiber spacing, shown predominately in the matrix cure shrinkage results as the mechanical loading results show virtually no interactions (see Appendix D), the magnitudes are very small. Thus the combined

effects show practically no interaction for the $2.5d_f$ fiber spacing. Figures 84 and 85 show the radial and shear stress distribution at the fiber-matrix interface due to the combination of mechanical loading, at their failure initiation load levels, and chemical shrinkage. Illustrating the point about the $6.0d_f$ and $2.5d_f$ fiber spacing groups discussed above; Figure 84 and 85 shows that their interfacial radial and shear stress distribution have practically the same shape but with slightly different magnitudes.

Having no or virtually no nearest neighboring fiber effects is not the case for the rest of the fiber spacing groups tested. As expected the interaction of the nearest neighbor fiber has the greatest effect at the point on the interface of the center fiber where the corner fiber is closest at $\theta = 45^\circ$. The rest of the fiber spacing groups; namely the $1.57d_f$, $1.75d_f$, $1.84d_f$, $1.9d_f$ and the $2.0d_f$, show combined nearest neighbor and matrix shrinkage effects by the hump in their interfacial radial stress distribution and by the unsymmetrical shape and shift in the maximum magnitude location for their interfacial shear stress distribution, as shown in Figure 84 and 85. The hump manifested in the radial stress distribution for the aforementioned fiber spacing groups is the hump in their distribution between approximately $\theta = 25^\circ$ and 50° . This manifestation is due to the combined effects from the mechanical load and matrix shrinkage as detailed in Appendix D. For the $1.57d_f$ fiber spacing these effect cause it to have it maximum radial stress magnitude at $\theta = 39.375^\circ$ and a fairly uniform radial stress from this point to $\theta = 90^\circ$.

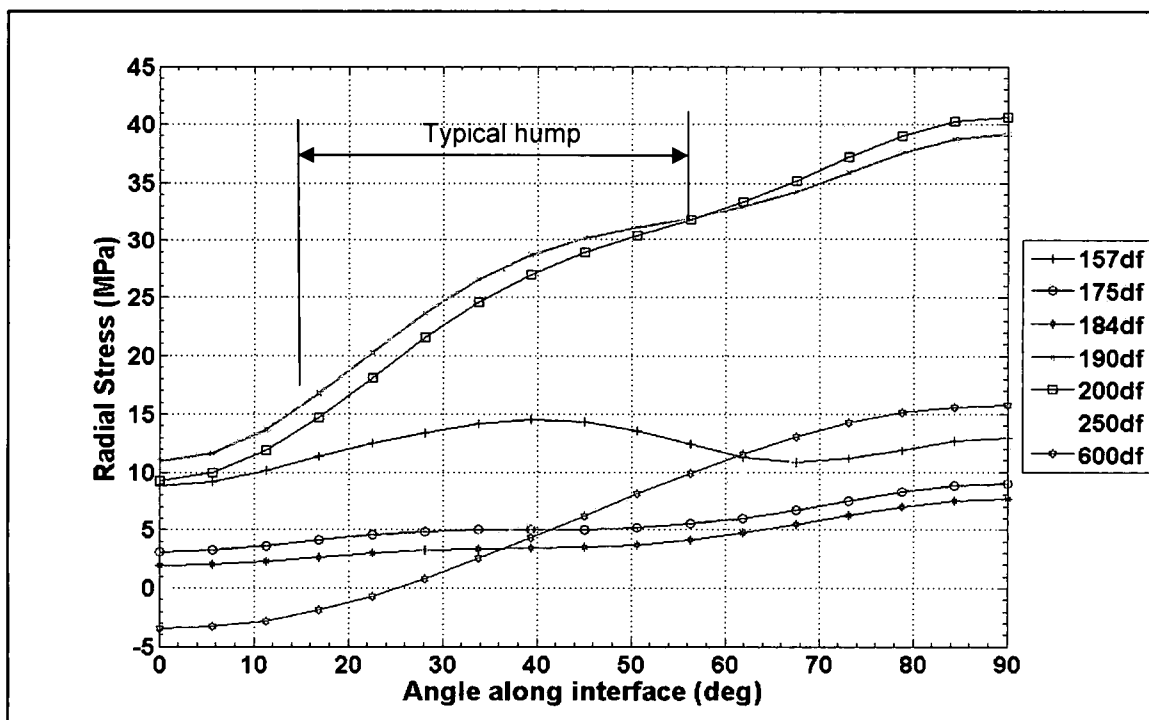


Figure 84: Radial stress distributions at the fiber-matrix interface due to the combination of mechanical loading and chemical shrinkage

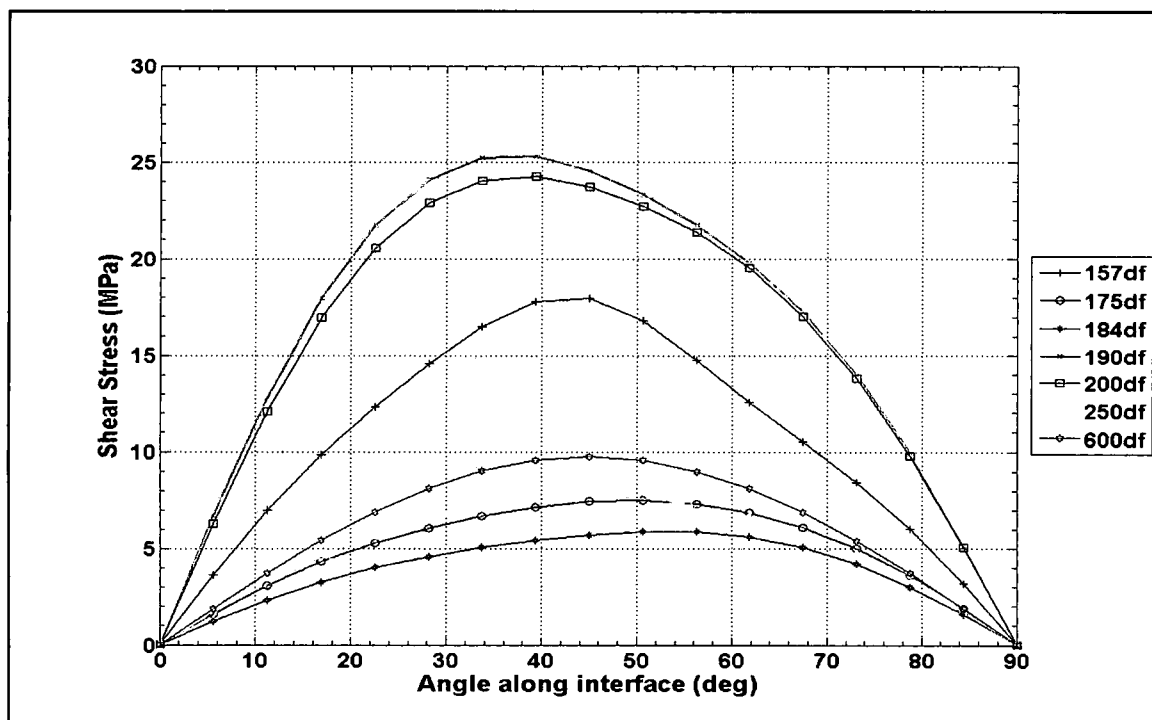


Figure 85: Shear stress distributions at the fiber-matrix interface due to the combination of mechanical loading and matrix chemical shrinkage

Corner Fiber Interface Results. The interfacial radial and shear analysis for the corner fiber discussed in detail in Appendix D is summarized in the following discussion. The corner fibers at the $6.0d_f$ fiber spacing group behave as isolated fibers showing no interaction to the center fiber from the applied mechanical load and the matrix cure shrinkage effects in all four quadrants. At the $2.5d_f$ fiber spacing the interfacial radial and shear stress distribution begin to show nearest neighbor effects predominately in the matrix cure shrinkage results. However, the mechanical loading results show virtually no interactions and are practically equal in magnitude to the $6.0d_f$ spacing. Thus the combined effects show nearly no interaction to the center fiber for the corner fiber at the $2.5d_f$ fiber spacing. However, this is not the case for the rest of the fiber spacing tested. As expected the interaction of the nearest neighbor fiber has the greatest effect in the third quadrant of the corner fiber where $\theta = 180^\circ$ to 270° . This quadrant is also closest to the center fiber; and both fibers show similar characteristics in their radial and shear stress distributions due to effects from one another. Figure 88 and 87 show the radial and shear stress distribution at the fiber-matrix interface due to the combination of mechanical loading and chemical shrinkage.

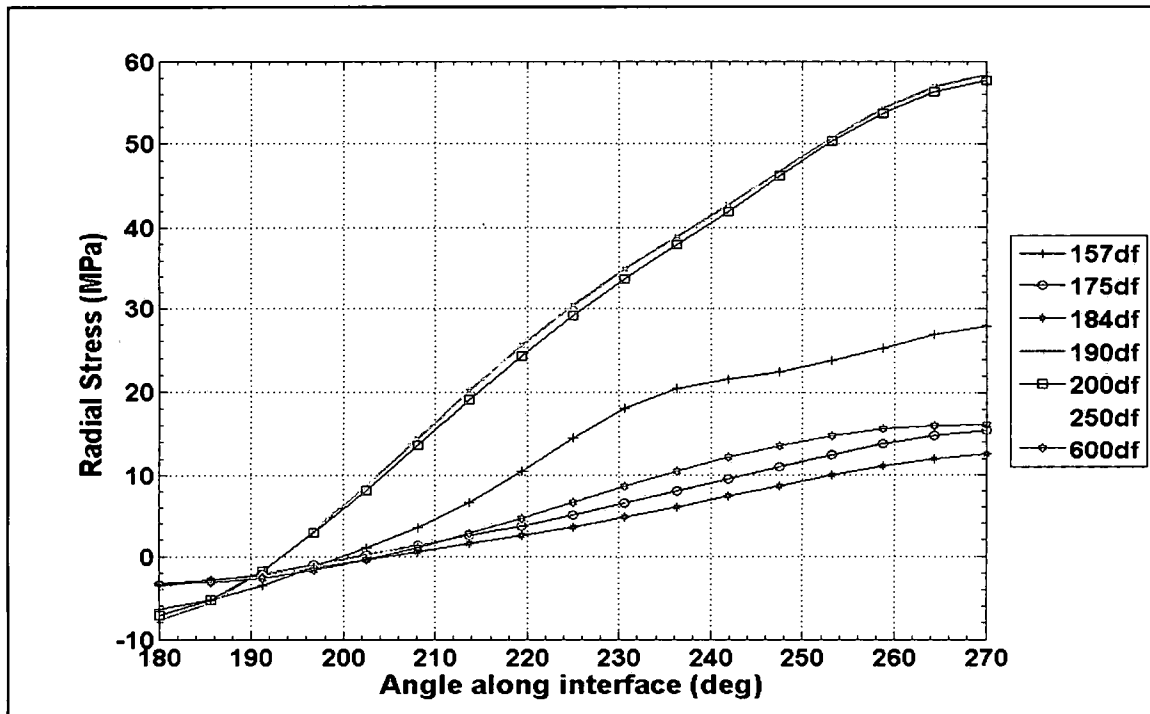


Figure 86: Radial stress distributions at the fiber-matrix interface due to the combination of mechanical loading and matrix chemical shrinkage from $\theta = 180^\circ$ to 270°

The $1.57d_f$, $1.75d_f$, $1.84d_f$, $1.9d_f$ and the $2.0d_f$ fiber spacing groups show nearest neighbor effects by the hump in their interfacial radial stress distribution shown in Figure 86. The nearest neighbor effects manifest themselves in the shear stress distribution by its unsymmetrical shape and shift in the maximum magnitude location for their interfacial shear stress distribution shown in Figure 87. Although effects from the center fiber are seen by the aforementioned fiber groups, they are most prominent at the $1.57d_f$ fiber spacing. As shown in Figure 86, the effects are indicated by the pronounced hump and almost constant magnitude in the radial stress distribution between $\theta = 210^\circ$ to 270° . They are also illustrated in the shift in maximum shear stress location from $\theta = 225^\circ$ to 219.375° and along with the concave distribution between approximately $\theta = 230^\circ$ to 260° , shown in Figure 87. Comparing Figures 84 to 86 and 85 to 87 the magnitudes of the radial and shear stresses are greater at the corner fiber. Thus it appears that the center fiber experiences a load shedding effect from the corner fibers by the reduction in stress magnitudes.

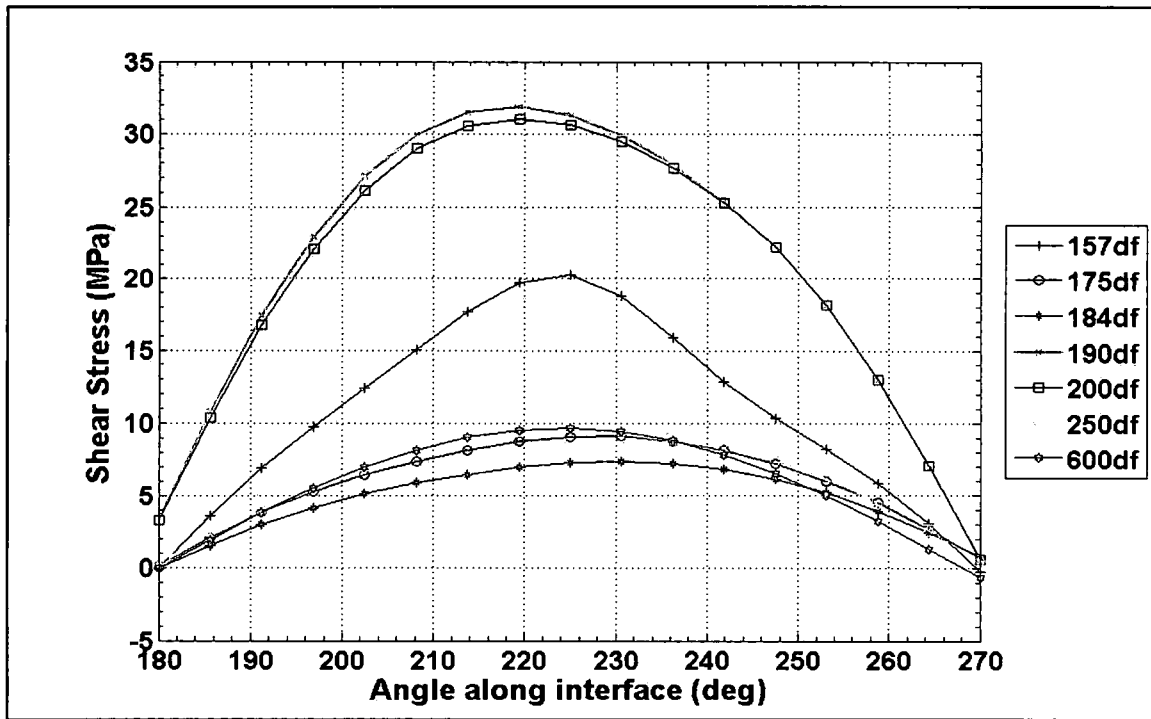


Figure 87: Shear stress distributions at the fiber-matrix interface due to the combination of mechanical loading and matrix chemical shrinkage from $\theta = 90^\circ$ to 180°

In the first, second and fourth quadrant very little effects by the center fiber are present in the interfacial stress distributions. The single fiber results, shown in the first quadrant of the corner fiber results (see Figure 193 Appendix D), illustrate a constant compressive radial stress and a near constant shear stress distribution due to the matrix cure shrinkage loading. It exhibits smooth radial and shear stress distribution having maximum magnitude locations at $\theta = 90^\circ$ for the radial stress and $\theta = 45^\circ$ for the shear stress. The single fiber (SF) is shown on the corner fiber stress distribution since the corner fiber is most physically similar to the single fiber with respect to loading and physical geometry to the specimen free edge. Specifically for the interface between $\theta = 0^\circ$ to $\theta = 90^\circ$ the load path and the uninterrupted distance from the fiber to the specimen free edge are basically identical. Elsewhere along the fiber-matrix interface, i.e. from $\theta = 90^\circ$ to $\theta = 360^\circ$ interaction with the surrounding fiber prohibit a correlation to analytical results with the multi-fiber specimens.

Analysis of the 1.9d_f and 2.0d_f Fiber Spacing Group Behavior. The 1.9d_f and 2.0d_f fiber spacing groups have the highest radial and shear stress magnitudes of all the fiber spacing groups tested as illustrated in Figures 84 – 87. Based on the parametric study results given in Appendix C, these two fiber groups should fall between the 1.57d_f and the 2.5d_f fiber spacing groups radial and shear stress distribution since they exhibited the same fiber-matrix debond failure initiation mechanism. However, they have the highest far-field stress at failure initiation of all multi-fiber cruciform specimens that initiated failure as a fiber-matrix debond. In an effort to explain this behavior the following tasks were under taken:

1. Nanoindentation tests were performed on 1.57d_f, 1.90d_f, 2.0d_f and 2.5d_f specimens for any changes in matrix properties around and extending from the fibers.
2. Five additional specimens were made and tested.
3. A thorough analysis of the failure initiation stress state at the center fiber and corner fiber for all fiber spacing groups was performed.
4. Parametric study analysis of specimen thickness was conducted.

A thorough discussion of the tasks undertaken to understand the unanticipated higher interfacial radial and shear stress occurring at the 1.9d_f and 2.0d_f fiber spacing is located in Appendix D. The results from the investigation show the following:

1. The nanoindentation results show no interphase exists and that the modulus of the matrix system for the 1.9d_f and 2.0d_f groups is the same as the 1.57d_f and 2.5d_f groups.
2. Test results from the five additional specimens at each fiber spacing show no significant difference in the far-field stress over the original group.
3. The SCF for both the corner and center fibers are only slightly above the other fiber spacing groups indicating that the analysis is correct.
4. The parametric studies show that radial and shear SCF for the multi-fiber cruciform are not sensitive to specimen thickness but that the radial and shear SCF for the single fiber are sensitive to changes in specimen thickness (see Figure 186, page 334 in Appendix C);

Based on the above listed results, then it is likely that the $1.9d_f$ and $2.0d_f$ fiber spacing is an optimum spacing where the fiber group acts more as a single unit much like the single fiber specimen. This is collaborated by the radial and shear stress distributions of the $1.9d_f$ and $2.0d_f$ fiber spacing groups being practically the same as the single fiber. See Figure 193, page 384 in Appendix D for the radial stress distribution and Figure 205, page 395 in Appendix D for the shear stress distribution. At these two spacing the applied load is efficiently spread to the fibers allowing the fiber group to effectively carry higher loads thus higher far-field stresses.

Fiber-Matrix Interface Analytical Results – Conclusions. Based upon the interfacial analytical results, nearest neighbor fiber interaction occurs in the region of the interface where the fibers are closest, namely first quadrant from $\theta = 0^\circ$ to 90° for the center fiber and in the third quadrant, between $\theta = 180^\circ$ to 270° for the corner fiber. The interactions are manifested in both the mechanical loading and the matrix shrinkage. Mechanical loading neighboring fiber effects are evident by the hump in the radial stress distribution for both fibers as shown in Figures 189 and 203 in Appendix D. The impact is evident as the length of fiber circumference at the interface over which the highest radial stresses act increases. In some cases the neighboring fiber causes the location of the maximum magnitude to change from along the direction of the applied load at $\theta = 90^\circ$ or 270° to $\theta = 45^\circ$ or 235° as evidence for the $1.57d_f$ spacing. Further indication of neighboring fiber effects manifest themselves by a change in the location of the maximum magnitude of the shear stress due to the mechanical loading only as shown in Figure 192 and 215 in Appendix D. The shape of the interfacial shear stress distribution also changes due to the neighboring fiber as illustrated in Figures 192 and 215 in Appendix D. The matrix shrinkage radial stress distributions, shown in Figures 188 and 199 in Appendix D, indicate an increasing radial stress as fiber spacing decreases due to the neighboring fibers. The maximum magnitude for all fiber spacing groups occurred at $\theta = 45^\circ$ or 225° . The matrix shrinkage shear stress distributions, shown in Figures 191 and 211 in Appendix D, show local maxima as the shear stress changes direction across the interface due to the effects from nearest neighboring fibers.

The impact of the matrix cure shrinkage on the interfacial radial stress is higher for the specimens having close fiber spacing, i.e. the $1.57d_f$, $1.75d_f$ and the $1.84d_f$ specimens, than for the specimens having the wider fiber spacing, the $1.9d_f$, $2.0d_f$, $2.5d_f$ and $6.0d_f$. The matrix cure shrinkage reduces the radial stress caused by the far-field load along the center fiber interface from 5% to 59% depending upon fiber spacing as listed in Table 57 in Appendix D. Similarly the corner fiber radial stress is reduced from 4% to 21% in the 1st, 2nd, and 4th quadrant depending upon fiber spacing as listed in Table 59 in Appendix D. Furthermore it is reduced from 4% to 59% in the 3rd quadrant of the corner fiber as listed in Table 60 in Appendix D. The matrix cure shrinkage effect on the interfacial shear stress is fairly consistent for both corner and center fibers. The shear stress is reduced from 1.7% to 14.7% along the center fiber interface depending upon fiber spacing as listed in Table 58 in Appendix D. Similarly, it is reduced along the interface of the corner fiber in the 2nd quadrant from 2.8% to 12.4 % and in the 3rd quadrant from 3.4% to 11.9% depending on fiber spacing as listed in Table 62 in Appendix D. for the 1st and 4th quadrants of the corner fiber, the interfacial shear stress is reduced from 1.1% to 6.3% depending on fiber spacing as listed in Table 62 in Appendix D.

The interfacial analysis also indicated that the $6.0d_f$ fiber spacing appears to behave as isolated fibers. No interactions occurred as evidence by the uniform radial and shear matrix cure shrinkage stresses. Additionally, no neighboring fiber effects occurred in the radial and shear stress distribution due to the mechanical load as discussed in Appendix D. Although behaving as an isolated fiber, the $6.0d_f$ spacing cannot be directly compared to the single fiber. The primary reason is that the specimen thickness was not held constant. However, a concentrated effort to keep the matrix cover from the fiber equator to the specimen free edge for all multi-fiber spacing groups was made. Since this was not done for the SF and the parametric study results show impact, see Figure 186 Appendix C a direct comparison cannot be made.

The $2.5d_f$ fiber spacing has negligible matrix cure shrinkage stresses in all four quadrants of the fiber as evidence by their low magnitudes. In addition, there is virtually no effect on the interfacial radial and shear stresses due to neighboring fibers from the mechanical loading. Thus

the $2.5d_f$ spacing can be considered at the very limits of the fiber spacing where the nearest neighboring fibers start to interact.

The preceding discussion points to the importance of including the matrix cure shrinkage stresses in any criterion development. Even though the 828/D-230 matrix system is a room temperature cured system, experimental measurements and the corresponding analytical analysis due to the matrix cure show a significant amount of stress relative to the mechanical loading only stresses at the interface. Consequently, to properly reflect the internal interfacial stress state the matrix cure stresses have to be incorporated into all failure criterion development.

Fiber-Matrix Interface Debond Criterion. As stated above, the literature review has indicated that a likely combination of fiber-matrix interface stresses to cause a fiber-matrix debond are the interfacial normal and shear stresses. In addition, it has been proposed that the combination of the interfacial normal and shear stresses can be expressed as a quadratic interaction criterion as shown in equation 1 above. In this work, it was shown in Chapter 2 that for the majority of the fiber spacing groups tested the locations of the fiber-matrix debond occurs at the corner fiber poles except for the $1.57d_f$ fiber spacing group where they occurred other than at the fiber pole. Conclusions drawn in Chapter 2 indicate that below a fiber spacing of $1.8d_f$, it appears that the preferred debond location is interior to the fiber group and those fiber spacing groups greater than $1.8d_f$ have no preference to debond location. The field of view for all cruciform tests show the 1st and 4th quadrants of the three fibers visible in the multi-fiber specimens, the top and bottom corner fibers and the center fiber. A detailed discussion correlating the debond measurements for the fiber spacing groups with the interfacial stress analysis at the corner fiber in the field of view is located in Appendix D. A summary of the results follows.

Each fiber spacing group experienced interfacial debonds over that part of the fiber exhibiting high magnitudes of radial stress. Moreover, the debond length covers portions of the fiber interface where the shear stress either reaches its maximum or its average magnitude over the initiated debond arc length is a significant percentage of the maximum magnitude. Table 32 lists the average debond measurements for the fiber spacing groups exhibiting fiber matrix

debonding as their failure initiation. The fact that the shear stress is critical and the interaction between the shear and normal or radial stress cannot be neglected is supported by the data in Table 32, which warrants a closer look. As described in Chapter 2 the experimental initiated debond widths were measured by extracting photomicrographs from the videotaped experiments. The debond width, location relative to fiber pole and also along fiber length, as well as debond type were tabulated for each specimen. The central angle and arc length were calculated and tabulated for each specimen as well as the corresponding FEM location in their respective fiber spacing groups. The average experimental debond width for each fiber spacing group where the debonds initiated in either fiber hemisphere is determined and the corresponding average debond central angle and average arc length are then calculated for that fiber spacing group. The experimental debond limits, listed in Table 32, are then determined from the average debond central angle for both the northern and southern hemisphere for each fiber spacing group.

The $1.57d_f$, $1.90d_f$ and the $2.0d_f$ debond limits cover 24%, 31% and 26% of the total circumference of the fiber which encompasses the location of highest radial and shear stresses. The $2.5d_f$ and $6.0d_f$ fiber spacing groups, on the other hand, debond only 12% and 13% of the fiber circumference respectively, that includes the location of maximum radial stress and a significant percentage of shear stress. These results lead to the conclusion that an interaction between the radial stress and shear stress be investigated as the interfacial debond criterion.

Table 32: Experimental fiber matrix debond measurements

Spec.	Average Debond Width, mm (Std dev)	Average Debond Central angle	Experimental Debond Limits	Arc Length, mm	% circumference
1.57d _f	0.053 (0.019)	91°	44.5° to 135.5° NP 224.5° to 315.5° SP	0.28	24
1.9d _f	0.083 (0.045)	116°	32° to 148° NP 212° to 328° SP	0.36	31
2.0d _f	0.075 (0.036)	110°	35° to 145° NP 215° to 325° SP	0.34	29
2.5d _f	0.015 (0.004)	47°	66.5° to 113.5° NP 246.5° to 293.5° SP	0.15	12
6.0d _f	0.0157 (0.0083)	48°	66° to 114° NP 246° to 294° SP	0.15	13
SF	0.07 (0.033)	106°	37° to 143° NP 217° to 323° SP	0.33	28

Matrix Failure Analytical Results. The experimentally observed form of matrix failure initiation is cavitation of the resin system. For matrix cavitation to occur a tensile tri-axial stress state must be present within the matrix. Cavitation creates micro-voids in the matrix material and for this reason evaluating stresses on the surface of the fiber or comparing the radial or shear stress components at the matrix interface will not work. Instead the matrix volumes have to be scanned checking the combination of stresses using various matrix failure criteria. Several matrix failure criterions, discussed above, are evaluated in the matrix regions of the cruciform specimen. Figure 88 shows how the finite element model is partitioned to investigate the state of stress within the model. In the development of the solid model it was determined early on that the best way for dealing with the large amounts of stress data was to subdivide the model into smaller volumes. Thus data extraction and evaluation could be done in the most expedient and efficient manner. Therefore, each FEM has 30 matrix volumes grouped into 2 distinct regions being the fiber matrix bands and the cruciform matrix volumes. The cruciform matrix volumes are further subdivided into sub-regions consisting of the between-the-fiber (BTF), the upper-between-the-fiber (UBTF), the exterior-matrix (EM), the upper-exterior matrix (UEM) and the upper-matrix (UM) sub-regions, as delineated in Figure 88. The fiber matrix bands are identified as the center band (CNB), the corner-band 0°-90° (CRB090), the corner-band 90°-180° (CRB90180), the corner-band 180°-270° (CRB180270) and the corner-band 270°-360° (CRB270360). Each region's results are

extracted from the finite element model then sorted based on positive principal stresses, thus capturing the locations that may be in a tensile tri-axial stress state. The tensile tri-axial stress state is pervasive in the cruciform matrix volumes but exists in small concentrated sub-volumes at either the fiber poles, equator or at both locations in the fiber matrix band volumes. Combining neighboring region's results was an effective way to evaluate the matrix failure criterions mentioned above. Thus, the EM region was combined with the UEM region and the BTF region was combined with the UBTF region to show analytical results correlated with the observed cruciform experimental location. Recall that the cruciform tests are videotaped from the specimen sides with the high magnification viewable area dimensions being approximately 2.0 mm high, in the direction of loading, by 4.0 mm wide along the fiber length for all the fiber spacing groups tested except the 6.0d_f fiber spacing. For this group the field of view is approximately 2.9 mm high by 4.4 mm wide to accommodate the wider fiber spacing. Since the analytical model is 1/8 the actual cruciform specimen all fiber matrix failure results are plotted having a field of view of approximately 1.4 mm high, in the direction of load, by 2.0 mm wide, along the fiber length. Consequently not all regions within the FEM are completely within view, namely the volume of matrix between the fibers, BTF, portions of the UBTF region and the corner fiber matrix bands from $\theta = 90^\circ$ to 270° .

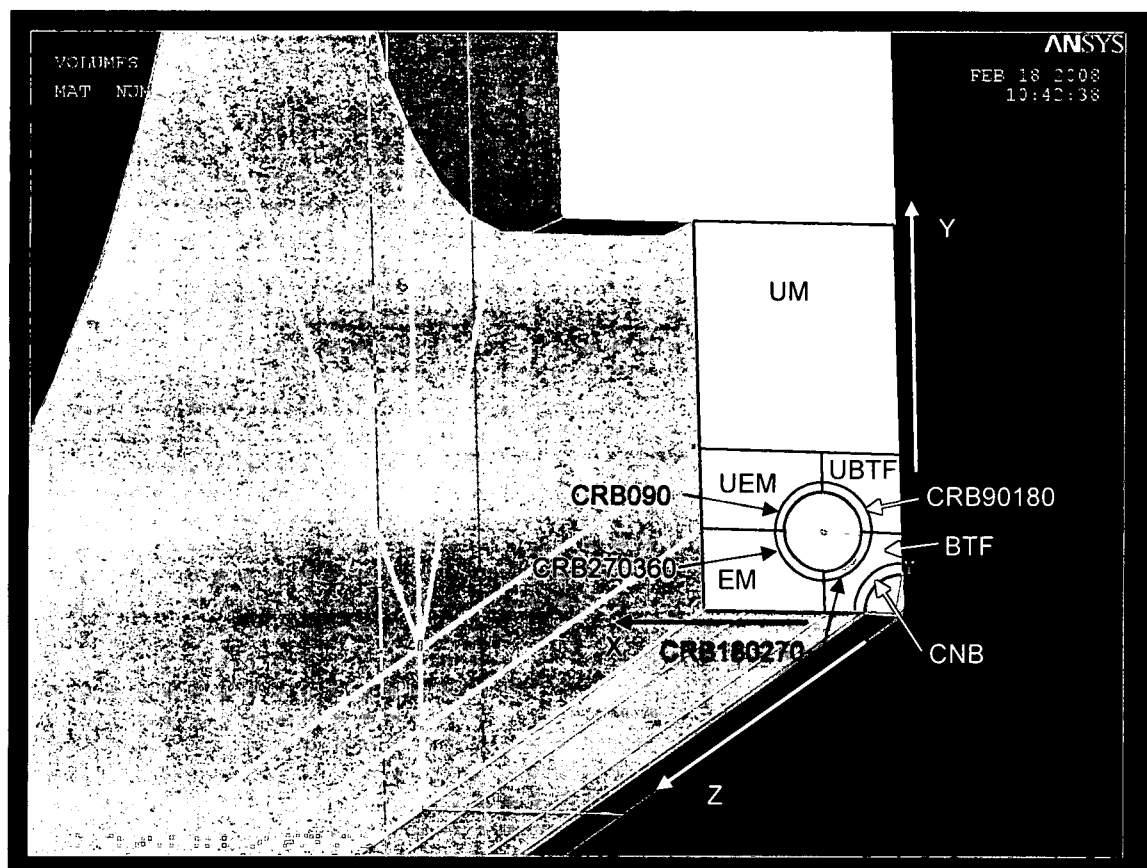


Figure 88: Finite Element Model plot showing the partitioning of the matrix volumes

To efficiently evaluate the criterion listed above for matrix failure, the analytical results of the EM and UEM regions of the FEM will be presented. Table 33 lists the limits of the exterior-matrix and upper-exterior-matrix regions of the FEM. As shown in Figure 88 the EM and UEM volumes encompass the corner fiber. Also listed in Table 33 are the locations of the bottom (south pole) and top (north pole) of the corner fiber matrix bands. Figure 89 shows the combined EM and UEM volumes of the FEM. This volume of matrix material exists in front of the fiber matrix bands and depicts a portion of the view of observation of the cruciform specimen experiments. The fiber and the matrix band surrounding the fibers are not shown. The X direction is through the cruciform specimen thickness, the Y direction is in the direction of the applied load and the Z direction is along the fiber length.

Table 33: Limits of the Exterior-Matrix and Upper-Exterior-Matrix regions and locations of the bottom and top corner fiber matrix band

Specimen	EM (mm)	UEM (mm)	Bottom Corner Fiber Band (mm)	Centerline Corner Fiber (mm)	Top Corner Fiber Band (mm)
1.57d _f	0.0 – 0.279	0.279 – 0.558	0.086	0.279	0.472
1.75d _f	0.0 – 0.311	0.311 – 0.623	0.093	0.311	0.529
1.84d _f	0.0 – 0.327	0.327 – 0.654	0.109	0.327	0.545
1.90d _f	0.0 – 0.338	0.338 – 0.676	0.120	0.338	0.556
2.0d _f	0.0 – 0.356	0.356 – 0.711	0.138	0.356	0.573
2.5d _f	0.0 – 0.445	0.445 – 0.889	0.227	0.445	0.662
6.0d _f	0.0 – 1.067	1.067 – 2.134	0.849	1.067	1.285

Post processing these results involved extracting all tensile tri-axial nodal solution data. Then organizing it within the field-of-view limits and creating a three-dimensional plot of the particular matrix failure criterion in the YZ plane of the specimen. The YZ plane is the field of view of experimental observation with Y being the vertical direction or in the direction of the applied load and Z being along the fiber length, sees Figure 88. For a 3D plot of Y, Z and the matrix criterion value, due to the way the FEM is meshed, nodes having the same Y and Z coordinate position along the X direction, the specimen thickness; the criterion value is averaged for that location on the YZ plane. In all cases the difference in magnitude of the criterion being evaluated at these locations in the different matrix volumes is very small. The averaged value of the criterion is less than 2% of the maximum value for the nodes having the same Y and Z coordinates in the individual volumes.

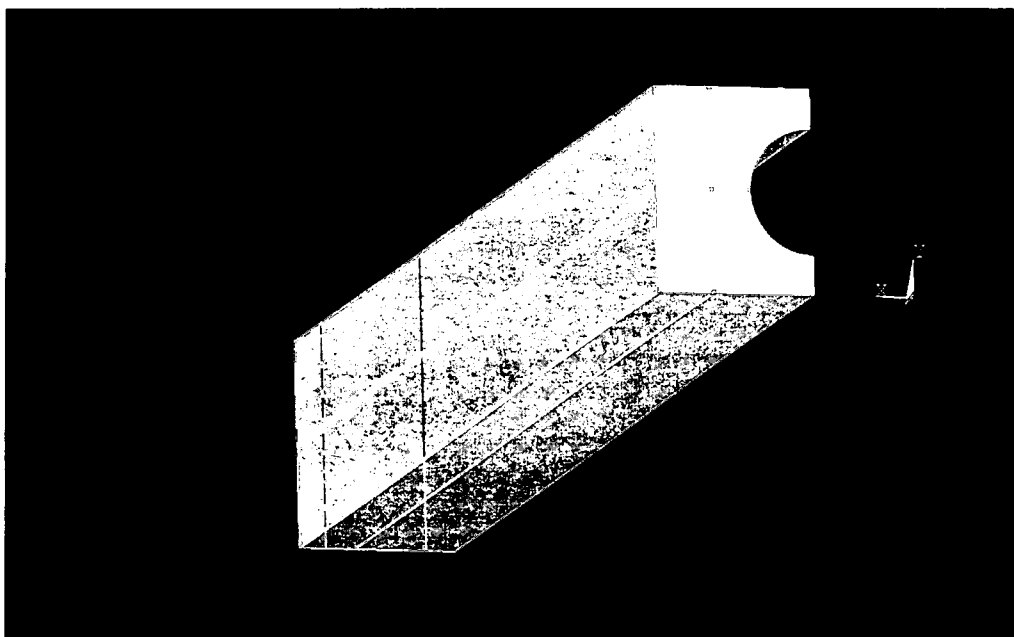


Figure 89: Exterior Matrix and Upper Exterior Matrix volumes of the Finite Element Model.

As discussed in the Matrix Failure Criterion section above the modified Tresca and Mohr-Coulomb criterion were down selected over several other possible candidates for further evaluation. These two were selected based on the indications from the fracture surface analysis that an interaction between the shear and tensile forces is working to create matrix cavitation. The fracture surface analysis also suggested that the shear strength is an upper limit for the cavitation forming under the stress state developed in the cruciform specimen. Furthermore, due to the tri-axial stress state causing dilatation of the matrix material, the limiting shear strength will be reduced at the onset of cavitation. In the following discussion both criteria will be plotted with in the field of view of the EM and UEM regions of the FEM.

As discussed in the Matrix Failure Criterion section above, the Tresca yield criterion modifies the critical shear stress to account for the tensile triaxial state of stress present for matrix failure initiation and, therefore, makes it more applicable to failure of a polymer. Figure 90 shows the distribution of the Modified-Tresca yield criterion in the YZ plane for the EM and UEM regions of the FEM due to the combination of mechanical loading and matrix cure shrinkage. The $1.75d_f$ and the $1.84d_f$ fiber spacing groups have the largest magnitudes for the Modified-Tresca

Criterion. It appears that the $2.5d_f$ and the $6.0d_f$ fiber spacing groups have virtually the same magnitude for the Modified-Tresca Criterion albeit less than that of the $1.75d_f$ and $1.84d_f$ fiber spacing. The magnitudes further decrease for the $1.57d_f$ fiber spacing with the $1.90d_f$ and the $2.0d_f$ fiber spacing having the lowest magnitude of all cruciform specimen fiber spacing groups tested. The distributions for all fiber spacing groups are symmetrical about the corner fiber horizontal centerline. Furthermore, the gap for which no criterion values exist in the YZ plane, in the Modified-Tresca Criterion distribution for all fiber spacing groups shown in Figure 90 is where a tensile tri-axial stress state does not exist, as previously mentioned for the other matrix failure criteria discussed above. This gap is primarily located in front of the corner fibers for each fiber spacing group where its vertical reach encompasses almost the entire diameter of the corner fiber and extends the entire length of the fiber in the FEM. Unlike the previously mentioned matrix failure criteria, the Modified-Tresca Criterion is uniform in magnitude for both the $1.75d_f$ and $1.84d_f$ fiber spacing groups from just above the south pole of the corner fiber to just below the north pole of the bottom corner fiber. In addition, it is also uniform from the north pole of the top corner fiber extending almost to the upper limit of the UEM volume for both the $1.75d_f$ and $1.84d_f$ fiber spacing groups. Furthermore, its maximum magnitude is practically constant for the $1.75d_f$ and $1.84d_f$ fiber spacing groups along the entire fiber length of the viewable area. Consequently, the Modified-Tresca Criterion has a large calculated value over a fairly large volume of matrix.

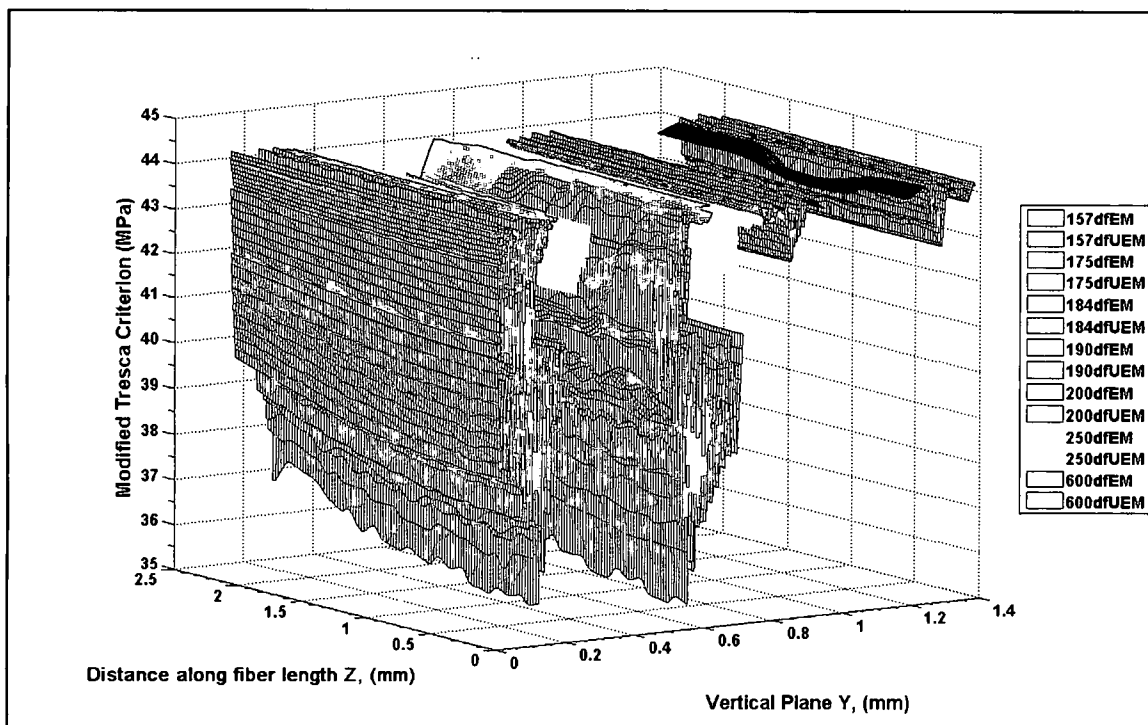


Figure 90: The Modified Tresca criterion YZ plane distribution in the Exterior-Matrix and Upper-Exterior-Matrix region for all fiber spacing groups tested

Lastly, another criterion that would possibly explain the observed matrix failure is the Mohr-Coulomb Criterion for the same reason mentioned for the modified Tresca Criterion. The distribution of the Mohr-Coulomb criterion in the YZ plane for the EM and UEM regions of the FEM is shown in Figure 91. Being very similar to the Modified-Tresca criterion in its form, the maximum magnitudes occur in the 1.75d_f and 1.84d_f fiber spacing groups, closely followed by the 2.5d_f and 6.0d_f fiber spacing groups with the 1.57d_f, 1.90d_f, and the 2.0d_f fiber spacing groups having the smallest magnitudes. The Mohr-Coulomb Criterion has virtually the same characteristics as the Modified-Tresca Criterion for all fiber spacing groups in that its maximum magnitude acts over the same volume of matrix in the EM and UEM regions of the FEM.

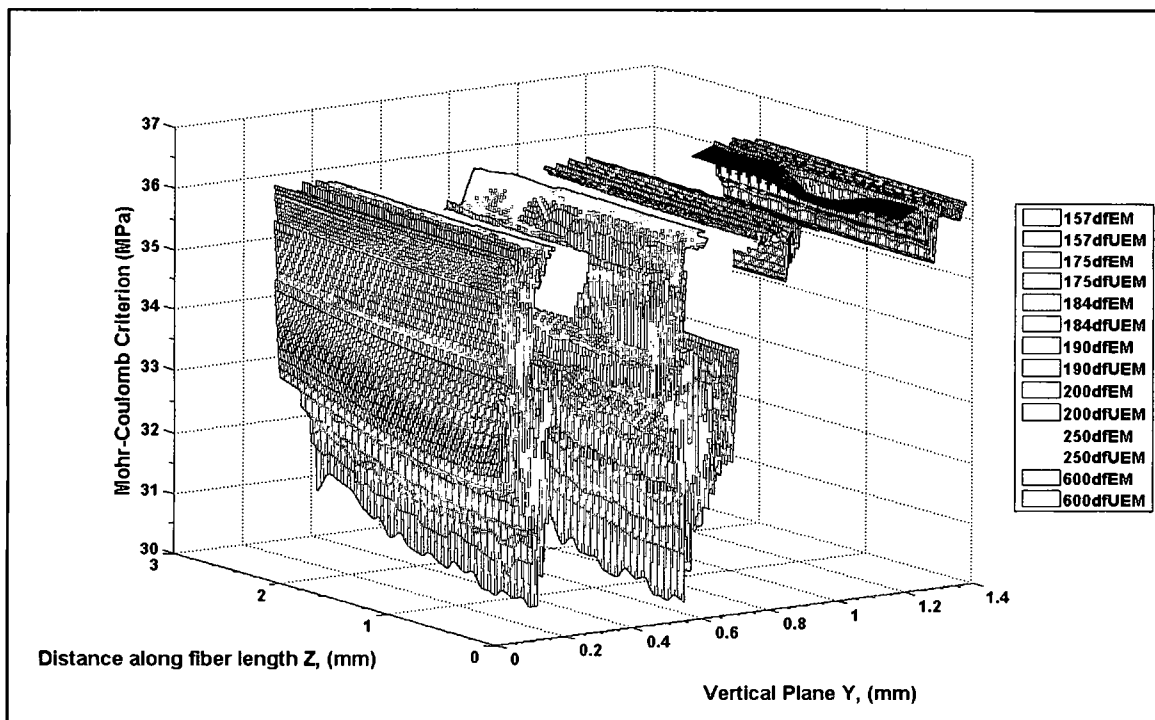


Figure 91: The Mohr-Coulomb criterion distribution acting in the YZ plane in the Exterior-Matrix and Upper-Exterior-matrix region for all fiber spacing groups tested

Matrix Failure Analytical Results Summary. The matrix failure for the 828/D-230 resin system is evaluated for all cruciform specimen fiber spacing groups tested. As discussed Matrix Failure Criterion section above, six possible failure criteria were identified that could explain the observed experimental results of matrix cavitation in the cruciform specimens tested. The criteria that best captures the effects on failure in the presence of shear stress together with the known sensitivity to hydrostatic stress of the polymer matrix are the Modified-Tresca and the Mohr-Coulomb criteria. Matrix failure or matrix cavitation occurs in a tensile tri-axial state of stress within the resin of the cruciform specimens. Only two cruciform specimen fiber spacing groups were observed exhibiting matrix cavitation failure as their first failure mechanism in the 828/D-230 resin system. They are the 1.75d_f and 1.84d_f fiber spacing groups. The analytical results indicate that a tensile tri-axial stress state exists in all matrix regions of the cruciform finite element model, as described above. Since the cruciform specimen experiments were videotaped from their side only the EM, UEM, UM and the CRB090 and CRB270360 are entirely visible. The corner matrix bands from 90

to 270 are partially visible as are the BTF matrix and the UBTF matrix volumes. For the initial evaluation of the six possible matrix failure criteria only the analytical results for the EM and UEM are presented.

The evaluation of the Modified-Tresca and the Mohr-Coulomb Criteria in the area of the matrix visible during the experiments show that the maximum magnitude occurs for the $1.75d_f$ and $1.84d_f$ cruciform fiber spacing groups, which are the two specimen spacing groups that exhibited matrix cavitation. Following the $1.75d_f$ and $1.84d_f$ fiber spacing groups in order of decreasing magnitude are the $2.5d_f$, $6.0d_f$, $1.57d_f$, with the $1.9d_f$ and $2.0d_f$ being practically equal at the lowest magnitude. Due to the Modified-Tresca and the Mohr-Coulomb matrix failure criteria constant magnitude from just below the south pole of the top corner fiber to just above the north pole of the bottom corner fiber plus from the north pole of the top corner fiber to almost the upper limit of the UEM volume; they act over the largest volume of matrix material correlating well to the observed failure initiation within the regions of the cruciform specimen.

862/W System

Fiber-Matrix Interface Analytical Results. Experimental results show that the $1.57d_f$, $1.75d_f$, $1.90d_f$, $2.50d_f$ and the $6.0d_f$ fiber spacing groups exhibited fiber-matrix debonds as their first failure mechanisms. For the $2.0d_f$ spacing its first failure mechanism is matrix cavitation. As explained above, two FEM models were constructed for each fiber spacing group to analyze the internal stresses due to the applied mechanical load from experimentation and from the residual stresses due to the matrix cure. Since the 862/W resin system is a non-linear material system the mechanical loading finite element analysis (FEA) is based on applying the displacement that achieves the far-field stress at first failure experienced from the cruciform tests. To determine the internal stresses due to the high temperature cure of the 862/W matrix system, the FEM is run having a temperature difference of 121°C using the effective coefficient of thermal expansion determined by photoelasticity methods described in Appendix B. The temperature difference of 121°C is when the matrix vitrifies locking in the residual stresses during the cure cycle.

The center and corner fiber interfacial radial and shear stress results are discussed in detail in Appendix D. Presented below are the summary discussions for center fiber and corner fiber followed by conclusions based on the interfacial analysis.

Center Fiber Interface Results. Summarizing the detail discussion of the interfacial analytical results contained in Appendix D; it is quite apparent that the center fiber of the $6.0d_f$ fiber spacing group is acting independently like an isolated single fiber. The analytical results indicate no nearest neighboring fiber interactions at the $6.0d_f$ spacing and a uniform residual stress present along its interface. However, for the $2.5d_f$ fiber spacing the nearest neighbor fiber effects are present but negligible. Analytical results show that the $2.5d_f$ spacing behaves similar to the $6.0d_f$ spacing but showed minor neighboring fiber interactions only involving the residual stresses. Both the $2.5d_f$ and $6.0d_f$ fiber spacing showed very similar behavior to their counterparts in the 828/D-230 matrix system. For the other fiber spacing groups tested neighboring fiber effects combined with the residual stress effects are manifested by a dip in the radial stress distribution as shown in Figure 92. Additionally, the combined effects result in the maximum shear stress magnitudes shifting location along the fiber matrix interface and their distribution exhibiting a change in shape becoming more asymmetric as shown in Figure 93. These behaviors are opposite to those shown in the 828/D-230 matrix system due to the high residual stresses imparted by the high temperature cure cycle.

It appears from inspection of Figure 93 that the residual stresses due to the matrix cure push the maximum shear stresses on the fiber-matrix interface toward the direction of applied load except at the $6.0d_f$ spacing. The maximum shear stresses due to the combined effects occur along the fiber-matrix interface and happen to be about where the radial stresses have their minimum magnitudes due to the combined effects for the $1.57d_f$, $1.75d_f$, $1.9d_f$ and $2.0d_f$ fiber spacing groups.

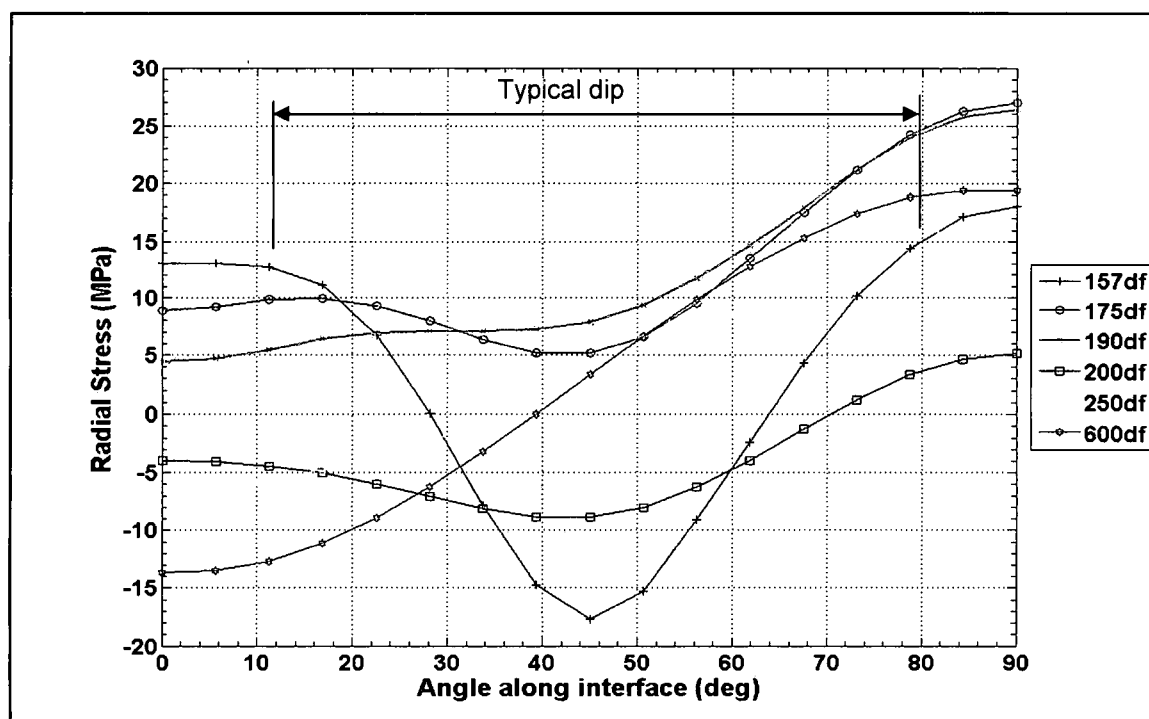


Figure 92: Radial stress distributions at the fiber-matrix interface due to the combination of mechanical loading and matrix residual stresses from cure cycle

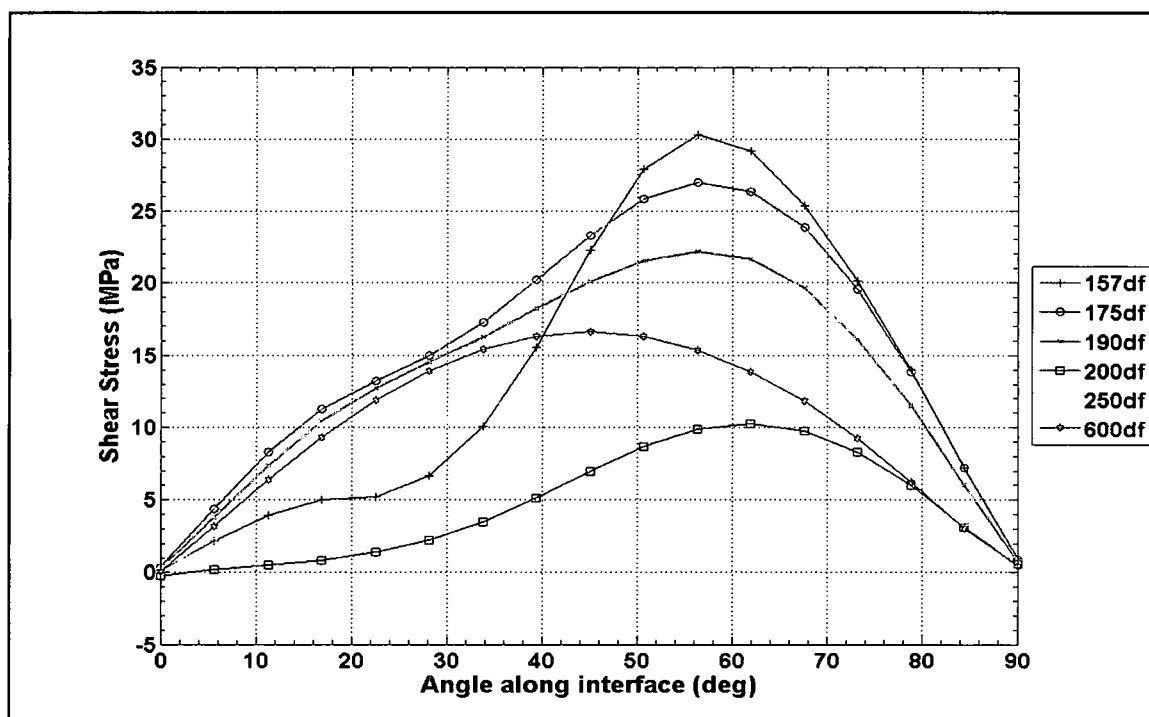


Figure 93: Shear stress distributions at the fiber-matrix interface due to the combination of mechanical loading and matrix residual stresses from cure cycle

Corner Fiber Results. Summarizing the detail discussion of the interfacial analytical results contained in Appendix D; the residual radial and shear stresses in general decrease the maximum magnitudes of the respective stresses due to mechanical loading for all fiber spacing groups in all four quadrants. The combination of the residual and mechanical loading creates a slight shift in the locations of their maximum shear stress magnitudes and slightly changes their interfacial distribution in quadrants 1, 2 and 4. Also, it appears that the residual stresses tend to increase the circumferential length over which the highest radial and shear stresses act for each fiber spacing group in the 1st, 2nd and 4th quadrants. In the 3rd quadrant nearest neighbor effects in combination with residual effects impose dramatic changes in the interfacial radial and shear stress distributions, as shown in Figures 94 and 95 respectively. The combination of residual stresses and nearest neighbor effects has the opposite effect in the 3rd quadrant reducing the circumferential length over which the highest radial and shear stresses act. The combined effects are evident by the dip in the radial stress distribution, shown in Figure 94, which is counter to that shown in the 828/D-230 system and due to the high temperature cure. Furthermore, the combined effects create a shift in maximum shear stress magnitude interfacial locations producing an asymmetric interfacial distribution as shown in Figures 95. The interfacial shear stress characteristics in the 862/W system are very similar to those shown in the 828/D-230 system.

It appears that the 6.0d_f fiber spacing group acts as an isolate fiber grouping since no nearest neighbor interaction exist in all four quadrants and its residual stresses are uniform along its interface. Although, neighboring fiber effects begin to manifest themselves at the 2.5d_f spacing their effects are very minor and are only evident in the residual stress analysis. Thus, the 2.5d_f fiber spacing group can be considered to also act as an isolated fiber grouping. The analytical results for these two fiber spacing groups are very consistent in both matrix systems.

Comparing Figures 92 to 94 and 93 to 95 the magnitudes of the radial and shear stresses are greater at the corner fiber. Thus, it appears that the center fiber experiences a load shedding effects from the corner fibers by the reduction in stress magnitude. This behavior is also very similar to that exhibited in the 828/D-230 matrix system.

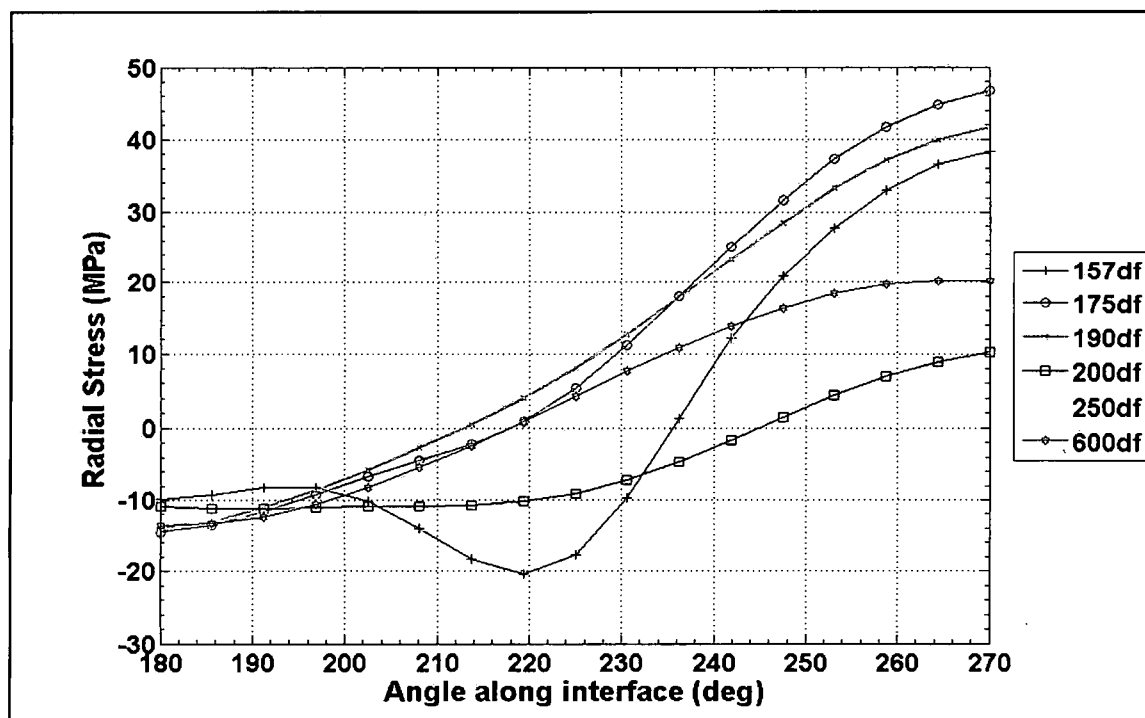


Figure 94: Radial stress distributions at the fiber-matrix interface due to the combination of mechanical loading and matrix cure residual stresses from $\theta = 180^\circ$ to 270°

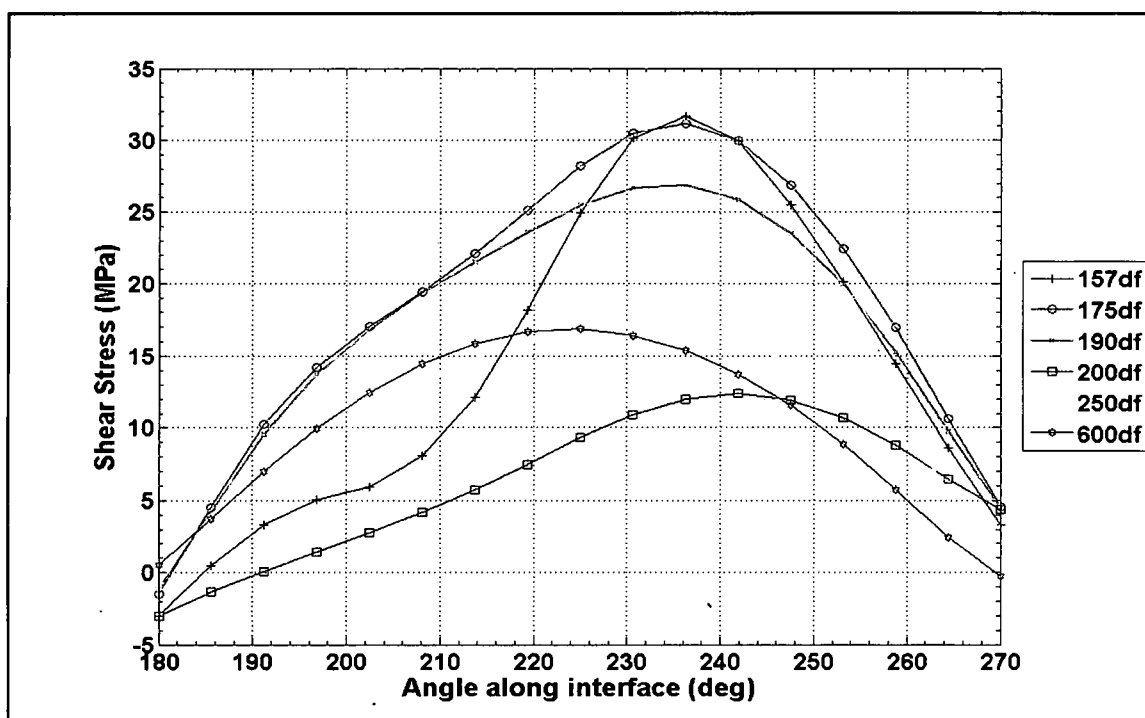


Figure 95: Shear stress distributions at the fiber-matrix interface due to the combination of mechanical loading and matrix cure residual stresses from $\theta = 180^\circ$ to 270°

Fiber-Matrix Interface Analytical Results – Conclusions. The interfacial analytical results indicate that nearest neighboring fiber interactions occur in the regions along the fiber interface where the fibers are closest together. This translates into the 1st quadrant for the center fiber and the 3rd quadrant of the corner fiber. The interactions are evident for both the mechanical loading and matrix residual stresses. Interaction effects due to the mechanical loading appear as a hump in the radial stress distribution for both fibers as shown in Figures 221 and 235 in Appendix D. The impact increases the length of fiber circumference at the interface over which the highest radial stresses act. Additionally, the impact changes the location of the maximum radial stress from along the direction of applied load, at $\theta = 90^\circ$ or 270° to $\theta = 45^\circ$ to 51° or 236° depending upon fiber spacing as shown in Figures 221 and 235 in Appendix D. Neighboring fiber interactions due to mechanical loading are also indicated by a shift in the location of the maximum magnitude of the shear stress and the shape of its distribution, as shown in Figures 224 and 239 in Appendix D. The matrix residual radial stress distributions impacts due to neighboring fiber effects result in an increase in stress as the fiber spacing decreases, as shown in Figures 220 and 231 in Appendix D. As expected, the largest effect occurs at $\theta = 45^\circ$ or 225° , the location where the distance between the fibers is shortest, but for the $2.5d_f$ and $6.0d_f$ their distribution is practically uniform. Similar to the radial stress, the shear stress distribution due to the matrix residual stresses increases as fiber spacing decreases as shown in Figures 223 and 243 in Appendix D. Also, the shear stress exhibits a change in direction as an inflection point occurs at approximately $\theta = 45^\circ$ or 225° across the fiber interface. For the $2.5d_f$ and $6.0d_f$ spacing the shear stress due to the matrix residual shear stresses is practically uniform and has a small magnitude similar to the radial stress. These nearest neighboring fiber behaviors exhibited in the 862/W system are very similar to those shown in the 828/D-230 system.

In general the impact from the matrix residual stress on the interfacial radial stresses is significant due to the high temperature cure and tends to increase as fiber spacing decreases. The radial residual stresses are compressive and thus reduce the radial stresses due to mechanical loading only along the center and corner fiber interface. The largest impact occurs where the fibers are closest together, 3rd quadrant corner fiber and 1st quadrant center fiber, and

ranges from 44% to as high as 194% depending on fiber spacing as listed in Tables 64 and 66 in Appendix D. At this location the impact is felt equally between the center and corner fiber. At the maximum radial stress location in 3rd quadrant corner fiber and 1st quadrant center fiber the impact is not as great but still significant ranging from 44% to 146% and is greatest at the center fiber. For the 1st and 2nd quadrants of the corner fiber, the impact of the matrix residual stresses reduces the radial stress from the mechanical load from 29% to 67% depending on the fiber spacing as listed in Table 67 in Appendix D. The impact on the 4th quadrant ranges from 16% to 57% depending on fiber spacing. The impact to the shear stresses due to the matrix residual stresses in corner fiber 3rd quadrant and center fiber 1st quadrant range from 9% to 65% depending on fiber spacing as listed in Tables 65 and 69 in Appendix D. The impact on the shear stress is greater at the center fiber. For the 1st and 4th quadrant of the corner fiber the residual stress impact to the shear stresses tend to be the least and range from 9% to 33% depending on fiber spacing as listed in Table 69 in Appendix D. The corner fiber 2nd quadrant exhibits a shear stress impact ranging from 11% to 33% depending on fiber spacing also listed in Table 69 in Appendix D.

The interfacial analysis indicates that the 6.0d_f and 2.5d_f fiber spacing groups can be considered to act as isolated fibers. The effects of nearest neighboring fibers due to mechanical loading are nonexistent for the 6.0d_f spacing and very minor at the 2.5d_f spacing. The residual stress effects at the 6.0d_f spacing are uniform across its interface and show only very minor effects from neighboring fibers at the 2.5d_f spacing. The analytical details particular to these two fiber spacing groups can be found in Appendix D.

Due to the high temperature cured 862/W epoxy system the magnitude of the residual stresses imparted during the curing cycle can be as large as or larger than those due to the mechanical loading. Therefore, it is imperative that the residual stresses be included in any failure criterion development. Failure to do so would result in not characterizing the internal stress state at failure initiation properly leading to erroneous results.

Fiber-Matrix Interface Debond Criteria. The debonds observed in the 862/W system are exactly as those in the 828/D-230 system. Similar correlations can be made between the cruciform tests and the analytical models in the 862/W system as for the 828/D-230 system. A detailed discussion correlating the debond measurements for the fiber spacing groups with the interfacial stress analysis at the corner fiber in the field of view is located in Appendix D. A summary of the results follows.

Each fiber spacing group experienced interfacial debonds over that part of the fiber exhibiting high magnitudes of radial stress. Furthermore, the debond length covers portions of the fiber interface where the shear stress either reaches its maximum or its average magnitude is a significant percentage of the maximum magnitude. Table 34 lists the average debond measurements for the fiber spacing groups exhibiting fiber matrix debonding as their failure initiation. The $1.57d_f$, $1.75d_f$, $1.9d_f$, $2.5d_f$ and the $6.0d_f$ debond limits cover 23%, 27%, 21%, 20% and 20% of the total fiber circumference respectively. These results lead to the conclusion that an interaction between the radial and shear stress acting at the fiber matrix interface contribute to the debond observed in the cruciform experiments.

Table 34: Experimental fiber matrix debond measurements

Spec.	Average Debond Width, mm (Std dev)	Average Debond Central angle	Experimental Debond Limits	Arc Length, mm	% circumference
$1.57d_f$	0.049 (0.024)	88°	46° to 134° NP 226° to 314° SP	0.27	23
$1.75d_f$	0.068 (0.041)	104°	38° to 142° NP 218° to 322° SP	0.32	27
$1.9d_f$	0.041 (0.041)	80°	50° to 130° NP 230° to 310° SP	0.25	21
$2.5d_f$	0.037 (0.021)	76°	52° to 128° NP 232° to 308° SP	0.24	20
$6.0d_f$	0.039 (0.0012)	78°	51° to 129° NP 231° to 309° SP	0.24	20
SF	0.023 (0.007)	54°	63° to 117° NP 243° to 297° SP	0.17	14

Matrix Failure Analytical Results. Like that shown in the 828/D-230 cruciform specimens, the experimentally observed form of matrix failure initiation is cavitation of the resin system. Recall that for matrix cavitation to occur a tensile tri-axial stress state must be present within the matrix of the cruciform specimen. As with the 828/D-230 system, several matrix failure criteria, as discussed in the Matrix Failure Criterion section of this chapter, were considered. For the same reasons discussed in the Matrix Failure Results Section for the 828/D-230 system, only two criteria will be plotted here and discussed. These are the modified Tresca and the Mohr-Coulomb matrix failure criteria. Only one fiber spacing, the $2.0d_f$ fiber spacing, experienced matrix cavitation in the 862/W resin system. The only regions of the FEM that exhibited the tri-axial stress state for the $2.0d_f$ fiber spacing is the Exterior Matrix (EM) region. See Figure 88 on how the finite element model is partitioned to investigate the state of stress within the model. The region results are extracted from the finite element model, in the same manner as for the 828/D-230 FEMs, then sorted based on positive principal stresses thus determining the locations that have a tensile tri-axial stress state. Figure 96 shows the EM region of the FEM where the tri-axial stress state occurs for the $2.0d_f$ fiber spacing. The EM volume extends only to the corner fiber horizontal centerline thus the FEM results indicate that matrix cavitation in the 862/W cruciform specimens will only occur in the matrix bounded by the corner fibers.

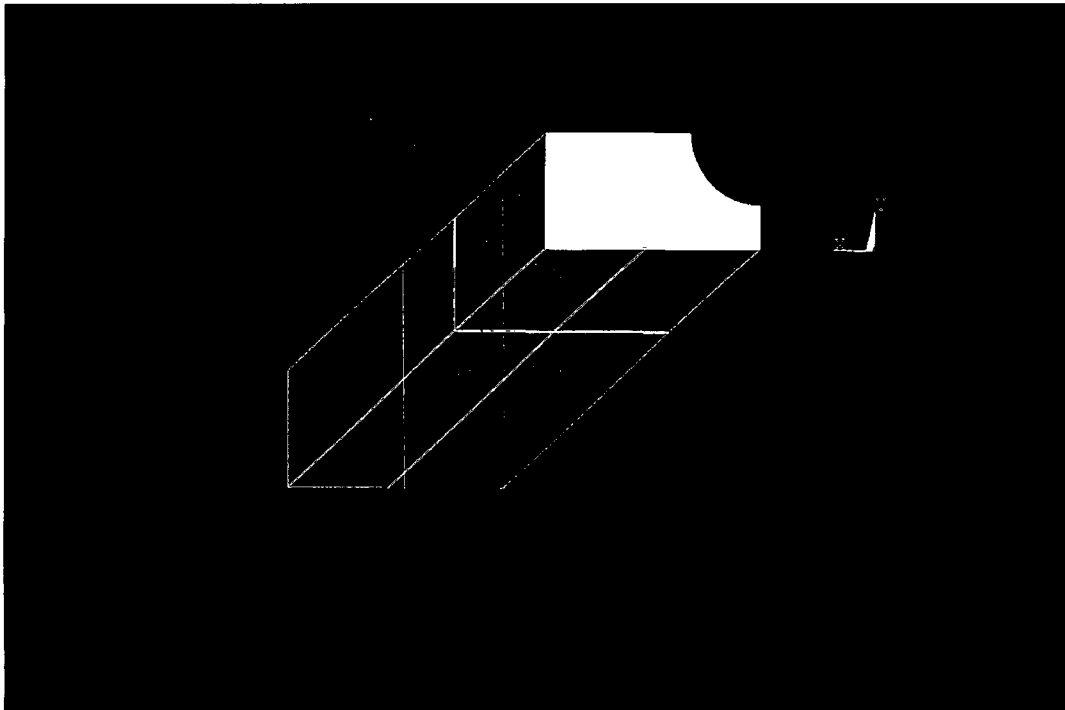


Figure 96: Exterior Matrix volume of the Finite Element Model for the 862/W cruciform specimen

The distribution of the Modified-Tresca matrix failure criterion due to the combination of mechanical load and matrix cure residual stresses in the YZ plane of the EM volume of the FEM is shown in Figure 97. The maximum magnitude of the Modified-Tresca Criterion occurs for the $2.0d_f$ fiber spacing, followed by the $2.5d_f$, $1.57d_f$, $1.90d_f$ and $1.75d_f$ fiber spacing groups, in decreasing order of magnitude. The maximum magnitude for both the $2.0d_f$ and $2.5d_f$ fiber spacing groups is practically uniform across the entire tri-axial stress volume of the EM region, in the vertical, Y direction and along the fiber length. The $1.57d_f$, $1.75d_f$ and the $1.90d_f$ fiber spacing group's maximum magnitudes are fairly constant across the tri-axial stress volume and have similar distribution characteristics.

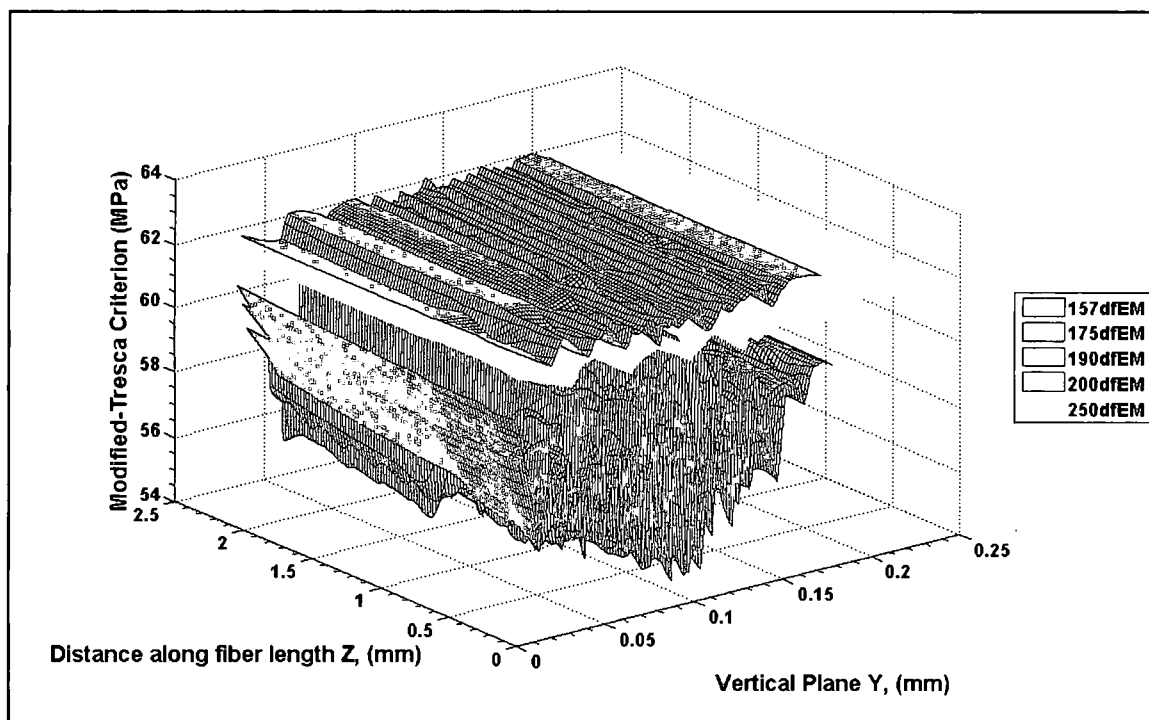


Figure 97: The Modified-Tresca criterion YZ plane distribution in the Exterior-Matrix region for all fiber spacing groups tested

The results for the Mohr-Coulomb matrix failure criterion due to the combination of mechanical load and matrix cure residual stresses in the YZ plane of the EM volume of the FEM are shown in Figure 98. Very similar to the Modified-Tresca Criterion, the maximum magnitude of the Mohr-Coulomb Criterion occurs for the $2.0d_f$ fiber spacing, followed in decreasing order of magnitude by the $2.5d_f$, $1.57d_f$, $1.9d_f$ and the $1.75d_f$ fiber spacing groups. Furthermore, the distribution of both the $2.0d_f$ and $2.5d_f$ fiber spacing groups is fairly uniform over the tri-axial stress volume. Whereas, the distribution for the $1.57d_f$, $1.75d_f$ and the $1.9d_f$ fiber spacing groups are very similar to the previously evaluated matrix failure criterion's mentioned above.

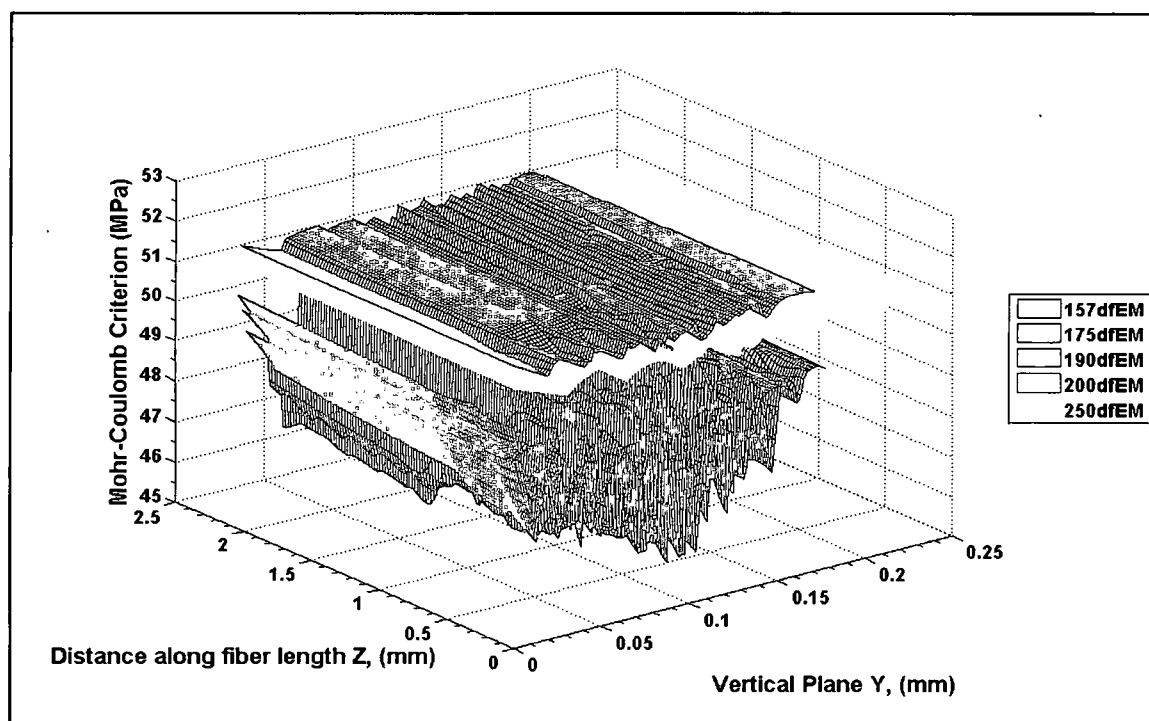


Figure 98: The Mohr-Coulomb criterion distribution acting in the YZ plane in the Exterior-Matrix region for all fiber spacing groups tested

Matrix Failure Analytical Results Summary. The matrix failure for the 862/W resin system for all cruciform specimen fiber spacing groups tested is evaluated using two possible failure criteria that would explain the observed experimental results. Matrix failure occurs under a tri-axial stress state within the matrix of the cruciform specimens. The only cruciform specimen fiber spacing observed exhibiting matrix failure as its first failure in the 862/W resin system is the $2.0d_f$ fiber spacing. The $2.0d_f$ fiber spacing exhibited a tri-axial stress state only in the exterior matrix (EM) region of the cruciform analytical model. In the evaluation of the possible matrix failure criteria in the EM region of the FEM, only the $6.0d_f$ fiber spacing did not have a tri-axial stress state in this particular volume of the finite element model.

The evaluation of the Modified-Tresca and the Mohr-Coulomb Criteria show that the maximum magnitude occurs for the $2.0d_f$ cruciform fiber spacing. Following the $2.0d_f$ fiber spacing in order of decreasing magnitude are the $2.5d_f$ and the $1.57d_f$, with the $1.75d_f$ and $1.90d_f$ being practically equal at the lowest magnitude.

Summary

This chapter summarized the development of an analytical model used to evaluate the internal stresses of the cruciform specimen at failure initiation. Beginning with a discussion of the appropriate failure criterion for the failure mechanisms observed during the cruciform tests; details of the FEM were discussed next in which results of the mesh sensitivity study arrived at the optimal mesh used throughout this work. This was followed by the parametric study results which lead to changes in the secondary camera position used for the remainder of the cruciform testing and served as a guide for determining what additional fiber spacing groups to order to complete the multi-fiber cruciform testing for this work. Next was a detailed discussion on each material system's interfacial stresses; followed by a treatise correlating the interfacial stress distributions with the observed experimental results. This confirmed the literature search results that an interaction exists between the normal or radial stresses and the shear stresses for initiating fiber-matrix debonds. These interactions between the interfacial radial and shear stresses will be further analyzed in Chapter 4 to formulate the fiber-matrix debond criterion.

Finally a discussion on the matrix stresses involved evaluating two of the most appropriate matrix failure criteria down selected from the six identified through the literature search results discussed above. The two most applicable criteria, a Modified-Tresca and a Mohr-Coulomb, were evaluated for all multi-fiber cruciform tests in both material systems in the EM and UEM regions of the FEM. Both criteria correlated the analytical results with the observed experimental results for both matrix systems. These two matrix failure criteria will be further scrutinized in Chapter 4.

References

1. Asp, L.E., L.A. Berglund, and R. Talreja, *Prediction of a matrix-initiated transverse failure in polymer composites*. Composites Science and Technology, 1996. **56**: p. 1089-1097.
2. Blackketter, D.M. and D. Upadhyaya, *Micromechanics prediction of the transverse tensile strength of carbon fiber/epoxy composites: The influence of the matrix and interface*. Polymer Composites, 1993. **14**(5): p. 437-446.

3. Busschen, A.T., *Micromechanical modeling of the transverse strength of unidirectional glass fiber reinforced polyester*, in *Engineering*. 1996, Delft Technical University: Delft, the Netherlands. p. 246.
4. Christensen, R.M. and J.A. Rinde, *Transverse tensile characteristics of fiber composites with flexible resins: Theory and test results*. *Polymer Engineering and Science*, 1979. **19**(7): p. 506-511.
5. Kok, J.M.M.d., *Deformation, yield and fracture of unidirectional composites in transverse loading*, in *Engineering*. 1995, Eindhoven University of technology: Eindhoven, the Netherlands. p. 141.
6. Kok, J.M.M.d. and H.E.H. Meijer, *Deformation, yield and fracture of unidirectional composites in transverse loading 1. Influence of fiber volume fraction and test-temperature*. *Composites Part A*, 1999. **30**: p. 905-916.
7. Kok, J.M.M.d., H.E.H. Meijer, and A.A.J.M. Peijs. *The influence of matrix plasticity on the failure strain of transversely loaded composite materials*. in *Composites Behavior, Proceedings ICCM-9*. 1993: Woodhead Publishing.
8. Rezaifard, A.H., M.G. Bader, and P.A. Smith, *Investigation of the transverse properties of a unidirectional carbon/epoxy laminate: Part 1-Matrix properties*. *Composites Science and Technology*, 1994. **52**: p. 275-285.
9. Varna, J., L.A. Berglund, and M.L. Ericson, *Transverse single-fiber test for interfacial debonding in composites 2: Modeling*. *Composites Part A*, 1997. **28**: p. 317-326.
10. Varna, J., F. Paris, and J.C. del Cano, *The effect of crack-face contact on fiber/matrix debonding in transverse tensile loading*. *Composites Science and Technology*, 1997. **57**: p. 523-532.
11. Zhang, H., et al., *Transverse single-fiber test for interfacial debonding in composites 1: Experimental observations*. *Composites Part A*, 1997. **28**: p. 309-315.
12. Schuller, T., et al., *Single-fiber transverse debonding: tensile test of a necked specimen*. *Composites Science and Technology*, 2000. **60**: p. 2077-2082.
13. Bulsara, V.N., R. Talreja, and J. Qu, *Damage initiation under transverse loading of unidirectional composites with arbitrary distributed fibers*. *Composites Science and Technology*, 1999. **59**: p. 673-682.
14. Ghosh, S., et al., *Interfacial debonding analysis in multiple fiber reinforced composites*. *Mechanics of Materials*, 2000. **32**: p. 561-591.

15. Kim, P. and S. Toll, *Stress spectra and the effective elastic and viscoelastic properties of unidirectional composites under transverse loading*. Journal of Composite Materials, 2000. **34**(17): p. 1418-1436.
16. Nimmer, R.P., P.A. Siemers, and M.R. Eggleston, *Fiber array geometry effects upon composite transverse tensile behavior*. 1991, GE Corporate Research and Development Center: Schenectady, NY. p. 369-370.
17. Wisnom, M.R., *Micromechanical modeling of the transverse tensile ductility of unidirectional silicon carbide/6061 aluminum*. Journal of Composites Technology and Research, 1992. **14**(2): p. 61-69.
18. Wriggers, P., G. Zavarise, and T.I. Zohdi, *A computational study of interfacial debonding damage in fibrous composite materials*. Computational Materials Science, 1998. **12**: p. 39-56.
19. Zhu, H. and J.D. Achenbach, *Radial matrix cracking and interphase failure in transversely loaded fiber composites*. Mechanics of Materials, 1991. **11**: p. 347-356.
20. Akser, E.O. and K.L. Choy, *Finite element analysis of the stress distribution in a thermally and transversely loaded Ti-6Al-4V/SiC fiber composite*. Composites Part A, 2001. **32**: p. 243-251.
21. Asp, L.E. and L.A. Berglund, *Effects of a composite-like stress state on the fracture of epoxies*. Composites Science and Technology, 1995. **53**: p. 27-37.
22. Asp, L.E., L.A. Berglund, and R. Talreja, *Effects of fiber and interphase on matrix-initiated transverse failure in polymer composites*. Composites Science and Technology, 1996. **56**: p. 657-665.
23. Fiedler, B., et al., *Finite-element modeling of initial matrix failure in CFRP under transverse tensile load*. Composites Science and Technology, 2001. **61**: p. 95-105.
24. Kok, J.M.M.d. and T. Peijs, *Deformation, yield and fracture of unidirectional composites in transverse loading 2. Influence of fiber-matrix adhesion*. Composites Part A, 1999. **30**: p. 917-932.
25. Piggott, M.R., *A new model for interface failure in fiber-reinforced polymers*. Composites Science and Technology, 1995. **55**: p. 269-276.
26. Gundel, D.B., B.S. Majumdar, and D.B. Miracle, *Evaluation of the transverse response of fiber-reinforced composites using a cross-shaped sample geometry*. Scripta Metallurgica et Materialia, 1995. **33**(12): p. 2057-2065.

27. Warriar, S.G., et al., *Interface effects on the micromechanical response of a transversely loaded single fiber SCS-6/Ti-6Al-4V composite*. Metallurgical and Materials Transactions A, 1996. **27A**: p. 2035-2043.
28. Warriar, S.G., et al., *Stress distribution in a transversely loaded cross-shaped single fiber SCS-6/Ti-6Al-4V composite*. Scripta Metallurgica et Materialia, 1996. **34**(2): p. 293-299.
29. Bechel, V.T. and G.P. Tandon, *Modified cruciform test for application to graphite/epoxy composites*. Mechanics of Advanced Materials and Structures, 2002. **9**: p. 1-17.
30. Tandon, G.P., R.Y. Kim, and V.T. Bechel, *Evaluation of interfacial normal strength in a SCS-0/epoxy composite with cruciform specimens*. Composites Science and Technology, 2000. **60**: p. 2281-2295.
31. Bechel, V.T. and G.P. Tandon. *Interfacial toughness measurement for a model SiC/epoxy composite*. in *SEM Annual Conference*. 2001. Portland, Oregon: SEM.
32. Bechel, V.T. and G.P. Tandon, *Characterization of interfacial failure using a reflected light technique*. Experimental Mechanics, 2002. **42**(2): p. 200-205.
33. Bechel, V.T., G.P. Tandon, and R.Y. Kim. *Fiber/Matrix Interface Debond Length Measurements under Transverse Loading in the Cruciform Test*. in *14th Annual Technical Conference of the American Society for Composites*. 1999. Fairborn, OH: American Society for Composites.
34. Tandon, G.P., R.Y. Kim, and V.T. Bechel. *Mixed-mode interfacial failure criteria using cruciform geometry*. in *16th Annual Technical Conference for the American Society for Composites*. 2001. Blacksburg, VA: American Society for Composites.
35. Tandon, G.P., R.Y. Kim, and V.T. Bechel, *Construction of the Fiber-Matrix Interfacial Failure Envelope in a Polymer Matrix Composite*. International Journal for Multiscale Computational Engineering, 2004. **2**(1): p. 65-77.
36. Tandon, G.P., R.Y. Kim, and R.E. Dutton, *Failure modes in unidirectional composites under transverse loading*. Journal of Reinforced Plastics and Composites, 1997. **16**(1): p. 33-49.
37. Tandon, G.P., et al., *influence of free edge and corner singularities on interfacial normal strength: application in model unidirectional composites*. Composites Part B, 1999. **30**: p. 115-134.
38. Asp, L.E., L.A. Berglund, and R. Talreja, *A criterion for crack initiation in glassy polymers subjected to a composite-like stress state*. Composites Science and Technology, 1996. **56**: p. 1291-1301.

39. Nicholls, D. *Effect of stress biaxiality on the transverse tensile strain-to-failure of composites*. in *Composite Materials Testing and Design (Seventh Conference)*, ASTM STP 893. 1986: ASTM.
40. Young, R.J. and P.A. Lovell, *Introduction to Polymers*. 2 ed. 1991, New York: Chapman and Hall.
41. Sultan, J.N. and F.J. McGarry, *Effect of Rubber Particle Size on Deformation Mechanics in Glassy Epoxy*. *Polymer Engineering and Science*, 1973. **13**(1): p. 29 - 34.
42. Tanaka, K., T. Mori, and T. Nakamura, *Cavity Formation at the Interface of a Spherical Inclusion in a Plastically Deformed Matrix*. *Phil Mag*, 1969. **21**: p. 267-279.
43. Bauwens, J.C., *Yield Condition and Propagation of Luders' Lines in Tension-Torsion Experiments on Poly(vinyl Chloride)*. *Journal of Polymer Science: Part A-2*, 1970. **8**: p. 893 - 901.
44. Rahhava, R. and R.M. Caddell, *The macroscopic yield behaviour of polymers*. *Journal of Materials Science*, 1973. **8**: p. 225 - 232.
45. Sterstein, S.S. and L. Ohgchin, *Yield Criteria for Plastic Deformation of Glassy High Polymers in General Stress Fields*. *American Chemical Society Polymer Preprints*, 1969. **10**(2): p. 1117 - 1124.
46. Tschoegl, N.W., *Failure Surfaces in Principal Stress Space*. *Polymer Science Symposium*, 1971. **32**: p. 239 - 267.
47. Ward, I.M., *Review: The Yield Behavior of Polymers*. *Journal of Materials Science*, 1971. **6**: p. 1397 - 1417.
48. Gosse, J.H. and S. Christensen, *Strain invariant failure criteria for polymers in composite materials*. 2001, American Institute of Aeronautics and Astronautics. p. 1-11.
49. Bowden, P.B. and J.A. Jukes, *The Plastic Flow of Isotropic Polymers*. *Journal of Materials Science*, 1972. **7**: p. 52 - 63.
50. Nadai, A., *Theory of Flow and Fracture of Solids*. 2 ed. Engineering Societies Monographs, ed. R.H. Phelps. Vol. 1. 1931, New York: McGraw-Hill Book Company. 572.

CHAPTER IV

RESULTS AND DISCUSSION

Introduction

In Chapter 2 a thorough discussion on the experimental results of the cruciform tests was presented detailing the fiber spacing groups' first damage initiation event. Chapter 3 discussed the analytical model developed to use for the determination of the stress state in the cruciform specimen at failure initiation. Also included in Chapter 3 was a brief discussion of the two failure criteria applicable for describing the experimentally observed damage initiation mechanisms. This chapter will discuss, in great detail, the fiber-matrix debonding criteria and the matrix failure criteria for each material system. Results for each criterion within the field of view of the cruciform analytical model will be thoroughly evaluated. For the sake of brevity, those areas in the cruciform model that are partially obstructed or completely obstructed from view by the fibers will be discussed in detail in Appendix E. Results of the detailed analysis from this chapter and Appendix E will be used to arrive at a fiber-matrix debonding and matrix failure criterion that best describes the failure initiation events observed in the test samples.

As previously stated, the objective of this proposed research is to establish a micromechanics based failure criterion for realistic composite materials loaded in tension transverse to the fiber direction. The experimental results confirm literature search findings showing two competing failure mechanisms of fiber-matrix debonding and matrix cavitation with varying fiber spacing. Both competing failure mechanisms were observed in model multi-fiber cruciform specimens in a room temperature cured 828/D-230 matrix system and in a high temperature cured 862/W matrix system. Several different fiber spacing cruciform specimen groups were utilized in both matrix systems where the fiber spacing is a constant multiple of the

fiber diameter. The fiber arrangement for all multi-fiber specimens consists of four fibers placed at the corners of a square and the fifth fiber located at the intersection of the face diagonals of the corner fibers. The fiber spacing is the distance between the centerline of the corner fibers with the center fiber remaining in the center of the cruciform specimen thickness. The specimen thickness varied with the fiber spacing. However, every attempt was made to keep the matrix cover, i.e. the distance from the corner fiber outside equator to the specimen free edge, constant for all fiber spacing groups. Common to both matrix systems were the $1.57d_f$, $1.75d_f$, $1.90d_f$, $2.0d_f$, $2.5d_f$ and $6.0d_f$ fiber spacing groups. The 828/D-230 system used one additional fiber spacing at $1.84d_f$. The different spacing groups were used to represent variations in the volume fraction of a composite material, i.e. from tightly packed fibers to widely spaced fibers. Some of these spacing represent volume fractions that are lower than seen in practical composites but were included in the study in order to investigate how the stresses and failure mechanism changed for a wide range of volume fractions. Table 35 lists the volume fraction based upon the area bounded by the center-to-center distance of the corner fibers and the cross sectional area of the enclosed fibers. The area of the enclosed fibers will always be equal to the cross sectional area of two fibers since the center fiber is wholly enclosed plus one-quarter of each corner fiber. Consequently the $1.57d_f$ spacing represents densely packed fiber spacing where the $1.75d_f$, $1.84d_f$, $1.90d_f$ and the $2.0d_f$ represent various degrees of moderately packed fibers. The $2.5d_f$ fiber spacing represents a sparsely packed fiber arrangement whereas the $6.0d_f$ spacing represents a wide fiber spacing array.

Table 35: Representative volume fraction of the multi-fiber cruciform specimen spacing groups

Fiber Spacing	Area (mm^2)	Enclosed Fiber Area, A_f (mm^2)	A_f/Area
$1.57d_f$	0.3117	0.198	0.64
$1.75d_f$	0.3873	0.198	0.51
$1.84d_f$	0.4281	0.198	0.46
$1.90d_f$	0.4565	0.198	0.43
$2.0d_f$	0.5058	0.198	0.39
$2.5d_f$	0.7903	0.198	0.25
$6.0d_f$	4.552	0.198	0.04

In addition to the multi-fiber cruciform specimens, a single fiber cruciform specimen was also tested in each matrix system. Table 36 lists the results of the cruciform specimen experimental results for each matrix system indicating the first failure mechanism and the far-field stress at the failure initiation. In the cases where the failure initiation is by matrix cavitation the far-field stress is considerably lower than the smallest fiber-matrix interface debond initiation far-field stress. For example, the $1.84d_f$ cruciform specimen in the 828/D-230 matrix system is just over 60% of the far-field stress of the $2.5d_f$ spacing that exhibited a fiber-matrix interface debond as its failure initiation. Likewise, the $2.0d_f$ cruciform fiber spacing in the 862/W matrix system is about 64% of the far-field stress of the $1.57d_f$ fiber spacing exhibiting the smallest fiber-matrix debonding failure initiation far-field stress. These examples offer a qualitative comparison illustrating the fact that matrix cavitation occurs at stress levels far below that for fiber-matrix debonding and ultimate failure. A quantitative comparison cannot be made between the different fiber spacing cruciform specimen groups since the stress state is dependent on several variables including the fiber spacing, the specimen's thickness and the distance from the corner fiber's outside equator to the specimen free edge, to name a few. Although there exists a large variation in the fiber-matrix debond initiation far-field stress relative in each matrix systems, the location of the failure initiation plays an important role in the explanation of the experimental results discussed in Chapter 2 and as shown in Table 36.

Table 36: Cruciform Specimen Experimental Results for both Matrix Systems showing first failure mechanisms and corresponding far-field stress at first failure

Fiber Spacing	828/D-230 Matrix System		862/W Matrix System	
	First Failure Mechanism	Average Far-Field Stress at First Failure (MPa)	First Failure Mechanism	Average Far-Field Stress at First Failure (MPa)
$1.57d_f$	Debond	8.29	Debond	12.04
$1.75d_f$	Cavitation	4.84	Debond	18.04
$1.84d_f$	Cavitation	3.97	-	-
$1.90d_f$	Debond	16.38	Debond	17.23
$2.0d_f$	Debond	15.66	Cavitation	7.76
$2.5d_f$	Debond	6.58	Debond	12.56
$6.0d_f$	Debond	10.7	Debond	21.44
SF	Debond	20.43	Debond	14.46

Recall that the cruciform specimen experiments are videotaped from the specimen's side. Figure 99 shows the typical view from the specimen's side used in all cruciform tests. Also shown in Figure 99 is the approximate high magnification viewing area. From this view the entire diameter of the corner fibers are visible for all cruciform tests. The center fiber, depending upon the fiber spacing is either partially obstructed by the corner fibers, the north and south poles are hidden, or the entire center fiber is within view. Table 37 lists the limits of the field of view for the center fiber for all fiber spacing groups tested.

In chapter 2 the fiber-matrix debond is characterized by a difference in shading on the fiber as shown in Figure 100. The debond typically initiates over a finite length instantaneously thus debonding a finite arc length of the fiber circumference. Figure 101 is a schematic diagram showing a fiber-matrix debond in the northern hemisphere of a fiber. The debond width is measured, in the vertical plane, from the still photos extracted from the videotaped experiments. From basic geometry, the central angle, 2α as defined in Figure 101 can be calculated.

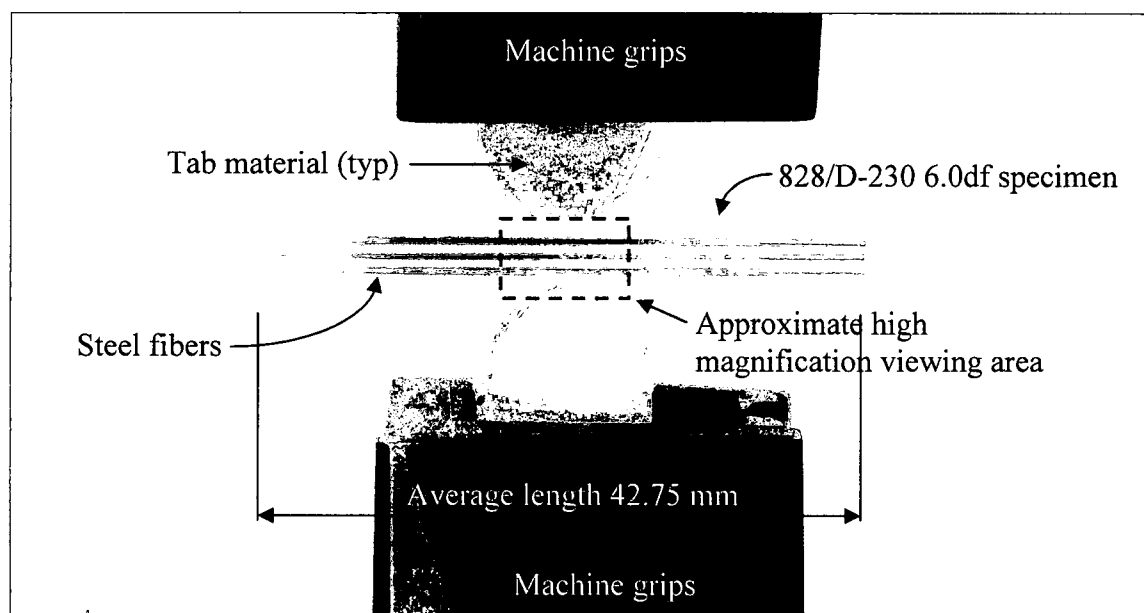


Figure 99: Typical video tape view of the cruciform specimen testing at low magnification

Table 37: The center fiber viewable area in multi-fiber cruciform specimens

Fiber Spacing	Distance between Corner Fiber poles (mm)	Angular sweep along fiber interface (deg)
$1.57d_f$	0.205	$0^\circ - 35^\circ$ & $360^\circ - 325^\circ$
$1.75d_f$	0.270	$0^\circ - 49^\circ$ & $360^\circ - 311^\circ$
$1.84d_f$	0.302	$0^\circ - 58^\circ$ & $360^\circ - 302^\circ$
$1.90d_f$	0.324	$0^\circ - 66^\circ$ & $360^\circ - 294^\circ$
$2.0d_f$	0.356	$0^\circ - 90^\circ$ & $360^\circ - 270^\circ$
$2.5d_f$	0.533	$0^\circ - 90^\circ$ & $360^\circ - 270^\circ$
$6.0d_f$	1.778	$0^\circ - 90^\circ$ & $360^\circ - 270^\circ$

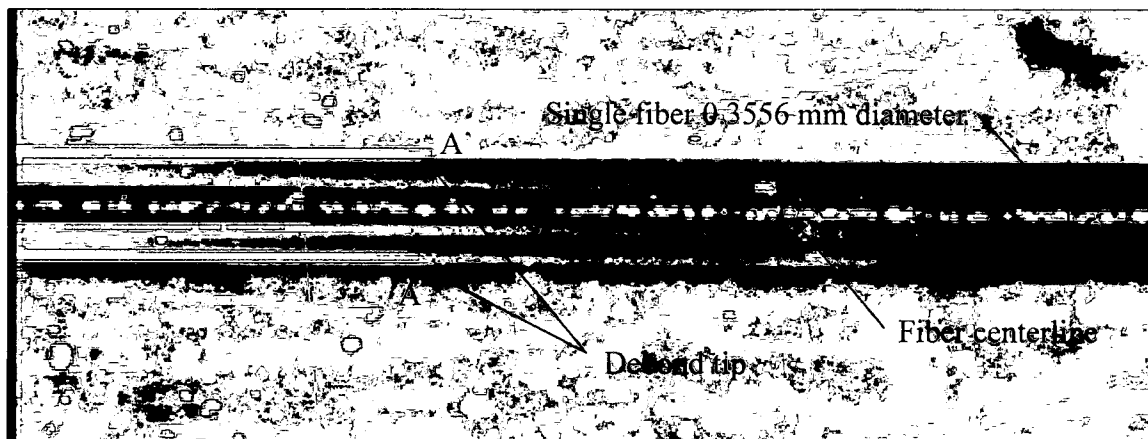


Figure 100: Typical fiber-matrix debonds in the north and south hemisphere of a single fiber specimen.

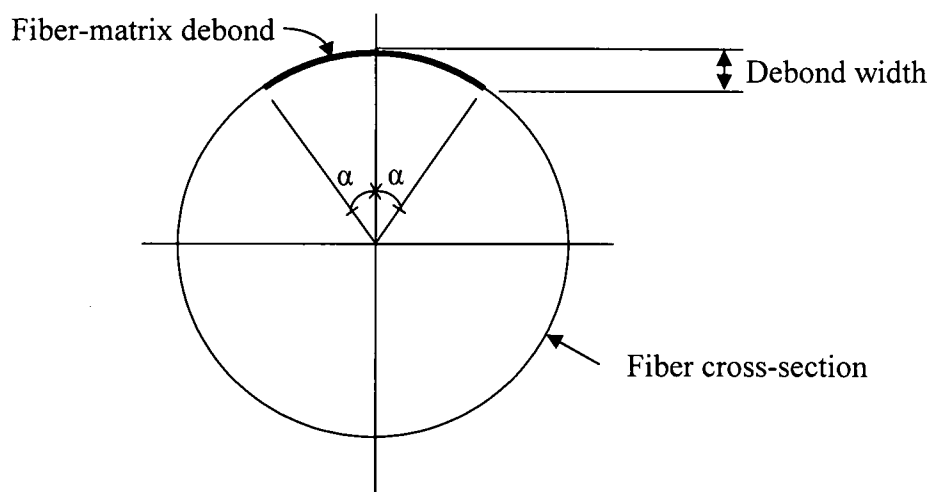


Figure 101: Fiber-matrix debond measurement schematic

Figure 102 shows the Cartesian directions and fiber interface angular orientation of the cruciform specimen. Accordingly, the corner fibers have a viewable fiber interface along the entire 1st quadrant from $\theta = 0^\circ$ to 90° and along the entire 4th quadrant from 270° to 360° or back to 0° . Whereas the center fiber's viewable area is dependent on fiber spacing and is listed in Table 37. From the FEM of the multi-fiber cruciform specimens described in Chapter 3, the corner fiber viewable areas are delineated as the CRB090 and CRB270360 matrix bands for the 1st and 4th quadrant respectively, and the center fiber is identified as CNB matrix band, see Figure 88. Figure 103 shows the break out of the CRB090, CRB270360 and the CNB volumes of the FEM in the field of view for a clear orientation.

Recall that in Chapter 2 the cruciform test results showed that the vast majority of fiber-matrix debonds occurred at the corner fiber in both matrix systems. Through the fracture surface analysis results discussed in Chapter 2, it was highly likely that a shear stress component along with a dominate tensile stress component created the debond initiation in both matrix systems. Through the interfacial stress analysis discussed in Chapter 3 and using the debond measurements obtained from the cruciform tests in Chapter 2, the fracture surface analysis was essentially confirmed. The analysis showed that in each matrix system each fiber spacing group experienced interfacial debonds over that part of the fiber exhibiting high magnitudes of radial and shear stresses. Specifically for the shear stress, the debond length covers portions of the fiber interface where it either reaches its maximum or its average magnitude is a significant percentage of the maximum magnitude. Therefore, the interfacial stresses at the corner fiber within the field of view, namely the 1st and 4th quadrants, will be thoroughly investigated and coupled with the experimental results to choose and apply a fiber-matrix debond criterion.

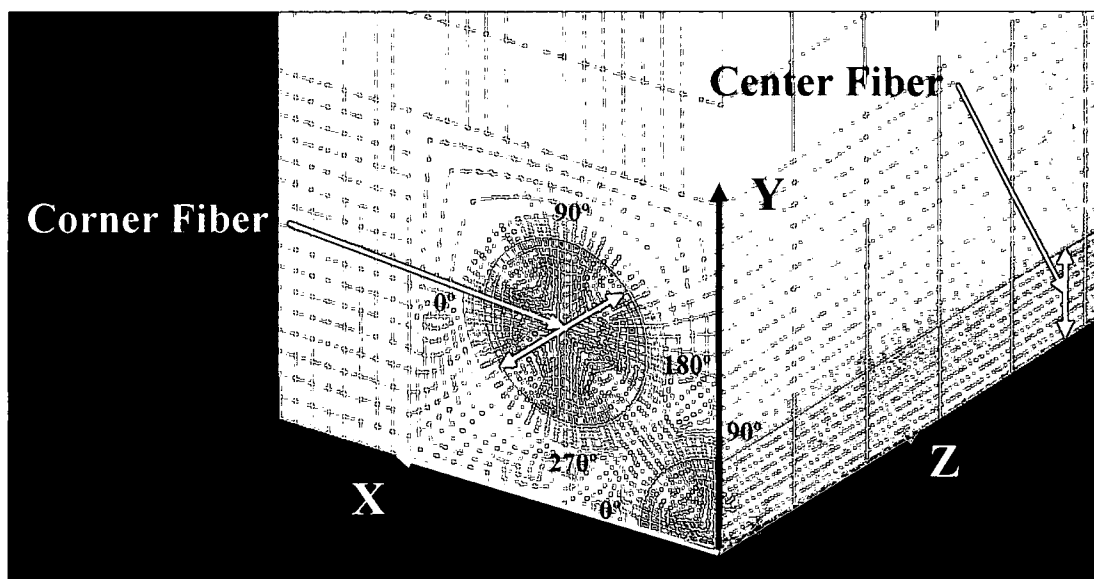


Figure 102: Cruciform specimen finite element model showing model Cartesian directions and fiber interface angular orientation

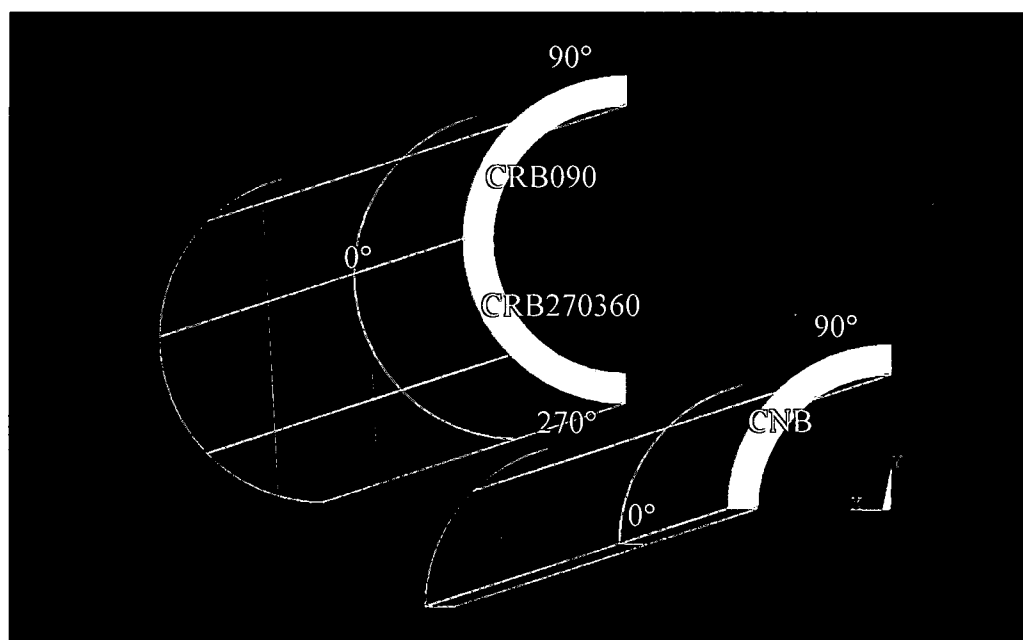


Figure 103: The multi-fiber cruciform FEM matrix volumes for the center and corner fiber in the experimental field of view

Chapter 2 also revealed that matrix cavitation developed in the $1.75d_f$ and $1.84d_f$ fiber spacing groups in the 828/D-230 matrix and at the $2.0d_f$ spacing in the 862/W matrix. Also, the test results show that the cavitations initiate in primarily the EM of both matrix systems. The 828/D-230 system had cavitations initiating in the UEM, UM, UBTF and CNB cruciform regions as well. Figure 104 shows the volumes in the FEM exhibiting matrix cavitation, namely the EM, UEM, UM, UBTF and CNB regions. In Chapter 3 six identified matrix failure criteria were down selected to two that best described the physics of the experimental observations. Consequently, these regions of the FEM will be thoroughly evaluated and coupled with the experimental results to choose and apply a matrix failure criterion capturing the cavitation for each matrix system.

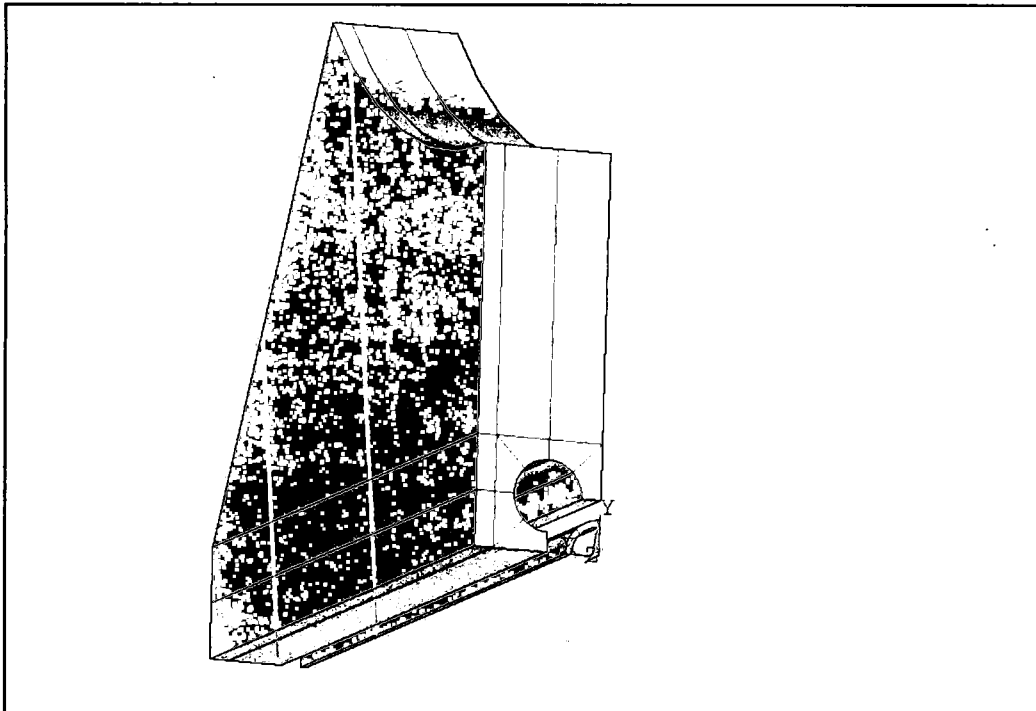


Figure 104: The multi-fiber cruciform FEM volumes for the EM, UEM, UM, UBTF and CNB in the experimental field of view

Fiber-Matrix Debond Initiation Criterion

Several forms of debonding criteria have been proposed in the literature ranging from a linear form, utilizing stress concentration factors (SCF), to quadratic forms, using the radial stress and shear stress terms at the fiber matrix interface. As discussed in Chapter 3, for a starting point in the determination of the most applicable debond criteria a quadratic form having a radial and shear stress interaction will be introduced.

The debond criterion most cited in the literature is a quadratic interaction between the normal and shear stress at the fiber-matrix interface [1]. The criterion shown in equation (1) is the squared ratio of the normal and shear stresses in the matrix at the interface to their respective matrix failure stresses under tension and shear alone. The constant C in equation (1) is usually 1 and when evaluated to be greater than 1, the criterion predicts debonding.

$$A \left(\frac{\sigma_r}{\sigma_{yt}} \right)^2 + B \left(\frac{\tau_{r\theta}}{\tau_y} \right)^2 \geq C \quad (1)$$

where σ_{yt} is the tensile strength and τ_y is the shear strength determined by neat resin tensile tests and torsion tests, respectively. σ_r and $\tau_{r\theta}$ are the interfacial radial stress and shear stress, respectively, determined by the cruciform FEA. The constants A and B are curve fitting parameters and can be regarded as a function of the adhesion properties between the matrix and fiber. The constant A can be considered a function of the adhesion strength of the matrix in tension or normal to the fiber interface and the constant B a function of the adhesion strength in shear.

Most linear debond criterion cited in the literature involve predicting the normal or shear debond initiation stress by applying a SCF to the applied far field stress summed with the particular residual stress component, either the radial or shear residual stress. These two forms are independent and may predict the debond stress in a pure radial or shear stress loading

condition. However, they do not cover the interaction of the radial and shear stresses occurring when load is applied normal to the direction of the fibers, i.e. in a more general loading case. In Appendix D from the 828/D-230 Fiber-Matrix Interface Debond Criterion Evaluation section, pages 408 to 417, it was shown that the radial stress was the dominate stress component and that its magnitude was compressive at the fiber equators. A problem with the proposed quadratic debond criterion stated above is that it does not reflect this stress state. Thus a linear version of equation 1 is introduced to capture the interaction between the radial stress and shear stress present at the fiber matrix interface when the applied load is transverse to the direction of the fibers. Furthermore, a linear version will also capture the compressive stress present at fiber equator along the fiber matrix interface as opposed to equation 1. The proposed linear debond criterion is shown by equation (2).

$$A \left(\frac{\sigma_r}{\sigma_{yt}} \right) + B \left(\frac{\tau_{r\theta}}{\tau_y} \right) \geq C \quad (2)$$

where σ_r and $\tau_{r\theta}$ are the interfacial radial and shear stress, respectively, in the matrix determined from the cruciform FEA and σ_{yt} and τ_y are the matrix tensile and shear strengths respectively, determined from the neat resin test results. The constants A and B are curve fitting parameters and can be considered a function of the adhesion properties between the matrix and fiber just as stated previously for equation (1). Like equation (1), the constant C is usually 1 and when equation (2) is evaluated to be greater than 1 a fiber matrix debond is predicted.

Quadratic Debond Initiation Criterion in the Field of View. Figures 105 and 106 show plots of the quadratic debond criterion distribution at the corner fiber in the 1st and 4th quadrant, respectively, at $Z = 0$ for all cruciform fiber spacing tested. The constants A and B have been set equal to 1.0. The debond criterion should be at its lowest magnitude for the 1.75d_f and 1.84d_f fiber spacing groups along the entire interface since they exhibited matrix cavitation as their failure initiation mechanism. The single fiber debond criterion distribution is also shown in the first

quadrant of the corner for reasons discussed in Chapter 3. Not surprisingly, the debond criterion distribution follows closely to the radial stress plot of all fiber spacing groups at the fiber interface in the first and fourth quadrants of the corner fiber. See Figures 193 and 196 of Appendix D. The largest magnitudes belong to the $1.9d_f$ and $2.0d_f$ followed by the SF, $1.57d_f$, $2.5d_f$, $6.0d_f$, $1.75d_f$ and $1.84d_f$ fiber spacing groups in decreasing order of magnitude.

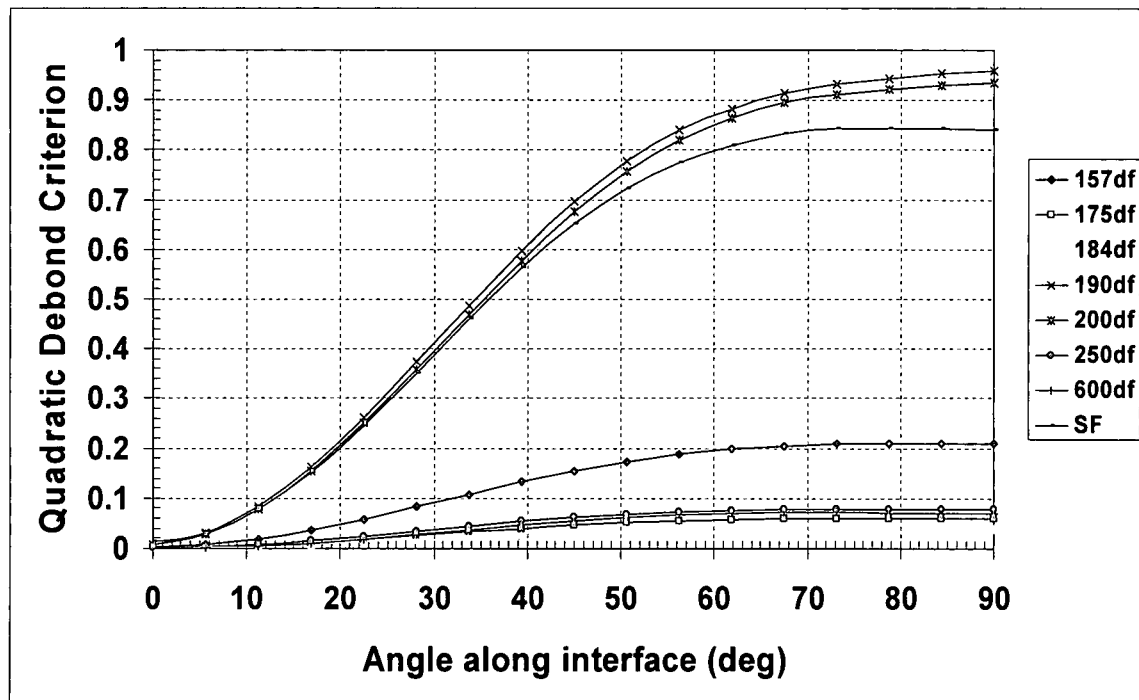


Figure 105: Quadratic Debond Criterion evaluated at the fiber matrix interface of the corner fiber in the field of view from $\theta = 0^\circ$ to 90° at $Z = 0$ with A and B equal to 1.0

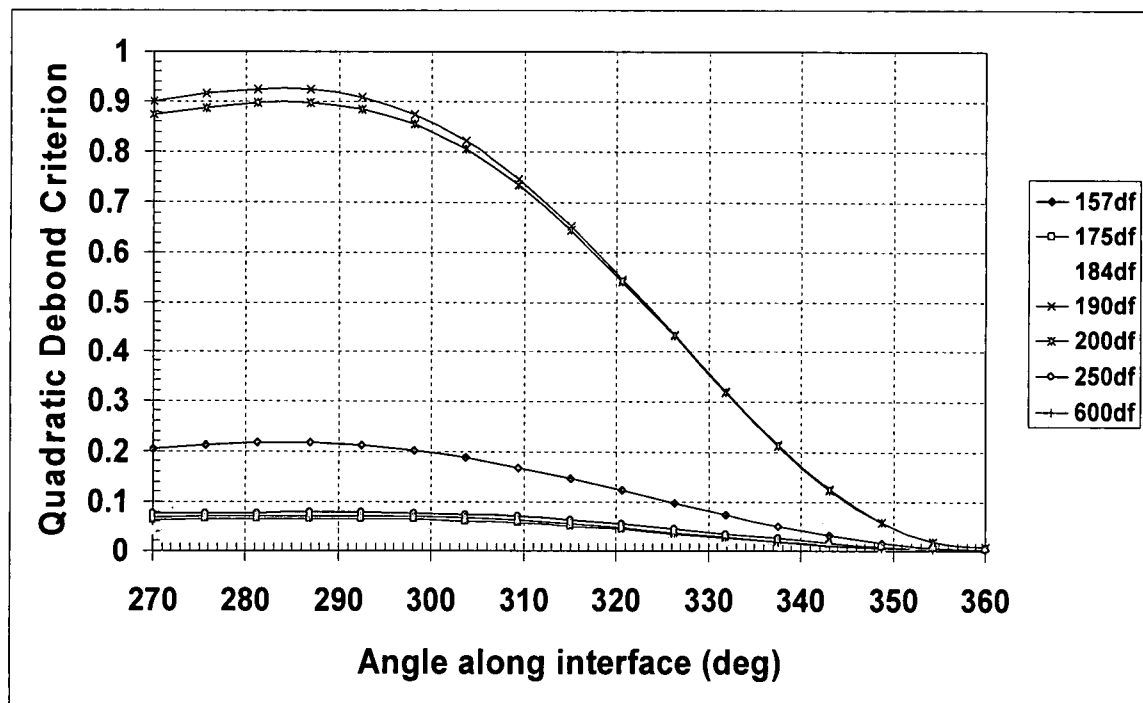


Figure 106: Quadratic Debond Criterion evaluated at the fiber matrix interface of the corner fiber in the field of view from $\theta = 270^\circ$ to 360° at $Z = 0$ with A and B equal to 1.0

By inspection of Figure 105 and 106 the constants, A and B , need to be such that the debond criterion distribution at the fiber interface is greater than 1.0 for the $1.57d_f$, $1.90d_f$, $2.0d_f$, $2.5d_f$ and the $6.0d_f$ fiber spacing groups. Manipulating the combination of the constants, A and B , for the fiber spacing groups that exhibited debonding as their failure initiation such that equation (1) is greater than 1.0 results in A equal to 15.0 and B equal to 1.0. Figures 107 and 108 are plots of the quadratic debond criterion evaluated in the 1st and 4th quadrants of the fiber matrix interface setting constants $A = 15.0$ and $B = 1.0$. Close inspection of both Debond Criterion distributions reveals that the $1.57d_f$, $1.90d_f$, $2.0d_f$, $2.5d_f$ and the $6.0d_f$ fiber spacing groups all exceed 1.0 indicating fiber matrix debond occurred correlating the experimental observations. The quadratic debond criterion also evaluates the $1.75d_f$ and $1.84d_f$ fiber spacing groups at less than 1.0 for both the first and fourth quadrants of the corner fiber, further correlating the experimental observations.

The angular location on the plot of where the distribution of the individual fiber spacing groups exceed 1.0 should correspond to the observed limits of the debond initiation. A measure of the soundness of the criterion predicting whether a debond occurs or not would be how close the criterion's debond limits are to the experimentally observed debond limits. The debond limits were determined from the photomicrograph analysis of the cruciform experiments. Table 74 lists the fiber matrix debond limits determined by the quadratic debond criterion evaluated from the cruciform FEM results for the corner fiber in the 1st and 4th quadrant as well as the experimental debond limits listed in Table 63. Also listed in Table 74 is the relative difference, expressed as a percentage, between the actual observed debond limit and the predicted debond limit determined by the quadratic debond criterion. The relative difference is taken as the ratio of the predicted angular measure to the observed angular measure expressed as a percentage, where the angular measure is the difference in angle along the interface between the respective pole to the debond limit, as shown in Figure 101.

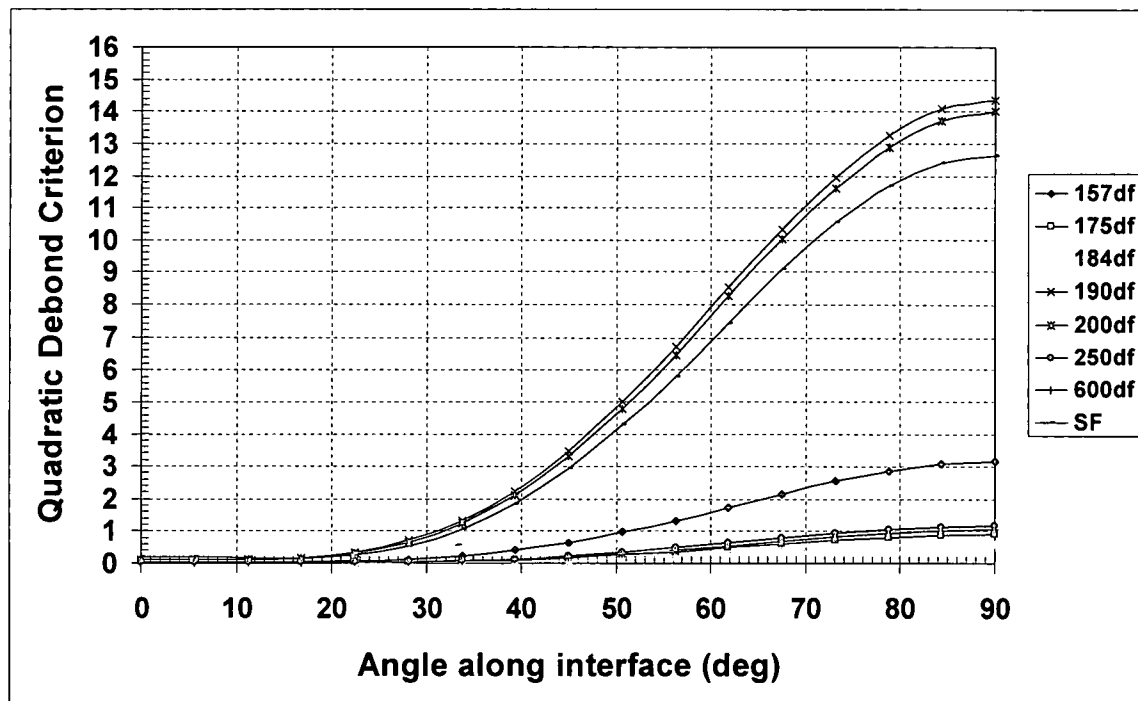


Figure 107: Quadratic Debond Criterion evaluated at the fiber matrix interface of the corner fiber in the field of view from $\theta = 0^\circ$ to 90° at $Z = 0$ with $A = 15.0$ and $B = 1.0$

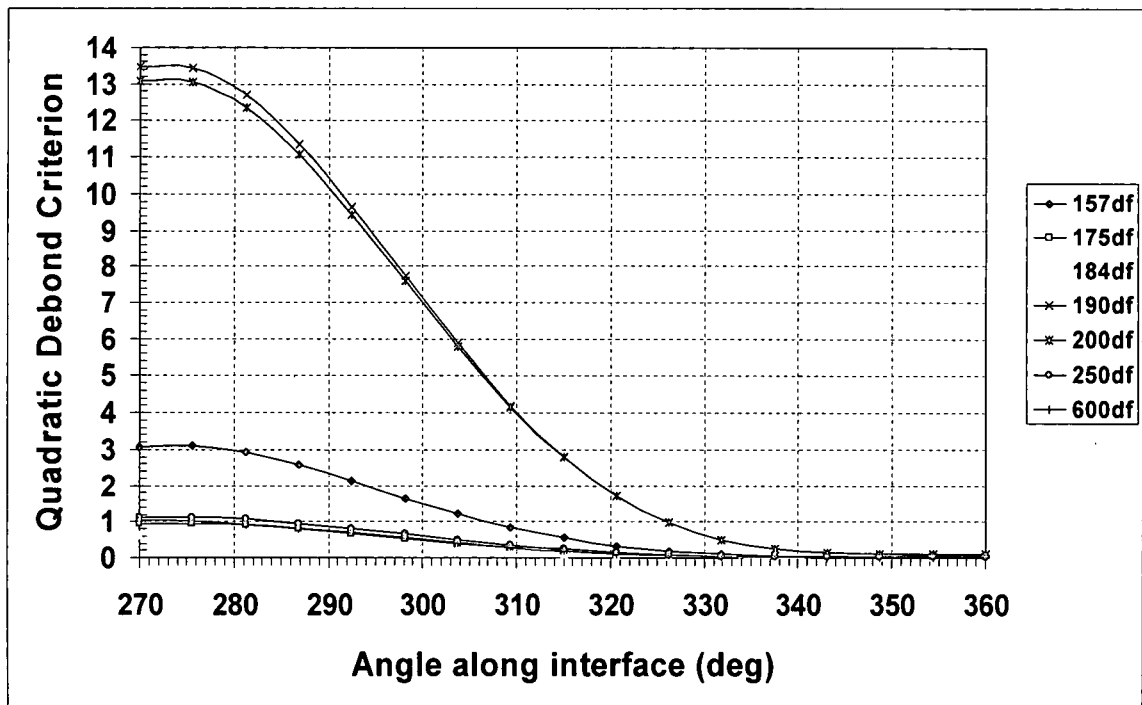


Figure 108: Quadratic Debond Criterion evaluated at the fiber matrix interface of the corner fiber in the field of view from $\theta = 270^\circ$ to 360° at $Z = 0$ with $A = 15.0$ and $B = 1.0$

Table 38: Fiber matrix debond limits for the corner fiber 1st and 4th quadrant determined by quadratic debond criterion evaluated from the cruciform FEM results

Fiber Spacing	Quadratic Debond Criterion Debond limits		Experimental Debond limits		% Δ	
	1 st Quad	4 th Quad	1 st Quad	4 th Quad	1 st Quad	4 th Quad
1.57d _f	51°	307°	44.5°	315.5°	14.3	18.7
1.9d _f	31°	326°	32°	328°	1.7	3.4
2.0d _f	31°	326°	35°	325°	7.3	1.8
2.5d _f	75°	285°	66.5°	293.5°	36.2	36.2
6.0d _f	81°	278°	66°	294°	62.5	66.7
SF	34°	-	37°	-	5.7	-

From Table 38 it appears that the quadratic debond criterion is fairly good in predicting the debond limits for the SF, 1.9d_f and 2.0d_f fiber spacing groups slightly over predicting their location as evidence of the small % Δ values. However, it has moderate success predicting the debond limits for the 1.57d_f fiber spacing under predicting the experimental observations. Furthermore, the quadratic criterion under predicts the debond limits by a rather large amount for

the $2.5d_f$ and $6.0d_f$ fiber spacing groups. Inspection of Figures 107 and 108 reveal that the quadratic debond criterion does not properly reflect the compression stress present at the fiber equator. The compressive stresses covered from 16% to 33% of the fiber interface as shown in Figure 193 and 196 in Appendix D. Although, the magnitudes are relatively small they could have an impact to the debond initiation location.

Linear Debond Initiation Criterion in the Field of View. Figures 109 and 110 show a plot of the linear debond criterion distribution in the 1st and 4th quadrants of the corner fiber, respectively, at $Z = 0$ having the constants A and B set equal to 1.0 for all cruciform fiber spacing groups tested. The debond criterion should be at its lowest magnitude for the $1.75d_f$ and $1.84d_f$ fiber spacing groups along the entire interface since these two exhibited matrix cavitation as their first failure mechanism. The single fiber debond criterion distribution is also shown in the first quadrant of the corner for reasons discussed in Chapter 3.

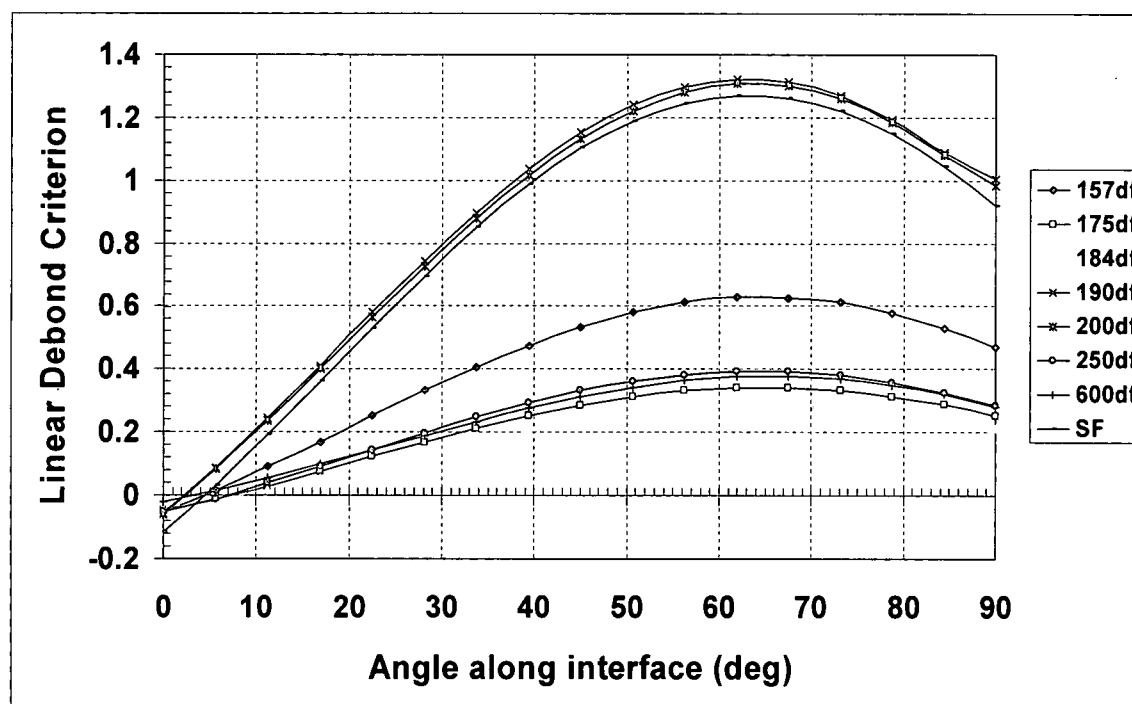


Figure 109: Linear Debond Criterion evaluated at the fiber matrix interface of the corner fiber in the field of view from $\theta = 0^\circ$ to 90° at $Z = 0$ with A and B equal to 1.0

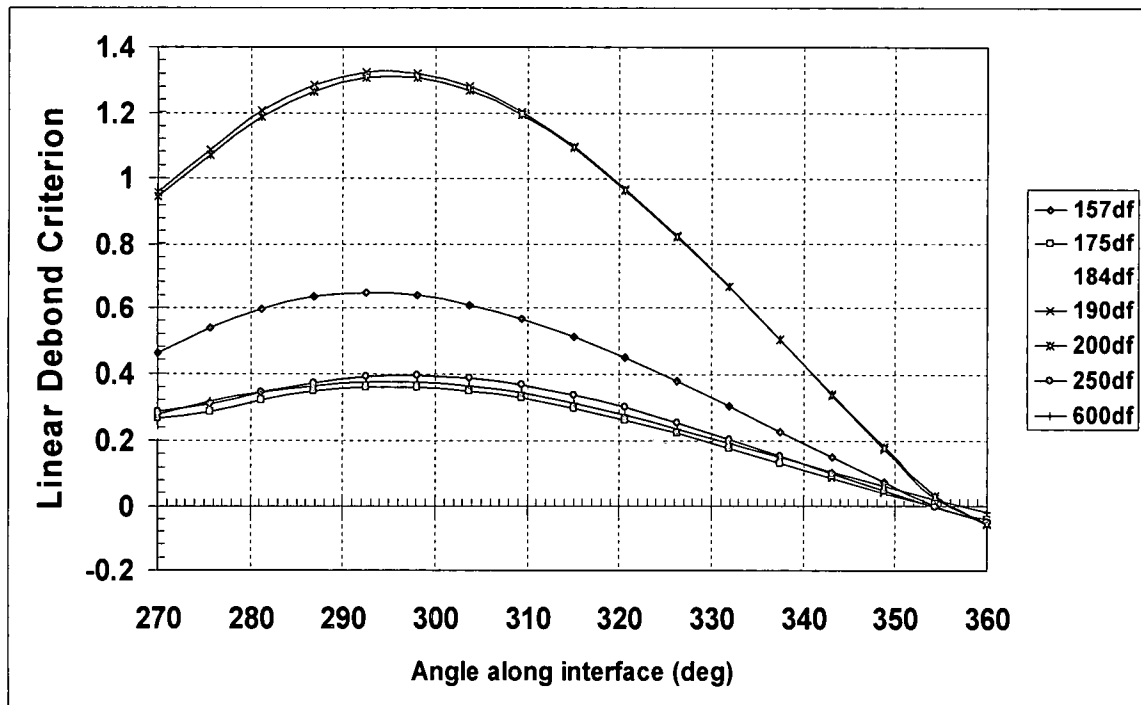


Figure 110: Linear Debond Criterion evaluated at the fiber matrix interface of the corner fiber in the field of view from $\theta = 270^\circ$ to 360° at $Z = 0$ with A and B equal to 1.0

Figure 109 and 110 show only that the SF, $1.9d_f$ and $2.0d_f$ fiber spacing groups should debond when it is observed that the $1.57d_f$, $2.5d_f$ and the $6.0d_f$ also debond. The debond criterion distribution also implies that the SF, $1.9d_f$ and $2.0d_f$ fiber spacing groups would only debond between 38° and 88° in the first quadrant and between 272° and 320° in the fourth quadrant. Clearly the experimental results show that this is not the case. Consequently, the constants A and B need adjusting to meet the characteristics of the actual observed fiber matrix debonds occurring for the $1.57d_f$, $1.9d_f$, $2.0d_f$, $2.5d_f$, $6.0d_f$ and the SF cruciform specimens. Figures 111 and 112 show the linear debond criterion distribution with $A = 11/3$ and $B = 4/3$ along the fiber matrix interface at $Z = 0$ in the 1st quadrant and 4th quadrant respectively. Inspection of Figure 111 and 112 shows that the $1.57d_f$, $1.9d_f$, $2.0d_f$, $2.5d_f$, $6.0d_f$ and the SF cruciform specimens exceed 1.0 indicating that debonds occurred correlating to the experimental observations. The $1.75d_f$ and $1.84d_f$ fiber spacing groups evaluate the linear debond criterion at less than 1.0 in the first quadrant. However, in the fourth quadrant the $1.75d_f$ spacing is at 1.0 but the $1.84d_f$ is clearly

less than 1.0. This correlates to the observed experimental results for the 1.75d_f and 1.84d_f fiber spacing groups as they exhibited matrix cavitation as their first failure mechanism. Figures 111 and 112 also reveal that the compressive stress state along the fiber interface at the fiber equator is adequately reflected by the linear debond criterion as shown by comparing them to Figure 193 and 196.

As indicated above, the location at which the debond criterion distribution exceeds 1.0 should correspond to the experimentally observed debond limits. The soundness of the criterion would then be reflected in the accuracy of the debond limits compared to the experimentally observed limits. Table 39 lists the fiber matrix debond limits determined by the linear debond criterion evaluated from the cruciform FEM results for the corner fiber in the 1st and 4th quadrant as well as the experimental debond limits shown in Table 74. Also listed in Table 39 is the percentage difference between the actual observed debond limit and the predicted debond limit determined by the linear debond criterion.

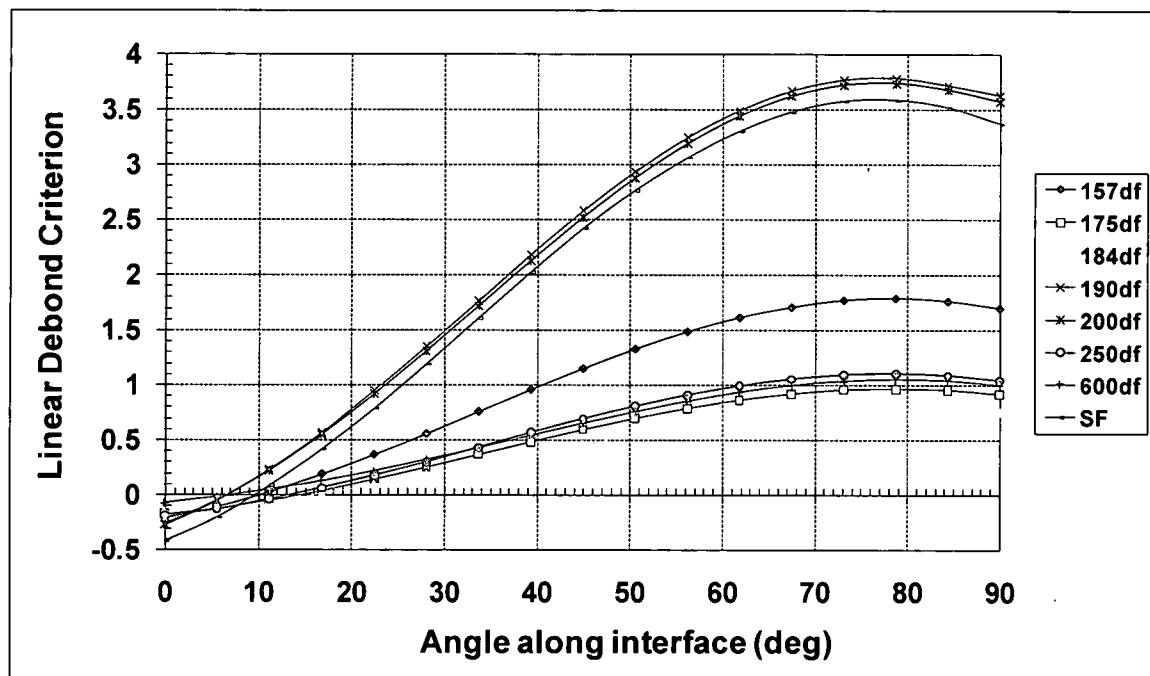


Figure 111: Linear Debond Criterion evaluated at the fiber matrix interface of the corner fiber in the field of view from $\theta = 0^\circ$ to 90° at $Z = 0$ with $A = 11/3$ and $B = 4/3$

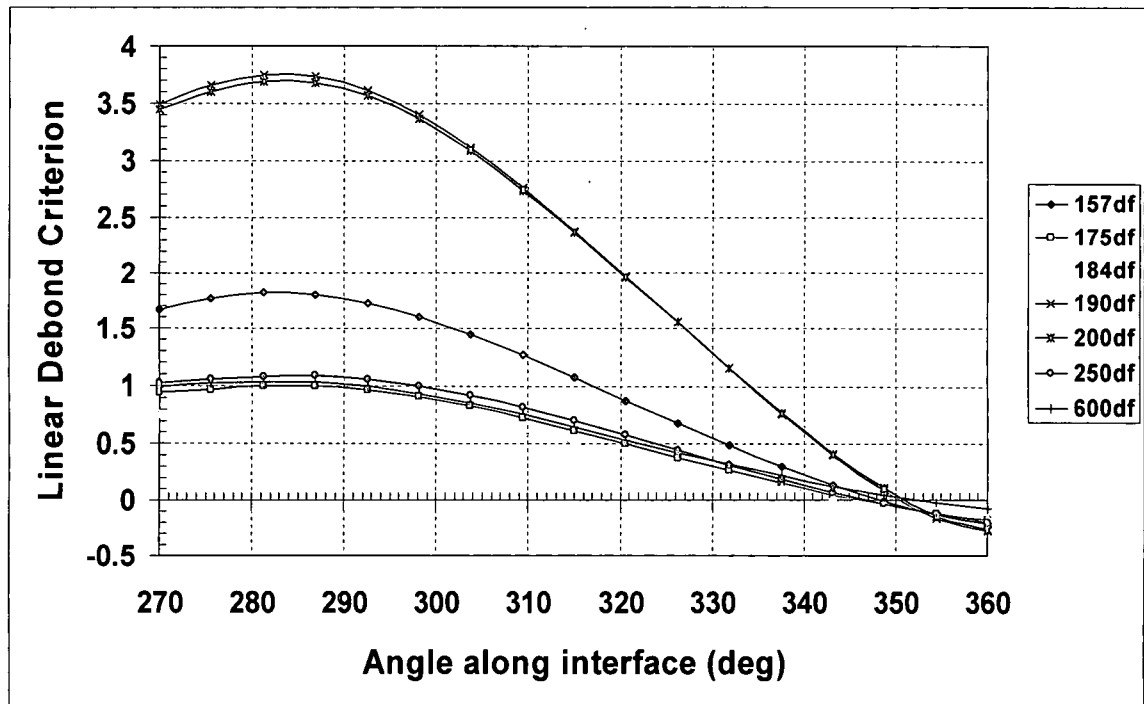


Figure 112: Linear Debond Criterion evaluated at the fiber matrix interface of the corner fiber in the field of view from $\theta = 270^\circ$ to 360° at $Z = 0$ with $A = 11/3$ and $B = 4/3$

Recall that the relative difference is taken as the ratio of the predicted angular measure to the observed angular measure expressed as a percentage; and that the angular measure is the difference in angle along the interface between the respective pole to the debond limit, as shown in Figure 101.

Table 39: Fiber matrix debond limits for the corner fiber 1st and 4th quadrant determined by linear debond criterion evaluated from the cruciform FEM results

Fiber Spacing	Linear Debond Criterion Debond limits		Experimental Debond limits		%Δ	
	1 st Quad	4 th Quad	1 st Quad	4 th Quad	1 st Quad	4 th Quad
1.57d _f	42°	314°	44.5°	315.5°	7.7	3.3
1.9d _f	24°	334°	32°	328°	15.5	10.3
2.0d _f	24°	334°	35°	325°	20	16.4
2.5d _f	65°	295°	66.5°	293.5°	10.6	6.4
6.0d _f	68°	292°	66°	294°	8.3	8.3
SF	26°	-	37°	-	20.8	-

From Table 39 the linear debond criterion is fairly accurate predicting the debond limits for the 1.57d_f and 6.0d_f fiber spacing groups in both the 1st and 4th quadrants of the corner fiber as evidenced by the low %Δ. The linear debond criterion over predicts the 1.57d_f spacing debond limit while under predicting the 6.0d_f spacing in the 1st quadrant. It under predicts the debond limits for both fiber spacing groups in the 4th quadrant. For the 1.9d_f, 2.0d_f, 2.5d_f and SF groups the linear debond criterion has moderate success predicting the debond limits as shown in Table 39. It is consistently over predicting the debond limits for the aforementioned fiber spacing groups in the 1st and 4th quadrant.

Quadratic vs. Linear Debond Criterion Evaluation. It appears that the Quadratic Debond Criterion is accurately predicting the debond limits for the 1.9d_f, 2.0d_f and SF cruciform specimens while the Linear Debond Criterion accurately predicts the debond limits for the 1.57d_f, 2.5d_f and 6.0d_f fiber spacing groups. To down select to the best fiber matrix debond criterion further evaluation is required. Since the corner fiber is completely visible in the field of view and the debond initiation locations along the fiber length can be readily measured, comparison of the debond limits in the northern hemisphere in the 1st quadrant of the corner fiber is listed in Table 40. The debond criterion distribution along the interface in the first quadrant of the corner fiber are shown in Figure 107 for the Quadratic Criterion and in Figure 111 for the Linear Criterion.

Table 40: Comparison of the fiber matrix debond limits predicted by the Quadratic and Linear Debond Criterion for the 1st quadrant of the corner fiber at the location of the debonds along the fiber

Fiber Spacing	Exp db Limits (deg)	Quadratic db Criterion limits (deg)	%Δ	Linear db Criterion limits (deg)	%Δ
1.57d _f	44.5	52	16.5	42	5.5
1.9d _f	32	32	0	24	13.9
2.0d _f	35	32	5.5	24	20
2.5d _f	66.5	81	38.3	65	6.4
6.0d _f	66	82	33.3	68	8.3
SF	37	33	7.5	26	20.8

The Linear Debond Criterion appears to predict the debond limits of the $6.0d_f$, $2.5d_f$ and $1.57d_f$ fiber spacing groups fairly well in the 1st quadrant of the corner fiber. Likewise, the Quadratic Debond Criterion predicts the SF, $2.0d_f$ and $1.9d_f$ fiber spacing groups fairly accurately. The bold italicized numbers in Table 40 delineate the lowest $\% \Delta$ values between the two debond criteria. Further scrutiny of Table 40 reveals a more consistent prediction for the Linear Criterion than the Quadratic Criterion in that the $\% \Delta$ for the fiber spacing groups that the Linear Criterion does not predict well is lower than for those fiber spacing groups that the Quadratic Criterion does not predict accurately. Furthermore, the Linear Criterion is more conservative for all fiber spacing groups except the $6.0d_f$ fiber spacing where it is fairly accurate in its prediction of the debond limits. For both criteria the $1.75d_f$ and $1.84d_f$ fiber spacing groups, whose first failure mechanism is matrix cavitation, are below 1.0.

The Quadratic and Linear Debond Criterion comparison for the 4th quadrant of the corner fiber at the location of debonds initiation along the fiber is listed in Table 41. The criterion distributions along the fiber interface for the Quadratic Debond Criterion is shown in Figure 108 and for the Linear Debond Criterion in Figure 112.

Table 41: Comparison of the fiber matrix debond limits predicted by the Quadratic and Linear Debond Criterion for the 4th quadrant of the corner fiber

Fiber Spacing	Exp db Limits (deg)	Quadratic db Criterion limits (deg)	$\% \Delta$	Linear db Criterion limits (deg)	$\% \Delta$
$1.57d_f$	315.5	306	20.9	316	1.1
$1.9d_f$	328	326	3.4	334	10.3
$2.0d_f$	325	326	1.8	334	16.4
$2.5d_f$	293.5	281	46.8	295	6.4
$6.0d_f$	294	275	79.8	290	16.7

It should be noted that due to the symmetry of the cruciform geometry that the single fiber south pole fiber matrix debond translate to the north pole for the FEA and thus are not part of this data set. Just like for the 1st quadrant of the corner fiber, the Quadratic Debond Criterion predicts the $1.9d_f$ and $2.0d_f$ fiber spacing groups more accurately than the Linear Debond Criterion in the 4th quadrant. Likewise, the Linear Debond Criterion predicts the debond limits

more accurately for the $6.0d_f$, $2.5d_f$ and the $1.57d_f$ fiber spacing than does the Quadratic Debond Criterion. The $1.75d_f$ and $1.84d_f$ fiber spacing groups have the lowest debond criteria evaluation along the fiber matrix interface just like in the 1st quadrant, although the $1.75d_f$ spacing does exceeds 1.0 by a mere 0.09% in the 4th quadrant. Again, the Linear Debond Criterion exhibits more consistency than the Quadratic Debond Criterion having lower percentages differences for the fiber spacing groups where the Quadratic Debond Criterion is more accurate.

Both the quadratic and linear debond criterion are thoroughly investigated and discussed in Appendix E for the 2nd and 3rd quadrants of the corner fiber as well as the center fiber. The criteria interfacial stress plots were used to measure their performance against the observed debond limits. A summary of all debond criterion evaluation results discussed above and in Appendix E follows.

Fiber-Matrix Debond Initiation Criterion – Summary. From the criterion evaluation previously discussed and that presented in Appendix E; the Quadratic Debond Criterion predicts the experimental debond limit more accurately for the $1.9d_f$ spacing in all 4 quadrants and the $2.0d_f$ fiber spacing in 3 of the 4 quadrants than did the Linear Debond Criterion. The $1.57d_f$ fiber spacing is better predicted by the Quadratic Debond Criterion in the 2nd and 3rd quadrants while the Linear Debond Criterion predicts it more accurately in the 1st and 4th quadrants. For both the $2.5d_f$ and $6.0d_f$ fiber spacing groups, the Linear Debond Criterion predicted the experimental debond limits much more accurately than the Quadratic Debond Criterion in all 4 quadrants. Lastly, the single fiber group debond limit is better represent by the Quadratic Debond Criterion than the Linear Criterion.

To summarize, the Quadratic Debond Criterion predicted the debonds for the majority of the fiber spacing groups, 3 out of 5, in the 2nd quadrant more accurately than the Linear Criterion. Both criteria predicted three fiber spacing groups more accurately than the other in the 1st quadrant. The Linear Debond Criterion, however, predicted the majority of fiber spacing groups with the greatest accuracy in both the 3rd and 4th quadrant. From a strictly scorecard perspective,

the Linear Debond Criterion out-performed the Quadratic Debond Criterion in quadrants 3 and 4, while the converse occurred in quadrant 2 and they tied in quadrant 1.

The Linear Debond Criterion, however, showed a more consistent prediction in that the percentage difference between the predicted debond limit and the experimental debond limit were smaller for the fiber spacing groups that were not predicted more accurately than the Quadratic Debond Criterion. For example, the relative difference between the Linear Criterion and the experimental debond limit in the 3rd quadrant for the 1.57d_f fiber spacing is 18.7% when the 1.57d_f fiber spacing is best predicted by the Quadratic Criterion. Whereas, the percentage difference between the Quadratic Criterion and the experimental debond limit in the 3rd quadrant for the 6.0d_f fiber spacing is 54.2% when the 6.0d_f fiber spacing is more accurately predicted by the Linear Criterion. The relative difference is much lower for the Linear Debond Criterion in the majority of all cases in all 4 quadrants. More importantly, the Linear Criterion relative differences for the fiber spacing groups that it did not more accurately predict than the Quadratic Criterion in both the 1st and 4th quadrant at the debond locations along the fiber are smaller than those when the Quadratic Criterion did not more accurately predict the debond limits, see Table 40 and 41 in Appendix E. Moreover, for the majority of the fiber spacing groups the Linear Debond Criterion over predicts the debond limits, meaning that the debond limit is greater than that observed from the cruciform experiments thus providing a conservative response. Lastly, the linear debond criterion more accurately reflects the compressive stresses at the fiber equator.

Therefore, based on the previous discussion and that presented in Appendix E the Linear Debond Criterion shown in equation (3) best describes the 828/D-230 fiber matrix debond failure initiation.

$$\frac{11}{3} \left(\frac{\sigma_r}{\sigma_{yt}} \right) + \frac{4}{3} \left(\frac{\tau_{r\theta}}{\tau_y} \right) \geq 1 \quad (3)$$

where σ_r and $\tau_{r\theta}$ are the interfacial radial and shear stress, respectively, determined from the cruciform FEA and σ_{yt} and τ_y are the tensile and shear strengths respectively, determined from the neat resin test results.

A true test of any failure criterion is when data from independent tests can be used in the criterion to predict the failure with a high degree of accuracy, as will be shown in the Matrix Failure Initiation Criterion following. However, other test methods available and used in previous work for understanding the physical basis of the fiber-matrix debonding mechanism, as described in Chapter 2, are fraught with effects from the specimen geometry that may mask the true failure mechanism. Since the data from another test method is not available in the literature, an independent evaluation cannot be done. However, it should be noted in the absence of shear stresses, as the radial stress increases to that of the tensile yield stress, the ratio, (σ_r/σ_{yt}) , becomes 1.0 and thus the criterion is satisfied. Likewise, in the absence of any radial stresses, as the shear stresses approach the shear yield stress the ratio, $(\tau_{r\theta}/\tau_y)$, becomes 1.0 and again the criterion is satisfied.

Residual Stress Impact to Fiber-Matrix Debond Initiation Criterion. Although the 828/D-230 matrix is a room temperature cured two part epoxy system, the effects of the cure shrinkage stress shown in Appendix D can be large. Table 68 on page 377 in Appendix D lists the reduction of the radial stress due to the mechanical load from the matrix cure shrinkage for the center fiber. From the table, the matrix cure shrinkage reduced the radial stress by an amount between 5% and 55% depending upon fiber spacing at the location of maximum mechanical radial stress. Similarly, the shear stress due to mechanical load at its maximum location has been reduced by an amount between 1.7% and 14.7%, depending on fiber spacing, by the matrix cure as depicted in Table 69 on page 381 in Appendix D. The radial stress due to the cure shrinkage had greater impacts where the fibers were closest together for each fiber spacing group, see Figure 188 page 374 in Appendix D, except at the 6.0d_f spacing. However, at these locations the mechanical radial stress was much lower. For the shear stress, the largest impacts due to the cure shrinkage

occurred approximately at $\theta = 28^\circ$ and again at $\theta = 62^\circ$ to 68° , see Figure 191 page 379 Appendix D. Like the radial stress, the shear stress due to the applied load was much lower at these locations. The resulting behavior of both the radial and shear stress due to the matrix cure caused the highest resulting stress to act over a larger length of the interface.

For the corner fiber the matrix cure shrinkage reduced the radial stress due to mechanical loading as shown in Tables 70 and 71 on page 393 in Appendix D. The impacts range from 4% to 21% at the location of maximum radial stress due to applied load, depending on fiber spacing, in the 1st, 2nd and 4th quadrants of the fiber. In the 3rd quadrant the impact ranged from 4% to 16% at the location of maximum radial stress due to the applied load depending on fiber spacing. In a similar fashion, the matrix cure reduced the shear stress by an amount between 0.4% and 2.8% in the 1st, 2nd and 4th quadrants at the location of maximum shear due to applied load, as shown in Table 72 on page 401 of Appendix D. In the 3rd quadrant it reduced the mechanical load shear by an amount between 0.4% and 6.4%. Similar to the center fiber, the corner fiber radial and shear stress due to the matrix cure had higher magnitudes at locations along the interface other than in the direction of the applied mechanical load (see Figures 197 – 200 pages 387 and 388 for the radial stress distributions and Figures 209 – 212 pages 399 and 400 for the shear stress distribution in Appendix D). The effects of the maximum radial and shear stress due to the matrix cure shrinkage resulted in a longer length of fiber-interface subjected to the highest radial and shear stress magnitudes.

The resulting impact due to the matrix cure shrinkage on the fiber-matrix debonding criterion in the field of view for the corner fiber 1st and 4th quadrant is shown in Figure 113 and 114. Quite evident is the fact that the criterion no longer accurately predicts the fiber spacing groups that exhibit fiber-matrix debonding as their failure initiation mechanism. The $1.75d_f$ spacing exceeds 1.0 while the $1.84d_f$ spacing is practically 1.0. Recall that the criterion predicts a fiber-matrix debond when equation (3) is evaluated greater than 1.0. Another indication of the impact of the residual stresses are the debond limits being much greater than those experimentally measured. The experimentally measured debond initiation limits should correspond to where the individual criterion distributions cross 1.0. For example, Figure 113 and

114 show a debond limit of the 1.57d_f fiber spacing group to be approximately 35° in the 1st quadrant and 319° in the 4th quadrant. The experimentally measured fiber-matrix debond initiation limit for the 1.57d_f spacing was 44.5° in the 1st quadrant and 315.5° in the 4th quadrant. When the matrix cure residual stresses were properly accounted for in the analysis the criterion evaluated the limits at 41° in the 1st quadrant and 314° in the 4th quadrant. The difference between the debond initiation limits when the matrix residual stresses are not accounted for are 9.5° in the 1st quadrant and 3.5° in the 4th quadrant. This equates to a 21.3% and 1.1% relative difference in the 1st and 4th quadrants respectively. When the matrix residual stresses are accounted for correctly in the analysis determining the internal stresses, the differences are 3.5° or 7.9% relative difference and 1.5° or 0.5% relative difference in the 1st and 4th quadrants respectively. These values are shown in Table 88 page 479 in Appendix E. The improvement in accuracy of the debond criterion when the residual stresses are included in the analysis is over twice when the residual stresses are not included in the analysis. Consequently, the linear debond criterion performs with greater accuracy when the matrix cure residual stresses are properly incorporated into the analysis.

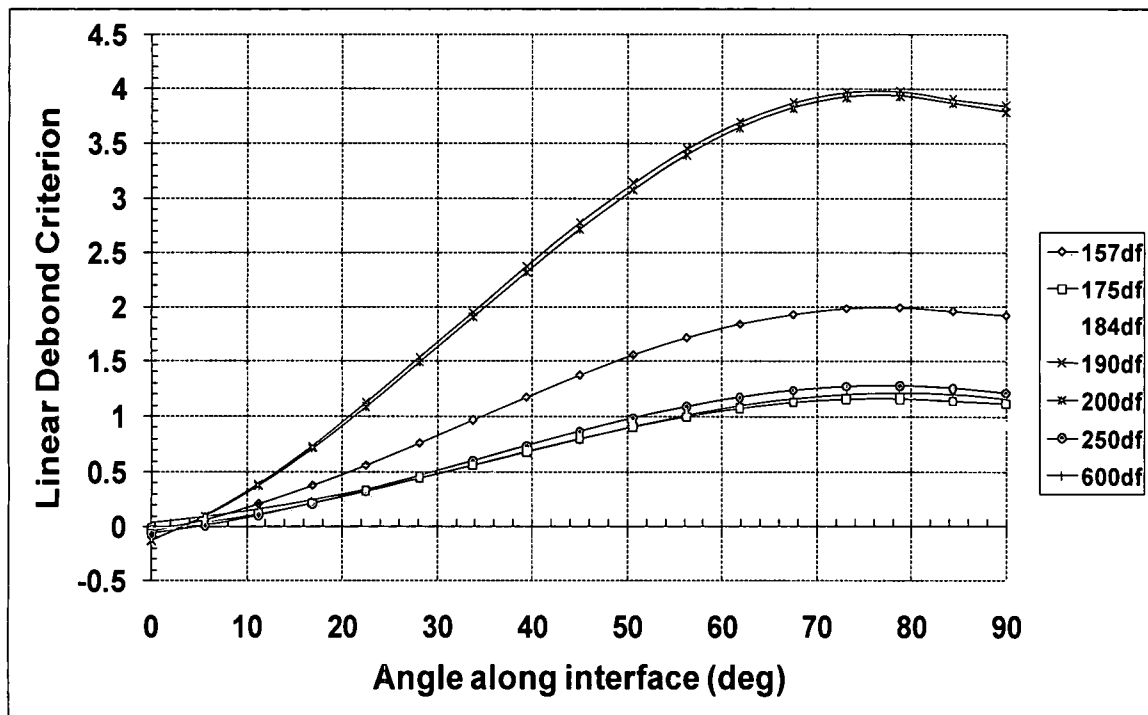


Figure 113: Effects of the matrix cure shrinkage residual stress on the Linear Debond Criterion in the 1st quadrant of the corner fiber

The 2nd and 3rd quadrants of the corner fiber show the same trends as the 1st and 4th quadrant. The 1.75d_f fiber spacing exceeded 1.0 and the 1.84d_f fiber spacing was evaluated at practically 1.0 when the linear debond criterion was evaluated in both quadrants. For the rest of the fiber spacing groups the debond limits were greater, by a substantial amount, than those experimentally measured.

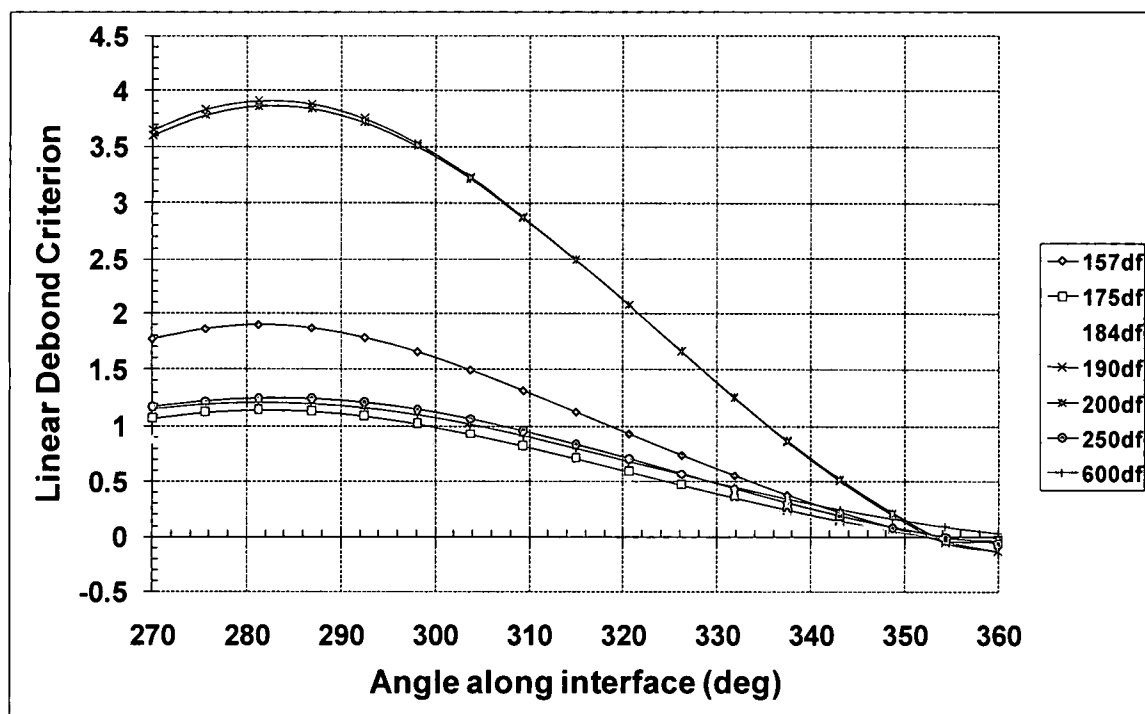


Figure 114: Effects of the matrix cure shrinkage residual stress on the Linear Debond Criterion in the 4th quadrant of the corner fiber

Matrix Failure Initiation Criterion

As previously discussed in Chapter 3, the literature indicates six matrix failure criteria that could possibly describe the initiation of failure within the matrix of the cruciform specimen. From the experimental results, only the 1.75d_f and 1.84d_f fiber spacing groups exhibited matrix failure as their first failure mechanism. The matrix failure initiation is manifested as matrix cavitation. Matrix cavitation is defined as the formation of small voids within the matrix volume away from the fiber matrix interface. The voids form as a result of the tri-axial state of tensile stress within the matrix material from the constraints due to the stiff fibers when the applied load is normal to the direction of the fibers. In the fiber spacing groups that exhibited matrix cavitation, all specimens in the 1.75d_f and 1.84d_f group formed multiple cavitations within the specimen as the applied load grew in magnitude. In all cases a fiber matrix debond also resulted as load continued to increase in magnitude after the formation of matrix cavitations. The cavitations appear the majority of the

time as white or light gray spots or in some instances very small white or light gray cracks. In few instances they appear as fairly dark gray spots. The spots can take a multitude of shapes ranging from smooth circular to jagged multifaceted polygons to thin lines. The key to the cavitations is that once formed they remain as loading increases. As illustrated in Chapter 2, the cavitations seem to form independent of one another and can grow in size as multiple cavitations form in very close proximity to each other. Fracture surface analyses of these two fiber spacing groups show cavitation features that indicate a shear force presence. As discussed in Chapter 3, the matrix cavitated under a large principal stress bias that created the cavitation features and thus placed the material under a shear stress.

Cavitation is a precursor to polymer crazing. The tensile tri-axial stress state creates voids causing a volume dilatation thus lowering the critical failure stress. Due to the large principal stress bias placing the material under the state of shear stress as indicated from the fracture surface analysis; only two failure criteria discussed in Chapter 3 would appropriately describe the physics causing the matrix cavitation, the Modified Tresca and the Mohr-Coulomb criteria. For the analytical evaluation of the matrix failure results discussed in Chapter 3, only the EM and UEM sub-regions were presented for the sake of efficiency. See Figure 89 for a picture of the EM and UEM volumes of the cruciform FEM.

The Modified-Tresca Criterion evaluated in Chapter 3 for the EM and UEM regions of the cruciform specimen FEM is repeated in equation (4).

$$\tau_s = \tau_s^0 - \mu \sigma_{on} \quad (4)$$

Using the shear yield stress, τ_y as determined by the torsion experiments as τ_s^0 and the octahedral normal stress determined by the FEA, the Modified-Tresca Criterion is evaluated in the EM and UEM region of the cruciform specimen.

The Mohr-Coulomb Criterion, also evaluated in Chapter 3 for the EM and UEM regions of the cruciform specimen FEM, is repeated in equation (5).

$$\tau_{oct} = \tau_o - \mu \sigma_{on} \quad (5)$$

For the Mohr-Coulomb, τ_o is the octahedral shear stress of the neat resin absent from any tri-axial stresses acting on the material and σ_{on} is the mean normal stress determined by the FEA. τ_o is calculated from the neat resin torsion experiments.

Results of independent neat resin tensile, compression and shear tests will be used to evaluate both criteria to see which one better describes the stress state at failure or at the onset of yielding. The Modified-Tresca predicts the critical shear stress, τ_s^0 , while the Mohr-Coulomb predicts the octahedral shear stress, τ_o .

From the tensile tests, $\sigma_1 = \sigma_{yt}$ is the applied stress where $\sigma_2 = \sigma_3 = 0$, the critical shear stress for the Modified-Tresca Criterion is

$$\tau_s = \frac{\sigma_{yt}}{2} \quad (6)$$

Likewise, for the Mohr-Coulomb the tensile test results in an octahedral shear stress given by

$$\tau_{oct} = \frac{1}{3} \left[(\sigma_1)^2 + (-\sigma_1)^2 \right]^{\frac{1}{2}} \quad (7)$$

From the torsion tests, $\sigma_1 = \tau_y$, $\sigma_2 = -\tau_y$ and $\sigma_3 = 0$ thus, the critical shear stress for the Modified-Tresca Criterion is

$$\tau_s = \tau_y \quad (8)$$

whereas, the torsion tests result in an octahedral shear stress for the Mohr-Coulomb Criterion of

$$\tau_{oct} = \frac{1}{3} \left[(\tau_y + \tau_y)^2 + (-\tau_y)^2 + (-\tau_y)^2 \right]^{\frac{1}{2}} \quad (9)$$

Lastly, from the compression tests $\sigma_1 = \sigma_3 = 0$ and $\sigma_2 = -\sigma_{yc}$ the Modified-Tresca critical shear stress is

$$\tau_s = \frac{1}{2} (\sigma_{yc}) \quad (10)$$

whereas, the octahedral shear stress for the Mohr-Coulomb Criterion becomes

$$\tau_{oct} = \frac{1}{3} \left[(\sigma_2)^2 + (-\sigma_2)^2 \right]^{\frac{1}{2}} \quad (11)$$

Table 42 compares the predicted critical shear values using the Modified-Tresca Criterion and the predicted octahedral shear values using the Mohr-Coulomb Criterion to the respective shear stresses obtained from the neat resin tests using equations (6) – (11).

Table 42: Criteria comparison using neat resin tests

	Mod-Tresca (MPa)	τ_s (MPa)	Δ	%Δ	Mohr-Coulomb (MPa)	τ_{oct} (MPa)	Δ	%Δ
Tensile	39.83	30.85	9.25	23.2	33.25	29.08	4.17	12.5
Shear	45.61	45.61	0	0	37.24	37.24	0	0
Compression	54.04	45.04	9.01	16.7	43.07	42.46	0.61	1.4

Both criteria predicted greater values than those calculated using data from the neat resin tests and equations (6) – (11). From Table 42 the Mohr-Coulomb Criterion predicts both the tensile and compression neat resin test results better than the Modified-Tresca Criterion. Since both criteria are based upon a shear failure of the material it is no surprise that both predicted their respective shear stresses dead on. The actual difference between the predicted octahedral shear stress of the Mohr-Coulomb Criterion and that calculated using the tensile tests and equation (7) is less than the standard deviation for the neat resin tensile tests results. From Appendix A the uniaxial compression failure of the neat resin actually fails in shear as an "X" pattern was observed developing on the specimen's side during the compression tests. The "X" pattern is the typical conical shape indicative of a shear failure [2]. The Mohr-Coulomb criterion predicted the octahedral shear more accurately using compression test data and equation (11) than the Modified Tresca criterion predicting the maximum shear using equation (10) and compression test data. The difference between the predicted octahedral shear stress using the Mohr-Coulomb criterion and that calculated using compression test data and equation (11) is less than the standard deviation for the neat resin compression tests. Therefore, because the Mohr-Coulomb Criterion predicted the octahedral shear stress better than the Modified Tresca criterion predicted the maximum shear stress using the neat resin data the Mohr-Coulomb criterion will be considered for further evaluation.

Matrix Failure Initiation Criterion Evaluation in the Field of View. Evaluating the Mohr-Coulomb criterion, expressed in equation (5) above, at these two fiber spacing groups involved extracting stills from the videotaped experiments and layering the images, on top of one another in chronological order, to detect any changes in the images due to the applied loading. Once the first failure is determined the location is measured relative to the center of the specimen or the north or south pole of the nearest corner fiber. The high magnification camera is always centered with respect to the cruciform specimen loading arm width and center fiber as shown in Figure 99, thus the location of the cavitation can be determined fairly accurately. However, since the observations are through highly polished polymers distortion will occur effecting the measurements in determining the location of the cavitation relative to the centerline of the center fiber or the north or south pole of the corner fiber. Since the cruciform specimen is symmetrical about its horizontal and vertical centerline, the location of the observed cavitation is translated into the appropriate FEM position. Knowing the coordinates of the cavitation site, the FEM model can be interrogated to find the maximum magnitude of the matrix failure criteria occurring at that location. Since the depth of the first cavitation site cannot be determined with sufficient accuracy due to the fact that each specimen was tested to failure, all FEM matrix sub-regions along the horizontal dimension are investigated. The nodal solution to the FEA is extracted from the FEM results and input into a spreadsheet. Each node is identified by its Cartesian coordinates and the nodal results closest to the cavitation site are tabulated. In the case where the cavitation site is a significant distance from any nodes the result is interpolated between the appropriate nodes. Table 43 lists the maximum Mohr-Coulomb Criterion value for each specimen exhibiting matrix cavitation and the corresponding FEM location of the maximum value.

Table 43: Cavitation locations for 1.75d_f and 1.84d_f fiber spacing groups and average apparent critical Mohr-Coulomb Criterion value

Specimen	Max-Mohr-Coulomb Criterion (MPa)	FEM Location	Y (mm)	Z (mm)
175R1C1-A	36.04	UBTF	0.62	0.46
175R1C1-B	36.29	UEM	0.53	0.69
175R1C1-C	36.30	EM	0.135	0.81
175R1C1-D	36.15	UM	1.28	1.04
175R1C1-E	36.29	UEM	0.53	0.69
175R1C1-F	36.11	UM	1.08	1.0
175R1C1-G	36.26	UEM	0.54	0
AVG		36.21		
Std-dev		0.10		
184R1C1-E	36.46	CNB (0.1978)	0	0
184R1C1-F	36.39	UEM	0.57	0.23
184R1C1-G	36.37	UEM	0.52	0
AVG		36.41		
Std-dev		0.04		
Total AVG		36.27		
Std-dev		0.12		

From Table 43 it appears that the majority of cavitation that is within view occurs in the upper exterior regions of the specimen. The majority of specimens seem to cavitate in the UEM region of the specimen which is in front of the northern hemisphere of the top corner fiber. See Figure 89 for locations of the FEM regions. The percent difference between the average value of the Mohr-Coulomb Criterion evaluated for the 1.75d_f and 1.84d_f fiber spacing groups is 0.4% indicating that very little variation between the two fiber spacing groups exhibiting cavitation. This gives confidence that the total average of the Mohr-Coulomb Criterion for all specimens exhibiting matrix cavitation appears to be the criterion's critical value. However, before establishing this value as the critical value for matrix cavitation a thorough evaluation of the FEM results needs to be done since there are areas not visible that may influence the critical value.

As discussed in Chapter 3 neighboring regions of the FEM are combined when illustrating the analytical results. Since Table 43 indicates that the majority of cavitation occurs in the UEM region of the specimen but also one specimen initiates cavitation in the EM region, these two regions will be combined when presenting the analytical results. Figure 115 shows the Mohr-Coulomb Criterion distribution in the YZ plane of the EM and UEM region of the specimen. Also shown in the distribution is a plane at the magnitude of the critical value and the black

vertical lines are the cavitation sites within the EM and UEM regions of the matrix as listed in Table 43.

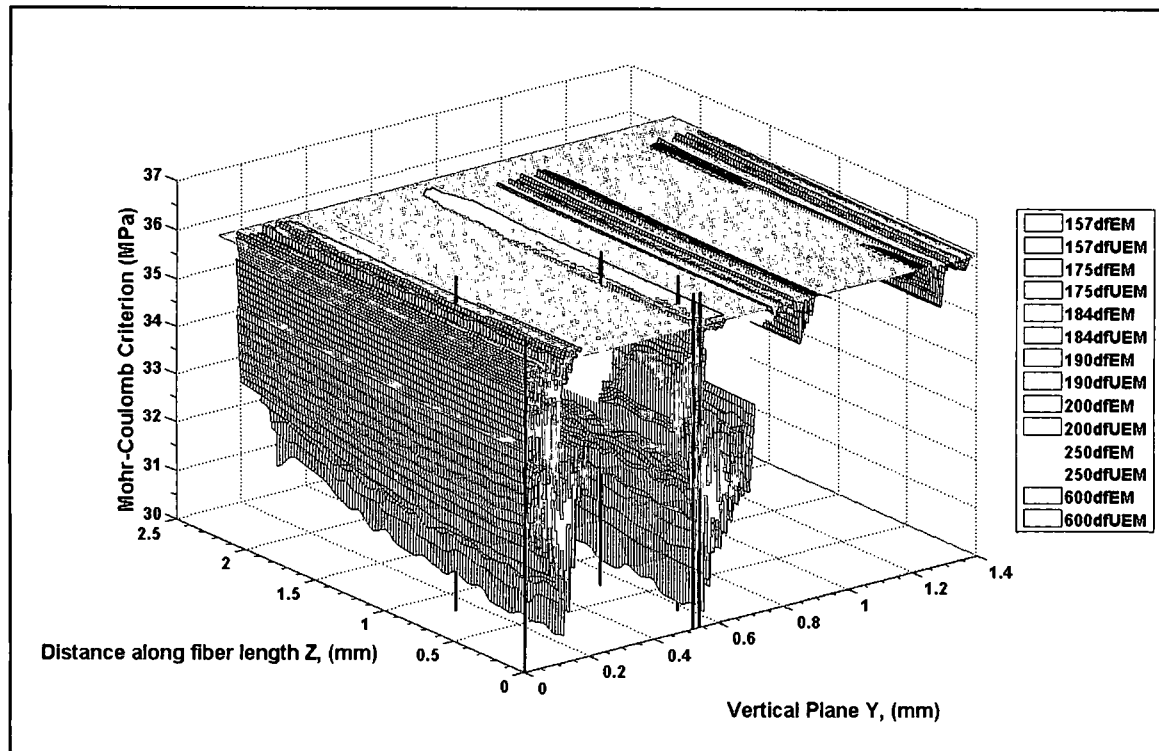


Figure 115: Mohr-Coulomb Criterion distribution in the YZ plane of the EM and UEM regions of the FEM

The Mohr-Coulomb distribution reveals that the $1.75d_f$, $1.84d_f$, $2.5d_f$ and the $6.0d_f$ fiber spacing groups exceed the apparent critical value, but only the former two groups' show cavitation as their first failure, the latter two exhibit fiber matrix debonding. Recall that the analytical results are the internal stresses occurring in the cruciform specimen at first failure. The $6.0d_f$ fiber spacing far-field stress at failure initiation is 10.7 MPa, and 6.58 MPa is the far-field stress at first failure for the $2.5d_f$ spacing. However, the $1.75d_f$ and $1.84d_f$ fiber spacing groups failed at 4.67 MPa and 3.97 MPa respectively; a considerably lower far-field stress than the $2.5d_f$ and $6.0d_f$ fiber spacing groups. Further scrutiny of Figure 115 particularly along the direction of loading, Y, at the center of the specimen, $Z = 0$, results in the Mohr-Coulomb Criterion plot shown

in Figure 116. Also shown in Figure 116 is the apparent critical value of the Mohr-Coulomb Criterion. This clearly shows that the criterion evaluated at the $1.75d_f$ and $1.84d_f$ fiber spacing groups has a larger magnitude than the $2.5d_f$ and $6.0d_f$ even though all four specimen groups have greater magnitudes than the apparent critical value as depicted in Figure 115. Closer inspection of Figure 116 reveals that the $2.5d_f$ fiber spacing does not exceed the apparent critical value at the center of the specimen. Figure 116 also confirms the vertical location of the Mohr-Coulomb values greater than the critical value. Referring to Figure 88 and Table 33, the $1.75d_f$ and $1.84d_f$ groups' the activity is located directly in front of the center fiber to about the 315° position of the corner fiber in the EM region and from above the north pole of the corner fiber band to the upper limit of the UEM region. For the $6.0d_f$ spacing its evaluated criterion maximum magnitudes occur from just below the south pole of the matrix band around the corner fiber to just in line with the south pole of the corner fiber in the EM region. The evaluated criterion maximum magnitudes continue from just below the north pole of the corner fiber for about 0.18 mm in the direction of the applied load.

Normal to the direction of applied load is the specimen thickness. Figure 117 shows the Mohr-Coulomb Criterion plotted in the XZ plane or along the specimen thickness at $Z = 0$. Similar to the results shown in Figure 116, the $1.75d_f$ and $1.84d_f$ have higher magnitudes than the $6.0d_f$ fiber spacing group even though all three exceed the apparent critical value. Figure 117 further pinpoints the location of the apparent critical criterion values at being from the outer matrix band at the corner fiber equator to just short of the specimen free edge for all three of the fiber spacing groups.

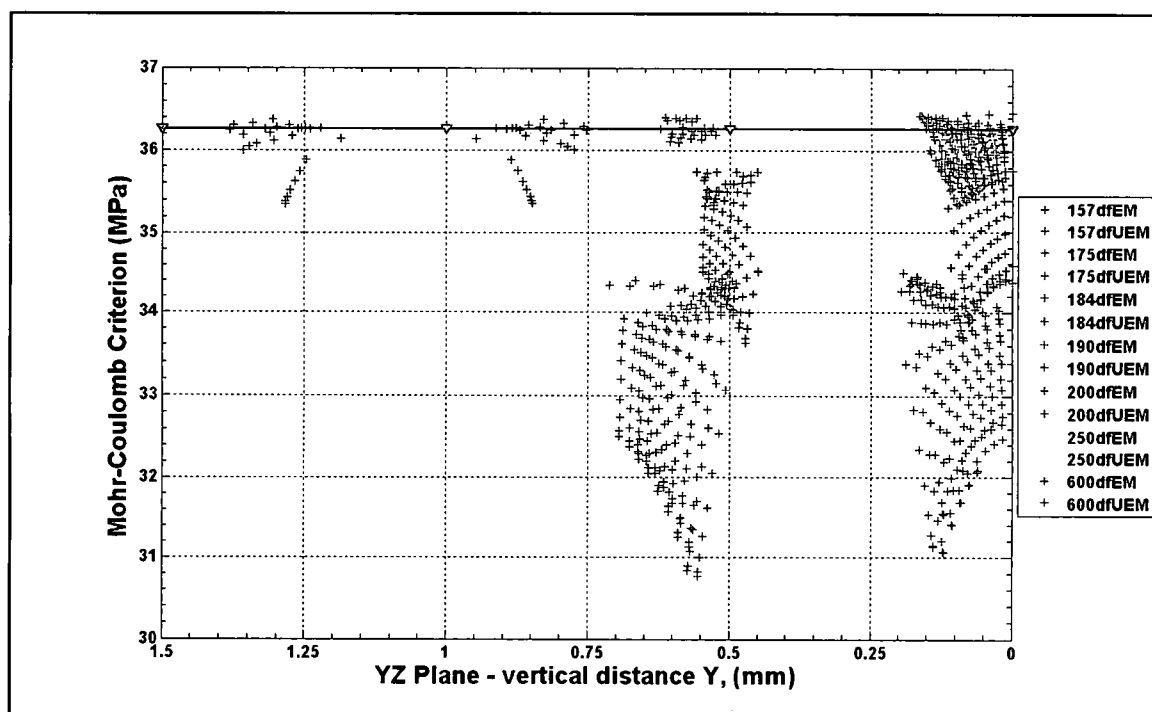


Figure 116: Mohr-Coulomb Criterion plot in the YZ plane along the vertical direction, Y, at Z=0 in the EM and UEM regions of the FEM.

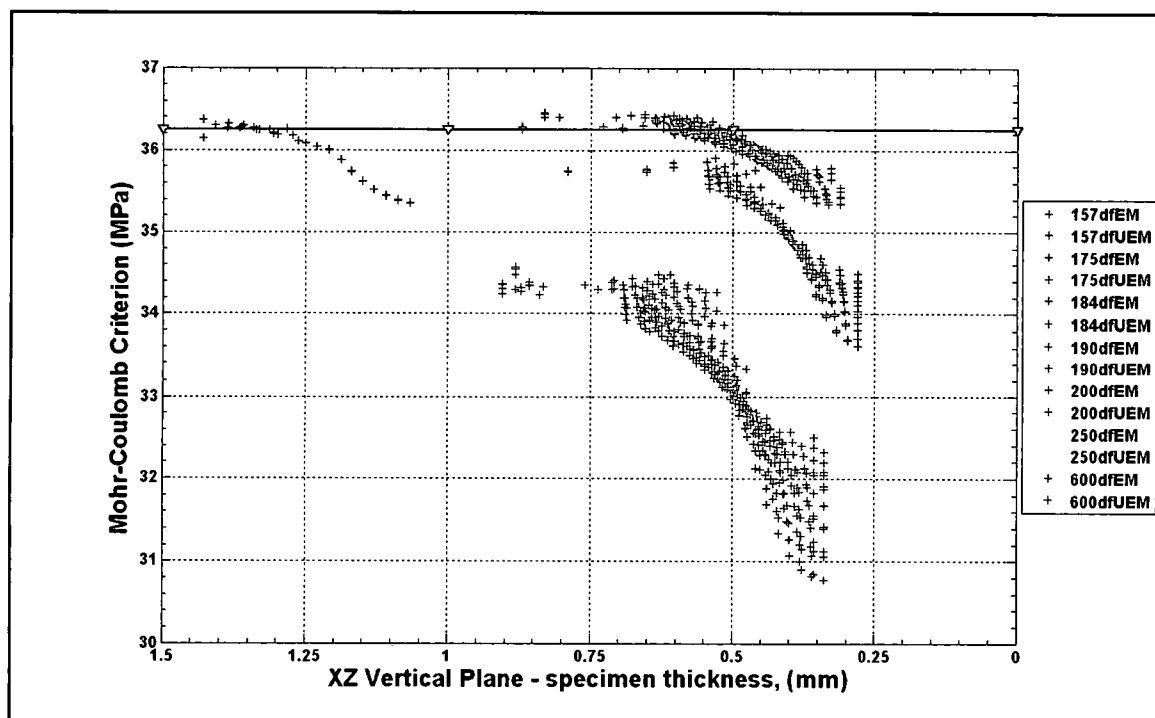


Figure 117: Mohr-Coulomb Criterion plot in the XZ plane along the specimen thickness, X, at Z=0 in the EM and UEM regions of the FEM.

The next region from Table 43 experiencing matrix cavitation is the UM region. Figure 118 is the Mohr-Coulomb Criterion distribution in the YZ plane of the UM region of the FEM. Also plotted is the apparent critical value plane of the Mohr-Coulomb Criterion and the cavitation locations of the UM region listed in Table 43 by the black vertical lines. Figure 118 reveals that the $1.84d_f$ fiber spacing group exceeds the apparent critical value of the criterion over a fairly large area in the UM region.

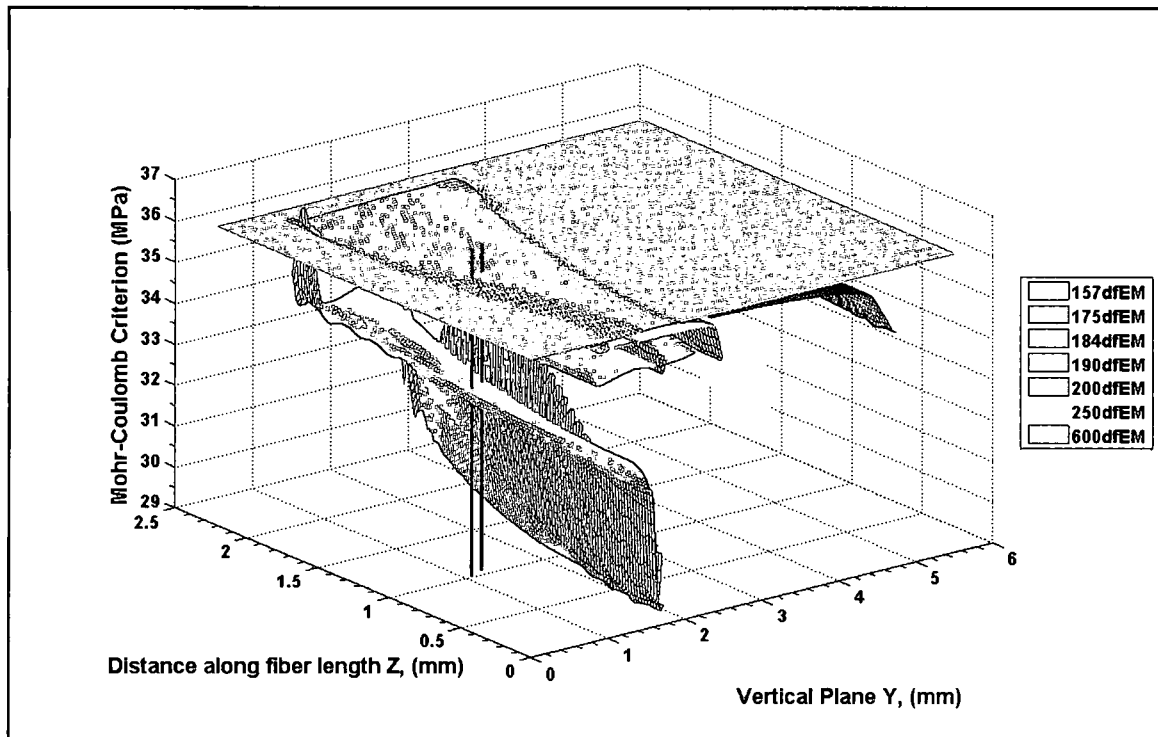


Figure 118: Mohr-Coulomb Criterion distribution in the YZ plane of the UM region of the FEM

The $1.75d_f$ fiber spacing group is just barely below the apparent failure criteria critical value plane. Also exceeding the apparent critical value are the $2.5d_f$ and $6.0d_f$ fiber spacing groups in very small isolated area of the region. Further scrutinizing the results shown in Figure 118 are the results shown in Figure 119 where the Mohr-Coulomb Criterion is plotted in the YZ plane along the vertical direction at $Z = 0$. Here it is shown that the $1.84d_f$ fiber spacing is the only fiber spacing group to exceed the apparent critical value of the matrix failure criterion. A plot of

the Mohr-Coulomb Criterion along the specimen thickness X , as shown in Figure 120, shows that the $1.75d_i$ and $1.84d_i$ are the only two specimens that exceed the apparent criterion.

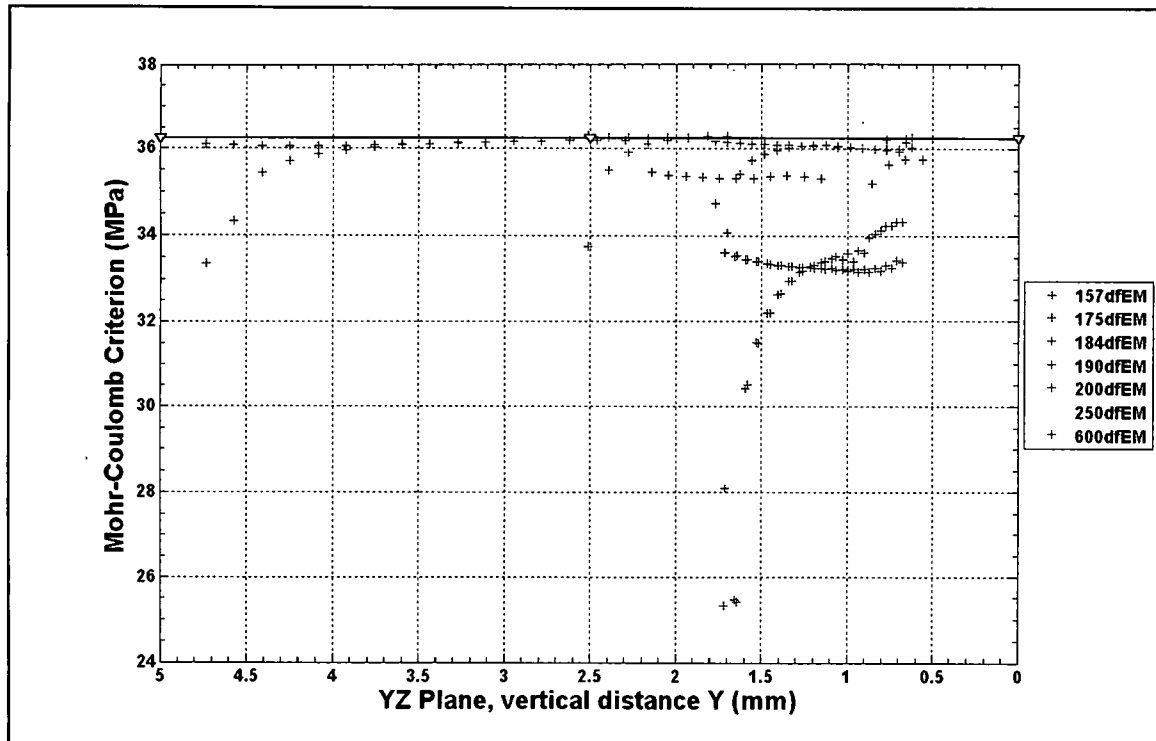


Figure 119: Mohr-Coulomb Criterion plot in the YZ plane along the vertical direction, Y, at $Z=0$ in the UM region of the FEM

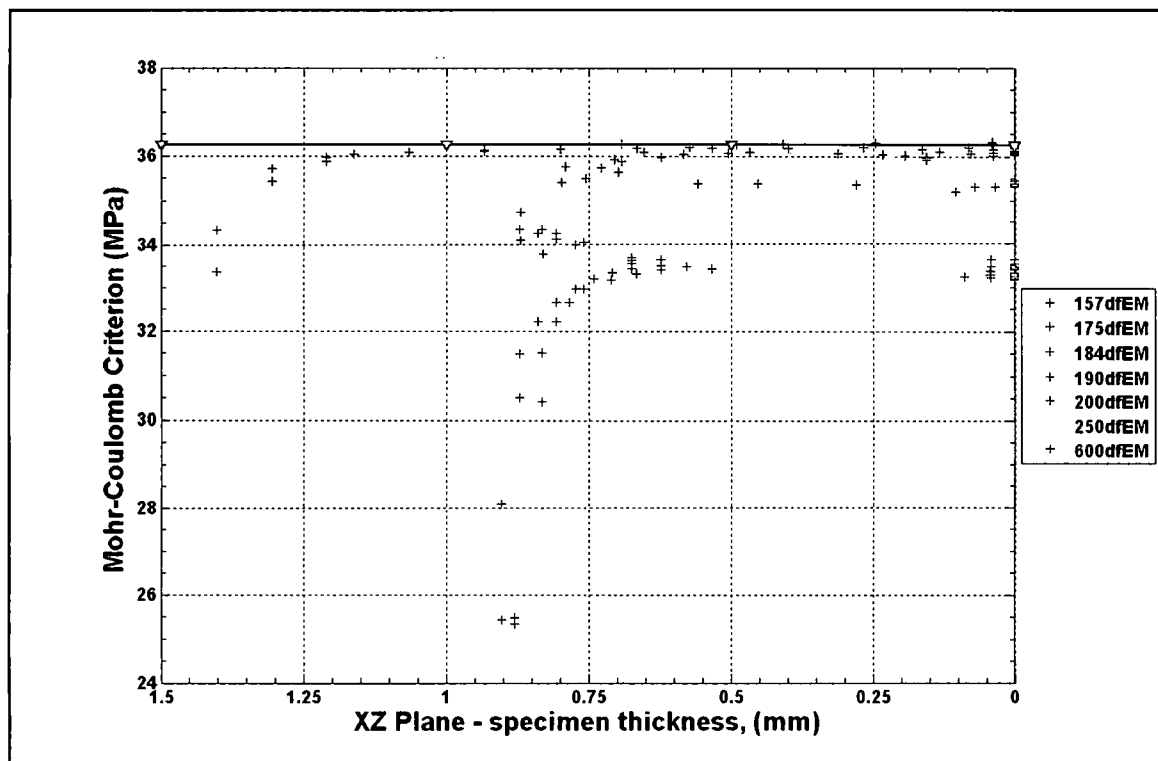


Figure 120: Mohr-Coulomb Criterion plot in the XZ plane along the specimen thickness, X, at Z=0 in the UM region of the FEM

Summarizing the analytical results in the EM, UEM and UM regions of the cruciform model; the 2.5d_f and 6.0d_f fiber spacing groups exceeded the critical criterion stress in only the EM and UEM regions. The 2.5d_f spacing exceeded the critical value by a very small amount and the 6.0d_f by a slightly larger magnitude. However, the 1.75d_f and 1.84d_f groups have larger magnitudes of the criterion than both the 6.0d_f and 2.5d_f in the EM and UEM regions, see Figures 116 and 117. Furthermore, the debond criterion evaluation for the 2.5d_f and 6.0d_f fiber spacing groups indicated debonds occurred, whereas for the 1.75d_f and 1.84d_f fiber spacing groups it did not. Although the 1.9d_f and 2.0d_f specimens maximum Mohr-Coulomb exceed the apparent critical value plane in one location at the edge of the field of view in the UM region (see Figure 118); no other fiber grouping exceeds the critical value except the ones that cavitared. Most likely the 1.9d_f and 2.0d_f location is a consequence of the plot routine used in the Matlab® program.

As previously mentioned Appendix E discusses the criterion evaluation in areas of the cruciform model either partially obstructed or completely obstructed from view. Also evaluated in Appendix E are the areas of the FEM where cavitation initiation was not identified to have occurred. The evaluation of the BTF and UBTF regions shows that the $1.75d_f$, $1.84d_f$ and $6.0d_f$ fiber spacing groups exceed the critical value as shown in Figure 257 in Appendix E. However, Figures 258 and 259 plot the criterion in the vertical and horizontal direction at $Z = 0$, respectively, show that the $1.75d_f$ and $1.84d_f$ specimens have higher magnitudes of the criterion than the $6.0d_f$ specimen. In addition, the $1.75d_f$ and $1.84d_f$ exceeded the critical value in the center fiber matrix band at the mid-plane, $R = 0.1978$ mm, and at the outer band limit, $R = 0.2178$ mm. At these two locations both the $2.5d_f$ and $6.0d_f$ groups had considerably lower magnitudes. Since no cavitation was observed as occurring as the first failure mechanism for the $2.5d_f$ and $6.0d_f$ fiber spacing groups then the apparent critical value may be too low. Adjusting the apparent critical Mohr-Coulomb criterion to 36.35 MPa, Figure 121 shows the cavitation locations are still contained within the area exhibiting maximum Mohr-Coulomb values for the $1.75d_f$ and $1.84d_f$ while the $6.0d_f$ is barely exceeding the critical plane in the EM and UEM regions of the FEM. The adjusted apparent critical value is within the standard deviation shown in Table 43. Appendix E contains the revised evaluations of all the FEM regions exhibiting matrix cavitation at the new critical value of 36.35 MPa. A summary of all matrix failure initiation results follows.

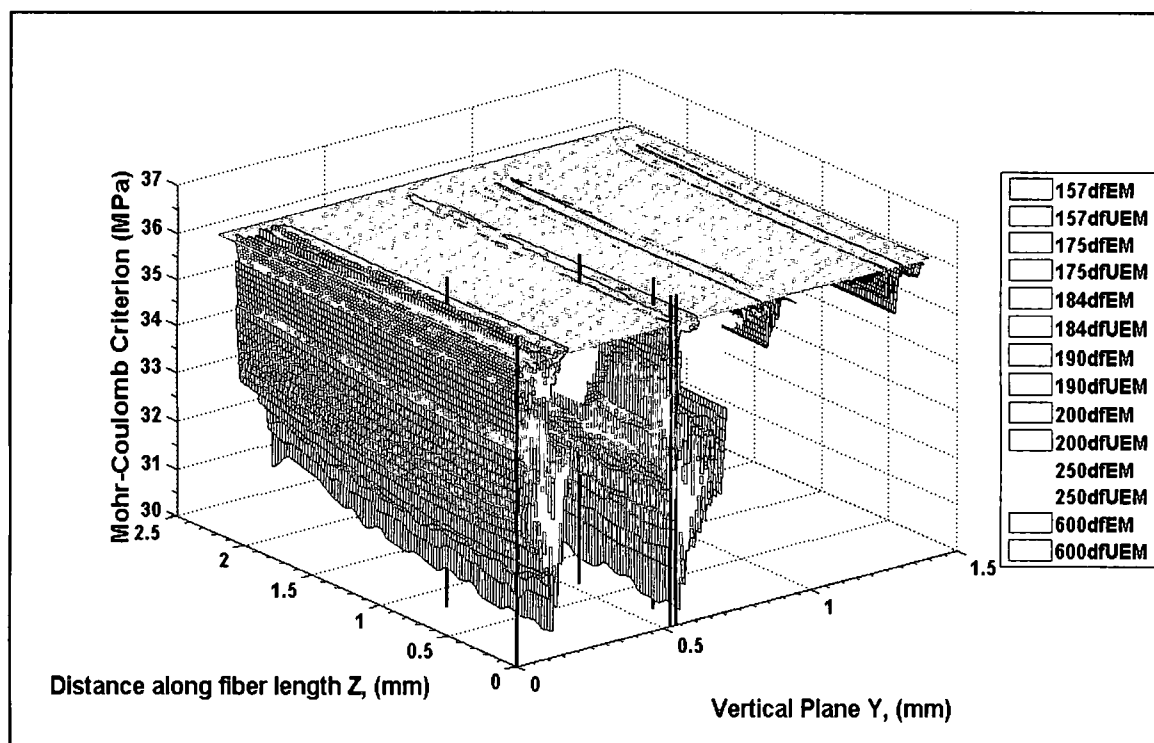


Figure 121: Mohr-Coulomb Criterion distribution in the YZ plane of the EM and UEM regions of the FEM showing the critical value plane at 36.35 MPa and cavitation locations

Matrix Failure Initiation Criterion – Summary. An apparent critical value of the Mohr-Coulomb Criterion was obtained by FEA based upon the location of the observed cavitation occurring in the 1.75d_f and 1.84d_f specimens. The apparent critical value was determined to be 36.35 MPa. The majority of the specimens initial cavitation was in the EM and UEM regions of the FEM, followed by the UM region then UBTF region and lastly by the CNB region at R = 0.1978 mm, see Table 43. In all cases the maximum Mohr-Coulomb values at the 1.75d_f and 1.84d_f fiber spacing exceeded the apparent critical value. However, the 6.0d_f specimen barely exceeded the critical Mohr-Coulomb in the EM, UEM and UBTF regions although no cavitations were observed during testing, see Figures 275 – 277 in Appendix E. When the initial cavitations locations are plotted, the ones occurring in the EM and UEM regions are contained in areas where the 1.75d_f and 1.84d_f exceed the apparent critical value. The cavitation locations occurring in the UM and UBTF regions are at the edge of the areas where the 1.75d_f and 1.84d_f exceed the apparent critical

value. The areas of the FEM exceeding the critical value correlate well with the experimentally observed matrix cavitations occurring in the cruciform specimen. Furthermore, the locations of the specimen's initial cavitation locations correlate very well to the observed experiments.

It should be noted that in each specimen where matrix cavitation was observed, it is the first instance of the damage mechanism that is recorded from which the far-field stress was determined. However, the FEA results in the EM, UEM, UBTF and the CNB regions show areas within the regions where the maximum Mohr-Coulomb criterion at the $1.75d_f$, $1.84d_f$ and $6.0d_f$ fiber spacing exceeds the apparent critical value, as mentioned above. Due to the FEM nodal solution the Mohr-Coulomb values at adjacent nodes will have slight variances differing tenths or hundreds of an MPa in magnitude. The plot routine employed in the Matlab® program interpolates between the nodal values of the Mohr-Coulomb to create the plane for the 3D plots used in this body of work. Close inspection of the plane reveals a wave or oscillation pattern. In reality these nodes or points within the continuum of the matrix would not have the oscillation but would be smooth. Most likely the plane representative of the actual value occurring in the matrix is probably somewhere between the peaks of the nodal points. Of course a finer mesh may smooth the plot as well but may not necessarily yield a better solution since the mesh density indicated very little improvement over what was used. These FEM resolution errors would likely show that the $6.0d_f$ does not exceed the critical value. Also, the locations of the cavitations were determined and measured with the best available tools and methodologies present. Due to the transparency of the matrix, distortion of the cavitation through the resin will cause errors in the location measurements which cannot be determined. Still, the areas of the cruciform specimen indicating matrix cavitations as predicted by the FEM and the locations of the cavitations correlate well with the experimental observations as mentioned above. Consequently, based upon the preceding discussion the Mohr-Coulomb criterion as presented by equation (5) very accurately describes the matrix cavitation occurring in the cruciform specimens have a fiber spacing at $1.75d_f$ and $1.84d_f$. The Mohr-Coulomb failure criterion critical magnitude is 36.35 MPa. Thus, when the Mohr-Coulomb criterion evaluates greater than 36.35 MPa matrix cavitation occurs. Due to the fact that the Mohr-Coulomb criterion best describes matrix cavitation there is strong

evidence that the matrix cavitation failure mechanism occurring in the cruciform specimens has a strong shear bias.

Residual Stress Impact to the Matrix Failure Initiation Criterion. In much the same way the matrix cure residual stresses affect the fiber-matrix debonding criterion, Figure 122 shows the residual stress effect on the Mohr-Coulomb criterion in the EM and UEM regions of the cruciform. By only incorporating the stresses due to the mechanical loading, other fiber spacing groups are shown exceeding the critical Mohr-Coulomb value. Figure 122 shows portions of the $2.5d_f$ fiber spacing and the all of the $6.0d_f$ fiber spacing exceeding the critical value indicating that matrix cavitation occurred in these specimens. The experimental results clearly have shown that the $2.5d_f$ and $6.0d_f$ fiber spacing groups did not exhibit matrix cavitation. Adjusting the critical value in the same manner as stated previously would cause the critical value to exceed its standard deviation. This would indicate that the criterion does not adequately describe the experimentally observed cavitation that occurred in the $1.75d_f$ and $1.84d_f$ fiber spacing specimen groups.

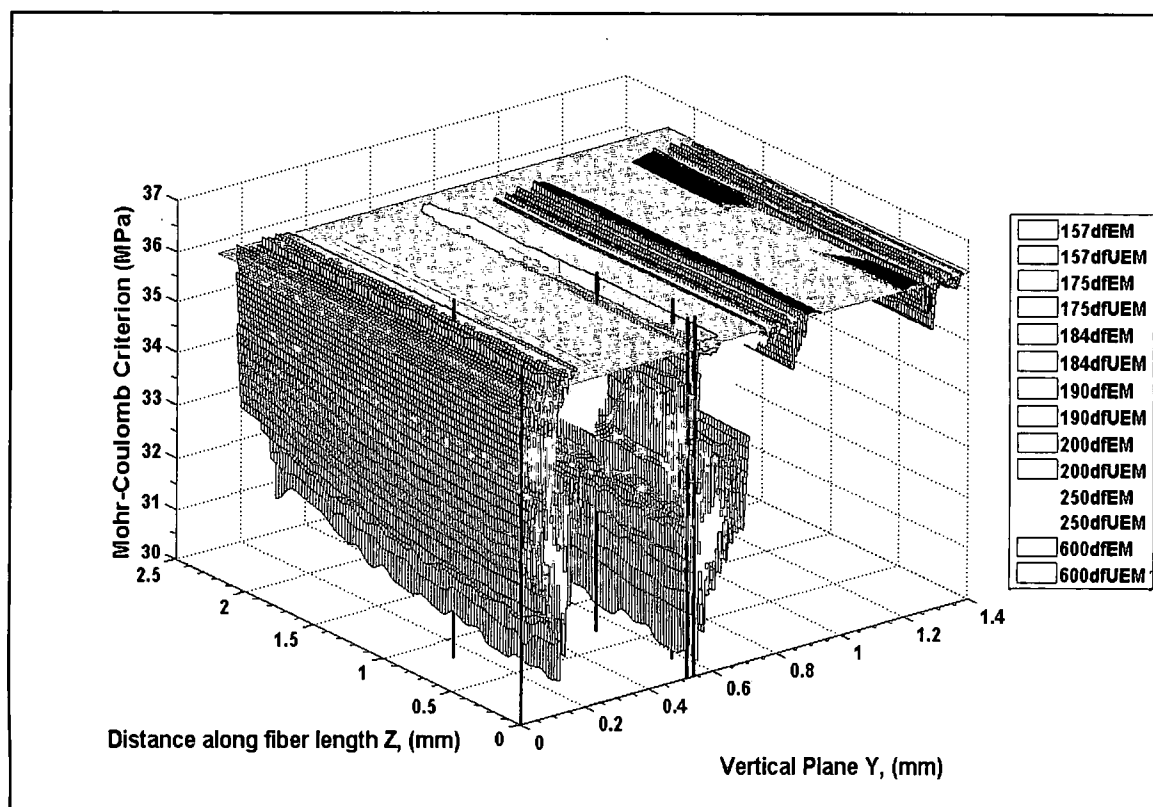


Figure 122: Matrix cure shrinkage residual stress effect on the Mohr-Coulomb matrix failure criterion showing results from the mechanical load only

The implications of not including the matrix cure shrinkage residual stresses in evaluating the matrix failure criterion would have disastrous consequences. It would lead to either selecting an erroneous existing criterion or developing a criterion that dramatically over predicts the stress state in which matrix cavitation occurs. Recall that the critical value was determined by the FEA at the locations of matrix cavitation from the experimental observations. Determining the Mohr-Coulomb critical value in the same manner using only the internal stress state due mechanical loading only would lead to a critical value far above when cavitation would actually occur. The consequences would be that the composite part would have micro-cracking due to matrix cavitation much sooner that the analysis would predict. This in turn would lead to final failure far sooner than the global failure criterion predicted.

862/W Matrix System

Fiber-Matrix Debond Initiation Criterion

Following the format used for the 828/D-230 matrix system debond criterion discussed above. An evaluation of the proposed quadratic and linear debonding criteria involving a radial and shear stress interaction within the field of view follows. Both criteria in the 2nd and 3rd quadrant will be thoroughly evaluated and discussed in Appendix E based upon the analytical results of the cruciform specimen FEM. A summary of all debond criteria evaluation follows.

Quadratic Debond Initiation Criterion in the Field of View. Following the same methodology as for the 828/D-230 quadratic debond criterion development, having the form shown in equation (1) and recognizing a larger shear component interaction based on the discussion above is presented for evaluation. Figure 123 and 124 are the distributions along the fiber matrix interface in the first and fourth quadrant of the corner fiber of the quadratic debond criterion shown in equation (12) having constants $A = 21$ and $B = 14$. Inspection of Figures 123 and 124 shows that

$$21 \left(\frac{\sigma_r}{\sigma_{yt}} \right)^2 + 14 \left(\frac{\tau_{r\theta}}{\tau_y} \right)^2 \geq 1 \quad (12)$$

for the 1.57d_f, 1.75d_f, 1.90d_f, 2.5d_f, 6.0d_f and the SF, all evaluate the quadratic debond greater than 1.0 in both quadrants indicating debond present and correlating the experimental results. Like for the 828/D-230 fiber-matrix debond criterion, the constant A can be considered a function of the adhesion strength of the matrix in tension or normal to the fiber interface and the constant B a function of the adhesion strength in shear.

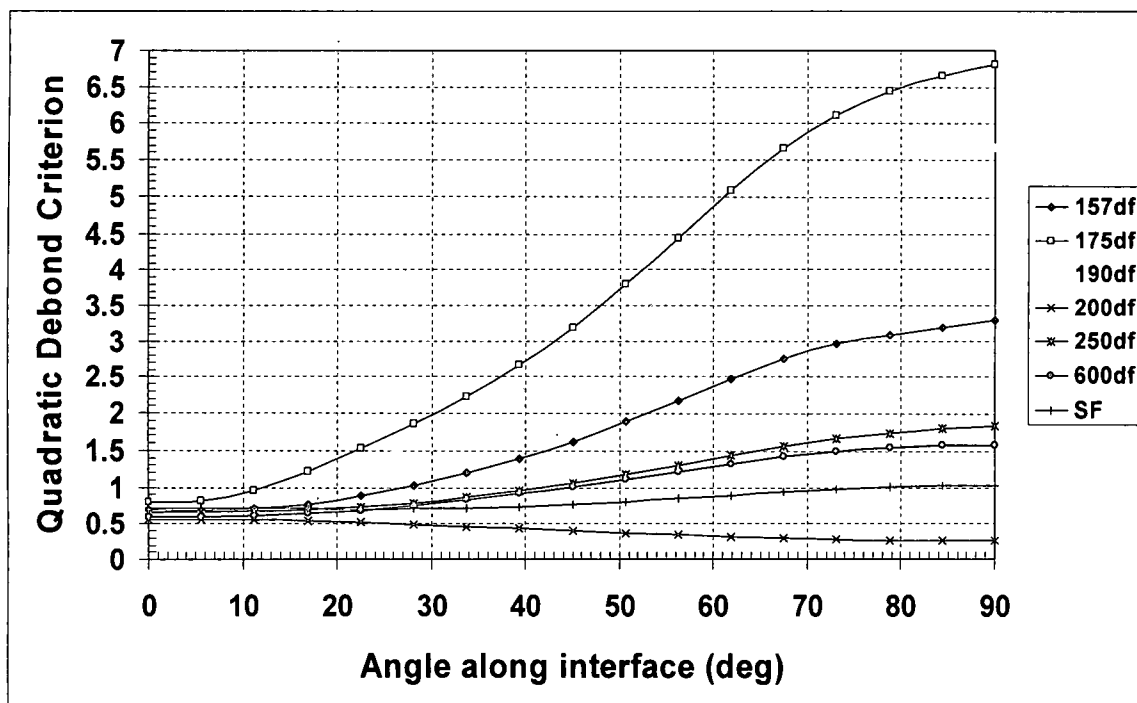


Figure 123: Quadratic Debond Criterion evaluated at the fiber matrix interface of the corner fiber in field of view from $\theta = 0^\circ$ to 90° at $Z = 0$ with $A = 21.0$ and $B = 14.0$

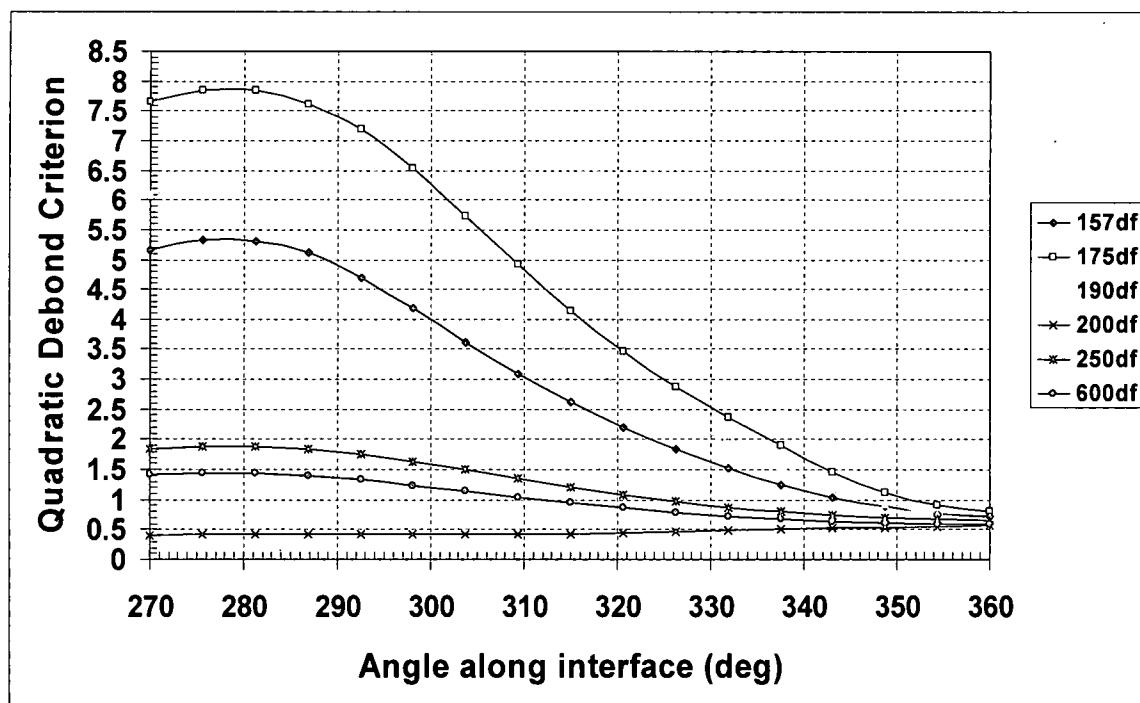


Figure 124: Quadratic Debond Criterion evaluated at the fiber matrix interface of the corner fiber in field of view from $\theta = 270^\circ$ to 360° at $Z = 0$ with $A = 21.0$ and $B = 14.0$

The quadratic debond criterion also evaluates the $2.0d_f$ fiber spacing, which exhibited matrix cavitation as its first failure mechanism, at less than 1.0 indicating that no debonds are present. Additionally, the angular location where the distribution of the individual fiber spacing groups exceed 1.0 should correspond to the limits of the debond measured from the photomicrograph taken of the cruciform experiments. Table 44 lists the fiber matrix debond limits determined by the quadratic debond criterion evaluated from the cruciform FEM results for the corner fiber in the 1st and 4th quadrants shown in Figure 123 and 124 respectively. Also listed in Table 44 are the experimentally measured debond limits, as shown in Table 34, as well as the relative difference between the criterion and the actual observed debond limit expressed as a percentage.

Table 44: Fiber matrix debond limits for the corner fiber 1st and 4th quadrant determined by quadratic debond criterion evaluated from the cruciform FEM results

Fiber Spacing	Quadratic Debond Criterion Debond limits		Experimental Debond limits		$\Delta\%$	
	1 st Quad	4 th Quad	1 st Quad	4 th Quad	1 st Quad	4 th Quad
$1.57d_f$	26°	344°	46°	314°	31.3	40.5
$1.75d_f$	12°	351°	38°	322°	33.3	35.8
$1.9d_f$	16°	347°	50°	310°	45.9	48.1
$2.5d_f$	41°	324°	52°	308°	22.4	29.6
$6.0d_f$	43°	310°	51°	309°	17	2.5
SF	77°	-	63°	-	51.9	-

It appears from the results presented in Table 44 that the quadratic debond criterion fairly accurately predicts the $6.0d_f$ fiber spacing group debond limit in the 4th quadrant only, while it's marginally close in the 1st quadrant at 17%. The relative differences for all other fiber spacing groups are quite large surpassing 20%. The debond criterion constantly over predicts the debond limits in both quadrants and does not accurately reflect the fairly large radial compressive stresses acting at the fiber equator.

Linear Debond Criterion in the Field of View. Again, following the methodology used for the 828/D-230 system discussed above a linear criterion having the form shown in equation (2) is presented for evaluation. Recognizing the higher tensile and shear yield strengths of the 862/W

matrix system, Figures 125 and 126 are the distributions of the linear debond criterion having the constants $A = 4.62$ and $B = 1.95$ for the corner fiber in the 1st quadrant and in the 4th quadrant. Since the constant A is tied to the ratio of the radial stress to the tensile yield strength in equation (2) the value of 4.62 is arrived by taking the value of A for the 828/D-230 system and multiplying it by the ratio of 862 tensile yield strength to the 828 tensile yield strength. Likewise, for the constant B since it is tied to the ratio of interfacial shear stress to the shear yield stress, its value for the 862/W system is arrived at by taking the value for the 828/D-230 system and multiplying it by the ratio of the shear yield strengths of the 862 to the 828 systems. Consequently, the linear debond criterion proposed for the 862/W matrix system is expressed in equation (13)

$$4.62 \left(\frac{\sigma_r}{\sigma_{yt}} \right) + 1.95 \left(\frac{\tau_{r\theta}}{\tau_y} \right) \geq 1 \quad (13)$$

Like for the 828/D-230 fiber-matrix debond criterion, the constant A can be considered a function of the adhesion strength of the matrix in tension or normal to the fiber interface and the constant B a function of the adhesion strength in shear.

Inspection of Figures 125 and 126 indicates that the criterion exceeds 1.0 for the $1.57d_f$, $1.75d_f$, $1.9d_f$, $2.5d_f$, $6.0d_f$ and the SF. Additionally, the $2.0d_f$ fiber spacing interfacial debond criterion is less than 1.0. Furthermore, the criterion accurately reflects the compressive stresses present at the fiber equator. These characteristics, shown in Figure 125 and 126, correlate with the experimental results. However, the angular position where each fiber spacing group's interfacial distribution exceeds 1.0 compared to the experimental measured results is the true test of the accuracy of the debond criterion.

Table 45 lists the fiber matrix debond limits determined by the linear debond criterion evaluated from the cruciform FEM results for the corner fiber in the 1st and 4th quadrant as well as the experimental debond limits listed in Table 34. Also listed is the relative difference expressed as a percentage between the criterion and the experimentally measure debond limits.

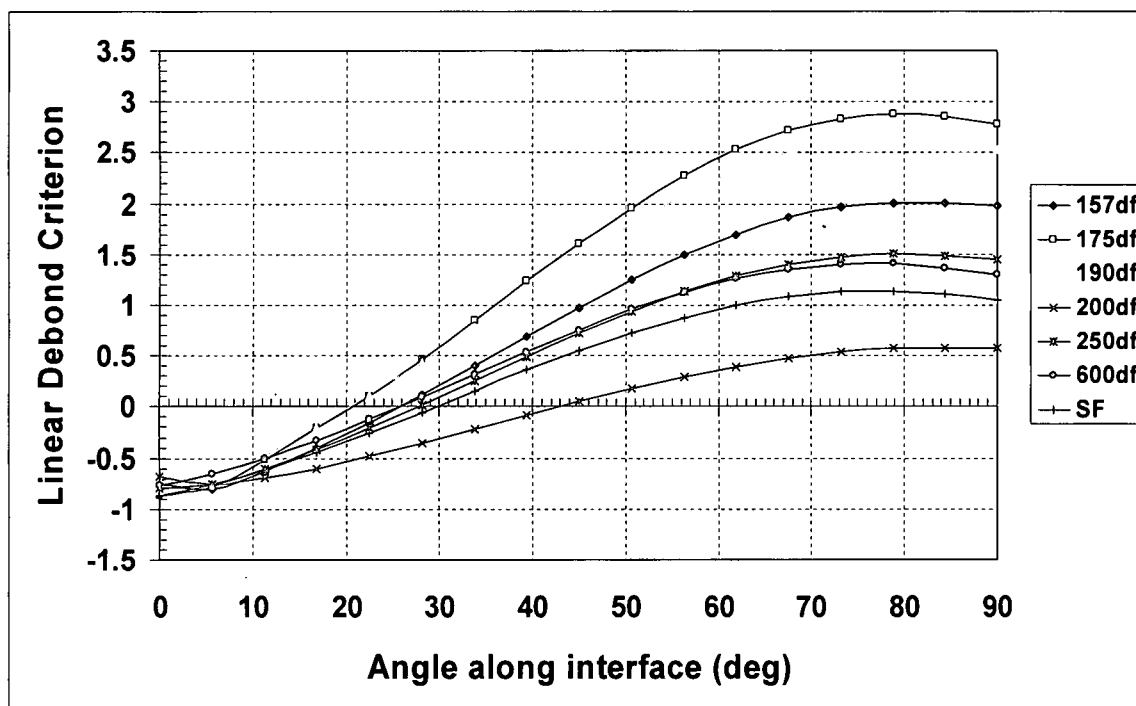


Figure 125: Linear Debond Criterion evaluated at the fiber matrix interface of the corner fiber in field of view from $\theta = 0^\circ$ to 90° at $Z = 0$ with $A = 4.62$ and $B = 1.95$

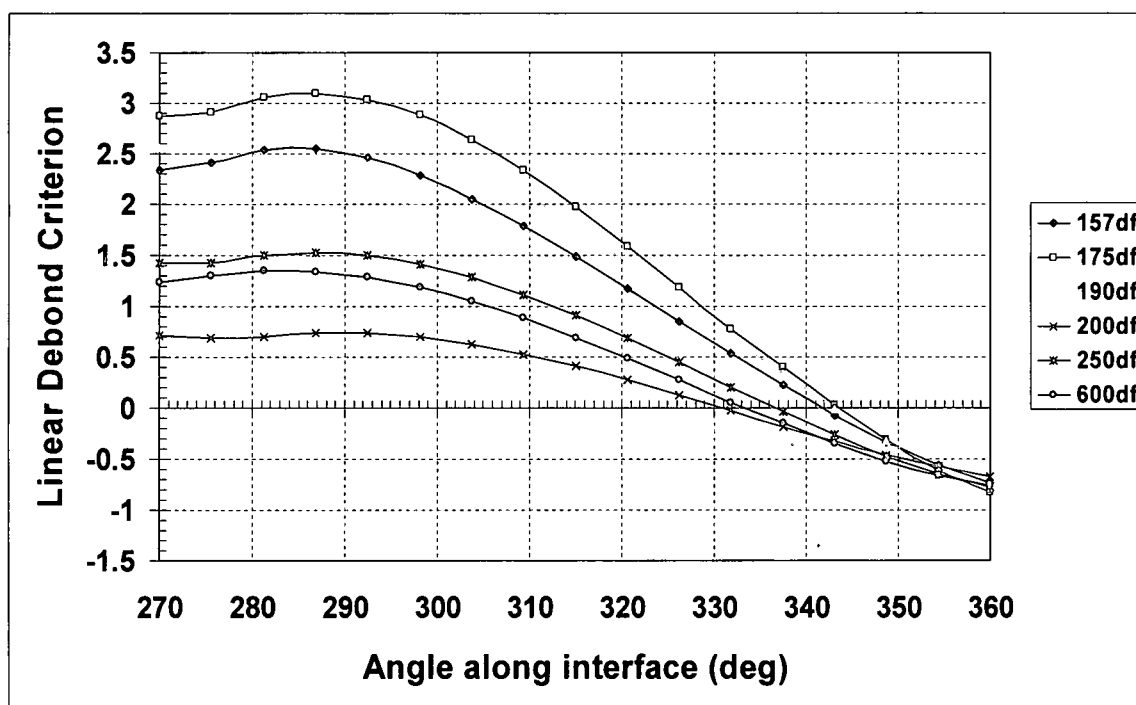


Figure 126: Linear Debond Criterion evaluated at the fiber matrix interface of the corner fiber in field of view from $\theta = 270^\circ$ to 360° at $Z = 0$ with $A = 4.62$ and $B = 1.95$

Table 45: Fiber matrix debond limits for the corner fiber 1st and 4th quadrant determined by the linear debond criterion evaluated from the cruciform FEM results

Fiber Spacing	Linear Debond Criterion Debond limits		Experimental Debond limits		$\Delta\%$	
	1 st Quad	4 th Quad	1 st Quad	4 th Quad	1 st Quad	4 th Quad
1.57d _f	46°	324°	46°	314°	0	18.5
1.75d _f	36°	329°	38°	322°	3.7	11.9
1.9d _f	37°	327°	50°	310°	24.5	29.8
2.5d _f	52°	313°	52°	308°	0	11.6
6.0d _f	52°	306°	51°	309°	2.6	7.7
SF	62°	-	63°	-	3.6	-

Table 45 shows that the linear debond criterion is quite accurate predicting the limits of the fiber matrix debonds for all fiber spacing groups except the 1.90d_f fiber spacing in the 1st quadrant of the corner fiber. It is only moderately accurate, at best, for predicting the debond limits in the 4th quadrant for all fiber spacing groups except the 1.9d_f. Due to the symmetry of the fiber arrangement the FEM is only 1/8 the actual specimen. Once the debond locations are determined they are translated to the appropriate FEM location. For all fiber spacing groups the majority of the debond locations within each group translated to the northern hemisphere of the top fiber. This correlating with the experimental observation that the majority of the debonds occurred externally to the fiber group. Thus the linear criterion is predicting the debond limits more accurately in the locations where they occur most frequently.

The reason for the high relative difference between the criterion and the experimental results at the 1.9d_f fiber spacing can be explained due to the fact only one specimen was observed debonding at the fiber pole. Recall that only three of eight specimens at this fiber spacing had their failure initiation mechanism observed; see Table 23, the other five exhibited debonds but they were completely obstructed from the field of view as described in Chapter 2. The one specimen whose debond was observed occurring centered at the fiber pole is the lone experimental data point at this fiber spacing and thus listed in Table 45. For the second specimen the fiber matrix debond occurred centered at the north pole of the top back fiber. This was directly observed due to fiber misalignment within the specimen but debond measurements are not possible as the front fiber partially obstructed the view. The third specimen initiated a thin debond in the southern hemisphere of the bottom fiber in the field of view, which translates to the northern

hemisphere of the top fiber for FEM comparisons. The limits for this debond are from $\theta = 25^\circ$ to 43° which encompasses the criterion debond limit for the $1.90d_f$ spacing of $\theta = 37^\circ$. Consequently, for the $1.9d_f$ fiber spacing it's difficult to make statistical comparisons with only one experimental data point for debond limits. Had more cameras been utilized it is quite possible that the $1.9d_f$ spacing debond limits would be closer to the $1.75d_f$ fiber spacing debond limits since the fiber spacing's are close to each other.

Quadratic vs. Linear Debond Criterion Evaluation. Combining Tables 44 and 45 along with the experimentally determined debond limits creates Table 46 for the 1st quadrant and Table 47 for the 4th quadrant of the corner fiber to compare the quadratic debond criterion to the linear debond criterion. From Table 46 it appears that the linear debond criterion is better at predicting the debond limits for all fiber spacing tested exhibiting fiber matrix debond as their failure initiation in the first quadrant of the corner fiber. The bold and italicized numbers represent the lowest relative difference expressed as a percentage between the two criteria. In fact, Table 46 indicates that the linear criterion predicts the exact debond limit for the $1.57d_f$ and $2.5d_f$ fiber spacing groups in the 1st quadrant.

Table 46: Comparison of the fiber matrix debond limits predicted by the Quadratic and Linear Debond Criterion for the 1st quadrant of the corner fiber at $Z = 0$

Fiber Spacing	Exp db Limits (deg)	Quadratic db Criterion limits (deg)	% Δ	Linear db Criterion limits (deg)	% Δ
$1.57d_f$	46	26	20	46	0
$1.75d_f$	38	12	26	36	3.7
$1.9d_f$	50	16	34	37	24.5
$2.5d_f$	52	41	11	52	0
$6.0d_f$	51	43	8	52	2.6
SF	63	77	17	62	3.6

Table 47 indicates that the quadratic debond criterion accurately predicts the debond limit for only the $6.0d_f$ fiber spacing group in the 4th quadrant. Whereas, the linear debond criterion predicts the debond limits more accurately for the remaining fiber spacing groups in the 4th quadrant of the corner fiber. Although the relative percent difference between the actual observed

debond limit and predicted linear debond limit are much larger in the 4th quadrant than in the 1st quadrant, the overall majority of the debonds in the 862/W matrix system occur exterior to the fiber group corresponding to the 1st quadrant with respect to the FEM. Consequently, the criterion is expected to perform better where the actual failure mechanism is happening. Both criteria are conservative in predicting the debond limits in the 4th quadrant, except at the 6.0d_f spacing for the linear criterion. However, the linear debond criterion is closer to the actual limits by a considerable amount than the quadratic criterion thus making the linear debond criterion a better fit.

Table 47: Comparison of the fiber matrix debond limits predicted by the Quadratic and Linear Debond Criterion for the 4th quadrant of the corner fiber at Z = 0

Fiber Spacing	Exp db Limits (deg)	Quadratic db Criterion limits (deg)	%Δ	Linear db Criterion limits (deg)	%Δ
1.57d _f	314	344	40.5	324	18.5
1.75d _f	322	351	35.8	329	11.9
1.9d _f	310	347	48.1	327	29.8
2.5d _f	308	324	29.6	313	11.6
6.0d _f	309	310	2.5	306	7.7

Although the linear debond criterion seems to be quite a better fit for predicting the debond limits in the 1st and 4th quadrants of the corner fiber, before down selecting to the recommended criterion a comparison at the debond locations on the corner fiber needs to be made. In addition, a performance analysis of the proposed criterion is made for the 2nd and 3rd quadrants of the corner fiber. The comparison and performance analysis are thoroughly evaluated and discussed in Appendix E. A summary of all debond criterion evaluation results discussed above and in Appendix E follows.

Fiber-Matrix Debond Initiation Criterion – Summary. A quadratic and linear debond criteria were investigated to see which one better predicted the debond limits observed in the cruciform experiments exhibiting fiber-matrix debond as their failure initiation for all fiber spacing groups. A thorough comparison was made between the two forms of the debond criteria in the visible 1st and 4th quadrants of the corner fiber presented above and in Appendix E. In addition, the criteria evaluation at the debond locations and in the 2nd and 3rd quadrant of the corner fiber are

thoroughly evaluated in Appendix E. From these results it was found that the linear debond criterion better predicted the debond limits for all fiber spacing groups in both quadrants except for the $6.0d_f$ fiber spacing group in the 4th quadrant. However, since the majority of the fiber-matrix debond occurred at the north pole of the corner fiber at the $6.0d_f$ fiber spacing and the debond was better described by the linear debond criterion in the visible 1st quadrant, it was concluded that the linear debond criterion is the best fit for the $6.0d_f$ spacing. Therefore, strong evidence exists that the linear debond criterion, shown in equation (13), best predicts the fiber-matrix debonds for all fiber spacing groups based upon its performance, shown above and in Appendix E. Furthermore, the linear debond criterion best described the interfacial stress state reflecting the compressive nature of the radial stress at the fiber equator which the quadratic criterion did not. Additionally, the experiments show that the linear debond criterion adequately predicts the debond limits of the quadrants of the corner fiber obstructed from view based on a symmetrical debond occurring at the fiber poles.

Residual Stress Impact to Fiber-Matrix Debond Initiation Criterion. The 862/W matrix is a high room temperature cured two part epoxy system and the effects of the cure shrinkage stress shown in Appendix D can be very large. Table 75 on page 422 in Appendix D lists the reduction of the radial stress due to the mechanical load from the matrix cure shrinkage for the center fiber. From the table, the matrix cure shrinkage reduced the radial stress by an amount between 44% and 146% depending upon fiber spacing at the location of maximum mechanical radial stress. Similarly, the shear stress due to mechanical load at its maximum location has been reduced by an amount between 9% and 65%, depending on fiber spacing, by the matrix cure as depicted in Table 76 on page 428 in Appendix D. The radial stress due to the cure shrinkage had greater impacts where the fibers were closest together for each fiber spacing group, see Figure 220 page 419 in Appendix D, except at the $6.0d_f$ spacing. However, at these locations the mechanical radial stress was much lower. For the shear stress, the largest impacts due to the cure shrinkage occurred approximately at $\theta = 28^\circ$ and again at $\theta = 62^\circ$ to 68° , see Figure 223 page 426 Appendix D. Like the radial stress, the shear stress due to the applied load was much lower. Just

as for the 828/D-230 matrix system, the resulting behavior of both the radial and shear stress due to the matrix cure caused the highest resulting stress to act over a larger length of the interface.

For the corner fiber the matrix cure shrinkage reduced the radial stress due to mechanical loading as shown in Tables 77 and 78 on page 441 and 442 in Appendix D. The impacts range by an amount between 16% and 67% at the location of maximum radial stress due to applied load, depending on fiber spacing, in the 1st, 2nd and 4th quadrants of the fiber. In the 3rd quadrant the impact ranged by an amount between 16% and 57% at the location of maximum radial stress due to the applied load depending on fiber spacing. In a similar fashion, the matrix cure reduced the shear stress by an amount between 2% and 33% in the 1st, 2nd and 4th quadrants at the location of maximum shear due to applied load, as shown in Table 80 on page 453 of Appendix D. In the 3rd quadrant it reduced the mechanical load shear by an amount between 11% and 43% depending upon fiber spacing. Similar to the center fiber, the corner fiber radial and shear stress due to the matrix cure had higher magnitudes at locations along the interface other than in the direction of the applied mechanical load (see Figures 229 – 232 pages 434 and 435 for the radial stress distributions and Figures 241 – 244 pages 447 and 448 for the shear stress distribution in Appendix D). The effects of the maximum radial and shear stress due to the matrix cure shrinkage at the corner fiber resulted in a longer length of fiber-interface subjected to the highest stress magnitudes, just as it was for the 828/D-230 matrix.

The resulting impact due to the matrix cure shrinkage on the fiber-matrix debonding criterion in the field of view for the corner fiber 1st and 4th quadrant is shown in Figure 127 and 128. Quite evident is the fact that the criterion no longer accurately predicts the fiber spacing groups that exhibit fiber-matrix debonding as their failure initiation mechanism. The $2.0d_f$ spacing exceeds 1.0 in both the 1st and 4th quadrants by a considerable amount. Recall that the criterion predicts a fiber-matrix debond when equation (3) is evaluated greater than 1.0. Another indication of the impact of the residual stresses are the debond limits being much greater than those experimentally measured. The experimentally measured debond initiation limits should correspond to where the individual criterion distributions cross 1.0. For example, Figure 127 and 128 show a debond limit of the $1.57d_f$ fiber spacing group to be approximately 25° in the 1st

quadrant and 329° in the 4th quadrant. The experimentally measured fiber-matrix debond initiation limit for the $1.57d_f$ spacing was 46° in the 1st quadrant and 314° in the 4th quadrant. When the matrix cure residual stresses were properly accounted for in the analysis the criterion evaluated the limits at 46° in the 1st quadrant and 324° in the 4th quadrant. The difference between the debond initiation limits when the matrix residual stresses are not accounted for are 21° in the 1st quadrant and 15° in the 4th quadrant. This equates to a 45.6% and 4.6% relative difference in the 1st and 4th quadrants respectively. When the matrix residual stresses are accounted for correctly in the analysis determining the internal stresses, the differences are zero in the 1st quadrant, meaning the criterion is very accurate in that it matches the observed debond length along the interface. Whereas, the differences are 10° or a 3.1% relative difference in the 4th quadrant between the observed debond and criterion. These values are shown in Table 92, page 507 of Appendix E. The improvement in accuracy of the debond criterion when the residual stresses are included in the analysis is dramatic in the 1st quadrant than when the residual stresses are not included in the analysis. In the 4th quadrant the improvement is 1.5%. Consequently, the linear debond criterion performs with greater accuracy when the matrix cure residual stresses are properly incorporated into the analysis.

The 2nd and 3rd quadrants of the corner fiber show the same trends as the 1st and 4th quadrant. The $2.0d_f$ fiber spacing exceeded 1.0 when the linear debond criterion was evaluated in both quadrants and the debond limits were greater, by a substantial amount, than those experimentally measured.

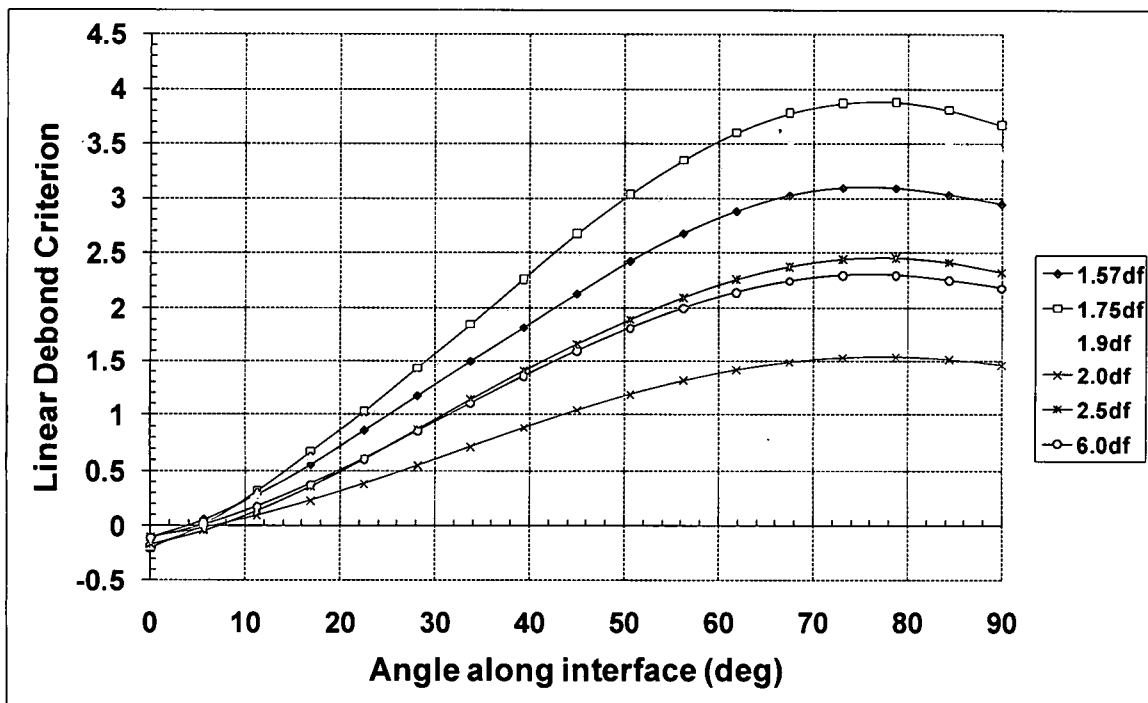


Figure 127: Effects of the matrix cure shrinkage residual stress on the Linear Debond Criterion in the 1st quadrant of the corner fiber

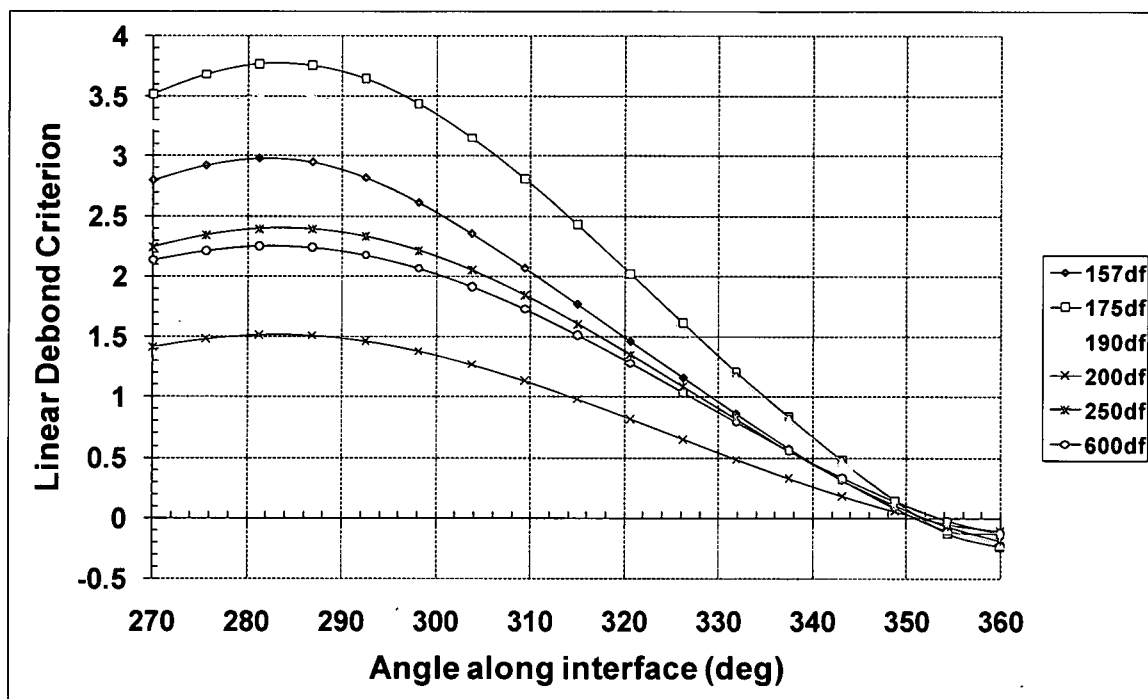


Figure 128: Effects of the matrix cure shrinkage residual stress on the Linear Debond Criterion in the 4th quadrant of the corner fiber

Matrix Failure Initiation Criterion

As mentioned in Chapter 3, literature search results list six possible failure criteria that could describe the matrix failure that was observed occurring in the multi-fiber cruciform specimens at the $2.0d_f$ fiber spacing. Furthermore, results of the analytical study conducted on the six candidates discussed in Chapter 3 indicate that only two concur with the observed experimental results, the Modified Tresca and the Mohr-Coulomb criteria. The analytical results also revealed that for all fiber spacing groups the UEM tri-axial state of stress existed at the specimen boundary. Due to this condition these analytical results will not be used. Also, for the $2.0d_f$ fiber spacing a tri-axial state of stress existed only in the EM region of the FEM within the field of view; in all other regions the tri-axial stresses either existed at the specimen boundary or were outside the field of view. In addition, for the $6.0d_f$ fiber spacing its tri-axial stresses occurred beyond the field of view in the EM region of the FEM. Consequently, only the EM region of the FEM for the $1.57d_f$, $1.75d_f$, $1.9d_f$, $2.0d_f$ and $2.5d_f$ fiber spacing groups will be used for the further evaluation of the matrix failure criterion. The EM volumes of the cruciform FEM are shown in Figure 96. For the Modified Tresca and Mohr-Coulomb matrix failure criteria, their distribution in the YZ plane of the EM sub-regions of the cruciform specimen show that the $2.0d_f$ fiber spacing has the maximum magnitude above all fiber spacing groups. See Figure 97 for the Modified Tresca distribution in the YZ plane and Figure 98 for the Mohr-Coulomb distribution in the YZ plane. Therefore, these two criteria will be further evaluated to determine which one best fits the experimental results.

Following the methodology used for the 828/D-230 matrix system for evaluating the appropriate matrix failure criterion; the neat resin tensile, compression and shear test results will be utilized. As discussed above, the Modified Tresca Criterion predicts the critical shear stress while the Mohr-Coulomb predicts the octahedral shear stress. Equation (7) is the critical shear stress and equation (8) is the octahedral shear stress from the neat resin tensile tests. The neat resin shear tests yield equation (9) for the Modified Tresca Criterion and equation (10) of the Mohr-Coulomb Criterion. The critical shear stress obtained from the compression tests results in equation (11) for the Modified Tresca Criterion while the octahedral shear stress is obtained from

equation (12) for the Mohr-Coulomb Criterion. Table 48 lists the results on the comparison between the Modified Tresca Criterion and the Mohr-Coulomb for predicting the critical shear stress and octahedral shear stress from the neat resin experiments.

Table 48: Criteria comparison using neat resin tests

	Mod-Tresca (MPa)	τ_s (MPa)	Δ	%Δ	Mohr-Coulomb (MPa)	τ_{oct} (MPa)	Δ	%Δ
Tensile	56.61	38.94	17.67	31.2	48.1	36.71	11.39	23.7
Shear	66.38	66.38	0	0	54.2	54.2	0	0
Compression	80.26	61.61	13.65	17	63.85	58.09	5.76	9

As with the 828/D-230 system, both criteria predicted greater values for the critical shear stress and the octahedral shear stress using data from the tension and compression tests than those calculated using equations (7) – (8) and (11) – (12). Since both criteria are based upon the shear failure of the material; it's no surprise that both criteria predicted their respective shear stresses exactly. The predicted shear stresses from both criteria are also closer to the shear stresses obtained from the compression test data due to the fact that the compression of a material usually fails in shear [2, 3]. This was observed during the compression tests of the neat resin samples described in Appendix A by shear bands forming at the specimens edges as load is increasing. Inspections of the fracture surface of the neat resin tensile dog-bone sample after failure revealed no indication of shear occurring. The surfaces were smooth and glassy indicating a pure tensile failure. As a result, from this analysis it appears that the Mohr-Coulomb Criterion best fits the neat resin data and thus will be considered for further evaluation. Therefore, a thorough evaluation of the Mohr-Coulomb criteria follows.

The procedure for locating the first cavitation is detailed in the Photomicrograph Image Analysis section in Chapter 2. Its vertical location in the YZ plane is measured from a reference, usually the centerline of a fiber, in the image capturing the cavitation initiation. Since the camera is centered for each specimen before testing begins the Z dimension is taken from the center of the image. Table 49 lists the results of the photomicrograph analysis determination of the first matrix cavitation failure mechanism. From Table 49 the locations of the cavitation determined from the photomicrograph analysis happen well within the EM region of the FEM. The field-of-

view for the $2.0d_f$ specimens averages a horizontal distance of 4.0 mm by a vertical distance of 3.6 mm which translates to a FEM field-of-view of 2.0 mm by 1.8 mm. The depth of the cavitations within the specimen, the X dimension, is impossible to determine through the photomicrograph analysis techniques but from the fracture surface analysis the X dimension can be measured from either the specimen edge or the from the fiber. Based upon the average vertical distance and the average horizontal distance along the fiber, it appears that the cavitation occur at the same elevation as the south pole of the corner fiber almost two fiber diameters from the center of the specimen. The results seem fairly constant as evidence by the low standard deviation thus the average maximum value of the Mohr-Coulomb Criterion as determined by equation (6) can be considered the apparent critical value.

Table 49: Cavitation locations for $2.0d_f$ fiber spacing group and average apparent critical Mohr-Coulomb Criterion value

Specimen	Max Mohr-Coulomb Criterion (MPa)	FEM Location	Y (mm)	Z (mm)
200R2C1-B	64.12	EM	0.195	0.45
200R2C1-C	64.38	EM	0.19	4.03*
200R2C1-D	64.04	EM	0.047	0.45
200R2C1-E	64.19	EM	0.31	0.45
200R2C1-F	64.19	EM	0.17	0.45
200R2C1-G	63.99	EM	0.012	0.67
200R2C1-H	64.24	EM	0.154	1.57
200R2C1-I	64.01	EM	0.27	0
200R2C1-J	64.06	EM	0.22	0.896
AVG	64.14			
Std-dev	0.12			
* delineates cavitation captured in far-field view camera				

Figure 129 is the Mohr-Coulomb Criterion distribution in the YZ plane of the EM region of the cruciform specimen for the aforementioned specimens exhibiting a tri-axial state of stress. Also plotted is a plane at the apparent critical value of the criterion as determined above and each individual specimen's cavitation location represented by the vertical lines. It is quite apparent that the $2.0d_f$ fiber spacing group has the maximum magnitude of the matrix failure criterion and exceeds the critical criterion value over all other fiber spacing groups. The individual specimen cavitation locations align quite well with the apparent critical value in that half are located in an

area where the critical value is greater than the magnitude at that particular location, while for the other half the converse is true. This indicates that the critical value is a good statistical representation of the sample size and thus can be considered the actual critical value of the Mohr-Coulomb Criterion. Confirmation of the critical value is shown in Figure 130 where the Mohr-Coulomb Criterion is plotted in the YZ plane at $Z = 0$, the center of the specimen. It is clear that the matrix failure criterion exceeds the critical value from about $Y = 0.09$ mm to about 0.17 mm. This range places the cavitation in front of the center fiber, approximately at the elevation of the 27° mark of the center fiber to the south pole of the corner fiber, of the EM region of the FEM. Figure 131 is Mohr-Coulomb Criterion plotted along the specimen thickness X at $Z = 0$. From this plot the cavitation occurs between approximately 0.65 mm to about 1.02 mm placing it just beyond the equator of the corner fiber matrix ring to just shy of the specimen boundary along the X direction. Furthermore, the plot of the Mohr-Coulomb Criterion in the YZ plane at $Z = 0.45$ mm as shown in Figure 132 indicates that the cavitation is occurring between approximately $Y = 0.045$ mm to approximately $Y = 0.19$ mm. whereas, the distribution in the XZ plane at $Z = 0.45$ mm shown in Figure 133 indicates the cavitation is located approximately between $X = 0.65$ mm to 1.02 mm. The locations indicated from the FEM results correlate very well with the experimental observation listed in Table 49. Thus it can be concluded that the critical value for the Mohr-Coulomb Criterion at matrix cavitation initiation is 64.14 MPa.

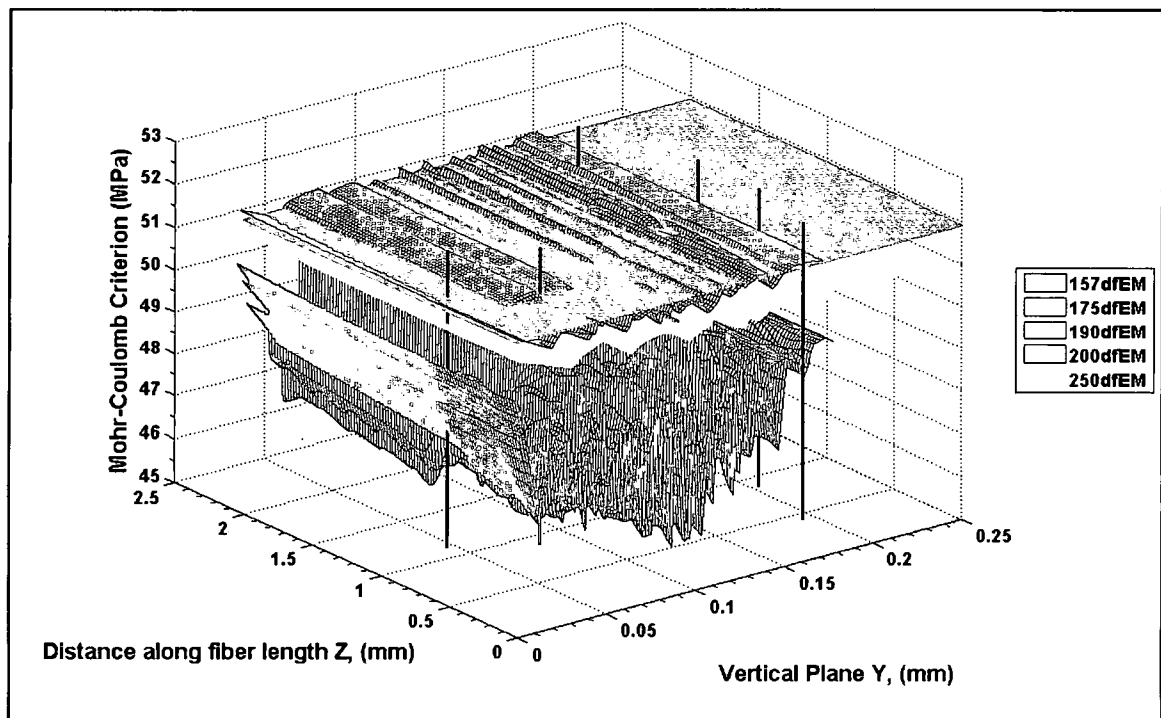


Figure 129: Mohr-Coulomb Criterion distribution in the YZ plane of the EM region of the FEM with each specimen's cavitation location

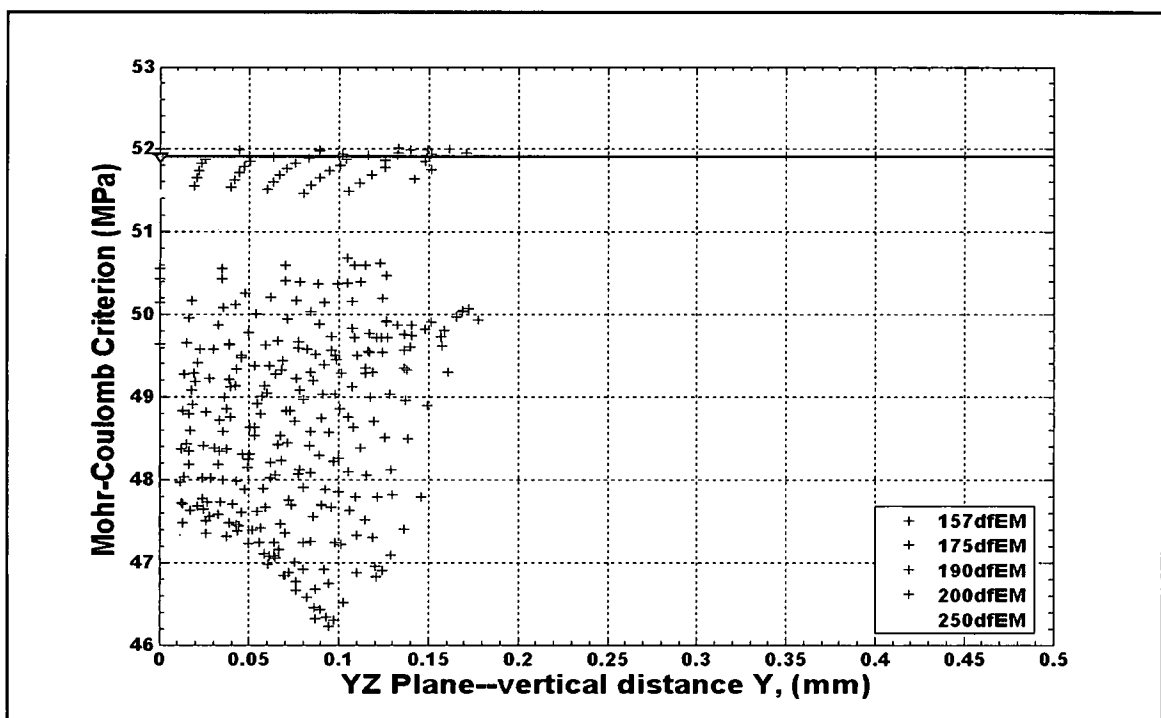


Figure 130: Mohr-Coulomb Criterion distribution in the YZ plane at $Z = 0$ of the EM region of the FEM

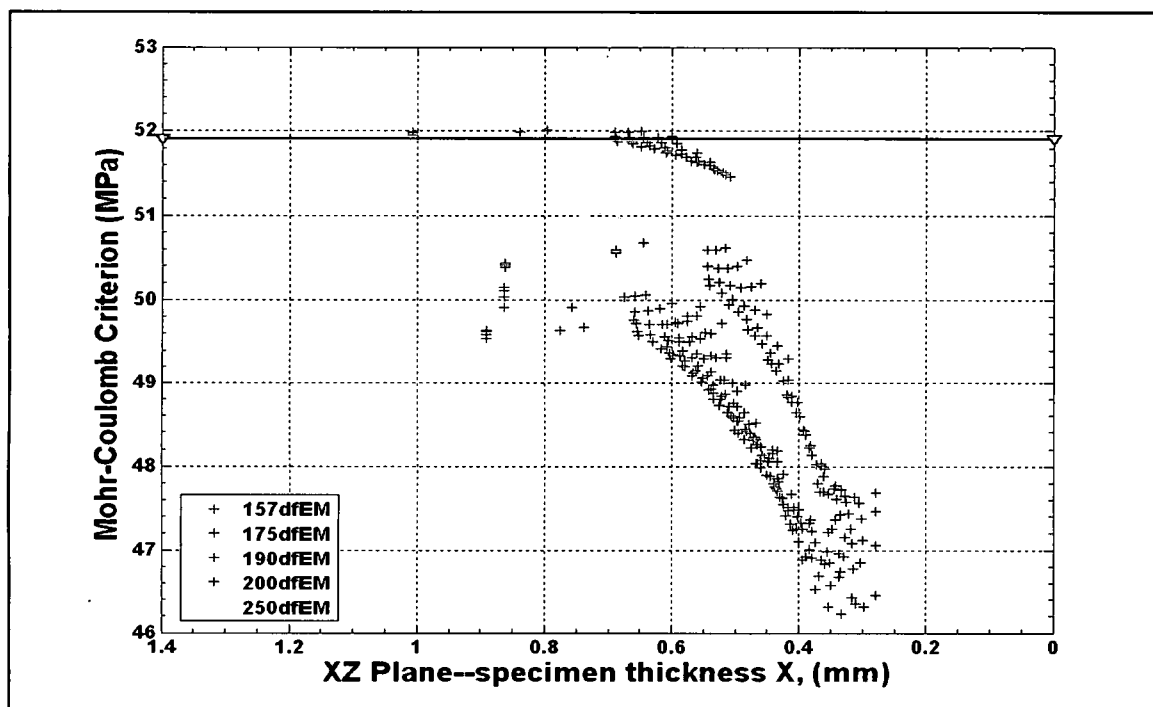


Figure 131: Mohr-Coulomb Criterion distribution in the XZ plane along the specimen thickness at $Z = 0$ of the EM region of the FEM

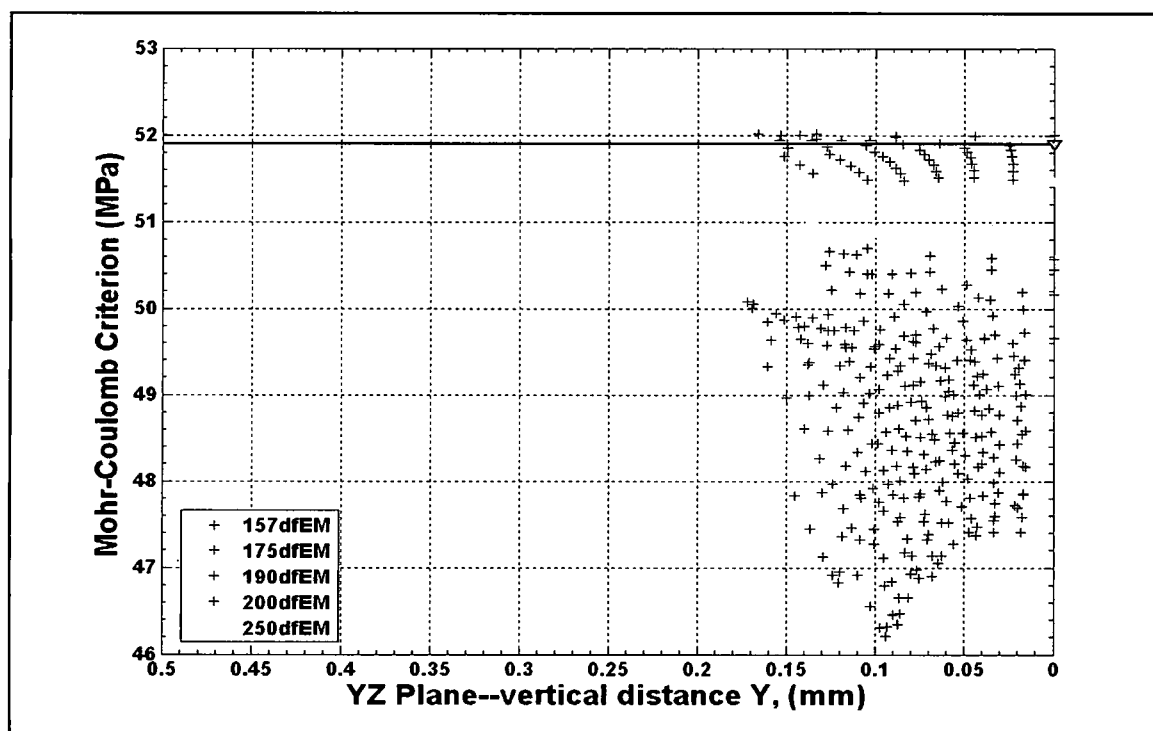


Figure 132: Mohr-Coulomb Criterion distribution in the YZ plane at $Z = 0.45$ of the EM region of the FEM

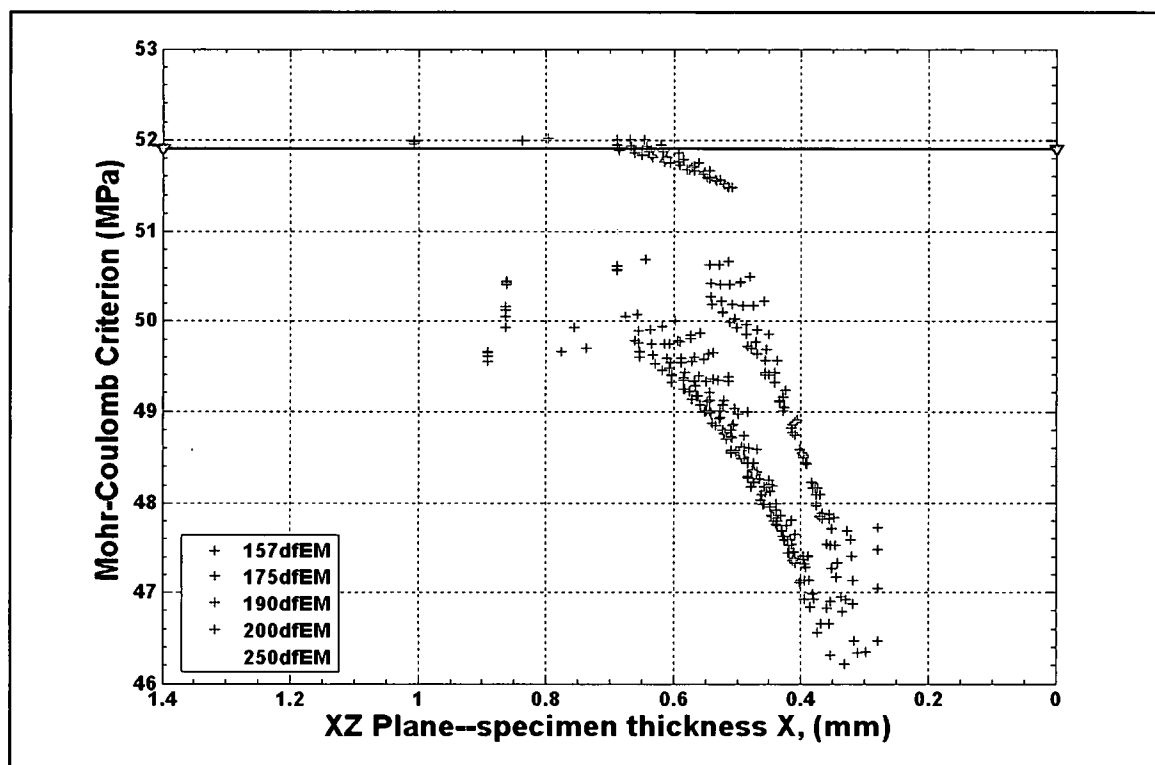


Figure 133: Mohr-Coulomb Criterion distribution in the XZ plane along the specimen thickness at $Z = 0.45$ of the EM region of the FEM

Matrix Failure Initiation Criterion – Summary. The Mohr-Coulomb Criterion more accurately predicts the octahedral shear stress than the Modified Tresca Criterion predicts the critical shear stress from the tensile and compression test results. In addition, the $2.0d_f$ fiber spacing group has the maximum magnitude of the Mohr-Coulomb Criterion than do all the other fiber spacing groups correlating the observed matrix cavitation developed in the cruciform specimens subjected to a uniaxial tensile stress. Furthermore, the cavitation locations determined by the finite element analysis evaluation of the Mohr-Coulomb Criterion correlates very well with the locations of the of the first failure cavitation determined via photomicrograph analysis for each specimen in the $2.0d_f$ fiber spacing group. Consequently, based upon the preceding discussion the Mohr-Coulomb criterion as presented by equation (6) very accurately describes the matrix cavitation occurring in the cruciform specimen have a fiber spacing at $2.0d_f$. The Mohr-Coulomb failure criterion critical magnitude is 64.14 MPa. Thus, when the Mohr-Coulomb criterion evaluates greater than 64.14

MPa matrix cavitation occurs. Due to the fact that the Mohr-Coulomb criterion best describes matrix cavitation there is strong evidence that the matrix cavitation failure mechanism occurring in the cruciform specimens has a strong shear bias.

Residual Stress Impact to the Matrix Failure Initiation Criterion. In much the same way the matrix cure residual stresses affects the fiber-matrix debonding criterion, Figure 134 shows the residual stress effect on the Mohr-Coulomb criterion in the EM regions of the cruciform. By only incorporating the stresses due to the mechanical loading, other fiber spacing groups are shown exceeding the critical Mohr-Coulomb value just like in the 828/D-230 matrix system. Figure 134 shows portions of the $1.57d_f$ and $2.5d_f$ fiber spacing groups exceeding the critical value indicating that matrix cavitation occurred in these specimens. The experimental results clearly have shown that the $1.57d_f$ and $2.5d_f$ fiber spacing groups did not exhibit matrix cavitation. Adjusting the critical value in the same manner as stated previously would cause the critical value to exceed its standard deviation. This would indicate that the criterion does not adequately describe the experimentally observed cavitation that occurred in the $2.0d_f$ fiber spacing specimen.

The implications of not including the matrix cure shrinkage residual stresses in evaluating the matrix failure criterion would have disastrous consequences. It would lead to either selecting an erroneous existing criterion or developing a criterion that dramatically over predicts the stress state in which matrix cavitation occurs. Recall that the critical value was determined by the FEA at the locations of matrix cavitation from the experimental observations. Determining the Mohr-Coulomb critical value in the same manner using only the internal stress state due mechanical loading only would lead to a critical value far above when cavitation would actually occur. The consequences would be that the composite part would have micro-cracking due to matrix cavitation much sooner than the analysis would predict. This in turn would lead to final failure far sooner than the global failure criterion predicted.

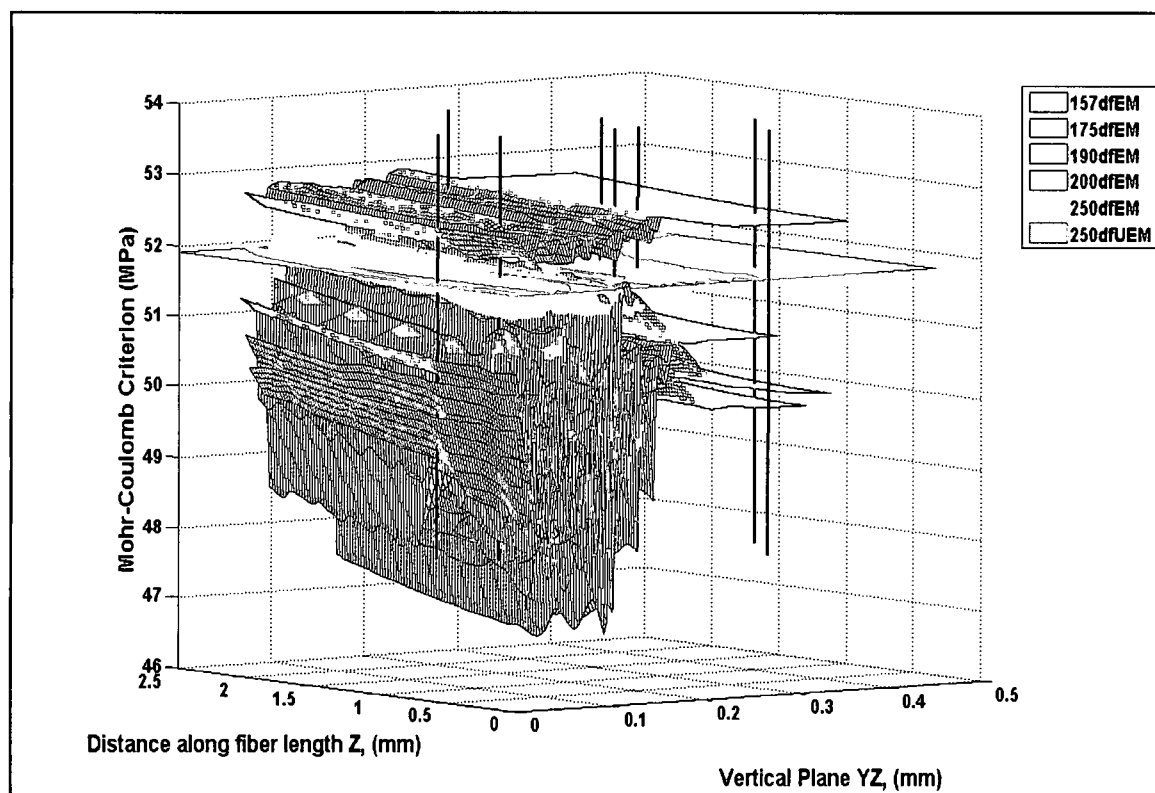


Figure 134: Matrix cure shrinkage residual stress effect on the Mohr-Coulomb matrix failure criterion showing results from the mechanical load only

Constants *A* and *B* of the Fiber-Matrix Debond Criterion

It has been shown that a linear debond initiation criterion having the general form shown in equation (2) accurately predicts the experimentally observed fiber-matrix debonds in both matrix systems. The constants ***A*** and ***B*** of equation (2) can be considered a function of the adhesion properties of the matrix systems utilized in this work. Constant ***A*** would then be a function of the normal interface strength between the fiber and matrix while constant ***B*** a function of the interfacial shear strength between the fiber and matrix. While the single fiber cruciform specimen tests were conducted, it was shown in the parametric study that the specimen thickness has an effect on the maximum radial and shear stresses. It was also shown that the fiber-matrix debond initiates under a combination of radial and shear stresses acting at the fiber-matrix interface for the single and multi-fiber cruciform specimens. Thus to effectively evaluate

the limiting radial or normal strength and the shear strength at the fiber-matrix interface both have to be evaluated separately. Literature search results reveal a rather large body of work investigating the adhesion bond strength of many adhesive and adherents. Most work involved the investigation and measurement of the "bond strength" which comprised the shear strength of the adhesive to the adherent. Many factors influence the bond strength such as the surface chemistry of the adherent, the chemistry of the adhesive, the surface preparation of the adherent, incorporation of spew fillets at the adherent edges, the thickness of the bond line and testing technique only to name a few. For this work several papers were found that dealt not only with the "bond strength" but also the "peel strength", the adhesive strength normal to the surface of the adherent, bonded to stainless steel, steel wires and using two part room temperature cured and high temperature cured epoxy adhesives [4-9].

Hobbiebrunken et al., [9], used a three point bend test varying the lamina stacking sequence between all 90° plies and various 90_x/0_y/90_x layups, where x and y are the number of plies to measure the radial and shear strengths of the fiber-matrix interface. The matrix materials were a high temperature cured epoxy and a room temperature cured epoxy, although the room temperature cured system was post cured at 80° C for 24 h. A unidirectional carbon fiber fabric consisting of 96% carbon fibers and 4% E-glass fibers as rovings was utilized as the individual plies. An oxidization treatment and a 1.25% epoxy sizing were used to optimize the matrix adhesion to the fibers. The experiments were observed in-situ via a SEM. The experimental results yielded an average radial stress of 123.4 MPa and shear stress of 43.4 MPa for the high temperature epoxy at the fiber-matrix interface. The room temperature cured epoxy results were an average radial stress and shear stress of 102.5 MPa and 41.0 MPa respectively at the fiber-matrix interface.

Seo et al., [7], utilized a high temperature cured two part epoxy bonded between 304L stainless steel adherents to measure the adhesive tensile strength of a butt joint. A dog-bone shaped stainless steel specimen was bonded together at the center of the gage section and tested in tension. The surface preparation of the specimens consisted of uniformly polishing the

bonded area with 400 grit SiC sandpaper. The experimental results varied from 30.83 MPa to 45.83 MPa depending upon the cross-sectional area of the dog-bone tensile specimen.

Zhandarov et al., [8], measured the bond strength between the fibers and matrix via fiber fragmentation and pull-out techniques. The bond strength in this case was defined as the interfacial shear strength of the fiber and matrix. It was not clear what matrix system was used but both carbon and E-glass fibers were employed in their experimental work. It was also not clear if any fiber sizing were used. The calculated local adhesive bond strength from the experimental results ranged from 97.7 MPa for the carbon fibers and 66.9 MPa for the E-glass fibers.

de Morais et al., [6], utilized AISI 304 stainless steel with a two-part room temperature cured and a two-part high temperature cured epoxy adhesives. Tests included butt joints and single-lap joints for the investigation of the bond strength. The butt joint test utilized bars having diameters of 20 mm and 30 mm while the single-lap joint tests used a constant width but varied the adhesive thickness and lap length. The stainless steel surfaces were sanded with 220 grade emery paper and cleaned and degreased with acetone. The butt joint test results were very consistent ranging from 32 MPa to 34 MPa for the high temperature system and from 33 MPa to 34 MPa for the room temperature system using the 20 mm and 30mm adherents respectively. These consistent test results indicate that alignment was not an issue, however, the test method suffers from high free edge stress concentrations and it does not appear that any fracture surface analysis was utilized to see if the failure was adhesive or cohesive in nature. The single-lap shear test results for the smallest lap shear area ranged from 26 MPa – 30 MPa for the high temperature system and from 17 MPa – 31 MPa for the room temperature system when a spew was present. When adhesive spew was not present the smallest lap shear test area results were 19 MPa – 28 MPa and 15 MPa – 29 MPa for the high and room temperature system respectively. De Morais also utilized a thick-adherent shear test similar to ISO 11003-2 for both epoxy systems. These test results were 34 MPa for the high temperature system and 33 MPa for the room temperature system.

Gorbatkina et al., [5], used a two-part epoxy and stainless steel wires to measure the bond strength between the matrix and wire. Again, the bond strength in this work is defined as the

interfacial shear strength between the epoxy and wire. The pull-out test method utilized involved a constant radius disk of epoxy having a varying thickness with a 150 μm diameter stainless steel wire positioned in the center of the disk axially aligned with the varying thickness and normal to the radius. The wire was surfaced cleaned with an acetone wash, rinsed with water and dried prior to casting the epoxy disk. The interfacial shear strengths ranged from 30 MPa to 130 MPa depending upon the bonded area.

Bradford et al., [4], utilized single fiber fragmentation tests to evaluate the adhesion level of various fiber surface treatments. Using the EPON 828 resin system with AS-4 carbon fibers, single fiber fragmentation specimens were manufactured via a special process to ensure high optical quality. Once the matrix material was placed into the specimens molds it was cured at 80° C for 2 h then post cured at 150° C for 2 hours. The interfacial shear strength was calculated using experimental results and ranged from 23.3 MPa for the unsized fiber surface treatment to 53.0 MPa for a custom surface treatment, which was the focus to this paper.

Table 50 summarizes the literature search data found to be most applicable in determining the validity of the constants **A** and **B** of the linear debond criterion. Although only one reference, [3], used one of the same epoxies utilized in this present body of work, EPON 828; Table 50 provides a range of epoxy adhesive strengths. The most common bond property, normally called the bond strength, is the interfacial shear strength and many experimental techniques were used to measure it. The least and probably the most difficult bond property is the normal or peel strength. The butt joint is the most common testing technique but it suffers from free edge stress concentrations, as previously stated, that affect the true strength of the adhesive. The notation used in Table 50 is defines as follows; HT is high temperature, RT is room temperature, CF is carbon fiber and THK is a thick bond line.

Table 50: Literature Search Summary of Interfacial Adhesive Normal and Shear Stress

Results for Various Two-Part Epoxy Systems

Stress	Reference					
	3	4	5	6	7	8
Interfacial Normal (MPa)	-	-	HT: 32 – 34	30.8 – 45.8	-	HT: 123.4
			RT: 33 – 34			RT: 102.4
Interfacial Shear (MPa)	23.3 – 53.0	30 – 130	HT: 19 – 30	-	CF: 97.7	HT: 43.4
			RT: 15 – 31		E-glass: 66.9	RT: 41.0
			THK HT: 34			
			THK RT: 33			

The experimentally observed debond, in both matrix systems, is a physical separation of the matrix from the fiber. Thus, the debond can be considered as severing the molecular bonds between the two materials at the fiber-matrix interface. Considering the constants **A** and **B** in the linear debond criterion and that the ultimate strength of the resin system is the actual failure of the neat matrix severing the molecular bonds, equation (14) represents that interfacial normal strength of the adhesion between the matrix and fiber. In a similar manner, equation (15) represents the interfacial shear strength of the adhesion between the matrix and fiber, although the torsion tests failed to fracture the specimens. In both cases the constants **A** and **B** can actually be considered the stress concentration factors relating the neat resin strength to that of the adhesion between the two materials.

$$\sigma_{ut} = A(\sigma_{at}) \quad (14)$$

$$\tau_y = B(\tau_{as}) \quad (15)$$

σ_{at} is the adhesive tensile strength, τ_{as} is the adhesive shear strength at the fiber-matrix interface, σ_{ut} is the ultimate tensile strength of the neat resin system and τ_y shear yield stress.

Using the σ_{ut} of the 828/D-230 and 862/W matrix systems, see Appendix A, and employing the respective constant **A** values of each matrix system results in σ_{at} of 15.92 MPa and 16.31 MPa for the 828/D-230 and 862/W systems respectively. These values are roughly half of those listed in Table 50. However, the experimental methods utilized to measure the tensile strength are very suspect, as previously mentioned. In addition, the adhesive system is not what

was used in this investigation and was most likely tailored to meet those specific use requirements of the referenced study. Although in two referenced studies the adherents are stainless steel, the experimental results appear to be dependent upon the length parameter of the test method used.

Although the torsion specimens never fractured during testing, the experiment was stopped after 1½ to 2 complete rotations when it was apparent that the maximum yield stress had been achieved. Thus the yield stress under torsion will be used to calculate the adhesive shear strength, τ_{as} , in the same manner as the adhesive tensile strength, σ_{at} . Referring to Appendix A for the shear yield strength of the 828/D-230 and 862/W matrix systems and employing the respective constant **B** values, results in the adhesive shear strength of 34.29 MPa for the 828 system and 34.04 MPa for the 862 system. These values appear to be quite in line with those listed in Table 50. Although the adhesive material systems tested are not the same as the matrix materials used in this work, the results specifically referenced in [5] where the adherents are stainless steel are very close. Even in references [3] and [5] employing carbon fibers in a high temperature cured epoxy system; the un-sized fiber interfacial adhesive shear strength is 23.3 MPa and 43.4 MPa for references [3] and [5] respectively. These are also quite in line with the calculated interfacial adhesive shear strength of the linear debonding criterion developed in this work for both matrix systems.

In summary, the calculated interfacial shear adhesive strength in both material systems of the linear debond criterion developed in this work falls in line with relevant referenced data giving confidence that the constant **B** is a function of the shear adhesion of the material system. Although not much data exists for the interfacial tensile or normal strength, its calculated value for the material systems utilized in this study is within the realm of the above relevant referenced values. This gives assurance that the constant A of the linear debond criterion is also a function of the tensile or normal adhesion strength of the material systems utilized in this body of work.

Summary

This chapter thoroughly evaluated the fiber-matrix debond initiation criterion and the matrix failure initiation criterion for each matrix system. It was shown that a linear debond criterion predicted the observed fiber-matrix debond limits quite well for each matrix system. For the 828/D-230 system the linear debond criterion, as shown in equation (3) is:

$$\frac{11}{3} \left(\frac{\sigma_r}{\sigma_{yt}} \right) + \frac{4}{3} \left(\frac{\tau_{r\theta}}{\tau_y} \right) \geq 1 \quad \text{828/D-230 Linear Debond Criterion}$$

The 862/W matrix system linear debond criterion, as shown in equation (13) is:

$$4.62 \left(\frac{\sigma_r}{\sigma_{yt}} \right) + 1.95 \left(\frac{\tau_{r\theta}}{\tau_y} \right) \geq 1 \quad \text{862/W Linear Debond Criterion}$$

Two matrix failure criteria were evaluated by independent neat resin tests. The independent test evaluations conducted in each material system resulted in the Mohr-Coulomb criterion best predicting the neat resin test results of both systems. It was then shown that the Mohr-Coulomb criterion best describe the experimentally observed matrix cavitation for both the 828/D-230 and 862/W matrix systems. The Mohr-Coulomb criterion, as shown in equation (6) is:

$$\tau_{oct} = \tau_o - \mu \sigma_{on} \quad \text{828/D-230 and 862/W Matrix Failure Criterion}$$

References

1. Wisnom, M.R., *Micromechanical modeling of the transverse tensile ductility of unidirectional silicon carbide/6061 aluminum*. Journal of Composites Technology and Research, 1992. **14**(2): p. 61-69.
2. Nadai, A., *Theory of Flow and Fracture of Solids*. 2 ed. Engineering Societies Monographs, ed. R.H. Phelps. Vol. 1. 1931, New York: McGraw-Hill Book Company. 572.
3. Tschoegl, N.W., *Failure Surfaces in Principal Stress Space*. Polymer Science Symposium, 1971. **32**: p. 239 - 267.
4. Bradford, D., K. Lease, and P.M.A. Sherwood, *Evaluation of the Effect of a Custom Fiber Surface Treatment on the Adhesion Level in a Polymer-Based Composite Using the Single Fragmentation Test*. Journal of Composite Technology & Research, 2000. **22**(2): p. 53 - 59.
5. Gorbatkina, Y.A. and V.G. Ivanova-Mumjjeva, *Variance of adhesive strength and fracture mechanism of fiber/matrix joints*. International Journal of Adhesion & Adhesives, 2001. **21**: p. 41 - 48.
6. Morais, A.B.d., et al., *Strength of epoxy adhesive-bonded stainless-steel joints*. International Journal of Adhesion & Adhesives, 2007. **27**: p. 679 - 686.
7. Seo, D.W. and J.K. Lim, *Tensile, bending and shear strength distributions of adhesive-bonded butt joint specimens*. Composites Science and Technology, 2005. **65**: p. 1421 - 1427.
8. Zhandarov, S.F. and E.V. Pisanova, *The Local Bond Strength and its Determination by Fragmentation and Pull-Out Tests*. Composites Science and Technology, 1997. **57**: p. 957 - 964.
9. Hobbiebrunken, T., et al., *Evaluation of interfacial strength in CF/epoxies using FEM and in-situ experiments*. Composites Part A: Applied Science and Manufacturing, 2006. **2006**: p. 2248 - 2256.

CHAPTER V

CONCLUSIONS AND RECOMMENDATIONS

Summary

The object of this research has been to develop a failure criterion for composite materials when loaded transverse to the fiber direction. A series of experiments and finite element analysis was done to investigate failure initiation in a model composite system. Using a novel experimental technique employing a cross shaped specimen with multiple fibers in two transparent epoxy systems, the failure initiation mechanisms were observed in-situ while being recorded for further analysis. Finite element models of the samples were developed to determine the internal state of stress at failure initiation. Failure initiation criterion, identified through the literature search, for each failure mechanism were carefully selected that best described the physics of the observed first damage.

Two transparent epoxy systems were utilized, a room temperature cured Epon 828 resin having the Jeffamine D-230 curing agent and a high temperature cured Epon 862 resin having the EPI-CURE W curing agent. The 828/D-230 epoxy system had a linear response to loading, whereas the 862/W system had highly non-linear response to loading. Both systems were fully characterized, see Appendix A, and the results were used as input parameters into the FEM. The residual stresses from the matrix cure kinetics were fully characterized, see Appendix B, and also utilized in the FEM. The residual FEA results were then coupled with the mechanical loading FEA results for a detailed examination of the internal stress state at first failure in the cruciform specimen.

A cruciform shaped specimen geometry was used with five stainless steel fibers each 0.36 mm in diameter. The fibers were arranged such that four fibers were placed at the corners of

a square and the fifth fiber was placed at the intersection of the face diagonals. The spacing of the corner fibers was varied as a function of the fiber diameter. In both epoxy systems the fiber spacing tested were the $1.57d_f$, $1.75d_f$, $1.90d_f$, $2.0d_f$, $2.5d_f$, $6.0d_f$ and the SF. For the 828/D-230 system, an extra fiber spacing was tested at $1.84d_f$. The specimens were machined flat and polished to a glassy surface smoothness ensuring the highest quality optical transparency. The specimen thickness varied as a function of fiber spacing but the amount of epoxy cover over the corner fibers was held constant to the best capability of the equipment utilized in this work.

All specimens were tested in tension utilizing the novel reflected light method and two high resolution video tape cameras. The reflected light method utilizes light reflected from internal failures due to the applied load. Once a fiber-matrix debond develops or a matrix cavitation occurs, the fracture surface of the damage caused the light passing through the specimen to reflect differently. Two high resolution cameras captured all failure initiation and growth to final failure under the applied load. One camera utilized a high magnification lens focused on an approximate 4 mm by 2 mm area at the center of the specimen while the other focused on an area approximately 12 mm by 5 mm encompassing the width of the loading arm. An image subtraction technique was developed and utilized to capture all damage initiation that occurred in each specimen. Failure initiation was defined as the first instance of damage occurring within the specimen detected by the high resolution cameras and was manifested as either a fiber-matrix debond or matrix cavitation. Since the cruciform tests were videotaped in-situ, the applied load at first damage was known. The far-field stress could then be calculated based upon the specimen dimensions and input into the FEM. The fracture surface of the cruciform specimens was investigated via an SEM. A sample set from all fiber spacing groups tested was used in the fracture surface analysis. All test results are presented in Chapter 2.

A solid finite element model of the cruciform specimen was utilized for this work to determine the internal stresses at failure initiation. The ANSYS commercial finite element code employing solid brick elements and the symmetrical fiber arrangement was used to analyze the different fiber spacing groups tested in both matrix systems. The cruciform FEM explicitly modeled the matrix and fiber assuming perfect adhesion between the two materials. The model

was sub-divided into regions for evaluation of the criterion describing the observed fiber-matrix debond and matrix cavitation initiation. The analytical results are presented in Chapter 3 with further details contained in Appendix C. The interfacial stress analysis results are presented in Appendix D.

Conclusions

Experimental results show that a fiber-matrix debond was the first failure mechanism occurring in the cruciform specimens having a fiber spacing of $1.57d_f$, $1.9d_f$, $2.0d_f$, $2.5d_f$, $6.0d_f$ and SF in the 828/D-230 matrix and at the $1.57d_f$, $1.75d_f$, $1.9d_f$, $2.5d_f$, $6.0d_f$ and SF fiber spacing in the 862/W. The fiber-matrix debonds occurred in either the northern or southern hemisphere of the corner fiber and appeared to be centered in the vicinity of the fiber pole, which is in the direction of the applied load. No preference to fiber-matrix debonding initiation with respect to the interior or exterior of the fiber group exists at fiber spacings larger than $1.9d_f$ in the 828/D-230 matrix and above $2.5d_f$ in the 862/W matrix. The preference for debond initiation in the 862/W matrix was shown to be within the interior of the fiber group below the $2.0d_f$ spacing. Although only one spacing groups exists below the $1.75d_f$ group in the 828/D-230 matrix, the debond initiation preference was interior to the fiber group. SEM fracture analysis of debond initiated specimens in both matrix systems show features indicating a shear stress present at final fracture.

Matrix cavitation was experimentally observed as the first failure mechanism at the fiber spacing of $1.75d_f$ and $1.84d_f$ in the 828/D-230 matrix and at the $2.0d_f$ fiber spacing in the 862/W matrix. Multiple cavitations occurred in each matrix system and were followed by fiber-matrix debonding in the vast majority of cases. The cavitations appear bounded within the specimen by an approximate fiber diameter from the corner fiber interface and occurred randomly after initiation. SEM fracture analysis of the cavitation initiated specimens show features on the fracture surface unique to these specimens and thus can be concluded are the micro-voids produced by the tri-axial stress state. These features also show a shear stress presence contributing to the development of the micro-voids.

The analytical results show that a linear debond criterion correlates extremely well with the experimental results in both matrix systems. The criterion expressed in equation (1) for both material systems, predicts the fiber spacing groups that exhibit fiber-matrix debonding as their failure initiation mechanism. For the 828/D-230 matrix $A = \frac{11}{3}$ and $B = \frac{4}{3}$ and for the 862/W matrix $A = 4.62$ and $B = 1.95$.

$$A \left(\frac{\sigma_r}{\sigma_{yt}} \right) + B \left(\frac{\tau_{r\theta}}{\tau_y} \right) \geq 1 \quad (1)$$

Furthermore, the criterion correlates very well to the observed debond limits measured from the photomicrographs taken from the videotaped experiments. Finally, the fiber-matrix debond criterion accurately reflects the compressive stress state at the fiber equator as shown in Chapter 4. Consequently, the fiber-matrix debond criterion developed in this work correctly describes the state of stress, with a high degree of confidence, within the cruciform specimens exhibiting fiber-matrix debonding as their failure initiation mechanism in both matrix systems investigated.

The constants **A** and **B** can be considered as a function of the radial and shear adhesion strength of the fiber-matrix interface respectively. The literature search had revealed ranges for the tensile or normal interfacial adhesion and the shear interfacial adhesion strengths for various two-part epoxy systems. It was found that the tensile interfacial adhesion strength can be expressed as a function of the neat resin ultimate strength as shown in equation (3) and that the shear interfacial adhesion strength can be expressed as a function of the shear yield strength as shown in equation (4). The calculated shear interfacial adhesion strengths were in line with literature search findings.

$$\sigma_{ut} = A(\sigma_{at}) \quad (3)$$

$$\tau_y = B(\tau_{as}) \quad (4)$$

However, the tensile interfacial adhesion strength is far more dependent on the testing technique and specifically formulated for tensile or normal stresses in bonded joints that practically no data with the material systems used in this study were found. Nevertheless, these findings give confidence that the constants are not strictly curve fitting parameters but functions of the adhesion of the matrix to the fibers.

For the matrix failure it was determined that the Mohr-Coulomb failure criterion, as shown in equation (5), best described the observed matrix cavitation occurring in both matrix systems. Details of the criteria evaluation are presented in Chapter 4 and Appendix E. Summarizing the analytical results show that the fiber spacing exhibiting matrix cavitation, in both matrix systems, had the highest Mohr-Coulomb stress correlating with the experimental observations. Thus, the Mohr-Coulomb predicted the fiber spacing of both matrix systems exhibiting matrix cavitation. In addition, the matrix failure initiation criterion predicted the locations within the cruciform specimen where the matrix cavitation initiation was observed.

$$\tau_{oct} = \tau_o - \mu\sigma_{on} \quad (5)$$

Furthermore, the criterion predicts the maximum magnitudes at the location of the cavitations measured from the experimental observations. Consequently, based upon the combination of the observed experimental results coupled with the analytical results, the Mohr-Coulomb correctly describes the stress state in the cruciform specimens exhibiting the matrix failure initiation.

Future Work Recommendations

The research presented here utilized a model composite system coupling experimental observations with analytical results to arrive at two failure initiation criteria that correctly describe

the experimental observations. This work provides a solid foundation from which to explore several factors involving both the experimental and analytical work to further enhance the failure initiation criterion conclusions. The recommendations that follow will improve the technical significance of understanding the micromechanics of failure initiation under a general state of stress.

Varying Fiber Diameters and Size Effects

As stated earlier, varying fiber diameters are pervasive in composite materials. In this research only one fiber diameter was used in the model composite cruciform specimens. Stainless steel fibers are available down to 0.127 mm in diameter at 0.025 mm increments and could be used within the five fiber configuration. Utilizing various fiber diameters in the same spacing arrangement would allow investigation of a more realistic composite cross section. This in turn would cause smaller regions of the specimen to have higher stresses due to the constraining effect of the stiffer fibers. These high stress regions would be comparable to a smaller fiber spacing sample but contained within one specimen. Thus a direct comparison between failure initiation mechanisms as a function of fiber spacing occurring within the same specimen can be made. The analytical results of this configuration would indicate the stress distribution occurring within the composite revealing the failure mode. Predictions could then be made of an actual composite cross-section as to the potential location of the failure initiation site as a possible quality control measure.

Possible size effects relative to the diameter of the fiber would be addressed by the use of the smaller diameter fibers. The smallest diameter available stainless steel fibers are in line with SiC fibers having diameters between 0.10 mm to 0.14 mm, although typical carbon fiber diameters are on the order of 0.004 mm to 0.008 mm.

Interfacial Adhesion Strength Determination

Literature search results reveal that the constants A and B of the linear debond criterion are functions of the interfacial adhesion of the material system. The actual bond strengths of the fiber-

matrix interface normal to the fiber surface and in shear at the fiber surface would need determined by experimentation and analysis. These findings would greatly enhance the physical meaning of the linear debond criterion developed in this body of work.

Fiber Arrangement Change

A five fiber arrangement where four fibers are placed at the corners of a square and the fifth fiber was placed at the intersection of the face diagonals was utilized for all of the multi-fiber cruciform specimens. Moving the center fiber where it would be in line with the top and bottom corner fibers or in line with the two top corner fibers would investigate fiber rich and resin rich areas within the same specimen. It would also emulate real fiber arrangements typically found in composite materials.

Realistic Composite Fibers

This work used stainless steel fibers for several reasons; for the ease of handling that allowed precise placement in distinct fiber arrangements and for the isotropic stiffness much greater than the softer matrix material emulating realistic composite materials. The isotropic stiffness reduced the number of FEM parameters was also a benefit for use. The use of SiC fibers or glass fibers that are used in more typical composite materials could be employed in the cruciform specimens to further advance the failure criteria developed presented here. With the use of glass fibers, light could possibly be transmitted through the fiber complementing the reflected light experimental method. Transmitting light through the fiber would possibly enhance the detection of the fiber-matrix debond pinpointing its location along the fiber-matrix interface. The current methodology could not pinpoint the exact location of the fiber-matrix debond initiation location.

Additional Camera to Cover Fifth Fiber and Opposite Side of Specimen

Two cameras were used for all cruciform experiments, except for the single fiber experimental runs. The second camera, for the majority of tests, was positioned above the

primary camera such that the width of the loading arm and four fibers were in the field of view. The fibers in the field of view were the near-field top and bottom corner fibers, the top far-field corner fiber and the center fiber. The far-field bottom corner fiber was not in any field of view of any video recorded experimental runs. A third camera positioned on the opposite side of the specimen in a similar manner to the second camera but from the bottom would cover the missing fiber. It would also capture any missed matrix cavitation that could be the explanation to the variance in the far-field stress at first damage in the 862/W 2.0d_f specimens. It would also cover the top corner fiber of that side, the bottom corner fiber on the opposite side as well as the center fiber. Recall that most of the 1.9d_f specimens in the 862/W matrix system debonded internally to the fiber grouping or unobservable due to the fiber position. The third camera would ensure all areas of the cruciform are observed for failure initiation detection. The third camera would greatly enhance the observation of damage initiation when utilizing varying fiber diameters and different fiber arrangements.

Polarized Light

The use of polarized light with the reflected light method would enhance the detection of matrix cavitation or fiber-matrix debonding better than using conventional white light. The lighting of the specimen was critical in getting the correct background shading so that the matrix cavitation would be clearly evident without the use of the image subtraction technique. Polarized light could also pinpoint the location along the fiber-matrix of the debond initiation.

Failure Initiation Surface Investigation

All specimens were tested to specimen fracture. This was done for two reasons; to determine the load at first failure and for future work in failure propagation. An alternative method for determining the load at first failure was also used as a check and was determined to be as effective as using the specimen fracture. Therefore, the first failure can be developed, the location determined and the test stopped. The specimen can then be sectioned at the failure initiation location and the site investigated utilizing a SEM. The fracture surface analysis combine with the

in-situ observation of the first damage mechanism would aid greatly in determining the stress state at failure initiation.

Increase FEM Mesh Density

Although the mesh sensitivity study showed no benefit of a more dense mesh than the one used for this work at the fiber-matrix interface, the study did not mesh the matrix portion of the model to the same level as the fiber portion at the interface. In addition, the mesh density along the fiber length was not as dense as that near the specimen center. Thus, an increased mesh density could possibly reveal a larger separation between the criteria describing the two different observed failure mechanisms.

Final Recommendation

This work focused on failure initiation, although all specimens were tested to complete failure. Since all tests were videotaped to final fracture that information is useful for further investigation on failure propagation. The fiber-matrix debond propagation can be measured both axially along the fiber length and circumferentially. The far-field stress due to the applied load is easily determined at every step of the failure propagation. Fracture analysis could be employed in the analysis of the fiber-matrix debond propagation. The influence of multiple matrix cavitation locations on the stress state and how the cavitations coalesce and propagate to the fiber-matrix interface can also be studied.

An additional recommendation would be to use the Air Force Research Laboratory in-house analysis code, the B-spline Analysis Method (BSAM), to investigate the stress state at the first damage load. Confirming the state of stress with another analysis code would give confidence to the analytical results used in this work.

APPENDIX A

MATERIALS CHARACTERIZATION

This section describes the effort characterizing the materials used in this work. Two transparent material systems are used to investigate the failure of unidirectional model composites when loaded transverse to the direction of the fiber. The model composite system consists of a clear room temperature cured two part epoxy system and an amber colored high temperature cured two part epoxy system. Isotropic stainless steel wires were used for the fibers. The stainless steel wires having a diameter of 0.36 mm are large enough to handle for precise placement in the cruciform specimen to represent resin-rich and/or fiber-rich areas common to commercially produced composites. In addition, multi-fiber cruciform specimens can be made to a specific fiber spacing in order to validate the failure criteria by providing multiple points on the failure surface. The stainless steel wires also reflect light well, enabling the use of the reflected light method, to capture the fiber-matrix debond initiation and aide in the capture of the cavitation of the matrix at or near the fiber-matrix interface. They are also known to bond to the resins systems being used in this work without the use of any surface treatments or sizing.

Room Temperature Cured 828/D-230 Epoxy System

Elastic Modulus Property Determination

The room temperature cured epoxy is the Epon 828 bisphenol A epoxy resin supplied by Miller-Stephenson Chemical Company. The curing agent used for the Epon 828 is the Jeffamine D-230 polyoxypropylenediamine supplied by the Huntsville Chemical Company. The mixing ratio used for the epoxy is 35% by weight Jeffamine D-230 to the Epon 828. It cures in approximately

seven days and has a linearly elastic response to loading. Fourteen dog-bone tensile tests were conducted to determine the modulus of elasticity. Seven specimens were tested on the Sintech tensile testing machine and seven were tested on the MTS tensile testing machine. This was done for several reasons; first to check the grips on the Sintech machine to see if the wedge grips interfere in any way with testing compared to pneumatic grips of the MTS testing system and secondly, to investigate any differences in the material response to the speed of the test. Both tests used a ½ inch extensometer to measure the strain. The test speed utilizing the MTS system is approximately 3 times faster than the Sintech system.

All specimens were prepared identically. The 828 epoxy was carefully placed into a plastic beaker zeroed on a scale capable of measuring its weight to the nearest 1/100 of a gram. The proper amount of D-230 curing agent was calculated as 35% of the weight of the 828 epoxy and placed into the same beaker. The resin system was vigorously hand stirred for minimum of 5 minutes with a tongue depressor then placed in a vacuum to de-bulk. Once all entrained air was removed from the matrix, de-bulked from between 30 to 45 minutes, it was carefully poured into the dog-bone specimen RTV molds so not to create air bubbles. Prior to pouring the matrix into the molds, the molds were cleaned with acetone and blown dry. They were then placed into aluminum pans. Once the molds were sufficiently filled with epoxy system, the aluminum pans were covered with aluminum foil and allowed to cure. If air bubbles formed as a consequence of pouring the matrix into the mold they were carefully brought to the surface using a stainless steel fiber. Once cured a minimum of 3 days the specimens were removed from the molds and prepared for testing.

Test preparation consisted of hand sanding to a uniform thickness using 240 grit sandpaper. Once the uniform thickness was achieved they were further sanded using 320, 400 and 600 grit sandpaper removing any surface marks from initial preparation. Careful attention was paid to the specimens' edges not to mark, gouge, or score the specimens in any way creating a possible surface flaw that would lead to premature failure. All specimens were kept in a sealed plastic bag once removed from the mold to testing. Previous work with this particular resin system yielded difference mechanical properties if tested before a full two weeks of cure.

Consequently the specimens were tested between 6 and 8 weeks after casting. Figure 135 shows a photograph of a typical 828/D-230 dog-bone specimen. The total length is approximately 113.3 mm, the grip width is approximately 19.0 mm, the gage width is approximately 6.48mm and the gage length is approximately 32.0 mm. The thickness depends upon the individual specimen preparation.

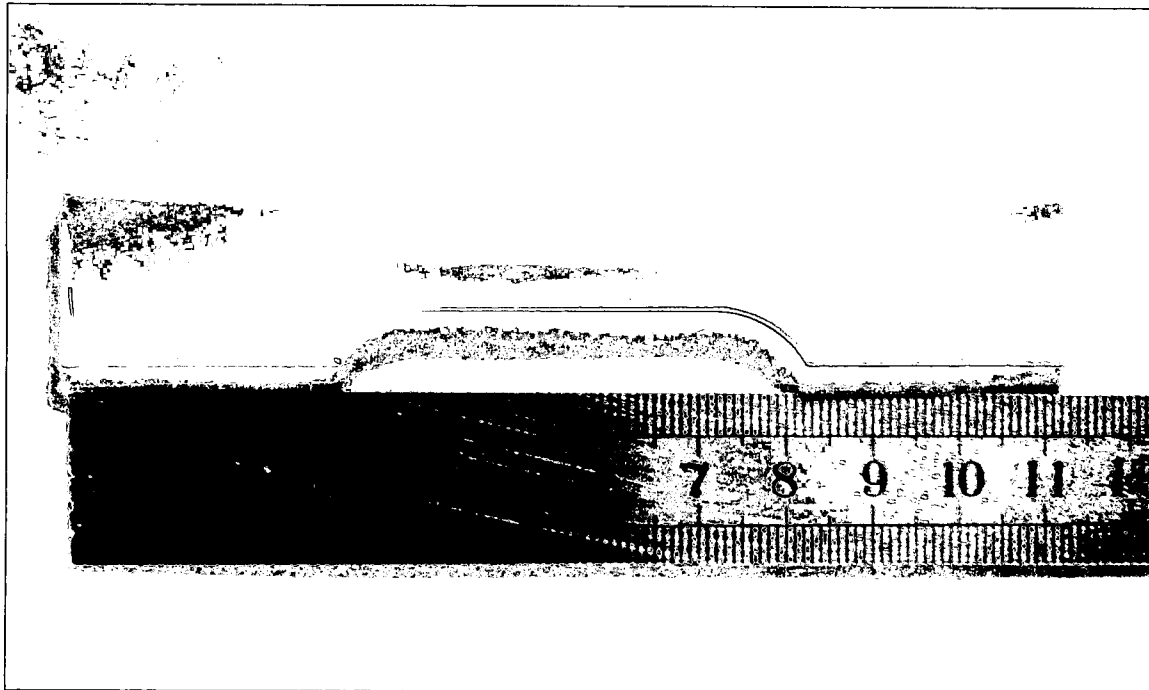


Figure 135: 828/D-230 typical neat resin dog bone specimen

Figure 136 shows the stress vs. strain curve for each test. The stress strain plot is linear for the bottom 2/3 of the curve, and then deviates very slightly until maximum stress. There is practically no spread in the data between the two testing machines used for this study as indicated by the small variance in the slope of the curves and at the maximum stress of each specimen. Table 51 list the maximum stress, maximum strain, ultimate stress, ultimate strain and the elastic modulus of all specimens tested. The average modulus between the MTS system and the Sintech system differs by less than 3%. This small variance is also shown in Figure 135 by the fact that the individual stress strain plots are practically the same. The elastic modulus is

calculated by plotting a straight line on the stress vs. strain curve of each specimen test and picking off the actual stress strain point very close to the origin and at the point where the curve begins to deviate from linearity. This method is compared to plotting an Excel trend line for the entire set of data with a Y-axis intercept selected by the program and with the Y-axis intercept equal to zero. The percent difference between the hand calculation and that of the Excel program for the program chosen Y-axis intercept and Y-axis intercept equal to zero is 8% and 5% respectively. Consequently there is no statistical significant difference between the elastic modulus determinations thus the hand calculated values will be used.

Table 51 also shows that the difference between the average maximum stresses between the testing systems is 2.3%, whereas the difference between the averages of the ultimate stress is 3.4%. For this work the maximum stress is defined as the maximum stress experienced during the tensile test, the peak load divided by the cross sectional area, whereas the ultimate stress is that stress at failure of the specimen. Figure 136 also shows a small variance between the maximum stresses of each specimen. The percentage difference between the two systems for average maximum strain is slightly above 8% and for the average ultimate strain is slightly greater than 33%. The maximum strain and ultimate strain are the strains corresponding to the maximum stress and ultimate stress defined above. The difference between the maximum strain and ultimate strain is clearly shown in Figure 136. There is a small variance for the maximum strain; however, the ultimate strain exhibits a rather large variance. This is attributed to several specimens failing in a rather ductile manner, indicated by the long tail of their stress strain curve after peak stress is achieved. The maximum and ultimate strain percentages are a bit

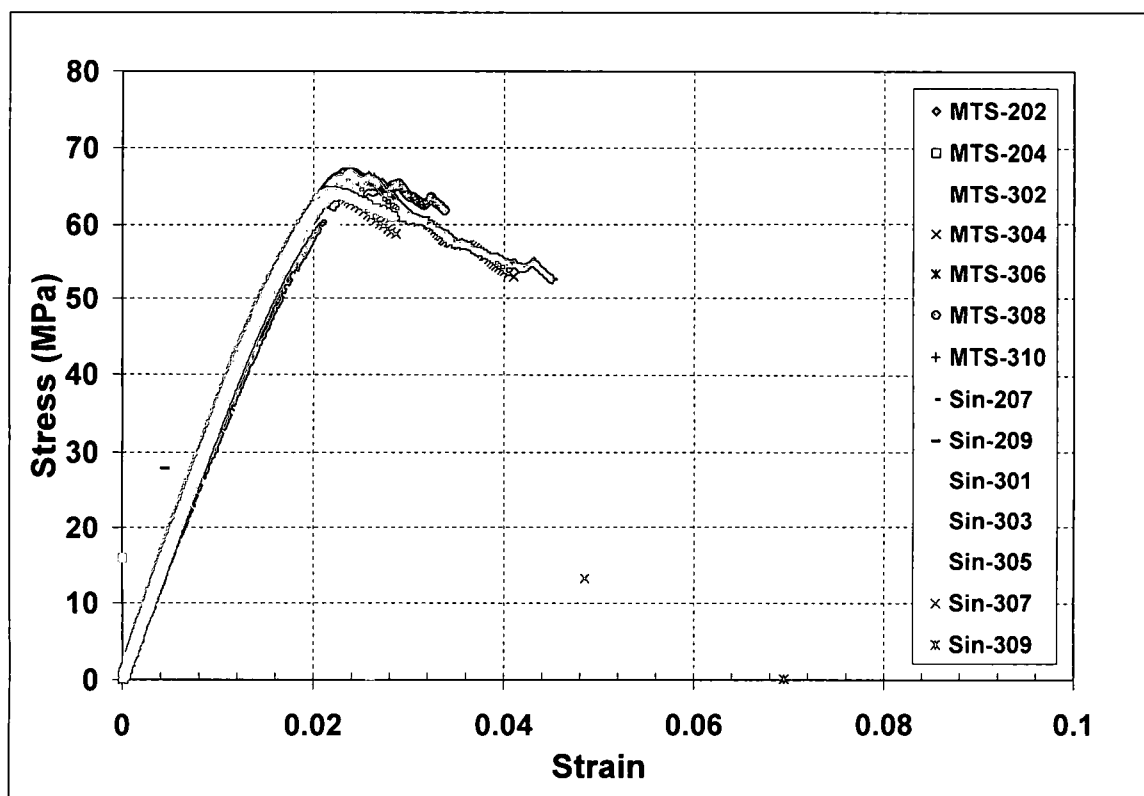


Figure 136: 828/D-230 Stress vs. Strain curve

misleading since the maximum strain measured by the Sintech system is 0.02 and by the MTS system 0.022, whereas the ultimate strain measured by the Sintech is 0.022 and by the MTS is 0.03. Consequently small differences in these values can lead to large percentage differences.

Previous experience and noted in the literature are mechanical property differences between batches of the same resin system. Due to this fact two different batches of the resin system were used to investigate any differences in mechanical properties between batches. The batches are designated by the 200 series and the 300 series specimen numbers listed in Table 51 and shown in Figure 136. The 200 series has a small sample size but nonetheless the percent difference between testing systems for the maximum stress is 10.1%, however, for the 300 series having a much greater sample size its percent difference for the maximum stress is just under 7%. For the maximum strain the percent differences between the testing systems are closer together and are 13% and 13.6% for the 200 series specimens and 300 series specimens

respectively. Comparing the modulus between testing systems for the 200 series specimens reveals a percent difference of less than 1% and for the 300 series a percent difference of 3.5%.

From the neat resin tensile test results it can be concluded that the 828/D-230 material system has no statistically significant response to testing speed and therefore viscoelastic effects will not be encountered in this work. In addition no differences in mechanical properties are expected between different manufacture batches of epoxy and curing agent. Furthermore, the specimen average values for maximum stress, maximum strain, ultimate stress, ultimate strain and elastic modulus will be used where appropriate through out this work.

Table 51: 828/D-230 specimen maximum stress and strain, ultimate stress and strain, and linear modulus

828 Specimen	Max Stress (MPa)	Max Strain	Ultimate Stress (MPa)	Ultimate Strain	Elastic Modulus (MPa)
Sin-207	58.0271	0.0186	58.0271	0.0186	3431.1025
Sin-209	58.9909	0.0190	58.9909	0.0190	3571.8033
Sin-301	57.1171	0.0176	57.1171	0.0176	3513.0253
Sin-303	64.2063	0.0219	60.9811	0.0283	3573.7409
Sin-305	61.6366	0.0211	59.0635	0.0228	3481.8940
Sin-307	64.0447	0.0224	58.7374	0.0287	3391.2768
Sin-309	62.8803	0.0207	62.8803	0.0207	3442.4704
Sin-AVG	60.9861	0.0202	59.3996	0.0222	3486.4733
MTS-202	57.7783	0.0182	57.7783	0.0182	3538.9768
MTS-204	47.4614	0.0145	47.4614	0.0145	3427.4778
MTS-302	67.0606	0.0238	65.5631	0.0270	3406.4476
MTS-304	65.2693	0.0231	52.8436	0.0410	3343.1315
MTS-306	65.6731	0.0253	64.1589	0.0284	3148.5561
MTS-308	66.7493	0.0241	61.8395	0.0338	3457.1769
MTS-310	66.7556	0.0238	52.5835	0.0452	3430.9851
MTS-AVG	62.3925	0.0218	57.4612	0.0297	3393.2503
DELTA	1.4064	0.0016	1.9385	0.0075	93.2231
% DELTA	2.3061	8.0980	3.3735	33.6009	2.7473
Specimen AVG (σ)	61.6893 (5.4167)	0.0210 (0.0031)	58.4304 (4.8869)	0.0260 (0.0091)	3439.8618 (107.6261)

Compression Property Determination

Compression tests were conducted to determine the compression strength of the 828/D-230 resin system. Tests were performed on rectangular specimens cut from 254 mm by 254 mm neat resin plates. The specimen's dimensions are approximately 134.6 mm by 25.4 mm by 3.6 mm. Based upon preliminary tests in which specimens were tested using the Northrop test fixture and the combined loading compression (CLC) fixture at gage lengths of 2.54 mm and 3.81 mm, the decision was made to use the CLC fixture since the Northrop fixture specimens exhibited signs of buckling. Compression tests at gage lengths of 2.54 mm and 3.81 mm using the CLC fixture indicated that no buckling had occurred; another preliminary test using the CLC fixture increasing the gage length to 7.62 mm was conducted. In this test strain gages were mounted on each side of the specimen for indications of specimen buckling. Test results confirmed no buckling occurred during the test at the 7.62 mm gage length and that the elastic modulus calculated from this test data, 3.26 GPa, agreed with that obtained from the tensile tests, 3.44 GPa, described above. This gives further evidence that the compression tests using the CLC fixture are being conducted properly and that the data obtained is good, however, no failure has occurred in the tests conducted using the 2.54 mm, 3.81 mm and the 7.62 mm gage lengths. Failure in this case is being defined as the specimen crushing into two pieces. In the third preliminary CLC compression test using strain gages at a gage length of 7.62 mm, the strain gages popped off at a compressive load of 7,409 N due to the formation of a local band of resin extruding from each side to the specimen. Load was continually applied until approximately 88,960 N hoping to fail the specimen, however, it never failed but exhibited a thin compression band of resin extruding from both sides approximately 2 mm. Further inspection of the local kink band revealed cross hatching within the thin compression band indicating a presence of shear stresses. Stress strain plots of the preliminary CLC tests having gage lengths of 2.54 mm, 3.81 mm and 7.62 mm showed that either a knee or "local" maximum occurs during the test.

Having concluded that compression specimens using the CLC test fixture do not buckle, seven specimens were tested at a gage length of 3.81 mm and seven at a gage length of 7.62 mm. Of the specimens tested at the 3.81 mm gage length, 3 of the seven, specimens 1, 3 and 5,

exhibited the local maximum in their load-displacement plots, another 3, specimens 2, 4 and 6, exhibited the knee in their load-displacement plots and the last one, specimen 7, was strain gage but due to the small gage length no usable data was collected. Of the specimens tested at the 7.62 mm gage length all specimens exhibited the local maximum in their load-displacement plots. Two of the seven specimens, 2-1a and 2-7, had strain gages applied to both sides of the specimens. Specimen 2-1a was loaded until its strain gage popped off at a load 7,562 N then it was retested until it reached its maximum load of 13,878 N. Specimen 2-7 strain gage popped off at a load of 8,718 N and it too was retested until reaching a maximum load of 8,798 N. Both of these specimens exhibited local maximum in their load-displacement plots upon retesting. Based upon these results failure is now defined as the load at which the local maximum is achieved in the load-displacement curve of each specimen. Additionally since the specimens utilizing the CLC fixture exhibited no buckling at all gage lengths tested, the compression strength will be determined by the combined data of the specimens exhibiting local maximums in their load-displacement curves at the gage lengths of 3.81 mm and 7.62 mm. The compression stresses vs. cross head displacement test results are shown in Figure 137. All specimens exhibited cross hatching within the deformation band indicating a shear stress presence as part of the failure mechanism.

In Figure 137 specimens 1, 3 and 5 were tested using a gage length of 3.81 mm, while the rest of the specimens used a gage length of 7.62 mm. As shown in Figure 137 the local maximum stress for all specimens has little variance therefore no significant differences exist between the different gage lengths. Table 52 lists the specimen dimensions, maximum load and corresponding maximum strength.

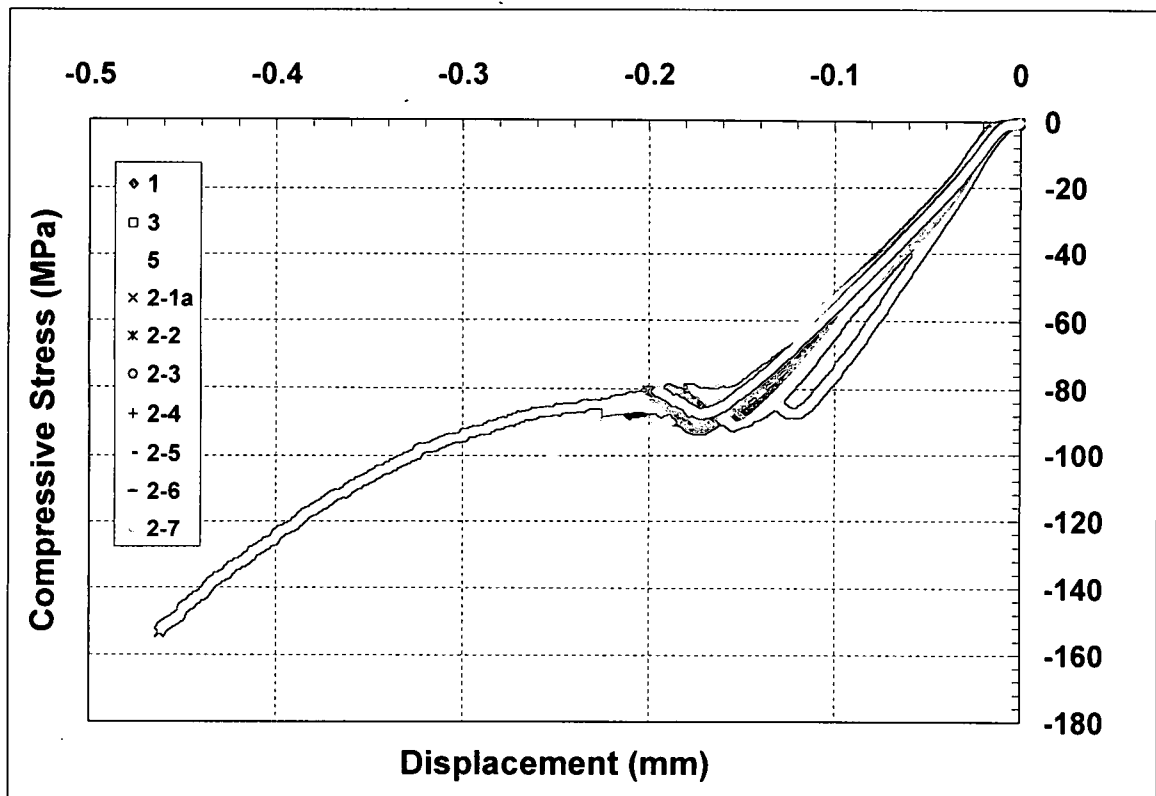


Figure 137: 828/D-230 Compression Stress vs. Displacement curve

Table 52: Compression specimen dimensions, maximum load and maximum strength

Specimen	w (mm)	t (mm)	X-sec Area (mm ²)	Maximum load (N)	Maximum Strength (MPa)
1	25.12	3.35	84.15	7468.10	88.75
3	25.15	3.25	81.74	7377.85	90.26
5	25.17	4.06	102.19	9429.49	92.27
2-1a	24.87	3.61	89.78	7846.18	87.39
2-2	24.69	3.73	92.09	8524.95	92.57
2-3	24.77	3.51	86.94	7815.31	89.89
2-4	24.71	3.84	94.89	8681.78	91.49
2-5	24.87	3.4	84.56	7464.98	89.46
2-6	24.61	3.3	81.21	7421.58	91.39
2-7	24.94	4.04	100.76	8797.92	87.32
AVG (σ)				8092.81 (677.20)	90.08 (1.78)

The standard deviations listed for the maximum load and corresponding maximum stress as listed in Table 52 confirm that shown in Figure 137 that there exist little variance thus the different gage length used for specimens 1, 3 and 5 have no statistical significance compared to

the specimens using the larger gage length. Consequently, the maximum compression strength of 90.08 MPa will be used for the 828/D-230 resin system

Poisson's Ratio Determination

Ten dog-bone specimens were tested for the determination of Poisson's Ratio of the 828/D-230 resin system. The dog-bone specimens were made in the exact same manner as described in the Elastic Modulus Property Determination section above, except that prior to testing strain gages were bonded within the gage length to each side of the specimen. One gage was bonded to measure the axial strain and the other was bonded to measure the transverse strain. Poisson's ratio is calculated by taking the ratio of transverse strain to axial strain. From these tests Poisson's ratio can be determined directly. Figure 138 shows the test results of the ten specimens.

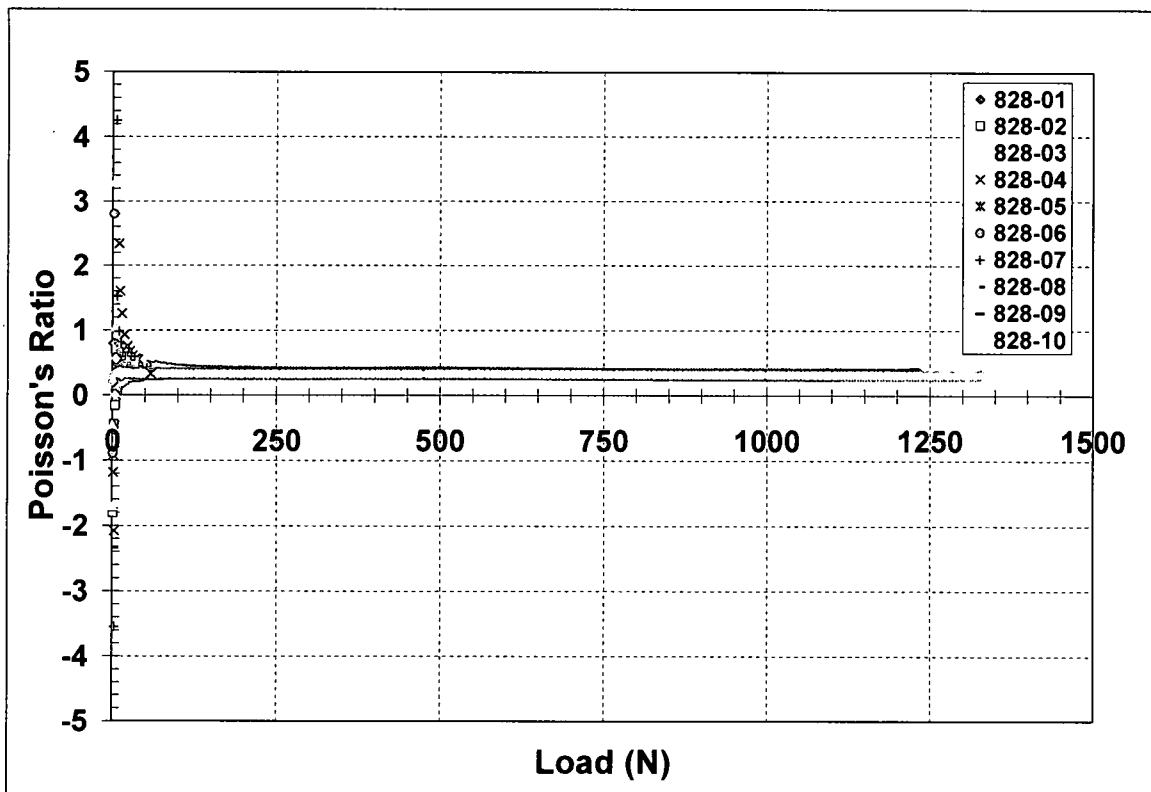


Figure 138: 828/D-230 Poisson's Ratio vs. load curve

As shown in Figure 138 the 828/D-230 resin system has a constant Poisson ratio over the entire loading range exhibiting very little scatter. The scatter shown between 0N to approximately 60N is attributed to the data collection system employed and is representative of system noise. Table 53 gives the individual specimen results. The average 828/D-230 specimen Poisson Ratio is 0.337 with a standard deviation of 0.0164.

Table 53: 828/D-230 Poisson's ratio specimen results

Specimen	Poisson's Ratio
828-01	0.3437
828-02	0.3384
828-03	0.3683
828-04	0.3639
828-05	0.3168
828-06	0.3281
828-07	0.3253
828-08	0.3226
828-09	0.3328
828-10	0.3277
AVG	0.3367
STDEV	0.0164

Coefficient of Thermal Expansion

Two 828/D-230 neat resin dog-bone specimens were tested to determine the coefficient of thermal expansion (CTE) of the matrix system. Two strain gages were bonded to each specimen, one on each side opposite each other, and then the temperature was increased from room temperature, 25.6° C (78° F) to 87.8° C (190° F). The temperature was incremented 3.3° C (6° F) per minute in steps of 22.2° C (40° F) with a 20 minute hold per step then decreased in the same manner. The material strain due to the temperature changes was recorded every minute. Figure 139 shows the results of the CTE of each specimen. The 828/D-230 resin system has a very linear CTE as exhibited by the plot and by the high multiple coefficient of determination, R^2 , of the trend lines plotted on Figure 139. The multiple coefficient of determination is the ratio of explained variation to the total variation thus a high value or an R^2 of close to one indicates very little variation. The average CTE of the 828/D-230 matrix system is 55.67 $\mu\epsilon/^\circ\text{C}$.

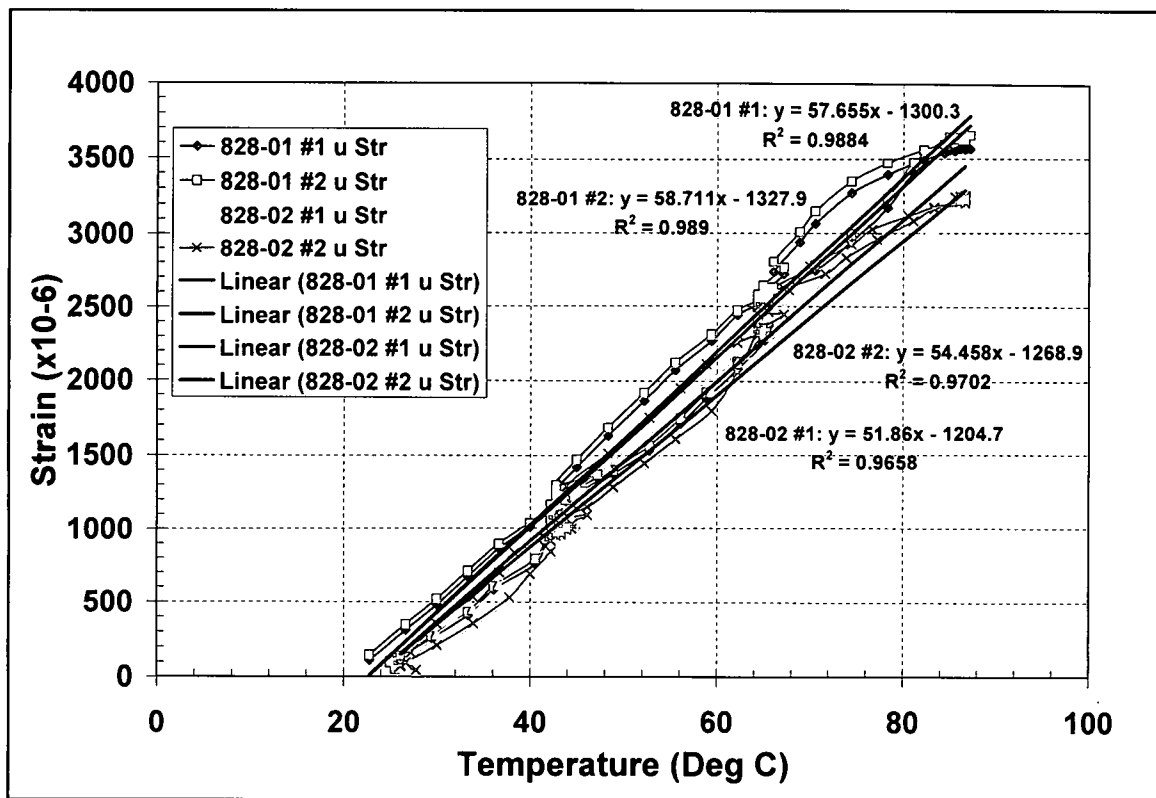


Figure 139: 828/D-230 strain vs. temperature plot with trend lines determining the CTE

Moisture uptake investigation

All material systems are susceptible to strains from moisture uptake. Typically the strains are swelling strains as a direct result of moisture gain and can have an effect on the failure initiation of the material system. To measure the moisture uptake of the 828/D-230 matrix system thirteen specimens were cut from a cast plate. Five specimens were cut into 25.4 mm (1 inch) squares labeled A specimens, four specimens were cut into 50.8 mm (2.0 inch) squares, labeled B specimens and four specimens were cut into 63.5 mm (2.5 inch) squares, labeled C specimens. All thirteen specimens were dried in an oven for 48 hours at 38°C (100°F) then weighed. The width, length and thickness of the B specimens and C specimens were measure after drying the specimens as shown in Figure 140. The A specimens were deemed too small to determine any swelling strains but were included in all moisture gain measurements. Once weighed and measured at the dry condition the specimens were then placed into a humidity

chamber at 60°C (140°F) and 90% relative humidity until saturated. Weight and specimen measurements were taken at 4, 8, and 24 hour increments once placed into the humidity chamber. Afterwards, for the first week, the weight and specimen measurements were taken daily at the same time of initial placement into the humidity chamber. After the first week into the humidity chamber weights and measurements were taken weekly until saturated.

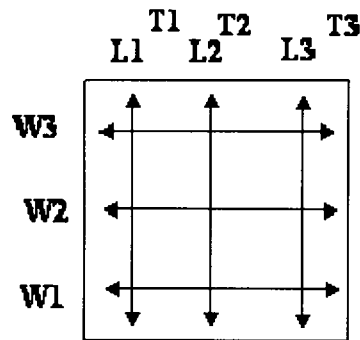


Figure 140: 828/D-230 moisture measurement diagram

Figure 141 is the plot of percent weight gain vs. time for all specimens in the investigation. Saturation is achieved after the 30th day at 3.03% weight gain. The dip at day 35 is due to power disruption to the equipment over a weekend; however, it did not affect the test. Figure 142 shows the average strain measured in the length and width directions as indicated in Figure 140. Even though saturation is achieved after 30 days the swelling seemed to continue as indicated in Figure 142. However after the 50th day the measurements began to oscillate, therefore we concluded the testing. Table 54 shows the average percent strain measurements of specimen B and C length and width. Once saturation was achieved the average percent strain for specimen B is 0.703% whereas the average percent strain for specimen C is 0.634%. The discrepancy is attributed to the difference in specimen dimensions. Consequently we can conclude that the 828/D-230 matrix system has a 0.669% swelling strain at saturation.

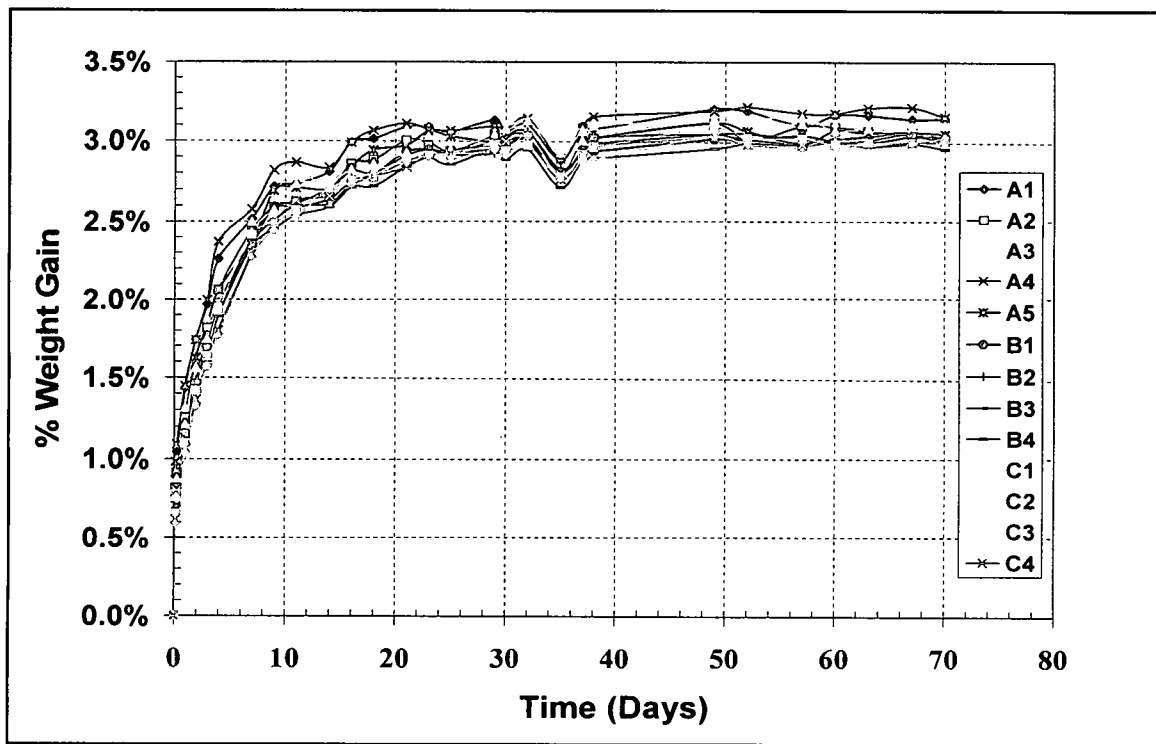


Figure 141: 828/D-230 Percent moisture gain

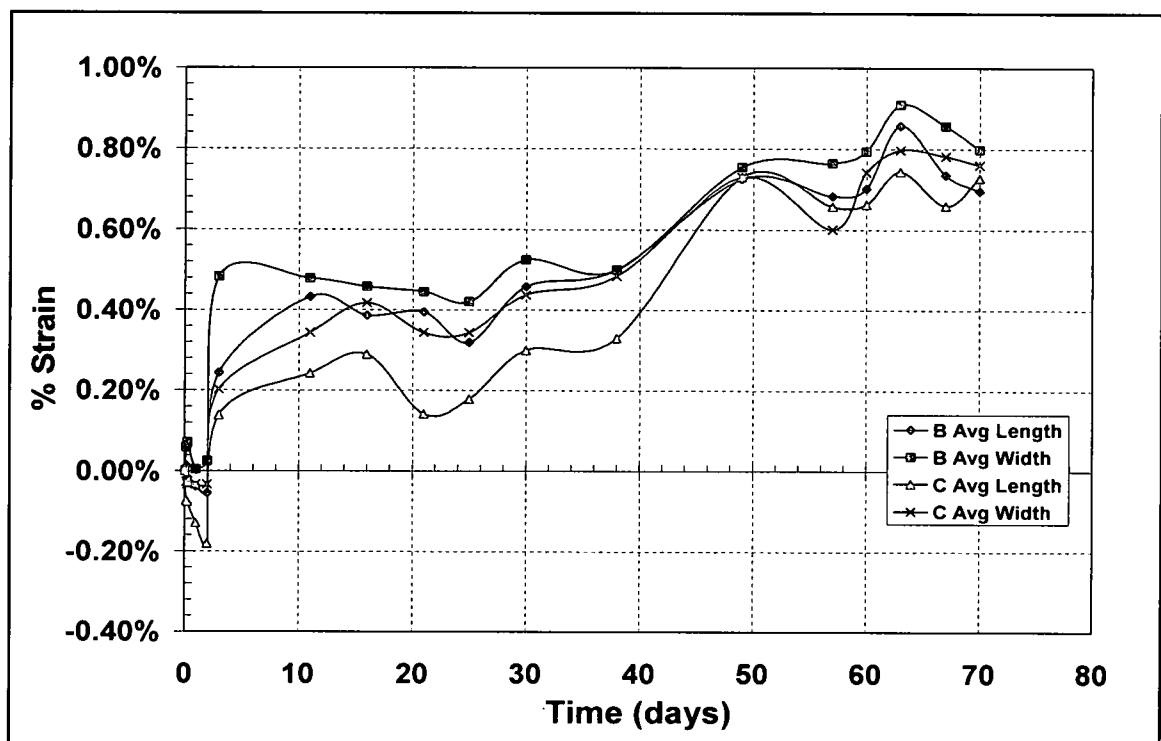


Figure 142: 828/D-230 Average Length and Width moisture strain

Table 54: 828/D-230 measured average length and width percent moisture strain

Days	Specimen B		Specimen C	
	Average Length	Average Width	Average Length	Average Width
0	0.000%	0.000%	0.000%	0.000%
0.17	0.012%	0.059%	-0.074%	-0.027%
0.27	-0.017%	0.071%	-0.077%	-0.034%
1	-0.038%	0.004%	-0.13%	-0.034%
2	-0.055%	0.025%	-0.181%	-0.034%
3	0.244%	0.483%	0.138%	0.202%
11	0.433%	0.479%	0.242%	0.343%
16	0.387%	0.458%	0.289%	0.417%
21	0.395%	0.445%	0.141%	0.343%
25	0.319%	0.420%	0.178%	0.343%
30	0.458%	0.525%	0.299%	0.437%
38	0.500%	0.500%	0.330%	0.484%
49	0.725%	0.754%	0.730%	0.730%
57	0.683%	0.764%	0.657%	0.600%
60	0.702%	0.794%	0.662%	0.742%
63	0.857%	0.909%	0.743%	0.797%
67	0.735%	0.857%	0.659%	0.782%
70	0.695%	0.798%	0.728%	0.760%
Saturated AVG	0.703%		0.634%	
	(days 49 thru 70)		(days 49 thru 70)	
Overall AVG	0.669% (days 49 thru 70)			

High Temperature Cured 862/W Epoxy System

Elastic Modulus Property Determination

The Epon 862 epoxy uses the EPI-CURE W curing agent in a ratio of 79.4% 862 to 20.6% W. It is an amber bisphenol-F/epichlorohydrin resin cured with an aromatic amine at 121.1° C (250°F) for 2 hours and post cured at 176.7° C (350°F) for 2 hours. Twelve dog-bone tensile tests were conducted to determine the modulus of elasticity. Six specimens were tested on the Sintech tensile testing machine and six were tested on the MTS tensile testing machine. This was done for the same reasons stated above for the 828/D-230 resin system; first to check the grips on the Sintech machine to see if the wedge grips interfere in any way with testing compared to pneumatic grips of the MTS testing system and secondly, to investigate any differences in the material response to the speed of the test. Both tests used a ½ inch

extensometer to measure the strain. The test speed utilizing the MTS system is approximately 3 times faster than the Sintech system. In addition, two different batches of the material was used to investigate any batch variations in mechanical properties.

All test specimens were prepared identically and in the same manner as stated above for the 828/D-230 matrix system, except that for this system the cure regime is 2 hours at 121.1° C (250°F) and 2 hours at 176.7° C (350°F). Sample preparation for testing is also identical to that described above for the 828/D-230 system. However, since this system has a high temperature cure with a high temperature post-cure testing can be begin as soon as the specimens are satisfactorily prepared. Figure 143 shows a photograph of a typical 862/W dog-bone specimen. The total length is approximately 113.3 mm, the grip width is approximately 19.0 mm, the gage width is approximately 6.48mm and the gage length is approximately 32.0 mm. The thickness depends upon the individual specimen preparation.

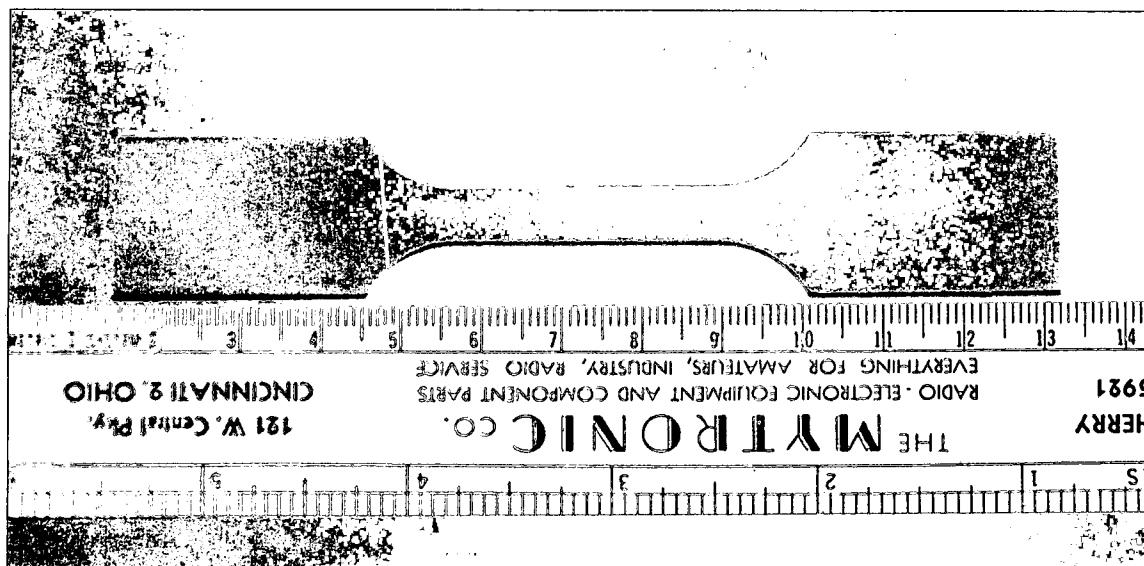


Figure 143: 862/W typical neat resin dog bone specimen

Figure 144 shows the stress vs. strain curve for each test. The stress strain plot is linear for approximately the bottom half of the curve, and then begins deviating gradually reaching a maximum stress at approximately 7.5% strain before ultimate stress is reached from 9% to 13% strain. There is practically no spread in the data between the two testing machines used for this

study as indicated by the small variance in the slope of the curves and at the maximum stress of each specimen.

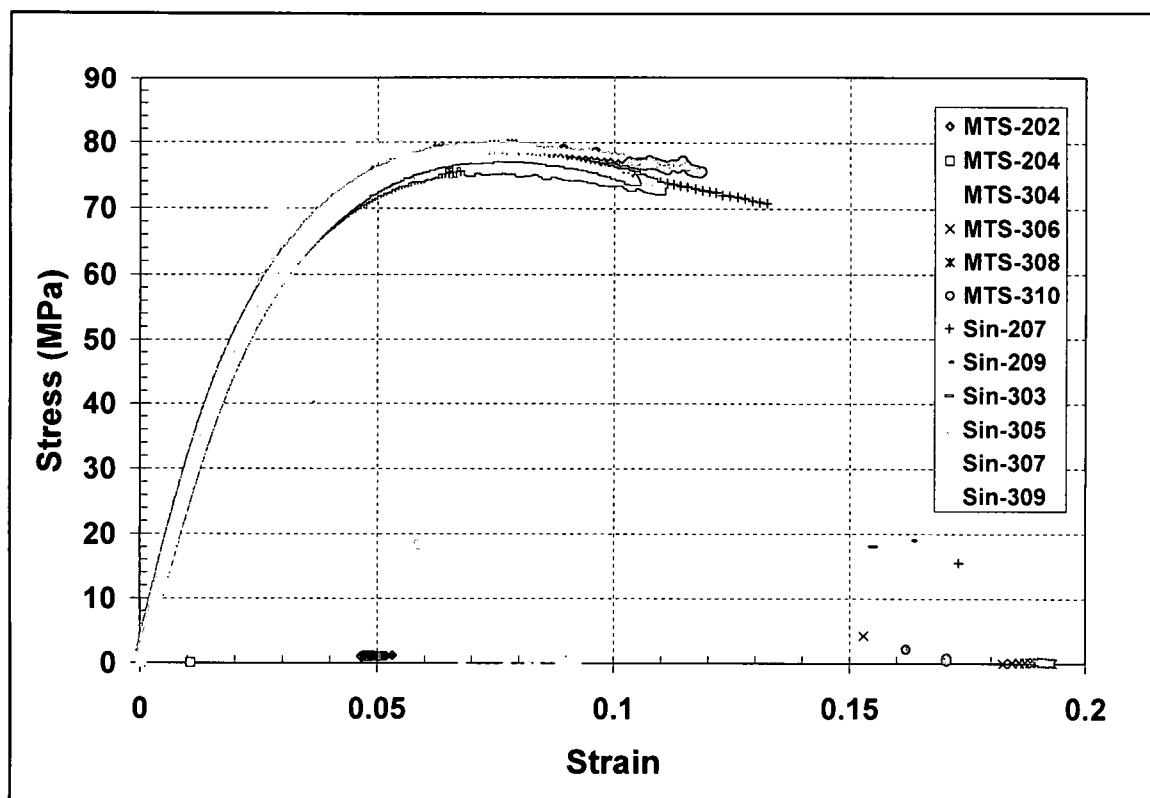


Figure 144: 862/W Stress vs. Strain curve

Table 55 lists the maximum stress, maximum strain, ultimate stress, the ultimate strain, and the linear modulus of all specimens tested. The average modulus between the MTS system and the Sintech system differs by less than 1%. This small variance is also shown in Figure 144 by the fact that the individual stress strain plots are almost identical. The individual specimen elastic modulus is calculated by plotting a straight line on the stress vs. strain curve of each specimen test and picking off the actual stress strain point at the point where the curve begins to deviate from linearity. Since all data begins at the origin the modulus is the stress divided by the strain of the selected point.

From the neat resin tensile test results it can be concluded that the 862/W material system has no statistically significant response to testing speed and therefore viscoelastic effects

will not be encountered in this work. In addition no differences in mechanical properties are expected between different manufactured batches of epoxy and curing agent. Furthermore, the specimen average values for maximum stress, maximum strain, ultimate stress, and ultimate strain will be used where appropriate through out this work. Due to the large non-linear behavior of the 862/W resin system the elastic modulus will be treated in a non-linear fashion. This comes to bear in the analytical models developed to determine the internal stresses at first failure. In the commercial finite element code ANSYS, utilized for all the analytical work in this thesis, provisions exists for a non-linear elastic material input. The input parameters allow for up to 100 input values of stress and corresponding strain with the provision that the first pair of values be that of the modulus at the end of linear portion of the of the curve. Specimen Sin-209 was chosen after careful scrutiny of all specimen plots to be representative of the data. Figure 145 shows the stress strain plot of specimen Sin-209 along with the values chosen for input into the analytical model.

Table 55: 862/W specimen maximum stress and strain, ultimate stress and strain, and linear modulus

862 Specimen	Max Stress (MPa)	Max Strain	Ultimate Stress (MPa)	Ultimate Strain	Linear Modulus (MPa)
Sin-207	76.2799	0.0801	70.8556	0.1324	2833.2952
Sin-209	77.9530	0.0779	75.7097	0.1045	2496.2494
Sin-303	76.6998	0.0784	74.4626	0.1083	2799.0647
Sin-305	78.9269	0.0759	77.8817	0.1016	2749.7477
Sin-307	79.4523	0.0749	79.1858	0.0827	2851.2275
Sin-309	77.9599	0.0741	74.4401	0.1044	2654.4347
Sin-AVG	77.8786	0.0769	75.4226	0.1057	2730.6699
MTS-202	72.8723	0.0466	72.7322	0.0469	2752.9878
MTS-204	77.1913	0.0712	72.8127	0.1100	2746.1685
MTS-304	79.9216	0.0448	75.6727	0.0653	2801.1205
MTS-306	78.4599	0.0748	76.3895	0.0957	2672.5787
MTS-308	79.8010	0.0783	78.5535	0.0791	2724.4193
MTS-310	79.0293	0.0892	75.6653	0.1187	2700.509
MTS-AVG	77.8792	0.0675	75.3043	0.0860	2732.9640
DELTA	0.0006	0.0094	0.1183	0.0197	2.2941
% DELTA	0.0008	12.2224	0.1568	18.6384	0.0839
Specimen AVG (σ)	77.8789 (1.8841)	0.0722 (0.0126)	75.3635 (2.3788)	0.0958 (0.0227)	2731.8169 (91.6887)

The modulus from the linear portion of the specimen data is 2496.23 MPa obtained from the actual values of stress at 33.07 MPa and a corresponding strain of 0.013. 53 points were selected as input and are also shown on the curve. One caveat of the input data is that the input must stop at the maximum stress, i.e. the finite element program can not handle a stress strain curve that continues to increase in strain while decreasing in stress after reaching the maximum stress. Although this specimen's modulus is the smallest of the test population, having a percent difference with the average modulus of just under 10%, it is the overall stress strain behavior that is most important in the analytical efforts since the FEM has to capture the far field stress at first failure of the experimental work to obtain the correct internal stresses. The input table for the non-linear elastic material is shown in Appendix C.

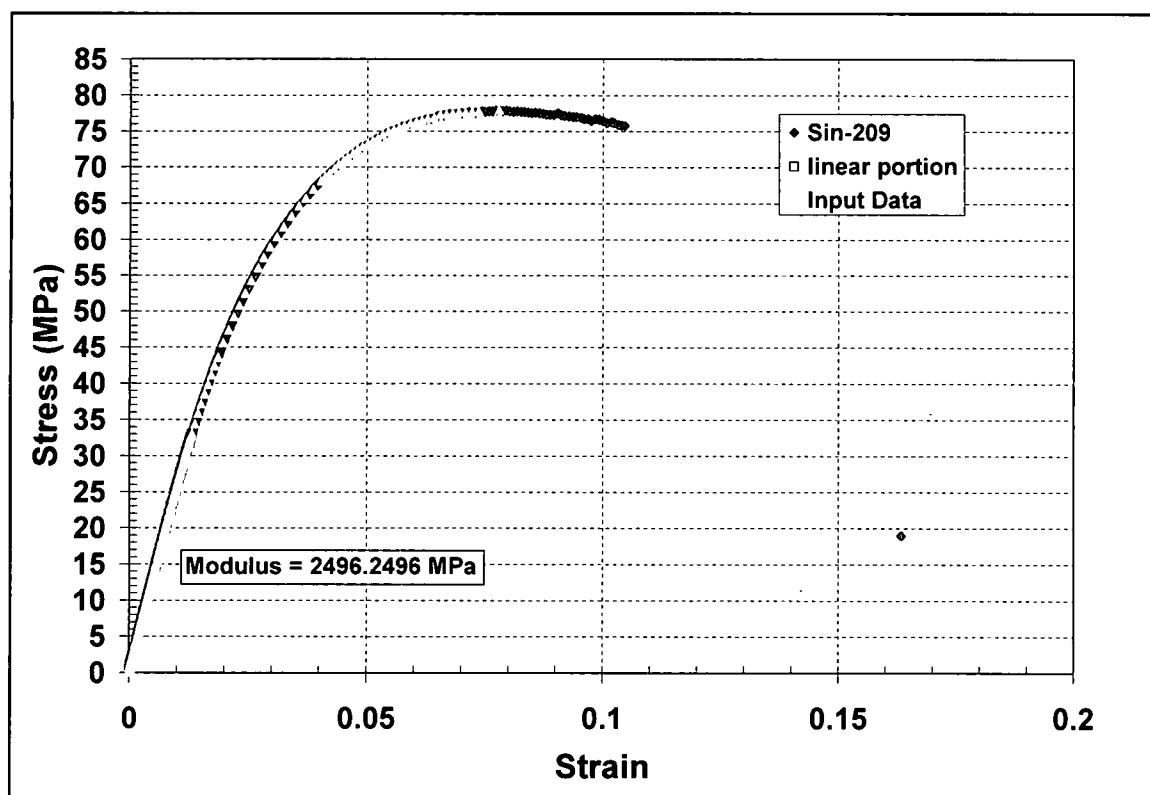


Figure 145: 862/W representative stress strain curve utilized for the finite element program

Compression Property Determination

Based on the findings of the 828/D-230 matrix comparing test fixtures, the CLC fixture was used to test the 862/W matrix system compression specimens at a gage length of 3.81 mm. A total of 16 specimens were tested, 10 at ½ inch wide and 6 at 1 inch wide. The specimens were cut from a neat resin plate approximately 10 inches square. Figure 146 is the compression stress vs. cross head displacement for all 16 specimens. Two specimens, one ½ inch wide and one 1 inch wide, had strain gages applied to each side of the specimen to measure any indication of buckling during the test. In both cases buckling was not present as both strain gages read almost the exact value of strain before separating from the specimen surface due to the extruded matrix material occurring within the compression zone during the test. A clear yield stress is apparent at about 125 MPa, as shown in Figure 146, as the compression stress reaches a maximum magnitude while the displacement continues to increase. For each individual specimen, the section where the compression stress exhibits its maximum magnitude is plotted over the range of displacement values to arrive at the point of yielding. Table 56 lists the width, thickness, load at yield and corresponding yield stress for each specimen tested. For each test the specimen exhibited an X shaped distortion and bulge at its edge during loading. Occurring simultaneously, the X shaped distortion was centered in the specimen thickness while the bulge occurred at the edge and along both faces at a finite width. As load was continually applied the bulge continued to get bigger extending away from the vertical planes of the specimen faces creating the extruded compression mentioned above. These features occurred as the load reached a peak under continued displacement definitely indicating that the yield stress had been reached. However, load was continually applied until oscillations in the load displacement curve were seen or the load was increasing under very little displacement as shown in Figure 146. The X shape distortion indicates a shear stress presence at the compression yield stress.

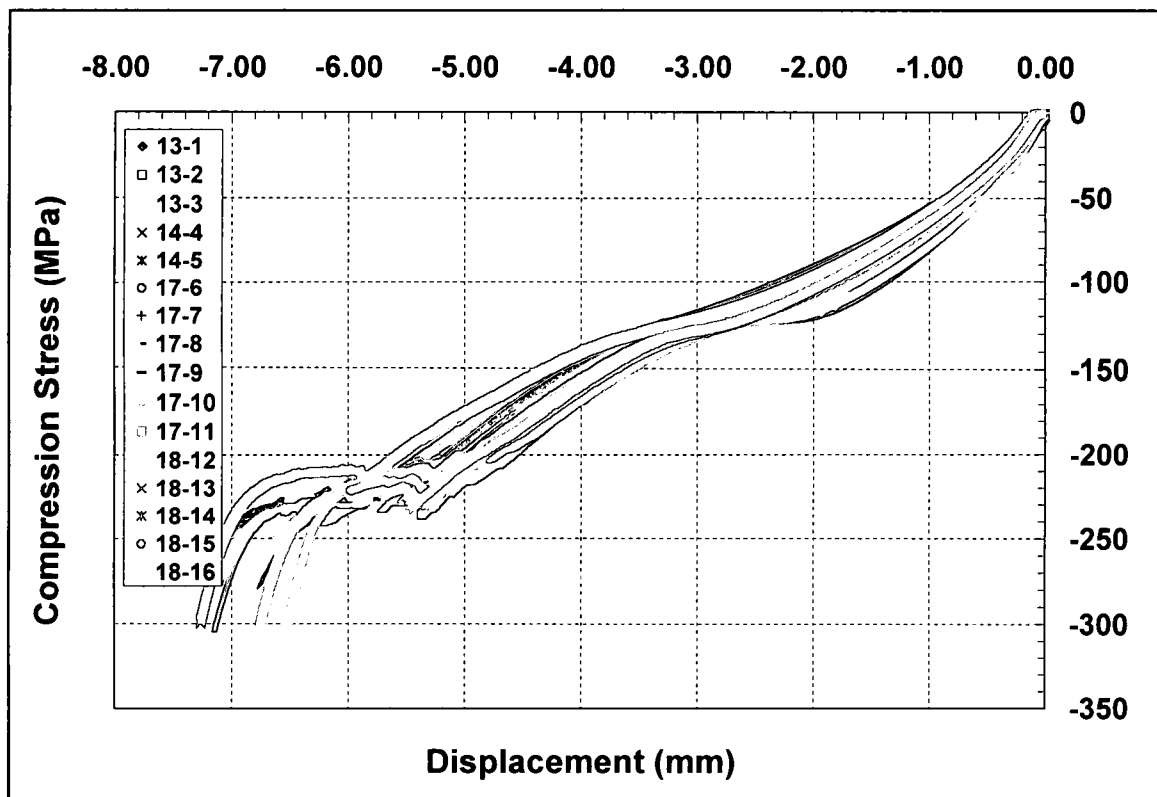


Figure 146: 862/W Compression stress vs. displacement curve

Table 56: 862/W Compression specimen dimension, maximum load and maximum strength

Specimen	Width (mm)	Thickness (mm)	X Sect Area (mm ²)	Load at yield (N)	Compressive yield stress (MPa)
13-1	0.495	0.233	0.115	13.90	120.495
13-2	0.497	0.238	0.118	14.24	120.383
13-3	0.493	0.237	0.117	13.72	117.959
14-4	0.499	0.235	0.117	14.30	121.966
14-5	1.004	0.223	0.224	29.20	130.407
17-6	0.498	0.232	0.116	13.81	119.585
17-7	0.502	0.230	0.115	13.71	118.701
17-8	0.503	0.227	0.114	13.64	119.493
17-9	0.496	0.230	0.114	13.31	116.664
17-10	0.496	0.239	0.119	14.49	122.228
17-11	0.495	0.237	0.117	14.39	122.701
18-12	1.002	0.215	0.215	27.95	129.73
18-13	0.986	0.224	0.221	28.00	126.779
18-14	0.996	0.227	0.226	28.70	126.393
18-15	1.003	0.223	0.224	28.79	128.72
18-16	1.001	0.217	0.217	27.98	128.802
AVG (std-dev)					123.22 (4.46)

The average compressive stress at yield for the 862/W matrix system that will be used throughout this work is 123.33 MPa.

Poisson's Ratio Determination

Ten dog-bone specimens were tested for the determination of Poisson's Ratio of the 862/W resin system. The dog-bone specimens were made in the exact same manner as described in the Elastic Modulus Property Determination section above, except that prior to testing strain gages were bonded within the gage length to each side of the specimen. One gage was bonded to measure the axial strain and the other was bonded to measure the transverse strain. Poisson's ratio is calculated by taking the ratio of transverse strain to axial strain. From these tests Poisson's ratio can be determined directly. Figure 147 shows the test results of nine of the ten specimens. One specimen, Y-3, encountered data collection difficulties during the test and therefore its data was determined not usable.

As shown in Figure 147 the 862/W resin system has a constant Poisson ratio over the entire loading range exhibiting very little scatter. The scatter shown between 0N to approximately 55N is attributed to the data collection system employed and is representative of system noise. Table 57 gives the individual specimen results. The average 862/W specimen Poisson Ratio is 0.3464 with a standard deviation of 0.0046.

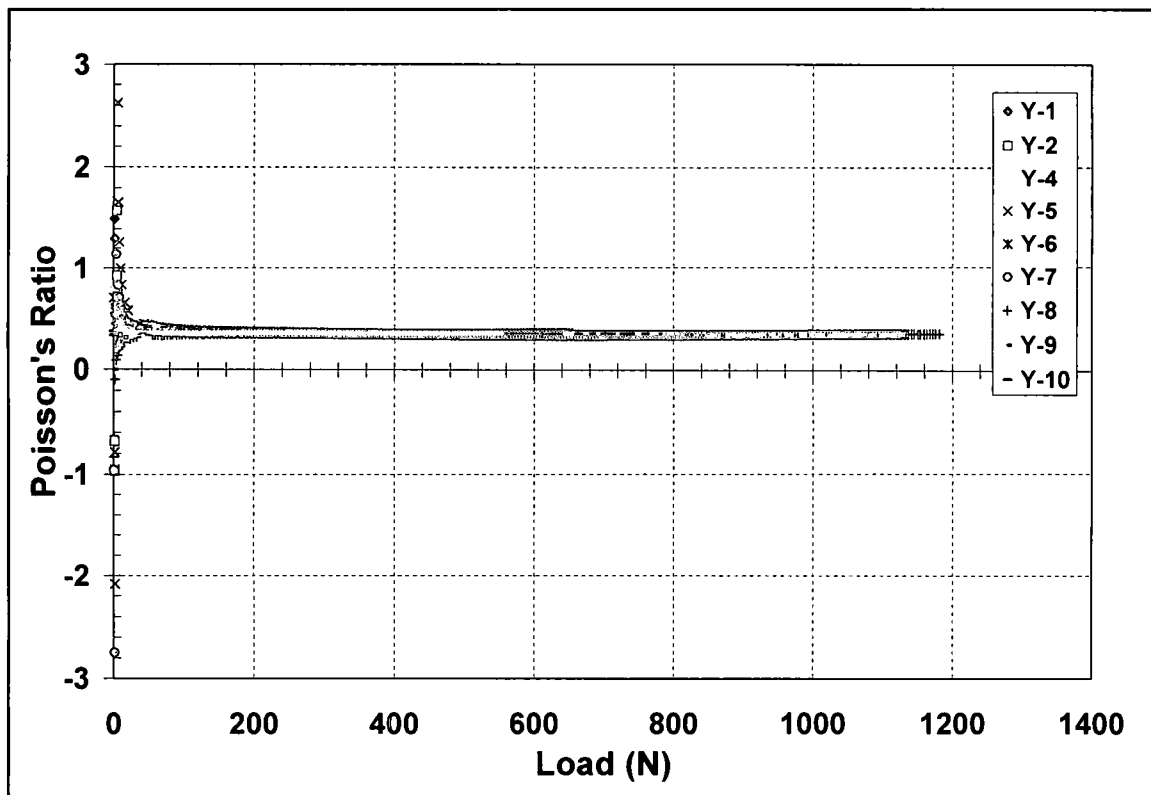


Figure 147: 862/W Poisson's Ratio vs. load curve

Table 57: 862/W Poisson's ratio specimen results

Specimen	Poisson's Ratio
862 Y-1	0.3412
862 Y-2	0.3481
862 Y-4	0.3474
862 Y-5	0.3532
862 Y-6	0.3383
862 Y-7	0.3434
862 Y-8	0.3448
862 Y-9	0.3513
862 Y-10	0.3496
AVG	0.3464
(STDEV)	(0.0046)

Coefficient of Thermal Expansion

Two 862/W neat resin dog-bone specimens were tested to determine the coefficient of thermal expansion (CTE) of the matrix system in the same manner as the 828/D-230 system. Two strain gages were bonded to each specimen, one each on opposite sides of the specimen.

The temperature was increased from room temperature at 25.6° C (78° F) to 110.0° C (230° F) in increments of 3.3° C (6° F) per minute and in steps of 22.2° C (40° F) with a 20 minute hold per step. It was then decreased in the same manner. The material strain due to the temperature changes was recorded every minute. Figure 148 shows the results of the CTE of each specimen. Like the 828/D-230 system the 862/W resin system has a very linear CTE as exhibited by the data plot and by the high multiple coefficient of determination, R^2 , of the trend lines shown on Figure 148. The multiple coefficient of determination is the ratio of explained variation to the total variation thus a high value or an R^2 of close to one indicates very little variation. The average CTE of the 862/W matrix system is 53.92 $\mu\epsilon/^\circ\text{C}$.

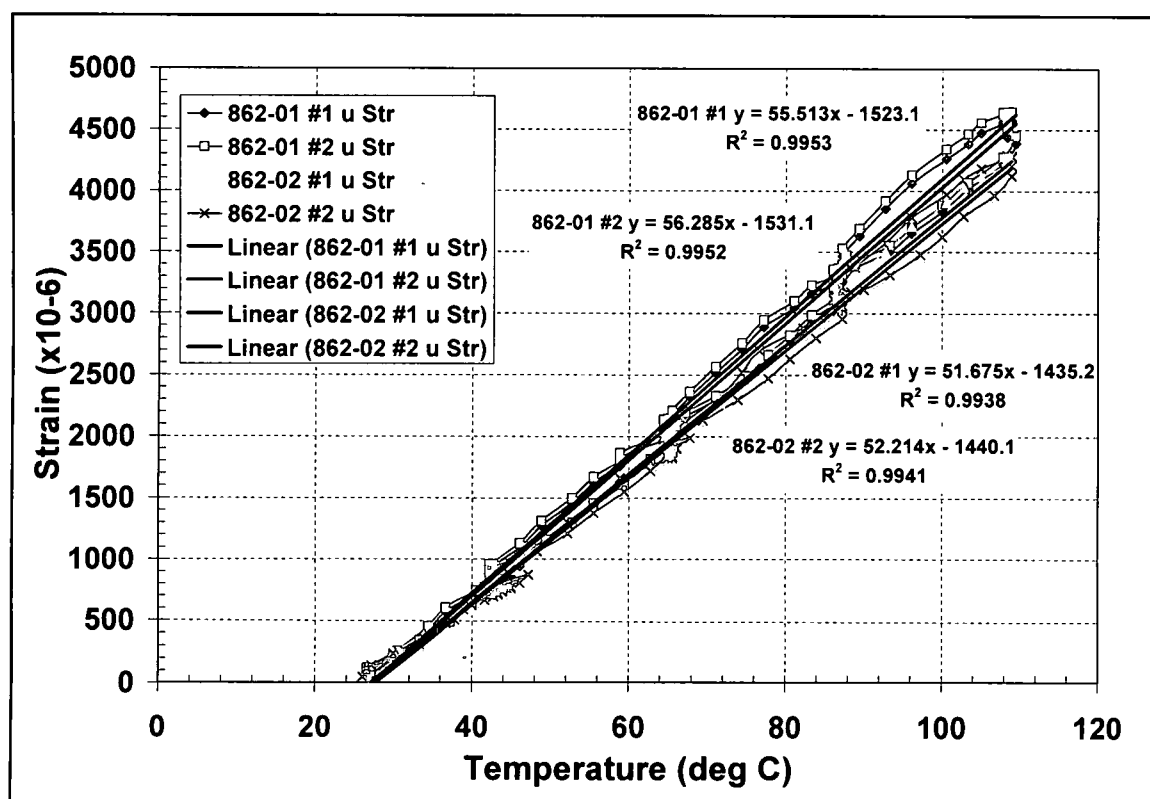


Figure 148: 862/W strain vs. temperature plot with trend lines determining the CTE

Moisture uptake investigation

To measure the moisture uptake of the 862/W resin system eleven specimens were cut from cast plates. Five of the specimens were cut into 44.45 mm (1.75 inch) squares and labeled

A specimens, five were cut into 76.2 mm (3 inch) squares and labeled C specimens and one was cut into 69.85 mm (2.75 inch) square and labeled B specimens. Since only one B specimen exists only the A and C specimens will be given for the length and width percent strain results from moisture gain. This investigation was carried out in the same manner as for the 828/D-230 investigation described above. Once placed in the humidity chamber they were weighed and measured after 6 and then 24 hours, then daily for the next 3 days. After which they were weighed and measured weekly until saturated. Figure 149 shows the percent weight gain vs. time for all specimens. The dip at day 49 was due to a power outage in the building but did not affect the results of this study. Saturation seems to occur at day 62 into this investigation as shown in Figure 149 by the leveling of the percent weight gain over time from this point to the end of the study at day 88. The average weight gain over this period of the 862/W matrix system is 1.88%.

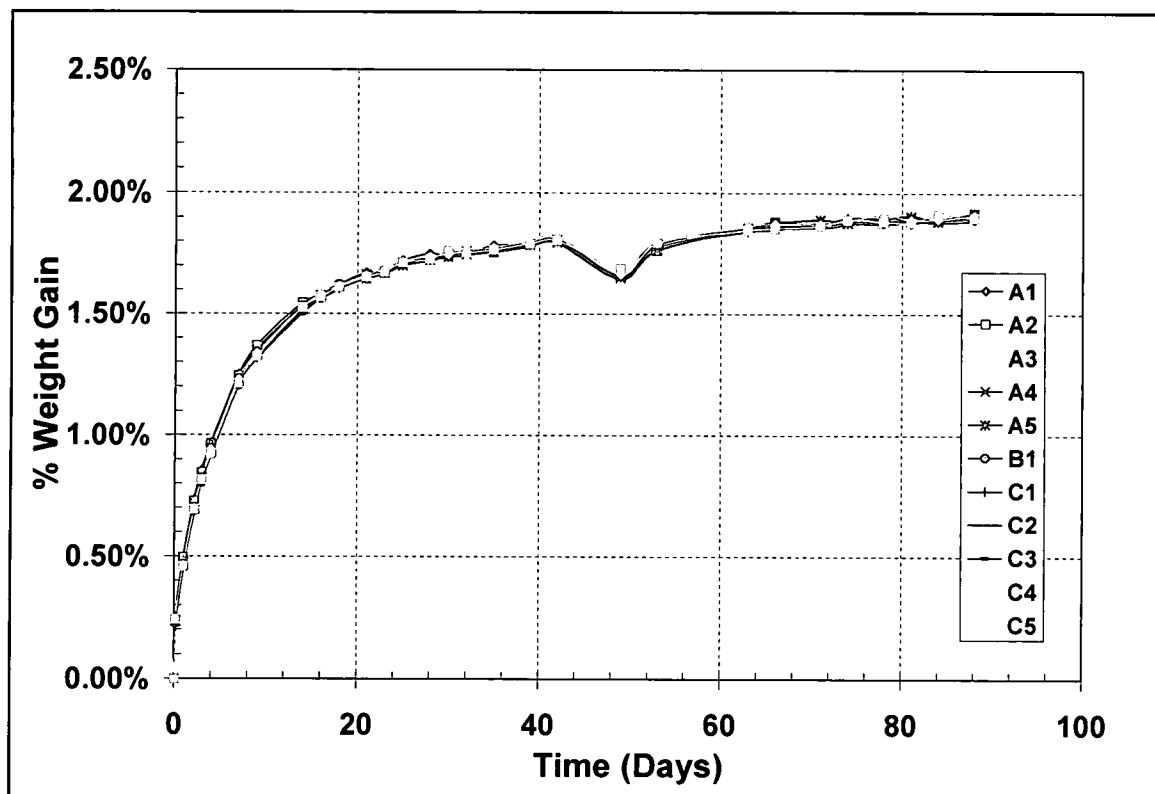


Figure 149: 862/W percent moisture gain

Unlike the 828/D-230 matrix system the 862/W matrix system did not continue to experience swelling strain after saturation was achieved. Figure 150 shows the percent strain of the average length and width over time for the A and C specimens. At saturation, on day 63, the swelling strain for the A specimens was 0.371% and for the C specimens is was 0.395%. After this point in time the average length and width swelling strains began to oscillate as shown in Figure 150, however the strain trend is slightly increasing. Table 58 shows the average percent strain measurements of specimen B and C length and width. The average swelling strain from the start of saturation, at day 63, to the end of the study at complete saturation, at day 88, of the 862/W matrix system is 0.397%.

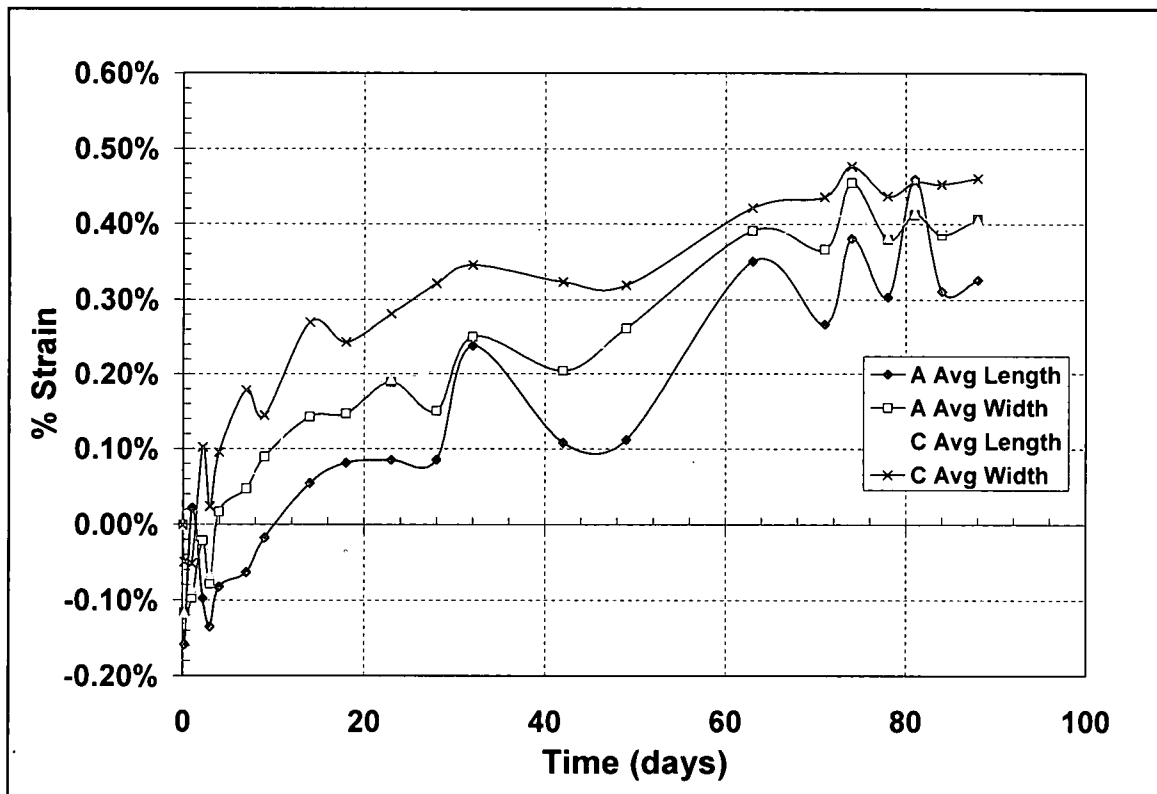


Figure 150: 862/W average length and width moisture strain

Table 58: 862/W measured average length and width percent moisture strain

Days	Specimen A		Specimen C	
	Average Length	Average Width	Average Length	Average Width
0	0.000%	0.000%	0.000%	0.000%
0.2	-0.16%	-0.12%	-0.1170%	-0.0490%
1	0.0220%	-0.0971%	-.0858%	-0.0512%
2.2	-0.0973%	-0.0209%	0.0212%	0.1026%
3	-0.1354%	-0.0780%	-0.0657%	0.0246%
4	-0.0823%	0.0173%	0.0435%	0.0959%
7	-0.063%	0.0478%	0.0702%	0.1783%
9	-0.0173%	0.0898%	0.0702%	0.1449%
14	0.0550%	0.1431%	0.1794%	0.2696%
18	0.0816%	0.1469%	0.1795%	0.2429%
23	0.0855%	0.1890%	0.1928%	0.2808%
28	0.0856%	0.1508%	0.2084%	0.3209%
32	0.2379%	0.2500%	0.2664%	0.3455%
42	0.1084%	0.2042%	0.2374%	0.3232%
49	0.1122%	0.2613%	0.2463%	0.3187%
63	0.3506%	0.3908%	0.3689%	0.4211%
71	0.2667%	0.3661%	0.4001%	0.4356%
74	0.3810%	0.4539%	0.4146%	0.4757%
78	0.3031%	0.3793%	0.3823%	0.4368%
81	0.4590%	0.4118%	0.4135%	0.4546%
84	0.3107%	0.3852%	0.3934%	0.4523%
88	0.3259%	0.4061%	0.4046%	0.4601%
Saturated AVG	0.3707%		0.4334%	
	(days 63 thru 88)		(days 63 thru 88)	
Overall AVG	0.397% (days 63 thru 88)			

Material Characterization Summary

The following table summarizes the material property values used for this work. It should be noted that for both matrix systems the compression tests revealed a shear stress presence in the yielding of the material. This would indicate that the compression of both matrix systems is not by a pure compression state; rather it initiates as shear-compression failure, where conical or wedge shaped volumes of material are being driven through the rest of the material volume by the applied loading. The material is essentially flowing across the slip planes where the pure compression within the specimen is at the points of the wedges and occupies a very small volume of material. This phenomenon clearly documented [1] is usually ignored for most materials since the bulk property is of interest, but for in this work failure is based upon the

initiation mechanism and this characteristic of the compressive yield stress should not be overlooked.

Table 59: Summary of matrix material properties used for this work

Material Property	828/D-230	862/W
Elastic Modulus	3439.86 MPa	2731.82 MPa (linear)
Maximum Tensile Yield Stress	61.69 MPa	77.88 MPa
Maximum Tensile Strain	2.10%	7.22%
Ultimate Tensile Stress	58.43 MPa	75.36 MPa
Ultimate Tensile Strain	2.60%	9.58%
Compression Yield Stress	90.08 MPa	123.22 MPa
Poisson's Ratio	0.337	0.347
CTE	55.67 $\mu\epsilon/^\circ\text{C}$	53.92 $\mu\epsilon/^\circ\text{C}$
Moisture Gain	3.03%	1.88%
Swelling Strain	0.669%	0.397%

References

1. Nadai, A., *Theory of Flow and Fracture of Solids*. 2 ed. Engineering Societies Monographs, ed. R.H. Phelps. Vol. 1. 1931, New York: McGraw-Hill Book Company. 572.

APPENDIX B

RESIDUAL STRESS DETERMINATION

Introduction

Cavitation induced matrix cracking and fiber-matrix debonding are two competing mechanisms responsible for damage initiation in composite materials loaded transverse to the fiber direction [1-7]. Obviously the fiber-matrix interface quality, i.e., a strong or weak interface, can cause a shift in the competing damage initiation mechanism. Previous analytical efforts indicated that the matrix residual stresses were affected by the fiber volume fraction; however, they are independent of interphase properties [1, 2]. Previous work also indicates that the residual stress components acting on the perimeter of the fiber can be either compressive, tensile or both [2]. Consequently the interaction of residual stresses and fiber spacing, especially varying spatial distribution, will have an impact on the failure initiation of a composite material.

In the investigation of transverse failure initiation in model multi-fiber composite cruciform specimens, [8], the need for an accurate method of measuring the residual shrinkage has become obvious. An accurate analysis of residual stresses brought about by the cure shrinkage for the room temperature cured matrix system as well as the residual stresses due to the thermal mismatch between the fibers and matrix and its own shrinkage cure for the high temperature cured matrix system is important for use in calculating the total mechanical and residual stress between fibers and along the fiber-matrix interface. Standard methods such as $(CTE)(\Delta T)$ are not expected to be sufficiently accurate because for a room temperature resin system the $\Delta T = 0$, however, the shrinkage strain is not zero as evidence by a volume decrease between un-cured specimens and cured specimens. As for the high temperature cured resin system it experiences both thermally induced stresses and shrinkage stresses due to its cure cycle. Additionally no

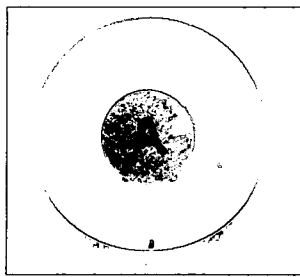
experimental method exists to separate the thermal stresses from the shrinkage stresses. Consequently due to the transparency of the model composite system used in this work, photoelasticity can be utilized to measure the residual stresses from each resin system cure cycle.

The approach for this study, derived by Bechel, et.al [9], utilizes a circular polariscope to measure the residual stresses induced in a 31.55 mm diameter model composite disk specimen comprised of 12.7 mm diameter aluminum rod surrounded by each matrix material. A finite element model (FEM) will be used to calculate the corresponding effective coefficient of thermal expansion for each material system. The model composite disks use two transparent epoxy resin systems. The first system is a room temperature cured Epon 828 epoxy using the Jeffamine D-230 curing agent (828/D-230). The second system is a high temperature cured Epon 862 epoxy using the EPI-CURE W curing agent (862/W). Experimental results using the circular polariscope were used in conjunction with a finite element analysis of the model composite disks to determine the effective coefficient of thermal expansion for the two matrix systems. The effective coefficient of thermal expansion was utilized to then estimate the contribution of residual stresses in the FEM of the cruciform specimens.

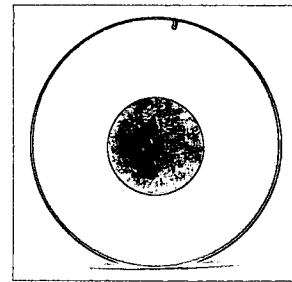
Experimental Technique

Specimen Geometry

The specimen, shown in Figure 151, is a concentric disk having an average diameter of 31.55 mm. In the center of the disk is placed an aluminum rod having a diameter of 12.7 mm. The specimen dimensions were chosen for convenience and for ease of specimen fabrication [10].



(a)



(b)

Figure 151: Photographs of an (a) 828 photoelastic specimen and (b) 862 photoelastic specimen

The specimen thickness is based upon the results of an earlier study [9] and preliminary experimentation. The disk specimens act as a temporary retardation plate because the stresses normal to the disk are zero and the principal stresses vary only slightly and can be assumed to be constant through the specimen thickness. Consequently the relative retardation of light passing through the specimen is directly proportional to the thickness of the specimen [10]. This means that for the 828/D-230 resin system, since it is anticipated that the shrinkage stresses will be lower than those of the 862/W resin system due to its room temperature cure, its specimen thickness must be greater than the 862/W specimens so an adequate number of fringes will appear for good experimental results. The average thickness for the 828/D-230 specimens is 16.98 mm and for the 862/W specimens are 12.87 mm.

Materials

The Epon 828 epoxy used the Jeffamine D-230 curing agent at 35% by weight of the 828. It cures in approximately seven days at room temperature. The 828/D-230 epoxy system is a clear difunctional bisphenol A/epichlorohydrin epoxy resin cured with an aliphatic amine [www.resin.com]. It is a simple system to make and cure and has a linear elastic response to loading, as shown in Figure 152. The Epon 862 epoxy uses the EPI-CURE W curing agent in a ratio of 79.4% 862 to 20.6% W. It is an amber bisphenol-F/epichlorohydrin resin cured with an

aromatic amine at 121.1° C for 2 hours and post cured at 176.7° C for 2 hours. The 862/W has a non-linear response to loading as shown in Figure 152.

The aluminum disks used in these specimens are 6061 aluminum alloy having a modulus of elasticity equal to 69.0 GPa.

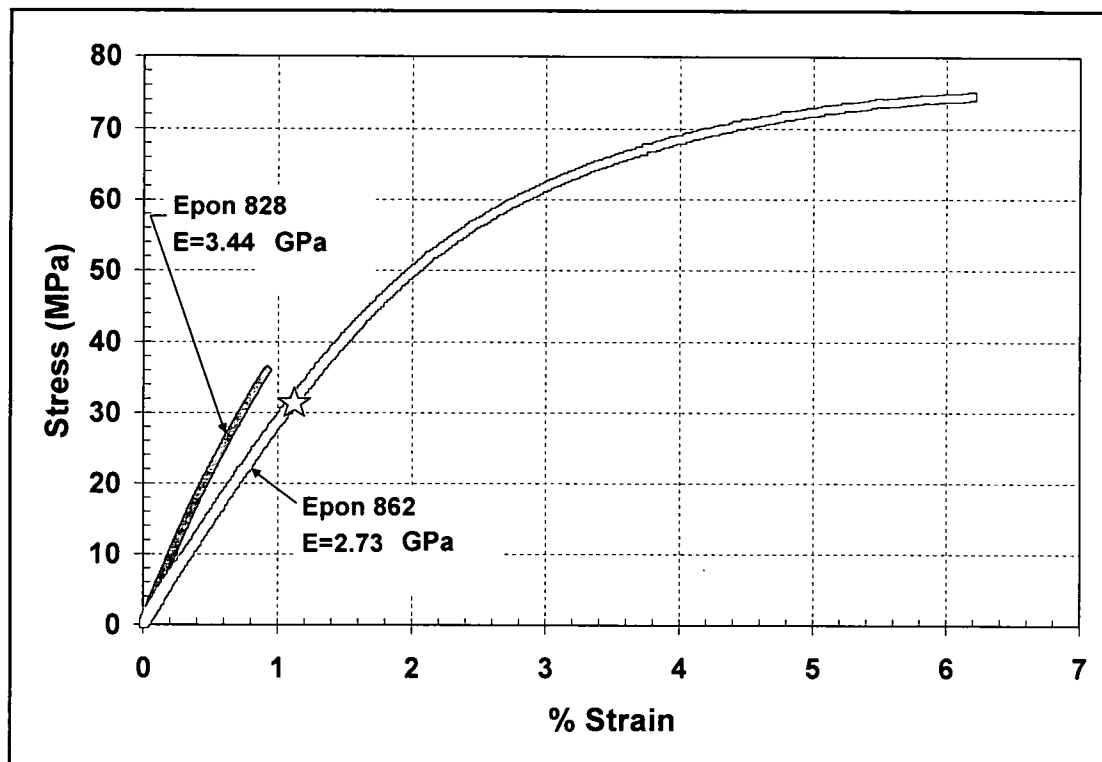


Figure 152: Stress-Strain response for both the 828/D-230 and the 862/W epoxy systems

Specimen Fabrication

Silicon rubber molds, 76.2 mm square as shown in Figure 153, were made for casting the epoxy disk specimens. The molds consisted of a square with a 31.75 mm diameter hole 19.05 mm deep. Once the molds cured they were thoroughly cleaned with an acetone wash prior to placement of each resin system. Aluminum rods, cut from bar stock and cleaned with an acetone wash, were placed in the center of the mold secured to the bottom by vacuum grease. Additional cleaning around the aluminum rod at the bottom of the mold by an acetone saturated Q-tip

removed any vacuum grease that may have squeezed out from underneath the aluminum rod after being centered in the rubber mold. Properly mixed and debulked 828 and 862 resin systems were then carefully poured in the mold without moving the aluminum rod and then cured following their respective curing cycles. For all specimens the molds were placed into an aluminum pan prior to pouring the resin and covered to prevent any dust or foreign particles from getting into the specimens. The 828/D-230 resin system was allowed to cure for three days before being removed from their molds, whereas the 862/W resin system followed its high temperature cure cycle and, once cool to the touch, were removed from their molds. The specimens were then placed in a desiccator to prevent any moisture absorption prior to testing.

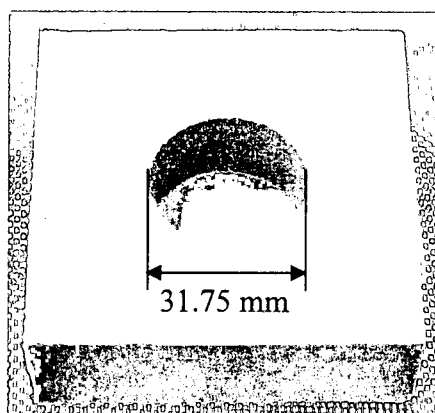


Figure 153: A typical silicon rubber mold used to cast the epoxy disk specimens.

For sharp images in the polariscope for the specimen's top and bottom should be exactly parallel and polished. Therefore, each specimen is sanded using 320, 400, and 600 grit sandpaper to a uniform thickness ensuring parallelism. After sanding the specimens are then highly polished, using alumina suspended in water on a polishing wheel, making the epoxy transparent through the thickness of each specimen. It should be noted that the disks always remained in the desiccator except during specimen preparation and testing.

Testing

Figure 154 shows the circular polariscope set-up used for all the experimental evaluations. The polariscope consists of a laser light source, objective lens and pin-hole, ground glass plate, collimating lens, polarizer, $\frac{1}{4}$ wave plate, the specimen, $\frac{1}{4}$ wave plate, analyzer, focusing lens, and a camera aligned on the same vertical plane in a perfect straight line along the laser beam. The laser light source is chosen due to its intensity and monochromatic attribute. However, lasers are also coherent light sources. Due to this fact we use a rotating ground glass to create the needed incoherent light source to avoid diffraction patterns in the image generated.

In general, for this arrangement, as the collimated and coherent laser light passes through the objective lens and pin-hole, the rotating glass plate, and the collimating lens the laser light now becomes expanded in size and incoherent. The expanded laser beam is needed for full coverage of the specimen while making the beam incoherent removes ghost fringes making the image sharper. As the beam passes through the polarizer it becomes plane polarized. Then as it passes through the first $\frac{1}{4}$ wave plate the light becomes circular polarized as it hits the specimen. As the circular polarized light passes through the specimen the internal stresses further rotate, or retard, the light waves that pass through the stressed area. The slow axis component of a light wave is retarded with respect to the fast axis component. The 2nd $\frac{1}{4}$ wave plate converts the light waves back to plane polarization. Next, as the light waves pass through the analyzer the waves that have been retarded, by passing through the stressed areas of the specimen, are removed. The removed light waves show up as fringes, black and white lines, in the image captured by the camera. The focusing lens fine-tunes the image for the camera. Depending upon how the polarizer/analyzer and the $\frac{1}{4}$ wave plates are aligned will create either a dark field or bright field. The fringe patterns for the circular polariscope are called isochromatics which depict the areas of equal principal stress difference.

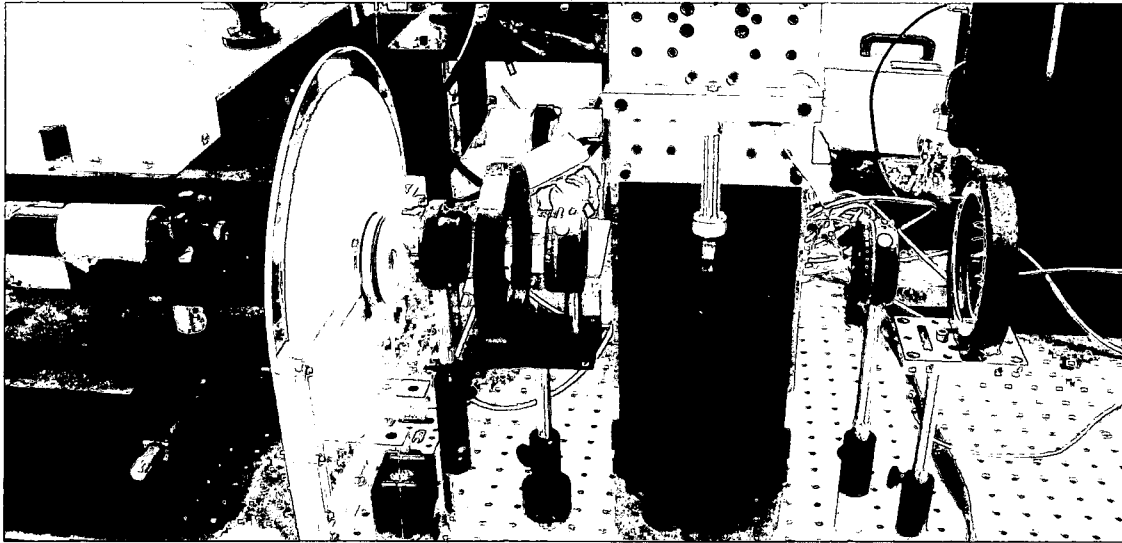


Figure 154: The polariscope set-up used for all experimentation. Not shown are the focusing lens and camera.

Experimental / Analytical Results

The Stress-Optic law [10] relates the angular phase shift of the light wave's component vectors, as it passes through the stressed specimen, to the difference in principal stresses in the specimen, the specimen thickness, and the wavelength of the light. Written for a two dimensional case the Stress-Optic law is expressed as

$$\sigma_1 - \sigma_2 = \frac{\Phi p}{2\pi hc} \quad (1)$$

Where, σ_1 and σ_2 are principal stresses, Φ is the angular phase shift of light passing through the specimen, p is the light's wave length, h is the specimen thickness and c is the stress optic coefficient of the material. The angular phase shift or the difference in the speed of light through the specimen can be expressed in terms relative to the retardation or interference as the light passes through the specimen. The fringe order, N , is the relative retardation or interference of the two components of the light wave passing through the specimen and is expressed as

$$N = \frac{\Phi}{2\pi} \quad (2)$$

For fringes to occur the intensity of light passing through the specimen has to be extinct. Since the intensity is the square of the amplitude of the light waves through the specimen; for extinction to occur the components of the light waves have to be out of phase by 180° or π radians. Due to the capability of the circular polariscope to produce both a dark field or destructive interference and a bright field or constructive interference; extinction of light occurs when $N = 0, 1, 2, 3, \dots$ for the dark field and $N = 0, 1/2, 3/2, 5/2, \dots$ for the bright field. Substituting (2) into (1) gives the principal stress difference as a function of the fringe order

$$\sigma_1 - \sigma_2 = \frac{Np}{hc} \quad (3)$$

The light's wave length, p , will be constant depending upon the source and the quantity

$$\frac{p}{c} = f_\sigma = \text{constant} \quad (4)$$

is the fringe constant of the particular material system. Substituting (4) into (3) yields

$$\sigma_1 - \sigma_2 = \frac{Nf_\sigma}{h} \quad (5)$$

The relationship between the photoelastic fringe order, N , and the average radial stress at the interface of the aluminum rod and resin system as derived by Bechel, et al. [9], for this axisymmetric problem, starts from equilibrium conditions

$$\partial \sigma_{xx} / \partial x = -\partial \sigma_{xy} / \partial y \quad (6)$$

and the Fundamental Theorem of Calculus

$$\int [\partial \sigma_{xx}(x, y_0) / \partial x] dx = \sigma_{xx}(x_0, y_0) - \sigma_{xx}(x, y_0) \quad (7)$$

relating the known value of σ_{xx} at one position, x_0 and y_0 , to the unknown value of σ_{xx} at another position x , and y_0 . Recognizing that along the x axis $\sigma_{xx}(x, 0)$ equals $\sigma_{rr}(x, 0)$ due to the geometry of the specimen, $y_0 = 0$, and x_0 is defined at the specimen edge, where the stress is zero, the equation for radial stress at the interface becomes

$$\sigma_{rr}(r, 0) = -[f_\sigma / h] \int \{ [N(x, 0) / x] \} dx \quad (8)$$

By setting r_0 equal to the radius of the specimen and r_f equal to the radius of the aluminum rod the integral is evaluated between the specimen's edge, $x = r_0$, and the interface, $x = r_f$.

In summary, the only two unknowns for calculating the radial stress due to the resin system curing cycle are the material fringe constant, f_σ , and the photoelastic fringe as a function of x , $N(x, 0)$.

Material fringe constant

Each resin system has a unique material fringe constant. This constant is determined by placing the neat resin under a known stress state. The material fringe constant for both resin systems used in this study is determined by placing a circular disk in diametric compression. The equation for the material fringe constant using this method [10] becomes

$$f_{\sigma} = \frac{8P}{\pi DN} \quad (9)$$

where P is the applied load, D is the diameter of the disk and N are the observed fringe value at the center of the disk.

The disk is loaded until a fringe at the center of the disk is seen. Additional load will produce additional fringes. A plot of load, P , verses fringe order, N , is made for a range of loads. A straight line is best fit through the data points where the slope of the line is $(\pi D/8) f_{\sigma}$. Figure 155 shows the load verses fringe order for the 828/D-230 resin system and the 862/W resin system.

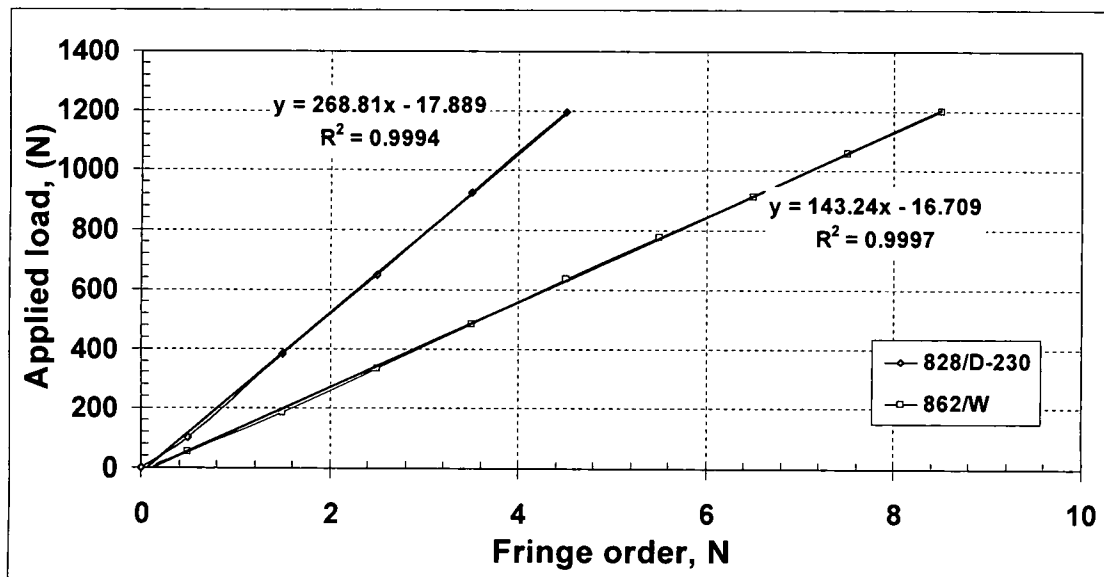


Figure 155: 828/D-230 and 862/W matrix system calibration curves used for experimentation.

Once the slope of each line is determined the fringe constant, f_{σ} , can be calculated. The fringe constant for the 828/D-230 resin system is 21.54 N/fringe-mm. The fringe constant for the 862/W resin system is 11.45 N/fringe-mm.

828/D-230 Cure Induced Residual Stress Results

Five 828/D-230 resin system disks are cast and allowed to cure for three days prior to removing from the mold. Once removed from the mold the specimens were sealed in a plastic bag and placed in a desiccator. After the disks were sanded and polished, as described earlier, photoelastic images of each specimen are taken in both the bright field and dark field. It should be noted that the manufacture, Epon, of this particular resin system states that a full cure occurs in 7 days at room temperature. All photoelastic images were taken a minimum of 45 days after casting of the specimens. Figure 156 shows a bright field photoelastic image of a typical 828/D-230 specimen. The fringes are concentric about the aluminum rod. Due to the room temperature cure of the 828/D-230 matrix system taking the bright and dark field images gives both half and full fringe orders of the matrix system. This in turn will provide a more accurate result for the interfacial radial stress.

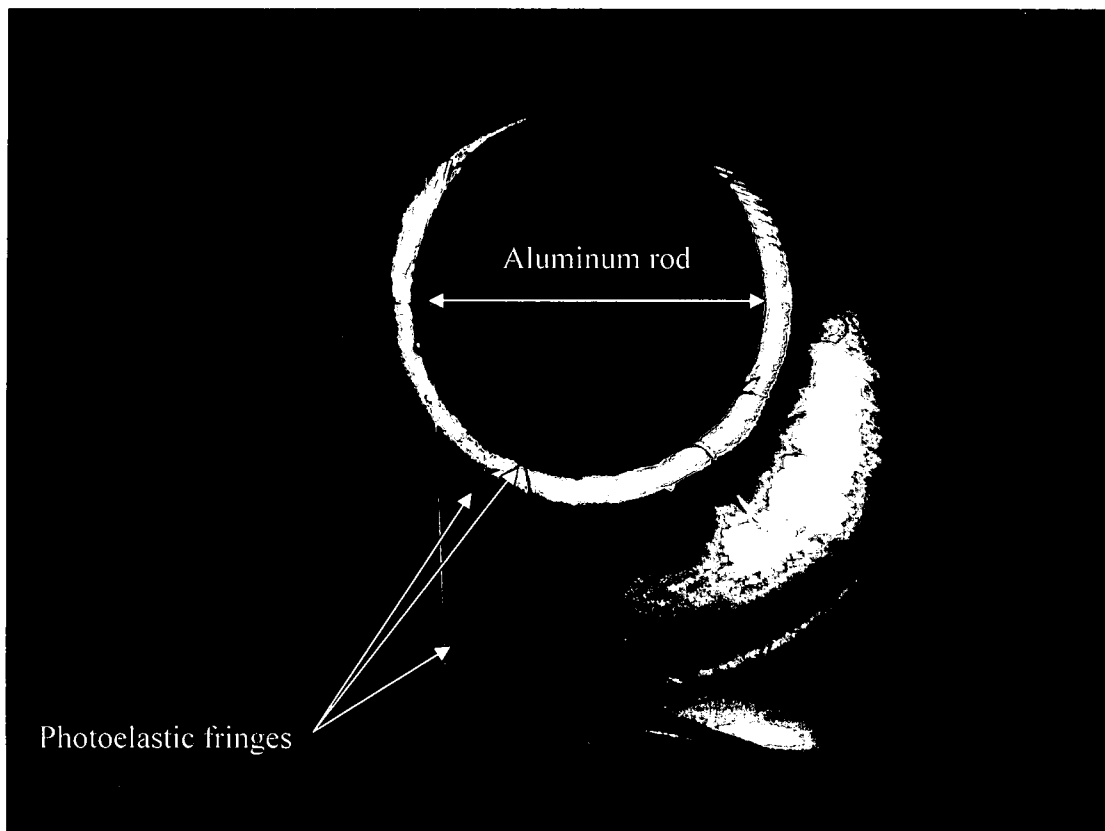


Figure 156: A bright field photoelastic image of an 828/D-230 disk specimen.

The full and half order isochromatic fringes are plotted versus radial distance beginning from the stress free boundary for all 5 specimens. Figure 157 shows a plot of the fringe order versus radial distance for specimen S201. From equation (8) the integral of $N(x,0)$ is evaluated from the free edge to the interface of the matrix and aluminum rod. For each specimen a curve of fringe order versus radial distance is fit through the data points from the test results. The cure induced residual stresses at the interface of the 828/D-230 resin system by the photoelastic method is listed in Table 60.

Table 60: Cure induced radial stresses for the 828/D-230 resin system at the interface.

Specimen	$\sigma_r(\text{MPa})$
828-S201	-2.19
828-S202	-2.34
828-S203	-1.96
828-S204	-1.98
828-S205	-1.84
AVG	-2.06

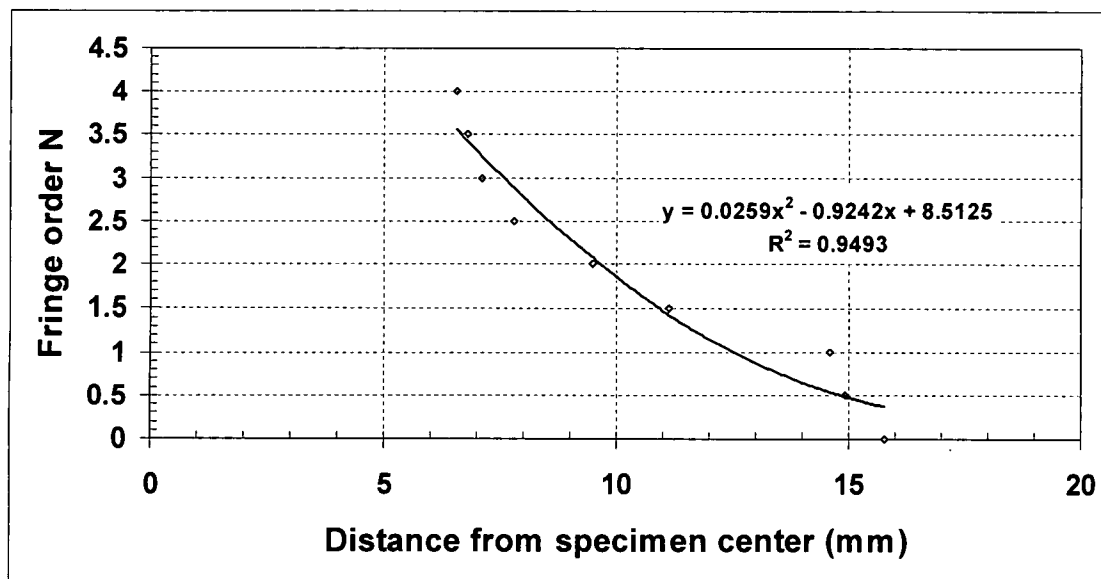


Figure 157: Bright and Dark Field Fringe order versus radial distance of 828/D-230 Specimen S201.

862/W Cure Induced Residual Stress Results

Four 862/W resin system disks are cast and cured at 121.1° C for 2 hours then post cured at 176.7° C for 2 hours. Once cooled, approximately 30 minutes after removal from the oven, they are removed from their molds and placed in a desiccator. Once the disks are prepared for testing, as described above, photoelastic images are taken of each specimen. Figure 158 shows a typical image of the 862/W specimen and its photoelastic fringes induced by the curing cycle. The photoelastic fringes are tightly packed and concentric about the aluminum rod. The tight spacing of the fringes is indicative of the expected high residual stresses due to the high temperature cure cycle. The half order isochromatic fringes, N , are plotted versus radial distance from the specimen stress free edge as shown in Figure 159. A curve is fit through the data points for each specimen tested and, from equation (8), the integral is evaluated to calculate the residual stress at the interface. The cure induced residual stresses at the interface of the 862/W resin system by the photoelastic method is listed in Table 61.

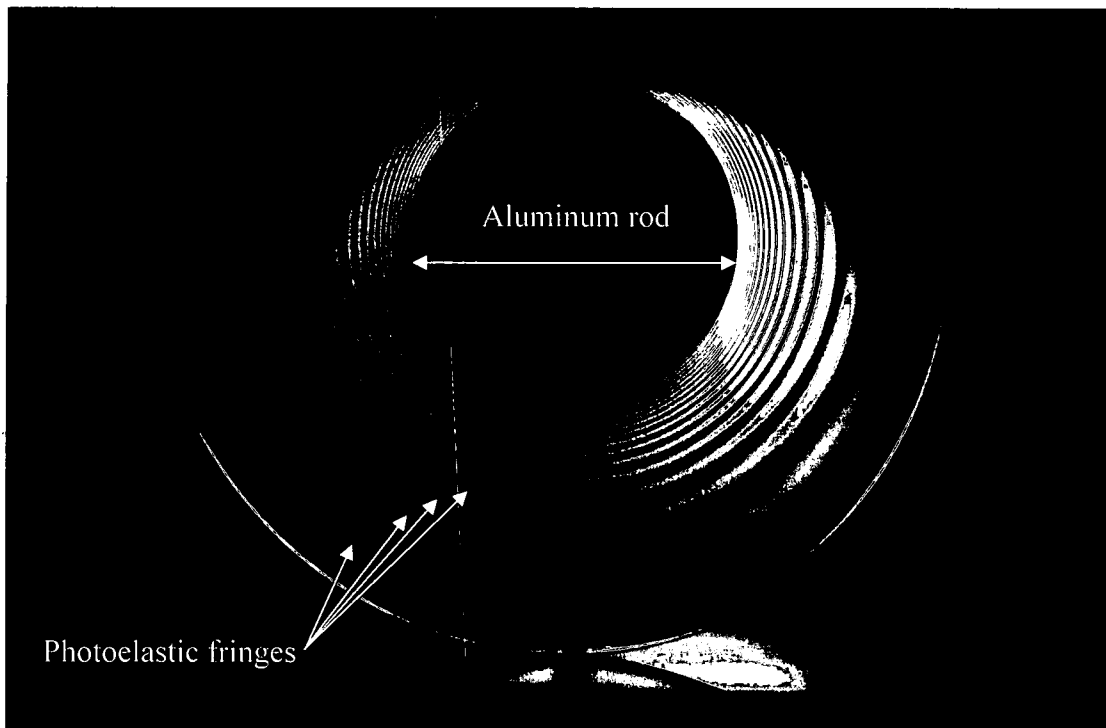


Figure 158: A bright field photoelastic image of an 862/W disk specimen.

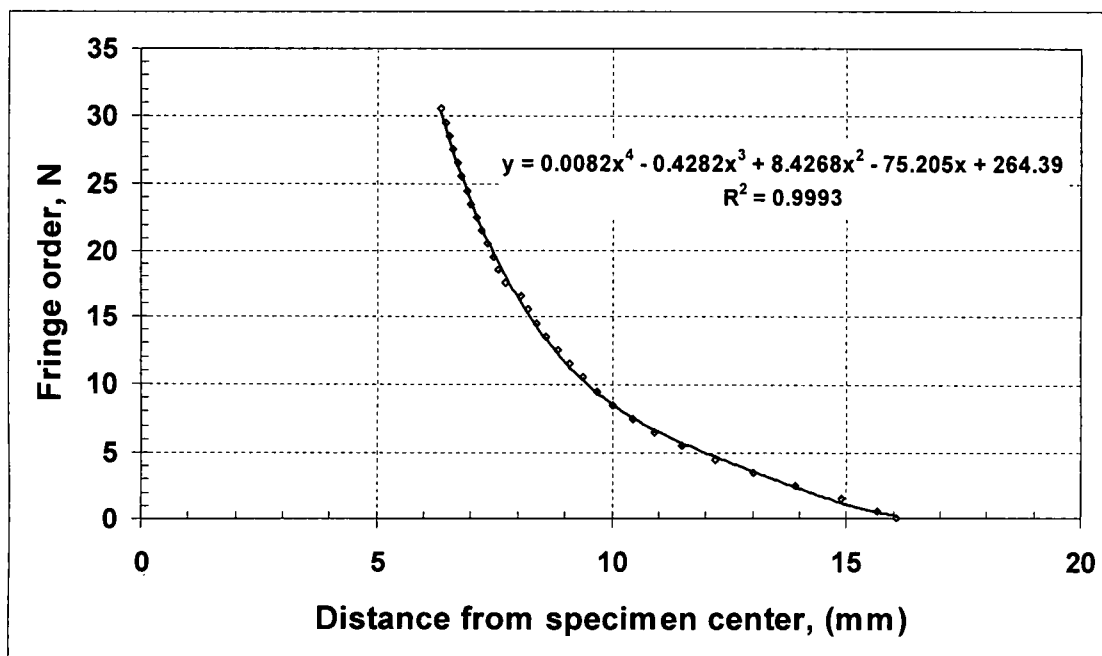


Figure 159: Bright Field Fringe order verses radial distance of 862/W Specimen A.

Table 61: Cure induced radial stresses for the 862/W resin system at the interface.

Specimen	σ_{rr} (MPa)
862-A	-8.88
862-B	-7.79
862-C	-7.81
862-D	-8.71
AVG.	-8.30

Analytical Results

A three-dimensional finite element analysis (FEA) utilizing the ANSYS [11] code is used to calculate the effective coefficient of thermal expansion. The concentric cylinder model for the 828/D-230 matrix system and 862/W system uses 387,072 elements having a total of 1,593,601 nodes. Figure 160 shows the element plots of both the 828/D-230 and 862/W FEM. Convergence studies were conducted using mesh refinement until further increases in mesh density results in less than 1.5% change in total stresses. The center of the model is fixed and a thermal load is

applied. The FEM is calibrated by adjusting the coefficient of thermal expansion until the analytical residual radial stress at the interface is equal to the experimentally obtained interface residual radial stress.

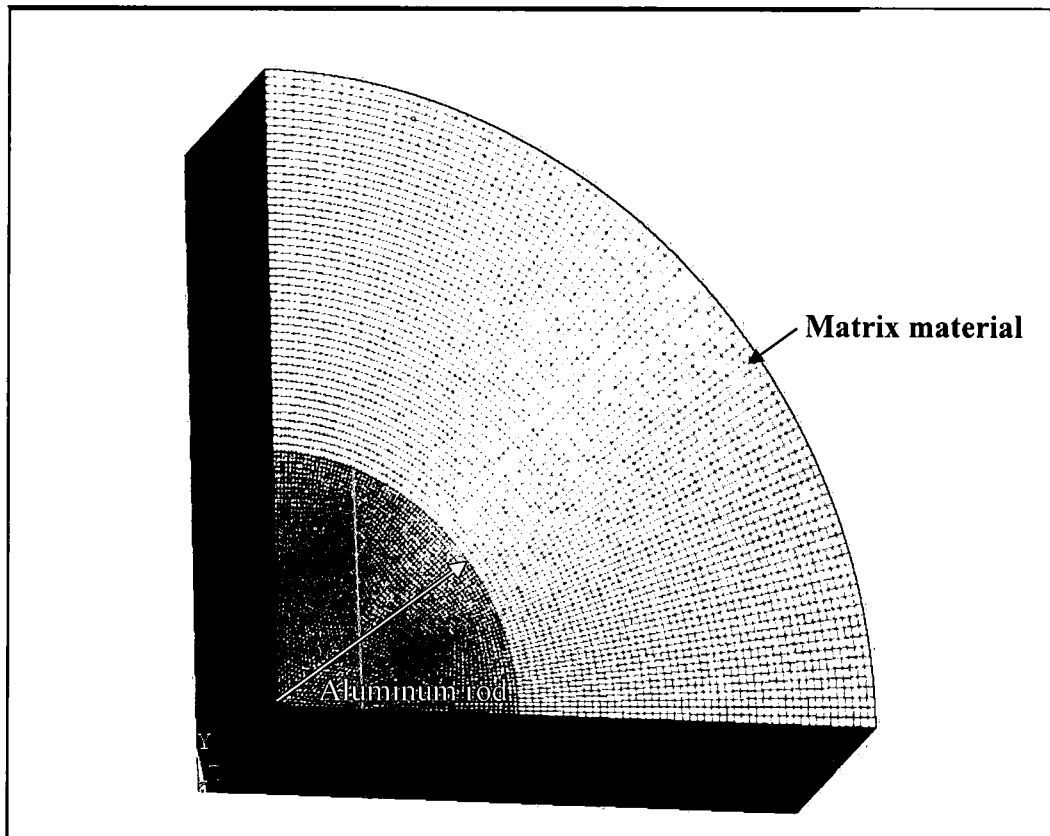


Figure 160: Finite element plot for the 828/D-230 and 862/W matrix systems residual stress models

For the 828/D-230 system a unit thermal load, $\Delta T = 1.0$, is applied. The CTE as determined by experimental test described in Appendix A is set as the initial FEM coefficient of thermal expansion. As mentioned above, the FEM CTE adjusted to obtain the compression stress at the interface of the aluminum rod experimentally determined from the photoelasticity tests described above. The experimentally obtained average stress due the cure shrinkage at the interface is -2.02 MPa resulting in an effective coefficient of thermal expansion of $741.83 \times 10^{-6}/^{\circ}\text{C}$. Likewise for the 862/W resin system, the thermal load applied in the FEM is -99°C . Since the

resin system vitrifies at 121.1° C the residual stresses are locked in at that temperature. Although the system continues with a post cure at 176.7° C for 2 hours, both the matrix and aluminum rod move together causing no further residual stresses. Consequently the ΔT input into the FEM is between the vitrification temperature and room temperature, thus $\Delta T = -99^{\circ}\text{C}$. Iterations are performed on the initial CTE model input, determined by experimentation described in Appendix A, until an average interfacial radial stress of -8.30 MPa is arrived. Therefore, the adjusted CTE results in an effective coefficient of thermal expansion of $67.4 \times 10^{-6}/^{\circ}\text{C}$. Both effective coefficient of thermal expansion values are then used in their respective cruciform FEM to determine the internal stresses caused by the matrix curing cycle process.

Conclusions

In this study the residual stresses due to the curing cycle of two model composite systems used in the work investigating failure mechanisms of composite materials loaded transverse to the direction of the fiber are determined experimentally by photoelastic methods. The experimental results are then used to calibrate a finite element model to determine an effective coefficient of thermal expansion. The experimental results show that for the 828/D-230 resin system the radial shrinkage stress at the interface is -2.06 MPa. Using a three-dimensional model of the photoelastic specimen an effective thermal coefficient of $741.83 \times 10^{-6}/^{\circ}\text{C}$ results in obtaining the radial shrinkage stress at the interface observed in the photoelastic specimens. Likewise, for the 862/W system, the experimental results show the residual radial stress induced by thermal loading and cure shrinkage at the interface is -8.3 MPa. The three-dimensional FEM results in an effective coefficient of thermal expansion of $67.4 \times 10^{-6}/^{\circ}\text{C}$ to obtain the observed interfacial radial stress from the photoelasticity experiments. The findings also show that a fairly significant amount of "pre-stress", i.e. a compressive radial stress, occurs around the fibers from the curing cycle of the room temperature cured 828/D-230 resin system while, as expected, a much larger pre-stress occurs from the high temperature cured 862/W resin system.

References

1. Asp, L.E. and L.A. Berglund, *Effects of a composite-like stress state on the fracture of epoxies*. Composites Science and Technology, 1995. **53**: p. 27-37.
2. Asp, L.E., L.A. Berglund, and R. Talreja, *Prediction of a matrix-initiated transverse failure in polymer composites*. Composites Science and Technology, 1996. **56**: p. 1089-1097.
3. Asp, L.E., L.A. Berglund, and R. Talreja, *A criterion for crack initiation in glassy polymers subjected to a composite-like stress state*. Composites Science and Technology, 1996. **56**: p. 1291-1301.
4. Bechel, V.T. and G.P. Tandon. *Interfacial toughness measurement for a model SiC/epoxy composite*. in *SEM Annual Conference*. 2001. Portland, Oregon: SEM.
5. Bechel, V.T. and G.P. Tandon, *Characterization of interfacial failure using a reflected light technique*. Experimental Mechanics, 2002. **42**(2): p. 200-205.
6. Busschen, A.T., *Micromechanical modeling of the transverse strength of unidirectional glass fiber reinforced polyester*, in *Engineering*. 1996, Delft Technical University: Delft, the Netherlands. p. 246.
7. Kok, J.M.M.d., *Deformation, yield and fracture of unidirectional composites in transverse loading*, in *Engineering*. 1995, Eindhoven University of technology: Eindhoven, the Netherlands. p. 141.
8. Foster, D.C., et al. *Residual Stress Effects on the Behavior of Unidirectional Composite Under Transverse Loading*. in *SAMPE 2004*. 2004. Long Beach, CA: Society for the Advancement of Material and Process Engineering, Covina CA.
9. Bechel, V.T., *The application of debond length measurements to examine the accuracy of composite interface properties derived from fiber pushout testing*, in *Engineering Mechanics*. 1997, University of Illinois at Urbana-Champaign: Urbana. p. 147.
10. Kobayashi, A., ed. *Handbook on Experimental Mechanics*. 1993, Society of Experimental Mechanics: New York. 165-261.
11. ANSYS, ANSYS, in *User's manual Release 10*. 2006: Cannonsburg, PA.

APPENDIX C

FINITE ELEMENT MODEL DETAILS

This appendix gives pertinent details of the finite element modeling used thorough out this work. Due to the differences between the material systems, different approaches were used for determining the internal stresses of the cruciform specimens at first damage. In addition, several preliminary studies were undertaken to determine the best mesh density and the effects of model parameters on the internal state of stress in the cruciform specimen. Finally, the ANSYS Parametric Design Language used thorough out the finite element modeling work is listed for the cruciform models and shrinkage models.

862/W Finite Element Model Unit Displacement Determination

Due to the nonlinear response of the 862/W matrix system each model was run at 3 or 4 different displacement values covering the observed far-field stress at failure initiation. The far-field stress versus displacement is plotted for each fiber spacing group with the equation of the line obtained to calculate the displacement required to achieve the far-field stress at first damage observed in the 862 cruciform experiments. Figure 161 shows a typical far-field stress verses displacement plot with the equation of the line indicated on the graph. This particular plot is for the 862 2.0d_f FEM where the far-field stress observed at first damage is plugged into the equation to obtain the required displacement to apply to the FEM. Table 62 lists the final displacements applied to the FEM to achieve the far-field stress at observed first damage.

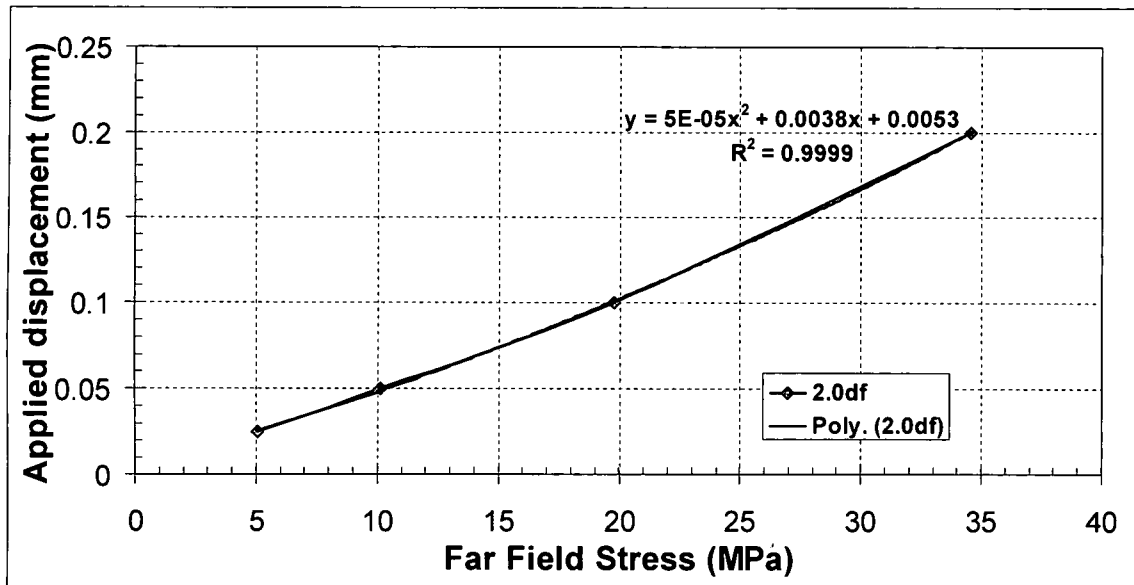


Figure 161: FEM applied displacement vs. FEM Far-field Stress results

Table 62: Final FEM applied displacements

Fiber Spacing	FEM Applied displacement (mm)
157d _f	0.05869
175d _f	0.08854
190d _f	0.08407
200d _f	0.03780
250d _f	0.07846
600d _f	0.08850
SF	0.05615

Table 63 shows the experimental far-field stress, the FEM far-field stress and the relative difference for each fiber spacing mechanical model run. The largest relative difference is 3.5% occurring at the 1.75d_f fiber spacing FEM while the smallest being 0.5% at the 6.0d_f model. Therefore, the mechanical FEM for the 862/W matrix system are accurately modeling the actual internal stress due to the applied loading at first damage as evidence by the small relative percent differences between the experimental and FEM far-field stress values listed in Table 63.

Table 63: Comparing Experimental far-field stress to 862 mechanical FEM far-field stress

862 Mechanical FEM	Experimental FF Stress (MPa)	FEM FF Stress (MPa)	% Δ
157d _f	12.04	11.88	1.3
175d _f	18.04	17.40	3.5
190d _f	17.23	16.75	2.8
200d _f	7.76	7.71	0.6
250d _f	13.66	12.63	0.6
600d _f	21.44	21.55	0.5
SF	14.46	14.56	0.7

Mesh Sensitivity Study

A study was conducted to measure the effects of the finite element mesh density on the calculated results. The linear 828 1.9d_f spacing FEM was used to gage these effects and the fiber matrix interface was investigated to see the differences of mesh density on the results. Three 3-D models were created, the 190dfRT-LDM, the 190dfRT, the 190dfRT-MDM, where the mesh densities varied as shown in Table 64. This resulted in meshes along the fiber matrix interface of the center fiber varying from 8, to 16, to 32 subdivisions and for the corner fiber from 32, to 64 to 128 subdivisions as shown in Figure 162 – 164. The elements were also increased in the radial direction from the center of each fiber to the fiber-matrix interface and further concentrated in a band around both fibers. From the outer limits of the band the elements fan outward in a uniform manner covering the rest of the matrix areas of the 3-D cruciform specimen model.

Table 64: Mesh density study statistics

Model	Elements	Nodes	Degrees of Freedom
190dfRT-LDM	22,112	95,760	287,280
190dfRT	138,048	576,800	1,730,400
190dfRT-MDM	1,104,384	4,515,321	13,545,963

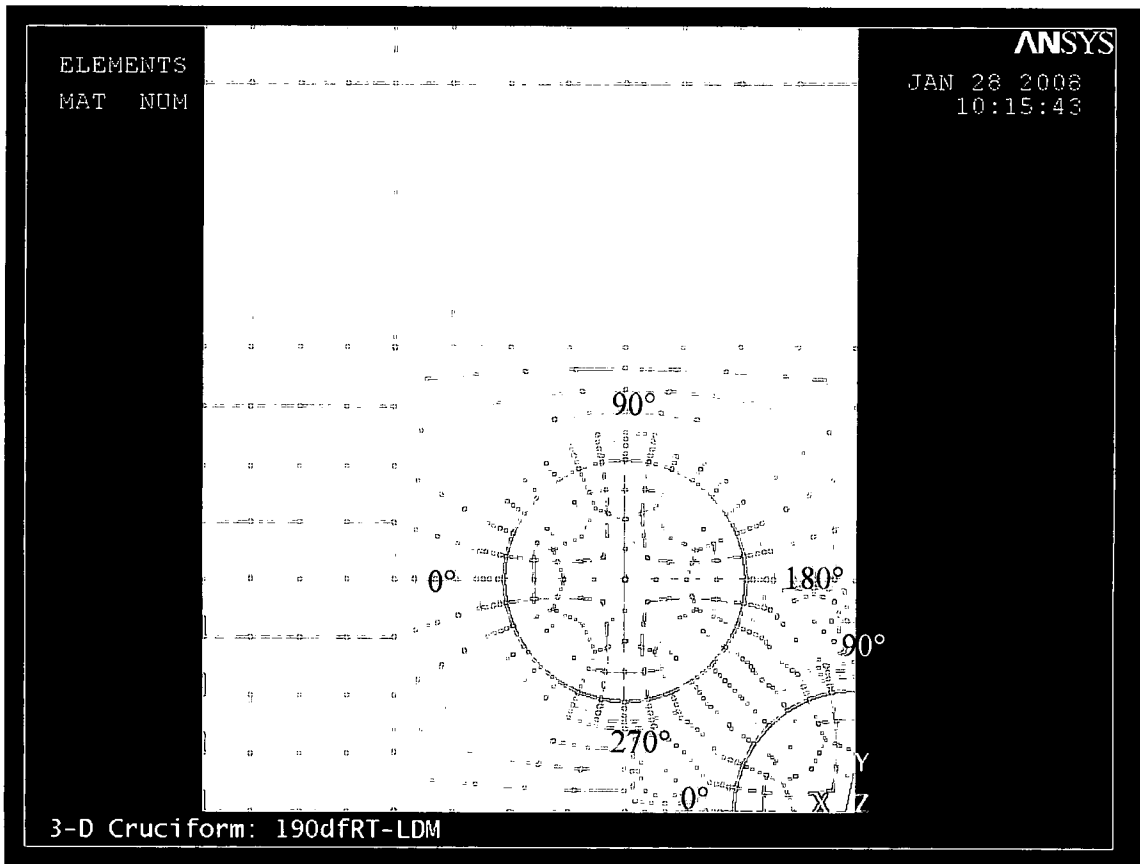


Figure 162: Element plots of the mesh density study models for the 190dfRT-LDM model

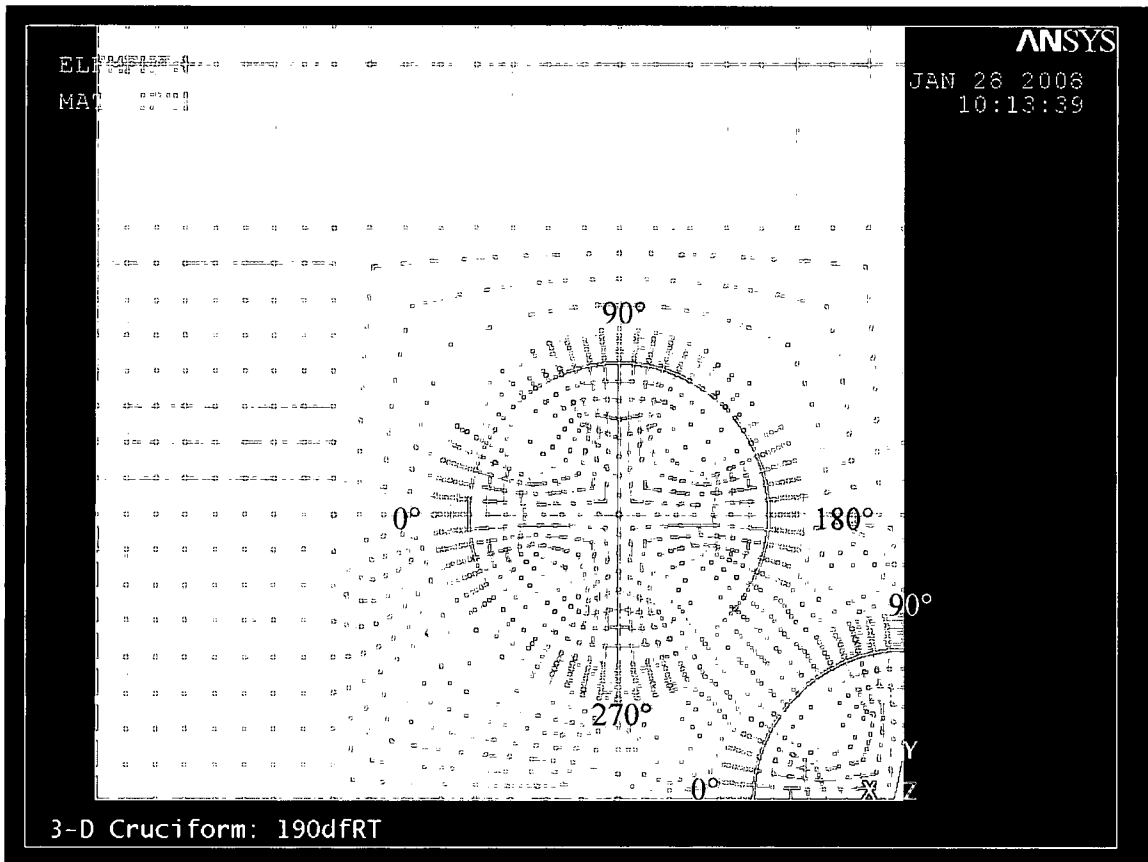


Figure 163: Element plots of the mesh density study models for the 190dfRT model

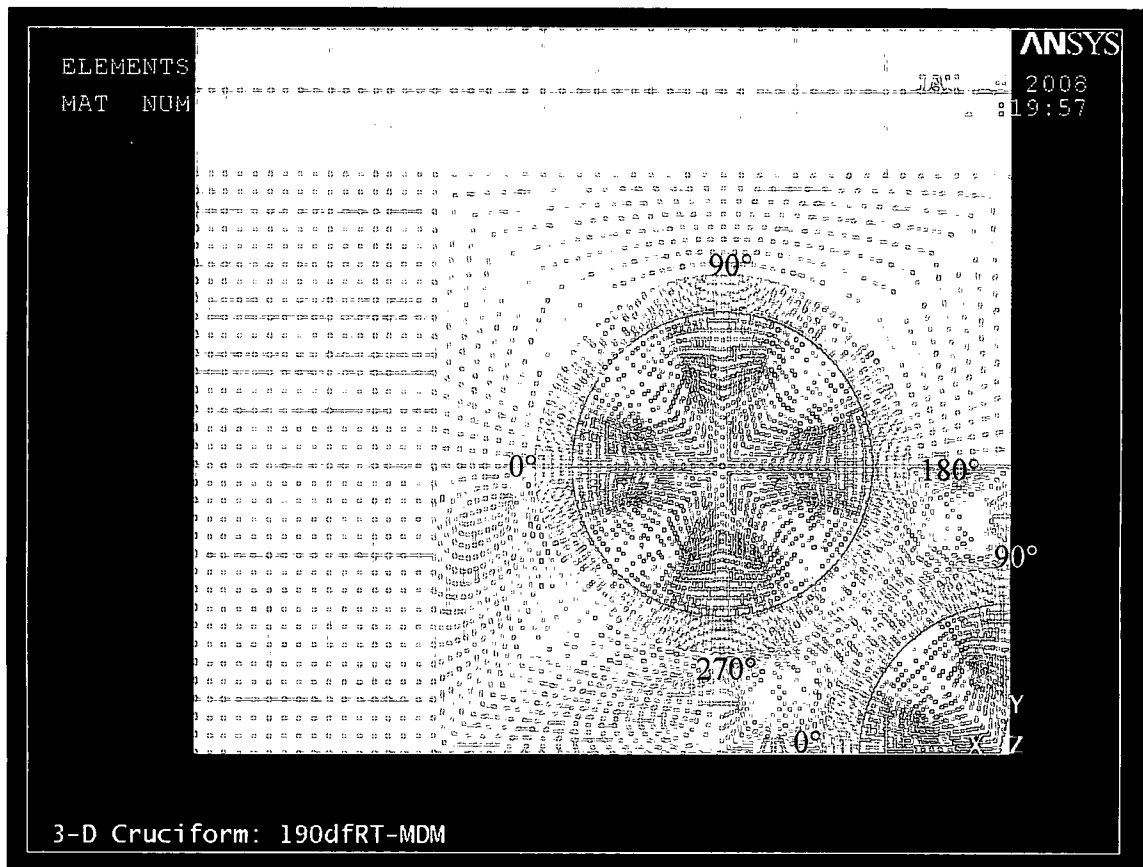


Figure 164: Element plots of the mesh density study models for the 190dfRT-MDM model

Figure 165 through 167 shows the radial, hoop and shear stress concentration factor (SCF) distribution along the center fiber, fiber-matrix interface at $Z = 0$ for the three models having the different mesh densities. All three models have the same shape for the interfacial radial, hoop and shear SCF distribution in the matrix as the plots practically lie on top of each other. For the radial and hoop SCF the minimum magnitude occurs at $\theta = 0^\circ$, normal to the direction of the load, and the maximum magnitude occurs at, in the direction of the load as expected. For the shear SCF the maximum magnitude for all three models appears to occur at $\theta = 34^\circ$ shifted from $\theta = 45^\circ$ due to nearest neighboring fiber effects. As expected, the smoothness of the interfacial distribution improves with mesh density, as evidence by comparing the 190dfRT-LDM, the 190dfRT and the 190dfRT-MDM plots in Figures 165, 166 and 167. The 190dfRT-LDM model shows oscillation in the Hoop SCF and Shear SCF plots along the center fiber interface.

This behavior is a leading indication that the mesh is not refined enough to capture the actual results along the center fiber interface.

Table 65 shows the interfacial center fiber radial (R), hoop (H) and shear (S) SCF results for the three differently meshed models at common angular positions along the interface. As expected, the largest relative differences exist between the least dense meshed model with the densest meshed model for radial, hoop and shear SCF. Whereas, the smallest differences occur between the 190dfRT and 190dfRT-MDM models relative to the radial, hoop and shear SCF. In fact, the largest differences occur at $\theta = 45^\circ$ between the 190dfRT and 190dfRT-MDM models for the radial and hoop SCF having only a relative difference of 1.2%. For the shear SCF the largest difference between 190dfRT and 190dfRT-MDM occurs at $\theta = 22.5^\circ$ having a relative difference of 1.5%.

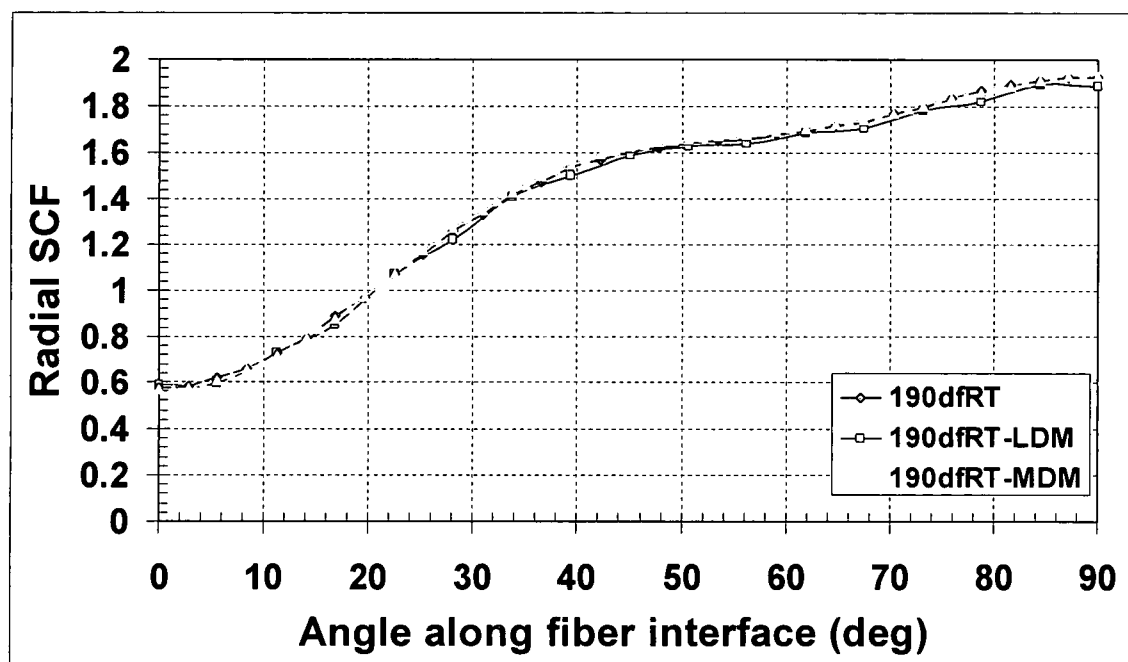


Figure 165: Center Fiber interface mesh density results for the Radial SCF

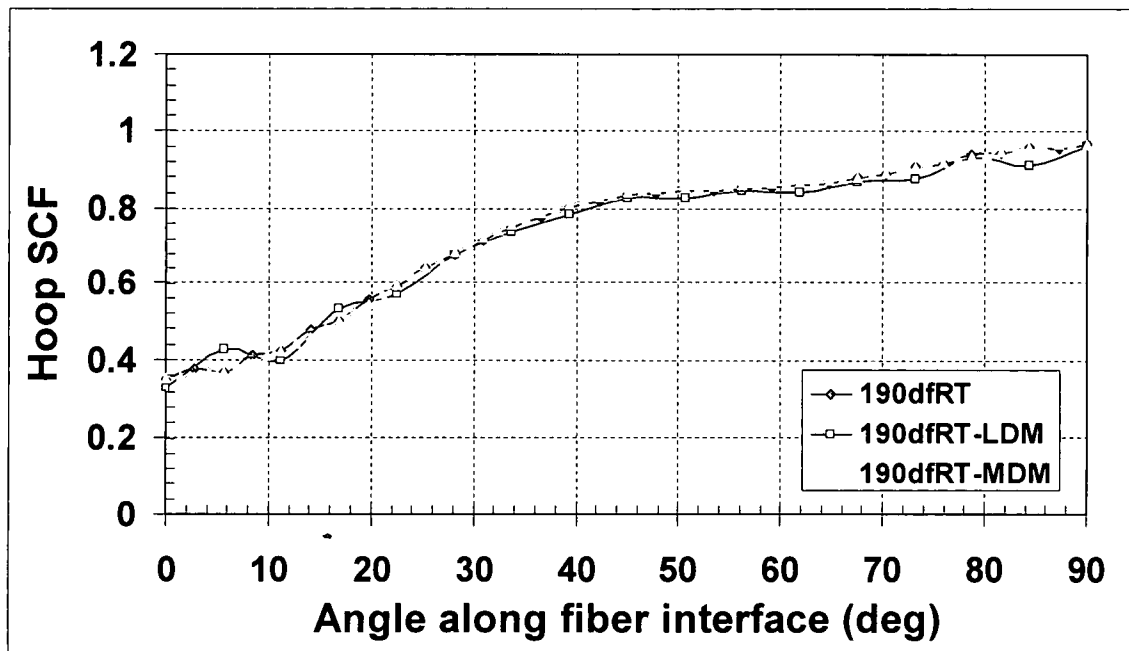


Figure 166: Center Fiber interface mesh density results for the Hoop SCF

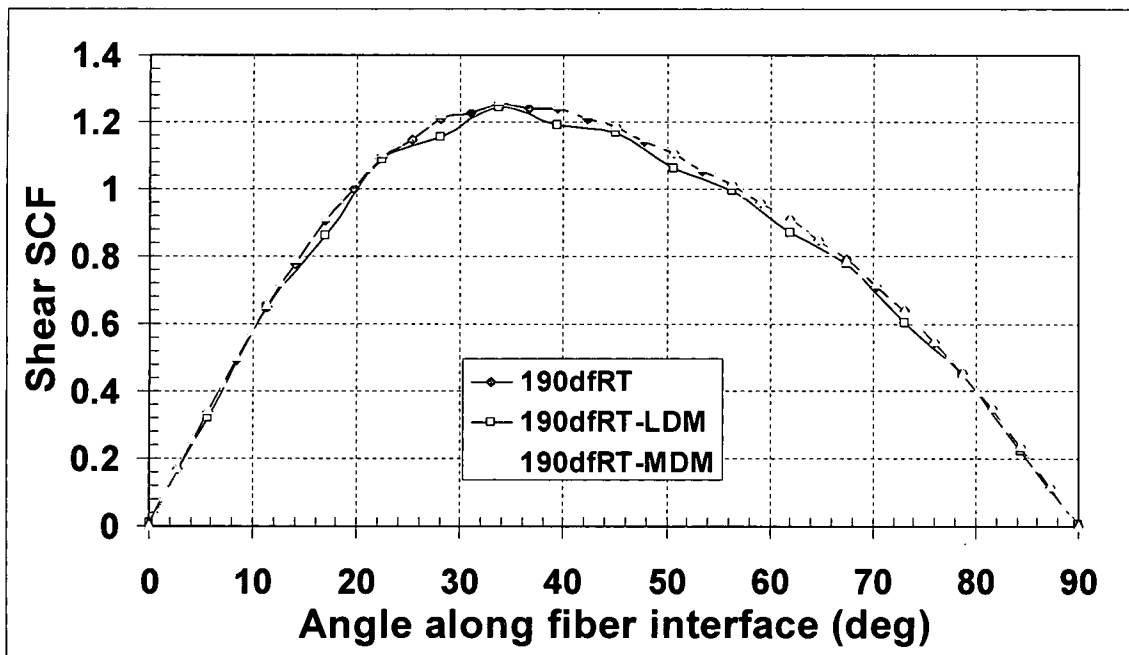


Figure 167: Center Fiber interface mesh density results for the Shear SCF

Table 65: Center Fiber interface SCF mesh density results for the 190dfTR-LDM, 190dfRT and 190dfRT-MDM FEM models

Angle	190dfRT-LDM			190dfRT			190dfRT-MDM		
	Radial	Hoop	Shear	Radial	Hoop	Shear	Radial	Hoop	Shear
0	0.59	0.38	0.01	0.57	0.35	0.0	0.57	0.35	0.0
22.5	1.07	0.57	1.09	1.07	0.59	1.09	1.07	0.59	1.11
45	1.59	0.83	1.17	1.60	0.83	1.19	1.62	0.84	1.19
67.5	1.70	0.87	0.78	1.73	0.88	0.79	1.74	0.88	0.79
90	1.89	0.96	0.01	1.92	0.97	0.0	1.93	0.97	0.0

To further gage the impact of mesh density on the analytical results the corner fiber interface between $\theta = 180^\circ$ to 270° is investigated. This region represents the section of fiber interface closest to the center fiber exhibiting high stresses due to their close proximity. Figures 168 through 170 shows the 3-D Corner Fiber FEM results for the Radial SCF, the Hoop SCF and the Shear SCF, respectively, at the interface between $\theta = 180^\circ$, normal to the direction of the load, and 270° , in the loading direction. Similar to the center fiber interface results between $\theta = 0^\circ$ and 90° , the corner fiber results between $\theta = 180^\circ$ and 270° for the three mesh densities have practically the same stress distribution. However, as shown in Figure 169 the Hoop SCF for the 190dfRT-LDM results oscillate between $\theta = 180^\circ$ to 202.5° and again between $\theta = 247.5^\circ$ and 270° . Furthermore, oscillation of 190dfRT-LDM model results is shown in the Shear SCF plot between $\theta = 196.875^\circ$ and 253.125° in Figure 170. As indicated above this particular behavior indicates that the mesh is not dense enough to adequately capture the correct results along the fiber-matrix interface.

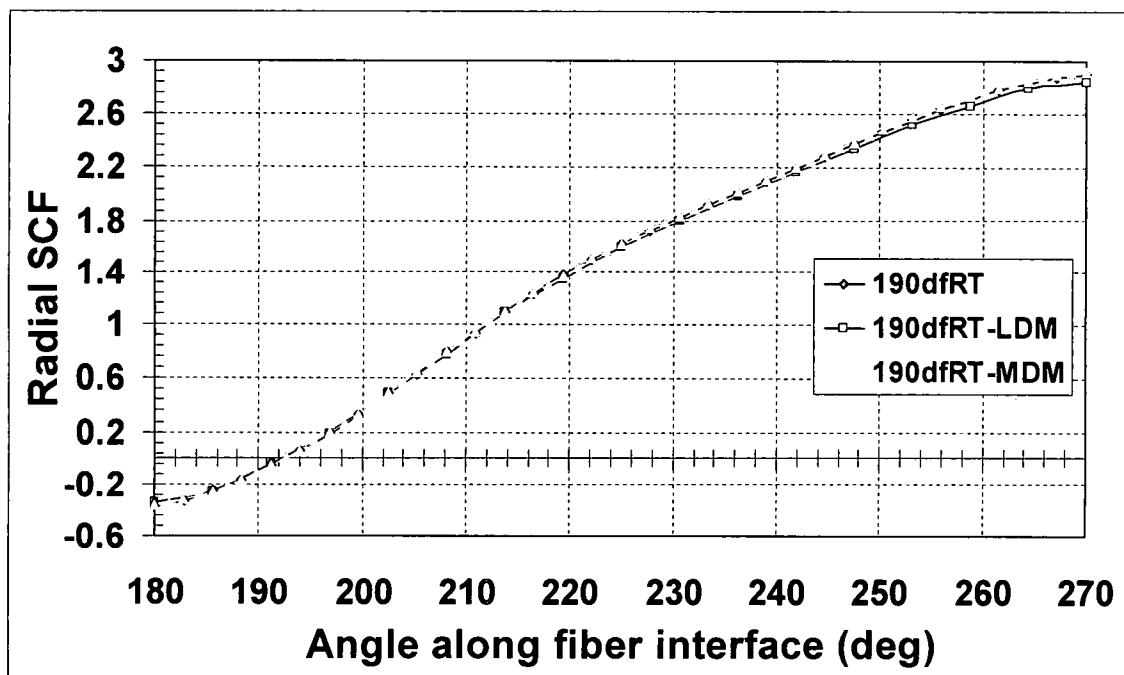


Figure 168: Corner Fiber mesh density results for the Radial SCF

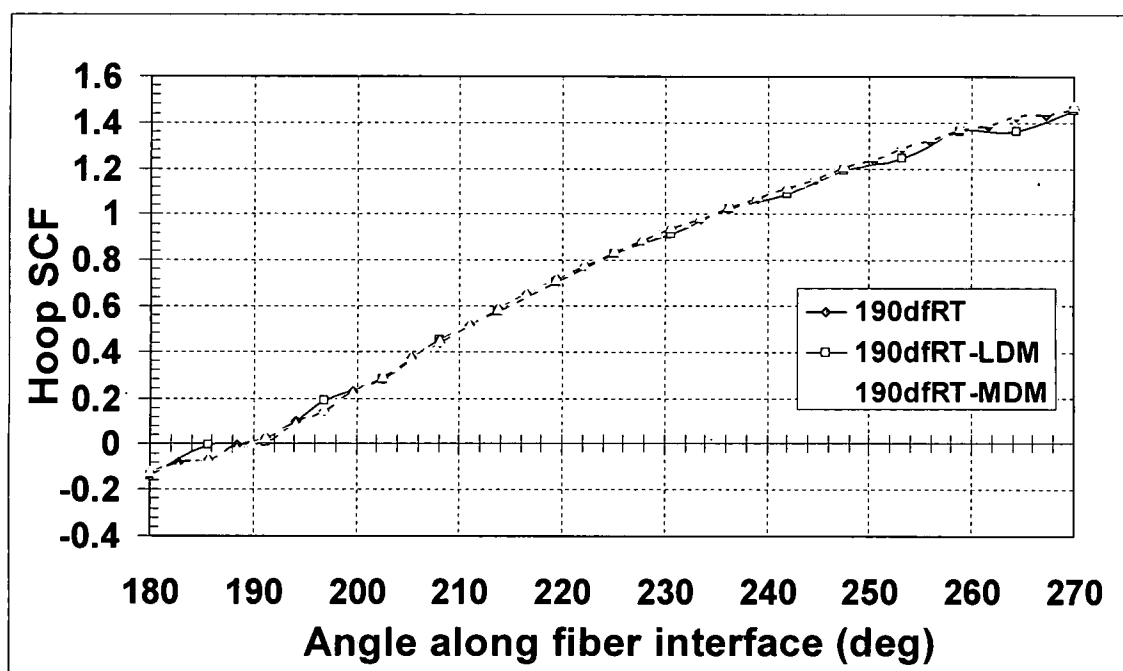


Figure 169: Corner Fiber mesh density results for the Hoop SCF

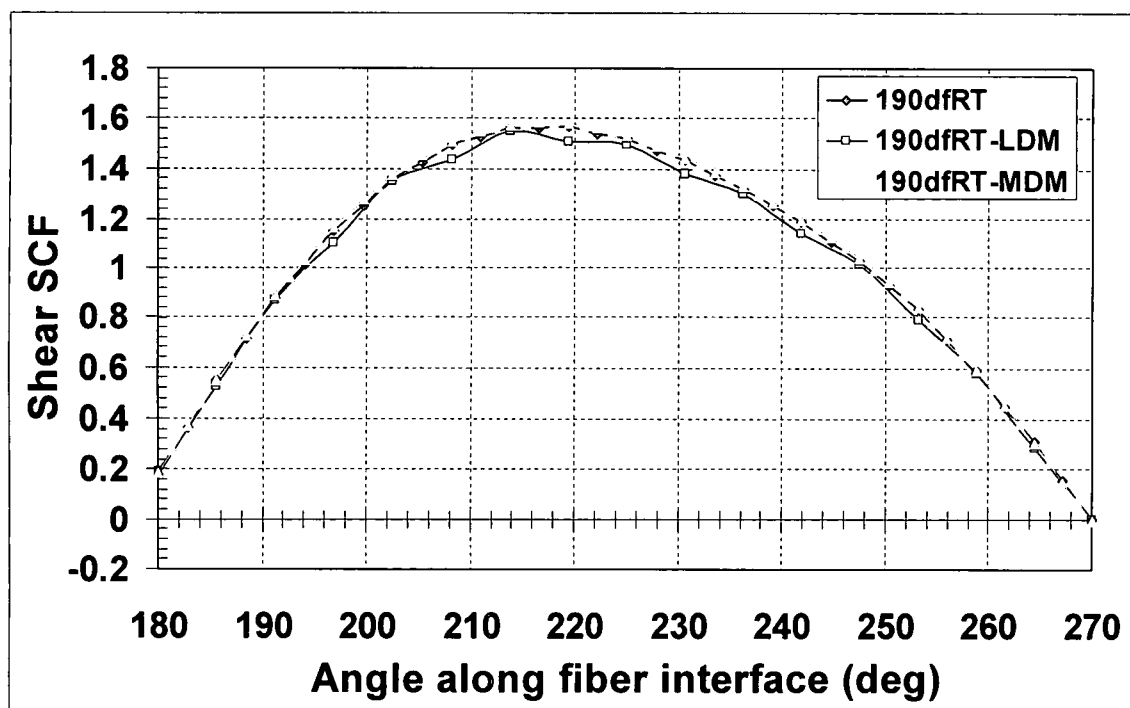


Figure 170: Corner Fiber mesh density results for the Shear SCF

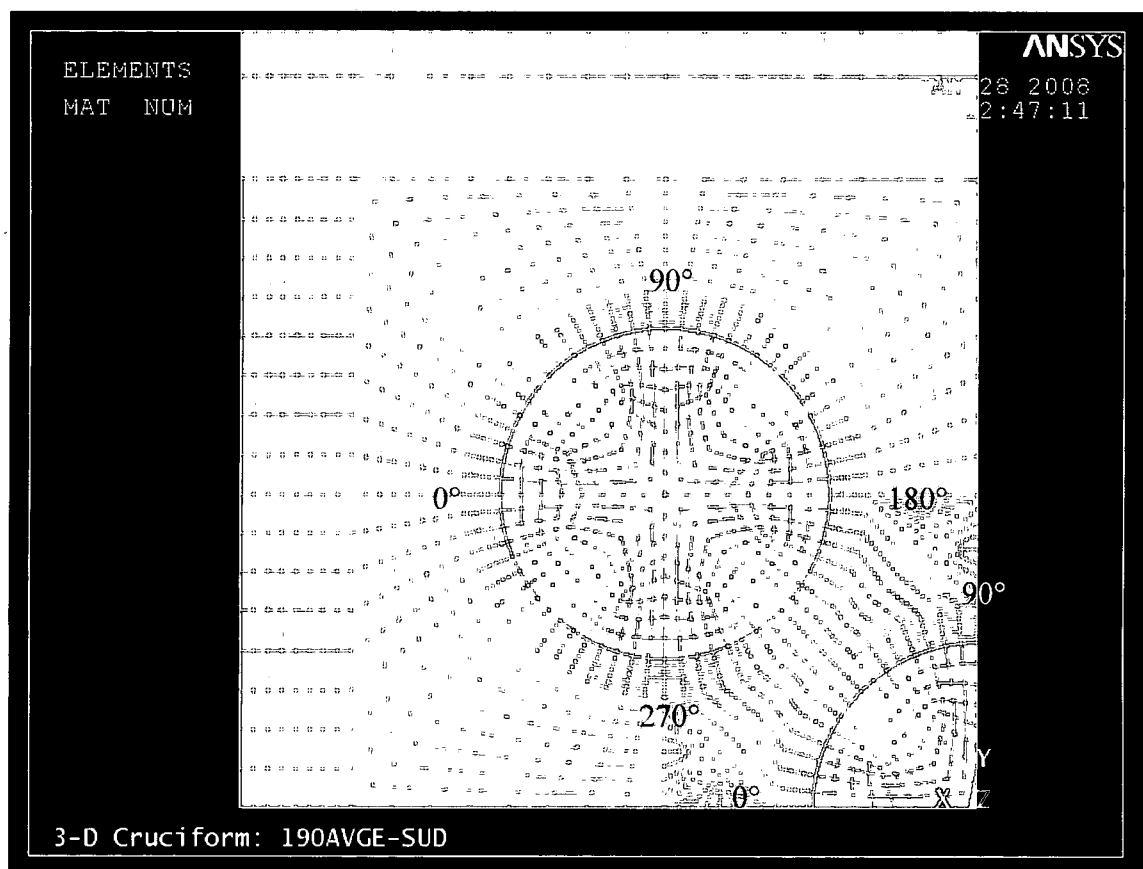
Table 66 lists the Radial SCF, the Hoop SCF, and the Shear SCF results of the three models at common angular positions selected along the corner fiber interface between 180° and 270°. The largest relative difference between the results for the radial, hoop and shear SCF magnitudes of the three FEM having different mesh densities occur primarily between the least dense meshed model and the most dense meshed model, as expected, except for the radial SCF at $\theta = 180^\circ$. Here the largest relative difference exists between the least dense meshed model and the regular meshed model. It is also anticipated that the smallest relative differences for the radial, hoop and shear SCF magnitudes exist between the regular meshed and most dense meshed model as revealed by Table 66.

Table 66: Corner Fiber interface SCF mesh density results

Angle	190dfRT-LDM			190dfRT			190dfRT-MDM		
	Radial	Hoop	Shear	Radial	Hoop	Shear	Radial	Hoop	Shear
180	-0.34	-0.14	0.19	-0.37	-0.13	0.18	-0.36	-0.12	0.18
202.5	0.50	0.28	1.35	0.49	0.29	1.36	0.49	0.29	1.37
225	1.59	0.83	1.50	1.61	0.84	1.52	1.62	0.84	1.53
247.5	2.34	1.19	1.01	2.37	1.20	1.03	2.39	1.21	1.03
270	2.88	1.45	0.0	2.89	1.46	0.0	2.92	1.47	-0.01

Mesh Sensitivity Study – Summary

Comparison of the data in Tables 65 and 66 indicate that the difference between results for the radial, hoop and shear SCF magnitudes are practically the same and do not justify the mesh density shown in the 190dfRT-MDM model. Furthermore, the oscillation exhibited for the interfacial results at the center and corner fiber indicates that the 190dfRT-LDM mesh density is not enough. Consequently the finite element model, 190dfRT, meshed twice over the least dense meshed model gives adequate results and thus this mesh density will be used throughout all finite element calculations for both matrix systems. Figure 171 shows the final configuration of the FEM mesh where further mesh refinement occurred beyond the outer band around the fibers deeper into the matrix regions of the cruciform model.



**Figure 171: Final mesh configuration showing mesh refinement over mesh density results
beyond outer band around fibers**

Parametric Study

A parametric study is performed to examine the effects of fiber spacing on the stress distributions as the fiber spacing is changed in the 828/D-230 matrix system. This effort was done to gain a better understanding of the locations within the cruciform specimen where failure is likely to occur. From previous experimental results of the $6.0d_f$, $2.5d_f$ and $1.84d_f$ fiber spacing groups where a change in failure initiation preference and mechanism was observed as the fiber spacing decreased. It was decided to focus on the interfacial length where the center and corner fiber are closest, thus from $\theta = 0^\circ$ to 90° for the center fiber and from $\theta = 180^\circ$ to 270° for the corner fiber, anticipating the highest magnitudes of stress in this location. In addition, the study shed light on the internal stress state of the multi-fiber cruciform specimen as the fiber spacing varied for potential changes in failure initiation mechanism already observed. Furthermore, the

parametric study revealed effects of cruciform parameters specific to the multi-fiber specimens not previously optimized or considered. It was also reasonable to expect similar behavior from the 862/W matrix system since both are isotropic materials although the 862/W is more compliant and stronger than the 828/D-230 matrix system.

Fiber Spacing Effects

The cruciform thickness in the finite element model is held constant at 4.75 mm while the center-to-center spacing between the central fiber and the corner fiber is varied. The study involves analyzing multi-fiber model composites having a fiber spacing of $1.57d_f$, $1.75d_f$, $1.9d_f$, $2.5d_f$, $6d_f$ and $12d_f$. The $1.57d_f$, $1.75d_f$, and $1.9d_f$ spacing represent varying degrees of densely packed fibers while the $2.5d_f$ spacing represent closely packed fibers and the $6d_f$ and $12d_f$ fiber spacing represent varying degrees of isolated fibers. For comparison with larger fiber spacing solutions, the limiting case of a single-fiber (SF) was also simulated. Due to symmetry conditions only 1/8 of the total multi-fiber cruciform specimen is modeled and its configuration is shown above in Figure 171.

The radial stress distributions due to the chemical shrinkage of the matrix at the fiber-matrix interface are shown in Figure 161 for the center fiber and Figure 173 for the third quadrant of the corner fiber. Recall that for the third quadrant of the corner fiber θ varies from 180° to 270° and also it is the quadrant closest to the center fiber as shown in Figure 164. These results represent the total stress due to the cure shrinkage by the matrix on the fibers in the cruciform specimens. The radial stress distributions for the $6d_f$, $12d_f$, and the single fiber are compressive and nearly uniform over the fiber-matrix interface. However, as the fiber spacing is decreased ($< 6d_f$), the radial stress ceases to be uniform and becomes a maximum at 45° for the center fiber and at 225° for the corner fiber. Moreover, the magnitude of the maximum radial stress increases with decrease in fiber spacing.

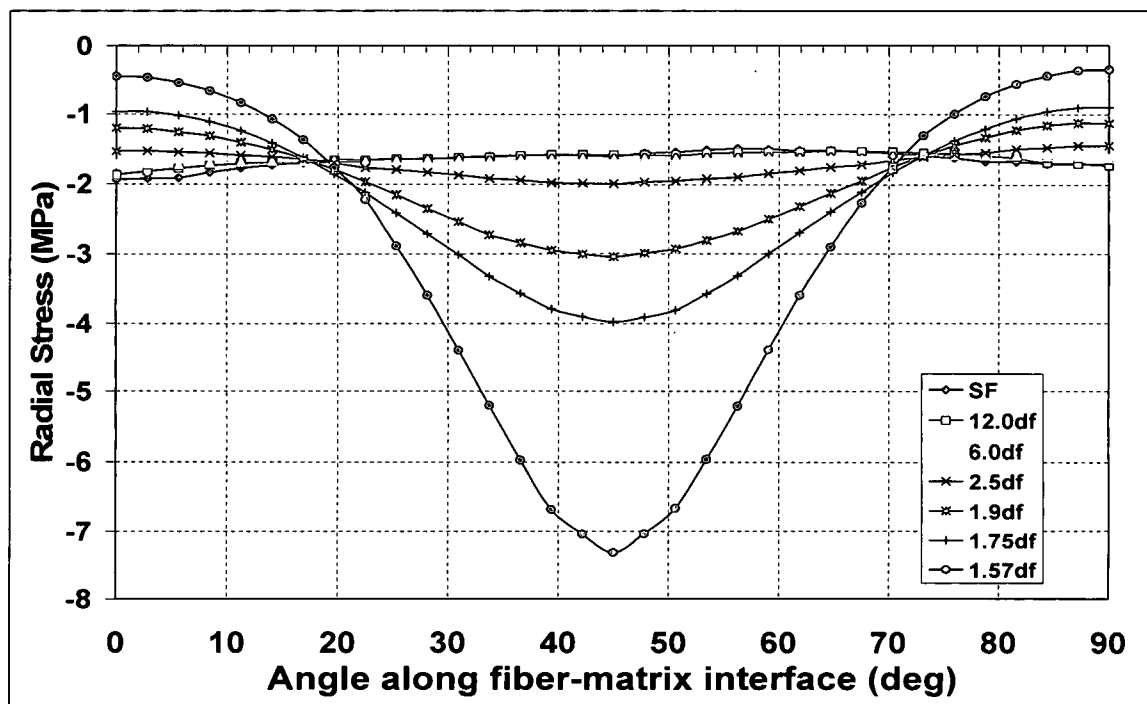


Figure 172: Variation of radial stress due to chemical shrinkage at the interface of the center fiber as a function of fiber spacing

The hoop stress distributions in the matrix due to the chemical shrinkage of the matrix at the fiber-matrix interface are shown in Figure 174 for the center fiber and Figure 175 for the corner fiber. The behavior of the hoop stress is similar to the radial stress distribution. However, the magnitude of the hoop stress is approximately 20% of the radial stress magnitude. The interfacial shear stresses due to the chemical shrinkage are also small in magnitude compared to the radial stress and are shown in Figure 176 and 177 for the center fiber and corner fiber respectively. Similar to the radial stress, the shear stress is approximately uniform over the fiber-matrix interface at larger spacings, but becomes non-uniform at smaller fiber spacings, with the maximum occurring at 28° and 62° for the center fiber, and at 208° and 242° for the corner fiber. The magnitude of the maximum shear stress is also seen to increase with decrease in fiber spacing.

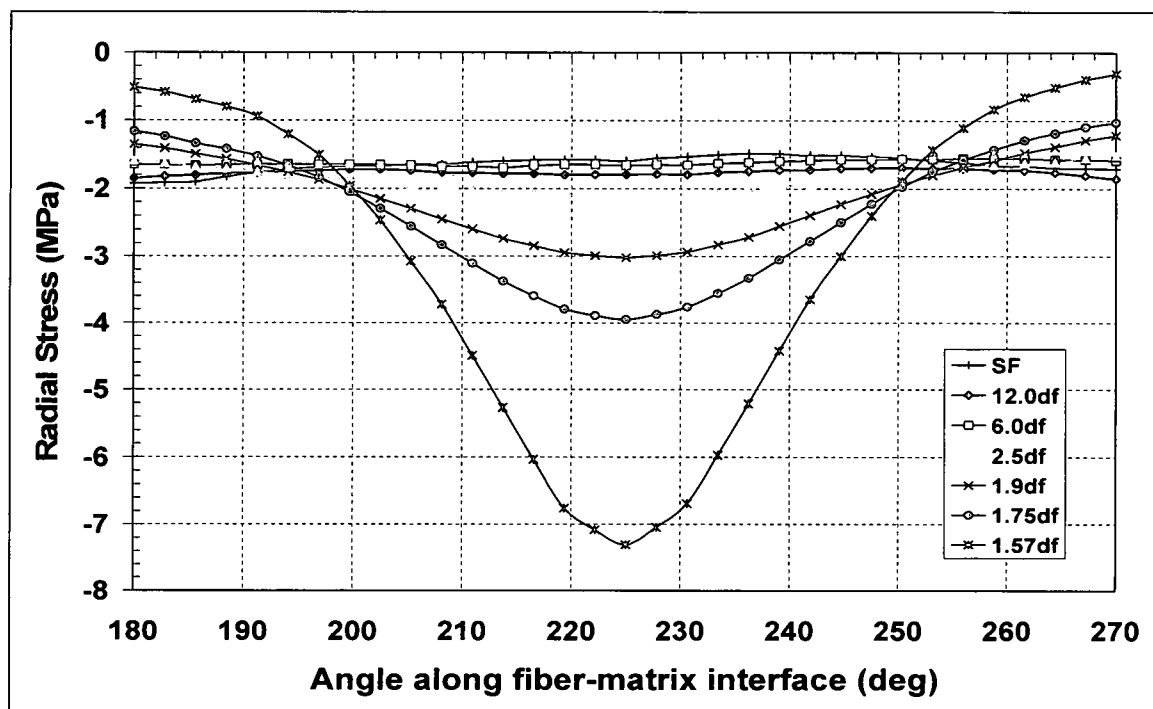


Figure 173: Variation of radial stress due to chemical shrinkage at the interface of the corner fiber as a function of fiber spacing

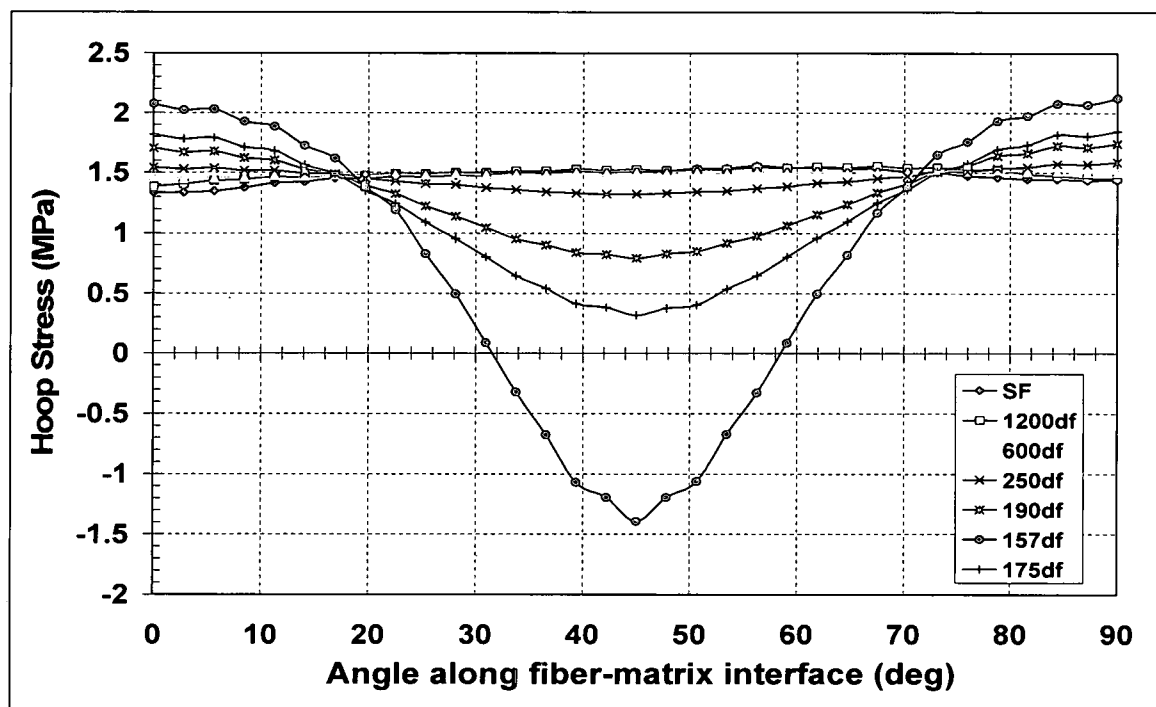


Figure 174: Variation of hoop stress due to chemical shrinkage at the interface of the center fiber as a function of fiber spacing

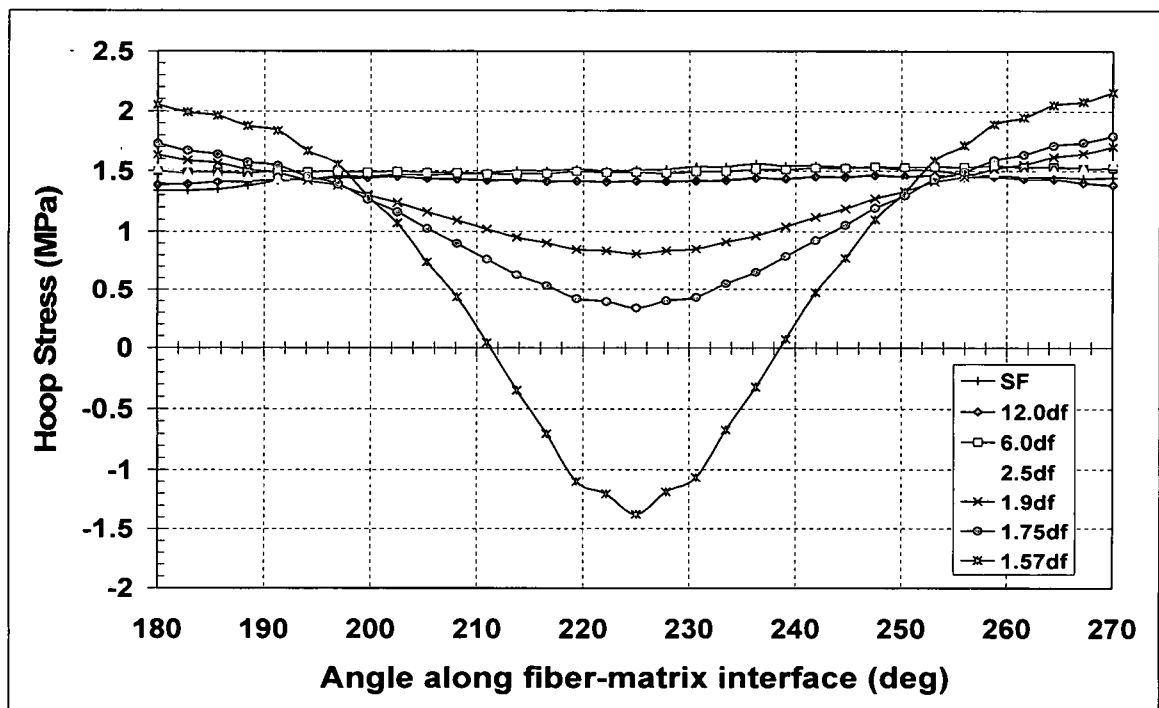


Figure 175: Variation of hoop stress due to chemical shrinkage at the interface of the corner fiber as a function of fiber spacing

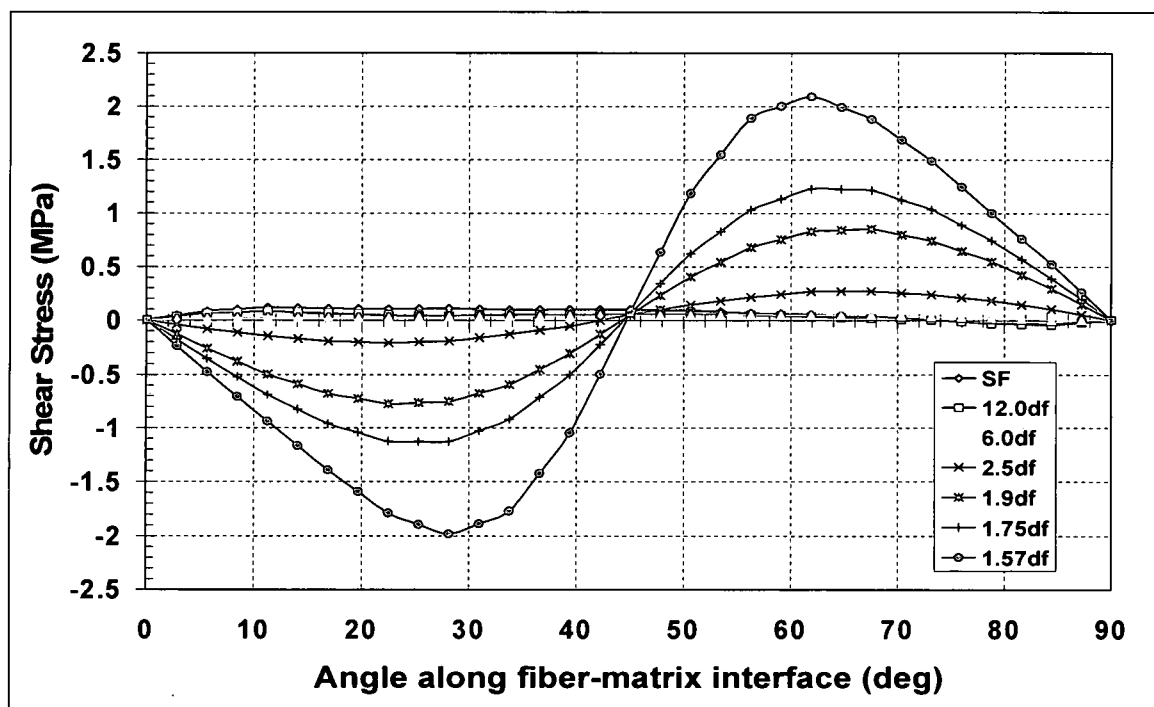


Figure 176: Variation of shear stress due to chemical shrinkage at the interface of the center fiber as a function of fiber spacing

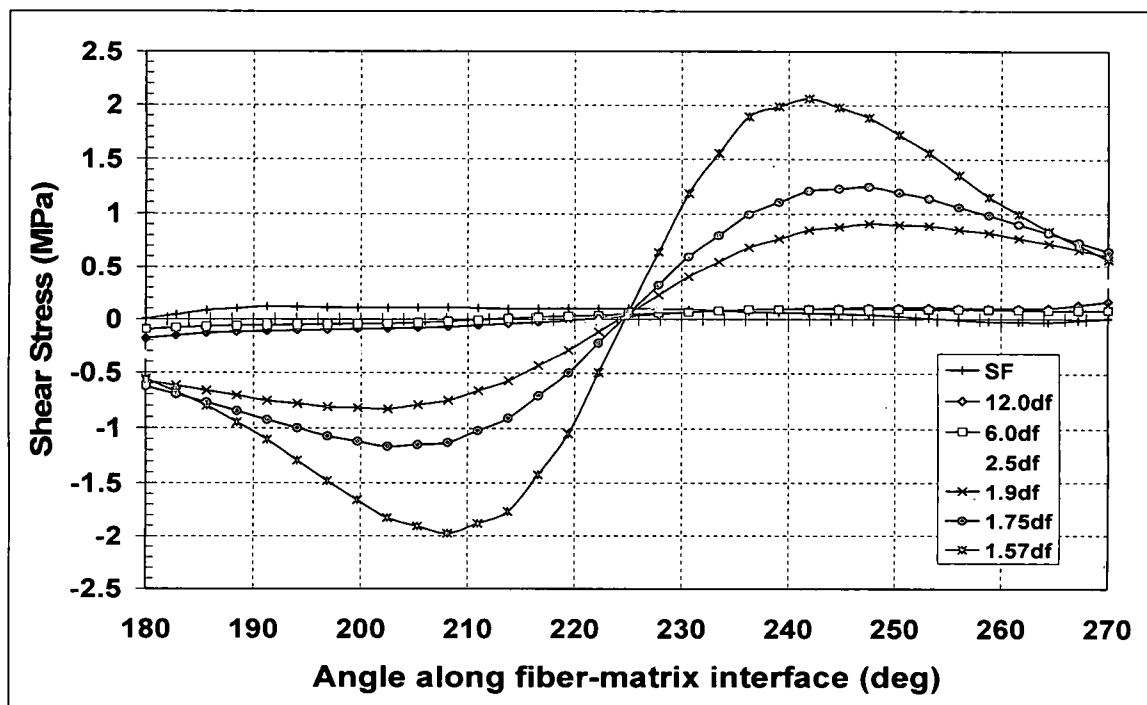


Figure 177: Variation of shear stress due to chemical shrinkage at the interface of the corner fiber as a function of fiber spacing

For the radial, hoop and shear stress distributions, the magnitudes increase as the fiber spacing decreases at both the center and corner fibers. This result reflects the influence of the nearest neighboring fiber on the interfacial stress distributions. However, for the 6.0df and the 12df no effects are indicated due to their uniform stress distribution exhibited for the interfacial radial, hoop and shear stresses just like those exhibited by the single fiber.

Figures 178 and 179 show the variation of radial stress in the matrix, at the fiber interface, due to the mechanical loading for the center and corner fiber, respectively. All the stress values reported from here onwards have been normalized with the average far-field stress values. Figure 178 shows that the multi-fiber analysis having the largest fiber spacing, 12df, has a maximum radial tensile stress at $\theta = 90^\circ$, in the direction of the load, while the minimum is normal to the direction of the load at $\theta = 0^\circ$. The SF analysis has practically the same radial stress distribution around the center fiber interface as the 12df multi-fiber model. Although slightly smaller in magnitude, the 6.0df has the same stress distribution as the 12df and the SF. Thus,

with wider $12d_f$ spacing and possibly the $6.0d_f$, the center fiber behaves like a single fiber. With a decrease in spacing to $2.5d_f$, the maximum radial stress continues to decrease while the minimum increases although the distribution remains similar to the $12d_f$ solution. With further decrease in spacing to $1.9d_f$, the radial stress at the interface tends to become more uniform over a larger portion of the interface close to the fiber north pole, with the maximum still occurring at $\theta = 90^\circ$. However, the $1.75d_f$ model shows a distinct shift in the location of the maximum radial stress from $\theta = 90^\circ$ to $\theta = 47.8^\circ$ while becoming more uniform over a larger portion of the interface. Note that the maximum radial stress for the $1.75d_f$ model at $\theta \sim 48^\circ$ is approximately equal to the $1.9d_f$ model at $\theta = 90^\circ$. As the fiber spacing is reduced further to $1.57d_f$, there is a significant shift in the location of the maximum radial stress with a distinct peak at $\theta \sim 45^\circ$. Further, the magnitude of the maximum radial stress at the interface for the $1.57d_f$ model is now larger compared to the $1.75d_f$, $1.9d_f$ and $2.5d_f$ results. The results of the $1.9d_f$, $1.75d_f$ and $1.57d_f$ FEA clearly show the influence of the neighboring fiber on the radial stress distribution at the fiber-matrix interface for the center fiber as the fiber spacing decreases.

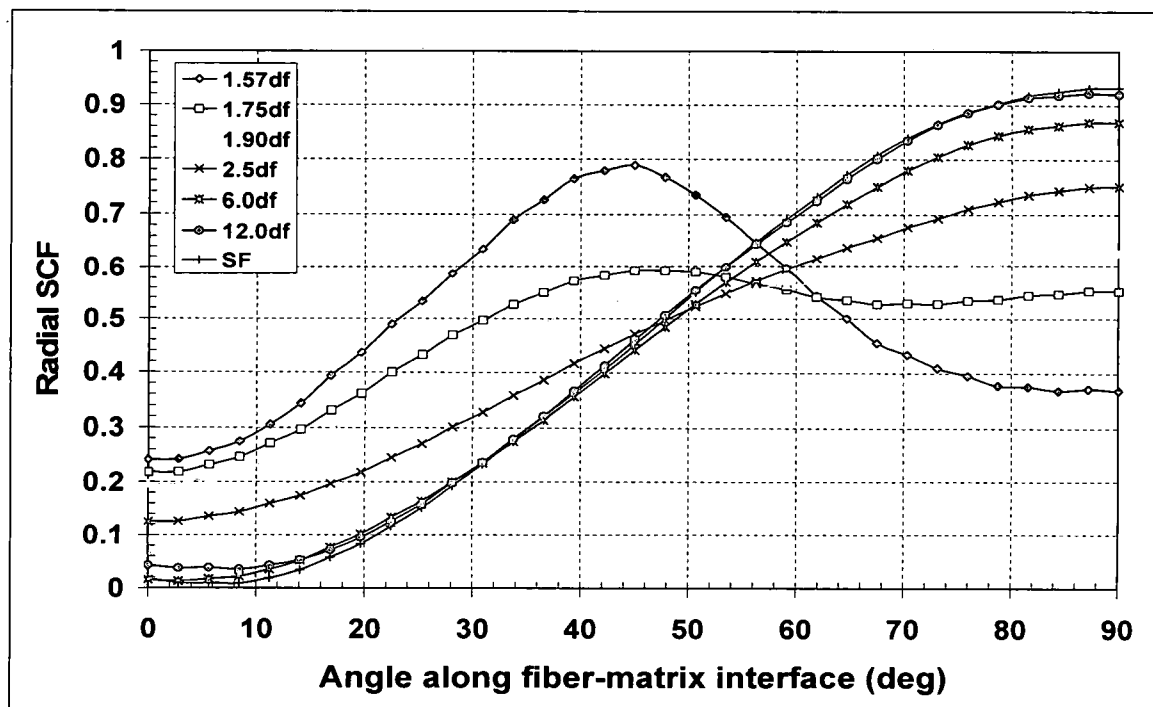


Figure 178: Variation of radial stress due to mechanical loading at the interface of the center fiber as a function of fiber spacing

Figure 179 shows the interface radial stress distribution for the section of corner fiber closest to the center fiber, i.e. from $\theta = 180^\circ$ to $\theta = 270^\circ$. The stress distribution for the $6.0d_f$ and $12d_f$ spacing for the corner fiber is similar to the results of the center fiber and SF solutions. Further, the radial stress distributions for the corner fiber follow trends similar to the center fiber as the fiber spacing is decreased, although the changes in the magnitude of maximum and minimum stress levels are lower. It is observed that at the smallest fiber spacing of $1.57d_f$, a distinct "hump" or "wave" begins to develop around $\theta \sim 233^\circ$ where the radial stress attains its maximum value. Moreover, the radial stress for the corner fiber is now approximately uniform over a larger portion of the interface extending from $\theta \sim 233^\circ$ to its south pole at $\theta = 270^\circ$. Thus, if failure was governed by a maximum radial stress criterion, any point on the interface between $\theta \sim 233^\circ$ and $\theta = 270^\circ$ could be a likely location. Another point to note is that for smaller fiber spacings ($< 6d_f$), the magnitude of the maximum radial stress at the interface for the corner fiber are larger compared to the center fiber. Thus, it is more likely that the corner fiber will debond first

at the smaller fiber spacings, whereas failure can initiate at either the corner fiber or center fiber interface at larger spacings ($> 6d_f$).

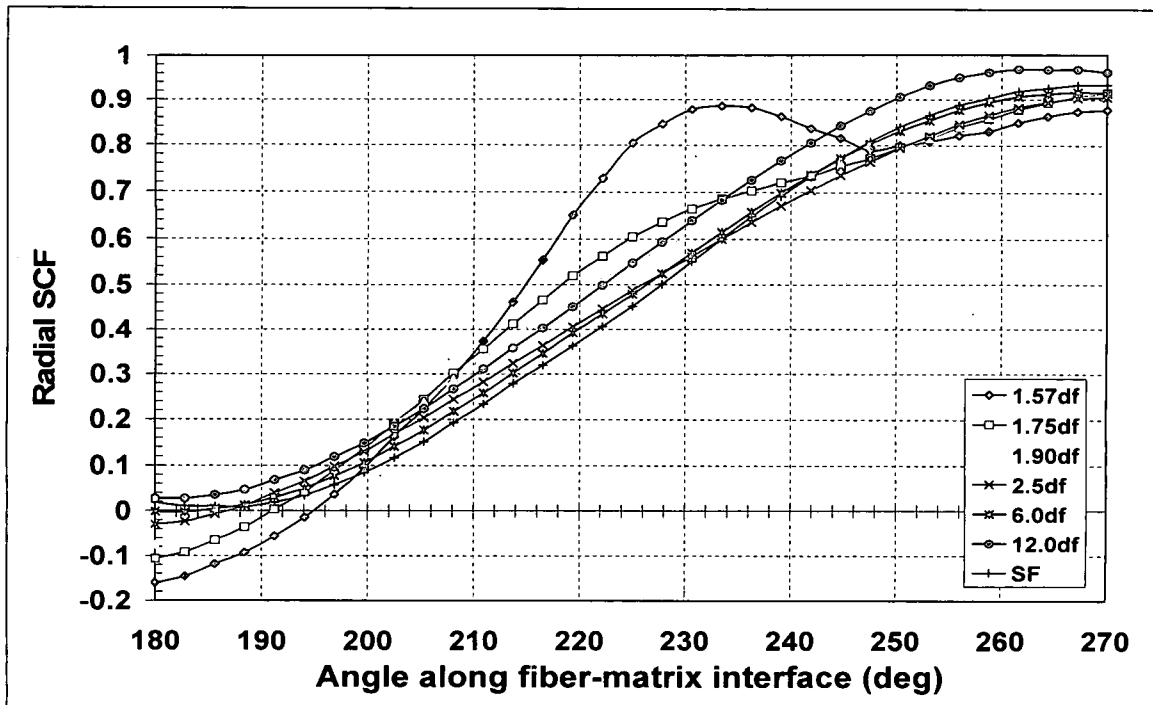


Figure 179: Variation of radial stress due to mechanical loading at the interface of the corner fiber as a function of fiber spacing

Figures 180 and 181 show the variation of the hoop stress distribution in the matrix at the fiber-matrix interface due to mechanical loading for the center and corner fiber, respectively. The stress distribution is very similar to that of the radial stress for both the center fiber and corner fiber. However, the magnitude of the hoop stress is approximately 50% of the corresponding radial stress.

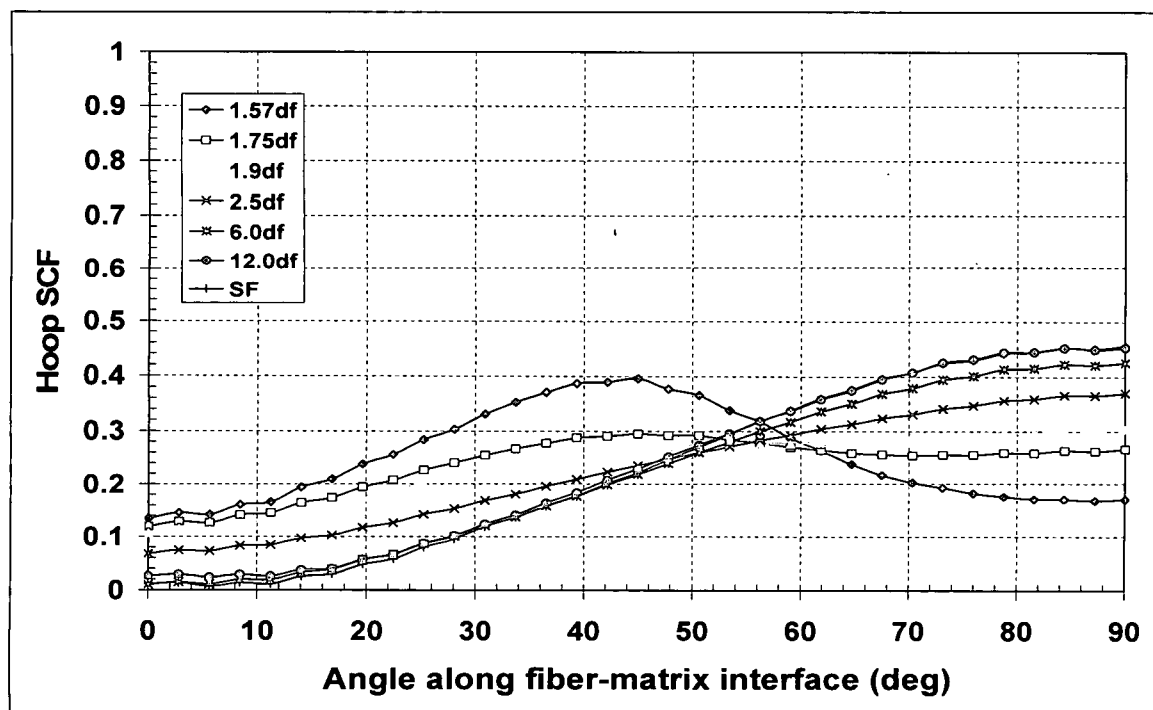


Figure 180: Variation of hoop stress due to mechanical loading at the interface of the center fiber as a function of fiber spacing

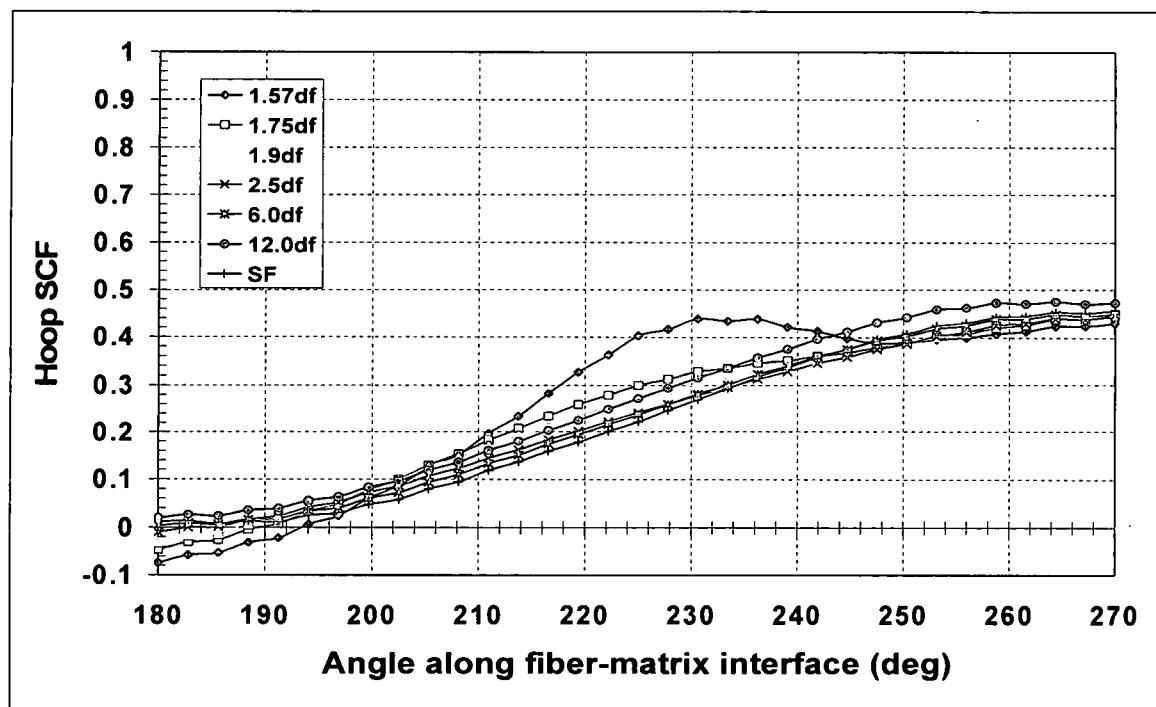


Figure 181: Variation of hoop stress due to mechanical loading at the interface of the corner fiber as a function of fiber spacing

Figures 182 and 183 show the variation of the shear stress distribution at the fiber-matrix interface due to mechanical loading for the center and corner fiber, respectively. For $12d_f$ spacing the shear stress distribution for the corner and center fiber are identical to the SF result, with the $6.0d_f$ spacing having practically the same distribution although at a slightly smaller magnitude. Thus at this fiber spacing no interaction takes place between neighboring fibers in a multi-fiber model. For the $6.0d_f$ spacing virtually no interactions exist as well. Similar to the radial stress distributions, both the magnitude and location of the maximum shear stress changes as the fiber spacing is varied. From Figure 182, the maximum shear stress for the center fiber for the SF, $12d_f$, $6d_f$, and $2.5d_f$ spacing occurs at $\theta = 45^\circ$ where the fibers are closest together while the magnitude of the maximum shear stress decreases as the fiber spacing decreases. However, with the $1.9d_f$ and lower fiber spacings, the magnitude of the maximum shear stress begins to increase as the stress distribution around the interface becomes skewed with the maximum occurring at angles $< 45^\circ$. For the smallest $1.57d_f$ spacing, the peak in the shear stress occurs at $\theta \sim 39^\circ$. The variation of shear stress distribution with fiber spacing for the corner fiber follow trends similar to the center fiber, as seen in Figure 183. However, for the corner fiber, the location of the maximum shear stress changes from $\theta = 225^\circ$ at large spacings ($> 2.5d_f$) to $\theta \sim 219^\circ$ for the $1.57d_f$ spacing. Similar to the radial stresses, it is further observed that for smaller fiber spacings ($< 6d_f$), the magnitude of the maximum shear stress at the interface for the corner fiber are larger compared to the center fiber. Thus, the corner fiber is likely to debond first in shear compared to central fiber for closely spaced fibers.

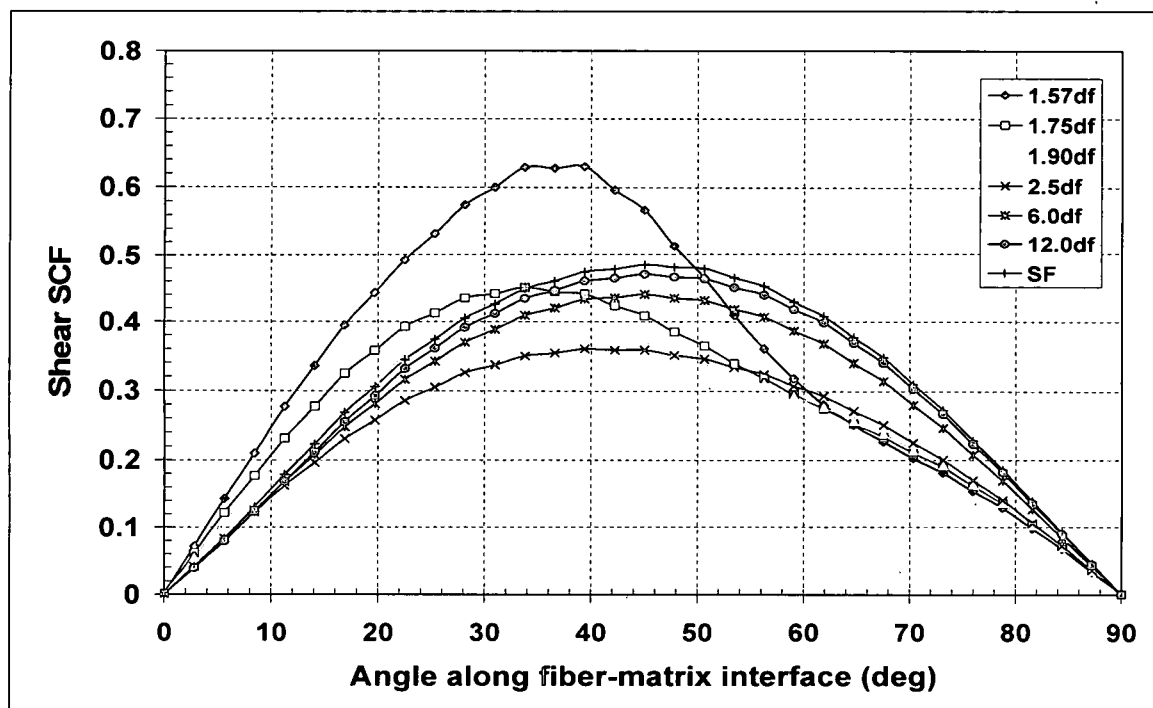


Figure 182: Variation of shear stress due to mechanical loading at the interface of the center fiber as a function of fiber spacing

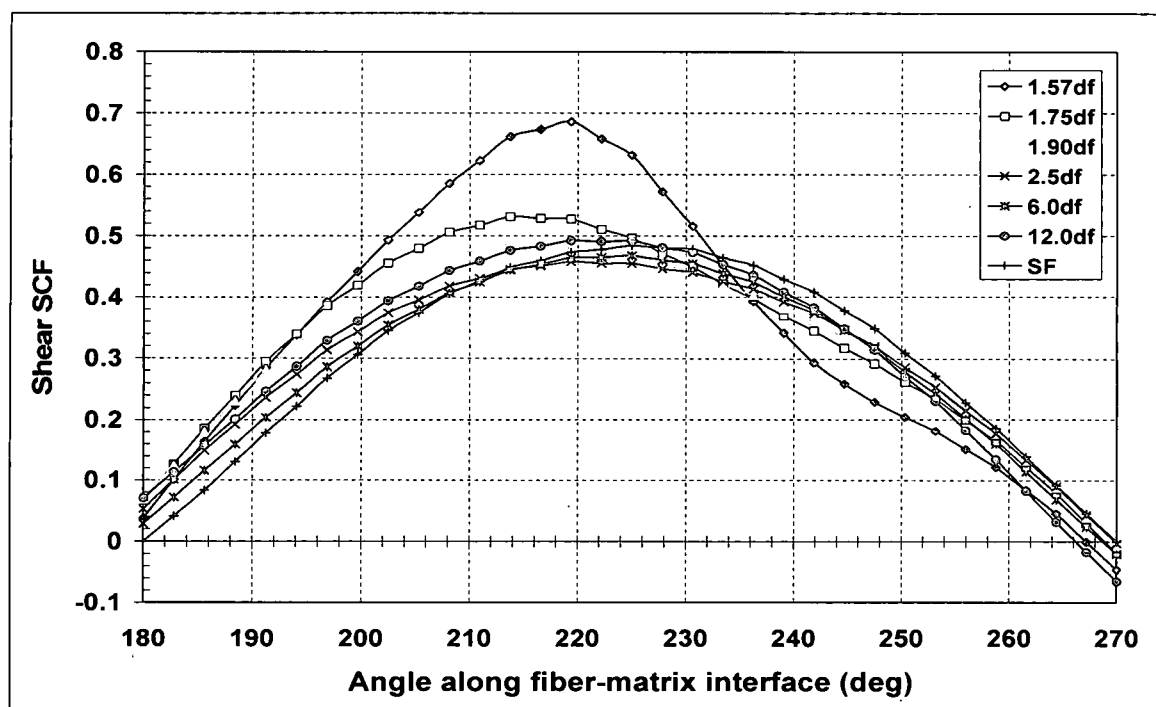


Figure 183: Variation of shear stress due to mechanical loading at the interface of the corner fiber as a function of fiber spacing

It should be noted that the shear SCF magnitudes range from 50% to 80% of the radial SCF magnitudes for both the center and corner fibers. It appears likely that an interaction between the radial and shear stress components along the fiber-matrix interface at the corner could create a debond over a maximum radial or shear stress.

The axial stress distribution due to mechanical loading along the length of the fiber at $\theta = 90^\circ$ for the center fiber and at $\theta = 270^\circ$ for the corner fiber as a function of fiber spacing is shown in Figure 184 and 185 respectively. For the center fiber, Figure 184, the axial stress in the center of the specimen, at $Z = 0$, is compressive for the $1.57d_f$ spacing and increases in magnitude as the fiber spacing increases. Additionally, the axial stress is practically uniform over the entire loading arm width at the $1.57d_f$ spacing but as the fiber spacing increases the length over which the magnitude of the axial stress is fairly uniform decreases becoming more concentrated in the center of the specimen. The axial stress magnitudes decrease for all fiber spacings across the fillet radius region of the specimen becoming slightly compressive until a very small free edge effect occurs at the end of the fiber length. The maximum magnitude of the axial stress for all fiber spacings is very small compared to the respective radial stress, hoop stress, and shear stress components. For the corner fiber the location at $\theta = 270^\circ$ was chosen because it is closest to the center fiber where the matrix stresses are expected to be the highest. The magnitude of the axial stress distribution along the corner fiber as a function of fiber spacing, shown in Figure 185, are very similar and follow the same trend except, for the magnitude of the single fiber, SF, which is considerably less. The highest stresses occur in the central third of the specimen loading arm decreasing considerably through the fillet region of the specimen becoming uniform and compressive along the rest of the fiber length. At the fiber ends a very small free edge stress concentration exists by the slight increase in stresses for all spacings except for the single fiber which decreases. The maximum magnitude of the axial stress for all fiber spacings at the corner fiber is very small compared to the respective radial stress, hoop stress, and shear stress components.

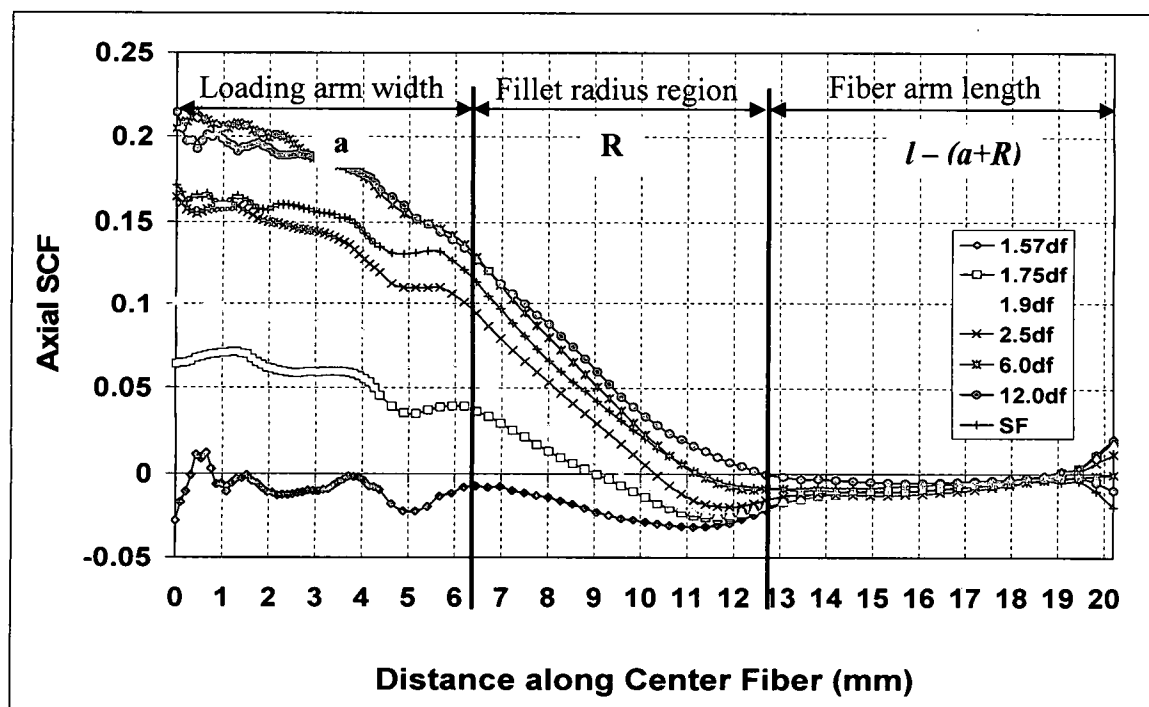


Figure 184: Variation of axial stress due to mechanical loading at the interface of the center fiber at $\theta = 90^\circ$ as a function of fiber spacing

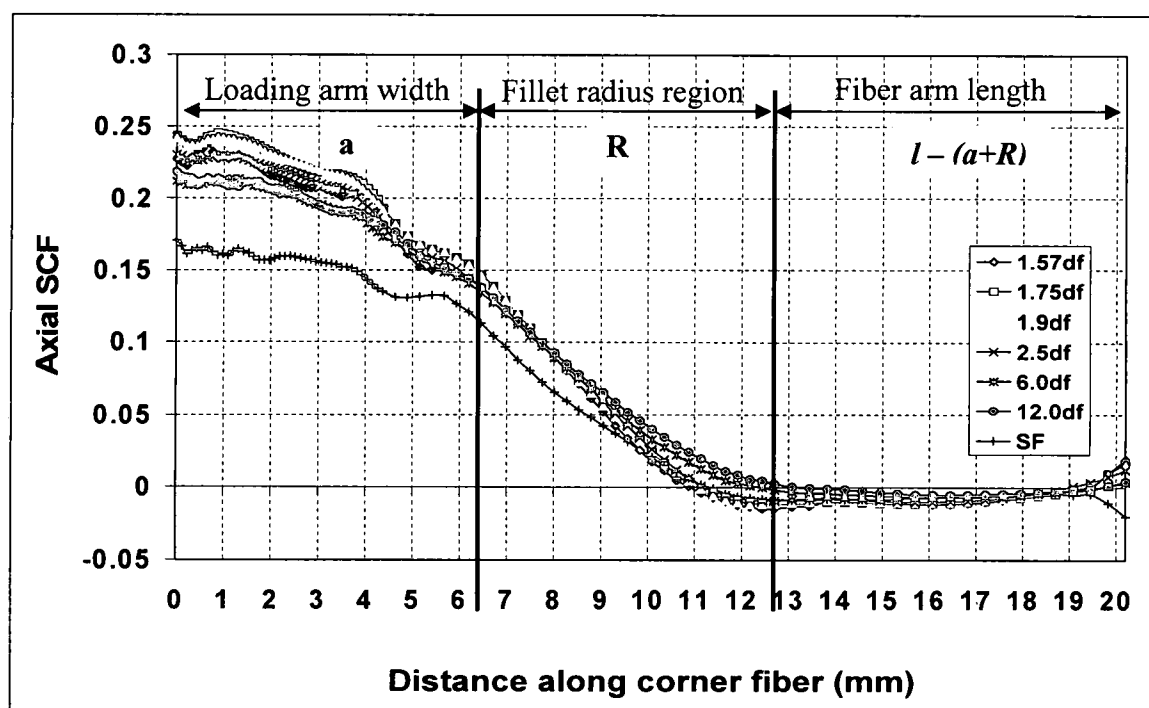


Figure 185: Variation of axial stress due to mechanical loading at the interface of the corner fiber at $\theta = 270^\circ$ as a function of fiber spacing

Fiber Spacing Effects - Summary

The interfacial radial and hoop stress distribution due to the chemical shrinkage for the center fiber from $\theta = 0^\circ$ to 90° and for the corner fiber from $\theta = 180^\circ$ to 270° are the same. However, the magnitudes of the radial stress are much greater than the hoop stress for both fibers. The shear stress distribution due to the chemical shrinkage for the center and corner fibers is also the same. For all stresses, the magnitude increases as the fiber spacing decreases indication effects from nearest neighbor fibers. It also appears, comparing Figures 172 to 177 between the center and corner fibers, that the magnitudes for the radial, hoop and shear stresses are practically the same.

The interfacial radial and hoop SCF distribution due to the mechanical load reveals nearest neighbor fiber effects for the $1.57d_f$, $1.75d_f$ and $1.9d_f$ fiber spacing groups at both center and corner fibers. Evidence of this is by a wave in their stress distribution at the location along the interface where the fibers are closest together. In addition, for the $1.75d_f$ and $1.9d_f$ groups the length of interface in which the maximum magnitude acts is larger. Further, the maximum magnitude of the $1.57d_f$ is greater than the $1.75d_f$, $1.9d_f$ and the $2.5d_f$. For the shear SCF distribution at both fibers the nearest neighbor effects are represented by a shift in the maximum magnitude location for the $1.57d_f$, $1.75d_f$ and $1.9d_f$ fiber spacing groups. For all stress components at both fibers no nearest neighbor effects are evident for the $6.0d_f$ and $12d_f$ other than small changes in magnitudes. Minor nearest neighbor effects are observed in the shear SCF distribution at the $2.5d_f$ spacing. Lastly, the magnitudes of the radial, hoop and shear SCF are greater at the corner fiber than at the center fiber, as expected, as evidence by comparing Figures 178 to 183.

In order to evaluate the total stresses due to mechanical loading and chemical shrinkage at initiation of damage, the results reported in Figures 178 to 183 will have to be scaled by the corresponding failure load and added to the shrinkage stresses shown in Figures 172 to 177. However, based on the shrinkage stress distribution in combination with the mechanical load distribution it appears that the interfacial length over which the largest magnitudes of the radial, hoop and shear stress acts will increase for the $1.57d_f$, $1.75d_f$ and $1.9d_f$ at both fibers coupled

with the mechanical loading results showing that the shear SCF magnitudes range from 50% to 80% of the radial SCF magnitudes at both fibers gives a strong indication that an interaction will exist creating a fiber-matrix debond in those specimens having this mechanism as their failure initiation.

Finally, from the axial SCF distribution of the center fiber at $\theta = 90^\circ$ and from the corner fiber at $\theta = 270^\circ$ the largest magnitudes occur within the loading arm width albeit they are considerably less than the radial, hoop and shear SCF magnitudes. Although, free edge effects are present at the fiber end as indicated but the increase in magnitude shown in Figure 184 and 185 they are minuscule in comparison to the magnitudes occurring at the center of the specimen.

Cruciform Specimen Thickness Effects

Since the corner fiber of the multi-fiber cruciform specimen is most physically similar to the single fiber with respect to loading and physical geometry to the specimen free edge, the single fiber will be used to study effects of the specimen thickness on the interfacial stress distribution. Five single fibers finite element models were made with the thickness set at 1.15 mm, 2.62 mm, 3.69 mm, 4.31 mm and 4.41 mm. Figure 186 is the variation of the maximum magnitudes for the radial, hoop and shear SCF as a function of the cover thickness over the fiber. It appears that when the cover thickness is just less than 1.4 mm the sensitivity of the SCF for all three components to thickness increases dramatically. These results imply that a cover thickness less than 1.4 mm would further increase the stresses at the corner fiber due to the applied mechanical loading.

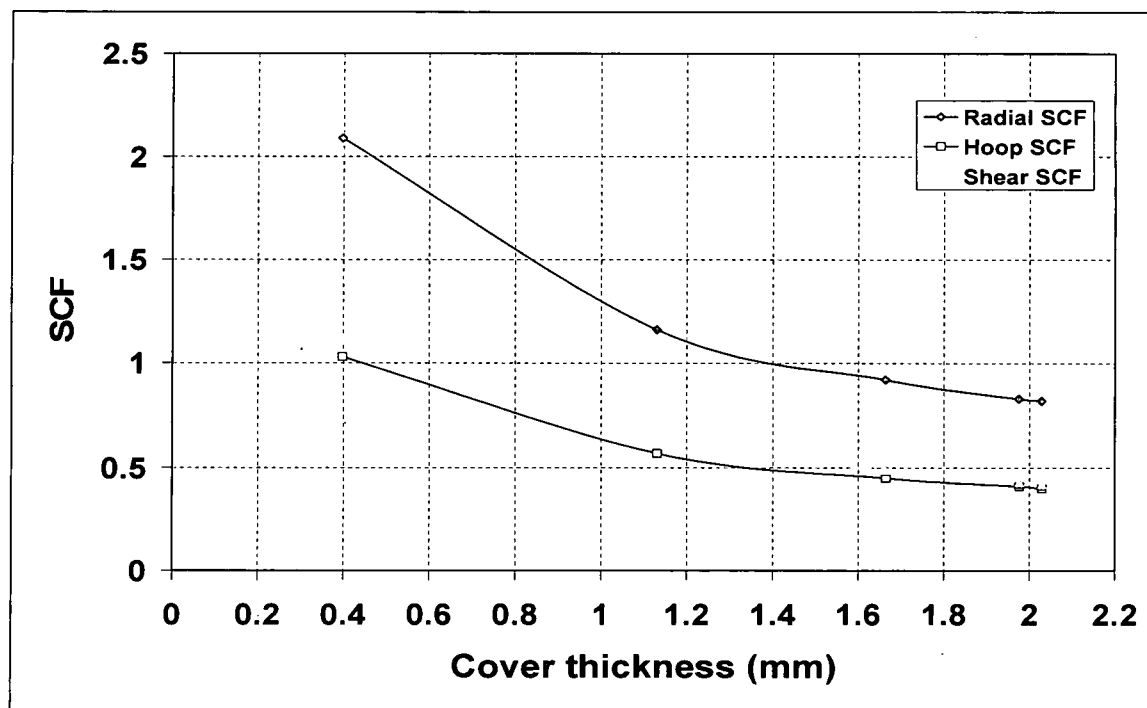


Figure 186: Radial SCF as a function of cover thickness

Parametric Study – Summary

The parametric study indicates that the nearest neighboring fiber has a large impact on the interfacial radial, hoop and shear stress distribution due to both the shrinkage stresses and mechanical load stresses at the center fiber and in the third quadrant of the corner fiber. Also, that the thickness of matrix cover over the corner fiber acts as to increase the radial, hoop and shear stress due to mechanical load as the cover decreases past a thickness of about 1.4 mm. In addition, the corner fiber experiences higher stress magnitudes due to the mechanical loading than the center fiber. Furthermore, the interfacial shear stress magnitude is from 50% to 80% of the interfacial radial stress magnitude at both the center and corner fiber. Thus, it is very likely that an interaction between the radial stress and shear stress contribute to create a fiber-matrix debond.

Due to the interfacial stress distributions the likelihood of observing first damage utilizing a secondary camera position located horizontally to the side of the primary camera is nil. Thus, based on these results the secondary camera position will be changed and be mounted above

the primary camera angled down viewing the front and back top corner fibers as well as portions of the center and front bottom corner fibers depending on fiber spacing. This angle will encompass the entire loading arm view to capture first damage within the high stressed areas of the sample.

Lastly, the results indicate that the $12d_f$ behaves virtually the same as the single fiber and $6.0d_f$ so there would be no need to fabricate specimens at this spacing. However, there appears to be a transition between the $2.5d_f$ and the $1.9d_f$ spacing. There exists a fairly wide gap and magnitude shift in the interfacial stress distributions. The magnitude shift obviously creates a different interface stress distribution but the difference between these two spacings warrant creating a specimen at $2.0d_f$ spacing.

ANSYS Parametric Design Language

The ANSYS Parametric Design Language (APDL) is a programming tool that runs within the ANSYS code and allows the user to automate various modeling tasks using parameters. For this work all finite element models were generated using macros designed with the APDL tool. The cruciform models are structured such that the average specimen dimensions, the fiber spacing and fiber diameters are input parameters to the macro that builds the solid model. The model is built via the bottom up approach, i.e. through the parameter inputs a key point subroutine is called first establishing all points of the cruciform model in the Cartesian coordinate system. Next the line subroutine is called followed by the volume subroutine and lastly the meshing subroutine that creates a meshed solid model. Model meshing involves dividing all lines into a certain number of spaces. Depending upon the specimen's average dimensions the macro subdivides the model along the fiber length and through its thickness. The number of volumes through the specimen thickness is held constant whereas the number of volumes along the fiber length is allowed to vary thus creating a uniform mesh in the areas of the specimen where the internal stresses are expected to be at a maximum. Material properties for the matrix, the fiber and the tab material are also input into a separate subroutine. The material properties used for all analysis inputs are shown in Table 67. All loading conditions and boundary conditions are also

included in the solid model via its own subroutine. Once the macro is run the data base is saved and the model is ready for analysis. Utilizing this approach for all the finite element models ensured consistency and repeatability for the analysis of the cruciform specimens. The model sizes ranged from 69,288 elements (296,008 nodes) for the single fiber models in both matrix systems to between 142,824 to 168,672 elements (595,764 - 702,172 nodes) for the 828 models and from 113,448 to 138,048 elements (475,528 - 576,800 nodes) for the 862 models.

Table 67: Material properties for the finite element model analysis

Constituent Materials	E _x (GPa)	ν	α_{eff}				
828/D-230	3.44	0.337	741.8×10^{-6}				
862/W	2.496	0.346	67.4×10^{-6}				
Stainless Steel	207	0.3	16×10^{-6}				
	E _y , E _z (GPa)	E _x (GPa)	ν_{xy}	ν_{yz}	ν_{xz}	G _{xy} , G _{xz} (GPa)	G _{zy} (GPa)
Glass/epoxy Tab	24.7	10.1	0.14	0.11	0.34	3.3	3.1

The Cruciform Model FEM Macro APDL Code

```

*****
!* Define Constants ---- millimeters
*****

rad1=0.1778
thk=0.04
rad2=rad1+thk

cent1x=0.33782    ! center of corner fiber is function of
cent1y=cent1x     ! of fiber spacing - define as user input
spthk=0.89

wht=2.53          ! fiber wing height
whl=17.95         ! fiber wing length - half of fiber arm
Ldam=6.31         ! load arm length
R_fillet=6.35     ! fillet radius
spthk=17.91       ! specimen height based on grip distance

ctaby=2.5
Rtab=3.905
tabthk=0.56
!
*****
!* Set materials 1 is for 828, 2 is for 862

```

```

|*****
|
|imat=2
|
|*****
|* Set meshing requirements
|*****
|
|n4=4
|n5=5
|n6=6
|n8=8
|n10=10
|n15=16 ! shown as 16 mesh divisions in notes
|n25=20 ! shown as 20 mesh divisions in notes
|r5=5
|
|*=====*|
|* Creates 3-D cruciform FEM *|
|*=====*|
|
|runName='190df862Ex-020L'
|/FILENAME,%runName%,1
|
|/TITLE, 3-D Cruciform: %runName%
|
|/PREP7
|
|/INPUT,materialRT,dat
|
|/INPUT,kpRT,dat
|/INPUT,lineRT,dat
|/INPUT,volRT,dat
|
|/INPUT,loadsRT,dat
|
|/INPUT,meshRT,dat
|
|SAVE,%runName%,db
|
|FINISH

```

The Key Point Generation APDL Code

```

|*****
|* Define Key Points for fiber spacing greater than 4 df
|*****
|
|*****
|* Fiber Area
|*****
|k,1,0,0,0
|k,2,rad1,0,0
|k,3,rad2,0,0
|k,4,rad1/SQRT(2),rad1/SQRT(2),0

```

```

k,5,rad2/SQRT(2),rad2/SQRT(2),0
k,6,0,rad1,0
k,7,0,rad2,0
k,8,cent1x,cent1y,0
k,9,cent1x+rad1,cent1y,0
k,10,cent1x+rad2,cent1y,0
k,11,cent1x+(rad1/SQRT(2)),cent1y+(rad1/SQRT(2)),0
k,12,cent1x+(rad2/SQRT(2)),cent1y+(rad2/SQRT(2)),0
k,13,cent1x,cent1y+rad1,0
k,14,cent1x,cent1y+rad2,0
k,15,cent1x-(rad1/SQRT(2)),cent1y+(rad1/SQRT(2)),0
k,16,cent1x-(rad2/SQRT(2)),cent1y+(rad2/SQRT(2)),0
k,17,cent1x-rad1,cent1y,0
k,18,cent1x-rad2,cent1y,0
k,19,cent1x-(rad1/SQRT(2)),cent1y-(rad1/SQRT(2)),0
k,20,cent1x-(rad2/SQRT(2)),cent1y-(rad2/SQRT(2)),0
k,21,cent1x,cent1y-rad1,0
k,22,cent1x,cent1y-rad2,0
k,23,cent1x+(rad1/SQRT(2)),cent1y-(rad1/SQRT(2)),0
k,24,cent1x+(rad2/SQRT(2)),cent1y-(rad2/SQRT(2)),0
k,25,0,cent1y,0
k,26,cent1x/2,cent1y/2,0
k,27,cent1x,0,0
!
*IF,sphk,LE,2*cent1x,THEN ! Set KP when sphk less that cent1x
  k,28,sphk,0,0
  k,30,sphk,cent1y,0
  k,34,sphk,cent1y*2,0
*ELSE
  k,28,cent1x*2,0,0
  k,29,sphk,0,0
  k,30,cent1x*2,cent1y,0
  k,31,sphk,cent1y,0
  k,34,cent1x*2,cent1y*2,0
  k,35,sphk,cent1y*2,0
*ENDIF
!
k,32,0,cent1y*2,0
k,33,cent1x,cent1y*2,0
!
k,40,0,wht+R_fillet,Ldam+R_fillet ! KP 40 center of fillet
k,41,cent1x,wht+R_fillet,Ldam+R_fillet ! KP 41 center of fillet
*IF,sphk,LE,2*cent1x,THEN ! Set KP when sphk less that cent1x
  k,42,sphk,wht+R_fillet,Ldam+R_fillet ! KP 42 center of fillet
*ELSE
  k,42,cent1x*2,wht+R_fillet,Ldam+R_fillet ! KP 42 center of fillet
  k,43,sphk,wht+R_fillet,Ldam+R_fillet ! KP 43 center of fillet
*ENDIF
!
!
k,36,(cent1x-rad2)/2,rad2+(cent1y-rad2)/2,0
k,37,rad2+(cent1x-rad2)/2,(cent1y-rad2)/2,0
!
*****
!* Loading Arm ---- 100 series points
*****

```

```

!
!* Find Y coordinate for key points 145 - 149
!
tabliney=((wht+R_fillet)-(ctaby+(Rtab-Rtab/SQRT(2))))
tablineZ=Ldam-(Rtab/SQRT(2))
tablineR=tabliney/tablineZ
taby=(tablineR*(wht-2*cent1y))
!
!
k,100,0,0,Ldam-(wht-2*cent1y)
k,101,0,ctaby,0 ! Apex of tab
k,102,cent1x,ctaby,0
!
*IF, spthk,LE,2*cent1x,then
  k,103,spthk,ctaby,0
  k,104,spthk+tabthk,ctaby,0
*ELSE
  k,103,cent1x*2,ctaby,0
  k,104,spthk,ctaby,0
  k,105,spthk+tabthk,ctaby,0
*ENDIF
!
*IF, spthk,LE,2*cent1x,then
  kgen,2,101,104,,0,Rtab,0,5 ! kp 106 - 109
  kgen,2,106,109,,0,(wht+R_fillet-(Rtab+ctaby)),0,5 ! kp 111 - 114
  kgen,2,111,114,,0,spht-(wht+R_fillet),0,5 ! kp 116 - 119
  kgen,2,116,119,,0,0,Rtab/SQRT(2),5 ! kp 121 - 124
  kgen,2,111,114,,0,0,Rtab/SQRT(2),15 ! kp 126 - 129
  kgen,2,106,109,,0,0,Rtab/SQRT(2),25 ! kp 131 - 134
  kgen,2,131,134,,0,-(Rtab/SQRT(2)),0,5 ! kp 136 - 139
  kgen,2,32,34,,0,0,(Ldam-(wht-2*cent1y)),109 ! kp 141 - 143
  kgen,2,121,124,,0,0,(Ldam-(wht-2*cent1y+Rtab/SQRT(2))),34 ! kp 155 - 158
  kgen,2,126,129,,0,0,(Ldam-(wht-2*cent1y+Rtab/SQRT(2))),24 ! kp 150 - 153
  kgen,2,150,153,,0,-taby,0,-5 ! kp 145 - 148
  kgen,2,155,158,,0,0,(wht-2*cent1y),5 ! kp 160 - 163
  kgen,2,150,153,,0,0,(wht-2*cent1y),15 ! kp 165 - 168
  kgen,2,40,42,,0,-(R_fillet/SQRT(2)),-(R_fillet/SQRT(2)),130 ! kp 170 - 172
  kgen,2,40,42,,0,-(R_fillet),0,134 ! kp 174 - 176
  kgen,2,174,176,,0,-(wht-2*cent1y),0,4 ! kp 178 - 181
  kgen,2,178,180,,0,-(2*cent1y),0,4 ! kp 182 - 184
  kgen,2,174,176,,0,0,(whl-(Ldam+R_fillet)),12 ! kp 186 - 188
  kgen,2,178,180,,0,0,(whl-(Ldam+R_fillet)),12 ! kp 190 - 192
  kgen,2,182,184,,0,0,(whl-(Ldam+R_fillet)),12 ! kp 194 - 196
*ELSE
  kgen,2,101,105,,0,Rtab,0,5 ! kp 106 - 110
  kgen,2,106,110,,0,(wht+R_fillet-(Rtab+ctaby)),0,5 ! kp 111 - 115
  kgen,2,111,115,,0,spht-(wht+R_fillet),0,5 ! kp 116 - 120
  kgen,2,116,120,,0,0,Rtab/SQRT(2),5 ! kp 121 - 125
  kgen,2,111,115,,0,0,Rtab/SQRT(2),15 ! kp 126 - 130
  kgen,2,106,110,,0,0,Rtab/SQRT(2),25 ! kp 131 - 135
  kgen,2,131,135,,0,-(Rtab/SQRT(2)),0,5 ! kp 136 - 140
  kgen,2,32,35,,0,0,(Ldam-(wht-2*cent1y)),109 ! kp 141 - 144
  kgen,2,121,125,,0,0,(Ldam-(wht-2*cent1y+Rtab/SQRT(2))),34 ! kp 155 - 159
  kgen,2,126,130,,0,0,(Ldam-(wht-2*cent1y+Rtab/SQRT(2))),24 ! kp 150 - 154
  kgen,2,150,154,,0,-taby,0,-5 ! kp 145 - 149
  kgen,2,155,159,,0,0,(wht-2*cent1y),5 ! kp 160 - 164

```

```

kgen,2,150,154,,0,0,(wht-2*cent1y),15 ! kp 165 - 169
kgen,2,40,43,,0,-(R_fillet/SQRT(2)),-(R_fillet/SQRT(2)),130 ! kp 170 - 173
kgen,2,40,43,,0,-(R_fillet),0,134 ! kp 174 - 177
kgen,2,174,177,,0,-(wht-2*cent1y),0,4 ! kp 178 - 181
kgen,2,178,181,,0,-(2*cent1y),0,4 ! kp 182 - 185
kgen,2,174,177,,0,0,(whl-(Ldam+R_fillet)),12 ! kp 186 - 189
kgen,2,178,181,,0,0,(whl-(Ldam+R_fillet)),12 ! kp 190 - 193
kgen,2,182,185,,0,0,(whl-(Ldam+R_fillet)),12 ! kp 194 - 197
*ENDIF
!
!* End of Key Points
!
```

The Line Generation APDL Code

```

|*****
!* Defines lines between keypoints and establishes the meshing
!* parameters
!*   L, P1, P2, NDIV, SPACE, XV1, YV1, ZV1, XV2, YV2, ZV2
!*
!* Defines a circular arc by end points and radius
!*   LARC, P1, P2, PC, RAD
!*
!* Specifies the divisions and spacing ration on UNMESHED lines
!*   LESIZE, NL1, SIZE, ANGSIZ, NDIV, SPACE, KFORC, LAYER1, LAYER2,
!*   KYNDIV
!*
!* Generates additional lines from a pattern of lines
!*   LGEN, ITIME, NL1, NL2, NINC, DX, DY, DZ, KINC, NOELEM, IMOVE
|*****
!*
numstr,line,1
|*****
!* Lines around fibers
|*****
l,1,2,n8 ! line 1
l,2,3,n6
l,3,27,n4
l,27,28,n8
l,28,30,n8 ! line 5
l,30,34,n8
l,34,33,n8
l,33,32,n8
l,32,25,n8
l,25,7,n4 ! line 10
l,7,6,n6
l,6,1,n8
l,1,4,n8
l,4,5,n6
l,5,26,n4 ! line 15
l,26,20,n4
l,20,19,n6
l,19,8,n8
l,8,11,n8
l,11,12,n6 ! line 20
l,12,34,n4
```

```

l,32,16,n4
l,16,15,n6
l,15,8,n8
l,8,23,n8 ! line 25
l,23,24,n6
l,24,28,n8
l,25,18,n4
l,18,17,n6
l,17,8,n8 ! line 30
l,8,9,n8
l,9,10,n6
l,10,30,n4
l,27,22,n4
l,22,21,n6 ! line 35
l,21,8,n8
l,8,13,n8
l,13,14,n6
l,14,33,n4
l,25,36,n4 ! line 40
l,36,26,n8
l,26,37,n8
l,37,27,n4
l,7,36,n4
l,36,18,n4 ! line 45
l,3,37,n4
l,37,22,n4
!
!* Center Fiber
!
larc,2,4,1,rad1
larc,4,6,1,rad1
larc,3,5,1,rad2 ! line 50
larc,5,7,1,rad2
!
!* Corner Fiber
!
larc,21,23,8,rad1
larc,23,9,8,rad1
larc,9,11,8,rad1
larc,11,13,8,rad1 ! line 55
larc,13,15,8,rad1
larc,15,17,8,rad1
larc,17,19,8,rad1
larc,19,21,8,rad1
larc,22,24,8,rad2 ! line 60
larc,24,10,8,rad2
larc,10,12,8,rad2
larc,12,14,8,rad2
larc,14,16,8,rad2
larc,16,18,8,rad2 ! line 65
larc,18,20,8,rad2
larc,20,22,8,rad2
!
!* Add outer sections id specimen thickness greater than 2*cent1x
!* and size fiber lines
!

```



```

*IF,spthk,LE,2*cent1x,then
  *do,iline,48,67 ! size lines around fibers
    lesize,iline,,,n8
  *enddo
*ELSE
  L,28,29,n8 ! create outside lines
  L,30,31,n8
  L,34,35,n8
  L,29,31,n8
  L,31,35,n8
  *do,iline,48,67 ! or else just size line around fibers
    lesize,iline,,,n8
  *enddo
*ENDIF
!
!*
!*****
!*
!* All X - dir lines = 200 series
!* All Y - dir lines = 100 series
!* All Z - dir lines = 300 series
!* All Fillet area lines = 500 series
!*
!*****
!*
!* Load arm section
!*
!* Y dir (vertical) lines
!*
numstr,line,101
!
*IF,spthk,LE,2*cent1x,then
  *do,ikp,32,34
    l,ikp,ikp+69,n15
  *enddo
*ELSE
  *do,ikp,32,35
    l,ikp,ikp+69,n15 ! lines 101 - 104
  *enddo
*ENDIF
!
*IF,spthk,LE,2*cent1x,then
  *do,ikp,101,104
    l,ikp,ikp+5,n15
  *enddo
*ELSE
  *do,ikp,101,105
    l,ikp,ikp+5,n15 ! lines 105 - 109
  *enddo
*ENDIF
!
*IF,spthk,LE,2*cent1x,then
  *do,ikp,106,109
    l,ikp,ikp+5,n10
  *enddo
*ELSE

```

```

*do,ikp,106,110
  l,ikp,ikp+5,n10 ! lines 110 - 114
*enddo
*ENDIF
!
*IF,spthk,LE,2*cent1x,then
  *do,ikp,111,114
    l,ikp,ikp+5,n10
  *enddo
*ELSE
  *do,ikp,111,115
    l,ikp,ikp+5,n10 ! lines 115 - 119
  *enddo
*ENDIF
!
*IF,spthk,LE,2*cent1x,then
  *do,ikp,136,139
    l,ikp,ikp-5,n15
  *enddo
*ELSE
  *do,ikp,136,140
    l,ikp,ikp-5,n15 ! lines 120 - 124
  *enddo
*ENDIF
!
*IF,spthk,LE,2*cent1x,then
  *do,ikp,131,134
    l,ikp,ikp-5,n10
  *enddo
*ELSE
  *do,ikp,131,135
    l,ikp,ikp-5,n10 ! lines 125 - 129
  *enddo
*ENDIF
!
*IF,spthk,LE,2*cent1x,then
  *do,ikp,126,129
    l,ikp,ikp-5,n10
  *enddo
*ELSE
  *do,ikp,126,130
    l,ikp,ikp-5,n10 ! lines 130 - 134
  *enddo
*ENDIF
!
*IF,spthk,LE,2*cent1x,then
  *do,ikp,141,143
    l,ikp,ikp+4,n15
  *enddo
*ELSE
  *do,ikp,141,144
    l,ikp,ikp+4,n15 ! lines 135 - 138
  *enddo
*ENDIF
!
*IF,spthk,LE,2*cent1x,then

```

```

*do,ikp,145,148
  l,ikp,ikp+5,n10
*enddo
*ELSE
  *do,ikp,145,149
    l,ikp,ikp+5,n10 ! lines 139 - 143
  *enddo
*ENDIF
!
*IF,spthk,LE,2*cent1x,then
  *do,ikp,150,153
    l,ikp,ikp+5,n10
  *enddo
*ELSE
  *do,ikp,150,154
    l,ikp,ikp+5,n10 ! lines 144 - 148
  *enddo
*ENDIF
!
*IF,spthk,LE,2*cent1x,then
  *do,ikp,165,168
    l,ikp,ikp-5,n10
  *enddo
*ELSE
  *do,ikp,165,169
    l,ikp,ikp-5,n10 ! lines 149 - 153
  *enddo
*ENDIF
!
*IF,spthk,LE,2*cent1x,then
  *do,ikp,174,176
    l,ikp,ikp+4,n10
  *enddo
*ELSE
  *do,ikp,174,177
    l,ikp,ikp+4,n10 ! lines 154 - 157
  *enddo
*ENDIF
*IF,spthk,LE,2*cent1x,then
  *do,ikp,186,188
    l,ikp,ikp+4,n10
  *enddo
*ELSE
  *do,ikp,186,189 ! lines 158 - 161
    l,ikp,ikp+4,n10
  *enddo
*ENDIF
*IF,spthk,LE,2*cent1x,then
  *do,ikp,141,143
    l,ikp,ikp-5,n15
  *enddo
*ELSE
  *do,ikp,141,144
    l,ikp,ikp-5,n15 ! lines 162 - 165
  *enddo
*ENDIF

```

```

!
!*
!* X - dir (horizontal) lines 200 series
!*
!* Load arm
!
numstr,line,201
!
*IF,spthk,LE,2*cent1x,then
  *do,ikp,101,103
    l,ikp,ikp+1,n8
  *enddo
*ELSE
  *do,ikp,101,104 ! lines 201 - 204
    l,ikp,ikp+1,n8
  *enddo
*ENDIF
!
*IF,spthk,LE,2*cent1x,then
  *do,ikp,106,108
    l,ikp,ikp+1,n8
  *enddo
*ELSE
  *do,ikp,106,109 ! lines 205 - 208
    l,ikp,ikp+1,n8
  *enddo
*ENDIF
!
*IF,spthk,LE,2*cent1x,then
  *do,ikp,111,113
    l,ikp,ikp+1,n8
  *enddo
*ELSE
  *do,ikp,111,114 ! lines 209 - 212
    l,ikp,ikp+1,n8
  *enddo
*ENDIF
!
*IF,spthk,LE,2*cent1x,then
  *do,ikp,116,118
    l,ikp,ikp+1,n8
  *enddo
*ELSE
  *do,ikp,116,119 ! lines 213 - 216
    l,ikp,ikp+1,n8
  *enddo
*ENDIF
!
*IF,spthk,LE,2*cent1x,then
  *do,ikp,121,123
    l,ikp,ikp+1,n8
  *enddo
*ELSE
  *do,ikp,121,124 ! lines 217 - 220
    l,ikp,ikp+1,n8
  *enddo

```

```

*ENDIF
!
*IF,spthk,LE,2*cent1x,then
  *do,ikp,126,128
    l,ikp,ikp+1,n8
  *enddo
*ELSE
  *do,ikp,126,129 ! lines 221 - 224
    l,ikp,ikp+1,n8
  *enddo
*ENDIF
!
*IF,spthk,LE,2*cent1x,then
  *do,ikp,131,133
    l,ikp,ikp+1,n8
  *enddo
*ELSE
  *do,ikp,131,134 ! lines 225 - 228
    l,ikp,ikp+1,n8
  *enddo
*ENDIF
!
*IF,spthk,LE,2*cent1x,then
  *do,ikp,136,138
    l,ikp,ikp+1,n8
  *enddo
*ELSE
  *do,ikp,136,139 ! lines 229 - 232
    l,ikp,ikp+1,n8
  *enddo
*ENDIF
!
*IF,spthk,LE,2*cent1x,then
  *do,ikp,141,142
    l,ikp,ikp+1,n8
  *enddo
*ELSE
  *do,ikp,141,143 ! lines 233 - 235
    l,ikp,ikp+1,n8
  *enddo
*ENDIF
!
*IF,spthk,LE,2*cent1x,then
  *do,ikp,145,147
    l,ikp,ikp+1,n8
  *enddo
*ELSE
  *do,ikp,145,148 ! lines 236 - 239
    l,ikp,ikp+1,n8
  *enddo
*ENDIF
!
*IF,spthk,LE,2*cent1x,then
  *do,ikp,150,152
    l,ikp,ikp+1,n8
  *enddo

```

```

*ELSE
  *do,ikp,150,153 ! lines 240 - 243
    l,ikp,ikp+1,n8
  *enddo
*ENDIF
!
*IF,spthk,LE,2*cent1x,then
  *do,ikp,155,157
    l,ikp,ikp+1,n8
  *enddo
*ELSE
  *do,ikp,155,158 ! lines 244 - 247
    l,ikp,ikp+1,n8
  *enddo
*ENDIF
!
*IF,spthk,LE,2*cent1x,then
  *do,ikp,160,162
    l,ikp,ikp+1,n8
  *enddo
*ELSE
  *do,ikp,160,163 ! lines 248 - 251
    l,ikp,ikp+1,n8
  *enddo
*ENDIF
!
*IF,spthk,LE,2*cent1x,then
  *do,ikp,165,167
    l,ikp,ikp+1,n8
  *enddo
*ELSE
  *do,ikp,165,168 ! lines 251 - 254
    l,ikp,ikp+1,n8
  *enddo
*ENDIF
!
*IF,spthk,LE,2*cent1x,then
  *do,ikp,174,175
    l,ikp,ikp+1,n8
  *enddo
*ELSE
  *do,ikp,174,176 ! lines 255 - 257
    l,ikp,ikp+1,n8
  *enddo
*ENDIF
!
*IF,spthk,LE,2*cent1x,then
  *do,ikp,186,187
    l,ikp,ikp+1,n8
  *enddo
*ELSE
  *do,ikp,186,188 ! lines 258 - 260
    l,ikp,ikp+1,n8
  *enddo
*ENDIF
!

```

```

*IF,spthk,LE,2*cent1x,then
  *do,ikp,178,179
    l,ikp,ikp+1,n8
  *enddo
*ELSE
  *do,ikp,178,180 ! lines 261 - 263
    l,ikp,ikp+1,n8
  *enddo
*ENDIF
!
*IF,spthk,LE,2*cent1x,then
  *do,ikp,190,191
    l,ikp,ikp+1,n8
  *enddo
*ELSE
  *do,ikp,190,192 ! lines 264 - 266
    l,ikp,ikp+1,n8
  *enddo
*ENDIF
!
!*****
!* Z dir (along fiber) lines 300 series
!*****
!
!* Load arm area
!
numstr,line,301
!
*IF,spthk,LE,2*cent1x,then
  *do,ikp,101,104
    larc,ikp,ikp+35,ikp+5,Rtab
  *enddo
*ELSE
  *do,ikp,101,105
    larc,ikp,ikp+35,ikp+5,Rtab ! line 301 - 305
  *enddo
*ENDIF
!
*IF,spthk,LE,2*cent1x,then
  *do,iline,301,304
    lesize,iline,,,n25
  *enddo
*ELSE
  *do,iline,301,305
    lesize,iline,,,n25
  *enddo
*ENDIF
!
!
*IF,spthk,LE,2*cent1x,then
  *do,ikp,136,139
    l,ikp,ikp+9,n15
  *enddo
*ELSE
  *do,ikp,136,140
    l,ikp,ikp+9,n15 ! line 306 - 310

```

```

*enddo
*ENDIF
!
*IF,spthk,LE,2*cent1x,then
  *do,ikp,106,109
    l,ikp,ikp+25,n25
  *enddo
*ELSE
  *do,ikp,106,110
    l,ikp,ikp+25,n25 ! line 311 - 315
  *enddo
*ENDIF
!
*IF,spthk,LE,2*cent1x,then
  *do,ikp,131,134
    l,ikp,ikp+14,n15
  *enddo
*ELSE
  *do,ikp,131,135
    l,ikp,ikp+14,n15 ! line 316 - 320
  *enddo
*ENDIF
!
*IF,spthk,LE,2*cent1x,then
  *do,ikp,145,148
    l,ikp,ikp+20,n10
  *enddo
*ELSE
  *do,ikp,145,149
    l,ikp,ikp+20,n10 ! line 321 - 325
  *enddo
*ENDIF
!
*IF,spthk,LE,2*cent1x,then
  *do,ikp,111,114
    l,ikp,ikp+15,n25
  *enddo
*ELSE
  *do,ikp,111,115
    l,ikp,ikp+15,n25 ! line 326 - 330
  *enddo
*ENDIF
!
*IF,spthk,LE,2*cent1x,then
  *do,ikp,126,129
    l,ikp,ikp+24,n15
  *enddo
*ELSE
  *do,ikp,126,130
    l,ikp,ikp+24,n15 ! line 331 - 335
  *enddo
*ENDIF
!
*IF,spthk,LE,2*cent1x,then
  *do,ikp,150,153
    l,ikp,ikp+15,n10

```



```

*enddo
*ELSE
  *do,ikp,150,154
    l,ikp,ikp+15,n10 ! line 336 - 340
  *enddo
*ENDIF
!
*IF,spthk,LE,2*cent1x,then
  *do,ikp,116,119
    l,ikp,ikp+5,n25
  *enddo
*ELSE
  *do,ikp,116,120
    l,ikp,ikp+5,n25 ! line 341 - 345
  *enddo
*ENDIF
!
*IF,spthk,LE,2*cent1x,then
  *do,ikp,121,124
    l,ikp,ikp+34,n15
  *enddo
*ELSE
  *do,ikp,121,125
    l,ikp,ikp+34,n15 ! line 346 - 350
  *enddo
*ENDIF
!
*IF,spthk,LE,2*cent1x,then
  *do,ikp,155,158
    l,ikp,ikp+5,n10
  *enddo
*ELSE
  *do,ikp,155,159
    l,ikp,ikp+5,n10 ! line 351 - 355
  *enddo
*ENDIF
!
*IF,spthk,LE,2*cent1x,then
  *do,ikp,174,176
    l,ikp,ikp+12,n10
  *enddo
*ELSE
  *do,ikp,174,177
    l,ikp,ikp+12,n10 ! line 356 - 359
  *enddo
*ENDIF
!
*IF,spthk,LE,2*cent1x,then
  *do,ikp,141,143
    l,ikp,ikp+37,n15
  *enddo
*ELSE
  *do,ikp,141,144
    l,ikp,ikp+37,n15 ! line 360 - 363
  *enddo
*ENDIF

```

```

!
*IF,spthk,LE,2*cent1x,then
  *do,ikp,178,180
    l,ikp,ikp+12,n10
  *enddo
*ELSE
  *do,ikp,178,181
    l,ikp,ikp+12,n10 ! line 364 - 367
  *enddo
*ENDIF
!
!*****
!* Fillet area
!*****
!
numstr,line,501
!
!* X dir (horizontal) lines
!
*IF,spthk,LE,2*cent1x,then
  *do,ikp,170,171
    l,ikp,ikp+1,n8
  *enddo
*ELSE
  *do,ikp,170,172
    l,ikp,ikp+1,n8 ! line 501 - 503
  *enddo
*ENDIF
!
*IF,spthk,LE,2*cent1x,then
  *do,ikp,141,143
    l,ikp,ikp+29,n10
  *enddo
*ELSE
  *do,ikp,141,144
    l,ikp,ikp+29,n10 ! line 504 - 507
  *enddo
*ENDIF
!
*IF,spthk,LE,2*cent1x,then
  *do,ikp,165,167
    larc,ikp,ikp+5,ikp-125,R_fillet
  *enddo
  *do,iline,506,508
    lesize,iline,,,n15
  *enddo
*ELSE
  *do,ikp,165,168
    larc,ikp,ikp+5,ikp-125,R_fillet ! line 508 - 511
  *enddo
  *do,iline,508,511
    lesize,iline,,,n15
  *enddo
*ENDIF
!
*IF,spthk,LE,2*cent1x,then

```

```

*do,ikp,170,172
  larc,ikp,ikp+4,ikp-130,R_fillet
*enddo
*do,iline,509,511
  lesize,iline,,,n15
*enddo
*ELSE
  *do,ikp,170,173
    larc,ikp,ikp+4,ikp-130,R_fillet ! line 512 - 515
  *enddo
  *do,iline,512,515
    lesize,iline,,,n15
  *enddo
*ENDIF
!
!*****
!* Construct line to drag areas making volumes
!*****
!
numstr,line,1001
l,1,100,n25 ! line 1001
l,100,182,n15 ! line 1002
l,182,194,n10 ! line 1003
!
!* Lines Done
!

```

The Volume Generation APDL Code

```

!*****
!* Constructs volumes from keypoints
!*****
!
!*****
!* Construct Area from KeyPoints for extruding volumes
!*****
!
ET,1,solid95 ! set element type for test of BC
!
numstr,area,1
!
!* Center fiber areas
!
a,1,2,4 ! area 1
a,1,4,6 ! area 2
!
!* Corner fiber areas
!
a,8,21,23 ! area 3
a,8,23,9 ! area 4
a,8,9,11 ! area 5
a,8,11,13 ! area 6
a,8,13,15 ! area 7
a,8,15,17 ! area 8

```

```

a,8,17,19 ! area 9
a,8,19,21 ! area 10
!
!* Center fiber matrix areas
!
a,2,3,5,4 ! area 11
a,4,5,7,6 ! area 12
!
!* Corner fiber matrix area
!
a,21,22,24,23 ! area 13
a,23,24,10,9 ! area 14
a,9,10,12,11 ! area 15
a,11,12,14,13 ! area 16
a,13,14,16,15 ! area 17
a,15,16,18,17 ! area 18
a,17,18,20,19 ! area 19
a,19,20,22,21 ! area 20
!
!* Matrix area between fibers
!
a,3,27,37 ! area 21
a,7,36,25 ! area 22
a,36,18,25 ! area 23
a,27,22,37 ! area 24
a,3,37,26,5 ! area 25
a,5,26,36,7 ! area 26
a,37,22,20,26 ! area 27
a,26,20,18,36 ! area 28
!
!* Matrix areas around corner fiber
!
*IF,spthk,LE,2*cent1x,then
a,27,28,24,22 ! area 29
a,24,28,30,10 ! area 30
a,10,30,34,12 ! area 31
a,12,34,33,14 ! area 32
a,14,33,32,16 ! area 33
a,16,32,25,18 ! area 34
*ELSE
a,27,28,24,22 ! area 29
a,24,28,30,10 ! area 30
a,10,30,34,12 ! area 31
a,12,34,33,14 ! area 32
a,14,33,32,16 ! area 33
a,16,32,25,18 ! area 34
a,28,29,31,30 ! area 35
a,30,31,35,34 ! area 36
*ENDIF
!
!
*****
!* Construct volumes in fiber region by extruding fiber areas
!* using the VDRAG command
*****

```

```

!
!
!
numstr,area,101
!
!* Create fiber volumes
!
numstr,volu,1
vsel,none
!
!* Fiber volumes 1 - 30
!
*do,ia,1,10
  vdrag,ia,,,,,1001
  vdrag,(ia*12)+92,,,,,1002
  vdrag,(ia*12)+96,,,,,1003
*enddo
!
vatt,3,, ! assign material 3 to steel fibers
!
!* Matrix volumes around Center Fiber
!
numstr,area,301
numstr,volu,101
vsel,none
*do,ia,1,2
  vdrag,(ia+10),,,,,,1001
  vdrag,(ia*15)+290,,,,,1002
  vdrag,(ia*15)+295,,,,,1003
*enddo
!
vatt,1,,
cm,CenFib_matrx,volu
!
!* Matrix volumes around Corner Fiber
!
vsel,none
*do,ia,3,10
  vdrag,(ia+10),,,,,,1001
  vdrag,(ia*15)+290,,,,,1002
  vdrag,(ia*15)+295,,,,,1003
*enddo
!
vatt,1,,
cm,CorFib_matrx,volu
!
!* Matrix between the fibers
!
vsel,none
numstr,area,501
!* Triangular areas 21,22,23,24
*do,ia,1,4

  vdrag,ia+20,,,,,1001
  vdrag,(ia*12)+492,,,,,1002
  vdrag,(ia*12)+496,,,,,1003

```

```

*enddo
!* Rectangular areas 25,26,27,28
*do,ia,1,4
  vdrag,(ia+24),,,,,,1001
  vdrag,(ia*15)+538,,,,,1002
  vdrag,(ia*15)+543,,,,,1003
*enddo
!
vatt,1,,
cm,BtwFib_matrx,volu
!
!* Matrix area rest of Fiber Wing
!
vsel,none
*IF,spthk,LE,2*cent1x,then
*do,ia,1,6
  vdrag,(ia+28),,,,,,1001
  vdrag,(ia*15)+598,,,,,1002
  vdrag,(ia*15)+603,,,,,1003
*enddo
*ELSE
*do,ia,1,8
  vdrag,(ia+28),,,,,,1001
  vdrag,(ia*15)+598,,,,,1002
  vdrag,(ia*15)+603,,,,,1003
*enddo
*ENDIF
!
vatt,1,,
!
!
!* Construct volumes in load arm
!
!
!* Create volumes in sector A
!
vsel,none
*IF,spthk,LE,2*cent1x,then
  v,32,141,136,101, 33,142,137,102
  v,33,142,137,102, 34,143,138,103
*ELSE
  v,32,141,136,101, 33,142,137,102
  v,33,142,137,102, 34,143,138,103
  v,34,143,138,103, 35,144,139,104
*ENDIF
vatt,1,,
!
!* Create volumes in Sector B
!
vsel,none
*IF,spthk,LE,2*cent1x,then
  *do,ikp,0,1
    v,101+ikp,136+ikp,131+ikp,106+ikp, 102+ikp,137+ikp,132+ikp,107+ikp
  *enddo
*ELSE

```

```

*do,ikp,0,2
  v,101+ikp,136+ikp,131+ikp,106+ikp, 102+ikp,137+ikp,132+ikp,107+ikp
*enddo
*ENDIF
vatt,1,,
!
!* Tab in Sector B
!
vsel,none
*IF,sphk,LE,2*cent1x,then
  ikp=2
  v,101+ikp,136+ikp,131+ikp,106+ikp, 102+ikp,137+ikp,132+ikp,107+ikp
*ELSE
  ikp=3
  v,101+ikp,136+ikp,131+ikp,106+ikp, 102+ikp,137+ikp,132+ikp,107+ikp
*ENDIF
vatt,4,, ! Set material 4 to tab material properties
!
!* Create volumes in Sector C
!
vsel,none
*IF,sphk,LE,2*cent1x,then
  *do,ikp,0,1
    v,106+ikp,131+ikp,126+ikp,111+ikp, 107+ikp,132+ikp,127+ikp,112+ikp
  *enddo
*ELSE
  *do,ikp,0,2
    v,106+ikp,131+ikp,126+ikp,111+ikp, 107+ikp,132+ikp,127+ikp,112+ikp
  *enddo
*ENDIF
vatt,1,,
!
!* Tab in Sector C
!
vsel,none
*IF,sphk,LE,2*cent1x,then
  ikp=2
  v,106+ikp,131+ikp,126+ikp,111+ikp, 107+ikp,132+ikp,127+ikp,112+ikp
*ELSE
  ikp=3
  v,106+ikp,131+ikp,126+ikp,111+ikp, 107+ikp,132+ikp,127+ikp,112+ikp
*ENDIF
vatt,4,,
!
!* Create volumes in Sector D
!
vsel,none
*IF,sphk,LE,2*cent1x,then
  *do,ikp,0,1
    v,111+ikp,126+ikp,121+ikp,116+ikp, 112+ikp,127+ikp,122+ikp,117+ikp
  *enddo
*ELSE
  *do,ikp,0,2
    v,111+ikp,126+ikp,121+ikp,116+ikp, 112+ikp,127+ikp,122+ikp,117+ikp
  *enddo
*ENDIF

```

```

vatt,1,,
!
!* Tab in Sector D
!
vsel,none
*IF,spthk,LE,2*cent1x,then
    ikp=2
    v,111+ikp,126+ikp,121+ikp,116+ikp, 112+ikp,127+ikp,122+ikp,117+ikp
*ELSE
    ikp=3
    v,111+ikp,126+ikp,121+ikp,116+ikp, 112+ikp,127+ikp,122+ikp,117+ikp
*ENDIF
vatt,4,,
!
!* Create volumes in Sector E
!
vsel,none
*IF,spthk,LE,2*cent1x,then
    *do,ikp,0,1
    v,136+ikp,141+ikp,145+ikp, 137+ikp,142+ikp,146+ikp
    *enddo
*ELSE
    *do,ikp,0,2
    v,136+ikp,141+ikp,145+ikp, 137+ikp,142+ikp,146+ikp
    *enddo
*ENDIF
vatt,1,,
!
!* Create volumes in Sector F
!
vsel,none
*IF,spthk,LE,2*cent1x,then
    *do,ikp,0,1
    v,136+ikp,145+ikp,131+ikp, 137+ikp,146+ikp,132+ikp
    *enddo
*ELSE
    *do,ikp,0,2
    v,136+ikp,145+ikp,131+ikp, 137+ikp,146+ikp,132+ikp
    *enddo
*ENDIF
vatt,1,,
!
!* Tab in Sector F
!
vsel,none
*IF,spthk,LE,2*cent1x,then
    ikp=2
    v,136+ikp,145+ikp,131+ikp, 137+ikp,146+ikp,132+ikp
*ELSE
    ikp=3
    v,136+ikp,145+ikp,131+ikp, 137+ikp,146+ikp,132+ikp
*ENDIF
vatt,4,,
!
!* Create volumes in Sector G
!

```



```

vsel,none
*IF,spthk,LE,2*cent1x,then
  *do,ikp,0,1
    v,131+ikp,145+ikp,150+ikp,126+ikp, 132+ikp,146+ikp,151+ikp,127+ikp
  *enddo
*ELSE
  *do,ikp,0,2
    v,131+ikp,145+ikp,150+ikp,126+ikp, 132+ikp,146+ikp,151+ikp,127+ikp
  *enddo
*ENDIF
vatt,1,,
!
!* Tab in Sector G
!
vsel,none
*IF,spthk,LE,2*cent1x,then
  ikp=2
  v,131+ikp,145+ikp,150+ikp,126+ikp, 132+ikp,146+ikp,151+ikp,127+ikp
*ELSE
  ikp=3
  v,131+ikp,145+ikp,150+ikp,126+ikp, 132+ikp,146+ikp,151+ikp,127+ikp
*ENDIF
vatt,4,,
!
!* Create volumes in Sector H
!
vsel,none
*IF,spthk,LE,2*cent1x,then
  *do,ikp,0,1
    v,126+ikp,150+ikp,155+ikp,121+ikp, 127+ikp,151+ikp,156+ikp,122+ikp
  *enddo
*ELSE
  *do,ikp,0,2
    v,126+ikp,150+ikp,155+ikp,121+ikp, 127+ikp,151+ikp,156+ikp,122+ikp
  *enddo
*ENDIF
vatt,1,,
!
!* Tab in Sector H
!
vsel,none
*IF,spthk,LE,2*cent1x,then
  ikp=2
  v,126+ikp,150+ikp,155+ikp,121+ikp, 127+ikp,151+ikp,156+ikp,122+ikp
*ELSE
  ikp=3
  v,126+ikp,150+ikp,155+ikp,121+ikp, 127+ikp,151+ikp,156+ikp,122+ikp
*ENDIF
vatt,4,,
!
!* Create volumes in Sector I
!
vsel,none
*IF,spthk,LE,2*cent1x,then
  *do,ikp,0,1
    v,141+ikp,170+ikp,165+ikp,145+ikp, 142+ikp,171+ikp,166+ikp,146+ikp

```

```

*enddo
*ELSE
  *do,ikp,0,2
    v,141+ikp,170+ikp,165+ikp,145+ikp, 142+ikp,171+ikp,166+ikp,146+ikp
  *enddo
*ENDIF
vatt,1,,
!
!* Create volumes in Sector J
!
vsel,none
*IF,spthk,LE,2*cent1x,then
  *do,ikp,0,1
    v,145+ikp,165+ikp,150+ikp, 146+ikp,166+ikp,151+ikp
  *enddo
*ELSE
  *do,ikp,0,2
    v,145+ikp,165+ikp,150+ikp, 146+ikp,166+ikp,151+ikp
  *enddo
*ENDIF
vatt,1,,
!
!* Tab in Sector J
!
vsel,none
*IF,spthk,LE,2*cent1x,then
  ikp=2
  v,145+ikp,165+ikp,150+ikp, 146+ikp,166+ikp,151+ikp
*ELSE
  ikp=3
  v,145+ikp,165+ikp,150+ikp, 146+ikp,166+ikp,151+ikp
*ENDIF
vatt,4,,
!
!* Create volumes in Sector K
!
vsel,none
*IF,spthk,LE,2*cent1x,then
  *do,ikp,0,1
    v,150+ikp,165+ikp,160+ikp,155+ikp, 151+ikp,166+ikp,161+ikp,156+ikp
  *enddo
*ELSE
  *do,ikp,0,2
    v,150+ikp,165+ikp,160+ikp,155+ikp, 151+ikp,166+ikp,161+ikp,156+ikp
  *enddo
*ENDIF
vatt,1,,
!
!* Tab in Sector K
!
vsel,none
*IF,spthk,LE,2*cent1x,then
  ikp=2
  v,150+ikp,165+ikp,160+ikp,155+ikp, 151+ikp,166+ikp,161+ikp,156+ikp
*ELSE
  ikp=3

```

```

v,150+ikp,165+ikp,160+ikp,155+ikp, 151+ikp,166+ikp,161+ikp,156+ikp
*ENDIF
vatt,4,,
!
!* Volumes in fiber arm (wing)
!
!* Create volumes in Sector L
!
vsel,none
*IF,spthk,LE,2*cent1x,then
*do,ikp,0,1
v,141+ikp,178+ikp,174+ikp,170+ikp, 142+ikp,179+ikp,175+ikp,171+ikp
*enddo
*ELSE
*do,ikp,0,2
v,141+ikp,178+ikp,174+ikp,170+ikp, 142+ikp,179+ikp,175+ikp,171+ikp
*enddo
*ENDIF
vatt,1,,
!
!* Create volumes in Sector M
!
vsel,none
*IF,spthk,LE,2*cent1x,then
*do,ikp,0,1
v,178+ikp,190+ikp,186+ikp,174+ikp, 179+ikp,191+ikp,187+ikp,175+ikp
*enddo
*ELSE
*do,ikp,0,2
v,178+ikp,190+ikp,186+ikp,174+ikp, 179+ikp,191+ikp,187+ikp,175+ikp
*enddo
*ENDIF
vatt,1,,
!
ALLSEL,ALL
!
!
!
*****
!* Delete tab for shrinkage analysis
*****
!
!ALLSEL,all
!VSEL,s,loc,x,spthk,spthk+tabthk,1
!VPLT,all
!VDELE,all,,,1
!ALLSEL,all
!
SAVE,%runName%_vol,db

```

The Applied Loading APDL Code

```

*****
!* Sets loading conditions
*****

```

```

!
!* Set shrinkage/thermal loads
!
ALLSEL,all
!

*IF,imat,EQ,1,then
  TREF,23      ! If imat = 1 Material is 828
  TUNIF,22
*ELSE
  TREF,121
  TUNIF,22      ! If imat = 2 Material is 862
*ENDIF
!
!* Set Static loads
!
ALLSEL, all

ASEL,s,loc,x,0 ! selects area for center cruciform fiber-dir symm BCs

DA,all,symm    ! creates center cruciform fiber-dir symm BCs

ALLSEL,all

ASEL,s,loc,y,0 ! selects areas for bottom symm BCs

DA,all,symm    ! creates bottom symm BCs

ALLSEL,all

ASEL,s,loc,z,0 ! selects areas for center thick symm BCs

DA,all,symm    ! creates center thick symm BCs

ALLSEL,all

ASEL,s,loc,y,spht ! selects areas at top of loading arm for loading

!DA,all,uy,1.0   ! creates unit displacement at top of load arm

ALLSEL,all

DK,1,ux,0,,,uy,uz,,, ! sets constraint at key point 1

ALLSEL,all

VPLOT,all

```

The FEM Mesh Generation APDL Code

```

!*=====
!* mesh
!*=====

MSHAPE,0,3-D ! 0 for quadrilateral, 1 for triangular.

```

MSHKEY,1 ! 0 for free mesh, 1 for mapped mesh, 2 for combined.

NUMMRG,ALL

VMESH,ALL

ALLSEL,ALL

/REPLOT

SBCTRAN

SAVE,%runName%_mesh,db

The FEM Materials APDL Code

!*=====*

!* define materials *!

!*=====*

!

ANTYPE,static

EQSLV,iter,1

ET,1,SOLID95

!imat=1 for 828, imat=2 for 862

*IF,imat,EQ,1,THEN

MP,EX,1,3.44e3 ! 828 Matrix

MP,PRXY,1,0.337

MP,ALPX,1,741.8e-6

! MP,ALPX,3,0.0

*ELSE

MP,EX,1,2.496e3 ! 862 Matrix

MP,PRXY,1,0.346

MP,ALPX,1,67.4e-6

!

!* Non-linear material input data

!

TB,MELAS,1,1,55,0

TBTEMP,22,1

TBPT,,0.013246,33.06532

TBPT,,0.013842,34.4337

TBPT,,0.01449,35.8918

TBPT,,0.015138,37.19288

TBPT,,0.015864,38.56125

TBPT,,0.016564,39.86233

TBPT,,0.017262,41.16341

TBPT,,0.017936,42.46449

TBPT,,0.018688,43.63097

TBPT,,0.019752,45.64989

TBPT,,0.020892,47.39961

TBPT,,0.02198,49.23907

TBPT,,0.023122,50.8542

TBPT,,0.02434,52.55906

```

TBPT,,0.025636,54.30878
TBPT,,0.027062,56.05851
TBPT,,0.028202,57.49418
TBPT,,0.029576,58.97472
TBPT,,0.031002,60.36552
TBPT,,0.032426,61.75633
TBPT,,0.03406,63.23687
TBPT,,0.035616,64.67254
TBPT,,0.037092,65.74929
TBPT,,0.038648,66.96064
TBPT,,0.04028,68.12713
TBPT,,0.041188,68.6655
TBPT,,0.042018,69.11415
TBPT,,0.043106,69.78712
TBPT,,0.043988,70.41523
TBPT,,0.045024,70.86388
TBPT,,0.045932,71.35739
TBPT,,0.046968,71.8509
TBPT,,0.048006,72.38928
TBPT,,0.049016,72.88279
TBPT,,0.050104,73.19685
TBPT,,0.05122,73.64549
TBPT,,0.052256,74.00441
TBPT,,0.053268,74.49792
TBPT,,0.054512,74.9017
TBPT,,0.055626,75.17089
TBPT,,0.056792,75.44008
TBPT,,0.057882,75.70927
TBPT,,0.059126,76.06819
TBPT,,0.060422,76.33738
TBPT,,0.061614,76.4271
TBPT,,0.062806,76.78602
TBPT,,0.064154,76.87575
TBPT,,0.06545,77.3244
TBPT,,0.066746,77.3244
TBPT,,0.068094,77.41413
TBPT,,0.069442,77.59359
TBPT,,0.070842,77.59359
TBPT,,0.07219,77.68332
TBPT,,0.073642,77.77305
TBPT,,0.077944,77.95251
!
*ENDIF
!
!* Stainless Steel wires Material 3
!
MP,EX,3,207e3
MP,PRXY,3,0.3
MP,ALPX,3,16.0e-6
!
!* Tab Material is Material 4
!
MP,EX,4,10.1e3
MP,EY,4,24.7e3
MP,EZ,4,24.7e3
MP,GXY,4,3.3e3

```

```

MP,GYZ,4,3.1e3
MP,GXZ,4,3.3e3
MP,PRXY,4,0.14
MP,PRYZ,4,0.11
MP,PRXZ,4,0.34
MP,ALPX,4,0

```

The APDL Code for the Residual Stress Models

The residual stress models for both matrix systems utilized the APDL programming tool to construct their FEM. Listed below is the APDL programming code used for the shrinkage analysis in the 828/D-230 matrix system and for the residual stress analysis in the 862/W matrix system.

The 828/D-230 Shrinkage Stress Analysis APDL Code

```

|*****
|* Shrinkage Model
|*****
|
|runName='828shrink'
|/FILENAME,%runName%,1
|/TITLE,3-D Shrinkage Analysis
|
|/PREP7
|ANTYPE,Static
|EQSLV,iter,1
|ET,1,SOLID95
|
|* Define constants
|
|radAL=6.35 ! in millimeters
|radS=15.7734 ! in millimeters
|Sthk=17.24152 ! in millimeters
|
|mesh=8
|MESH=8
|*
|* Define Material Properties
|*
|* 828 Matrix material is number 1
|*
|MP,EX,1,3.44e3
|MP,PRXY,1,0.337
|MP,ALPX,1,965.7e-6
|*
|* Aluminum disk is material number 2
|*
|MP,EX,2,70e3 ! from matweb.com general aluminum alloys
|MP,PRXY,2,0.33 ! from matweb.com general aluminum alloys
|MP,ALPX,0 ! 24x10-6 m/m-C from matweb.com general aluminum alloys
|

```

```

!* Define specimen geometry
!
!* Keypoints
!
k,1,0,0,0
k,2,radAL,0,0
k,3,radS,0,0
k,4,(radS/SQRT(2)),(radS/SQRT(2)),0
k,5,0,radS,0
k,6,(radAL/SQRT(2)),(radAL/SQRT(2)),0
k,7,0,radAL,0
k,8,0,0,Sthk
k,9,radAL,0,Sthk
k,10,radS,0,Sthk
k,11,(radS/SQRT(2)),(radS/SQRT(2)),Sthk
k,12,0,radS,Sthk
k,13,(radAL/SQRT(2)),(radAL/SQRT(2)),Sthk
k,14,0,radAL,Sthk
!
!* Define lines
!
L,1,2,mesh ! line 1
L,2,3,mesh
L,1,6,mesh
L,6,4,MESH
L,1,7,MESH ! LINE 5
L,7,5,MESH
L,8,9,MESH
L,9,10,MESH
L,8,13,MESH
L,13,11,MESH ! LINE 10
L,8,14,MESH
L,14,12,MESH
L,5,12,MESH
L,7,14,MESH
L,1,8,MESH ! LINE 15
L,2,9,MESH
L,3,10,MESH
L,4,11,MESH
L,6,13,MESH
LARC,3,4,1,radS ! line 20
LARC,4,5,1,radS
LARC,10,11,8,radS
LARC,11,12,8,radS
LARC,2,6,1,radAL
LARC,6,7,1,radAL
LARC,9,13,8,radAL
LARC,13,14,8,radAL
!*
!* mesh arc lines
!*
*do,iline,20,27
  lesize,iline,,,mesh
*enddo
!*
!* Construct volumes

```



```

!*
!* Aluminum Rod volumes
!*
vsel,none
V,1,2,6,8,9,13 ! Volume 1 Aluminum
V,1,6,7,8,13,14 ! Volume 2 Aluminum
vatt,2
!
!* Matrix Volumes
!
vesl,none
V,2,3,4,6, 9,10,11,13 ! Volume 3 Matrix
V,6,4,5,7, 13,11,12,14 ! Volume 4 Matrix
vatt,1
!
!
!* Apply shrinkage load
!
ALLSEL,all
TREF,23
TUNIF,22
VPLOT,all
!
!* Apply BC constraints at center KP
!
ALLSEL,all
DK,1,ux,0,,,uy,uz,,, ! sets constraint at key point 1
!
ALLSEL,all
VPLOT,all
!
!* Mesh Model
!
MSHAPE,0,3D ! 0 for quadrilateral, 1 for triangular
MSHKEY,1 ! 0 for free mesh, 1 for mapped mesh, 2 for combined
NUMMRG,ALL
VMESH,ALL
ALLSEL,all
/REPLOT
!
SBCTRAN
!
SAVE,%runName%,db

FINISH

```

The 862/W Residual Stress Analysis APDL Code

```

*****
!* Shrinkage Model
*****
!
runName='862shrink-6xMFNL'
/FILNAME,%runName%,1
/TITLE,3-D Shrinkage Analysis

```

```

!
/PREP7
!ANTYPE,Static
!EQSLV,PCG,,
ET,1,SOLID95
!
!* Define constants for 1/8 model
!
radAL=6.35 ! in millimeters
radS=15.79 ! in millimeters
Sthk=8.77 ! in millimeters
!
mesh=48
MESH=48
!*
!* Define Material Properties
!*
!* 862 Matrix material is number 1
!*
MP,EX,1,2.496e3
MP,PRXY,1,0.346
MP,ALPX,1,64.0e-6
!*
TB,MELAS,1,1,55,0
TBTEMP,22,1
TBPT,,0.013246,33.06532
TBPT,,0.013842,34.4337
TBPT,,0.01449,35.8918
TBPT,,0.015138,37.19288
TBPT,,0.015864,38.56125
TBPT,,0.016564,39.86233
TBPT,,0.017262,41.16341
TBPT,,0.017936,42.46449
TBPT,,0.018688,43.63097
TBPT,,0.019752,45.64989
TBPT,,0.020892,47.39961
TBPT,,0.02198,49.23907
TBPT,,0.023122,50.8542
TBPT,,0.02434,52.55906
TBPT,,0.025636,54.30878
TBPT,,0.027062,56.05851
TBPT,,0.028202,57.49418
TBPT,,0.029576,58.97472
TBPT,,0.031002,60.36552
TBPT,,0.032426,61.75633
TBPT,,0.03406,63.23687
TBPT,,0.035616,64.67254
TBPT,,0.037092,65.74929
TBPT,,0.038648,66.96064
TBPT,,0.04028,68.12713
TBPT,,0.041188,68.6655
TBPT,,0.042018,69.11415
TBPT,,0.043106,69.78712
TBPT,,0.043988,70.41523
TBPT,,0.045024,70.86388
TBPT,,0.045932,71.35739

```

TBPT,,0.046968,71.8509
 TBPT,,0.048006,72.38928
 TBPT,,0.049016,72.88279
 TBPT,,0.050104,73.19685
 TBPT,,0.05122,73.64549
 TBPT,,0.052256,74.00441
 TBPT,,0.053268,74.49792
 TBPT,,0.054512,74.9017
 TBPT,,0.055626,75.17089
 TBPT,,0.056792,75.44008
 TBPT,,0.057882,75.70927
 TBPT,,0.059126,76.06819
 TBPT,,0.060422,76.33738
 TBPT,,0.061614,76.4271
 TBPT,,0.062806,76.78602
 TBPT,,0.064154,76.87575
 TBPT,,0.06545,77.3244
 TBPT,,0.066746,77.3244
 TBPT,,0.068094,77.41413
 TBPT,,0.069442,77.59359
 TBPT,,0.070842,77.59359
 TBPT,,0.07219,77.68332
 TBPT,,0.073642,77.77305
 TBPT,,0.077944,77.95251

!

!* Aluminum disk is material number 2

!

MP,EX,2,70e3 ! from matweb.com general aluminum alloys

MP,PRXY,2,0.33 ! from matweb.com general aluminum alloys

MP,ALPX,2,24.0e-6 ! 24x10-6 m/m-C from matweb.com general aluminum alloys

!

!* Define specimen geometry

!

!* Keypoints

!

k,1,0,0,0

k,2,radAL,0,0

k,3,radS,0,0

k,4,(radS/SQRT(2)),(radS/SQRT(2)),0

k,5,0,radS,0

k,6,(radAL/SQRT(2)),(radAL/SQRT(2)),0

k,7,0,radAL,0

k,8,0,0,Sthk

k,9,radAL,0,Sthk

k,10,radS,0,Sthk

k,11,(radS/SQRT(2)),(radS/SQRT(2)),Sthk

k,12,0,radS,Sthk

k,13,(radAL/SQRT(2)),(radAL/SQRT(2)),Sthk

k,14,0,radAL,Sthk

!

!* Define lines

!

L,1,2,mesh ! line 1

L,2,3,mesh

L,1,6,mesh

L,6,4,MESH

```

L,1,7,MESH ! LINE 5
L,7,5,MESH
L,8,9,MESH
L,9,10,MESH
L,8,13,MESH
L,13,11,MESH ! LINE 10
L,8,14,MESH
L,14,12,MESH
L,5,12,MESH
L,7,14,MESH
L,1,8,MESH ! LINE 15
L,2,9,MESH
L,3,10,MESH
L,4,11,MESH
L,6,13,MESH
LARC,3,4,1,radS ! line 20
LARC,4,5,1,radS
LARC,10,11,8,radS
LARC,11,12,8,radS
LARC,2,6,1,radAL
LARC,6,7,1,radAL
LARC,9,13,8,radAL
LARC,13,14,8,radAL
!*
!* mesh arc lines
!*
*do,iline,20,27
  lesize,iline,,,mesh
*enddo
!*
!* Construct volumes
!*
!* Aluminum Rod volumes
!*
vsel,none
V,1,2,6,8,9,13 ! Volume 1 Aluminum
V,1,6,7,8,13,14 ! Volume 2 Aluminum
vatt,2,,
!
!* Matrix Volumes
!
vsel,none
V,2,3,4,6, 9,10,11,13 ! Volume 3 Matrix
V,6,4,5,7, 13,11,12,14 ! Volume 4 Matrix
vatt,1,,
!
!
!* Apply shrinkage load
!
ALLSEL,all
TREF,121
TUNIF,22
VPLOT,all
!
!* Apply BC constraints at center KP
!

```

```

ALLSEL,all
DK,1,ux,0,,,uy,uz,,, ! sets constraint at key point 1
!
!* select area normal to x for symmetrical BCs
!
ALLSEL,all
ASEL,s,loc,x,0 ! selects area normal to x for symm BC
DA,all,symm
!
!* select area normal to y for symmetrical BCs
!
ALLSEL,all
ASEL,s,loc,y,0 ! selects area normal to y for symm BC
DA,all,symm
!
!* select area normal to z for symmetrical BCs
!
ALLSEL,all
ASEL,s,loc,z,0 ! selects area normal to z for symm BC
DA,all,symm
!
ALLSEL,all
VPLOT,all
!
!* Mesh Model
!
MSHAPE,0,3D ! 0 for quadrilateral, 1 for triangular
MSHKEY,1 ! 0 for free mesh, 1 for mapped mesh, 2 for combined
NUMMRG,ALL
VMESH,ALL
ALLSEL,all
/REPLOT
!
SBCTRAN
!
!OUTRES,NSOL,LAST
!
SAVE,%runName%,db
!
!/SOLU
!ANTYPE,Static
!NLGEOM,on
!NROPT,full
!EQSLV,PCG,,
!NSUBST,990,1500,100
!EQSLV,PCG,1E-6
!TIME,1
!
!SOLVE
!
FINISH

```

APPENDIX D

INTERFACIAL ANALYTICAL RESULTS

In this appendix is a compilation of the interfacial analytical results for the center and corner fiber in both the 828/D-230 and 862/W matrix systems. The interfacial radial and shear stress results are discussed in detail starting with the combined mechanical load and matrix residual stresses followed by the matrix residual stresses then by the mechanical load stresses. The impacts of the matrix residual stresses on the mechanical load stresses are noted as well as the effects from neighboring fibers at all loadings. Following the interfacial stress discussion is a thorough evaluation of the analytical results correlating the experimentally observed debonds to the fiber-matrix interfacial debond criterion. Finally the analysis of the 828/D-230 1.9d_f and 2.0d_f fiber spacing group behavior is presented. In this discussion nanoindentation study results, additional cruciform testing results, a failure initiation stress state analysis and results from a cruciform thickness parametric study are presented to correlate to the observed behavior.

828/D-230 System Fiber-Interface Analytical Results

Center Fiber Interface Results – Radial Stress

Figure 187 shows the radial stress distribution for the center fiber at the fiber-matrix interface due to the combination of mechanical load and matrix chemical shrinkage for the seven fiber spacing groups tested. The maximum radial stress occurs at $\theta = 90^\circ$, in the direction of loading, for all fiber spacing's except for the 1.57d_f specimens, where its maximum occurs at $\theta = 39.375^\circ$. The minimum radial stress occurs as $\theta = 0^\circ$, normal to direction of loading. The

magnitude is negative or compressive for the maximum fiber spacing of $6.0d_f$, but increases becoming positive or tensile as the fiber spacing decreases.

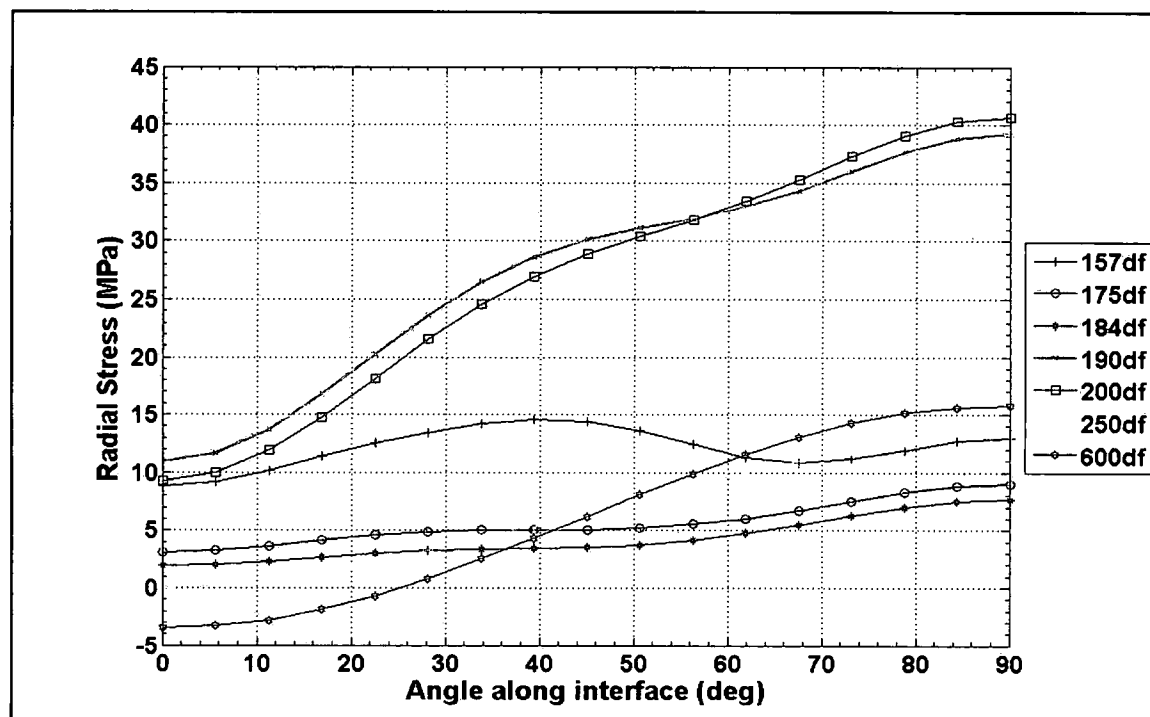


Figure 187: Radial stress distributions at the fiber-matrix interface due to the combination of mechanical loading and chemical shrinkage

The $1.57d_f$ specimen has a fairly uniform radial stress distribution from $\theta = 0^\circ$ to $\theta = 90^\circ$ varying a little over 5 MPa over the entire range, however, its maximum radial stress occurs at $\theta = 39.375^\circ$, as mentioned above, instead at $\theta = 90^\circ$ like all the other fiber spacing groups. This can be attributed to the effects of its nearest neighbor fiber, the corner fiber, which is closest to the center fiber at $\theta = 45^\circ$ on the center fiber interface. For the $1.75d_f$ and $1.84d_f$ specimens the radial stress variation is practically the same, being almost parallel to each other, and fairly uniform varying from approximately 2 MPa to 8 MPa for the $1.75d_f$ spacing and from approximately 3 MPa to 9 MPa for the $1.84d_f$ spacing. Like the $1.57d_f$ spacing, these two fiber spacing groups exhibit a local maximum at $\theta = 39.375^\circ$, albeit not as pronounced as the $1.57d_f$ spacing, due to the corner fiber as evidenced by the hump or wave in their matrix-interface stress distribution. The largest magnitude for both the minimum and the maximum interface radial stresses occur for the $1.9d_f$

and $2.0d_f$ specimens as they vary from about 10 MPa to approximately 40 MPa. Their distributions are practically parallel up to about $\theta = 40^\circ$ with the $1.9d_f$ spacing having a slightly larger magnitude. At this point the $1.9d_f$ radial stress starts to converge with the $2.0d_f$ spacing finally switching magnitudes around the 60° location on the interface. Thence becoming parallel again at about $\theta = 75^\circ$ to $\theta = 90^\circ$. Similarly to the $1.57d_f$, the $1.75d_f$ and the $1.84d_f$ spacing groups, these two fiber spacing groups show nearest neighbor effects in the same position along their interface, centered at approximately $\theta = 40^\circ$, as shown by the hump or wave in their interface stress distribution. The $2.5d_f$ and $6.0d_f$ interfacial radial stress variation from $\theta = 0^\circ$ to $\theta = 90^\circ$ have the same smooth shape without any evidence of nearest neighbor effects exhibited by the other fiber spacing groups. However, the $2.5d_f$ spacing is not compressive at its minimum radial stress at $\theta = 0^\circ$ and is slightly less than the $6.0d_f$ spacing at their maximum radial stress occurring at $\theta = 90^\circ$, as shown in Figure 187.

To appreciate the nearest neighbor effects, the radial stresses due the room temperature matrix chemical shrinkage and due to the mechanical load are plotted separately along the fiber-matrix interface for the center fiber. Figure 188 shows matrix shrinkage radial stress distribution along the fiber-matrix interface of the center fiber for the range of fiber spacing groups tested. The maximum radial stress is compressive and occurs at $\theta = 45^\circ$ for all fiber spacing groups except for the $6.0d_f$ spacing. At the $6.0d_f$ spacing, the radial stress distribution is almost uniform across the entire interface varying less than 0.25 MPa from $\theta = 0^\circ$ to $\theta = 90^\circ$.

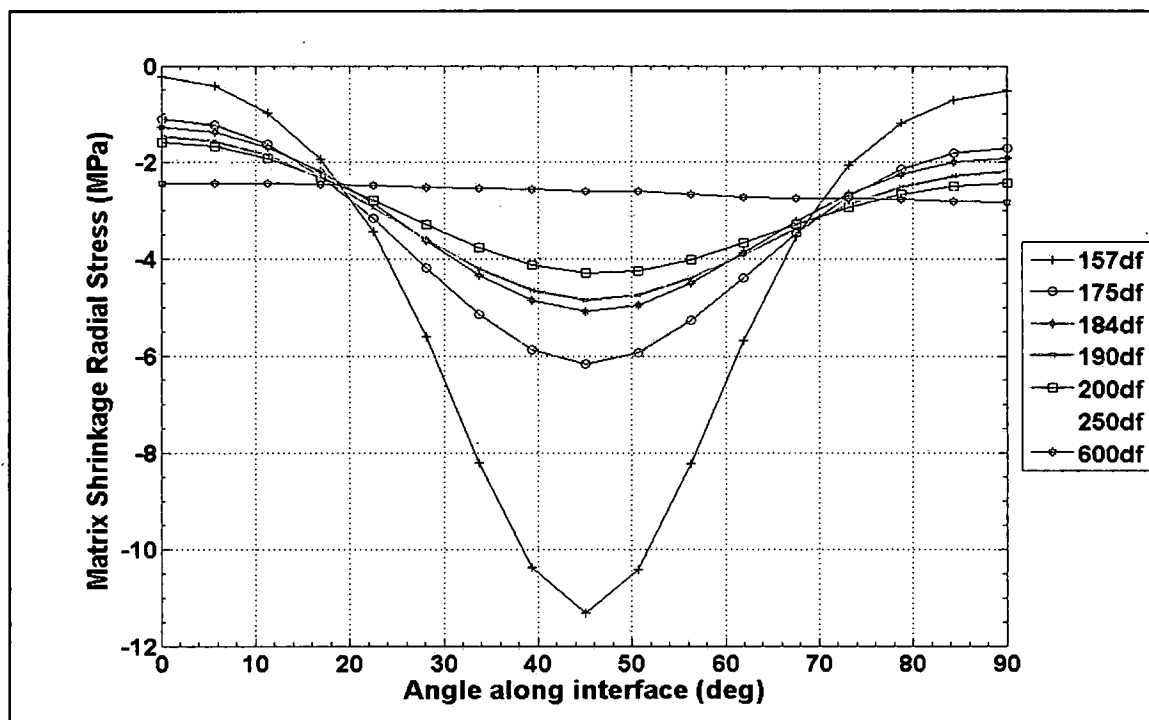


Figure 188: Radial stress distributions at the fiber-matrix interface due to the matrix chemical shrinkage

Effects from nearest neighbors on the room temperature cured chemical shrinkage of the matrix begin to manifest themselves at the $2.5d_f$ spacing as the radial stress is maximum at $\theta = 45^\circ$, the location along the center fiber interface where the corner fiber is closest. The nearest neighbor effects due to matrix chemical shrinkage further increase as the fiber spacing decreases, as shown in Figure 188, where the maximum magnitude for each fiber spacing occurs at $\theta = 45^\circ$. The effects decrease from the maximum magnitude location in both directions along the interface reaching minimum compressive stress values at $\theta = 0^\circ$ and $\theta = 90^\circ$. Consequently as the fiber spacing decreases, the radial stress along the fiber-matrix interface due to the matrix chemical shrinkage changes from a uniform compressive stress distribution, shown by the $6.0d_f$ spacing, to a maximum compressive radial stress at $\theta = 45^\circ$, the location closest to the corner fiber, and minimum compressive radial stresses at $\theta = 0^\circ$ and $\theta = 90^\circ$.

Figure 189 shows the radial stress distribution due to the mechanical load only for the seven fiber spacing groups investigated. The maximum radial stresses due to the mechanical loading are all positive or tensile and occur at $\theta = 90^\circ$ with the exception of the $1.57d_f$ and $1.75d_f$ spacing. At these fiber spacing groups their location of the maximum radial stress occurs at $\theta = 45^\circ$. The minimum radial stresses occur at $\theta = 0^\circ$ for all the fiber spacing groups tested and are positive or tensile with the exception of the $6.0d_f$ spacing where its minimum is slightly compressive.

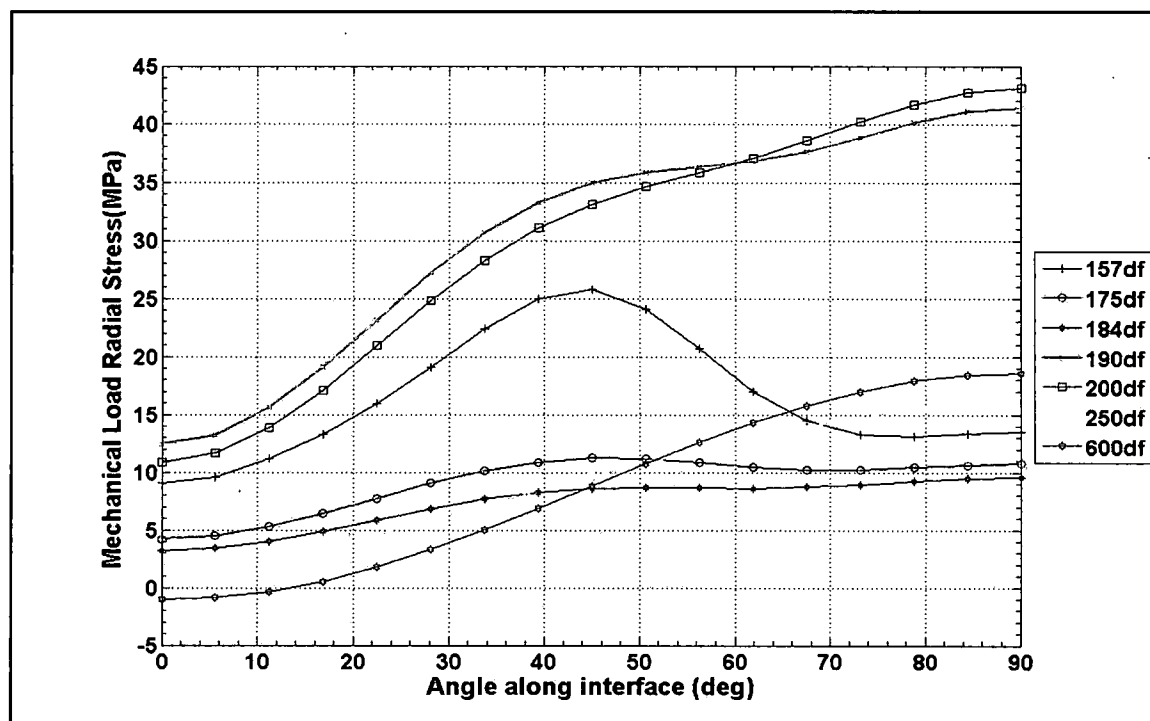


Figure 189: Radial stress distributions at the fiber-matrix interface due to the mechanical loading

As shown in Figure 189, nearest neighbor effects due to the mechanical loading clearly manifest themselves at the $1.57d_f$ spacing as its maximum radial stress occurs at $\theta = 45^\circ$, the point on the interface at which the corner fiber is closest to the center fiber. The radial stress dramatically drops off in magnitude from this point in both directions, as θ goes to 0° and 90° , along the fiber-matrix interface. Although not as pronounced, the same behavior exists for the $1.75d_f$ and $1.84d_f$ fiber spacing groups except their magnitude is quite uniform from about $\theta = 40^\circ$

to $\theta = 90^\circ$, as shown in Figure 189. Also, the behavior is seen in the $1.90d_f$ and $2.0d_f$ fiber spacing specimens where the hump or wave is prevalent and centered at approximately $\theta = 45^\circ$ along the fiber-matrix interface. The interfacial radial stress distribution due to the mechanical loading for the $2.5d_f$ and $6.0d_f$ fiber spacing specimens are both smooth, having the same basic shape and show no evidence of nearest neighbor effects, as shown in Figure 189.

In summary for the radial stress, with the exception of the $1.57d_f$ fiber spacing, the maximum radial stress occurs at $\theta = 90^\circ$ for the combined mechanical load and matrix chemical shrinkage effects, while the minimum radial stress occurs at $\theta = 0^\circ$ for all fiber spacing groups. The $1.57d_f$, $1.75d_f$, $1.84d_f$, $1.90d_f$ and $2.0d_f$ fiber spacing groups experience nearest neighbor effects as evidence by the wave in their interfacial radial stress distribution between approximately $\theta = 20^\circ$ to 50° , as shown in Figure 187. The fibers in the $2.5d_f$ and $6.0d_f$ fiber spacing specimens appear to act independently as their interfacial radial stress variation due to the mechanical loading only is smooth showing no signs of nearest neighbor effects by the lack of a hump or wave in the stress distribution common to the other fiber spacing groups. The matrix chemical shrinkage stresses increase as fiber spacing decreases indicating nearest neighbor effects, as shown in Figure 188. The maximum stresses occur at $\theta = 45^\circ$ except for the $6.0d_f$ fiber spacing group and to a lesser extent the $2.5d_f$ fiber spacing; as these two spacing have practically a uniform shrinkage stress along the fiber matrix interface. For all fiber spacing groups the shrinkage stresses are compressive along the fiber-matrix interface. The interfacial radial stress distribution due to the mechanical load only, as shown in Figure 189, is very similar to the radial stress distribution of the combined mechanical load and shrinkage effects shown in Figure 187. Nearest neighbor effects clearly manifest themselves by the wave in the distribution for the $1.57d_f$, $1.75d_f$, $1.84d_f$, $1.9d_f$ and $2.0d_f$ fiber spacing groups. Similar to the combined loading the $2.5d_f$ and $6.0d_f$ appear to act independently showing no signs of nearest neighbor effects by the lack of the wave, as shown in Figure 189. The impact of the matrix cure shrinkage stress due to its interfacial compressive stress over the mechanical load radial stress for all fiber spacing is listed in Table 68 at the location of maximum radial shrinkage stress and at maximum radial stress due to mechanical load. It appears that the smaller fiber spacing has the largest impacts

due to the matrix shrinkage stress and in general the impact reduces as the fiber spacing increases.

Table 68: The percent reduction of the radial stress over the mechanical load due to the matrix chemical shrinkage

Fiber Spacing	Max Matrix Resdl Stress (MPa)	Mech @ Max Resdl (MPa)	Loc	%	Max Mech Stress (MPa)	Resdl Stress @ Max Mech (MPa)	Loc	%
1.57d _f	-11.33	25.74	45°	44	25.74	-11.33	45°	44
1.75d _f	-6.18	11.22	45°	55	11.22	-6.18	45°	55
1.84d _f	-5.09	8.62	45°	59	9.56	-1.91	90°	20
1.90d _f	-4.86	34.98	45°	14	41.44	-2.19	90°	5
2.0d _f	-4.30	33.13	45°	13	43.09	-2.43	90°	6
2.5d _f	-3.10	10.79	50.6°	29	16.0	-2.66	90°	17
6.0d _f	-2.84	18.61	90°	15	18.61	-2.81	90°	15

Center Fiber Interface Results – Shear Stress

Figure 190 shows the interfacial shear stress distribution along the center fiber due to the combination of mechanical loading and room temperature matrix cure shrinkage. The 6.0d_f and 2.5d_f fiber spacing shear stress distributions are smooth, having a symmetrical shape, and their maximum shear stress occurs at $\theta = 45^\circ$, hence exhibiting no or minimal nearest neighbor effects. However, the rest of the fiber spacing groups tested exhibit signs of interaction with the corner fiber as either a shift in the location of the maximum shear stress occurs or the stress distribution exhibits an irregular asymmetrical shape compared to the 6.0d_f and 2.5d_f spacing.

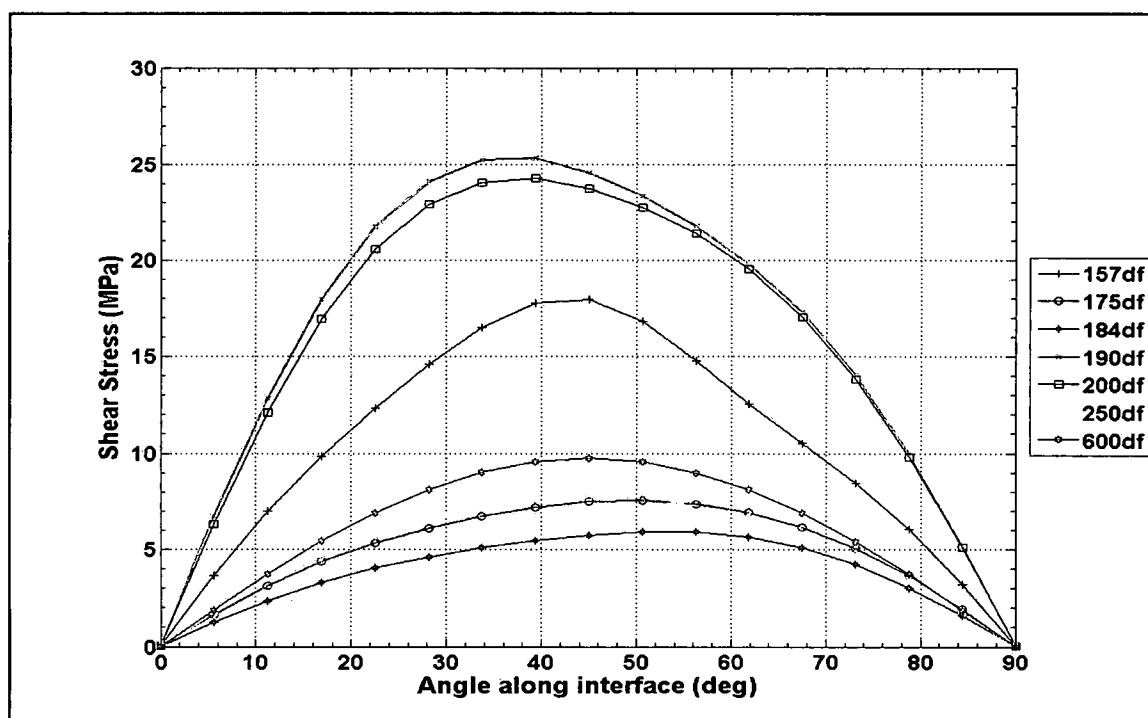


Figure 190: Shear stress distributions at the fiber-matrix interface due to the combination of mechanical loading and matrix chemical shrinkage

For the $2.0d_f$ and $1.90d_f$ shear stress distribution, shown in Figure 190, the maximum shear stress occurs at $\theta = 39.375^\circ$ thus creating an asymmetrical shape to the plot as the rate of change of slope decreases between $\theta = 39.375^\circ$ to $\theta = 90^\circ$. This behavior also exists for the $1.84d_f$ and $1.75d_f$ spacing specimens except in the opposite fashion, where the maximum shear stress occurs at $\theta = 56.25^\circ$ and 50.625° respectively. Notice the rate of change of slope is greater before the maximum shear stress for the $1.90d_f$ and $2.0d_f$; while it is after the maximum shear stress magnitude for the $1.75d_f$ and $1.84d_f$. As for the $1.57d_f$ fiber spacing, its maximum occurs at $\theta = 45^\circ$ but it shows a more radical rate of change in slope between $\theta = 45^\circ$ and $\theta = 90^\circ$ as the shear stress distribution is concave between $\theta = 50.625^\circ$ and $\theta = 67.5^\circ$.

Similar to the radial stress distribution, the room temperature matrix shrinkage shear stress plays a large role in the interfacial shear stress distribution due to the combined loading. Figure 191 shows the interfacial shear stress distribution due to the room temperature cure of the matrix. The shear stress distribution for the $6.0d_f$ fiber spacing is negligible being barely 0.2 MPa

for its maximum magnitude at $\theta = 45^\circ$. The other fiber spacing groups show an inflection point between $\theta = 46^\circ$ to $\theta = 54^\circ$ as the shear stress changes direction across the fiber-matrix interface, as shown in Figure 191, exhibiting local maxima at approximately $\theta = 28.125^\circ$ and between $\theta = 61.875^\circ$ to $\theta = 67.5^\circ$. The effects from nearest neighbor fibers is seen for the $1.57d_f$, $1.75d_f$, $1.84d_f$, $1.90d_f$, $2.0d_f$ and $2.5d_f$ fiber spacing groups as the shear stress magnitudes increase as the fiber spacing decreases affecting the shear stress distribution differently depending on the position along the fiber-matrix interface.

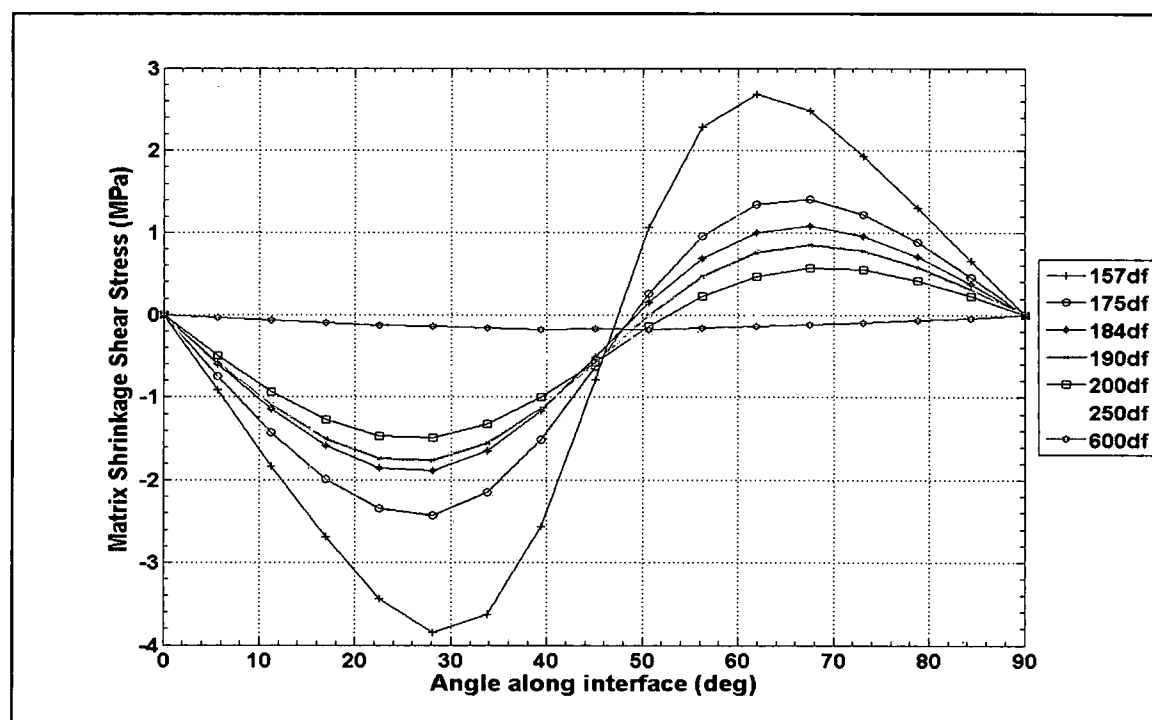


Figure 191: Shear stress distributions at the fiber-matrix interface due to the matrix chemical shrinkage

Although not having a uniform shear stress distribution along its interface, the $2.5d_f$ fiber spacing interfacial shear stress, as shown in Figure 191, is negligible since its maximum magnitude is less than 0.8 MPa.

Figure 192 shows the shear stress distribution due to the mechanical load only for the seven fiber spacing groups tested. With the exception of the $6.0d_f$ fiber spacing, all fiber spacing

groups show effects from the corner fiber as their maximum magnitude of the shear stress shifts from $\theta = 45^\circ$ to a location between $\theta = 33.75^\circ$ to 39.375° and the distributions for each fiber spacing group is asymmetrical.

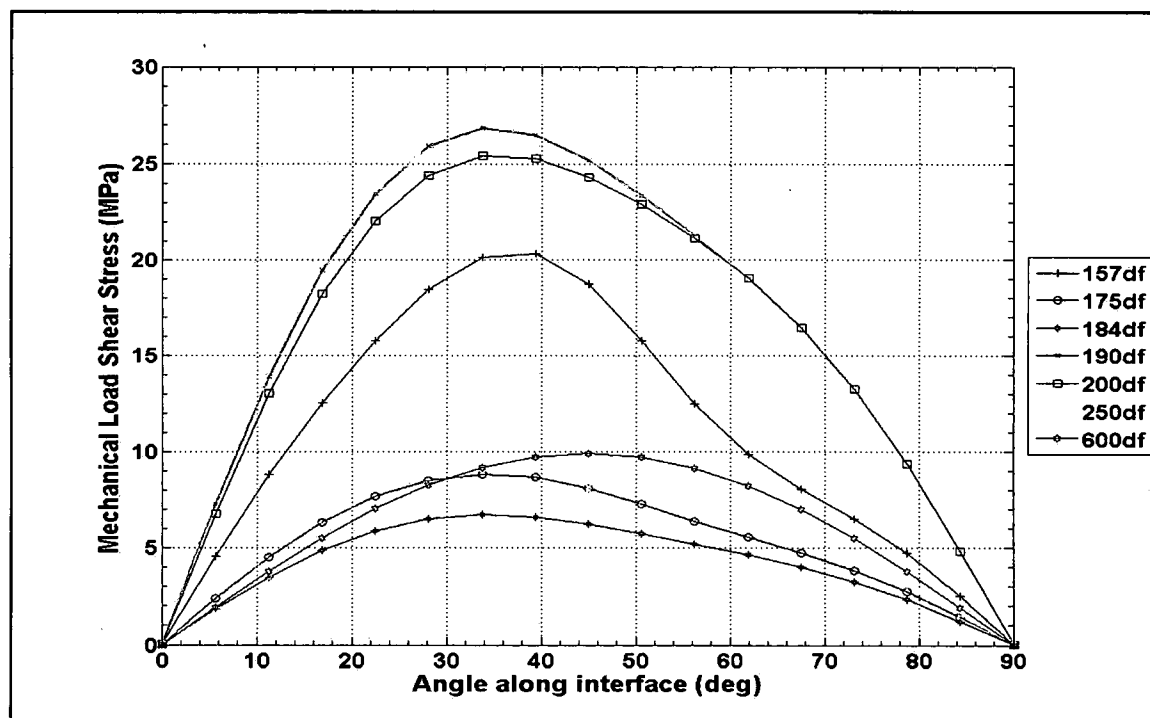


Figure 192: Shear stress distributions at the fiber-matrix interface due to the mechanical loading

The 6.0d_f fiber spacing group's smooth symmetrical interfacial shear stress distribution with its maximum magnitude occurring at $\theta = 45^\circ$ indicates no nearest neighbor effects. The 2.5d_f fiber spacing, on the other hand, shows minor nearest neighbor effects as a shift occurs at its maximum magnitude where it is almost equal at $\theta = 39.375^\circ$ and at $\theta = 45^\circ$. Whereas, the 2.0d_f, 1.90d_f, 1.84d_f and 1.75d_f fiber spacing groups show larger influence to the corner fiber on the mechanical loading as evidence of a shift in the maximum shear stress is shown in Figure 192 as the magnitude occurs at $\theta = 33.75^\circ$ instead of $\theta = 45^\circ$. Furthermore, their shear stress distribution is unsymmetrical further indicating nearest neighbor effects. For the 1.57d_f fiber spacing its maximum shear stress occurs at $\theta = 39.375^\circ$ and shows drastic difference in the rate

of slope change from $\theta = 39.375^\circ$ to $\theta = 90^\circ$ as the shear stress distribution is concave between $\theta = 50.625^\circ$ and $\theta = 73.125^\circ$.

Summarizing the shear stress results, it appears that the $6.0d_f$ fiber spacing groups has no nearest neighboring fiber interaction as its shear stress distribution is smooth and symmetrical about its maximum magnitude occurring at $\theta = 45^\circ$. Whereas, the other fiber spacing groups show varying degrees of nearest neighbor interaction as evidenced by a shift in their maximum shear stress magnitude location and the asymmetrical shape to their interfacial distribution. Although the magnitude of the matrix cure shrinkage shear stress is small, combining it with the mechanical load effects further impacts the interfacial shear stress as evidence by the change in location of the maximum stress and the asymmetrical distribution shape for the $2.0d_f$, $1.90d_f$, $1.84d_f$, $1.75d_f$ and the $1.57d_f$ fiber spacing groups. Table 69 lists the maximum variation of the shear stress across the interface due to the matrix shrinkage and the percentage reduction of the maximum shear stress by the shrinkage stress. The maximum variation is taken as the difference between the local peaks for each fiber spacing group shown in Figure 191 and is an indication of the effects from the corner fiber. From Table 69 the variation decreases, thus having less of an impact, as the fiber spacing increases. However, due to the shrinkage stress interfacial distribution it causes the mechanical load to act over a larger portion of the fiber interface readily observed by comparing Figure 190 and 192.

Table 69: Maximum shear stress variation due to matrix shrinkage and percent reduction of the maximum shear stress due to the mechanical load

Fiber Spacing	Maximum Shear Stress Variation (MPa)	Percent reduction of Maximum Shear by Shrinkage Stress
$1.57d_f$	6.53	11.8%
$1.75d_f$	3.84	14.7%
$1.84d_f$	2.97	12.1%
$1.90d_f$	2.61	5.6%
$2.0d_f$	2.07	4.5%
$2.5d_f$	0.79	6.2%
$6.0d_f$	0.18	1.7%

Center Fiber Interface Results – Summary

In summary for the center fiber the $6.0d_f$ fiber spacing group behaves as if the fibers were isolated from each other showing no interaction to the corner fibers due to the applied mechanical loads and the matrix cure shrinkage effects. Although nearest neighbor effects begin to manifest themselves at the $2.5d_f$ fiber spacing, shown predominately in the matrix cure shrinkage results as the mechanical loading results show virtually no interactions (see Figure 188 and 191), the magnitudes are very small. Thus the combined effects show practically no interaction for the $2.5d_f$ fiber spacing. This is not the case for the rest of the fiber spacing tested. Figure 187 and 190 show the radial and shear stress distribution at the fiber-matrix interface due to the combination of mechanical loading and chemical shrinkage. As expected the interaction of the nearest neighbor fiber has the greatest effect at the point on the interface of the center fiber where the corner fiber is closest at $\theta = 45^\circ$. The rest of the fiber spacing groups; namely the $1.57d_f$, $1.75d_f$, $1.84d_f$, $1.9d_f$ and the $2.0d_f$, show nearest neighbor effects by the wave in their interfacial radial stress distribution and by the unsymmetrical shape and shift in the maximum magnitude location for their interfacial shear stress distribution.

Corner Fiber Interface Results – Radial Stress

The radial stress distribution at the fiber-matrix interface due to the combined effects of mechanical loading and matrix cure shrinkage is shown in Figure 193 for the first quadrant; Figure 194 for the second quadrant; Figure 195 for the third quadrant and in Figure 196 for the fourth quadrant. As expected the maximum radial stress is tensile and in the direction of the mechanical load at $\theta = 90^\circ$ and 270° , whereas the minimum radial stress is compressive for all fiber spacing groups and occurs at $\theta = 0^\circ$ and 180° , normal to the applied load, as shown in Figure 193 - 196. The maximum magnitude of the radial stress is practically the same at the corner fiber and at the center fiber for the $6.0d_f$ spacing. However, it is significantly larger for the other fiber spacing groups. While the minimum radial stress is compressive for all fiber spacing groups at the corner fiber it is only compressive for the $6.0d_f$ fiber spacing at the center fiber. The single fiber (SF) is shown on the corner fiber stress distribution, see Figure 193, since the corner

fiber is most physically similar to the single fiber with respect to loading and physical geometry to the specimen free edge. Specifically for the interface between $\theta = 0^\circ$ to $\theta = 90^\circ$ the load path and the uninterrupted distance from the fiber to the specimen free edge are basically identical. Elsewhere along the fiber-matrix interface, i.e. from $\theta = 90^\circ$ to $\theta = 360^\circ$ interaction with the surrounding fiber prohibit a correlation to analytical results with the multi-fiber specimens. For the most part there appears to be no interaction with nearest neighboring fibers evident in quadrants 1, 2 and 4. The interfacial radial stress distributions are smooth and reach maximum magnitude in the direction of the applied load and have minimum magnitudes normal to the direction of loading. Interaction effects from the center fiber appear along the interface between $\theta = 180^\circ$ and 270° which is the range where the corner fiber is closest to the center fiber, as shown in Figure 195 for the $2.0d_f$, $1.90d_f$, $1.84d_f$, $1.75d_f$ and $1.57d_f$ fiber spacing groups. The magnitude of the interaction effects is very slight compared to the center fiber. Similar to the center fiber, the nearest neighbor effects manifest themselves as a wave along the fiber-matrix interface approximately between $\theta = 210^\circ$ to $\theta = 245^\circ$ for the $2.0d_f$ and $1.90d_f$ fiber spacing; between $\theta = 216^\circ$ to $\theta = 250^\circ$ for the $1.57d_f$ fiber spacing; and between $\theta = 200^\circ$ to $\theta = 220^\circ$ for the $1.84d_f$ and $1.75d_f$ fiber spacing.

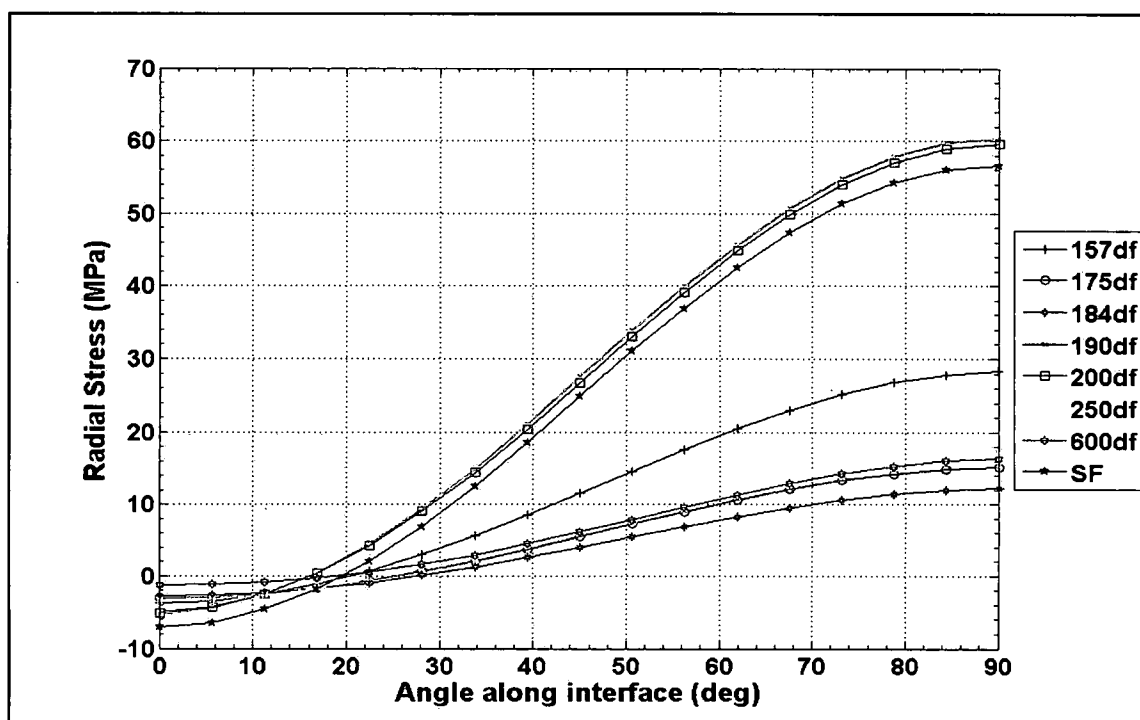


Figure 193: Radial stress distributions at the fiber-matrix interface due to the combination of mechanical loading and matrix chemical shrinkage from $\theta = 0^\circ$ to 90°

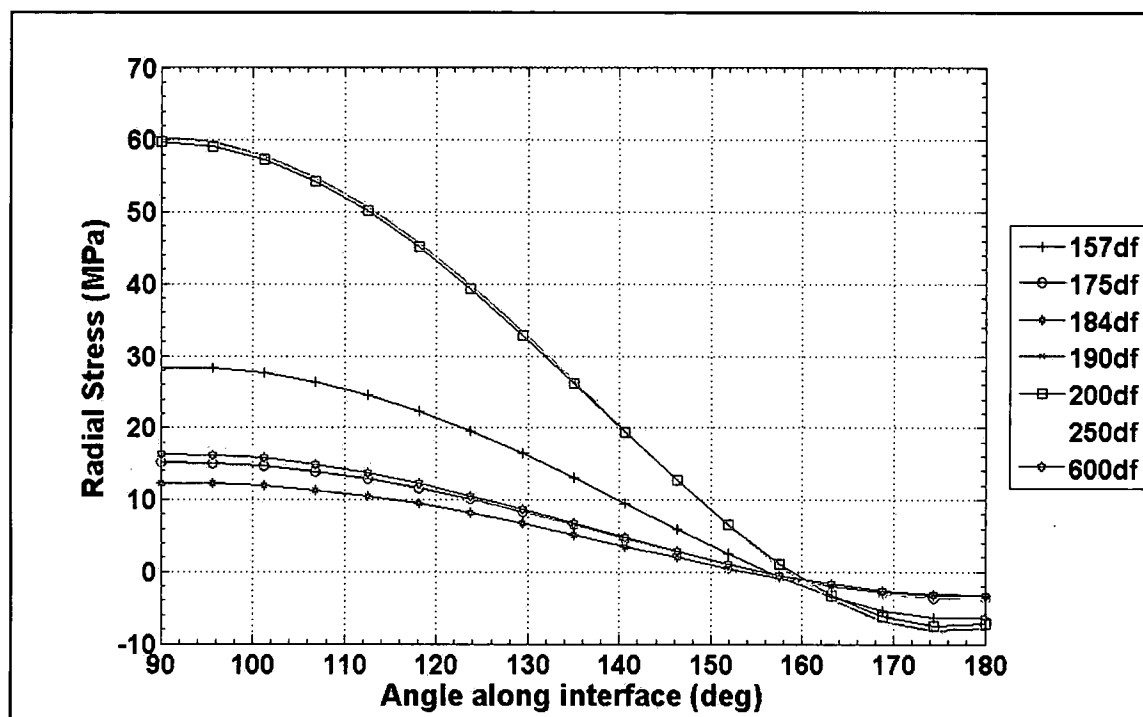


Figure 194: Radial stress distributions at the fiber-matrix interface due to the combination of mechanical loading and matrix chemical shrinkage from $\theta = 90^\circ$ to 180°

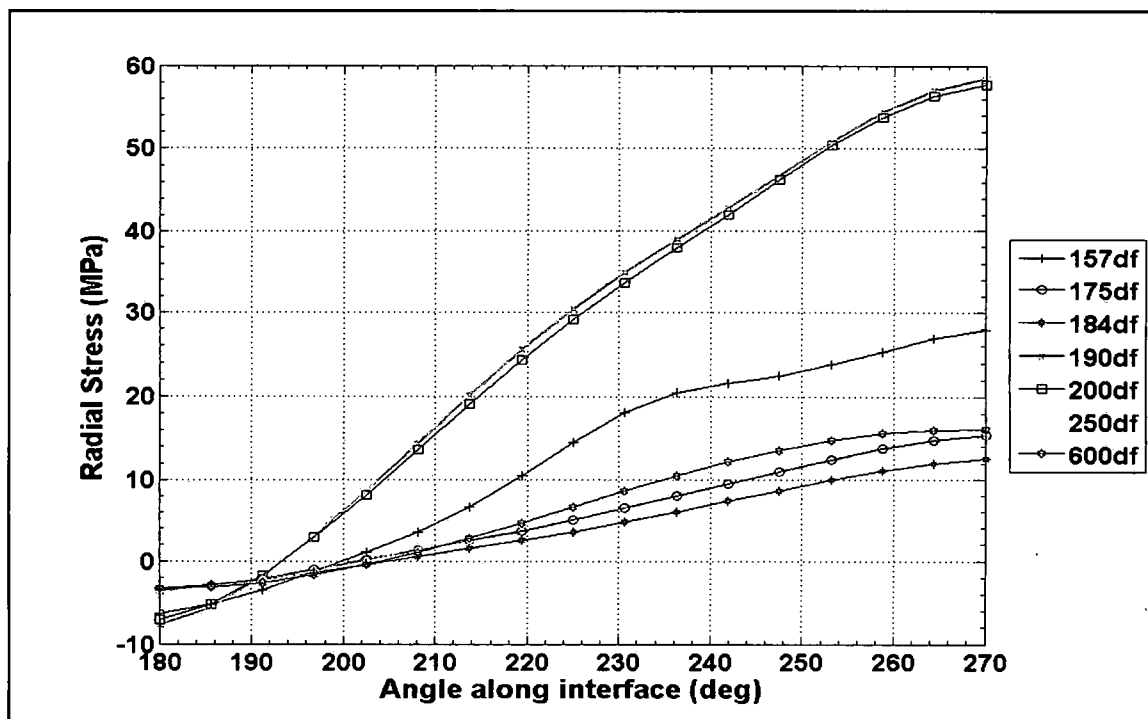


Figure 195: Radial stress distributions at the fiber-matrix interface due to the combination of mechanical loading and matrix chemical shrinkage from $\theta = 180^\circ$ to 270°

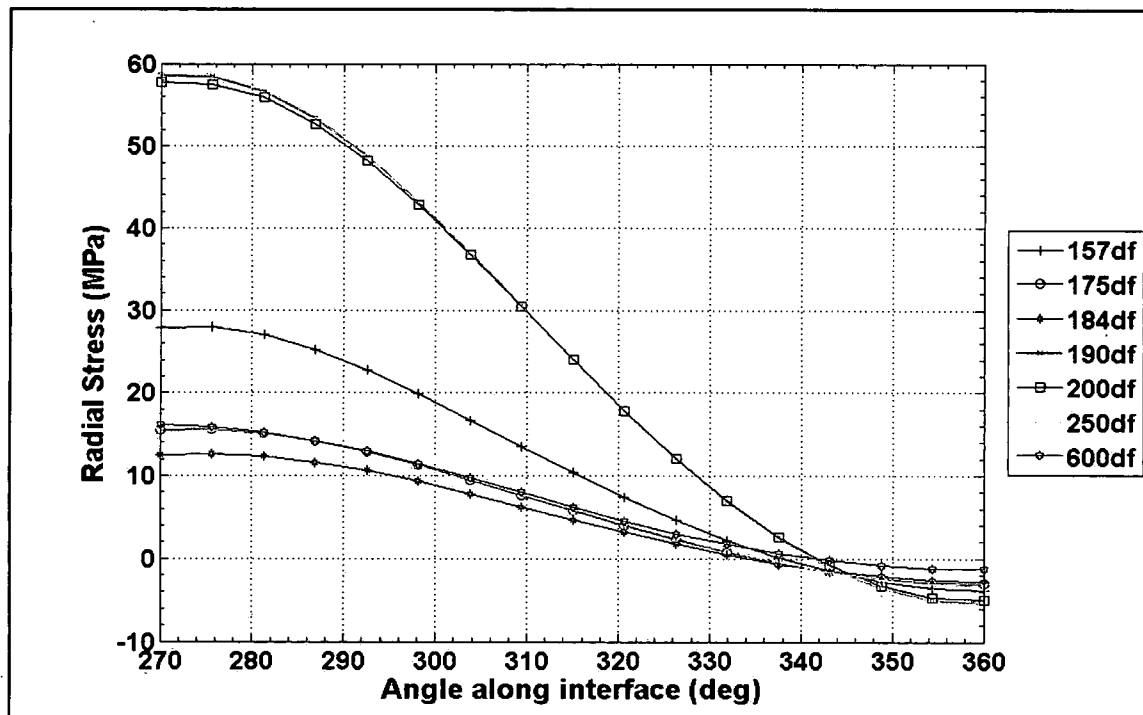


Figure 196: Radial stress distributions at the fiber-matrix interface due to the combination of mechanical loading and matrix chemical shrinkage from $\theta = 270^\circ$ to 360°

Investigating the interfacial radial stress due to the matrix cure shrinkage reveals a compressive stress around the entire circumference of the fiber as shown in Figure 197 for the first quadrant; in Figure 198 for the second quadrant; in Figure 199 for the third quadrant and in Figure 200 for fourth quadrant. As mentioned previously the single fiber results are plotted with the corner fiber results from $\theta = 0^\circ$ to $\theta = 90^\circ$. As shown in Figure 197 the single fiber interfacial radial stress distribution is fairly uniform from $\theta = 0^\circ$ to $\theta = 90^\circ$, as expected, as the matrix is free to shrink around the interface unobstructed due to its cure kinetics imparting a compressive prestress. In the first quadrant of the corner fiber, $\theta = 0^\circ$ to $\theta = 90^\circ$, the interfacial radial stress tend to increase, i.e. become more compressive, as the fiber spacing decreases as shown in Figure 197. The increasing trend is most likely caused by the specimen edge. The point closest to the specimen edge is at $\theta = 0^\circ$, while moving along the interface to 90° increases the distance from the edge. From about $\theta = 50^\circ$ to 110° the radial shrinkage stresses are fairly uniform for the $1.57d_f$, $1.75d_f$, $1.84d_f$, $1.90d_f$ and the $2.0d_f$ fiber spacing groups and reach their respective maximum magnitudes between $\theta = 65^\circ$ to 85° . In the second quadrant, $\theta = 90^\circ$ to 180° , the interfacial matrix cure shrinkage radial stresses decrease in magnitude, i.e. becoming less compressive, as the fiber spacing decreases and as they traverse along the interface to 180° . This behavior would be caused by the effects of the other corner fiber. The maximum magnitude of the radial compressive stresses due to the chemical shrinkage occurring between $\theta = 65^\circ$ to 85° is also caused by the effects from the other corner fiber disrupting the unobstructed due to its cure kinetics observed for the single fiber.

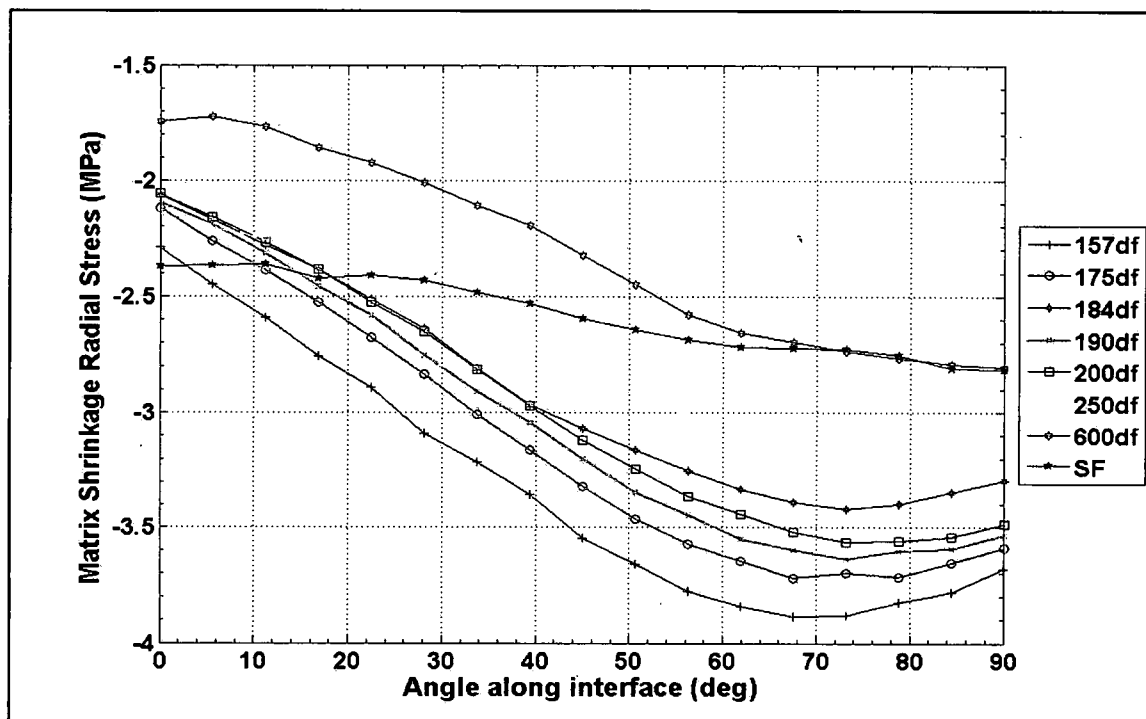


Figure 197: Radial stress distributions at the fiber-matrix interface due to the matrix chemical shrinkage from $\theta = 0^\circ$ to 90°

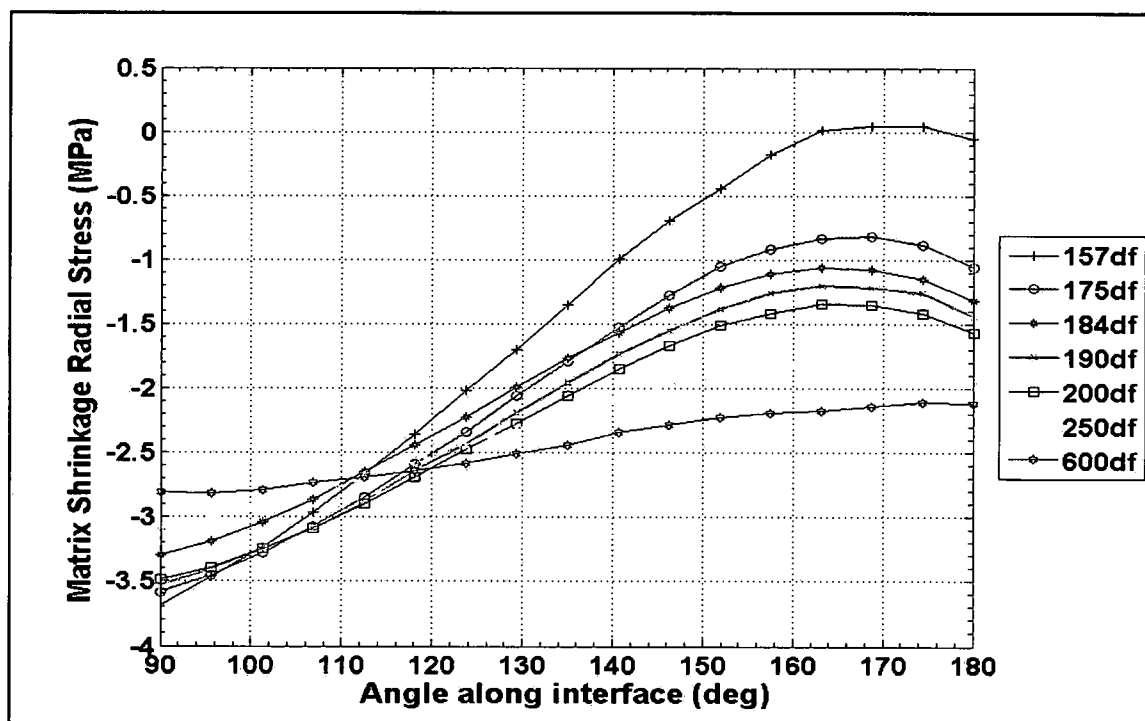


Figure 198: Radial stress distributions at the fiber-matrix interface due to the matrix chemical shrinkage from $\theta = 90^\circ$ to 180°

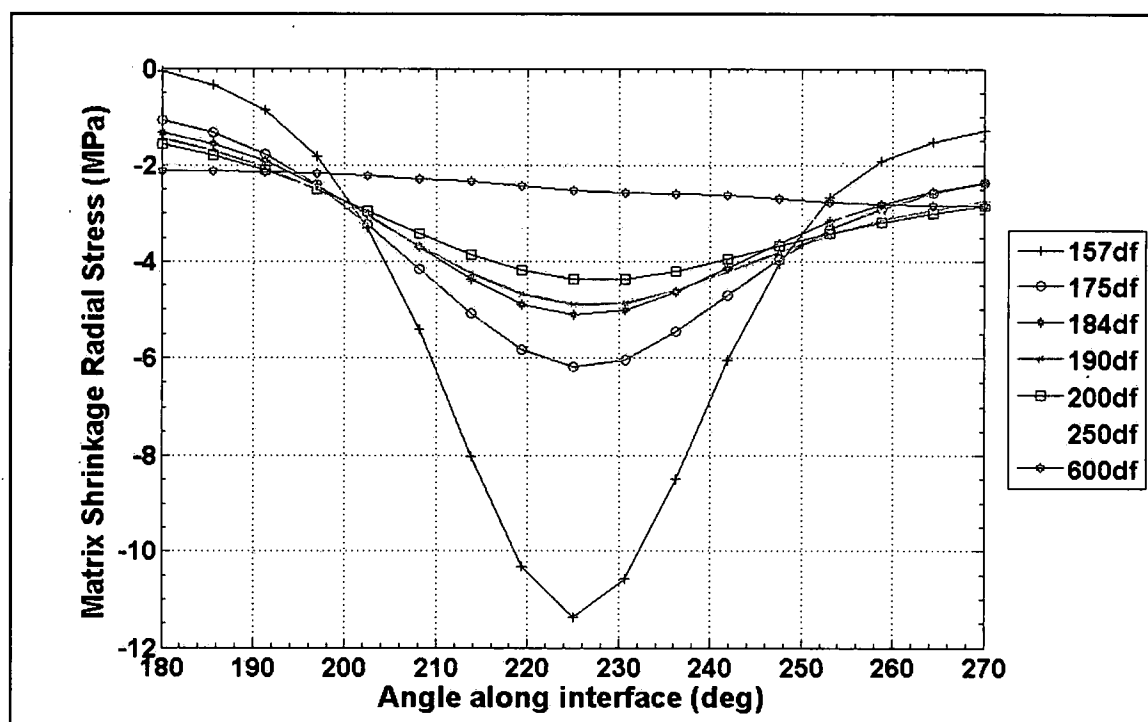


Figure 199: Radial stress distributions at the fiber-matrix interface due to the matrix chemical shrinkage from $\theta = 180^\circ$ to 270°

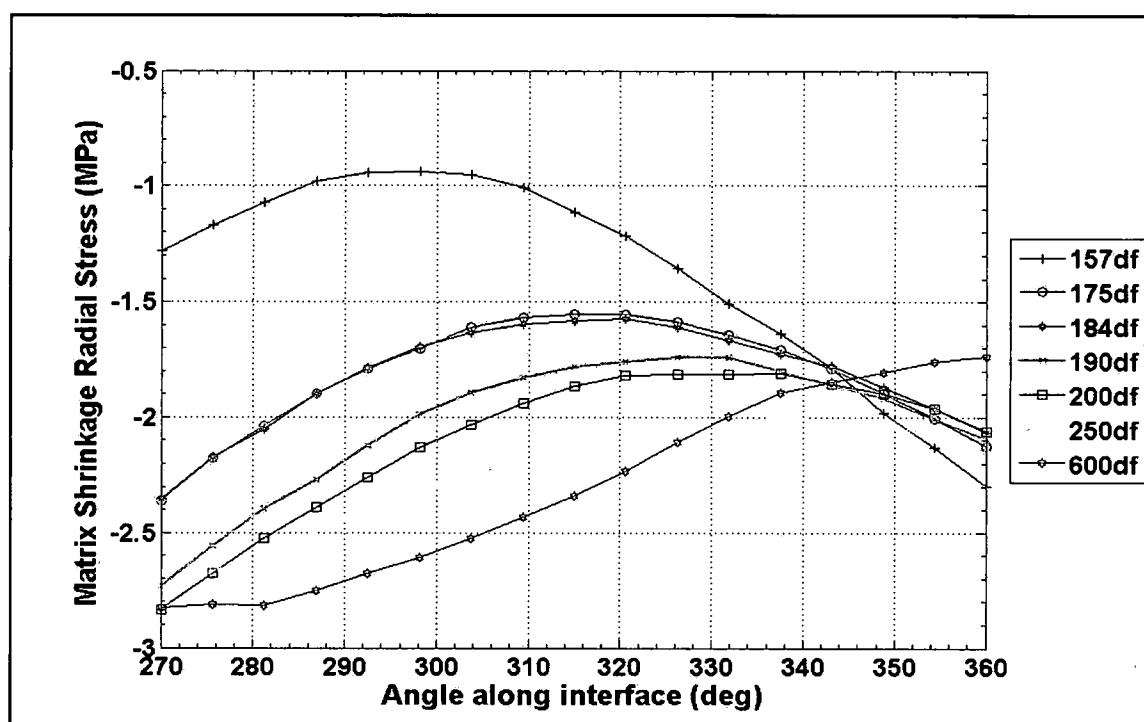


Figure 200: Radial stress distributions at the fiber-matrix interface due to the matrix chemical shrinkage from $\theta = 270^\circ$ to 360°

The radial stress component of the matrix cure shrinkage in the fourth quadrant, i.e. $\theta = 270^\circ$ to 360° appears to be affected by both the center fiber and the third corner fiber. For the third quadrant of the corner fiber, $\theta = 180^\circ$ to 270° , the interfacial radial stress of the matrix cure shrinkage exhibits the same behavior as the center fiber where the stresses increase as the fiber spacing decreases. The third quadrant of the corner fiber is closest to the center fiber and the interactions are quite apparent as the maximum magnitudes are at $\theta = 225^\circ$ for all fiber spacing groups except the $6.0d_f$ spacing.

Figure 201 to 204 shows the radial stress distribution in all four quadrants of the corner fiber at the fiber-matrix interface due to the mechanical load only. Similar to the radial stress distribution of the combined mechanical load and matrix cure shrinkage, the maximum magnitudes occur in the direction of the applied load at $\theta = 90^\circ$ and 270° and are all tensile. Whereas, the minimum magnitudes occur at $\theta = 0^\circ$ and 180° , normal to the applied loading direction and are mostly compressive except for the $6.0d_f$ fiber spacing in the first and fourth quadrant where its magnitude is practically zero. As mentioned above the single fiber results are plotted with the first quadrant corner fiber results and are practically parallel to the $1.9d_f$ and $2.0d_f$ interfacial radial stress results, albeit slightly smaller in magnitude. Comparing to the first, second and fourth quadrants of the radial stress due to the combined mechanical and shrinkage loads, see Figure 193, 194 and 196 to the same quadrants due only to the mechanical loading, see Figure 201, 202 and 203; not much difference exists between the radial stress distributions at the fiber-matrix interface for the fiber spacing groups tested except the small change in magnitudes due to the matrix cure shrinkage compressive radial stresses. Nearest neighbor effects manifest themselves in the third quadrant of the corner fiber as shown in Figure 203, by the characteristic wave present in the radial stress distribution due to the mechanical loading for the $2.0d_f$, $1.90d_f$, $1.84d_f$, $1.75d_f$ and $1.57d_f$ fiber spacing groups. Recall this quadrant of the corner fiber is closest to the center fiber. The maximum radial stress for the $1.57d_f$ fiber spacing occurs at $\theta = 236.25^\circ$ and remains fairly constant to $\theta = 270^\circ$. Whereas, a slight wave exists for the $1.75d_f$ and the $1.84d_f$ fiber spacing groups between $\theta = 210^\circ$ and $\theta = 240^\circ$ and for the $1.90d_f$ and $2.0d_f$ fiber spacing group between $\theta = 213.75^\circ$ and $\theta = 236.25^\circ$. The $2.5d_f$ and $6.0d_f$ fiber spacing group indicates no

interaction with the center fiber as their interfacial radial stress distribution is smooth, parallel and practically equal to each other.

Although, it appears that the shrinkage effects are sensitive to both the proximity to the specimen edge and the closest neighboring fiber, as seen in Figures 197, 198 and 200; dramatic impacts of the interfacial radial stress due to the matrix cure shrinkage is predominately seen in the third quadrant of the corner fiber, where the corner fiber and center fiber are closest. Table 70 lists the percent reduction of the radial stress due to the mechanical load from the matrix chemical shrinkage radial stress for quadrants 1, 2 and 4 of the corner fiber. Although in quadrant 1 the radial shrinkage stresses are maximum between $\theta = 70^\circ$ to 78° for most of the fiber spacing groups as shown in Figure 197, Table 70 lists the impact at the location of maximum radial stress due to the mechanical load since radial shrinkage stresses are practically uniform from $\theta = 70^\circ$ to 90° . From Table 70 the impacts due to the chemical shrinkage on the radial stress, both in percent reduction and magnitude, are consistent for all fiber spacing groups in quadrants 1, 2 and 4 except for the $1.57d_f$ spacing in the 4th quadrant where the impact is less. The impacts for the SF, $1.90d_f$ and the $2.0d_f$ are practically equal and are virtually the same compared to the same fiber spacing groups at the center fiber.

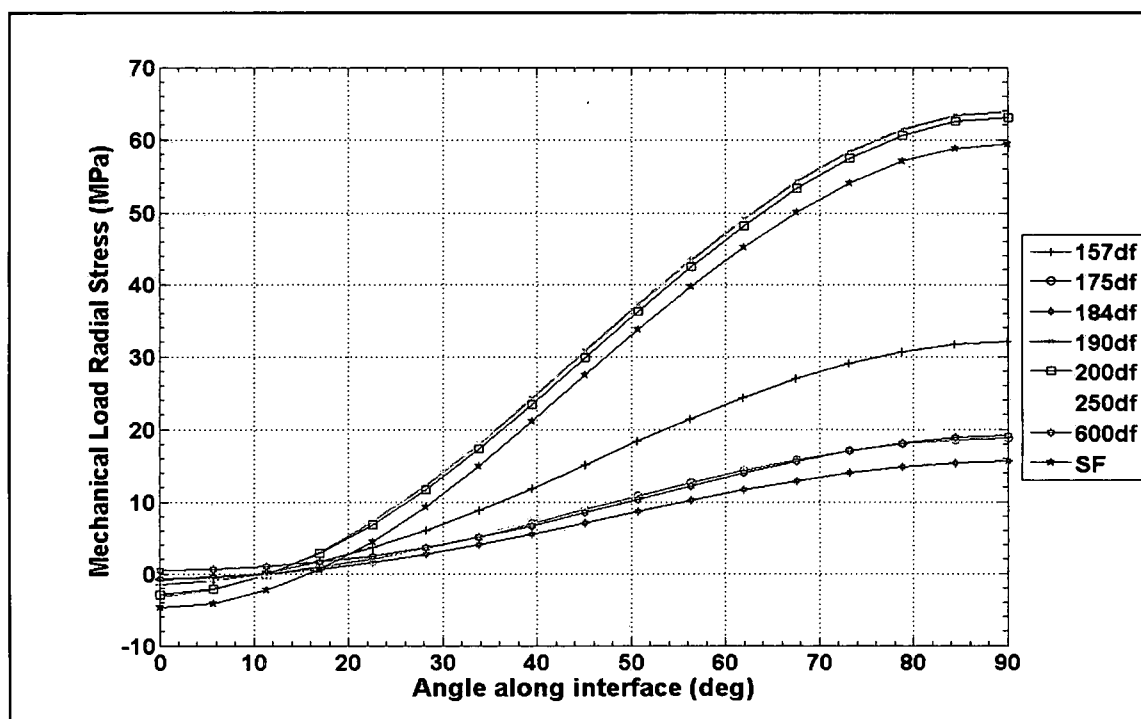


Figure 201: Radial stress distributions at the fiber-matrix interface due to the mechanical loading from $\theta = 0^\circ$ to 90°

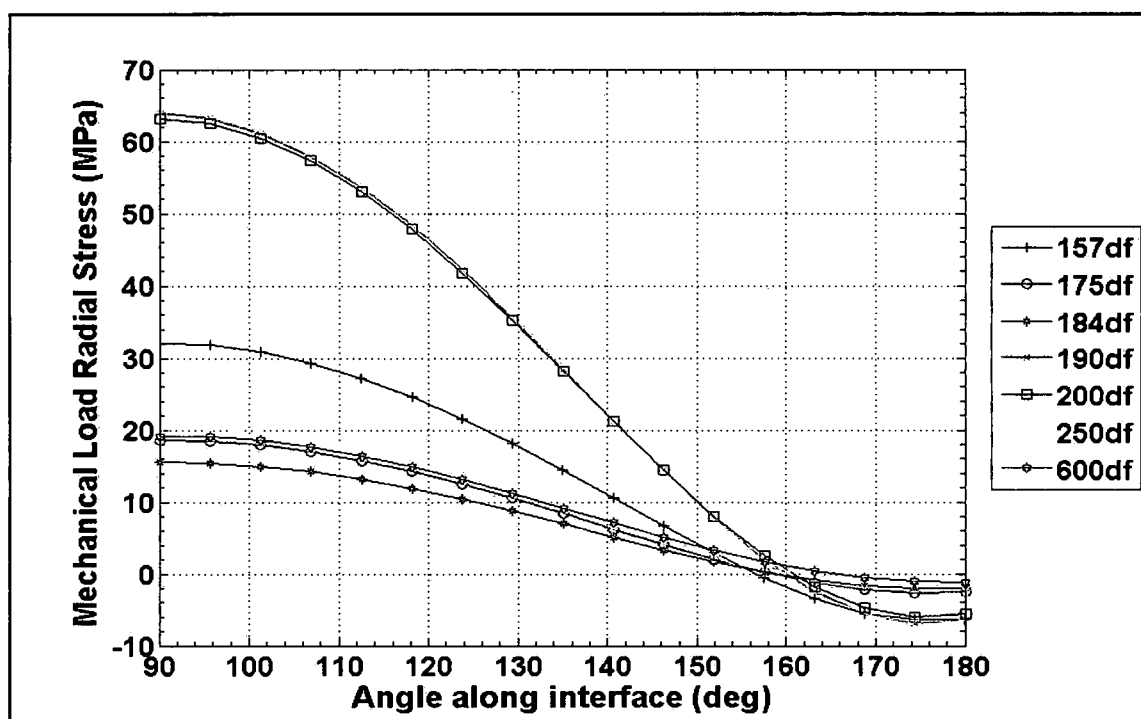


Figure 202: Radial stress distributions at the fiber-matrix interface due to the mechanical loading from $\theta = 90^\circ$ to 180°

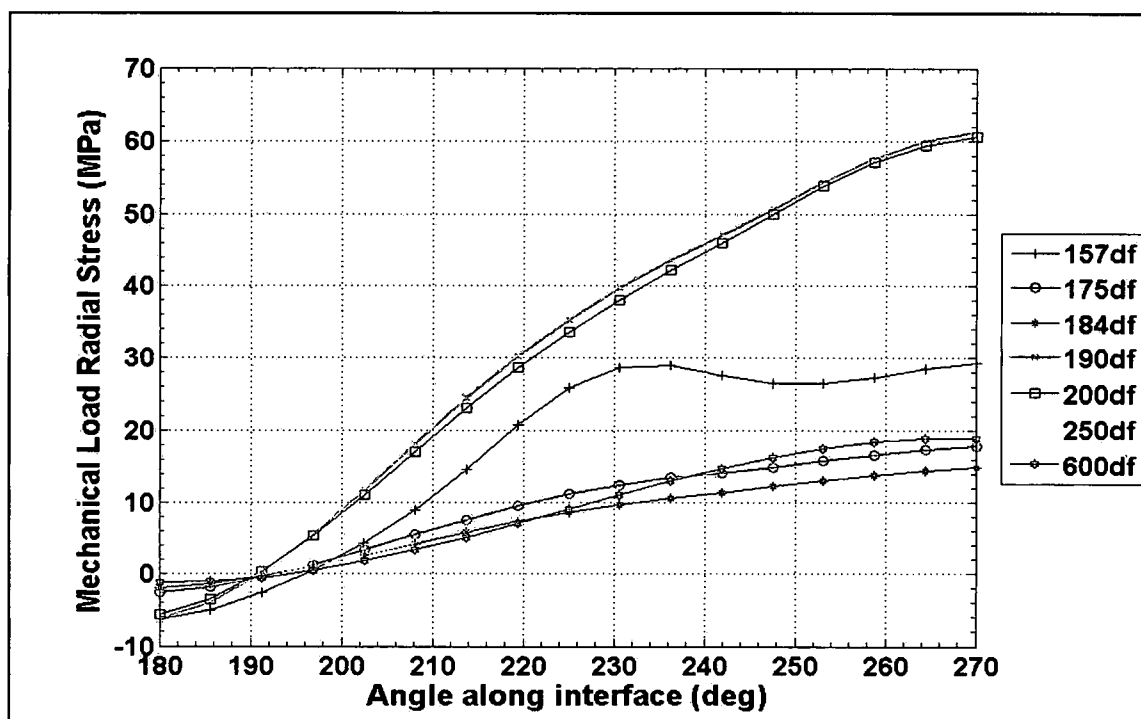


Figure 203: Radial stress distributions at the fiber-matrix interface due to the mechanical loading from $\theta = 180^\circ$ to 270°

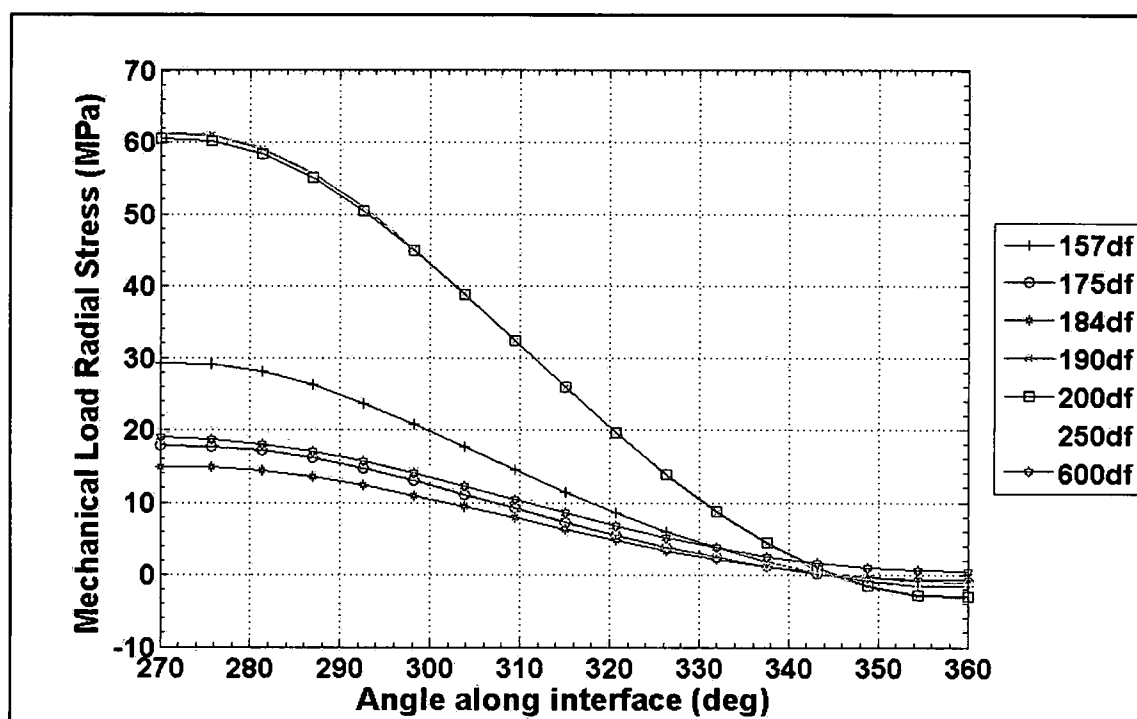


Figure 204: Radial stress distributions at the fiber-matrix interface due to the mechanical loading from $\theta = 270^\circ$ to 360°

Table 70: The percent reduction of the radial stress over the mechanical load due to the matrix chemical shrinkage for quadrants 1, 2, and 4 of the corner fiber

Fiber Spacing	1 st and 2 nd Quadrant				4 th Quadrant			
	Max Mech Radial Stress	Residual Stress @ Max Mech Radial Stress	Loc θ	%	Max Mech Radial Stress	Residual Stress @ Max Mech Radial Stress	Loc θ	%
1.57d _f	31.99	-3.68	90°	12	29.20	-1.28	270°	4
1.75d _f	18.70	-3.59	90°	19	17.82	-2.36	270°	13
1.84d _f	15.54	-3.30	90°	21	14.88	-2.35	270°	16
1.9d _f	63.89	-3.53	90°	6	61.22	-2.73	270°	4
2.0d _f	63.14	-3.49	90°	6	60.50	-2.83	270°	5
2.5d _f	20.35	-3.07	90°	15	19.64	-2.76	270°	14
6.0d _f	19.13	-2.81	90°	15	18.99	-2.83	270°	15
SF	59.38	-2.81	90°	5	-			

For the third quadrant, comparing Figure 195 to Figure 203 the matrix cure shrinkage effects are rather large at the maximum matrix cure shrinkage location of $\theta = 225^\circ$ for the 1.57d_f, 1.75d_f and 1.84d_f fiber spacing groups. Table 71 lists the percent reduction of the radial stress due to the mechanical load from the matrix chemical shrinkage radial stress for the third quadrant of the corner fiber. It is very apparent, from Table 71, the impact that the matrix shrinkage imparts on the radial stress for all fiber spacing groups predominately at the location where the fibers are closest together. At the location of maximum radial stress magnitude due to the mechanical load the impacts due to the matrix shrinkage are quite less but consistent with the impacts exhibited in the other quadrants. What is very consistent is the behavior of the 6.0d_f fiber spacing across all quadrants of the corner fiber.

Table 71: The percent reduction of the radial stress over the mechanical load due to the matrix chemical shrinkage for quadrant 3 of the corner fiber

Fiber Spacing	Max Matrix Resdl Stress (MPa)	Mech @ Max Resdl (MPa)	Loc	%	Max Mech Stress (MPa)	Resdl Stress @ Max Mech (MPa)	Loc	%
1.57d _f	-11.38	25.92	225°	44	29.19	-1.28	270°	4
1.75d _f	-6.20	11.23	225°	55	17.82	-2.36	270°	13
1.84d _f	-5.12	8.69	225°	59	14.88	-2.35	270°	16
1.90d _f	-4.91	35.28	225°	14	61.21	-2.73	270°	4
2.0d _f	-4.38	33.53	225°	13	60.49	-2.83	270°	5
2.5d _f	-3.30	11.58	230.6°	28	19.64	-2.76	270°	14
6.0d _f	-2.83	18.90	264.4°	15	18.99	-2.82	270°	15

In summarizing the radial stress distribution around the corner fiber, it appears that the shrinkage radial stress is sensitive to the specimen geometry in addition to neighboring fibers. Consequently these effects are felt along the entire circumference of the corner fiber. The radial stress due to the matrix cure shrinkage increases as the fiber spacing decreases in the first and third quadrants, whereas, the opposite occurs in the second and fourth quadrants. As the matrix cures it is highly constrained by the comparative closeness of the fiber spacing creating relative high compressive stresses. Thus the magnitude of the radial stress increases as the fiber spacing decreases, as witnessed in the third quadrant. To maintain equilibrium the other quadrants must compensate causing the radial stress to decrease as the fiber spacing decreases, as witnessed in the second and fourth quadrant. The first quadrant must maintain the equilibrium thus its radial stress increase as the fiber spacing decreases. For the $6.0d_f$ fiber spacing the shrinkage radial stress is fairly constant across the entire interface of the corner fiber as shown in Figure 197 – 200 and in Tables 70 and 71. Nearest neighboring fibers affect the interfacial radial stress distribution due to the mechanical loading predominately in the third quadrant as evidence by the characteristic wave in the distribution as shown in Figure 203. Comparing Figure 189 to Figure 203 the maximum magnitudes of the radial stresses are greater for the corner fiber than for the center fiber for the fiber groups experiencing nearest neighbor interactions, namely the $1.57d_f$, $1.75d_f$, $1.84d_f$, $1.90d_f$ and $2.0d_f$. Furthermore, in this quadrant for these fiber spacing groups the radial stress acts over a longer arc length on the corner fiber due to the mechanical load. However, due to the shrinkage affects the radial stress acts over a longer portion of the fiber-matrix interface than just due to the mechanical loading

Corner Fiber Interface Results – Shear Stress

The interfacial shear stress results all four quadrants of the corner fiber due to the combination of mechanical load and matrix cure shrinkage are shown in Figures 205 through 208. In the first, second and fourth quadrants the shear stress distribution follows an expected pattern of behavior, i.e. that the maximum magnitude for each fiber spacing group is located at the midpoint of the quadrant. Furthermore, the interfacial distribution is symmetrical about the

midpoint and the minimum magnitudes approach zero at the quadrant end points. Minor differences exist for the $6.0d_f$ spacing in the 1st and 4th quadrant and for the $1.57d_f$ fiber spacing in the 2nd and 4th quadrant relative to their specific maximum magnitude locations.

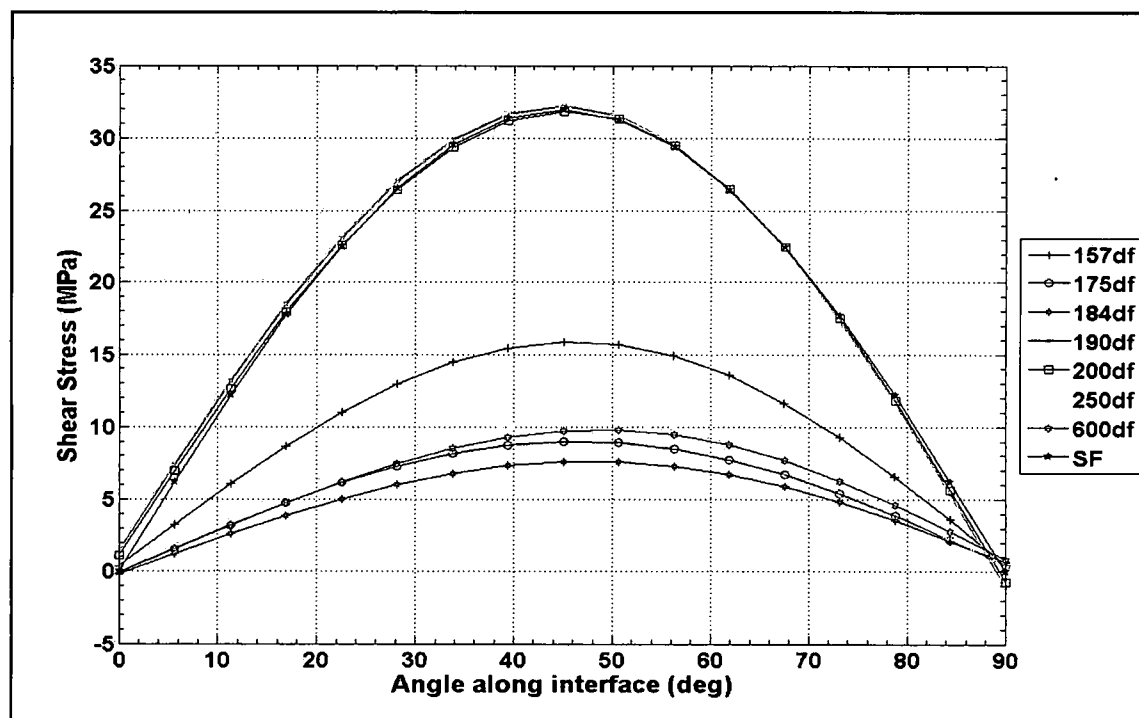


Figure 205: Shear stress distributions at the fiber-matrix interface due to the combination of mechanical loading and matrix chemical shrinkage from $\theta = 0^\circ$ to 90°

The single fiber interfacial shear stress distribution due to the combination of mechanical loading and matrix cure shrinkage tracks practically equal to the $1.9d_f$ and $2.0d_f$ fiber spacing groups. The SF is shown here in the first quadrant of the corner fiber for reason previously mentioned.

The nearest neighbor interactions manifest themselves in the third quadrant of the corner fiber. Comparing the center fiber interfacial shear stress distribution, as shown in Figure 190, to the corner fiber interfacial shear stress distribution, as shown in Figure 207, show virtually the same stress distribution at the fiber-matrix interface albeit the corner fiber has slightly higher stress magnitudes. The maximum magnitude locations for each fiber spacing distribution for the

corner fiber shown in Figure 207 has the same corresponding shift as the center fiber, shown in Figure 190.

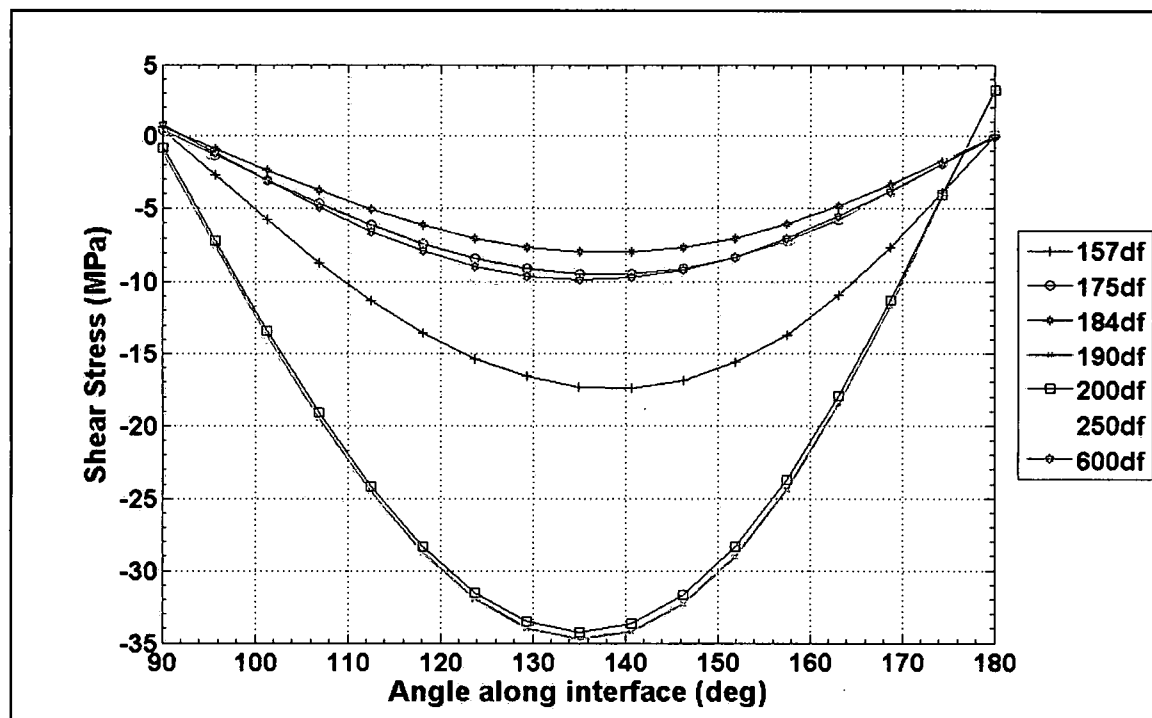


Figure 206: Shear stress distributions at the fiber-matrix interface due to the combination of mechanical loading and matrix chemical shrinkage from $\theta = 90^\circ$ to 180°

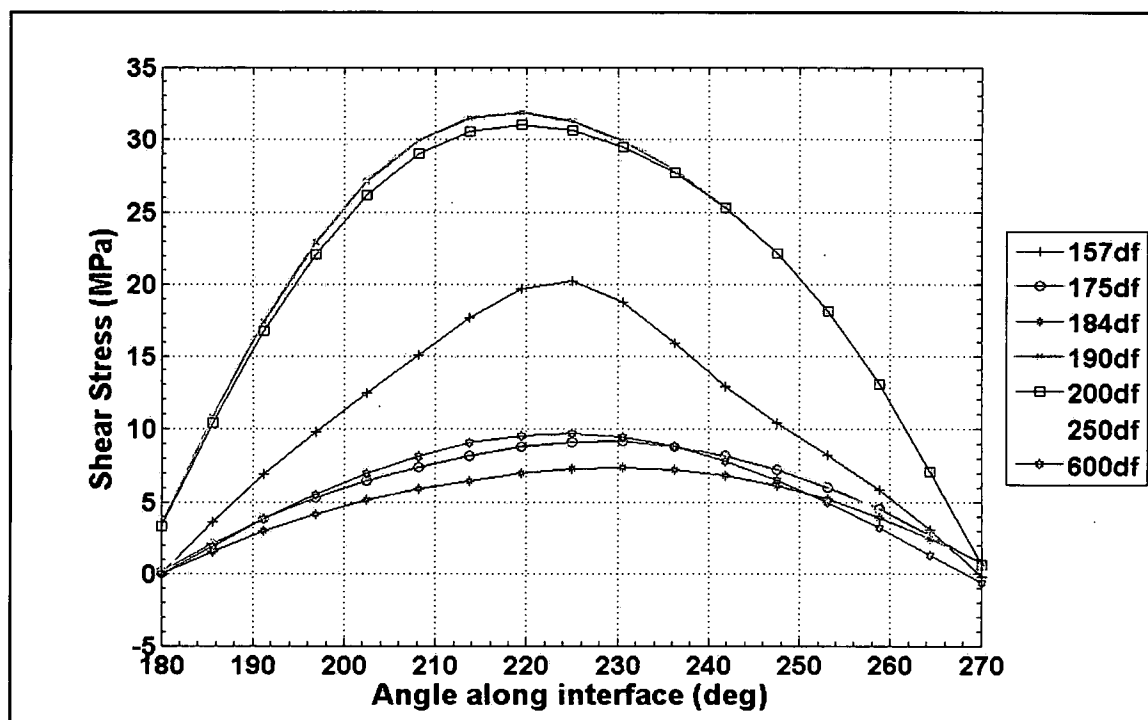


Figure 207: Shear stress distributions at the fiber-matrix interface due to the combination of mechanical loading and matrix chemical shrinkage from $\theta = 180^\circ$ to 270°

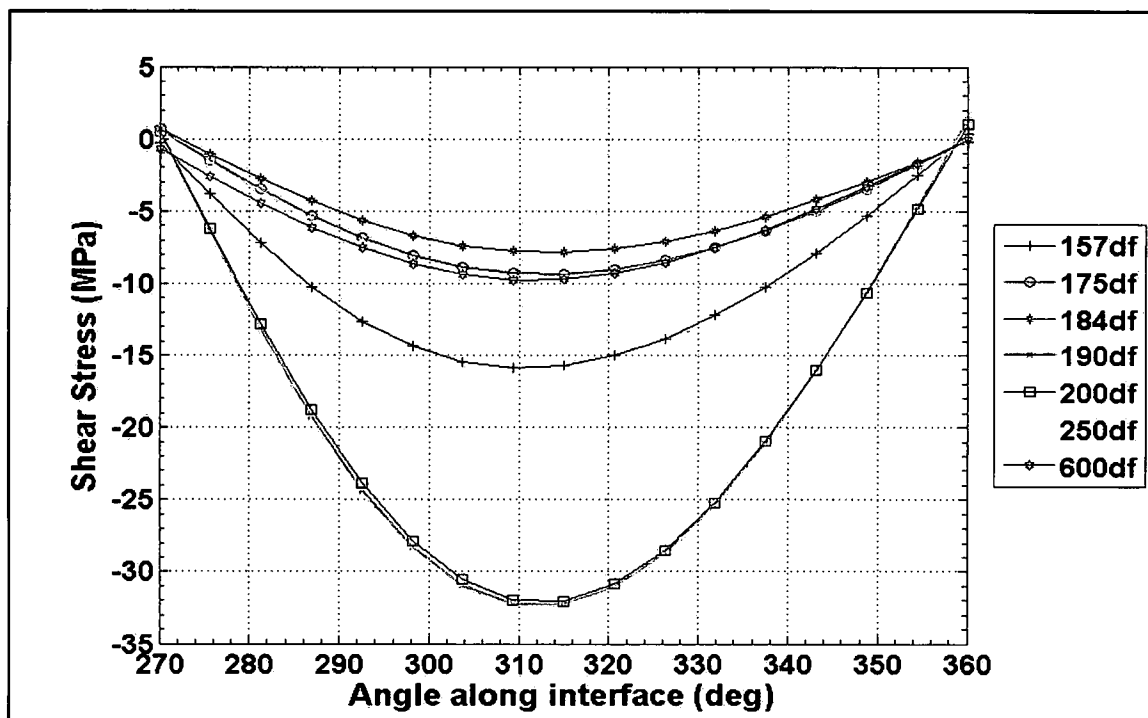


Figure 208: Shear stress distributions at the fiber-matrix interface due to the combination of mechanical loading and matrix chemical shrinkage from $\theta = 270^\circ$ to 360°

This behavior for the corner fiber, being similar to that of the center fiber, is explained in part by examining the interfacial shear stress distributions due to the matrix cure shrinkage. Figure 209 to 212 shows the shear stress distribution at the fiber-matrix interface due to the matrix cure shrinkage in all four quadrants of the corner fiber. The SF distribution is shown in the first quadrant of the corner fiber for reasons previously mentioned. Its magnitude is virtually constant across the entire quadrant. The relative magnitudes of the shear stress distribution in quadrants one, two and four for the rest of the fiber spacing groups are small compared to the shear stress due to the combination of the mechanical load and the matrix cure shrinkage, shown in Figure 205, 206 and 208, indicating very little neighboring fiber effects. For their relative maximum magnitudes they tend to increase as the fiber spacing decreases showing the effects of the neighboring fibers. Consequently the shear stresses due to the matrix cure shrinkage have minor impacts to the stress distribution in these quadrants of the corner fiber. The nearest neighbor interactions appear in the third quadrant of the corner fiber, namely from $\theta = 180^\circ$ to 270° as shown in Figure 211, and are virtually identical to the corresponding shear stress distribution for the center fiber as shown in Figure 191. The shear stress distribution for the 6.0d_r fiber spacing is negligible having a maximum magnitude of only 0.4 MPa at $\theta = 315^\circ$. The other fiber spacing groups show an inflection point between $\theta = 225^\circ$ to $\theta = 240^\circ$ as the shear stress changes direction across the fiber-matrix interface, as shown in Figure 211. Although not uniform the 2.5d_r fiber spacing interfacial shear stress distribution, as shown in Figure 211, is negligible since its maximum magnitude is less than 0.9 MPa. For the rest of the fiber spacing groups exhibit local maxima occurring between $\theta = 202.5^\circ$ and 208.125° and again between $\theta = 241.875^\circ$ to 270° . Furthermore, they tend to increase as the fiber spacing decrease, showing interaction with neighboring fibers like the center fiber, affecting the shear stress distribution differently depending on the interfacial position, as shown in Figure 211.

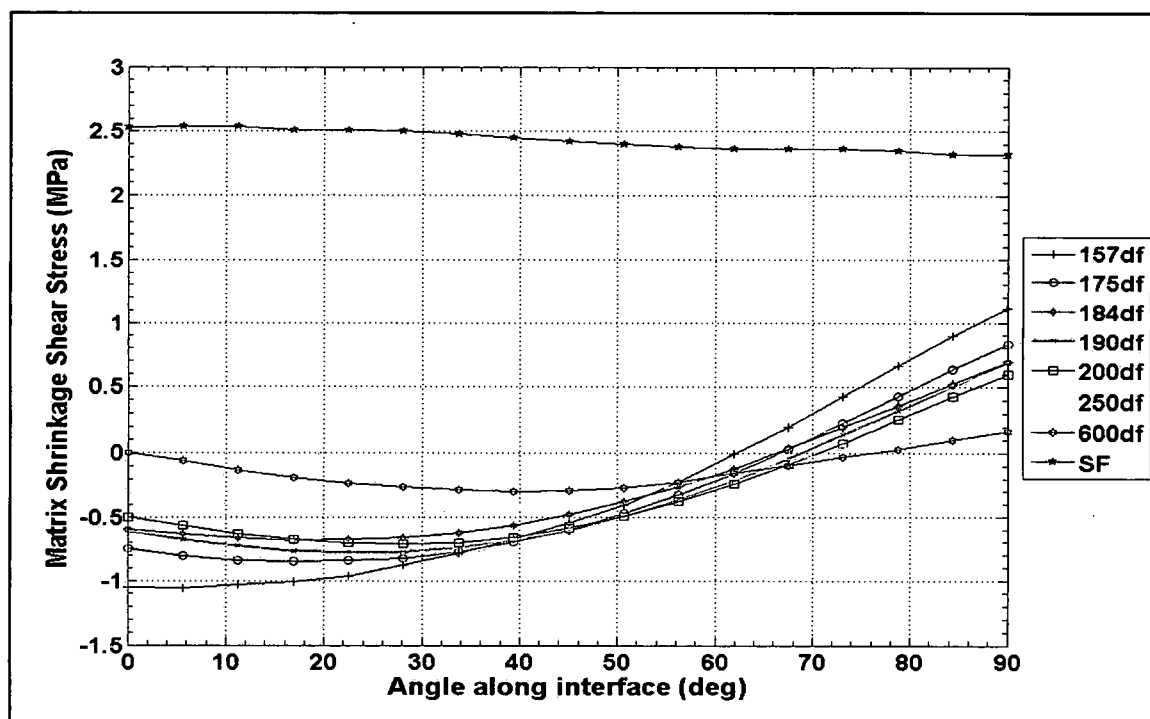


Figure 209: Shear stress distributions at the fiber-matrix interface due to the matrix chemical shrinkage from $\theta = 0^\circ$ to 90°

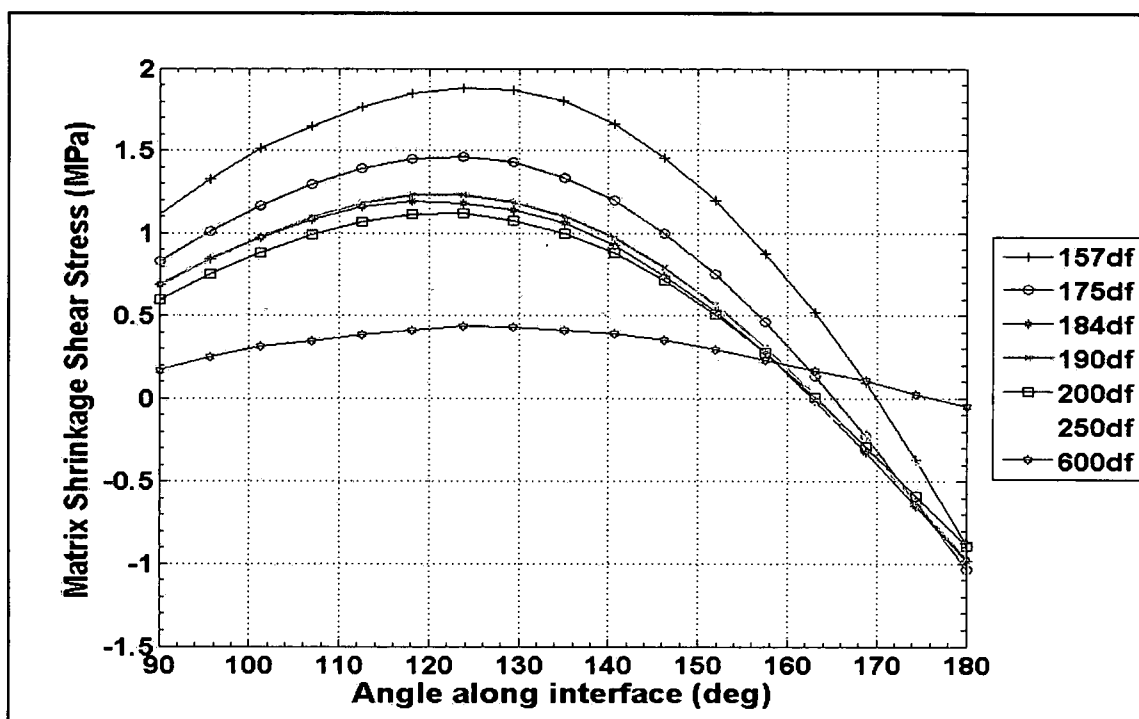


Figure 210: Shear stress distributions at the fiber-matrix interface due to the matrix chemical shrinkage from $\theta = 90^\circ$ to 180°

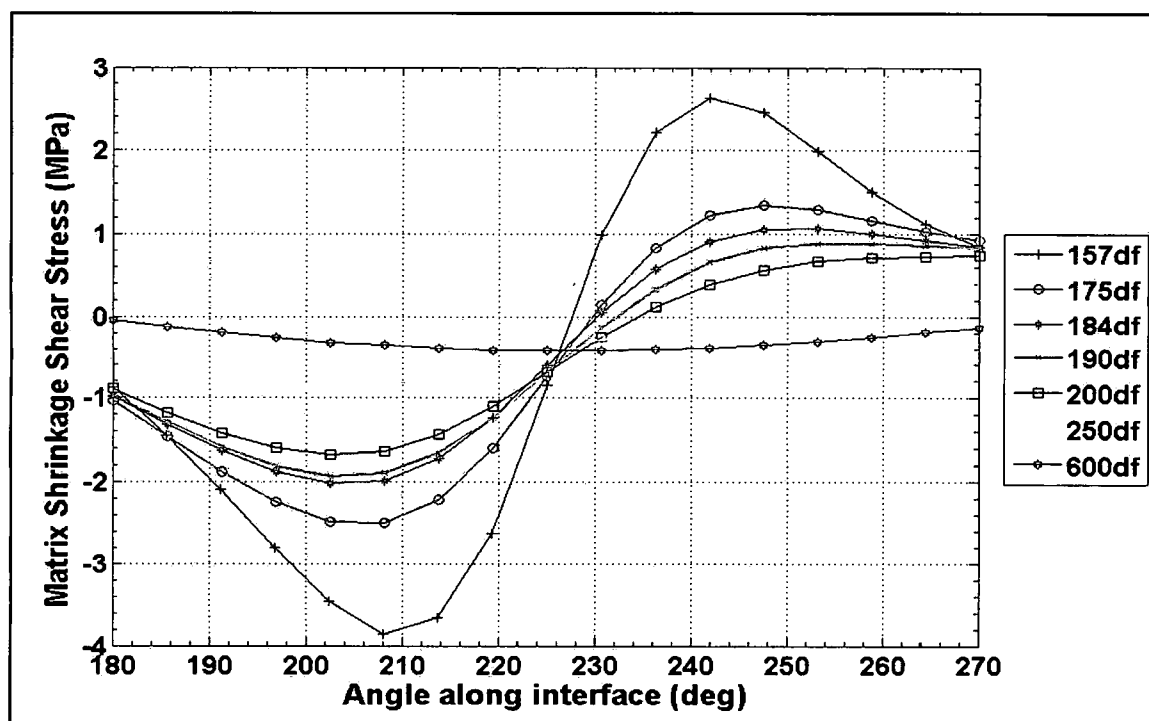


Figure 211: Shear stress distributions at the fiber-matrix interface due to the matrix chemical shrinkage from $\theta = 180^\circ$ to 270°

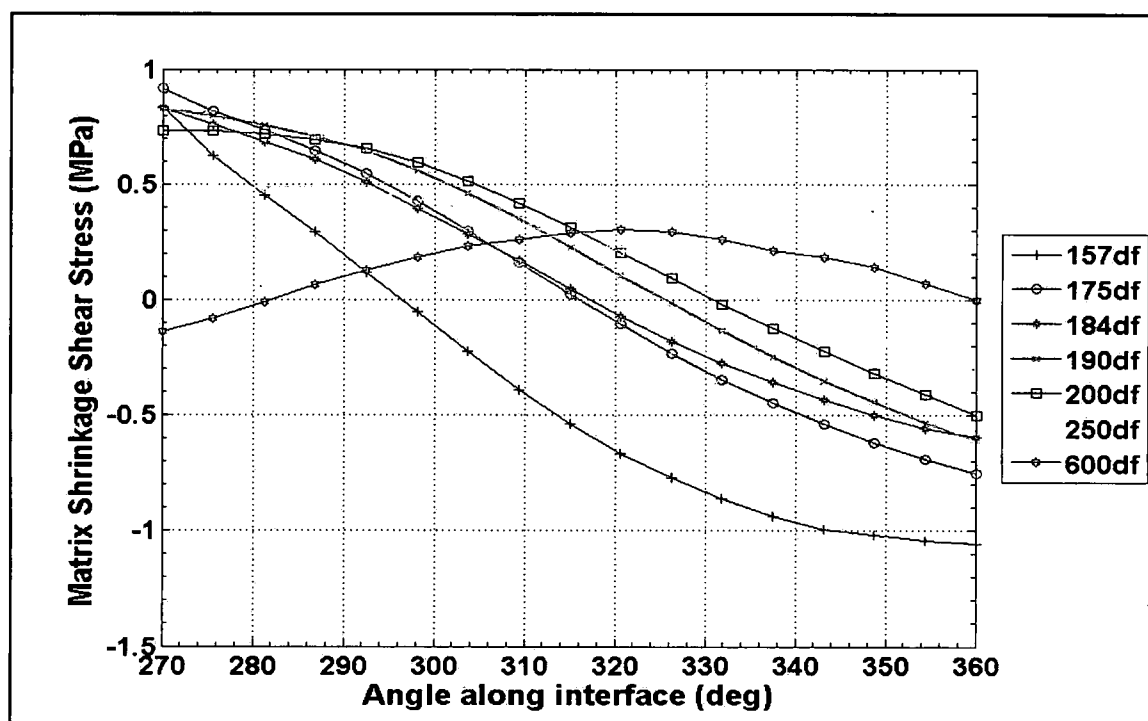


Figure 212: Shear stress distributions at the fiber-matrix interface due to the matrix chemical shrinkage from $\theta = 270^\circ$ to 360°

Table 72 lists the shear stress variations across the four quadrants of the corner fiber. For each quadrant it reveals that the matrix residual shear stresses decreases as the fiber spacing increases. The maximum shear stress magnitudes are fairly consistent in the first and fourth quadrants with respect to fiber spacing as shown in Table 72. The 2nd quadrant shear stress variation increases for all fiber spacing groups compared to the 1st and 4th quadrants. However, the 3rd quadrant shows the influence of neighboring fibers as its shear stress variation is greatest for each fiber spacing. Nearest neighbor effects manifest themselves quite clearly as the primary maximum magnitudes occur at $\theta = 208.125^\circ$ and secondary maximum magnitudes occur between $\theta = 241.875^\circ$ to $\theta = 270^\circ$, thus affecting the shear stress differently depending on the position along the fiber-matrix interface in the 3rd quadrant as shown in Figure 203. The 6.0d_f has a very minimal shear stress thus a very small variation across all four quadrants of the corner fiber.

Table 72: Maximum Shear Stress variation in all four quadrants of the Corner Fiber

Fiber Spacing	1 st and 4 th Quadrant Maximum Shear Stress Variation (MPa)	2 nd Quadrant Maximum Shear Stress Variation (MPa)	3 rd Quadrant Maximum Shear Stress Variation (MPa)
1.57d _f	2.2	2.8	6.4
1.75d _f	1.7	2.5	4.0
1.84d _f	1.4	2.2	3.0
1.9d _f	1.4	2.2	2.8
2.0d _f	1.3	2.2	2.4
2.5d _f	0.9	1.1	1.2
6.0d _f	0.4	0.4	0.4

Figure 213 to 216 shows the interfacial shear stress distribution in all four quadrants of the corner fiber due to the mechanical load. The SF distribution is shown in the first quadrant for reasons previously mentioned and track almost equal to the 1.90d_f and 2.0d_f fiber spacing groups. Figure 213, 214 and 216 are virtually a carbon copy of the shear stress distribution at the fiber-matrix-interface due to the combination of mechanical loading and the matrix cure shrinkage stresses, as shown in Figure 205, 206 and 208, indicating that the matrix cure shrinkage effects are very minimal for the corner fiber from $\theta = 0^\circ$ to $\theta = 180^\circ$ and from $\theta = 270^\circ$ to $\theta = 360^\circ$.

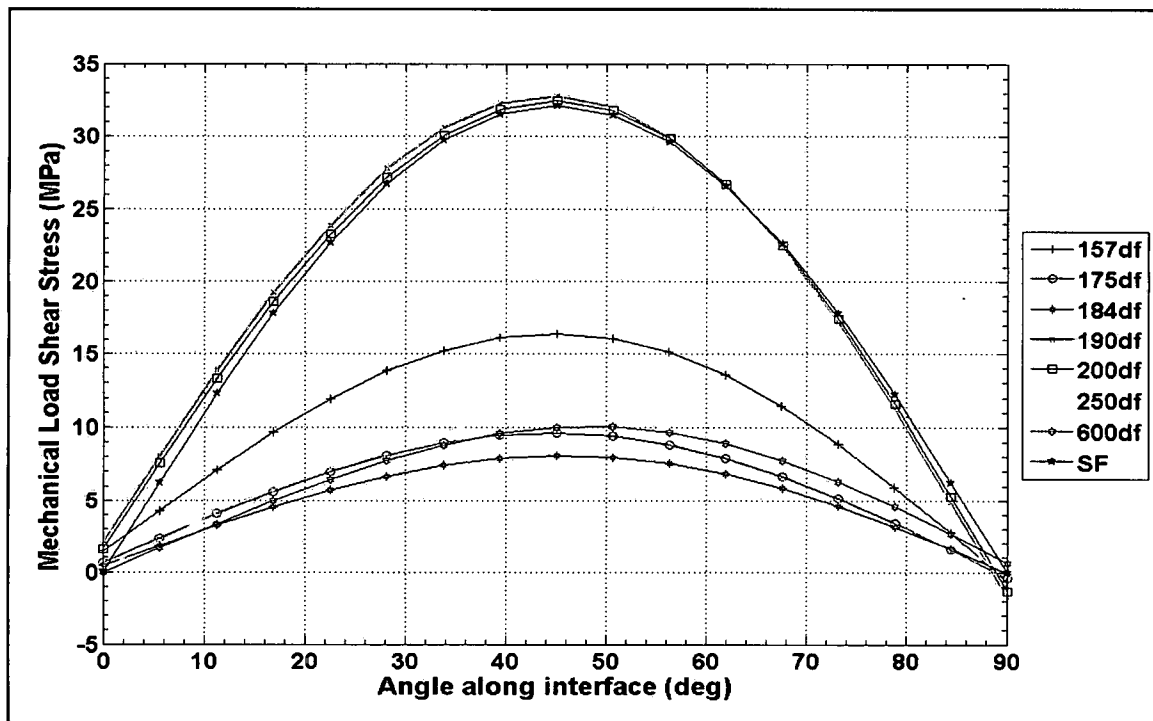


Figure 213: Shear stress distributions at the fiber-matrix interface due to the mechanical loading from $\theta = 0^\circ$ to 90°

The corner fiber shear stress results in the third quadrant, shown in Figure 215, confirm nearest neighbor interaction effects by the shift in the location of the maximum magnitude and exhibiting an asymmetrical shape as opposed to the other quadrants of the corner fiber nearly symmetrical interfacial distribution. These interfacial shear stress distributions are almost the same behavior as that shown Figure 192 for the center fiber. More precisely, the influence by the center fiber for $2.0d_f$, $1.90d_f$, $1.84d_f$, $1.75d_f$ and the $1.57d_f$ fiber spacing groups due the mechanical loading shifts the maximum shear stress to $\theta = 219.375^\circ$ instead of $\theta = 225^\circ$, as shown in Figure 215. Shifting the maximum magnitude location creates the asymmetrical shear stress distribution for these fiber spacing groups. However, the $1.57d_f$ fiber spacing shows a more drastic influence to the center fiber by the rate of slope change from $\theta = 225^\circ$ to 253.125° as the distribution is concave between $\theta = 230.625^\circ$ and 253.125° . Like the center fiber, the $6.0d_f$ fiber spacing corner fiber shows no neighboring fiber effects by its smooth symmetrical interfacial shear stress distribution and maximum magnitude occurring at $\theta = 225^\circ$, as shown in Figure 215.

For the $2.5d_f$ fiber spacing its maximum magnitude is almost equal at $\theta = 219.375^\circ$ and at 225° indicating nearest neighbor effects can be neglected.

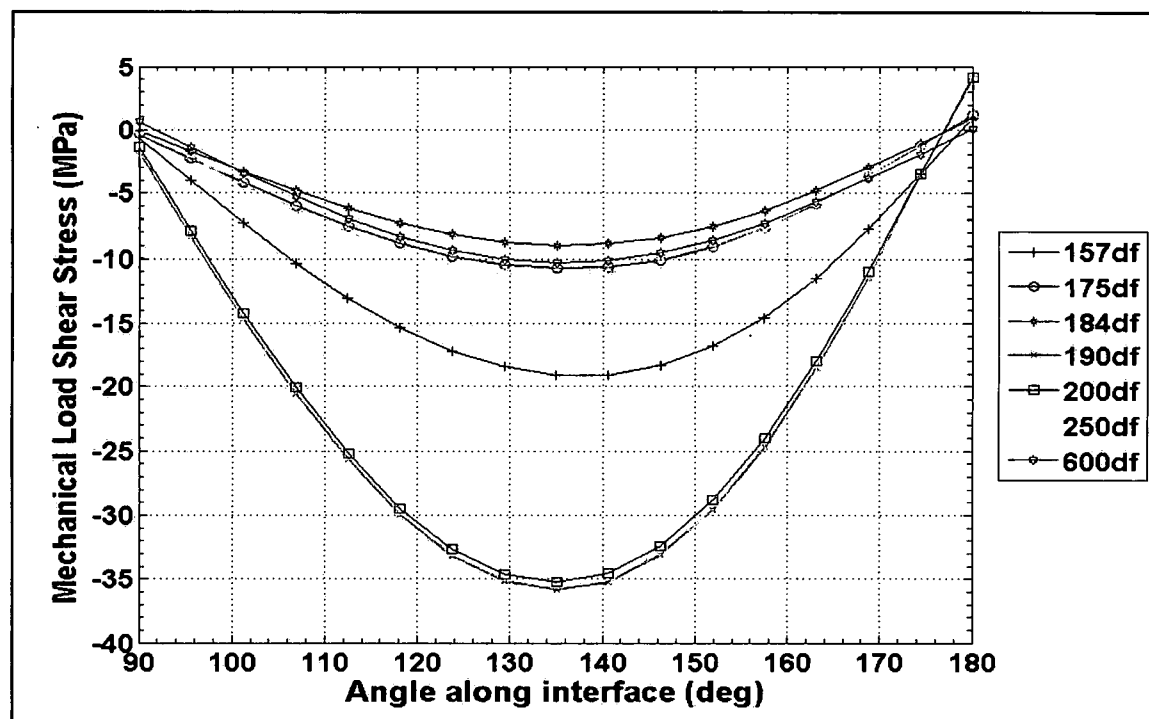


Figure 214: Shear stress distributions at the fiber-matrix interface due to the mechanical loading from $\theta = 90^\circ$ to 180°

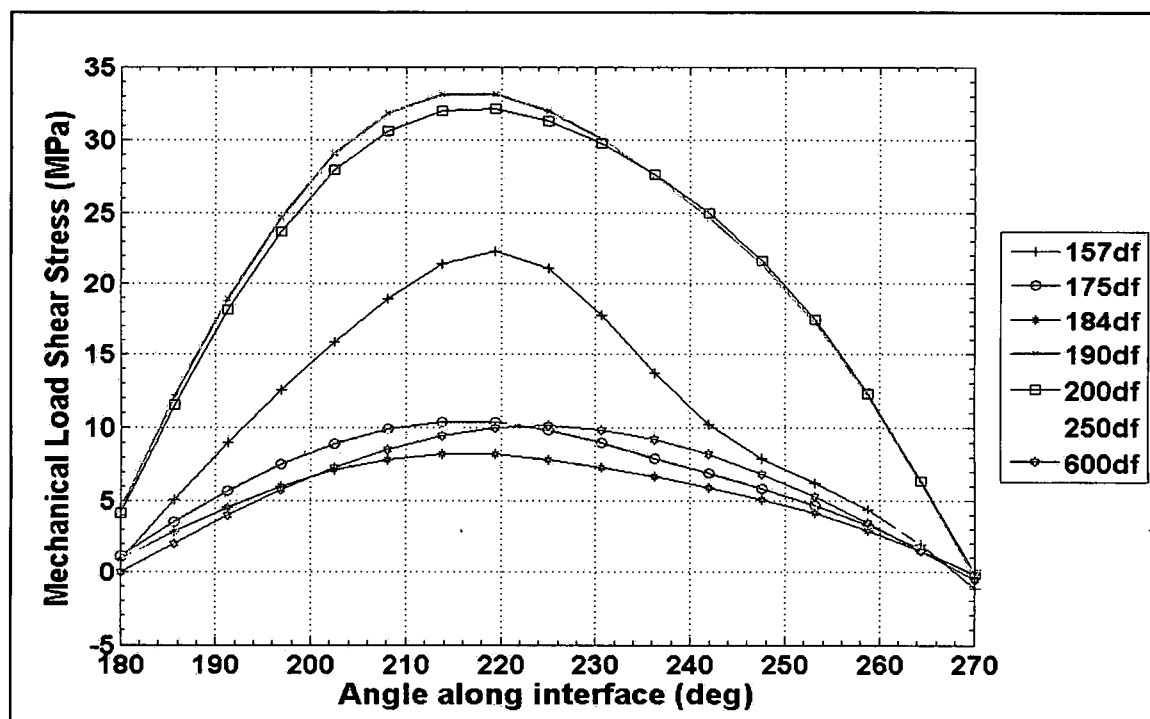


Figure 215: Shear stress distributions at the fiber-matrix interface due to the mechanical loading from $\theta = 180^\circ$ to 270°

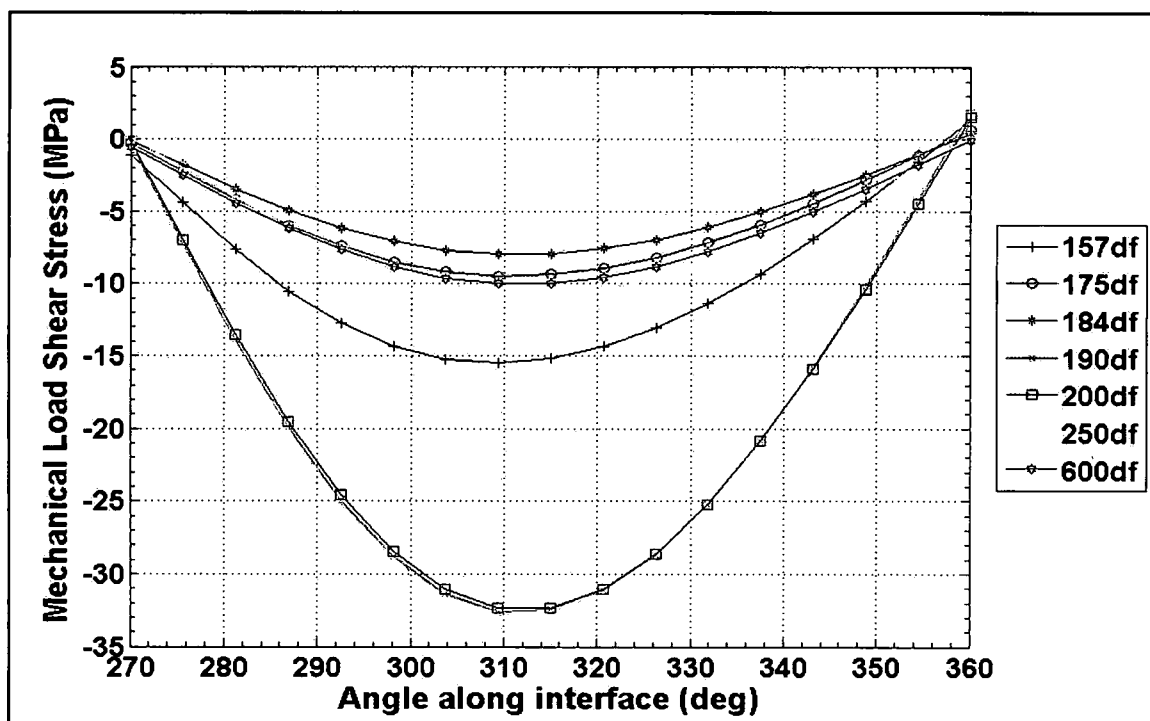


Figure 216: Shear stress distributions at the fiber-matrix interface due to the mechanical loading from $\theta = 270^\circ$ to 360°

The matrix cure shrinkage effects on the shear stress distribution are negligible in the first, second and fourth quadrants for the corner fiber as evidence by the relatively low magnitudes of the interfacial shear stresses, shown in Figure 209, 210 and 212, compared to the magnitudes of the shear stress due to the mechanical loading shown in Figure 213, 214 and 216. In addition, practically no changes exists between the interfacial shear stress due to the combination of mechanical load and matrix cure stresses and the mechanical loading only as seen by comparing Figures 205, 206 and 208 to Figure 213, 214 and 216. However, like the center fiber, the matrix cure shrinkage shear stress results for the third quadrant of the corner fiber, shown in Figure 211, impact the shear stresses from the mechanical loading, see Figure 215, by shifting the location of maximum magnitude and changing the symmetry of the distribution to that shown in Figure 207. As mentioned above the $6.0d_f$ fiber spacing matrix cure shrinkage shear stresses are virtually nonexistent having maximum magnitude of only 0.46 MPa. Table 73 lists the maximum shear stress variation for the matrix shrinkage load in all four quadrants and its percent reduction of the maximum shear stress due to the mechanical loading. The maximum variations of the shear stress due to the matrix shrinkage are fairly small in all four quadrants and tend to decrease with increasing fiber spacing. Obviously, the largest variations occur in the third quadrant where the fibers are closest together. The most dramatically impacted from the matrix cure shrinkage shear stresses are the $1.57d_f$, $1.75d_f$ and the $1.84d_f$ fiber spacing groups in the second and third quadrants. For the $1.90d_f$, $2.0d_f$, $2.5d_f$ and the $6.0d_f$ fiber spacing groups the impacts from the matrix cure shrinkage over the mechanical load are rather insignificant in all four quadrants.

Table 73: Maximum shear stress variation due to matrix shrinkage and percent reduction of the maximum mechanical load shear stress for all four quadrants of the corner fiber

Spacing	1 st Quad Max Shear Var (MPa)	Impact to Max shear %	2 nd Quad Max Shear Var (MPa)	Impact to Max shear %	3 rd Quad Max Shear Var (MPa)	Impact to Max shear %	4 th Quad Max Shear Var (MPa)	Impact to Max shear %
1.57d _f	2.17	3.3	2.75	9.5	6.50	9.5	1.90	2.5
1.75d _f	1.68	6.3	2.49	12.4	3.83	11.9	1.66	1.2
1.84d _f	1.37	5.9	2.17	11.8	3.07	10.1	1.43	1.3
1.90d _f	1.46	1.9	2.20	3.1	2.81	3.8	1.44	1.1
2.0d _f	1.31	1.8	2.01	2.8	2.41	3.4	1.23	1.1
2.5d _f	0.82	3.6	1.21	5.0	1.32	4.5	0.79	2.7
6.0d _f	0.46	2.7	0.48	4.1	0.38	4.2	0.45	2.6
SF	0.21	0.7	-	-	-	-	-	-

Summarizing the interfacial shear stress results for the corner fiber due to the combination of mechanical load and matrix cure shrinkage; the interfacial shear stress distribution for all fiber spacing groups is smooth and symmetrical having their maximum magnitudes at the midpoint in each quadrant for the first, second and fourth quadrants. Even though they exhibit the typical symmetrical shear stress plot by virtue of their shear stress magnitudes are the fiber spacing groups showing effects due to the fiber spacing, except for the 1.9d_f and 2.0d_f fiber spacing groups which will be reasoned below. It should also be mentioned that the analysis is based on the far-field stress at first damage. Comparing the 1.57d_f, 2.5d_f and 6.0d_f fiber spacing groups whose far-field stress at first damage is 8.29 MPa, 6.58 MPa and 10.7 MPa respectively; the results show an increase in shear stress magnitude as fiber spacing decreases. The shrinkage shear stresses have minimal impact on the mechanical shear stresses in quadrants 1, 2 and 4; however, they tend to increase in relative magnitude as fiber spacing decreases. The shrinkage shear stresses have the highest impact on the mechanical load shear stresses in the 3rd quadrant. Here local maxims exist for all fiber spacing groups except the 6.0d_f spacing where its shrinkage shear stress distribution is rather uniform. At the local maxims the shear stresses increase with decreasing fiber spacing clearly showing effects from neighboring fibers. The shear stress distribution due to the mechanical load only for all fiber spacing groups is practically the same as for the combined effects in quadrants 1, 2 and 4. For the third quadrant the nearest neighbor effects are clearly present by the wave in the interfacial shear stress distribution for all

fiber spacing groups except the $6.0d_f$ group and with the $2.5d_f$ group showing very minor effects from neighboring fibers. The SF is shown in the first quadrant of the corner fiber for the reason explained above. Its interfacial shear stress distribution is practically the same for the combined loading and due to mechanical loading only. It has a practically uniform shrinkage shear stress distribution.

Corner Fiber Interface Results – Summary

In summary, for the corner fiber the $6.0d_f$ fiber spacing group behaves as isolated fibers showing no interaction to the center fiber from the applied mechanical load and the matrix cure shrinkage effects in the same manner as at the center fiber. For the $2.5d_f$ fiber spacing the interfacial radial and shear stress distribution of the corner and center fiber show very similar trends as nearest neighbor effects begin to manifest themselves at this spacing. The neighboring fiber effects are predominately shown in the matrix cure shrinkage results, however, the mechanical loading results show virtually no interactions (see Figure 201 to 204 and 213 to 216) as the magnitudes are very small. Thus the combined effects show practically no interaction for the $2.5d_f$ fiber spacing at the corner fiber. This is not the case for the rest of the fiber spacing tested. As expected the interaction of the nearest neighbor fiber has the greatest effect in the third quadrant. The $1.57d_f$, $1.75d_f$, $1.84d_f$, $1.9d_f$ and the $2.0d_f$ fiber spacing groups show nearest neighbor effects by the wave in their interfacial radial stress distribution and by the unsymmetrical shape and shift in the maximum magnitude location for their interfacial shear stress distribution. The effects from the center fiber are most prominent in the $1.57d_f$ fiber spacing by the pronounced wave and almost constant magnitude in the radial stress distribution between $\theta = 210^\circ$ to 270° ; as well as the shift in maximum shear stress location along with the concave distribution between approximately $\theta = 230^\circ$ to 260° . In the first, second and fourth quadrant very little effects by the center fiber are present in the interfacial stress distributions. The single fiber results, shown in the first quadrant of the corner fiber results for reasons previously explained, show a constant compressive radial stress and a near constant shear stress distribution due to the matrix cure shrinkage loading. It exhibits typical radial and shear stress distribution and

maximum magnitude locations, i.e. at $\theta = 90^\circ$ for the radial stress and $\theta = 45^\circ$ for the shear stress.

828/D-230 Fiber-Matrix Interface Debond Criterion Evaluation

The location of the fiber-matrix debond occurs at the corner fiber poles in cases where the fiber-matrix debond is the first failure, except for the $1.57d_f$ fiber spacing group. Inspection of Table 14 shows that 5 of the 12 specimens having the $1.57d_f$ fiber spacing initiate their debond other than at the fiber pole. For the $6.0d_f$ and the $2.0d_f$ fiber spacing groups the majority of the debond initiation occurred interior to the fiber group, i.e. the debond initiated either at the south pole of the top corner fiber, the north pole of the bottom corner fiber or on the center fiber, see Tables 4 and 8 respectively. Conversely for the $2.5d_f$ and $1.9d_f$ fiber spacing groups the majority of the debond initiation occurred exterior to the fiber group, see Tables 6 and 10 respectively. Only for the $1.57d_f$ fiber spacing did an equal number of specimens initiate internal or external to the fiber group, Table 14. By incorporating the first debond observed in the specimens that exhibited both failure mechanisms, it appears that for specimens having a fiber spacing greater than $1.8d_f$ the fiber-matrix debond is independent of location relative to the fiber group. However, for specimens having a fiber spacing less than $1.8d_f$ the preference for the fiber-matrix debond is interior to the fiber group. Therefore, the CRB090 and CRB270360 regions of the finite element analysis (FEA) are utilized to efficiently address the state of stress within the cruciform specimens corresponding to the observed location of the interface debonds to investigate a fiber-matrix debond criterion.

The radial stress distribution along the fiber interface is symmetrical about the fiber pole, $\theta = 90^\circ$ for the CRB090 and $\theta = 270^\circ$ for CRB270360, as shown in Figure 193 and 196. Similarly, the shear stress for the CRB090 and the CRB270360 FEM regions are virtually equal in magnitude along the fiber interface for all fiber spacing groups comparing Figures 205 and 208, although of opposite sign. Consequently only the radial and shear stress distribution due to the

combination of mechanical load and matrix cure shrinkage of the CRB090 region of the FEM will be presented for discussion.

The radial stress distribution along the fiber-matrix interface in the viewable area of the corner fiber from $\theta = 0^\circ$ to 90° due the combination of mechanical load and matrix cure shrinkage at $Z = 0$ is shown in Figure 217. The maximum radial stress is located at the fiber poles for all fiber spacing groups. The largest radial stresses belong to the $1.90d_f$ and $2.0d_f$ fiber spacing groups followed by the $1.57d_f$, $2.5d_f$ and the $6.0d_f$ groups in decreasing order of magnitude, as shown in Figure 217. All these fiber spacing groups have exhibited fiber-matrix debonding as their first failure mechanism. The lowest radial stresses are those from the specimens that exhibited matrix cavitation, namely the $1.75d_f$ and $1.84d_f$ fiber spacing groups. From Figure 217 the maximum magnitudes are also fairly constant for all fiber spacing groups over a 20° sweep of the interface centered at the poles.

The shear stress distribution along the fiber-matrix interface in the viewable area of the corner fiber from $\theta = 0^\circ$ to 90° due to the combination of mechanical load and matrix cure shrinkage at $Z = 0$ is shown in Figure 218. The maximum magnitudes for the shear stress distribution occur at the midpoint of the fiber interface for the CRB090 and CRB270360 FEM regions, namely at $\theta = 45^\circ$ and 315° . Similar to the radial stress, the $1.9d_f$ and $2.0d_f$ fiber spacing groups have the largest magnitude of all fiber spacing groups followed by the $1.57d_f$, $2.5d_f$ and the $6.0d_f$ specimens in decreasing order of magnitude, as shown in Figure 218. All of these specimens exhibited fiber matrix debonding as their first failure mechanism. The two lowest maximum magnitudes occur for the fiber spacing groups exhibiting matrix cavitation as their first failure, specifically the $1.75d_f$ and $1.84d_f$ fiber spacing groups as shown in Figure 218. The interfacial shear stress distribution, Figure 218, also reveals that the length of fiber interface over which a relatively high shear stress acts is independent of fiber spacing. Although all are centered on the midpoint of the CRB090 region, the length of interface for which a relatively high shear stress acts on the $1.90d_f$ and $2.0d_f$ fiber spacing groups is about 10° . Whereas, for the $1.57d_f$ fiber spacing the interfacial length increases to approximately 20° and for the $2.5d_f$ and $6.0d_f$ the interfacial length increases further to almost 30° . For the $1.75d_f$ and $1.84d_f$ fiber spacing groups

the circumferential length over which a relatively high magnitude of shear stress acts is between 27° to 30°, similar to the 2.5d_f and 6.0d_f spacing groups.

It should be noted that the debonds extend over into the 2nd and 3rd quadrant of the corner fiber but are not visible. The analysis indicates that the magnitude of the interfacial radial and shear stresses in the 2nd quadrant are virtually equal to those in the 1st quadrant indicating a nearly symmetrical debond. However, in the 3rd quadrant the nearest neighboring fiber effects are more pronounced as the fiber spacing decreases. These effects tend to shift the shear stress distribution away from the fiber pole and reduce the circumferential length that the highest radial stresses act. This could create an unsymmetrical debond or a smaller debond at the south pole.

For the 6.0d_f fiber spacing group, all fiber matrix debonds in all five specimens initiate as a spot at the fiber pole and slowly, over a several seconds, propagate along the fiber pole while sweeping around the fiber circumference, as explained in Chapter 2. Furthermore all specimens fiber matrix debonds initiate on fibers within the field of view. The observed fiber-matrix debonds average an instantaneous debond width of approximately 0.0157 mm making a central angle of 48° creating an arc length of 0.15 mm. Thus the debond covers 13% of the fiber circumference. Over this same fiber interface arc length, the 6.0d_f fiber spacing experiences an average radial stress of approximately 14.6 MPa, or 89% of its maximum radial stress magnitude, as shown in Figure 217. Correspondingly, the average shear stress over this same arc length of fiber interface is approximately 5.03 MPa or 52% of its maximum shear stress magnitude as shown in Figure 218. The observed fiber matrix debond occurs at the fiber pole and instantaneously covers the length of fiber interface having the highest magnitude of radial stress, from $\theta = 66^\circ$ to 90° shown in Figure 217. Additionally, from Figure 217, the minimum radial stress at the debond limit of the interface at $\theta = 66^\circ$ is 77% of the maximum radial stress. Furthermore, a rather significant amount of shear stress is present over this same interfacial length contributing to the fiber matrix debond as the shear stress at the debond limit is 82% of the maximum. Figure 218 shows that the shear stresses over the interfacial debond length are 52% of the maximum shear stress.

All of the cruciform specimens having the 2.5d_f fiber spacing group debonded at the fiber poles. In four of the five specimens the debond occurred on a fiber in the field of view. In the fifth

specimen the fiber debonded on a back corner fiber obstructed from view. All of the observed fiber-matrix debonds initiated as either a spot or over a very small length and propagated slowly over a few seconds along the fiber pole. The four observed fiber matrix debonds averaged a debond width of approximately 0.015mm which make a central angle of 47° creating an arc length of 0.15 mm. This in turn caused about 12% of the fiber circumference to debond. Over this circumferential arc length from $\theta = 66.5^\circ$ to 90° , the $2.5d_f$ fiber spacing group experiences an average radial stress of 15.6 MPa, or just over 90% of its maximum magnitude. From Figure 217 the radial stresses at the fiber matrix debond limit are 78% of the maximum magnitude. The shear stress at the debond limits are approximately 8.0 MPa, as shown in Figure 218 where the average shear stress over the interfacial debond length is 4.8 MPa which amounts to 47% of the maximum shear stress. Consequently, over the observed fiber matrix debond limits, from $\theta = 66.5^\circ$ to 90° , the radial stress ranges from its maximum magnitude to approximately 78% of its maximum and the shear stress reaches 47% of its maximum magnitude. Therefore, the debond occurs over an interfacial length having the largest magnitudes of radial stress and a considerable amount of shear stress contributing to the fiber matrix debond failure initiation.

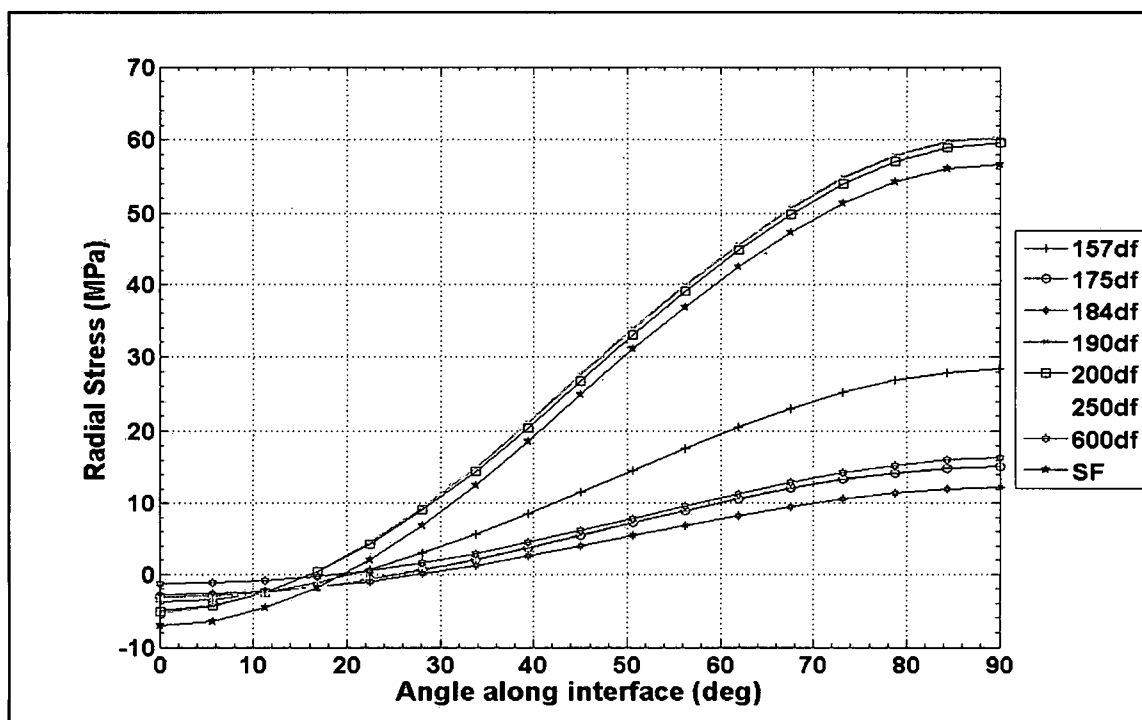


Figure 217: Radial stress distributions along the corner fiber-matrix interface from $\theta = 0^\circ$ to 90° at $Z = 0$ due to the combination of mechanical loading and matrix chemical shrinkage

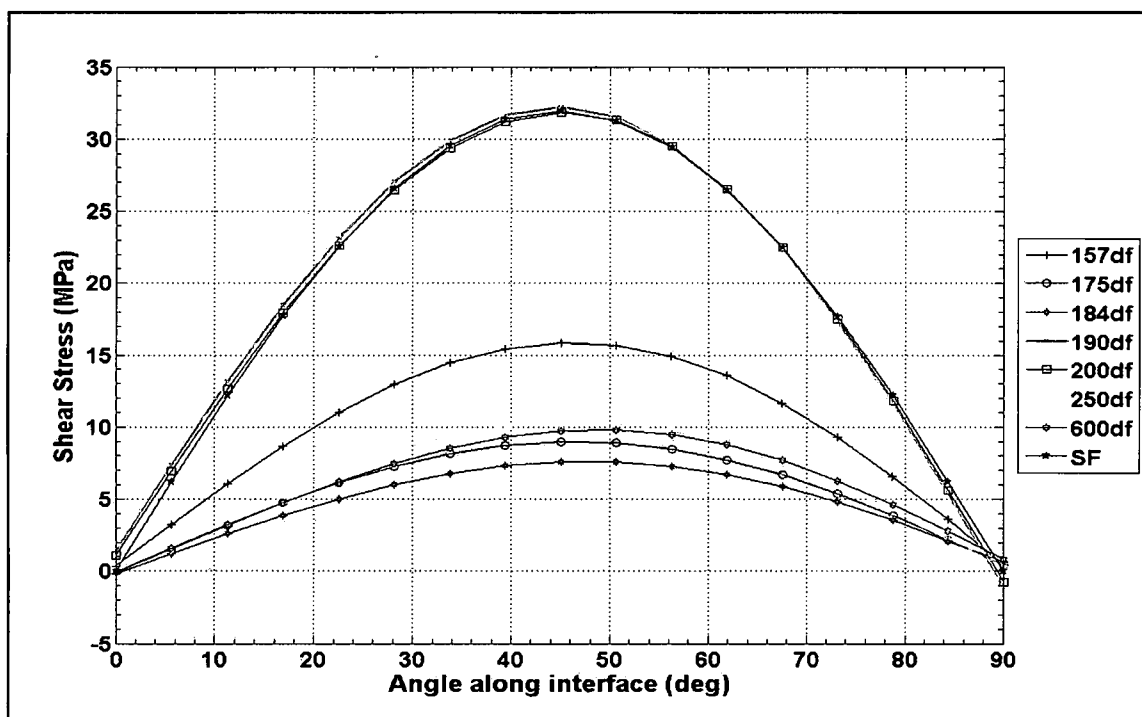


Figure 218: Shear stress distributions along the corner fiber-matrix interface from $\theta = 0^\circ$ to 90° at $Z = 0$ due to the combination of mechanical loading and matrix chemical shrinkage

The 1.9d_f and 2.0d_f fiber spacing groups have practically the same magnitudes of radial and shear stress according to Figures 217 and 218. Furthermore, all specimens at these two fiber spacings exhibit fiber matrix debonding as their first failure and it occurs at the fiber poles. Of the 19 total specimens between the two fiber spacing groups, 9 specimens at the 2.0d_f spacing and 10 specimens at the 1.9d_f spacing, a total of 5 specimen's debond failure initiation was obstructed from view, one at the 2.0d_f spacing and four at the 1.9d_f spacing. The similarities between the two fiber spacing groups seem to end at this point in that fairly large differences between the observed debond widths occur. For the 1.9d_f fiber spacing group the average observed debond width is 0.083 mm. This makes a central angle of 116° creating a debond arc length of 0.36 mm debonding approximately 31% of the fiber circumference. From the analytical results, Figure 217 indicates that the 1.9d_f fiber spacing has an average radial stress over the interfacial debonded length of about 39.3 MPa or about 66% of its maximum magnitude. That is, the debond length covers the area having the largest magnitude of the radial stress distribution starting at $\theta = 32^\circ$ to the maximum magnitude at $\theta = 90^\circ$. At the debond limit, $\theta = 32^\circ$, the magnitude of the radial stress is approximately 13.2 MPa. For the shear stress, Figure 218 shows that the 1.9d_f spacing debond covers over half of the shear stress distribution encompassing the maximum magnitude, from $\theta = 32^\circ$ to 90° . At the limit of the interfacial debond the shear stress is about 29.0 MPa. Where the average shear stresses experienced over this interfacial debond length is approximately 22.3 MPa or about 69% of the maximum shear stress. It appears that for fiber matrix debonds occurring at the 1.90d_f fiber spacing they encompass a very large range of interface where the radial stress the shear stress reaches their maximum magnitude. Consequently, the 1.90d_f specimens experience a radial and shear stress interaction contributing to the fiber matrix debond.

The 2.0d_f fiber spacing group has a much smaller observed average debond width of 0.065 mm, which in turn makes a central angle of 101°. This creates a debond arc length of 0.31 mm covering approximately 26% of the fiber circumference. Figure 217 shows that at the fiber matrix debond limits, at $\theta = 39.5^\circ$, the radial stresses are approximately 20.4 MPa and that over the debond length the average radial stress is 74% of the maximum magnitude or 44.3 MPa. For

the shear stress, Figure 218 indicates that the average shear stress over the interface debond is about 20.9 MPa which equates to approximately 65% of the maximum shear stress. In addition, Figure 218 also reveals that the limit of the debond occurring at $\theta = 39.5^\circ$ is very close to the maximum shear stress magnitude and is equal to approximately 31.2 MPa or about 98% of the maximum shear stress. From the experimental and analytical results it appears that the $2.0d_f$ fiber spacing cruciform specimens fiber matrix debonds occur over the fiber interface where the maximum radial stress is located and encompass a large range of relatively high radial stresses. Furthermore, the location of the fiber matrix debond limit is close to the maximum shear stress magnitude and that the interfacial debond encompass a significant amount of shear stress. Consistent with the $1.90d_f$ fiber spacing group, the $2.0d_f$ fiber spacing group experiences an interaction between the radial and shear stress contributing to its fiber matrix debond.

Of the twelve cruciform specimens having the $1.57d_f$ fiber spacing nine exhibited fiber matrix debonding at the corner fiber and eight were in the field of view. The other three specimen had their debond initiate on the center fiber. For the eight specimens that debonded at the corner fiber in the field of view, five initiated at the fiber pole, whereas three exhibited their debond on the bottom corner fiber at 43° , 38° and 347° . The average debonds width for the five specimens that debonded in the field of view is 0.053 mm. This translates into a central angle of 91° creating a debond arc length of 0.28 mm which comprises 24% of the circumference of the fiber. From Figure 217 the radial stress at the debond limits of $\theta = 44.5^\circ$ is about 11.5 MPa and that the average radial stress over the debond length is approximately 21.7 MPa which is 77% of the maximum magnitude for the $1.57d_f$ fiber spacing. The debond limit, $\theta = 44.5^\circ$, for the shear stress shown in Figure 218 is very close to the location of maximum shear stress magnitude at $\theta = 45^\circ$, consequently the shear stress at the debond limit is 15.84 MPa. The average shear stress over the debond length is approximately 10.2 MPa which is 64% of the maximum shear stress. For the specimen that initiated its debond on the bottom corner fiber at $\theta = 43^\circ$ the radial stress is approximately 10.3 MPa or about 36% of the maximum, as shown in Figure 217. The shear stress at this location on the fiber interface shown in Figure 218 is approximately 15.6 MPa and is very close to the maximum shear stress magnitude since it is over 98% of the maximum. Similarly

for the specimen that exhibited a debond initiation failure on the bottom corner fiber at $\theta = 38^\circ$, Figure 217 shows that the radial stress at this location is approximately 8.0 MPa which is just over 28% of the maximum radial stress. Whereas, Figure 218 indicates that the shear stress at $\theta = 38^\circ$ is approximately 15.3 MPa, or just under 97% of the maximum reflecting that its location is very close to the maximum shear stress. Lastly, for the $1.57d_f$ cruciform specimen that debonded on the bottom corner at $\theta = 347^\circ$, this location on the fiber interface translates to an angle of $\theta = 13^\circ$ due to the symmetry of the cruciform specimen. Figure 217 reveals that at this location the radial stress is compressive and at a magnitude of approximately 2.2 MPa. Whereas, the shear stress shown in Figure 218 has a magnitude of 6.8 MPa at $\theta = 13^\circ$, which is approximately 43% of the maximum shear stress magnitude. Except for this last specimen that debonded on the bottom corner fiber at $\theta = 347^\circ$, all of the specimens having the observed debond failure initiation have a very high shear stress influence as evidence by the length and limits of the interface debond. Furthermore, for the specimens that debonded at the corner fiber poles, the location of the debond length around the fiber interface encompasses the highest radial stress subjected to the corner fiber.

Twenty-one single fiber cruciform specimens were tested and in all cases the failure initiation is by fiber-matrix debond at the fiber poles. The average debond width for the single fiber 0.07 mm creating a central angle of 106° debonding an arc length of 0.33 mm which comprised 28% of the fiber circumference. The debond limits are between 37° to 143° for the north pole and between 217° to 323° for the south pole. From Figure 217 the radial stress at the debond limit of 37° is 16.0 MPa. The average radial stress over the debond limit is 39.59 MPa which is about 70% of the maximum magnitude. From Figure 218 the shear stress at the debond limit of 37° is 30.59 MPa and the average shear stress over the debond limit is 21.78 MPa being 68% of the maximum magnitude. Consequently, the single fiber experiences both high radial and shear stresses over its interface within the debond limits as indicated that the average radial and shear stresses are 70% and 68% respectively of their corresponding maximum magnitudes. Furthermore, the debond limits encompass both the maximum magnitude radial and shear stress magnitudes.

In summary, each fiber spacing group experienced interfacial debonds over that part of the fiber exhibiting high magnitudes of radial stress. Furthermore, the debond length covers portions of the fiber interface where the shear stress either reaches its maximum or its average magnitude is a significant percentage of the maximum magnitude. Table 4 lists the average debond measurements for the fiber spacing groups exhibiting fiber matrix debonding as their failure initiation. The fact that the shear stress is critical and the interaction between the shear and normal or radial stress cannot be neglected is supported by the data in Table 74, which warrants a closer look. As described in Chapter 2 the experimental debond widths were measured by extracting photomicrographs from the videotaped experiments. The debond width, location relative to fiber pole and also along fiber length, as well as debond type were tabulated for each specimen. The central angle and arc length were calculated and tabulated for each specimen as well as the corresponding FEM location in their respective fiber spacing groups. The average experimental debond width for each fiber spacing group where the debonds initiated at either fiber pole is determined and the corresponding average debond central angle and average arc length are then calculated for that fiber spacing group. The experimental debond limits, listed in Table 74, are then determined from the average debond central angle for both the north and south poles for each fiber spacing group.

The $1.57d_f$, $1.90d_f$ and the $2.0d_f$ debond limits cover 24%, 31% and 26% of the total circumference of the fiber which encompasses the location of highest radial and shear stresses. The $2.5d_f$ and $6.0d_f$ fiber spacing groups, on the other hand, debond only 12% and 13% of the fiber circumference respectively, that includes the location of maximum radial stress and a significant percentage of shear stress. These results lead to the conclusion that an interaction between the radial stress and shear stress be investigated as the interfacial debond criterion.

Table 74: Experimental fiber matrix debond measurements

Spec.	Average Debond Width, mm (Std dev)	Average Debond Central angle	Experimental Debond Limits	Arc Length, mm	% circumference
1.57d _f	0.053 (0.019)	91°	44.5° to 135.5° NP 224.5° to 315.5° SP	0.28	24
1.9d _f	0.083 (0.045)	116°	32° to 148° NP 212° to 328° SP	0.36	31
2.0d _f	0.075 (0.036)	110°	35° to 145° NP 215° to 325° SP	0.34	29
2.5d _f	0.015 (0.004)	47°	66.5° to 113.5° NP 246.5° to 293.5° SP	0.15	12
6.0d _f	0.0157 (0.0083)	48°	66° to 114° NP 246° to 294° SP	0.15	13
SF	0.07 (0.033)	106°	37° to 143° NP 217° to 323° SP	0.33	28

862/W System Fiber-Interface Analytical Results**Center Fiber Interface Results – Radial Stress**

The interfacial radial stress results for the six multi-fiber cruciform specimen groups tested due to the combination of mechanical loading and matrix residual stresses are shown in Figure 219. Similar to the center fiber results of the 828/D-230 matrix, the maximum stress occurs in the direction of applied load at $\theta = 90^\circ$ and all are tensile. However, for the 1.57d_f, 1.75d_f, and 2.0d_f fiber spacing groups the minimum magnitude of the radial stress occurs at $\theta = 45^\circ$. Figure 219 points out the dramatic stress reversal for the 1.57d_f spacing where the maximum compressive stress, occurring at $\theta = 45^\circ$, is almost equal to its maximum tensile stress, occurring at $\theta = 90^\circ$. Less dramatic but having similar radial stress distributions are the 1.75d_f, 1.90d_f and the 2.0d_f fiber spacing groups; where the 1.75d_f and 2.0d_f have their minimum radial stress magnitudes at $\theta = 45^\circ$ too. For the rest of the fiber spacing groups their minimum radial stress magnitude occurs at $\theta = 0^\circ$ and is compressive for the 6.0d_f and 2.5d_f fiber spacing groups.

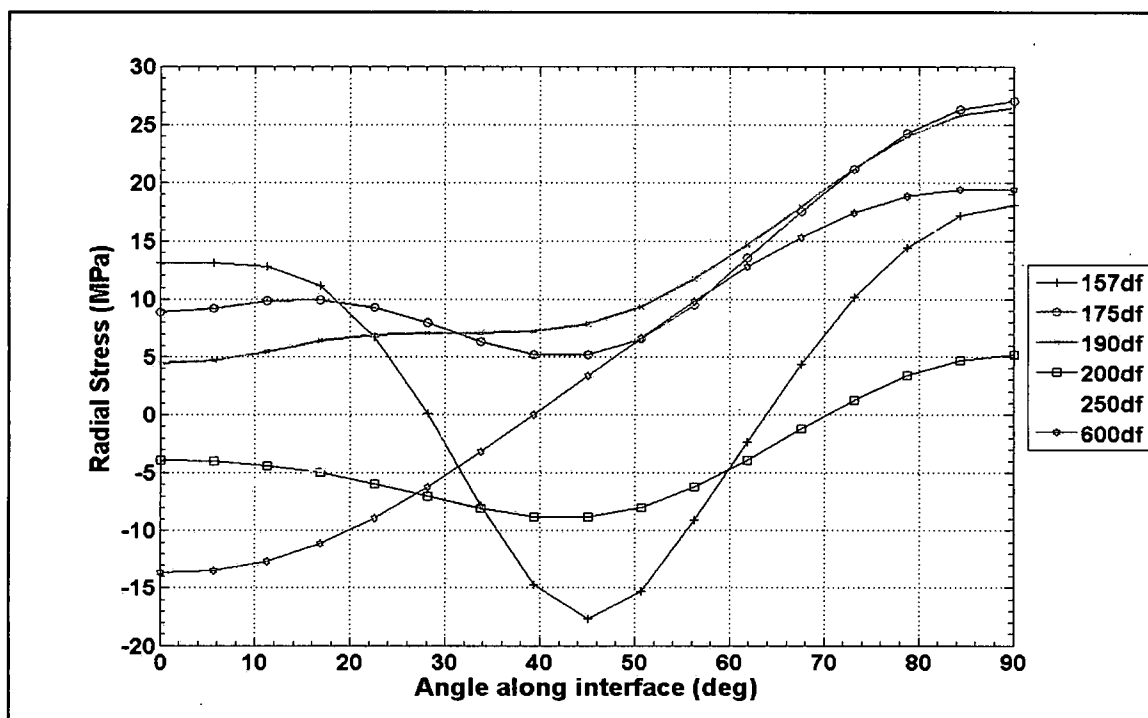


Figure 219: Radial stress distributions at the fiber-matrix interface due to the combination of mechanical loading and matrix residual stresses from cure cycle

Differences between the two resin systems, however, are the indicators of neighboring fiber effects. In the 862/W matrix system these effects are evident by the "dip" in the interfacial stress distribution, shown for the 1.57d_f, 1.75d_f, 1.9d_f and 2.0d_f fiber spacing groups occurring at $\theta = 45^\circ$. For the 828/D-230 matrix system a wave in the interfacial radial stress distribution, at approximately the same angular location as in the 862/W system, indicates the presence of neighboring fiber interactions. An explanation of this behavior is evident by the radial stress distribution due to the residual stress from the matrix cure cycle.

The 6.0d_f and 2.5d_f have the classical radial stress distribution exhibited for a circular inclusion or hole where the maximum magnitudes are in the direction of applied loading and the minimum magnitudes are normal to the applied loading. Consequently nearest neighboring effects are absent or very minimal, which is similar to the same fiber spacing groups in the 828/D-230 matrix system.

The radial stress distribution around the fiber-matrix interface due to the matrix cure is shown in Figure 220. The distribution is identical to that of the 828/D-230 matrix system shown in Figure 188 except that the 862/W system has much larger magnitudes due to the fact its cure temperature is 121°C versus room temperature for the 828/D-230 system. Figure 220 shows that the residual stresses from the matrix cure impart a compressive stress along the fiber-matrix interface for all fiber spacing groups.

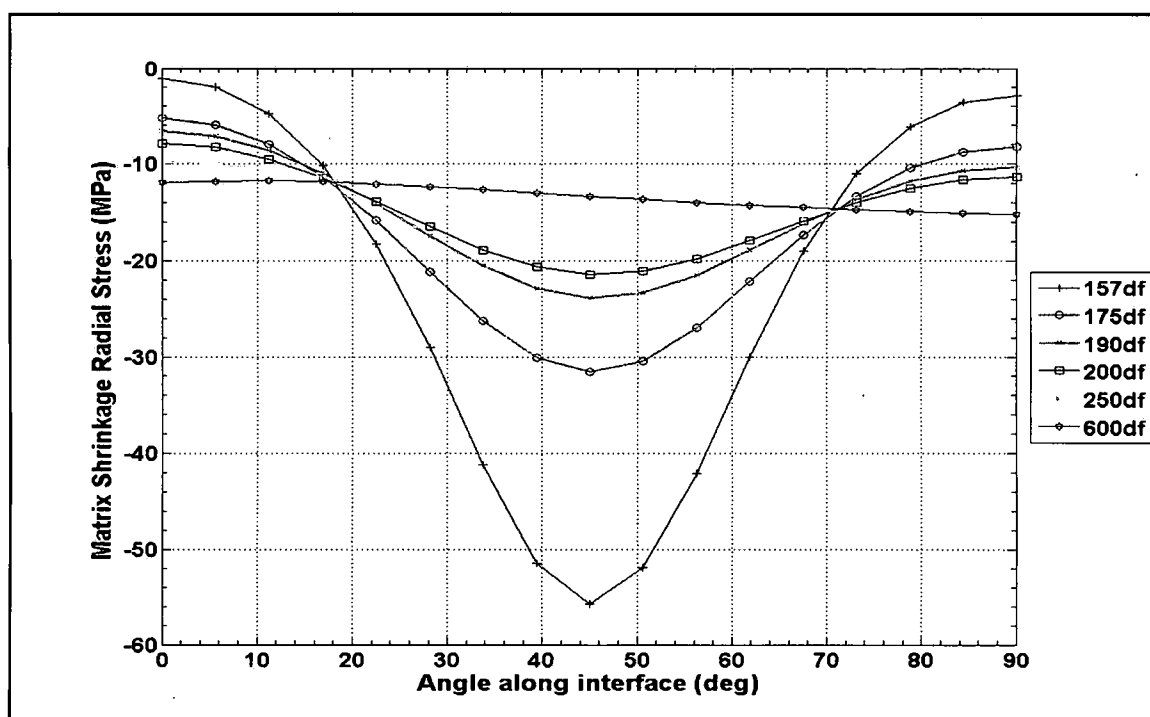


Figure 220: Radial stress distributions at the fiber-matrix interface due to the matrix residual stresses from cure cycle

Effects from nearest neighbors on the high temperature cured residual stresses of the matrix begin to manifest themselves at the 2.5d_f spacing as its radial stress is maximum at $\theta \sim 50^\circ$, however, the magnitudes vary little over this range. For the 6.0d_f fiber spacing the magnitude of the radial stress due to the residual stress from the matrix cure is practically uniform varying just over 1.5 MPa over this range. The maximum magnitude for the rest of the fiber spacing groups occur very close to the location along the center fiber interface where the distance to the

corner fiber is smallest, at $\theta = 45^\circ$. Figure 220 indicates that as the fiber spacing decreases the residual stresses increases.

The influence of the mechanical load on the six cruciform fiber spacing groups tested is shown in Figure 221. The maximum magnitude of the radial stress are all tensile and occur at $\theta = 90^\circ$, in the direction of applied load, for each fiber spacing group except for the $1.57d_f$ and $1.75d_f$ fiber spacing groups. For all fiber spacing groups the minimum magnitudes of the radial stresses are tensile except for the $6.0d_f$ fiber spacing, where it's slightly compressive. Nearest neighbor effects are prominent at the $1.57d_f$, $1.75d_f$ and $1.9d_f$ fiber spacing groups and to a lesser extend at the $2.0d_f$ spacing. These effects are evident by the wave occurring around $\theta = 45^\circ$ in the interfacial distribution, also observed in the 828/D-230 center fiber radial interfacial stress distribution. The maximum magnitude of the $1.57d_f$ fiber spacing occurs at $\theta = 45^\circ$ then its magnitude drops rapidly as θ increases to 90° and as θ decreases to 0° . The magnitudes of the radial stress due to the mechanical load are close at $\theta = 0^\circ$ and 90° only differing by approximately 7MPa.

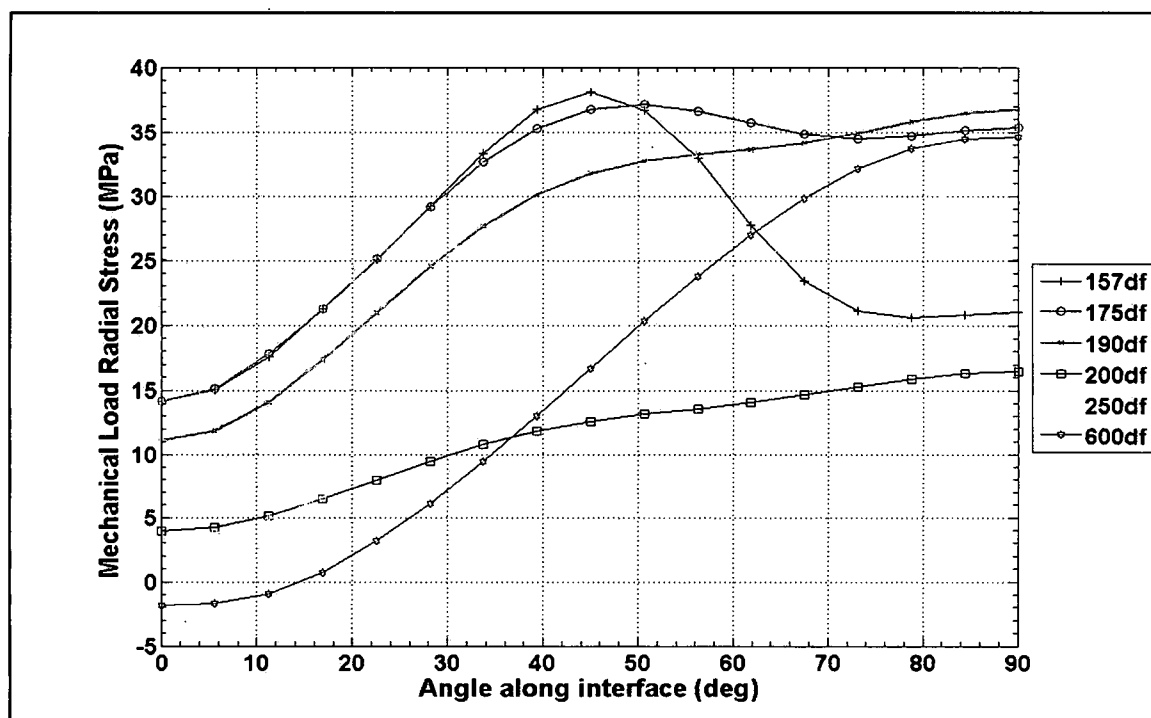


Figure 221: Radial stress distributions at the fiber-matrix interface due to the mechanical loading

For the 1.75d_f fiber spacing nearest neighbor effects manifest themselves causing its maximum magnitude to occur at $\theta = 50.625^\circ$. From this point the magnitude of the radial stress distribution is fairly uniform from $\theta = 50.625^\circ$ to 90° only varying approximately 2 MPa. Although the 1.90d_f fiber spacing has its maximum magnitude at $\theta = 90^\circ$, the behavior is similar to the 1.75d_f fiber spacing as the magnitude of the radial stress is almost uniform from $\theta \sim 50^\circ$ to 90° varying a little over 5 MPa showing effects of the corner fiber over this range. Correspondingly, neighboring fiber effects are evident for the 2.0d_f fiber spacing as the magnitude of the radial stress is rather uniform from $\theta = 45^\circ$ to 90° varying slightly over 4MPa over this range. For the 2.5d_f and 6.0d_f fiber spacing groups their interfacial radial stress distribution is smooth from $\theta = 0^\circ$ to 90° showing no effects from their nearest neighbor fibers, as shown if Figure 221.

Table 75 lists the maximum radial stress due from the residual stresses and the mechanical loading at two locations which give the impact that the residual stresses have on the mechanical load radial stress. The first location is where the radial stress from the matrix cure is a

maximum and the second location is at the maximum radial stress due to the mechanical load. From Table 75 it is apparent that the high temperature cure imparts very high radial stresses and in some cases it is greater than the mechanical load at both locations. For the 1.57d_f fiber spacing the radial stress due to the matrix cure is almost 1.5 times that due to the mechanical load and the maximum magnitudes for both loading conditions occur at the same location on the interface. Similarly, for the 2.0d_f fiber spacing the matrix cure radial stress is 194% of the radial stress due to the mechanical load at the location of maximum residual stresses.

Table 75: The percent reduction of the radial stress over the mechanical load due to the residual stress from the high temperature matrix cure

Fiber Spacing	Max Matrix Resdl Stress (MPa)	Mech @ Max Resdl (MPa)	Loc	%	Max Mech Stress (MPa)	Resdl Stress @ Max Mech (MPa)	Loc	%
1.57d _f	-55.74	38.09	45°	146	38.09	-55.74	45°	146
1.75d _f	-31.62	36.79	45°	86	37.13	-30.54	45°	82
1.90d _f	-23.93	31.77	45°	75	36.72	-10.32	90°	28
2.0d _f	-24.44	12.61	45°	194	16.45	-11.32	90°	69
2.5d _f	-16.09	20.76	45°	78	30.61	-13.90	90°	45
6.0d _f	-13.74	34.60	90°	44	34.60	-15.18	90°	44

For the 1.90d_f, 2.0d_f, 2.5d_f and 6.0d_f fiber spacing groups the high residual radial stress has a relatively high impact at the location of maximum radial stress due to the mechanical load. However, the impact for the 6.0d_f fiber spacing is constant across the interface, as shown in Figure 222 and indicated in Table 75. The high impacts of the matrix curing stresses, as shown in Table 75, combined with the nearest neighboring effects cause the radial stress to act over a smaller length of the fiber-matrix interface as evidence by comparing Figures 219 and 221 for all fiber spacing groups except the 6.0df. Most affected are the close fiber spacing groups especially, the 1.75d_f and 1.90d_f fiber spacing specimens. At these two fiber spacing groups the radial stress due to mechanical load acts over practically half the fiber circumference is cut down to less than 1/10 the circumference due to the residual stresses. The 2.5d_f fiber spacing is least affected and actually increases the length of influence the radial stress acts along the circumference. For the

1.57d_f fiber spacing, the location of influence of the radial stress on the interface changes location when effects are combined.

In summary the radial stress distributions and due to the mechanical load for the 862/W matrix system are similar to the 828/D-230 system for the corresponding fiber spacing groups; even though the 1.75d_f and the 2.0d_f fiber spacing groups exhibit different failure initiation mechanisms in the 862/W system. For the cases where the fiber spacing and first failure mechanism is the same, the 862/W matrix system has greater radial stress magnitudes than the 828/D-230 system except for the 1.90d_f spacing where the magnitudes are virtually equal. The radial stress distribution due to the matrix cure for both resin system have virtually the same distribution, however, the magnitudes for the 862/W system are approximately 5 times greater than those of the 828/D-230 system. It is quite apparent that the high temperature cure of the 862/W matrix system imparts a compressive stress around the circumference of the center fiber. The net result of this compressive prestress reduces the radial stress due to the mechanical loading is evident by comparing Figure 219 to Figure 221. Additionally, the residual stresses coupled with the neighboring fiber effects drastically change the radial stress distribution and reduce the length that the radial stress acts along the fiber-matrix interface for the 1.57d_f, 1.75d_f, 1.9d_f and 2.0d_f fiber spacing groups, also seen by comparison of Figures 219 with 221. The 6.0d_f and for the most part the 2.5d_f fiber spacing groups have no or virtually no nearest neighbor fiber effects, essentially acting as isolated fibers. These two fiber spacing groups behave in the same manner in the 828/D-230 matrix system.

Center Fiber Interface Results – Shear Stress

The analytical shear stress distribution at the fiber-matrix interface due to the combination of mechanical loading and residual stress for the six multi-fiber cruciform specimen fiber spacing groups tested is shown in Figure 222. Neighboring fiber effects clearly present themselves as the location of the maximum shear stress shifts from $\theta = 45^\circ$ to $\theta = 56.25^\circ$ for the 1.57d_f, 1.75d_f, 1.90d_f fiber spacing groups and to $\theta = 61.875^\circ$ for the 2.0d_f spacing creating an asymmetric stress distribution for each fiber spacing. A slight shift from $\theta = 45^\circ$ to 50.625° occurs for the 2.5d_f

fiber spacing as shown in Figure 222, indicating very modest effects from its corner fiber. However, for the $6.0d_f$ fiber spacing its distribution is symmetrical about its maximum magnitude location occurring at $\theta = 45^\circ$ signifying no nearest neighbor fiber effects. Additional nearest neighbor effects are shown in the $1.57d_f$, $1.75d_f$, $1.90d_f$ and $2.0d_f$ fiber spacing groups as the shear stresses exhibit a concave stress distribution between $\theta = 0^\circ$ to 50.625° , with the $1.57d_f$ spacing exhibiting the most drastic impact to its corner fiber. Lastly, the minimum magnitude of the shear stress for all fiber spacing groups is zero or practically zero at $\theta = 0^\circ$ and 90° .

It is worth noting that the effects of the corner fibers manifest themselves in the same manner by shifting the maximum magnitude location and affecting the rate of slope of the interfacial distribution in both matrix system. however, the shift in the maximum location is toward the interfacial location in line with the applied loading in the 862/W system and away from it in the 828/D-230 system.

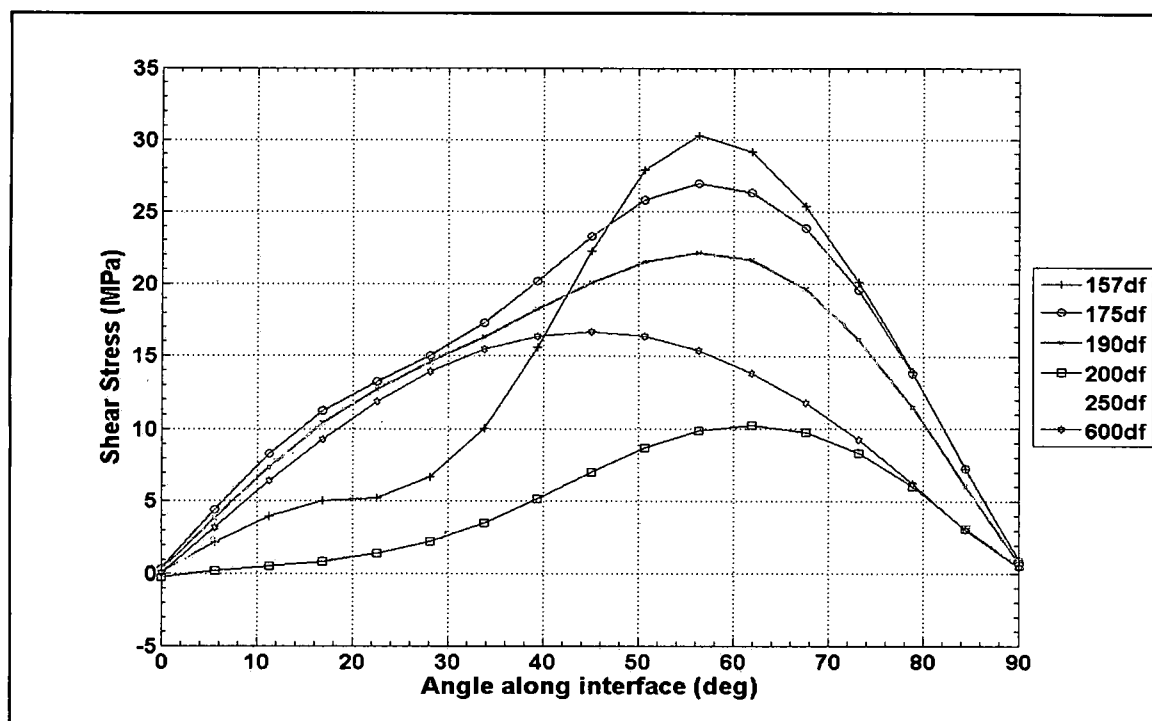


Figure 222: Shear stress distributions at the fiber-matrix interface due to the combination of mechanical loading and matrix residual stresses from cure cycle

The major contributor to this behavior is seen by examining the residual stress around the fiber-matrix interface due to the matrix cure cycle. Figure 223 shows the interfacial residual shear stresses for the six cruciform specimen fiber spacing groups tested due to the high temperature matrix cure. The 862/W matrix system has the exact same shear stress distribution for the residual stresses as the 828/D-230 matrix system for the matrix cure shrinkage shear stresses. Like the 828/D-230 system, the $6.0d_f$ fiber spacing in the 862/W system has negligible residual shear stress since its maximum magnitude at $\theta = 45^\circ$ is barely 2.0 MPa. For the $1.57d_f$, $1.75d_f$, $1.9d_f$ and the $2.0d_f$ fiber spacing groups an inflection point between $\theta = 48^\circ$ to 52° exists as the shear stress changes direction across the fiber-matrix interface, as shown in Figure 222. Although nearest neighbor effects appear at the $2.5d_f$ fiber spacing as evident of its shear stress distribution along its interface, as shown in Figure 222, its interfacial shear stress can be considered negligible since its maximum magnitude is just less than 4.0 MPa. For the rest of the fiber spacing groups, however, nearest neighbor effects manifest themselves quite clearly as two maxims occur at $\theta = 28.125^\circ$ and between $\theta = 61.875^\circ$ to 67.5° . Just like the 828/D-230 system, the 862/W system nearest neighbor effects of the matrix residual shear stresses tend to increase as the fiber spacing decrease affecting the shear stress distribution differently depending on the position along the fiber-matrix interface, as shown in Figure 223.

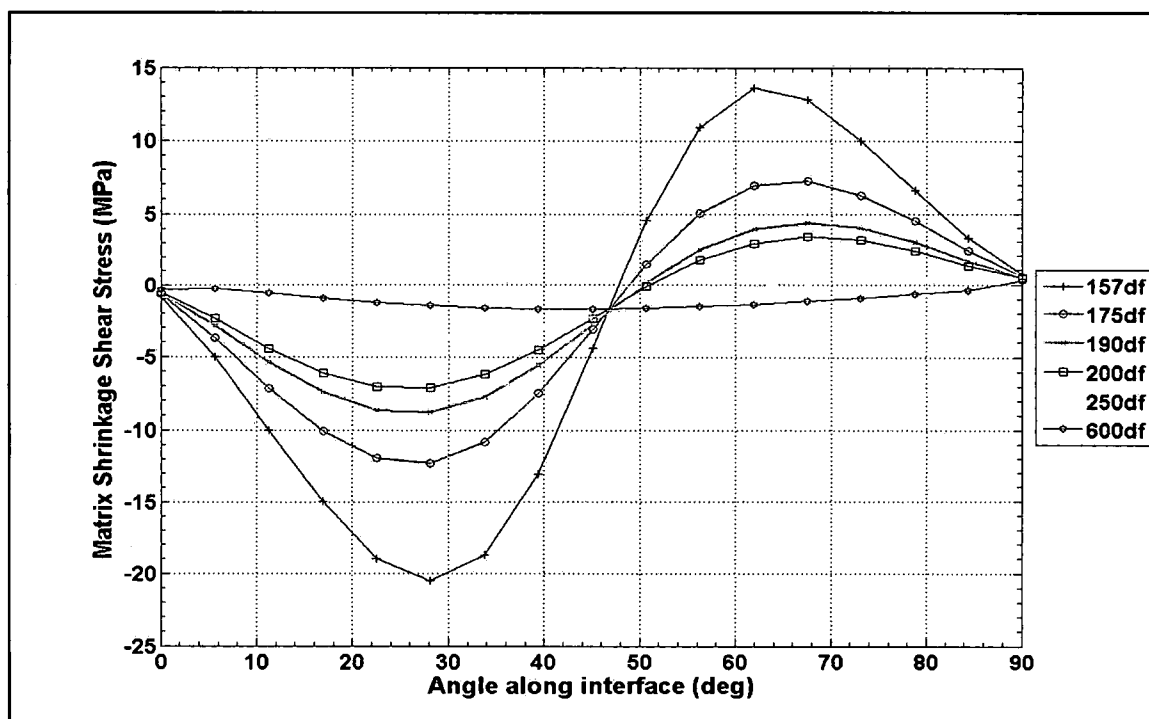


Figure 223: Shear stress distributions at the fiber-matrix interface due to the matrix residual stresses from cure cycle

Figure 224 shows the analytical results of the interfacial shear stress due to the mechanical loading for all multi-fiber cruciform spacing groups tested. Similar to the 828/D-230 shear stress distribution; all but the 6.0d_f fiber spacing in the 862/W matrix system indicate effects from the corner fiber by the shift in the location of their maximum magnitude shear stresses. The maximum magnitude locations occur at $\theta = 33.75^\circ$ for the 1.57d_f, 1.75d_f, 1.90d_f and 2.0d_f fiber spacing groups whereas the maximum magnitude for the 2.5d_f occurs at $\theta = 39.375^\circ$. The nearest neighbor effects tend to increase the shear stress as fiber spacing decreases for the close fiber spacing groups, namely the 1.57d_f, 1.75d_f and 1.90d_f, when comparing fiber spacing groups having the same first failure mode. In addition, effects are also exhibited by the asymmetrical shape of the distribution. The 1.57d_f fiber spacing exhibits the most drastic effect of the corner fiber as is shear stress distribution from its maximum magnitude location to $\theta = 90^\circ$ is concave at $\theta = 61.875^\circ$. Whereas, for the 1.75d_f, 1.90d_f and 2.0d_f fiber spacing groups their interfacial shear stress distribution from their respective maximum magnitude locations to $\theta = 90^\circ$

exhibits a constant slope as opposed to variable change in slope in some section of this interface region.

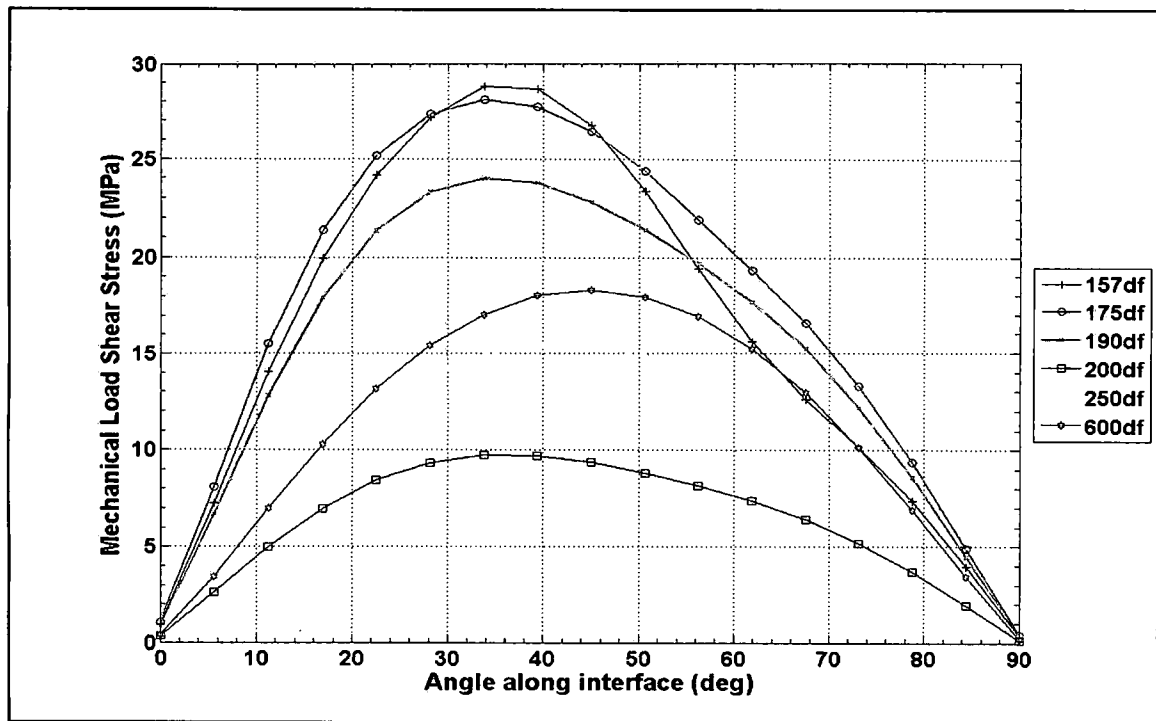


Figure 224: Shear stress distributions at the fiber-matrix interface due to the mechanical loading

Although the maximum magnitude location shifts for the 2.5d_f fiber spacing to $\theta = 39.375^\circ$ the difference at this location to the magnitude at $\theta = 45^\circ$, where the maximum magnitude would occur if no nearest neighbor effects were present, is 0.08%. Because the effect is very small the distribution at the 2.5d_f fiber spacing is virtually symmetrical about the maximum location and consequently the effects from the corner fiber due to the mechanical loading can be neglected.

Table 76 lists the variation of the shear stress across the interface due to the matrix cure and the percent reduction of the maximum shear stress due to the mechanical load.

Table 76: Maximum shear stress variation due to matrix cure and percent reduction of the maximum shear stress due to mechanical load

Fiber Spacing	Maximum Shear Stress Variation (MPa)	Impact Maximum Shear By Residual Stress
1.57d _f	34.1	65%
1.75d _f	19.6	39%
1.90d _f	13.2	32%
2.0d _f	10.4	64%
2.5d _f	4.2	19%
6.0d _f	1.7	9%

The variation is the absolute sum of the maximum shear stresses shown in Figure 223. The impact on the maximum shear stress is the ratio, expressed as a percentage, of the maximum shear stress due to the matrix cure to the shear stress due to the mechanical load at the location of maximum shear due to mechanical load. In all cases the maximum shear stress from the matrix cure is of opposite sign than the maximum shear stress from the mechanical load. It is evident from Table 76 by the high variation in shear stress across the interface of the center fiber and the large percentage impacts that the high temperature cure matrix has large effects on the shear stresses over the mechanical load. For example, at the 1.57d_f spacing the shear stress due to the matrix cure is 65% of the shear stress due to the mechanical load; i.e. the high temperature matrix cure imparts shear stresses having magnitudes as high as almost 2/3 of the shear stress due the mechanical load. Also evident are the effects on the shear stress from nearest neighboring fibers in combination with the residual effects since the variation decreases as the fiber spacing increases. Consistent with the radial stress the 6.0d_f fiber spacing has very little effect from the corner fiber as its variation is just less than 2.0 MPa. The net result of the impact due to the residual stress is the shift in location of the maximum shear stress.

Summarizing the interfacial shear stress results show that the residual stresses due to the matrix cure have considerable impact on the shear stress due to mechanical loading only for the 1.57d_f, 1.75d_f, 1.9d_f and 2.0d_f fiber spacing groups by comparison of Figures 222, 223 and 224. This is indicated by the dramatic shift in the location of the maximum magnitude of the shear stresses and the shape of the interfacial distribution. The peak shear stress location shifts 28.125° from an original location due to the mechanical loading at $\theta = 28.125^\circ$ to the location of θ

= 56.25° due to the combination of mechanical load and residual stress from the matrix cure. In addition, the region of the interface distribution indicative of the effects of the corner fiber, sees slope changes from the location of maximum magnitude to $\theta = 90^\circ$, and again from the location of the maximum magnitude to $\theta = 0^\circ$. For the $2.5d_f$ fiber spacing the impact of the residual stresses due to the matrix cure have a slight effect on the mechanical loading shear stresses as evident of the slight shift in the location of maximum shear stress magnitude as shown in Figure 222. The $6.0d_f$ fiber spacing, on the other hand, shows no effects from its corner fiber as there is no evidence of a shift in the location of maximum magnitude of the shear stress and that the distribution is smooth and symmetrical about the maximum shear, as shown in Figure 222.

Center Fiber Interface Results - Summary

In summary for the center fiber it appears that the residual stress due to the matrix cure pushes the maximum shear stresses on the fiber-matrix interface toward the direction of applied load. The maximum shear stresses due to the combined effects occur along the fiber-matrix interface and happen to be about where the radial stresses have their minimum magnitudes due to the combined effects for the $1.57d_f$, $1.75d_f$, $1.9d_f$ and $2.0d_f$ fiber spacing groups. Since the $1.57d_f$, $1.75d_f$ and the $1.9d_f$ fiber spacing groups exhibit fiber-matrix debonding as the first failure mechanism it could be surmised that the interfacial radial and shear stresses interact for the debond to occur. It is quite apparent that the center fiber of the $6.0d_f$ fiber spacing group is acting independently like an isolated single fiber. However, for the $2.5d_f$ fiber spacing the nearest neighbor fiber effects are present but negligible.

Corner Fiber Interface Results – Radial Stress

The interfacial radial stress distribution due to the combination of mechanical load and residual matrix curing stresses in all four quadrants are shown in Figures 225 to 228 for the cruciform fiber spacing groups tested. These results are very similar to the corresponding corner fiber radial stresses of the 828/D-230 matrix system.

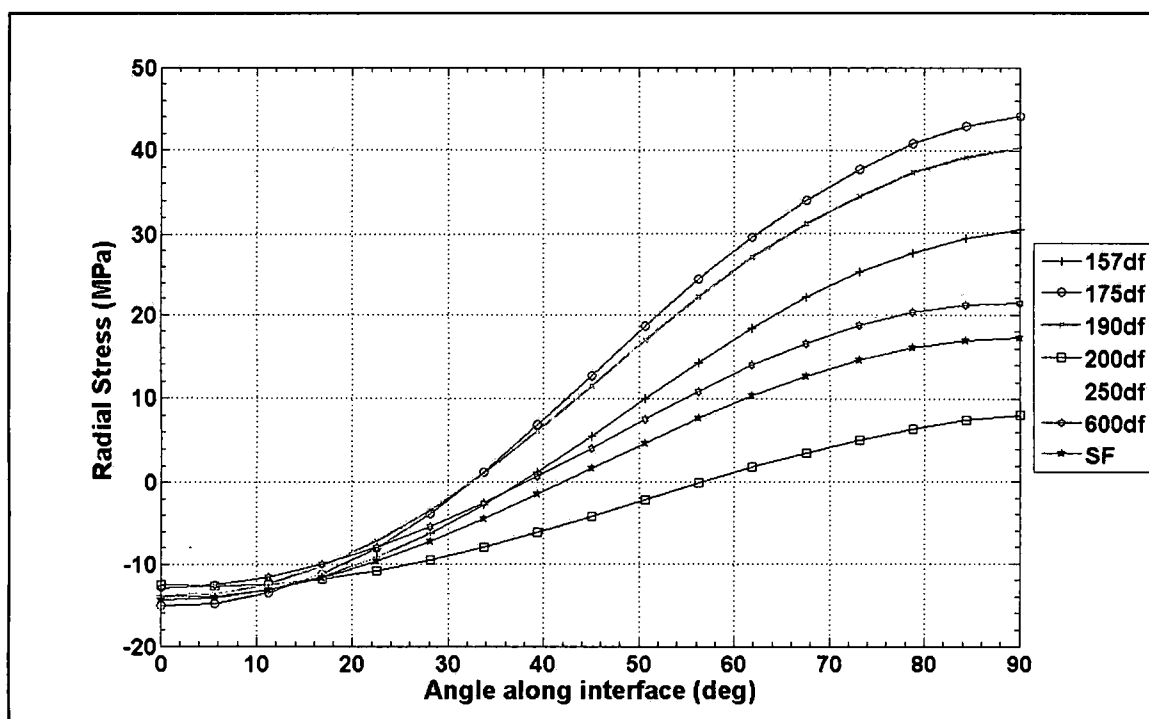


Figure 225: Radial stress distributions at the fiber-matrix interface due to the combination of mechanical loading and matrix cure residual stresses from $\theta = 0^\circ$ to 90°

For all fiber spacing cases in the first, second and fourth quadrant of the corner fiber the maximum magnitude of the radial stress is tensile and occurs at $\theta = 90^\circ$ at the location in the direction of applied load. The minimum magnitude of the radial stress is compressive and occurs at $\theta = 0^\circ$ for all fiber spacing groups in the first, second and fourth quadrants, as shown in Figure 225, 226 and 228.

Like in the 828/D-230 matrix system, nearest neighbor effects in the 862/W matrix system are presented in the third quadrant of the corner fiber, as shown in Figure 227. However, unlike the 828/D-230 matrix system where a "wave" shows the effects of the nearest neighbor fibers, the effects in the 862/W system from the corner fiber are distinguished by a concave stress distribution or "dip", shown in Figure 227. Specifically for the $1.57d_f$ fiber spacing the concave stress distribution occurs from $\theta = 191.25^\circ$ to approximately 247.50° . Similarly for the $1.75d_f$ and $1.90d_f$ the dip occurs approximately between $\theta = 202.5^\circ$ and 236.25° and for the $2.0d_f$ fiber spacing it occurs roughly between $\theta = 202.5^\circ$ to 230.625° .

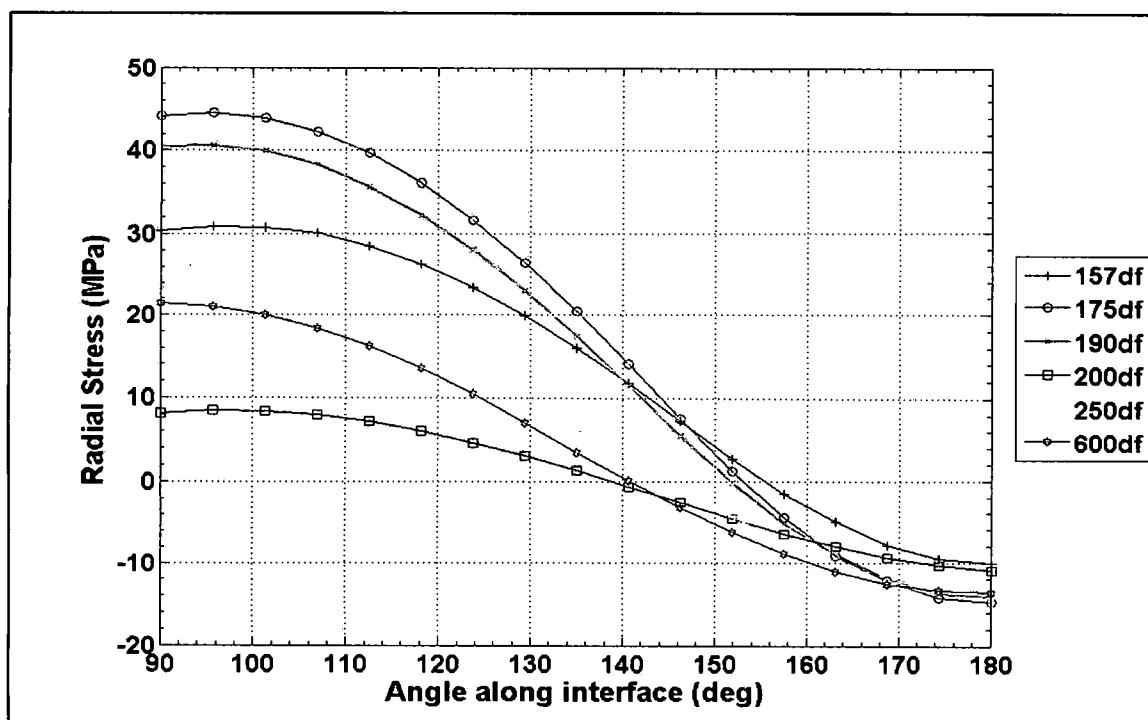


Figure 226: Radial stress distributions at the fiber-matrix interface due to the combination of mechanical loading and matrix cure residual stresses from $\theta = 90^\circ$ to 180°

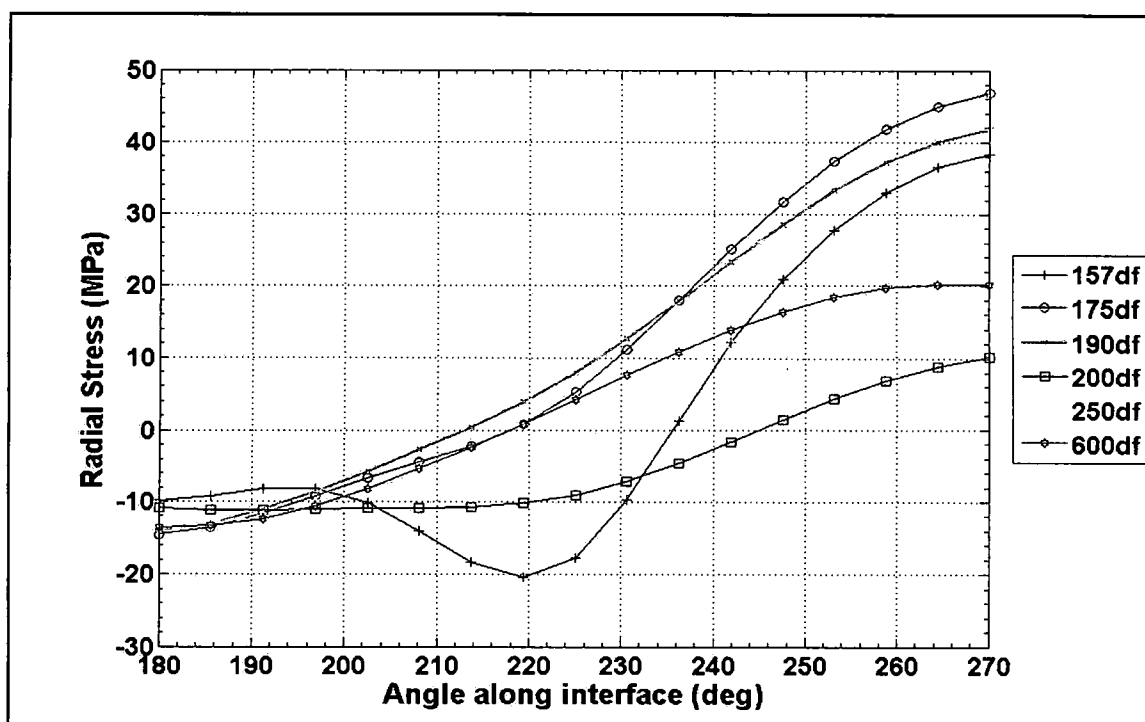


Figure 227: Radial stress distributions at the fiber-matrix interface due to the combination of mechanical loading and matrix cure residual stresses from $\theta = 180^\circ$ to 270°

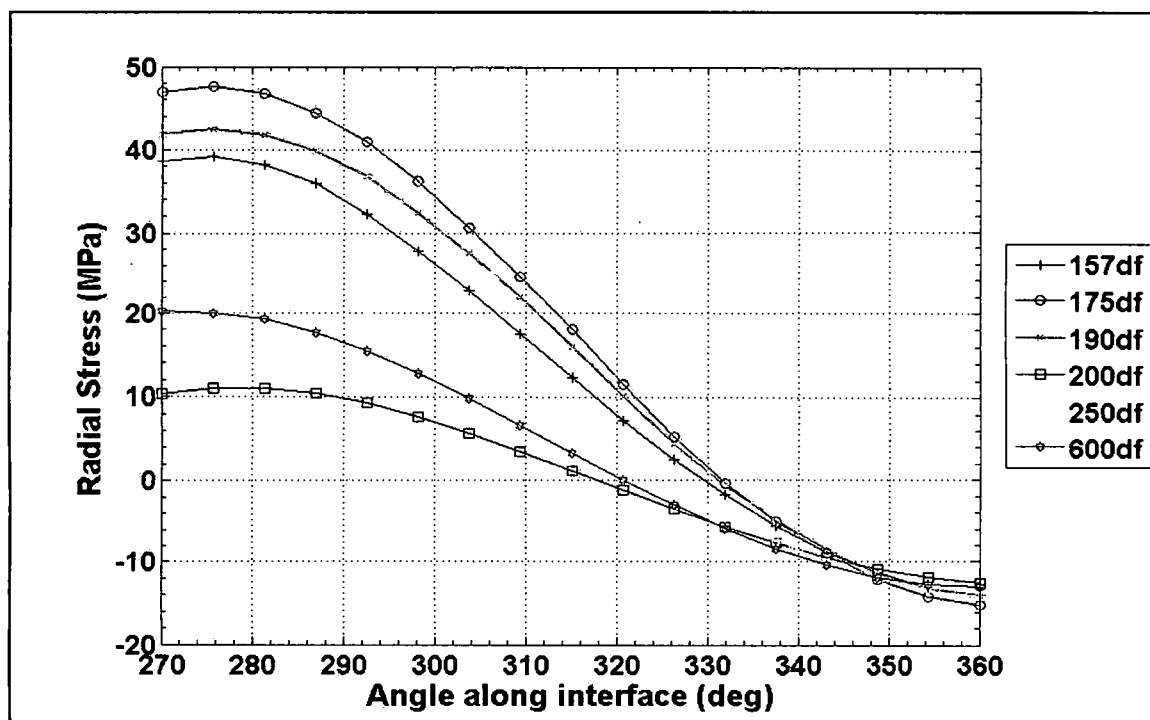


Figure 228: Radial stress distributions at the fiber-matrix interface due to the combination of mechanical loading and matrix cure residual stresses from $\theta = 270^\circ$ to 360°

The 2.5d_f and 6.0d_f fiber spacing groups radial stress distribution due to the combined mechanical load and matrix residual stress from the curing cycle have practically the same stress distribution, as shown in Figure 227 and are similar to that for the 828/D-230 matrix system shown in Figure 195. In addition, no effects from their nearest neighbor fibers exist as no indication of a dip is present in the radial stress distribution. Furthermore, the radial stress magnitudes for the 2.5d_f and 6.0d_f fiber spacing groups are basically equal in the third quadrant.

The single fiber interfacial radial stress distribution due to the combination of mechanical load and matrix residual stresses from its cure cycle is also in Figure 225 for the same reason discussed above in the 828/D-230 section. The SF radial stress distribution is virtually the same, although slightly less in magnitude, as the 2.5d_f and 6.0d_f radial stress distribution.

It should be pointed out that the maximum magnitudes for all fiber spacing groups except the 6.0d_f group occur at $\theta = 95.625^\circ$ in the second quadrant and at $\theta = 275.625^\circ$ in the fourth

quadrant. Although minor in nature, this effect is caused by the residual stresses due to the matrix cure cycle and the interaction with neighboring fibers.

The interfacial radial stress distribution due to the residual stress from the high temperature 862/W cure cycle, shown in Figures 229 to 232 in all four quadrants, sheds some light on the behavior of the radial stress distribution due to the combination of mechanical load and matrix curing stresses shown in Figures 225 to 228. Although both matrix systems have the same general radial stress distribution due to their matrix curing cycle, the 862/W system has much greater magnitudes. Another similarity with the 828/D-230 system is that the entire radial stresses, except for a very small segment in the second quadrant of the corner fiber between $\theta = 158^\circ$ and $\theta = 182^\circ$ are compressive around the fiber-matrix interface. In the first quadrant of the corner fiber, $\theta = 0^\circ$ to $\theta = 90^\circ$, the interfacial radial stress tend to increase as the fiber spacing decreases as shown in Figure 225. All the fiber spacing groups except the SF have a fairly uniform radial stress distribution from $\theta = 58^\circ$ to 90° . The 6.0d_f fiber spacing also has a fairly uniform radial stress distribution from $\theta = 0^\circ$ to 28° . Whereas, the SF radial stress distribution can be considered fairly uniform across the entire quadrant varying slightly more than 2.0 MPa. In the second quadrant and fourth quadrant the interfacial matrix residual radial stresses decrease in magnitude as the fiber spacing decreases, as shown in Figure 230 and 232. For all practical purposes the residual stresses can be considered acting in a virtually uniform manner from about $\theta = 150^\circ$ to 180° in the second quadrant, shown in Figure 230, for all fiber spacing groups. In the fourth quadrant the residual stresses are acting in virtually uniform manner from approximately $\theta = 300^\circ$ to 342° , shown in Figure 232, for all fiber spacing groups except the 1.57d_f group. Here it acts in a uniform manner from about $\theta = 280^\circ$ to 320° .

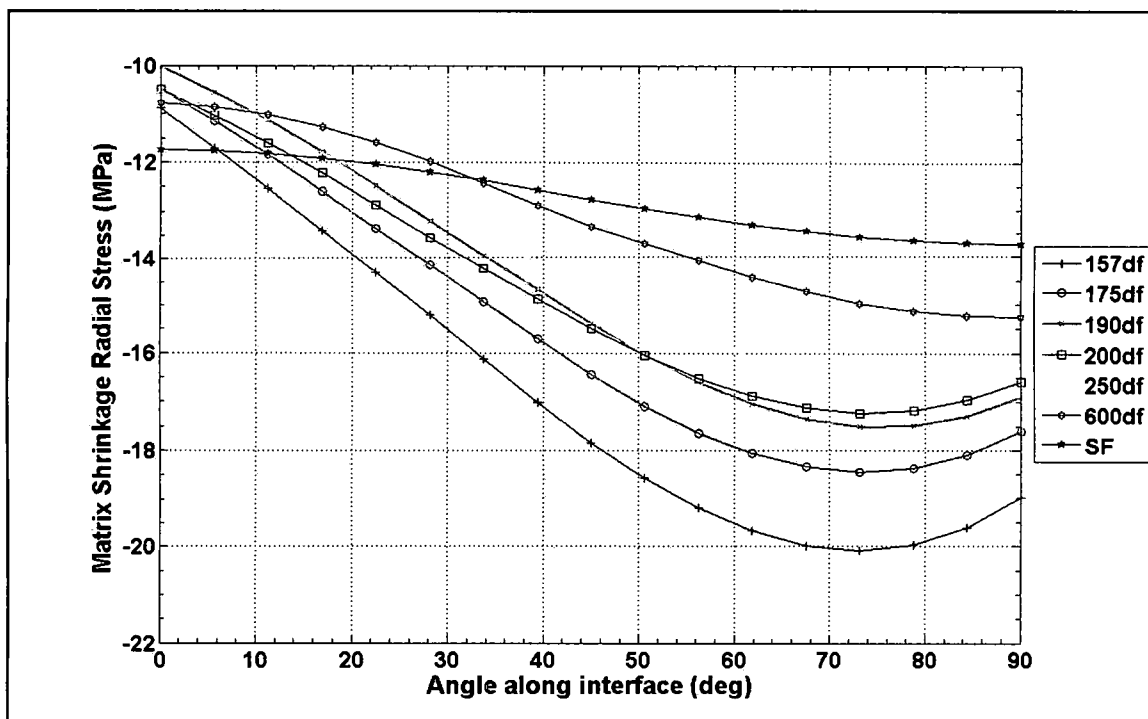


Figure 229: Radial stress distributions at the fiber-matrix interface due to the matrix cure residual stress from $\theta = 0^\circ$ to 90°

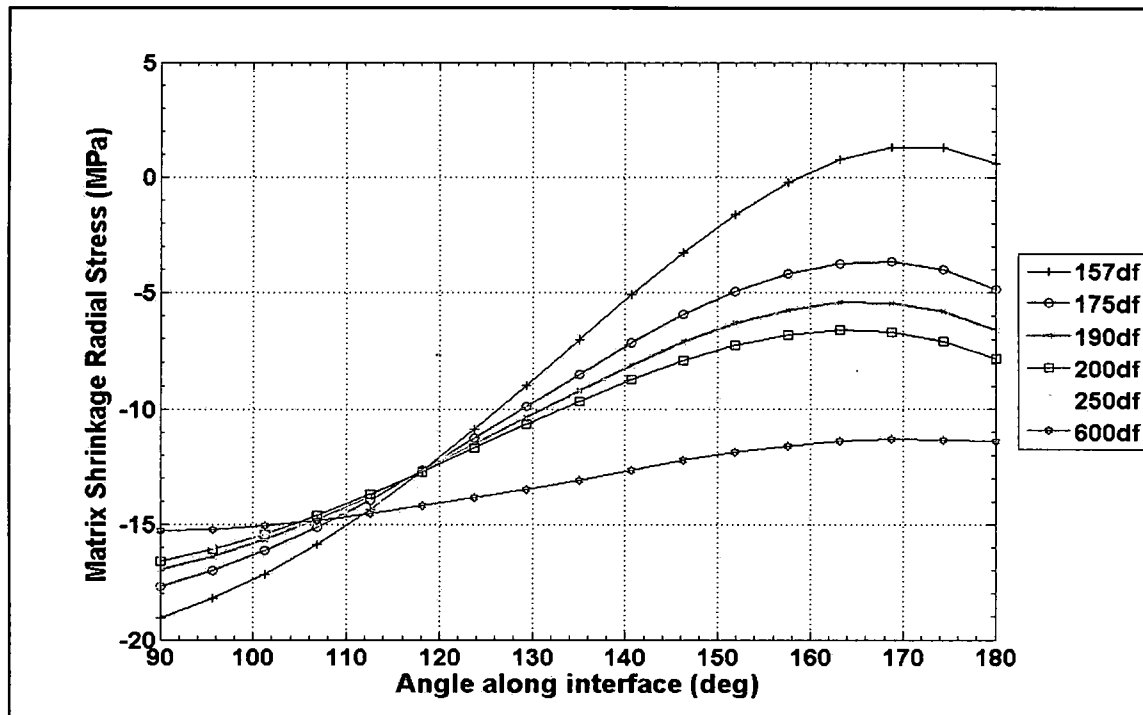


Figure 230: Radial stress distributions at the fiber-matrix interface due to the matrix cure residual stress from $\theta = 90^\circ$ to 180°

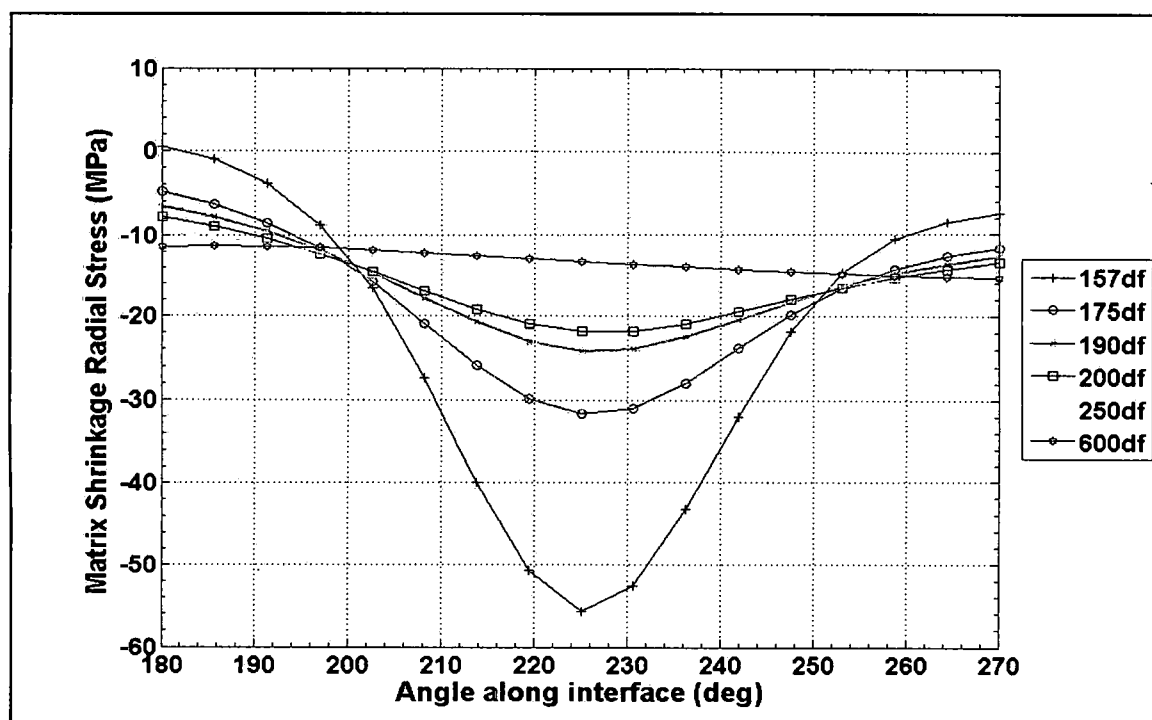


Figure 231: Radial stress distributions at the fiber-matrix interface due to the matrix cure residual stress from $\theta = 180^\circ$ to 270°

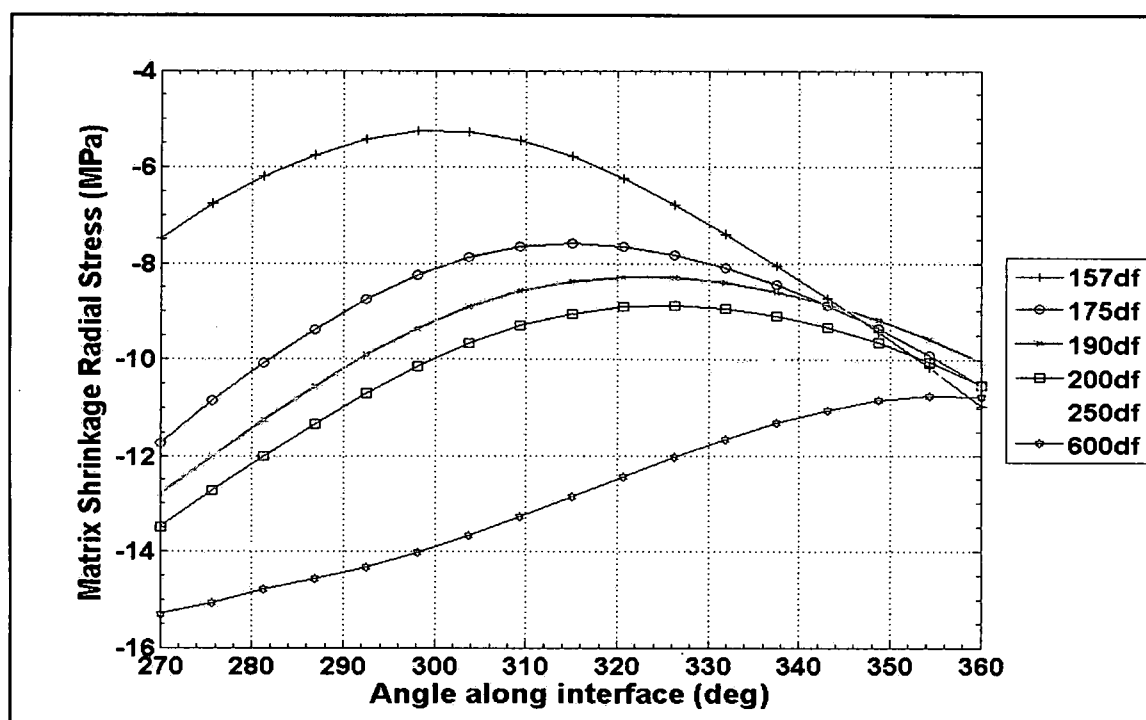


Figure 232: Radial stress distributions at the fiber-matrix interface due to the matrix cure residual stress from $\theta = 270^\circ$ to 360°

In the third quadrant of the corner fiber the interfacial radial stress due to the matrix cure residual stresses exhibits the same behavior as the center fiber where the maximum magnitude stresses increase as the fiber spacing decreases. The third quadrant of the corner fiber is closest to the center fiber and the interactions are quite apparent as the maximum magnitudes are at $\theta = 225^\circ$ for all fiber spacing groups except the $6.0d_f$ spacing. For all practical purposes the $6.0d_f$ fiber spacing has a uniform radial stress due to the residual stress from the high temperature matrix cure across the entire third quadrant having a total variance of just under 4.0MPa.

The nearest neighbor effects are felt along the entire circumference of the corner fiber is evident by inspection of Figures 229 – 232. The radial stress due to the matrix cure residual stress increases as the fiber spacing decreases in the first and third quadrants, whereas, the opposite occurs in the second and fourth quadrants. For the high temperature cured 862/W matrix system the residual stresses occur due to the complex combination of thermal coefficient of expansion mismatch between the resin system and the stainless steel fibers as well as the shrinkage the matrix experiences as it vitrifies. As the matrix vitrifies at the high temperature it bonds and clamps, due to the shrinkage, to the stainless steel fibers, already expanded from the temperature change, creating high compressive forces. As the system cools the fibers shrink, both in the radial direction across the cross section and axially, however, the matrix remains bonded and clamped to the fiber. The matrix is also highly constrained by the comparative closeness of the fiber spacing. This creates a complex three-dimensional state of stress as the matrix tries to stop the fiber from returning to its original state while being constrained by the fiber grouping. This in turn reduces some of the compressive stress around the interface as shown in the second and fourth quadrant of the corner fiber in Figure 230 and 232. Furthermore, the radial stresses increase in the third quadrant due to the nearest neighbor fibers further constraining the matrix. Equilibrium must be maintained thus the radial stress increase as the fiber spacing decreases in the first quadrant as this quadrant is closest to the specimen free edge without any nearest neighbor effects.

The interfacial radial stress distribution due to the mechanical loading for the 862/W matrix system in all four quadrants of the corner fiber for all cruciform specimens' fiber spacing

groups is shown in Figures 233 to 236. As expected, the radial stress distribution due to the mechanical loading is very similar to the radial stress distribution due to the combination of mechanical loading and residual stresses from the matrix cure in the first, second and fourth quadrants. Furthermore, the 862/W radial stress distribution is very similar to the 828/D-230 radial stress distribution. In all cases, the maximum magnitudes occur in the direction of applied load at $\theta = 90^\circ$ for the first and second quadrant and at $\theta = 270^\circ$ for the third and fourth quadrant. The minimum magnitude occurs at $\theta = 0^\circ$ in the first and second quadrant and at $\theta = 180^\circ$ in the third and fourth quadrants, normal to the direction of applied load, for all fiber spacing groups as well.

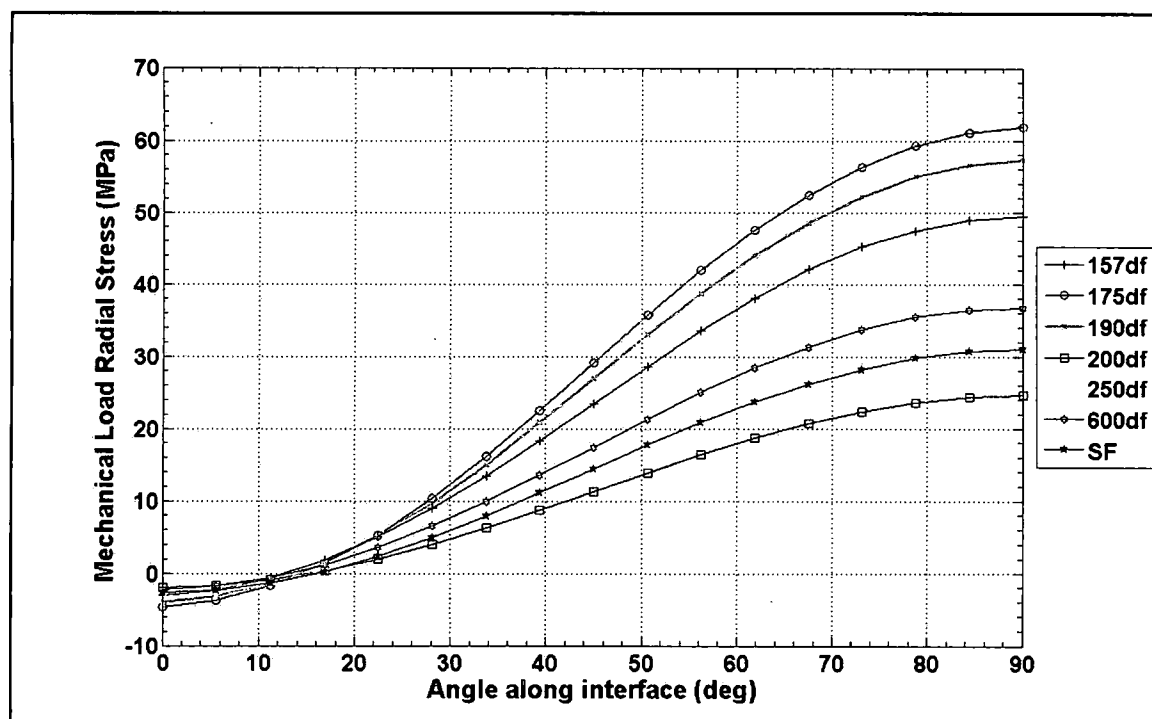


Figure 233: Radial stress distributions at the fiber-matrix interface due to the mechanical loading from $\theta = 0^\circ$ to 90°

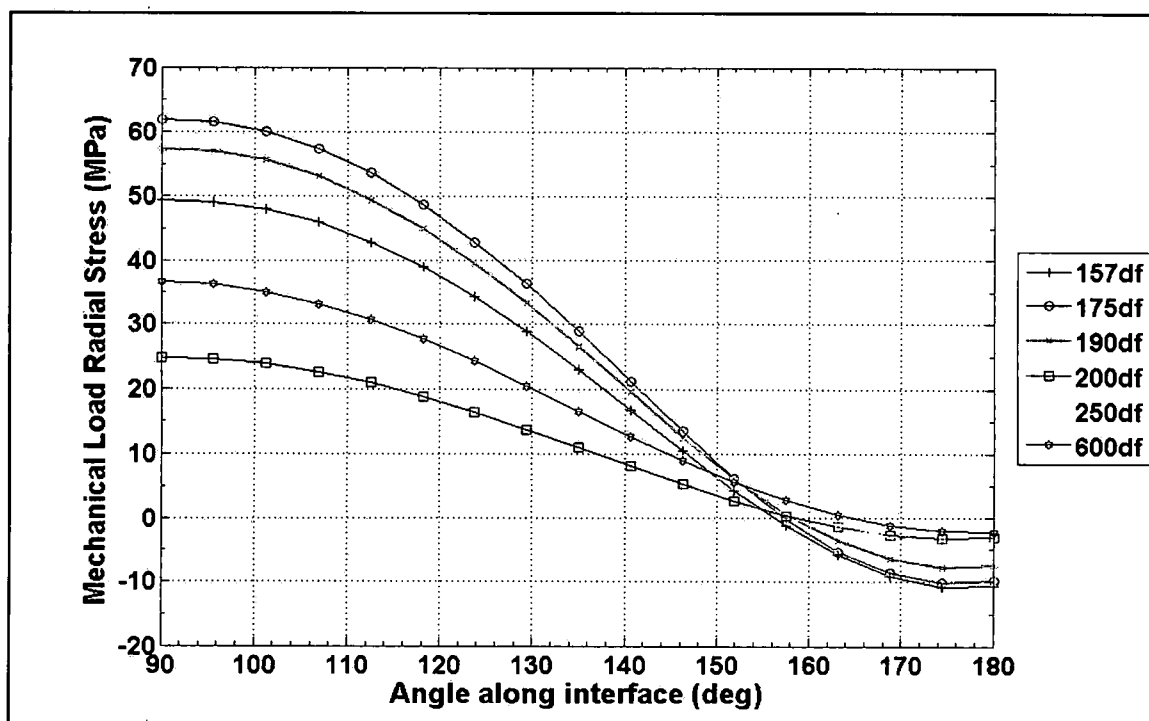


Figure 234: Radial stress distributions at the fiber-matrix interface due to the mechanical loading from $\theta = 90^\circ$ to 180°

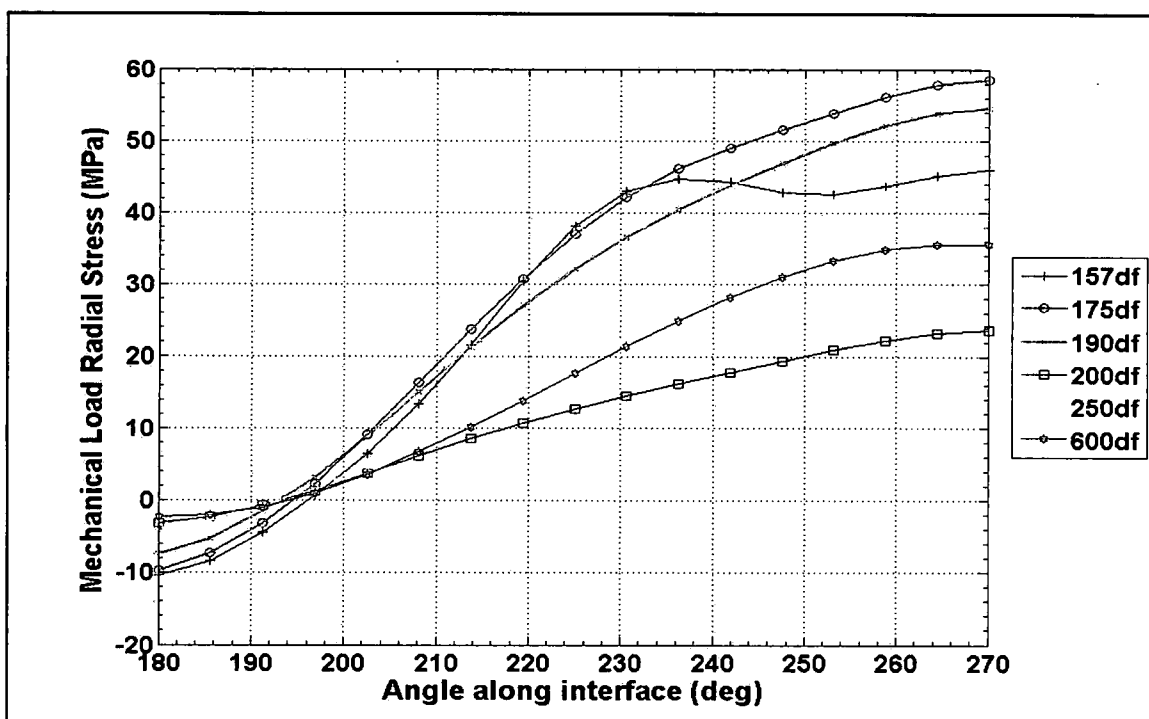


Figure 235: Radial stress distributions at the fiber-matrix interface due to the mechanical loading from $\theta = 180^\circ$ to 270°

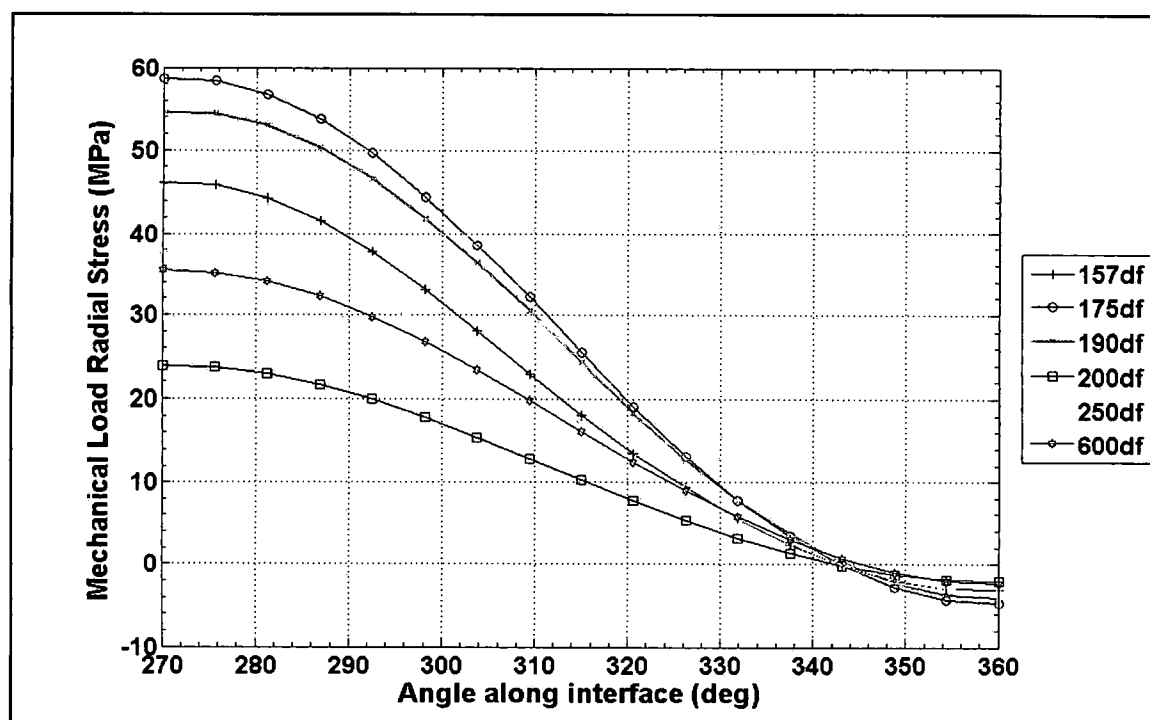


Figure 236: Radial stress distributions at the fiber-matrix interface due to the mechanical loading from $\theta = 270^\circ$ to 360°

The nearest neighbor fiber effects present themselves in the third quadrant of the corner fiber for the $1.57d_f$, $1.75d_f$, $1.9d_f$ fiber spacing groups in the same manner as in the 828/D-230 matrix system by the presence of a "wave" in the stress distribution as shown in Figure 235. The maximum radial stress for the $1.57d_f$ fiber spacing occurs at $\theta = 270^\circ$ but is practically equal to the magnitude at $\theta = 236.25^\circ$ consequently it remains fairly constant from this point to $\theta = 270^\circ$. A slight wave exists for the $1.75d_f$ and the $1.9d_f$ fiber spacing groups between $\theta = 216^\circ$ and $\theta = 250^\circ$ causing the higher radial stresses to act over a longer length of interface. For the $2.0d_f$ fiber spacing, its slope is less in the 3rd quadrant than in the other quadrants. The $2.5d_f$ and $6.0d_f$ fiber spacing group indicates no interaction with the center fiber as their interfacial radial stress distribution is smooth, parallel and practically equal to each other.

Comparing the center fiber radial stress distribution due to mechanical load, see Figure 221, to the corner fiber radial stress distribution due to mechanical load, see Figure 235, the maximum magnitudes of the radial stresses are greater for the corner fiber than for the center

fiber for all cases. However, for the 6.0df fiber spacing, its maximum magnitude of the radial stress on the center fiber is practically equal to its maximum magnitude of the radial stress on the corner fiber. Even though the maximum magnitudes for the radial stresses are greater on the corner fiber than on the center fiber it appears that the nearest neighbor interactions are greater on the center fiber than on the corner fiber for those fiber groups experiencing interactions, namely the 1.57d_f, 1.75d_f, 1.90d_f and to a lesser extent the 2.0d_f. Also, for these fiber spacing groups the radial stress acts over a larger portion of the center fiber than on the corner fiber.

Similar to the 828/D-230 matrix system the impacts of the matrix residual stresses due to the matrix cure of the 862/W resin system on the radial stress distribution at the fiber-matrix interface are predominate in the third quadrant of the corner fiber. This is evident by comparing Figures 227, 231, and 235, where the nearest neighbors create a "dip" in the radial stress distribution due to the combined loading from the mechanical load and residual stresses, as shown in Figure 227, but the corner fiber effects due to mechanical load only are manifested by a "wave" as shown in Figure 235. By inspection of Figure 231, the magnitudes of the residual stresses due to the cure cycle are quite large and in some cases greater than those from the mechanical load only, especially at $\theta = 225^\circ$ where the center and corner fiber are closest. Table 77 lists the percentage of the mechanical load radial stress to the matrix cure residual radial stress in the third quadrant at two locations along the fiber matrix interface. The first location is the point on the interface of maximum residual stress due to matrix cure and the second location is at the point of maximum mechanical load. The maximum radial stresses due to matrix cure are in some cases are much greater than the radial stress imparted by mechanical load, as mentioned above. The high compressive stresses due to the matrix cure for the 1.57d_f, 1.75d_f, 1.90d_f and the 2.5d_f fiber spacing groups occurring at $\theta = 225^\circ$, shown in Table 77, create the dramatic change in the radial stress distribution seen when comparing Figures 227 and 235. The net result is a reduction of the radial stress at the point of maximum stress due to the mechanical load, i.e. at $\theta = 270^\circ$.

**Table 77: Third quadrant percent reduction of the radial stress over the mechanical load
due to the residual stress from the high temperature matrix cure**

Fiber Spacing	Max Matrix Resdl Stress (MPa)	Mech @ Max Resdl (MPa)	Loc	%	Max Mech Stress (MPa)	Resdl Stress @ Max Mech (MPa)	Loc	%
1.57d _f	-55.73	38.07	225°	146	45.89	-7.49	270°	16
1.75d _f	-31.67	37.0	225°	86	58.53	-11.74	270°	20
1.90d _f	-24.16	32.10	225°	75	54.53	-12.82	270°	24
2.0d _f	-21.85	12.77	225°	171	23.77	-13.51	270°	57
2.5d _f	-17.12	25.62	225°	67	37.8	-14.84	270°	39
6.0d _f	-15.33	35.51	270°	43	35.51	-15.33	270°	43

For the first, second and fourth quadrant of the corner fiber the biggest impact of the residual radial stresses on the mechanical loading radial stress is at the point in the direction of applied loading, i.e. at $\theta = 90^\circ$ and 270° . Table 78 lists the percentage of the mechanical load radial stresses to the residual stresses from the matrix cure for the three quadrants. Although not as high as in the 3rd quadrant, the matrix cure residual stresses are still quite significant ranging from 29% to 67% in the 1st and 2nd quadrant and from 16% to 57% in the 4th quadrant of the mechanical stress due to the applied load. Even comparing the percentage of the residual stress to the mechanical load stresses at $\theta = 90^\circ$ and 270° significant differences exist due in part to the combination of nearest neighbors and the specimen free edge as mentioned above. It appears that at the 6.0d_f fiber spacing the residual radial stress is uniform across the entire fiber circumference and its magnitude is practically equal to that for the SF. This suggests that at the 6.0d_f spacing the fibers are acting as isolated fibers.

Table 78: Percent reduction of the radial stress of the mechanical load by the residual stress due to the matrix cure at the location of maximum mechanical radial stress

Fiber Spacing	1 st and 2 nd Quadrant				4 th Quadrant			
	Max Mech Radial Stress	Residual Stress @ Max Mech Radial Stress	Loc θ	%	Max Mech Radial Stress	Residual Stress @ Max Mech Radial Stress	Loc θ	%
1.57d _f	49.41	-19.05	90°	38	45.98	-7.49	270°	16
1.75d _f	61.81	-17.64	90°	29	58.59	-11.74	270°	20
1.9d _f	57.29	-16.93	90°	30	54.58	-12.81	270°	23
2.0d _f	24.71	-16.60	90°	67	23.80	-13.51	270°	57
2.5d _f	39.26	-16.24	90°	41	37.82	-14.83	270°	39
6.0d _f	36.67	-15.27	90°	42	35.51	-15.32	270°	43
SF	30.99	-13.74	90°	44	-	-	-	-

Summarizing the corner fiber radial stress results, it is quite apparent that the high temperature cure 862/W matrix imparts a relatively high residual compressive radial stress around the fiber-matrix interface. In general the radial stresses due to the matrix cure tend to increase as the fiber spacing decreases in the first and third quadrants, whereas, the opposite is true in the second and fourth quadrants, as shown in Figures 229 to 232. The net resulting action of the compression stresses reduces the radial stress as shown by comparing Figures 225 through 228 to Figures 233 through 236 and also shown in Tables 77 and 78. Nearest neighbor effects on the radial stresses due to the matrix cure slightly shift the maximum radial stress location for all fiber spacing groups except the 6.0d_f in all four quadrants. In quadrants one and two the nearest neighbor effects combined with the residual effects increase the interfacial length over which the radial stress acts. In quadrant three neighboring fiber effects are clearly shown at the location on the interface where the fibers are closest together, i.e. $\theta = 225^\circ$, and decrease as the fiber spacing increases as shown in Figure 232. Furthermore, in quadrant 3 the combination of loading and nearest neighbor effects reduces the length that the radial stress acts along the circumference for all fiber spacing groups except for the 6.0d_f. The 6.0d_f spacing, on the other hand, exhibits no neighboring fiber interaction effects and has a rather uniform radial compressive stress along its entire fiber circumference.

Corner Fiber Interface Results – Shear Stress

The interfacial shear stress results for all four quadrants of the corner fiber due to the combination of mechanical load and the residual stress from the matrix cure are shown in Figures 237 to 240. Evidence of nearest neighbor effects for the corner fiber are a shift of the maximum shear stress location from the midpoint of the quadrant, the asymmetrical shape of the distribution and the minimum magnitude of the shear stress at the limits of each quadrant not equal to zero. Minor effects are prevalent in first, second and fourth quadrants as shown in Figure 237, 238 and 240.

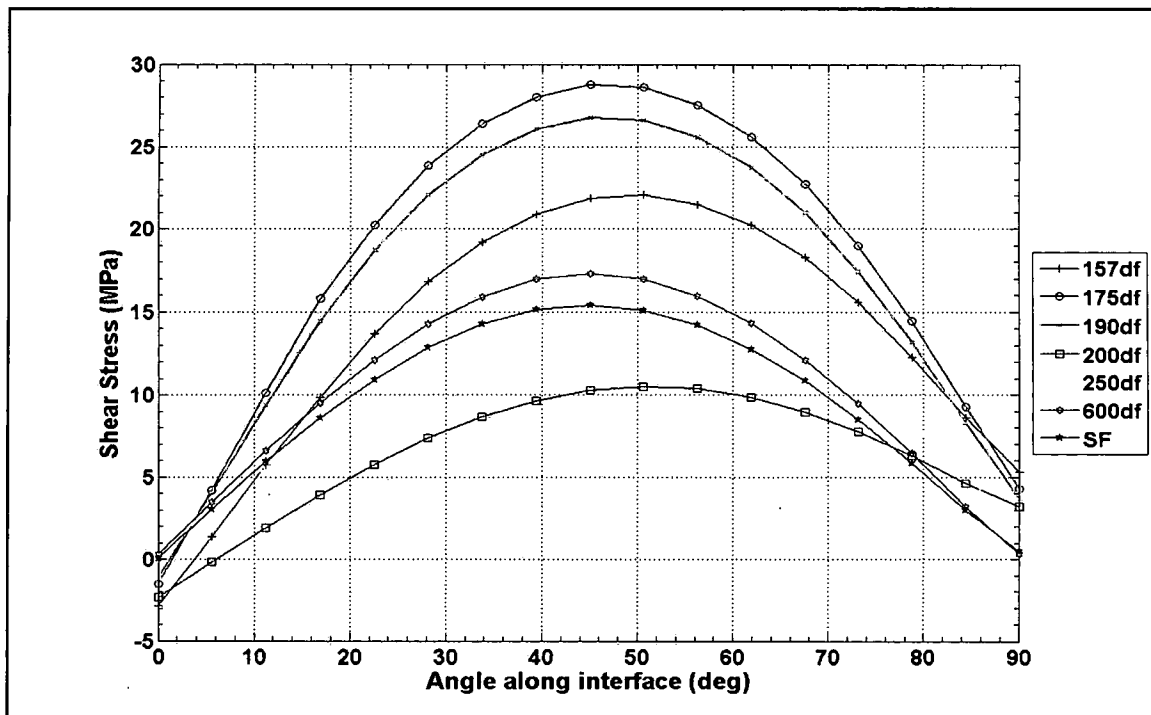


Figure 237: Shear stress distributions at the fiber-matrix interface due to the combination of mechanical loading and matrix cure residual stresses from $\theta = 0^\circ$ to 90°

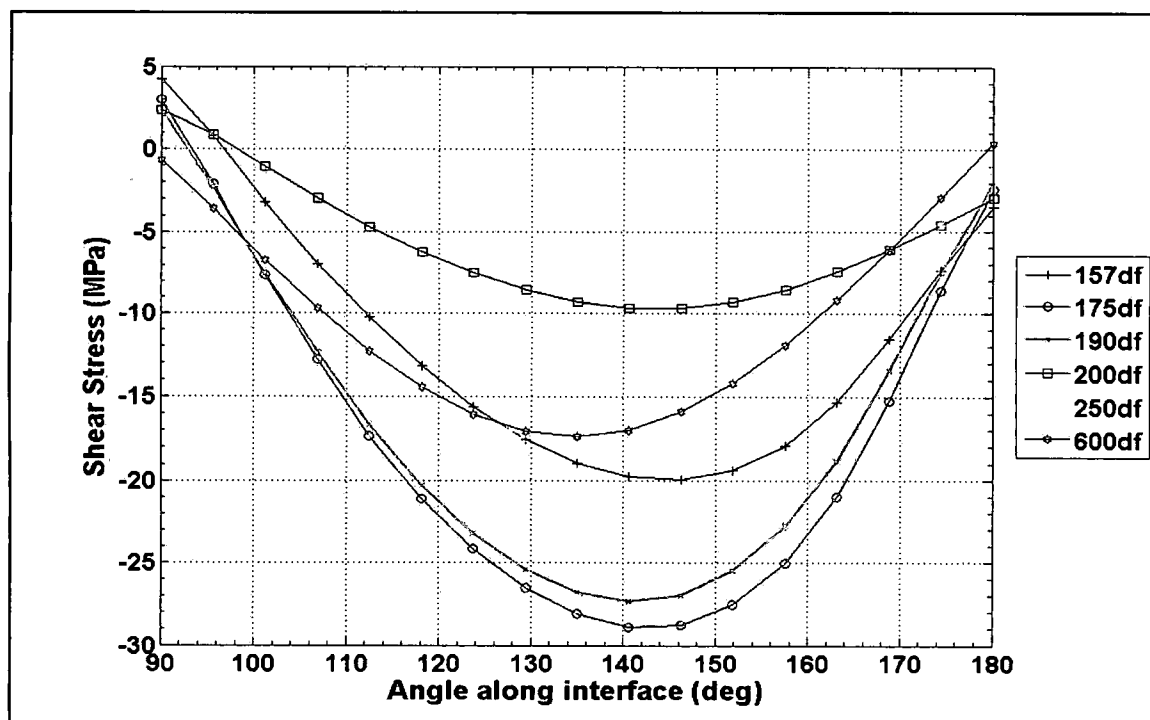


Figure 238: Shear stress distributions at the fiber-matrix interface due to the combination of mechanical loading and matrix cure residual stresses from $\theta = 90^\circ$ to 180°

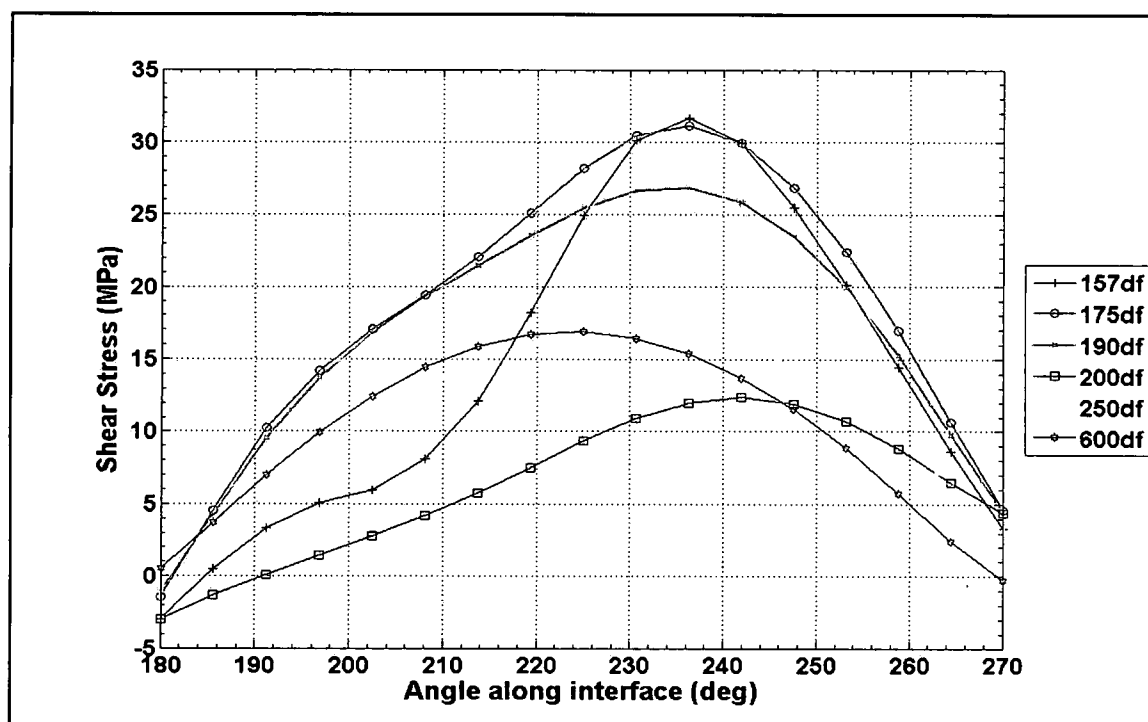


Figure 239: Shear stress distributions at the fiber-matrix interface due to the combination of mechanical loading and matrix cure residual stresses from $\theta = 180^\circ$ to 270°

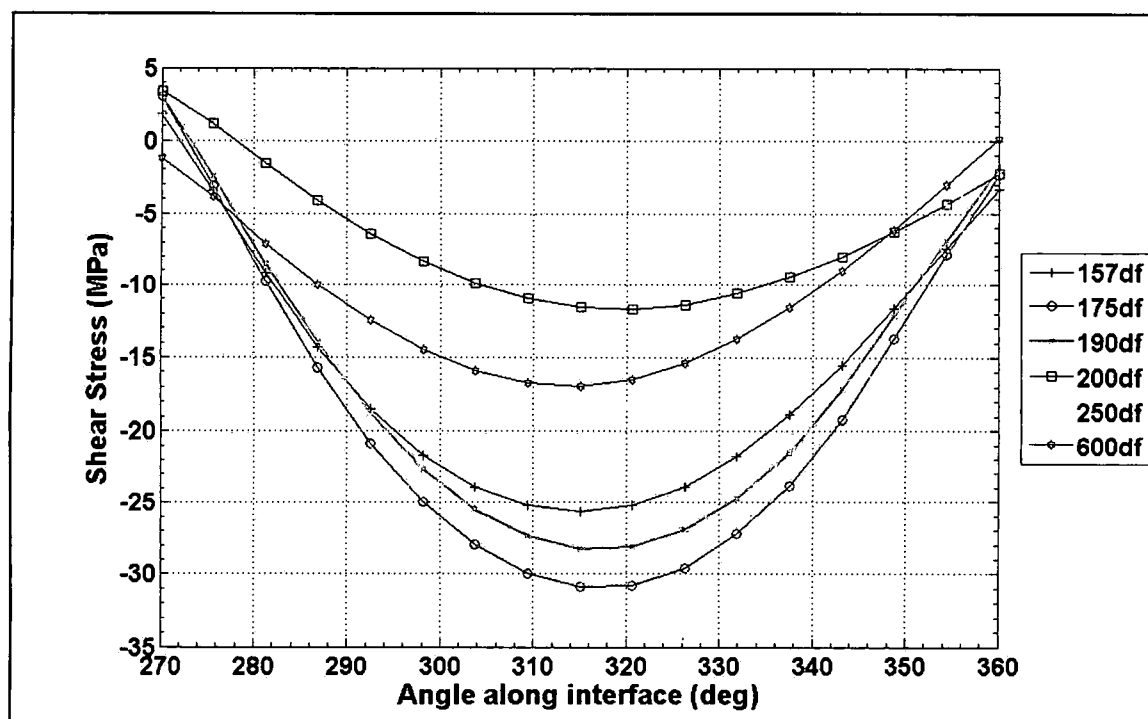


Figure 240: Shear stress distributions at the fiber-matrix interface due to the combination of mechanical loading and matrix cure residual stresses from $\theta = 270^\circ$ to 360°

The location of the maximum shear stress magnitude shifts slightly for the $1.57d_f$ and $2.0d_f$ fiber spacing groups in the 1st quadrant and for the $2.0d_f$ fiber spacing group in the 4th quadrant; while all but the $6.0d_f$ groups exhibit shifts in their maximum magnitude locations in the 2nd quadrant. However, the most telltale sign of the influence of the residual stresses occurring in quadrants 1, 2 and 4 are that the minimum magnitudes of the shear stress for all fiber spacing groups except the $6.0d_f$ and SF, is not zero at $\theta = 0^\circ, 90^\circ, 270^\circ$ and 360° .

Like the 828/D-230 corner fiber shear stress results, the 862/W shear stress results show prominent nearest neighbor effects in the third quadrant as shown in Figure 239. Here the shear stress distributions have a similarity between matrix systems; the shear stress distribution of the 862/W center fiber is almost identical to the 3rd quadrant corner fiber distribution of the 828/D-230, see Figure 222 and Figure 239. Neighboring fiber effects clearly present themselves as the location of the maximum shear stress shifts from $\theta = 225^\circ$ to 236.25° for the $1.57d_f, 1.75d_f, 1.90d_f$ fiber spacing groups and to $\theta = 241.875^\circ$ for the $2.0d_f$ spacing creating an asymmetric stress

distribution for each fiber spacing. Between $\theta = 180^\circ$ to 236.25° the distribution is concave for the $1.57d_f$, $1.75d_f$, $1.9d_f$ and the $2.0d_f$ fiber spacing groups, with the most dramatic change belonging to the $1.57d_f$ group. A slight shift from $\theta = 225^\circ$ to 230.625° occurs for the $2.5d_f$ fiber spacing as shown in Figure 239, indicating very modest effects from its corner fiber. However, for the $6.0d_f$ fiber spacing its distribution is symmetrical about its maximum magnitude location occurring at $\theta = 225^\circ$ and its minimum magnitudes return to zero signifying no nearest neighbor fiber effects. Furthermore, the minimum magnitude of the shear stress for all fiber spacing groups do not return to zero at $\theta = 180^\circ$ and 270° .

The residual stresses around the fiber-matrix interface due to the matrix cure cycle are major contributors to the behavior described above. Figures 241 through 244 show the interfacial residual shear stresses for the cruciform specimen fiber spacing groups tested due to the high temperature matrix cure for all four quadrants of the corner fiber. The 862/W matrix system has a very similar shear stress distribution for the residual stresses as the 828/D-230 matrix system has for the matrix cure shrinkage shear stresses, albeit with much larger relative magnitudes.

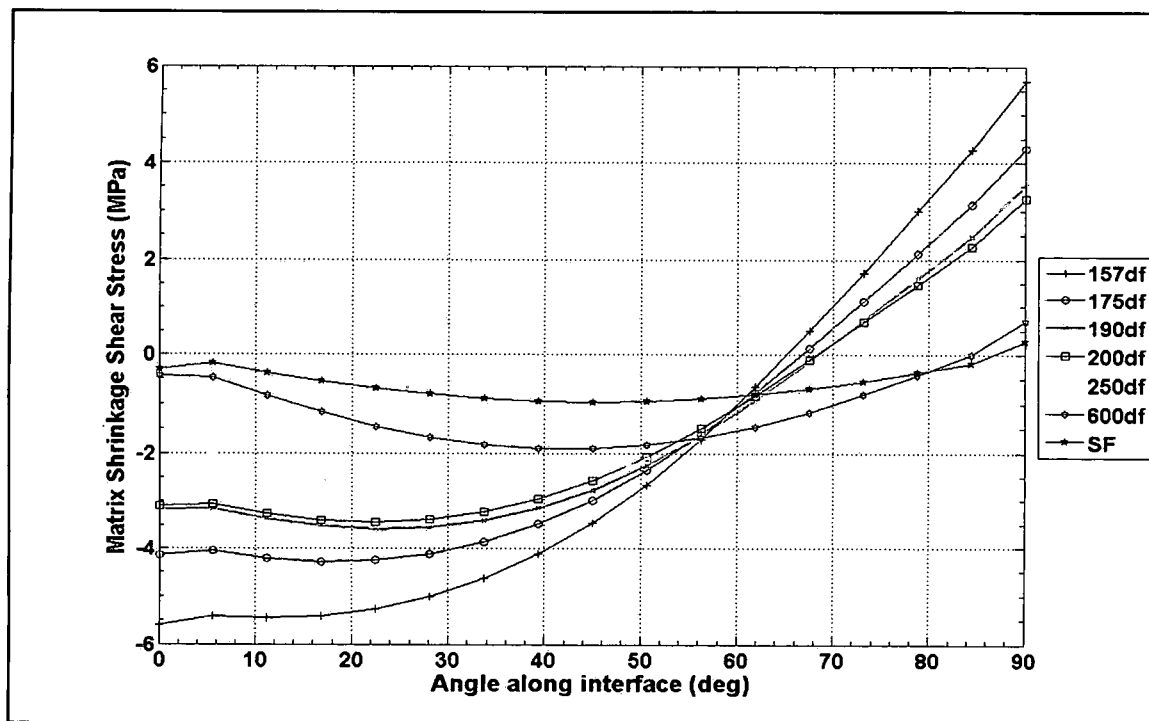


Figure 241: Shear stress distributions at the fiber-matrix interface due to the matrix cure residual stress from $\theta = 0^\circ$ to 90°

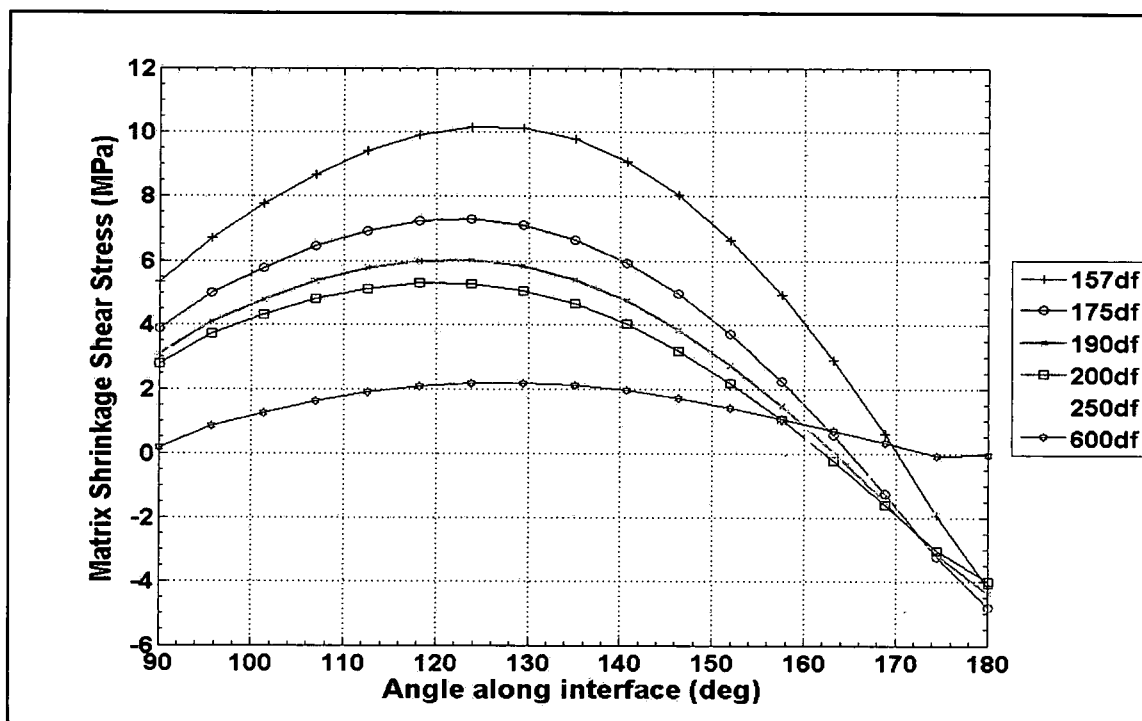


Figure 242: Shear stress distributions at the fiber-matrix interface due to the matrix cure residual stress from $\theta = 90^\circ$ to 180°

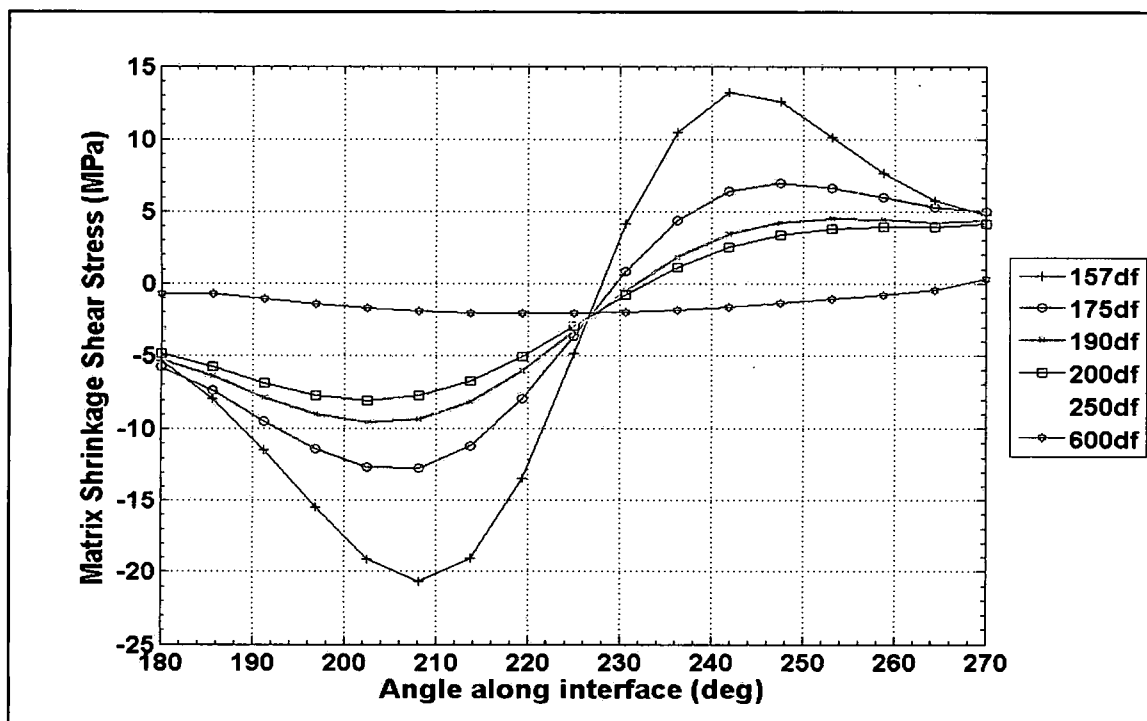


Figure 243: Shear stress distributions at the fiber-matrix interface due to the matrix cure residual stress from $\theta = 180^\circ$ to 270°

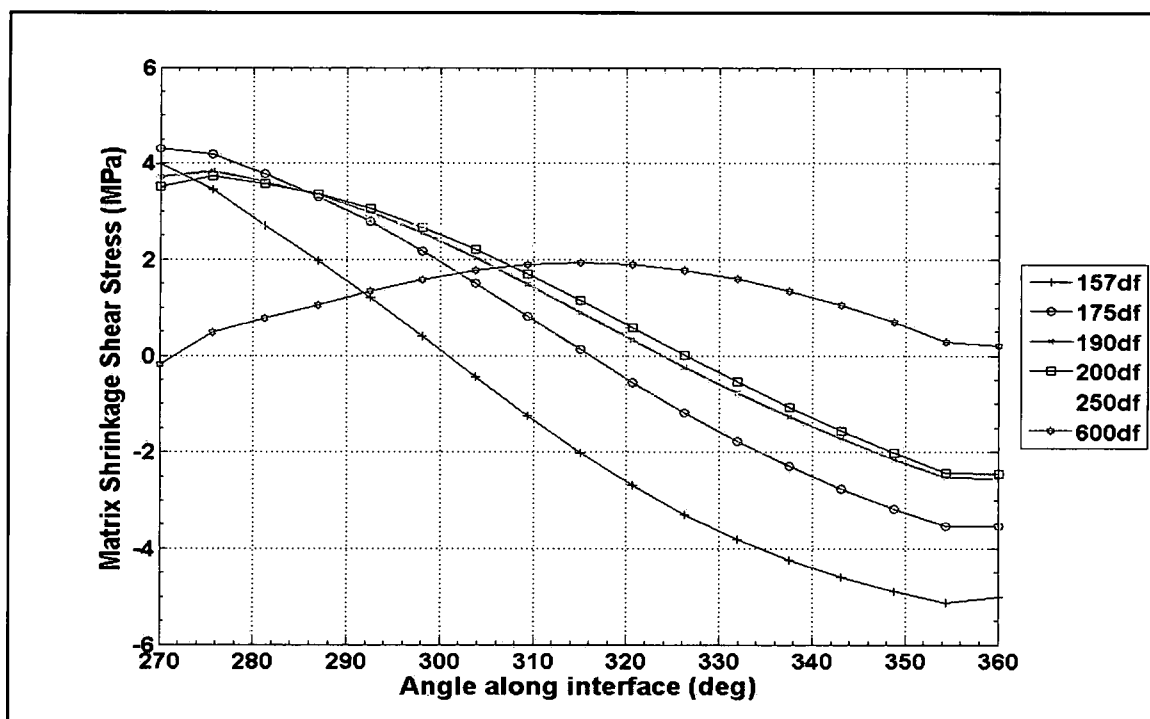


Figure 244: Shear stress distributions at the fiber-matrix interface due to the matrix cure residual stress from $\theta = 270^\circ$ to 360°

Like the 828/D-230 system, the $6.0d_f$ fiber spacing in the 862/W system has negligible residual shear stress since its maximum magnitude is approximately 2.0 MPa for all four quadrants. Similarly the SF has insignificant shear stress due to the matrix cure as its maximum magnitude is just over 1.0 MPa shown in the first quadrant of the corner fiber in Figure 241. For the $1.57d_f$, $1.75d_f$, $1.9d_f$, $2.0d_f$ and the $2.5d_f$ fiber spacing groups in the first, second, and fourth quadrants, the magnitude of the shear stress due to the residual stress from the matrix cure tend to increase as the fiber spacing decreases. Furthermore, an inflection point exists as the shear stress changes direction across the fiber-matrix interface, as shown in Figure 241, 242 and 244. For most cases in these quadrants the maximum shear stress magnitudes generally occurring at the quadrant limits are practically equal but are opposite sign. Only in the second quadrant are the maximum shear stress magnitudes significantly greater than at the quadrant limits of $\theta = 90^\circ$ and 180° .

Table 79 lists the shear stress variations across the four quadrants of the corner fiber. For each quadrant it reveals that the matrix residual shear stresses decreases as the fiber spacing increases. The maximum shear stress magnitudes are fairly consistent in the first and fourth quadrants with respect to fiber spacing as shown in Table 79. The 2nd quadrant shear stress variation increases for all fiber spacing groups compared to the 1st and 4th quadrants. However, the 3rd quadrant shows the influence of neighboring fibers as its shear stress variation is greatest for each fiber spacing. Nearest neighbor effects manifest themselves quite clearly as the primary maximum magnitudes occur at $\theta = 208.125^\circ$ and secondary maximum magnitudes occur between $\theta = 241.875^\circ$ to $\theta = 270^\circ$, thus affecting the shear stress differently depending on the position along the fiber-matrix interface in the 3rd quadrant as shown in Figure 243.

Table 79: Maximum Shear Stress variation in all four quadrants of the Corner Fiber

Fiber Spacing	1 st and 4 th Quadrant Maximum Shear Stress Variation (MPa)	2 nd Quadrant Maximum Shear Stress Variation (MPa)	3 rd Quadrant Maximum Shear Stress Variation (MPa)
$1.57d_f$	11.0	14.0	34
$1.75d_f$	8.5	12.5	20
$1.90d_f$	7.5	10.5	15
$2.0d_f$	6.5	9.5	12
$2.5d_f$	5.0	6.5	8

Figures 245 through 248 show the analytical results of the interfacial shear stress due to the mechanical loading for all cruciform multi-fiber spacing groups tested for all four quadrants of the corner fiber. Similar to the 828/D-230 shear stress distribution shown in Figures 213 through 216; all but the 6.0d_f fiber spacing in the 862/W matrix system shown minor effects from the center fiber in quadrants 1, 2 and 4 by the slight shift in the location of their maximum magnitude shear stresses shown in Figure 245, 246 and 248, but for the most part, their distributions are symmetrical about their maximum magnitude. Likewise for the corner and center fiber in the 828/D-230 system, neighboring fiber effects impact the third quadrant where the fibers are closest.

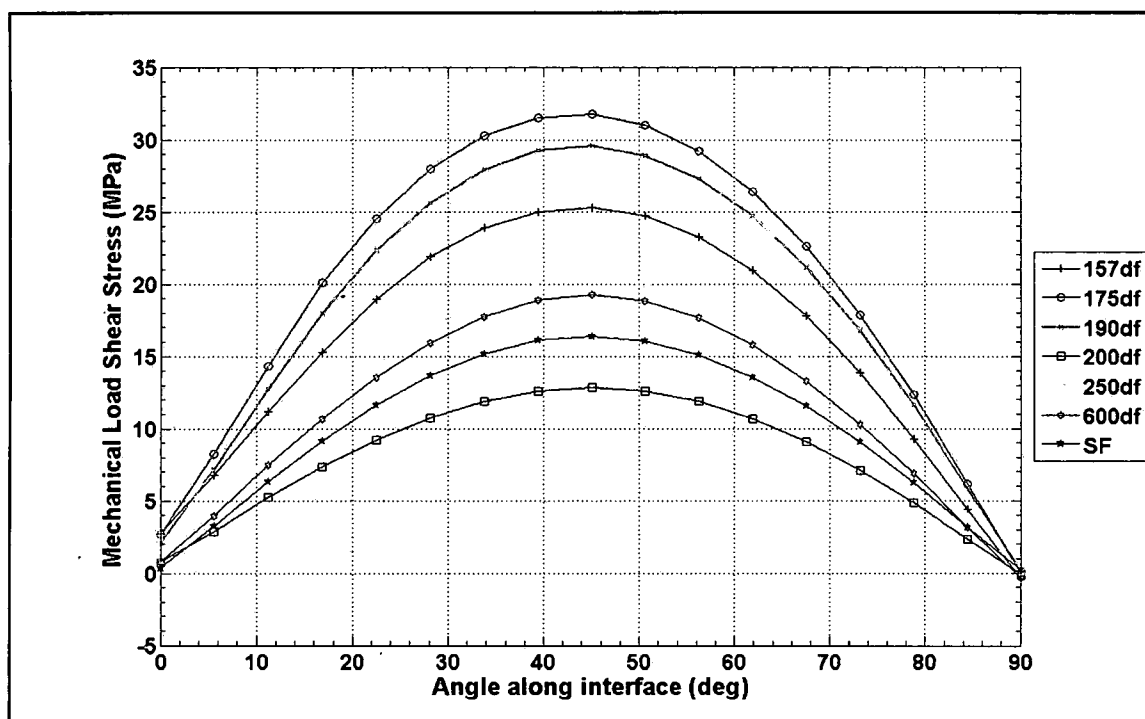


Figure 245: Shear stress distributions at the fiber-matrix interface due to the mechanical loading from $\theta = 0^\circ$ to 90°

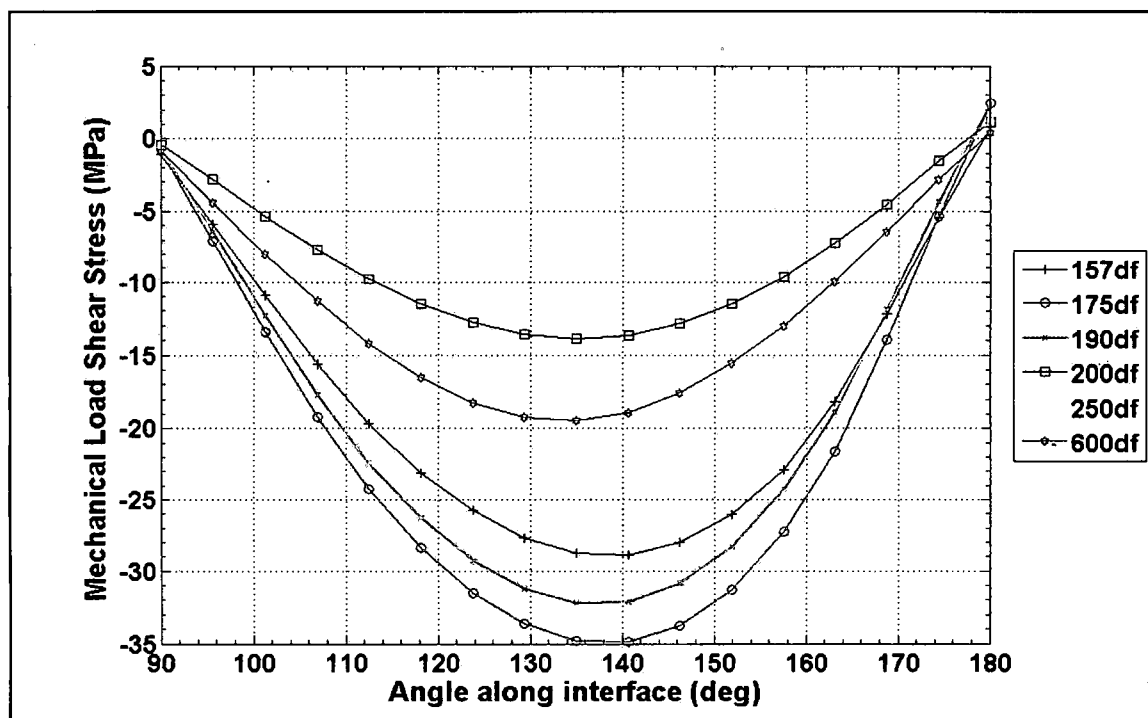


Figure 246: Shear stress distributions at the fiber-matrix interface due to the mechanical loading from $\theta = 90^\circ$ to 180°

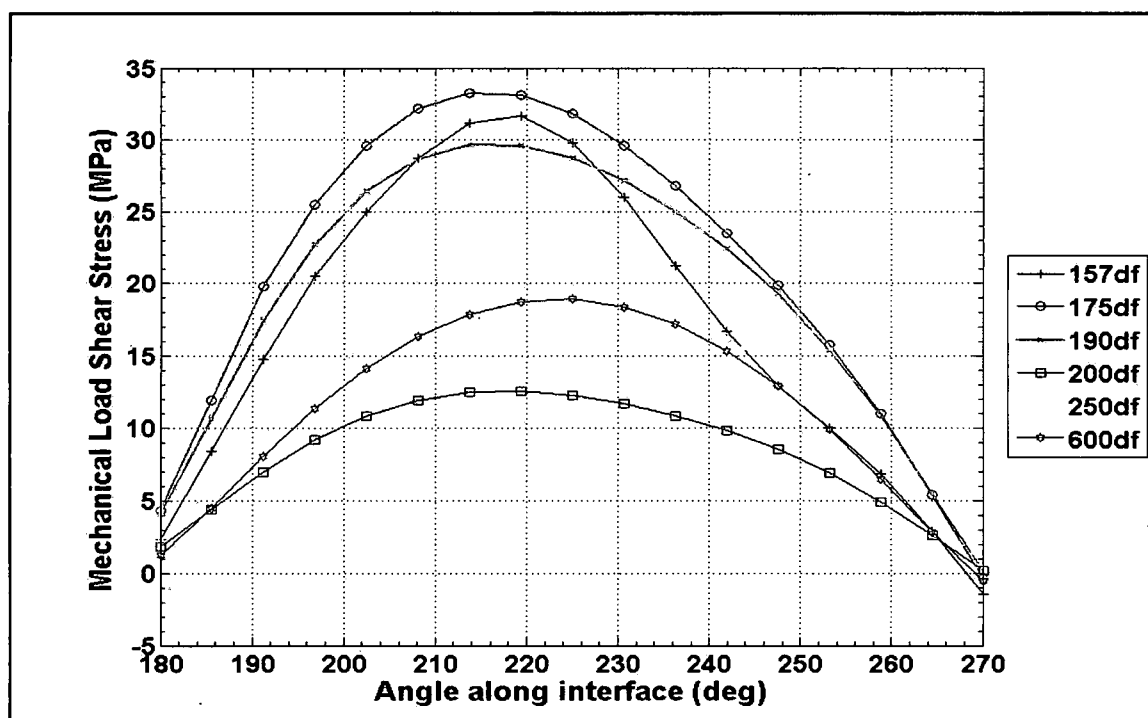


Figure 247: Shear stress distributions at the fiber-matrix interface due to the mechanical loading from $\theta = 180^\circ$ to 270°

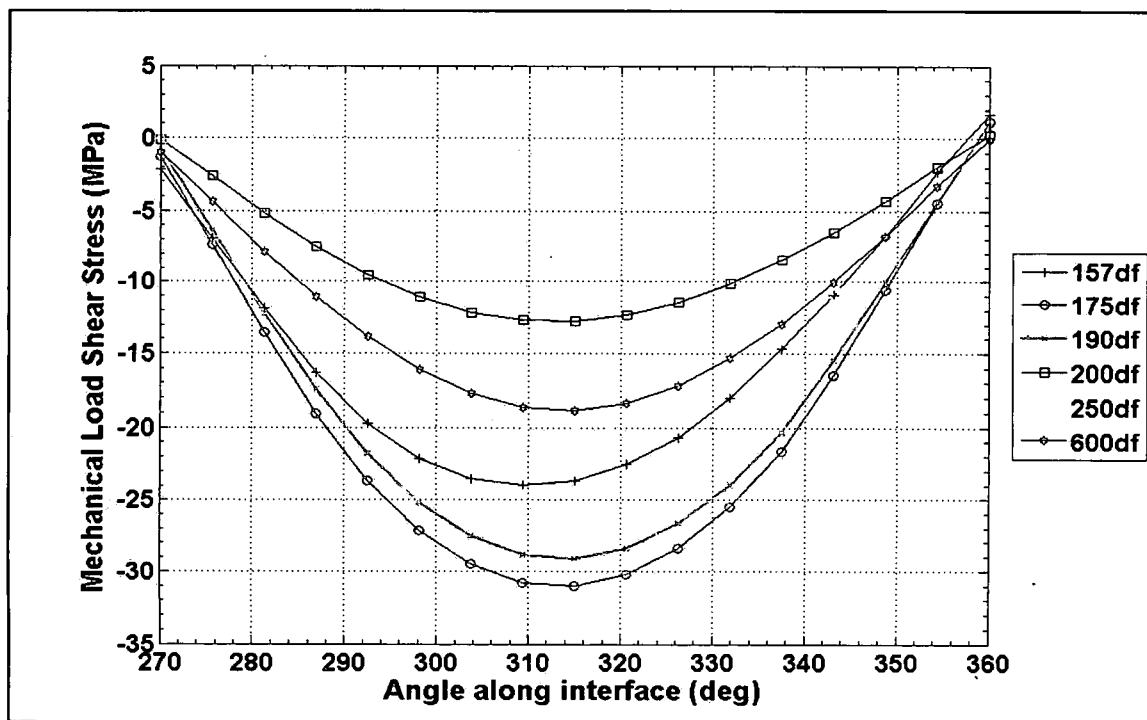


Figure 248: Shear stress distributions at the fiber-matrix interface due to the mechanical loading from $\theta = 270^\circ$ to 360°

The nearest neighbor effects are clearly revealed in the third quadrant as shown in Figure 247. The maximum magnitude locations occur at $\theta = 219.375^\circ$ for the $1.57d_f$, $2.0d_f$ and $2.5d_f$ and at $\theta = 213.75^\circ$ for the $1.75d_f$ and $1.90d_f$ fiber spacing groups. Nearest neighbor effects are also exhibited by all the fiber spacing groups in the 3rd quadrant, except the $6.0d_f$ spacing, by the asymmetrical shape of the shear stress distribution, as shown in Figure 247. The $1.57d_f$ fiber spacing exhibits the most drastic effect of the center fiber as its shear stress distribution from its maximum magnitude location at $\theta = 219.375^\circ$ to $\theta = 270^\circ$ is concave. Whereas, for the $1.75d_f$, $1.90d_f$ and $2.0d_f$ fiber spacing groups their interfacial shear stress distribution from their respective maximum magnitude locations to $\theta = 270^\circ$ exhibits a constant slope as opposed to variable change in slope in some sections of this interface region. Although the maximum magnitude location shifts for the $2.5d_f$ fiber spacing to $\theta = 219.375^\circ$ the difference at this location to the magnitude at $\theta = 225^\circ$, where the maximum magnitude would occur if no nearest neighbor effects were present, is 0.15%. Because the effect is very small the distribution at the $2.5d_f$ fiber

spacing is virtually symmetrical about the maximum location and consequently the effects from the corner fiber due to the mechanical loading can most likely be neglected. Like in the 828/D-230 matrix system the 6.0d_f fiber spacing in the 862/W matrix system has a smooth symmetrical interfacial shear stress distribution with its maximum magnitude occurring at $\theta = 225^\circ$, as shown in Figure 247, indicating no corner fiber effects.

Table 80 lists the percentage reduction of the maximum shear stress due to the residual stress from the matrix cure for all four quadrants of the corner fiber at the location of maximum shear due to the mechanical loading. From Table 80 in the 1st and 4th quadrants the impacts are relatively small and fairly close for all fiber groups, except the 2.0d_f group in the 1st quadrant, ranging from 9% to 14% and 2% to 10%. In the 1st quadrant the 2.0d_f fiber spacing group experiences a 20% impact due to the residual shear stress over the mechanical shear stress.

Table 80: Percent reduction of maximum shear stress due to residual stress from matrix cure at the location of maximum shear due to mechanical loading

Fiber Sp	1 st Quad Impact Max Shear by Residual stress	2 nd Quad Impact Max Shear by Residual stress	3 rd Quad Impact Max Shear by Residual stress	4 th Quad Impact Max Shear by Residual stress
1.57d _f	14%	31%	43%	5%
1.75d _f	9%	17%	34%	2%
1.9d _f	9%	17%	28%	3%
2.0d _f	20%	33%	40%	9%
2.5d _f	12%	16%	18%	10%
6.0d _f	10%	11%	11%	10%

In the second quadrant the impacts of the residual stresses increase considerably over the 1st and 4th quadrant, in some cases by over a factor of 2, as shown in Table 80. The largest impact the residual stresses have on the mechanical shear stress is in quadrant three as shown in Figures 239, 243 and 247 plus as depicted in Table 80. For the close fiber spacing groups, the 1.57d_f, the 1.75d_f and the 1.9d_f, the residual stresses range from almost 30% to over 40% of the shear stress due to the mechanical load. It is in this quadrant that the maximum magnitude location shifts and the interfacial distribution becomes asymmetrical for all but the 6.0d_f fiber spacing as described above. In addition the minimum shear stress magnitudes increase

underscoring the impact of the residual stresses on the overall shear stress distribution at the fiber-matrix interface of the corner fiber. Table 80 also reveals that the residual stress impact on the $6.0d_f$ fiber spacing is very consistent along the entire interface giving further credence that the fibers at this spacing are behaving as an isolated fiber having no impact with their neighboring fibers.

In summary practically no neighboring fiber effects are observed in the first quadrant due to mechanical loading only and very minor effects from neighboring fibers occur in the second and fourth quadrant, see Figure 245, 246 and 248. Nearest neighbor effects are dramatically illustrated in the third quadrant due to the mechanical loading where a shift in the maximum shear stress location occurs and the interfacial distribution changes as shown in Figure 247. The net results of the residual shear stresses on the mechanical load shear stresses are a decrease in the maximum shear magnitude, shown in Table 80, as well as a shift in their location resulting in a change of the interfacial shear stress distribution, shown by comparing Figures 237 through 240 and 245 through 248. These effects slightly increase the interface length over which the shear stress acts for quadrants one, two and four. In quadrant three, these effects decrease the length over which the shear stress acts for the $1.57d_f$, $1.75d_f$ and $1.9d_f$ fiber spacing groups but increase the length for the $2.0d_f$ and $2.5d_f$ spacing. The single fiber shows no increase along the fiber-matrix interface in which the shear stress acts. For the $6.0d_f$ fiber spacing there is either no change or practically no change of the length of fiber-matrix interface in which the shear stress acts in all four quadrants. The maximum magnitude shift along the fiber-matrix interface tends toward the direction of applied loading. This is shown quite clearly by comparing Figure 247 to 239. The $6.0d_f$ fiber spacing cruciform specimen appears to behave as isolated fibers since negligible effects from neighboring fibers are seen in Figures 237 through 248. Although the nearest neighbor effects are present, the $2.5d_f$ fiber spacing cruciform specimen can be considered as also acting as isolated fibers since the effects are very minor as shown in Figures 237 through 248.

Corner Fiber Interface Results - Summary

The residual radial and residual shear stress in general decrease the maximum magnitudes of the total radial and shear stresses for all fiber spacing groups in all four quadrants and cause a slight shift in their maximum magnitude location in quadrants 1, 2 and 4. Nearest neighbor effects in combination with residual effects impose dramatic changes in the interfacial radial and shear stress distributions in the 3rd quadrant. It appears that the residual stresses tend to increase the circumferential length over which the highest radial and shear stresses act for each fiber spacing in the 1st, 2nd and 4th quadrants. The combination of residual stresses and nearest neighbor effects has the opposite effect in the 3rd quadrant. It appears that the 6.0d_f fiber spacing group acts as an isolate fiber grouping since no nearest neighbor interaction exist in all four quadrants and its residual effects are very similar to the single fiber. Although, neighboring fiber effects begin to manifest themselves at the 2.5d_f spacing their effects are very minor such that the 2.5d_f fiber spacing groups can be considered to also act as an isolated fiber grouping.

862/W Fiber-Matrix Interface Debond Criterion Evaluation

The majority of the fiber matrix debonds occurring in the 862/W matrix system occur at the corner fiber. For the 6.0d_f fiber spacing, fiber matrix debonding was observed for all eight specimens and Table 18 lists the location of the debonds relative to the top, center and bottom fibers. It also reveals that of the eight specimens, four debond at the pole of the corner fiber exterior to the fiber group, whereas one debonds at the corner fiber in the northern hemisphere at $\theta = 54.5^\circ$. The remaining three specimens debond at the center fiber. All nine specimens at the 2.5d_f fiber spacing were observed exhibiting fiber matrix debonds and Table 20 lists their location. Eight of the nine specimens at the 2.5d_f spacing debond at the corner fiber, three internally to the fiber group and five externally. For the 1.9d_f fiber spacing, six of the nine specimen's debond was obstructed from view as explained in Chapter 2. As listed in Table 23, three of the nine specimens were directly observed exhibiting a fiber matrix debond at the corner fiber, two externally to the fiber group and one internally. At the 1.75d_f spacing Table 24 lists the location of the debonds and reveals that three of the twelve specimens were obstructed from view. All nine

specimens were observed exhibiting fiber matrix debonds, seven of the nine specimens observed debonding at the corner fiber and two debonding at the center fiber. Of the seven debonding at the corner fiber, three debonded internal to the fiber group and four debond external to the debond group. For the $1.57d_f$ fiber spacing listed in Table 26, all sixteen specimens were observed exhibiting debonds. Fourteen of the sixteen specimens debonded at the corner fiber. Of the fourteen specimens debonding at the corner fiber half debond internally and half externally to the fiber group. Although for the two latter fiber spacing groups previously mentioned there seems to be no preference to debond location relative to fiber grouping in that half, $1.57d_f$ or nearly half, $1.75d_f$, debond internal or external to the fiber group. The majority of the debonds occurring at the $6.0d_f$ and $2.5d_f$ fiber spacing groups mentioned above are externally to the fiber group; while the majority of those at the $1.9d_f$ spacing debond internally to the fiber group. Thus, the CRB090 region of the FEM at the fiber interface will be used to address the state of stress within the cruciform specimens corresponding to the observed location of the interface debonds to develop a fiber-matrix debond criterion.

The radial stress distribution along the fiber-matrix interface in the viewable area of the corner fiber from $\theta = 0^\circ$ to 90° due the combination of mechanical load and matrix cure residual stresses at $Z = 0$ is shown in Figure 249. The maximum radial stress is located at the fiber poles for all fiber spacing groups. The largest radial stresses belong to the $1.75d_f$ fiber spacing group followed by the $1.90d_f$, $1.57d_f$, $2.5d_f$, $6.0d_f$ and SF groups in decreasing order of magnitude, as shown in Figure 249. All these fiber spacing groups have exhibited fiber-matrix debonding as their first failure mechanism. The lowest radial stresses are those from the specimens that exhibited matrix cavitation, namely the $2.0d_f$ fiber spacing group. From Figure 249 the maximum magnitudes are also fairly constant for all fiber spacing groups over an approximate 20° sweep of the interface centered at the poles.

The shear stress distribution along the fiber-matrix interface in the viewable area of the corner fiber from $\theta = 0^\circ$ to 90° due to the combination of mechanical load and matrix cure residual stresses at $Z = 0$ is shown in Figure 250. The maximum magnitudes for the shear stress distribution occur at the midpoint of the fiber interface, at $\theta = 45^\circ$, for the $1.75d_f$, $1.9d_f$, $2.5d_f$, $6.0d_f$

and SF groups but are shifted slightly to $\theta = 50.625^\circ$ for the $1.57d_f$ and $2.0d_f$ fiber spacing groups. Similar to the radial stress, the $1.75d_f$ fiber spacing has the largest magnitude of all fiber spacing groups followed by the $1.90d_f$, $1.57d_f$, $2.5d_f$, $6.0d_f$ and the SF specimens in decreasing order of magnitude, as shown in Figure 250. All of these specimens exhibited fiber matrix debonding as their first failure mechanism. The lowest maximum magnitudes occur for the fiber spacing group exhibiting matrix cavitation as their first failure, specifically the $2.0d_f$ fiber spacing as shown in Figure 250. The interfacial shear stress distribution, Figure 250, also reveals that the length of fiber interface in which a relatively high shear stress acts is fairly consistent for fiber spacing groups exhibiting debonding. Although all are centered at the midpoint or close to the midpoint of the CRB090 region, the length of interface for which a relatively high shear stress acts ranges between 17° to 21° . Whereas, for the $2.0d_f$ fiber spacing the interfacial length increases to approximately 26° .

It should be noted that the debonds extend over into the 2nd and 3rd quadrant of the corner fiber but are not visible. The analysis indicates that the magnitude of the interfacial radial and shear stresses in the 2nd quadrant are virtually equal to those in the 1st quadrant indicating a nearly symmetrical debond. However, in the 3rd quadrant the nearest neighboring fiber effects are more pronounced as the fiber spacing decreases. These effects tend to shift the stress distribution toward the fiber pole especially for the shear stress. This could create an unsymmetrical debond.

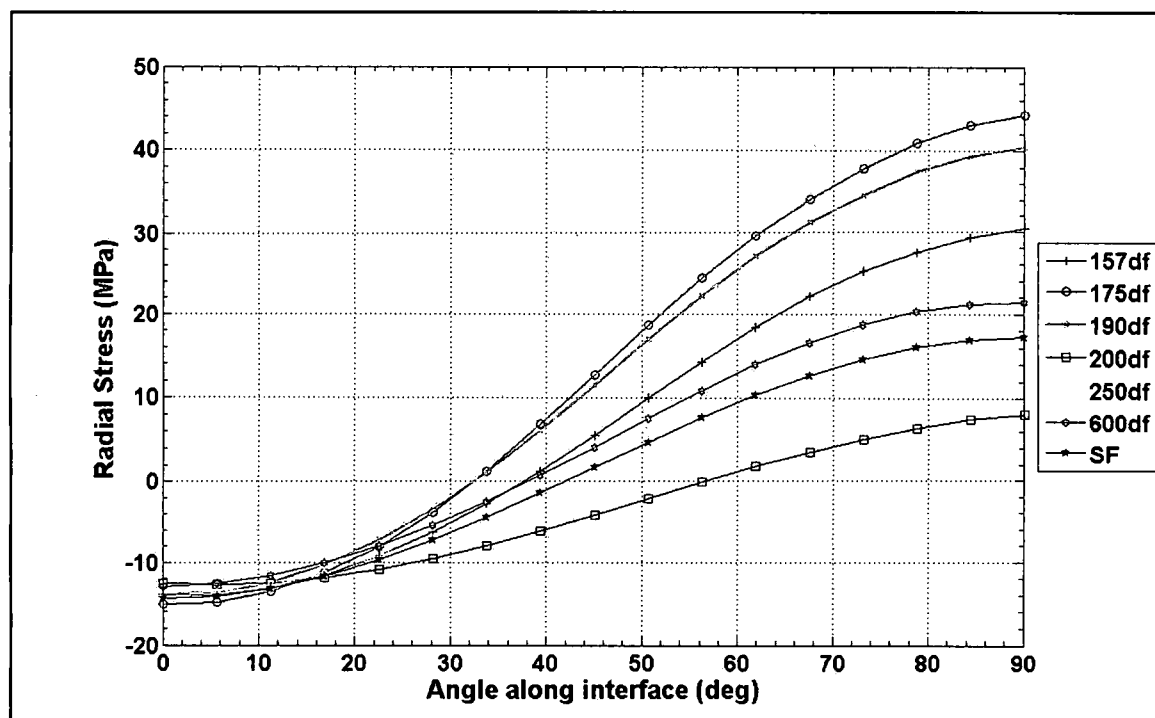


Figure 249: Radial stress distributions along the corner fiber-matrix interface from $\theta = 0^\circ$ to 90° at $Z = 0$ due to the combination of mechanical loading and matrix residual stresses

Although all of the 6.0d_f fiber spacing group specimens debonded, of the four specimens debonding at the pole of the corner fiber only three were observed with the high magnification camera and were used for debond measurements. One specimen debonded at the pole of the top corner fiber but its initiation was observed with the far-field camera without sufficient resolution thus making debond measurements practically impossible. The other three specimens debonded either in the northern or southern hemisphere of the fiber. The observed fiber matrix debonds average an instantaneous debond width of approximately 0.039 mm making a central angle of 78° creating an arc length of 0.24 mm, which debonds about 20% of the total fiber circumference. Over this same interfacial distance the 6.0d_f fiber spacing experiences an average radial stress of 16.36 MPa or 76% of the maximum magnitude, according to the interfacial radial stress distribution shown in Figure 249. Likewise, the average shear stress over the debonded interface is approximately 57% of the maximum shear stress magnitude or about 9.86 MPa, as shown in the interfacial shear stress distribution of Figure 250. At the debond limit of $\theta = 51^\circ$ the

radial stress is 7.83 MPa or 37% of its maximum, whereas the shear stress is 16.94 MPa or 98% of its maximum. Consequently, the average debond arc length for the 6.0d_f fiber spacing debonds a length of fiber interface, from $\theta = 90^\circ$ to 51° in the first quadrant of the corner fiber, that has the largest magnitude of radial stress and a substantial amount of shear stress present contributing to the fiber matrix debond.

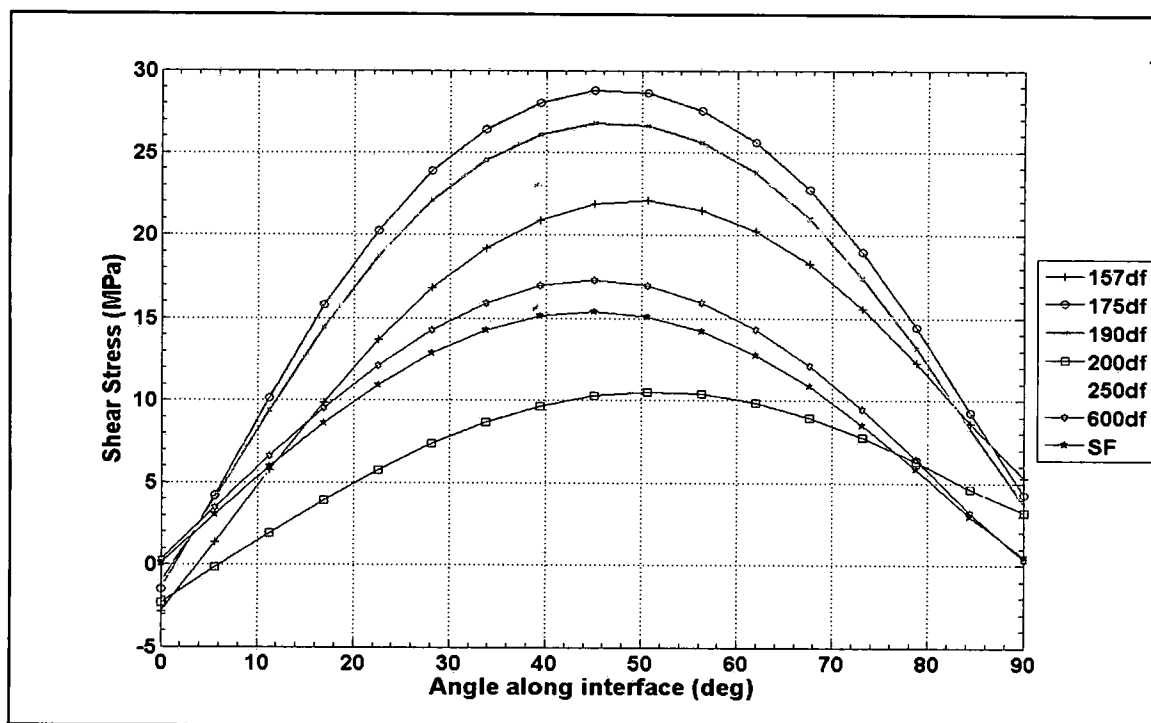


Figure 250: Shear stress distributions along the corner fiber-matrix interface from $\theta = 0^\circ$ to 90° at $Z = 0$ due to the combination of mechanical loading and matrix residual stresses

At the 2.5d_f fiber spacing all nine specimens were observed exhibiting fiber matrix debonding as their first failure mechanism. Eight of the nine were in full view and thus debond measurements could be taken, while in one specimen the top back fiber was observed, due to misalignment, thus the debond limits were not obtainable. Only three of the eight observed debonds was instantaneous while the others were spot debonds slowly propagating at final failure. All debonds occurred at the pole of the fibers. The observed average debond width was measured to be 0.037 mm making a central angle of 76° thus debonding an arc length along the

interface of 0.24 mm. Over this interfacial debond arc length the average radial stress exhibited by the applied load is 16.74 MPa or approximately 73% of the maximum radial stress as shown in Figure 249. The corresponding shear stress experienced over the interfacial debond length is 11.41 MPa or about 64% of the maximum shear stress magnitude, as shown in Figure 250. At the debond limits of $\theta = 52^\circ$, figure 249 shows that the radial stress is 7.75 MPa which is 34% of the maximum, while Figure 250 shows the shear stress is 99% of its maximum being 17.71 MPa. As a result, over the observed fiber matrix debond limits, from $\theta = 90^\circ$ to 52° in the first quadrant of the corner fiber, the radial stress ranges from its maximum magnitude to approximately 64% of its maximum while the shear stress reaches 64% of its maximum magnitude. Therefore, the debond occurs over an interfacial length having the largest magnitudes of radial stress and a considerable amount of shear stress causing the fiber matrix debond failure initiation.

For the $1.9d_f$ fiber spacing group, all eight specimens exhibited fiber matrix debonds, however, only three were visible. Of the three visible debonds, one was obstructed, one debonded in the southern hemisphere of the bottom corner fiber and the third debonded north pole of the bottom corner fiber. Consequently, only one debond measurement could be made, which resulted in a debond width of 0.041 mm. This translates into a central angle of 80° making an arc length of 0.25 mm. although using only one data point, the debond traverses an interface arc length experiencing an average radial stress of approximately 29.47 MPa, according to Figure 249, which is about 73% of the maximum radial stress magnitude. Likewise the average shear stress is about 18.47 MPa, as shown in Figure 250, which is approximately 69% of the maximum shear stress magnitude. At the debond limit of $\theta = 50^\circ$ the radial stress is 16.34 MPa or 40% of the maximum value, as shown in Figure 249, while the shear stress is 26.66 MPa or about 99% of the maximum shear stress, as shown in Figure 250. Thus, the $1.9d_f$ fiber spacing group debond limit of $\theta = 90^\circ$ to 50° in the first quadrant of the corner fiber, experiences a radial stress over the debond length ranging from its maximum magnitude to 40% of its maximum while the shear stress reaches 99% of its maximum magnitude. As a result, the $1.9d_f$ fiber spacing, like the $6.0d_f$ and the $2.5d_f$ fiber spacing group, experiences considerable combination of radial and shear stress contributing to the fiber matrix debond initiation.

The 1.75d_f fiber spacing group exhibited fiber matrix debond in all twelve specimens but only nine were directly observable due to the others being obstructed. Of the nine observed debonds five occurred at the fiber pole and four of those five debonded instantaneously across the field of view. The other was a spot debond that slowly propagated along the fiber achieving a length of about 0.053 mm at final failure. The average debond width measured for the five debonds occurring at the fiber pole is 0.068 mm. This translates into a central angle of 104° making an arc length of 0.32 mm. Over this debonded interfacial length the average radial stress is approximately 27.08 MPa which is about 61% of the maximum magnitude as shown in Figure 249. Whereas, the average shear stress over the debond length is about 21.45 MPa corresponding to approximately 75% of the maximum magnitude according to Figure 250. The radial stress at the debond limit of $\theta = 38^\circ$ is 5.47 MPa, as shown in Figure 249, and encompasses about 90% of the tensile radial stress exhibited at the fiber interface due to the applied load at failure initiation. The shear stress is 27.64 MPa at the debond limit as shown in Figure 250 and encompasses approximately 64% of the shear stress imparted at the interface by the applied load at failure initiation. Like the other fiber spacing groups exhibiting fiber matrix debonds, the 1.75d_f spacing experiences the majority of the radial stress and a large shear stress component acting along the debond limits of $\theta = 90^\circ$ to 38° in the first quadrant of the corner fiber, contributing to the fiber debonding observed experimentally.

Lastly the 1.57d_f fiber spacing group of the multi-fiber cruciform specimens is no different than the other specimens exhibiting fiber matrix debond as their first failure mechanism in that it experiences a large majority of the radial and shear stress over its debond length. All 16 specimens debonded at the fiber pole and 13 were directly observed. The average debond width is 0.049 mm creating a central angle of 88° making an arc length of 0.27 mm. The average radial stress experienced over the debond length, as shown in Figure 249, is 20.37 MPa or about 67% of the maximum radial stress magnitude. The average shear stress over the debond length shown in Figure 250 is 16.2 MPa or about 73% of the maximum shear stress. At the debond limit of $\theta = 46^\circ$ the radial stress equates to 6.36 MPa and encompasses over 83% of the tensile radial

stress imparted by the load at first failure. While the shear stress is 21.87 MPa, it encompasses over 59% of the shear stress imparted by the loading along the debond length.

The SF also exhibited fiber matrix debonding as its first failure mechanism and all six specimens debonded with three at the fiber pole, two in the southern hemisphere and one in the northern hemisphere. The average debond measurement at the fiber pole is 0.023 mm that creates a central angle of 54° making an arc length of 0.17 mm. Over this debond length the average radial stress at the fiber interface is approximately 14.77 MPa or about 86% of the maximum radial stress. The average shear stress over the debond length is about 6.85 MPa or approximately 44% of the maximum shear stress magnitude. At the debond limit of $\theta = 63^\circ$ the radial stress is approximately 10.87 MPa or 63% of the maximum magnitude and encompasses 56% of all tensile radial stress at the interface imparted by the failure initiation load. Likewise the shear stress at the debond limit is about 12.39 MPa which is approximately 80% of the maximum. Therefore, the SF specimen debond limit of $\theta = 90^\circ$ to 63° in the first quadrant of the fiber encompasses the largest portion of the radial stress acting along the interface as well as reaching 80% of the maximum shear stress. Consequently, a radial stress and shear stress interact to create the fiber matrix debond observed in the single fiber cruciform specimens.

In summary, each fiber spacing group experienced interfacial debonds over that part of the fiber exhibiting high magnitudes of radial stress. Furthermore, the debond length covers portions of the fiber interface where the shear stress either reaches its maximum or its average magnitude is a significant percentage of the maximum magnitude. Table 81 lists the average debond measurements for the fiber spacing groups exhibiting fiber matrix debonding as their failure initiation. The debond measurements were made in the same manner as discussed above. The $1.57d_f$, $1.75d_f$, $1.9d_f$, $2.5d_f$ and the $6.0d_f$ debond limits cover 23%, 27%, 21%, 20% and 20% of the total fiber circumference respectively. These results lead to the conclusion that an interaction between the radial and shear stress acting at the fiber matrix interface contribute to the debond observed in the cruciform experiments.

Table 81: Experimental fiber matrix debond measurements

Spec.	Average Debond Width, mm (Std dev)	Average Debond Central angle	Experimental Debond Limits	Arc Length, mm	% circumference
1.57d _f	0.049 (0.024)	88°	46° to 134° NP 226° to 314° SP	0.27	23
1.75d _f	0.068 (0.041)	104°	38° to 142° NP 218° to 322° SP	0.32	27
1.9d _f	0.041 (0.041)	80°	50° to 130° NP 230° to 310° SP	0.25	21
2.5d _f	0.037 (0.021)	76°	52° to 128° NP 232° to 308° SP	0.24	20
6.0d _f	0.039 (0.0012)	78°	51° to 129° NP 231° to 309° SP	0.24	20
SF	0.023 (0.007)	54°	63° to 117° NP 243° to 297° SP	0.17	14

Analysis of the 828/D-230 1.9d_f and 2.0d_f Fiber Spacing Group Behavior

Nanoindentation Study

The 1.9d_f and 2.0d_f fiber spacing groups have the highest radial and shear stress magnitudes of all the fiber spacing groups tested. Based on the parametric study results given in Appendix C, these two fiber groups should fall between the 1.57d_f and the 2.5d_f fiber spacing groups radial and shear stress distribution since they exhibited the same fiber-matrix debond failure initiation mechanism. However, they have the highest far-field stress at failure initiation of all multi-fiber cruciform specimens that initiated failure as a fiber-matrix debond. In an effort to explain this behavior, nanoindentation tests were performed on the specimens having the 1.57d_f, 1.9d_f, 2.0d_f and 2.5d_f fiber spacing to see if any interphase was formed. As mentioned earlier the 1.9d_f and 2.0d_f spacing have the largest magnitude of the interfacial radial and shear stress of all specimens tested in the 828/D-230 matrix system. Comparing the 1.9d_f and 2.0d_f to the 1.57d_f and 2.5d_f nanoindentation results would show deviations of the material properties between the specimens closest to their spacing exhibiting the same failure mode. An interphase around the fibers could exist due to fiber surface chemical reactions with the matrix. The interphase material could have very different material properties than those of the neat resin and could explain the

behavior of the 1.9d_f and 2.0d_f fiber spacing groups. The nanoindentation tests used a Nano Indentor[®] XP (MTS NanoInstruments, Oak Ridge, TN) with a Berkovich (three-sided pyramidal) indenter. A continuous stiffness measurement that involved a series of loading and unloading cycles was conducted until the final indentation depth was achieved, generating a series of hardness and modulus values as a function of indentation depth. Nanoindentation tests were first performed on fused silica for tip calibration and the modulus, 70-72 GPa, was used as an internal reference. Indentations were made from the fiber-matrix interface outward toward the matrix in a spiral pattern to void overlapping of plastic deformation zones onto neighboring. Twelve equally spaced spiral patterns were made around the circumference of the fiber. A 500 nm indentation depth was used with spacing between adjacent indents of 8, 14, 20, 30, 40, 50, 60, 75, and 90 micrometer. Figure 251 shows the spiral patterns and indentation spacing of nanoindentation tests for the 1.9d_f fiber spacing cruciform specimen. The average modulus was averaged from twelve indents for each fiber spacing group.

Nanoindentation tests were done on the 1.57d_f, 1.90d_f, 2.0d_f and 2.5d_f fiber spacing cruciform specimens to measure the modulus of the matrix. Table 82 lists the test results of 9 individual nanoindentation tests on each specimen measuring the modulus of the matrix as a function of distance from the interface. Test results confirmed no interphase regions around the fiber had formed and that all four cruciform specimens had similar modulus values for the matrix. Fiber spacing measurements were also done for each specimen and revealed slight variation in the fiber spacing but not enough to explain the relatively high radial and shear stress magnitudes.

Table 82: Nanoindentation Modulus Results

Distance from Interface (μm)	Modulus (MPa)			
	157d _f	190d _f	200d _f	250d _f
8	3.708	3.644	3.738	3.849
14	3.658	3.619	3.749	3.838
20	3.657	3.642	3.709	3.838
30	3.649	-	3.692	3.853
40	3.610	3.641	3.695	3.803
50	3.613	3.702	3.672	3.825
60	3.587	3.683	3.654	3.795
75	3.613	3.647	3.697	3.743
90	3.603	3.616	3.694	3.796
AVG	3.635	3.649	3.700	3.816

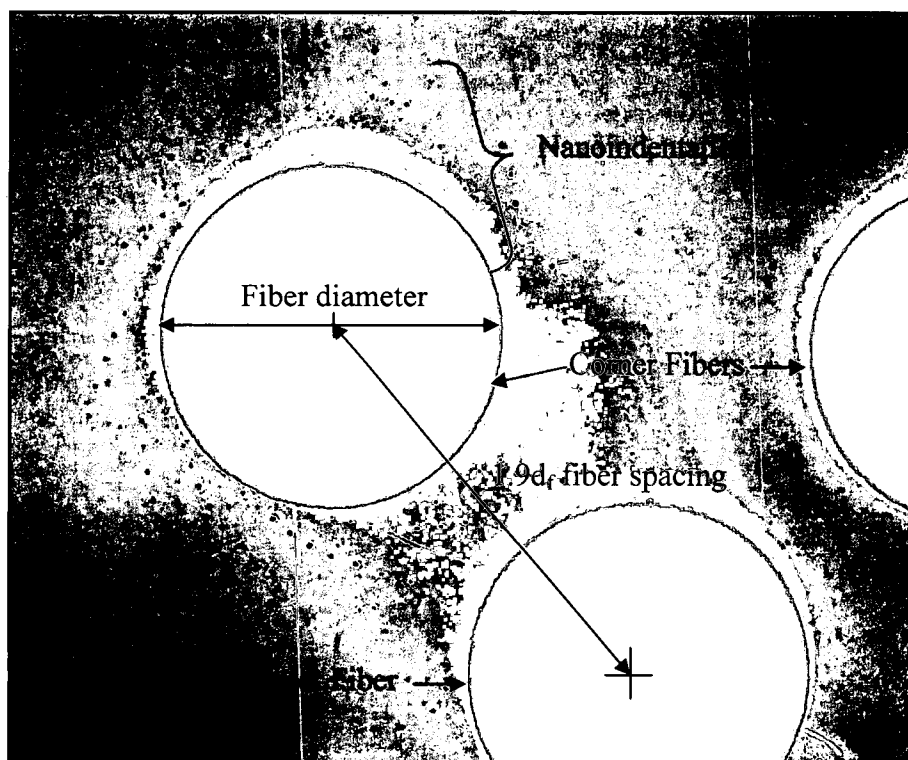


Figure 251: Photomicrograph of nanoindentation pattern for the 1.9d_f fiber spacing cruciform specimen

Additional Cruciform Specimen Testing at the 1.9d_f and 2.0d_f Fiber Spacing

Five additional specimens each were made at the 1.9d_f and 2.0d_f fiber spacing and tested. In all cases at both fiber spacing groups the failure initiation was fiber-matrix debonding. Table 83 lists the average far-field stress at first damage for the additional tests, designated S190R1C1XX and S200R1C1XX, along with the average far-field stress of the original test matrix for the 1.90d_f and 2.0d_f fiber spacing groups. The difference between the average of additional tests and the original tests is less than 1.0 MPa in both cases. With the 828/D-230 matrix being a linearly elastic material the FEM results will not be significantly different between the old and new tests for both fiber spacing groups. Consequently no errors were made in making and preparing the specimens and no significant resin material batch differences exist.

Table 83: Average far-field applied stress for the additional specimens and the original specimens at the 1.9d_f and 2.0d_f fiber spacing

Specimen	Avg Far-field Stress at debond initiation (MPa)	Specimen	Avg Far-field Stress at debond initiation (MPa)
S190R1C1-AA	15.75	S200R1C1-AA	16.65
S190R1C1-BB	16.56	S200R1C1-BB	16.86
S190R1C1-CC	15.16	S200R1C1-CC	10.55
S190R1C1-DD	15.33	S200R1C1-DD	17.38
S190R1C1-EE	14.57	S200R1C1-EE	18.56
AVG	15.47	AVG	16.00
S190R1C1-G	13.24	S200R1C1-A	18.19
S190R1C1-H	14.47	S200R1C1-B	12.48
S190R1C1-I	14.97	S200R1C1-C	16.80
S190R1C1-J	16.89	S200R1C1-D	18.32
S190R1C1-K	16.57	S200R1C1-E	12.14
S190R1C1-L	18.25	S200R1C1-F	13.21
S190R1C1-M	18.81	S200R1C1-G	13.12
S190R1C1-N	15.51	S200R1C1-H	14.85
S190R1C1-O	16.60	S200R1C1-I	-
S190R1C1-P	18.48	S200R1C1-J	21.86
AVG	16.38	AVG	15.66
Δ	0.91	Δ	0.34

Failure Initiation Stress State Analysis

Table 84 lists the stress concentration factor (SCF) of center fiber for all fiber spacing groups tested for the radial and shear stress located at $\theta = 90^\circ$ and 45° , respectively, on the interface. The SCF is the ratio of the FEM results for the maximum interfacial radial and shear stress at their respective location to the applied far-field stress. The radial SCF for the 1.9d_f and 2.0d_f are only slightly above those of the 1.57d_f and 2.5d_f not indicative of the large difference in the actual stress magnitudes. Likewise, the shear SCF for the 1.9d_f and 2.0d_f are equal and very close to the other fiber spacing groups. Recall that the 1.75d_f and 1.84d_f specimen exhibited matrix cavitation as their first failure mechanism.

Table 84: Center fiber radial and shear SCF for all fiber spacing groups tested where FF is defined as Far-Field

Specimen	FF Stress at 1 st failure	Max Radial Stress At $\theta = 90^\circ$	Radial SCF	Max Shear Stress At $\theta = 45^\circ$	Shear SCF
S157R1C1	8.29	14.58	1.8	11.32	1.4
S175R1C1	4.67	9.04	1.9	7.54	1.6
S184R1C1	3.97	7.65	1.9	5.91	1.5
S190R1C1	16.38	39.25	2.4	25.29	1.5
S200R1C1	15.66	40.66	2.6	24.25	1.5
S250R1C1	6.58	13.34	2.0	7.74	1.2
S600R1C1	10.7	15.27	1.5	9.75	0.9

Table 85 lists the radial and shear SCF in the first quadrant of the corner fiber for all fiber spacing groups tested. Similar to the center fiber SCF, the corner fiber radial and shear SCF for the 1.9d_r and 2.0d_r are only slightly larger than the other fiber spacing groups. It should be noted that the calculated maximum radial and shear stress for the 1.9d_r and 2.0d_r are very close to the SF, although their respective SCF are slightly different. The interfacial radial and shear distribution are also practically the same as shown in the first quadrant of the corner fiber, see Figures 193 and 205. The SCF results for the other quadrants of the corner fiber are very similar to the first quadrant.

Table 85: Corner fiber radial and shear SCF for all fiber spacing groups tested

Specimen	FF Stress at 1 st failure	Max Radial Stress At $\theta = 90^\circ$	Radial SCF	Max Shear Stress At $\theta = 45^\circ$	Shear SCF
S157R1C1	8.29	28.3	3.4	15.85	1.9
S175R1C1	4.67	15.10	3.2	9.0	1.9
S184R1C1	3.97	12.24	3.1	7.57	1.9
S190R1C1	16.38	60.36	3.7	32.18	2.0
S200R1C1	15.66	59.65	3.8	31.84	2.0
S250R1C1	6.58	17.28	2.6	10.32	1.6
S600R1C1	10.7	16.32	1.5	9.78	0.9
SF	20.43	56.57	2.8	31.93	1.6

The experimental results show that for the 1.9d_r spacing, 9 of 10 specimens debond initiated at the corner fiber and in 4 of the 9 they debonded at the north pole. For the 2.0d_r spacing, 7 of 9 specimens debond initiated at the corner fiber and 4 of the 7 debonded at the north pole. Both fiber spacing groups exhibited multiple debonds with the far-field stress of each

debond being fairly close together. Furthermore the time to final failure was shortly after the final observed debond.

Cruciform Specimen Thickness Parametric Study

According to the parametric study discussed in Appendix C, the thickness of the specimen had little influence on the radial and shear SCF at the corner fiber for the multi-fiber cruciform cases analyzed. In this study the specimen thickness was held constant while the fiber spacing varied. This in turn changes the distance between the specimen free edge and the fiber. For the cases studied this distance ranged from 1.9182 mm for the $1.57d_f$ spacing to 0.0636 mm for the $12d_f$ spacing. However, specimen thickness has a rather large influence on the radial and shear SCF of a single fiber specimen. It was shown that decreasing thickness increases the radial and shear SCF and the distances ranged from 0.3972 mm to 2.0282 mm in this analysis. For the SF study, the radial and shear SCF increased by 80% with a specimen thickness decrease of 56%. The actual average specimen thickness for the single fiber cruciform specimens tested is 2.3 mm while the averages for the $1.9d_f$ and $2.0d_f$ cruciform specimens are 1.87 mm and 1.81 mm respectively.

Summary

828/D-230 Matrix system interfacial stress results

The $6.0d_f$ fiber spacing behaves as if the fibers were isolated from each other showing no signs of interaction from its neighboring fiber due to the mechanical or residual loads. Nearest neighboring fiber effects begin to manifest themselves due to the residual stress and to a lesser extent from the mechanical loading at the $2.5d_f$ fiber spacing. These effects have minimal impact, i.e. the magnitudes of the stresses are very low thus the $2.5d_f$ spacing can also be considered as acting as isolated fibers. From the $2.5d_f$ spacing the interaction of neighboring fiber impacts increase as the fiber spacing decreases in the quadrants where the fibers are closest together.

The largest impacts are centered at $\theta = 45^\circ$ for the center fiber and in the 3rd quadrant at $\theta = 225^\circ$ for the corner fiber. The effects are shown in the radial stress distribution as a wave and in the shear stress distribution as a shift in the location of the maximum magnitude as well as a dip in the distribution at around $\theta = 230^\circ$ to 260° . In the 2nd and 3rd quadrants of the corner fiber neighboring fiber effects are minimal and practically nonexistent in the 1st quadrant of the corner fiber. The single fiber results, shown in the first quadrant of the corner fiber results for reasons previously explained, show a constant compressive radial stress and a near constant shear stress distribution due to the matrix cure shrinkage loading. It exhibits typical radial and shear stress distribution and maximum magnitude locations, i.e. at $\theta = 90^\circ$ for the radial stress and $\theta = 45^\circ$ for the shear stress. Lastly, the corner fiber exhibits higher magnitudes of the radial and shear stresses than does the center fiber because the corner sheds load from the center fiber as the applied load propagates through the bulk matrix of the specimen.

862/W Matrix system interfacial stress results

The 6.0d_f and 2.5d_f fiber spacing groups behave like their counter parts in the 828/D-230 matrix system. Just like in the 828/D-230 system, the corner fiber exhibits higher magnitudes of the radial and shear stresses than does the center fiber because the corner sheds load from the center fiber as the applied load propagates through the bulk matrix of the specimen. However, that is where the similarities end. For the center fiber it appears that the residual stress due to the matrix cure pushes the maximum shear stresses on the fiber-matrix interface toward the direction of applied load. The maximum shear stresses due to the combined effects occur along the fiber-matrix interface and happen to be about where the radial stresses have their minimum magnitudes due to the combined effects for the 1.57d_f, 1.75d_f, 1.9d_f and 2.0d_f fiber spacing groups. Since the 1.57d_f, 1.75d_f and the 1.9d_f fiber spacing groups exhibit fiber-matrix debonding as the first failure mechanism it could be surmised that the interfacial radial and shear stresses interact for the debond to occur. At the corner fiber, the residual radial and residual shear stress in general decrease the maximum magnitudes of the total radial and shear stresses for all fiber spacing groups in all four quadrants and cause a slight shift in their maximum magnitude location

in quadrants 1, 2 and 4. Nearest neighbor effects in combination with residual effects impose dramatic changes in the interfacial radial and shear stress distributions in the 3rd quadrant. It appears that the residual stresses tend to increase the circumferential length over which the highest radial and shear stresses act for each fiber spacing in the 1st, 2nd and 4th quadrants. The combination of residual stresses and nearest neighbor effects has the opposite effect in the 3rd quadrant.

Fiber-Matrix Interfacial Debond Criterion Evaluation results

A thorough evaluation of the fiber-matrix interfacial debond criterion, for both matrix systems, indicate that an interaction exists between the radial and shear stresses to initiate a debond. In all cases at fiber spacings that exhibited debonding as their failure initiation, the debond arc length covered that section of the fiber interface experiencing the highest interfacial radial stress and a large percentage or up to the maximum shear stress.

Analysis of the 828/D-230 1.9d_f and 2.0d_f Fiber Spacing Group Behavior results

The nanoindentation results show no interphase exists and that the modulus of the matrix system for the 1.9d_f and 2.0d_f groups is the same as the 1.57d_f and 2.5d_f groups. Test results from the five additional specimens at each fiber spacing show no significant difference in the far-field stress over the original group. This indicates that no mistakes in the matrix formulation were made in the original group and that no errors in the testing were made as well. Additionally, the SCF for both the corner and center fibers are only slightly above the other fiber spacing groups indicating that the analysis is correct. Lastly the parametric studies show that radial and shear SCF for the multi-fiber cruciform are not sensitive to specimen thickness but that the radial and shear SCF for the single fiber are sensitive to changes in specimen thickness. Therefore, it is likely that the 1.9d_f and 2.0d_f fiber spacing is an optimum spacing where the fiber group acts more as a single unit much like the single fiber specimen. This is collaborated by the radial and shear stress distributions of the 1.9d_f and 2.0d_f fiber spacing groups being practically the same as the

single fiber. At these two spacing the applied load is efficiently spread to the fibers allowing the fiber group to effectively carry higher loads thus higher far-field stresses.

APPENDIX E

FIBER – MATRIX DEBOND AND MATRIX FAILURE CRITERIA EVALUATION

Chapter 4 proposed that two debond criteria involving the interaction between the radial and shear stresses, a quadratic interaction criteria and linear interaction criteria, could predict the fiber-matrix debond initiation. Chapter 4 also proposed two matrix failure criteria, a Modified Tresca criterion and the Mohr-Coulomb criterion, which could predict matrix cavitation. The failure criteria describing the fiber-matrix debond initiation and the matrix cavitation within the field of view was presented in Chapter 4. This Appendix thoroughly evaluates and discusses the aforementioned criteria in the portions of the cruciform specimen either partially or completely obstructed from view. In addition, revisions to the matrix failure criterion in the 828/D-230 system discussed in Chapter 4 are thoroughly evaluated. Furthermore, the fiber-matrix debond criterion evaluated at the location of the debond initiation for the 862/W matrix system is also presented to choose which one best predicts the experimentally observed results.

828/D-230 Fiber-Matrix Debond Criterion Evaluation

Quadratic Debond Criterion

As mentioned in Chapter 3, the debond criterion most cited in the literature is a quadratic interaction between the normal and shear stress at the fiber-matrix interface. The criterion shown in equation (1) is the squared ratio of the normal and shear stresses at the interface to their respective failure stresses under tension and shear alone. The constant C in equation (1) is usually 1 and when evaluated to be greater than 1, the criterion predicts debonding.

$$A \left(\frac{\sigma_r}{\sigma_{yt}} \right)^2 + B \left(\frac{\tau_{r\theta}}{\tau_y} \right)^2 \geq C \quad (1)$$

Where σ_{yt} is the tensile strength and τ_y is the shear strength determined by neat resin tensile tests and torsion tests, respectively, and σ_r and $\tau_{r\theta}$ are the interfacial radial stress and shear stress, respectively, determined by the cruciform FEA. The constants A and B are curve fitting parameters and can be considered proportional to the adhesion properties of the matrix in tension, or normal to the fiber, and shear respectively.

Linear Debond Criterion

Previously mentioned in Chapter 4, most linear debond criterion cited in the literature involve predicting the normal or shear debond initiation stress by applying a SCF to the applied far field stress. In some cases it is summed with the particular residual stress component, either the radial or shear residual stress. The linear forms only address one stress state and not any interaction of stresses most likely occurring in the multi-fiber cruciform fiber-matrix debond initiation case when loaded transverse to the fiber direction. Thus a linear version of equation 1 is introduced to capture the interaction between the radial stress and shear stress present at the fiber matrix interface when the applied load is transverse to the direction of the fibers. Furthermore, a linear version will also capture the compressive stress present at fiber equator along the fiber matrix interface as opposed to equation 1. The proposed linear debond criterion is shown by equation 2:

$$A \left(\frac{\sigma_r}{\sigma_{yt}} \right) + B \left(\frac{\tau_{r\theta}}{\tau_y} \right) \geq C \quad (2)$$

where σ_r and $\tau_{r\theta}$ are the interfacial radial and shear stress, respectively, determined from the cruciform FEA and σ_{yt} and τ_y are the tensile and shear strengths respectively, determined from

the neat resin test results. The constants A and B are curve fitting parameters and can be considered proportional to the adhesion properties of the matrix just as for equation (1) previously mentioned. Like equation (1), the constant C is usually 1 and when equation (2) is evaluated to be greater than 1 a fiber matrix debond is predicted.

Quadratic vs. Linear Debond Criterion Evaluation in the 2nd and 3rd Quadrants of the Corner Fiber

The second and third quadrants of the corner fiber provide further examination for evaluation of the two proposed fiber-matrix debond criteria. Table 86 lists the Quadratic and Linear Debond Criterion comparison for the 2nd quadrant of the corner fiber at the location of debonds initiation at $Z = 0$, or at the center of the cruciform specimen. Figures 252 and 253 show the debond criteria distribution for the Quadratic Debond Criterion and the Linear Debond Criterion, respectively, at $Z = 0$ in the 2nd quadrant of the corner fiber. The results for the 2nd quadrant are similar to the 1st quadrant except that the Quadratic Debond Criterion predicts the results better for the $1.57d_f$ spacing instead of the Linear Criterion, as shown in Table 86. The rest of the fiber spacing groups are following the trends established in the 1st and 4th quadrants as far as accuracy in predicting the fiber matrix debonds between the Quadratic and Linear Debond Criteria are concerned. In addition, the $1.75d_f$ and $1.84d_f$ are also following the trend of having the smallest debond criteria evaluation for both proposed criteria just like that shown in 1st and 4th quadrants. The Linear Debond Criterion is again more constant than the Quadratic Debond Criterion in predicting the debond limits for the fiber spacing groups as discussed above.

Table 86: Comparison of the fiber matrix debond limits predicted by the Quadratic and Linear Debond Criterion for the 2nd quadrant of the corner fiber

Fiber Spacing	Exp db Limits (deg)	Quadratic db Criterion limits (deg)	% Δ	Linear db Criterion limits (deg)	% Δ
1.57d _f	135.5	132	7.7	143	16.5
1.9d _f	148	147	1.7	154	10.3
2.0d _f	145	147	3.6	154	16.4
2.5d _f	113.5	107	27.7	119	23.4
6.0d _f	114	100	58.3	113	4.2

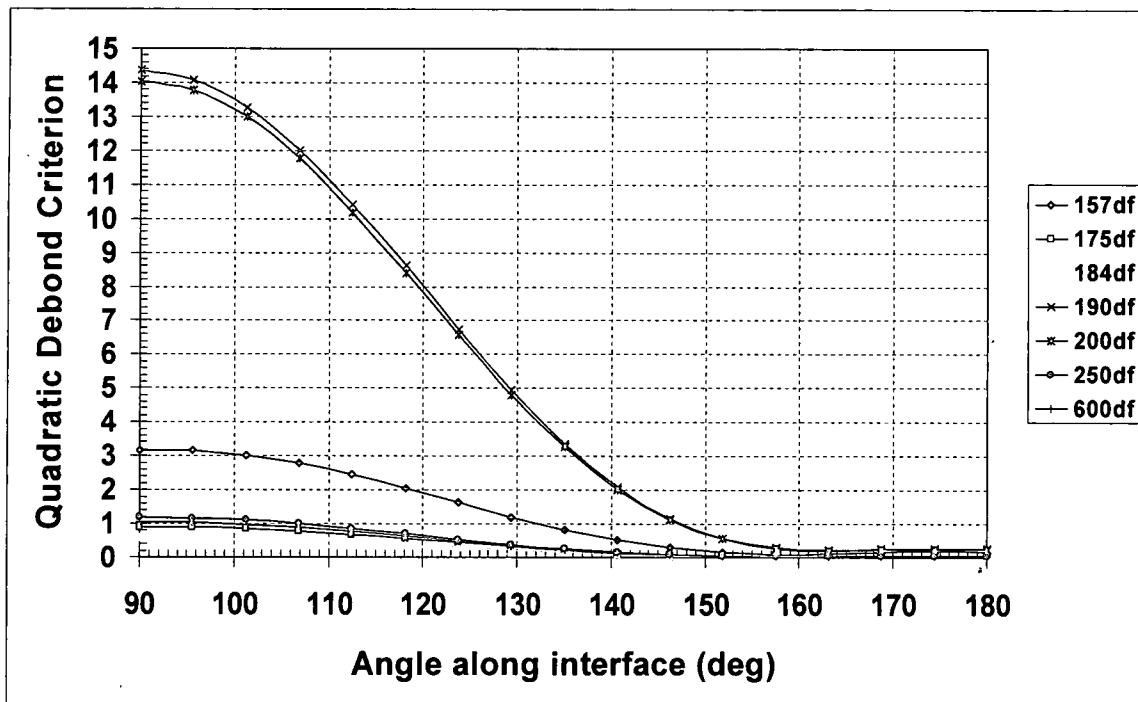


Figure 252: Quadratic Debond Criterion evaluated at the debond locations in the 2nd quadrant of the corner fiber with $A = 15.0$ and $B = 1.0$

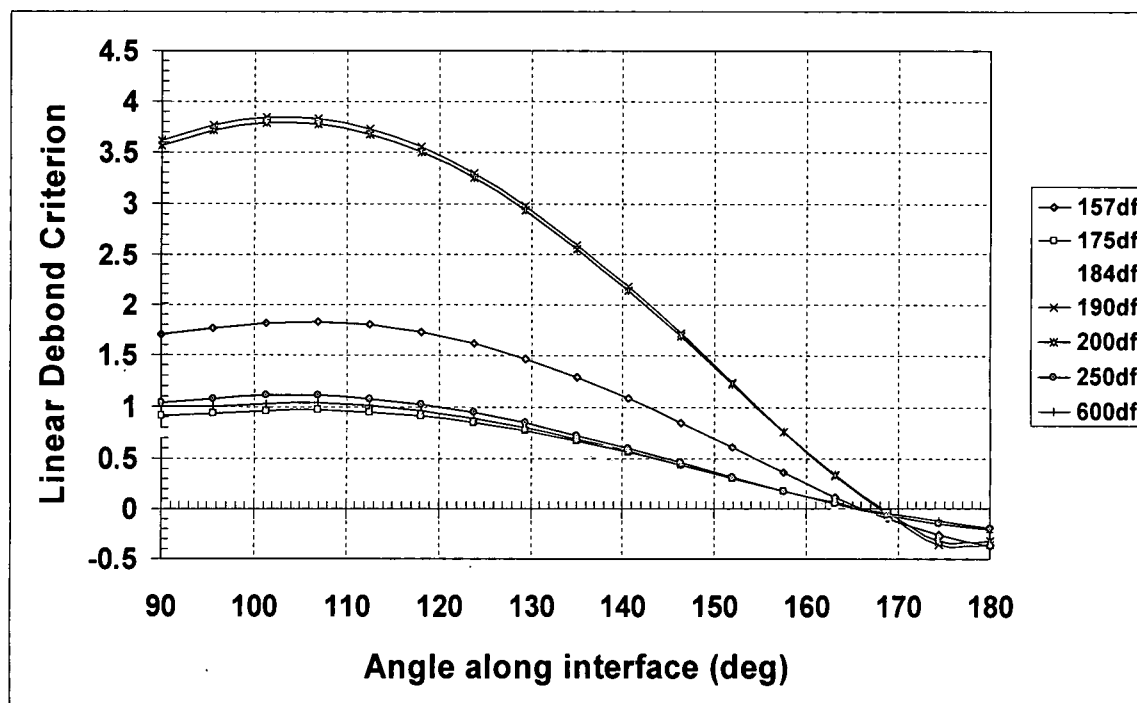


Figure 253: Linear Debond Criterion evaluated at the debond locations in the 2nd quadrant of the corner fiber with $A = 11/3$ and $B = 4/3$

The 3rd quadrant of the corner fiber debond criteria evaluation results are tabulated in Table 87. The debond criteria distribution for the Quadratic Debond Criterion and the Linear Debond Criterion are shown in Figures 254 and 255, respectively, at $Z = 0$ in the 3rd quadrant of the corner fiber. It appears that the Linear Debond Criterion predicts the 6.0d_f, 2.5d_f and 2.0d_f fiber spacing groups better than the Quadratic Debond Criterion, however, the for the 1.90d_f and 1.57d_f fiber spacing groups the opposite is true. The trends for the 1.75d_f and 1.84d_f fiber spacing groups remain the same for this quadrant compared to the other quadrants. Lastly, the Linear Debond Criterion exhibits the consistency of its debond limit prediction for the 3rd quadrant just as before in the 1st, 2nd and 4th quadrants.

Table 87: Comparison of the fiber matrix debond limits predicted by the Quadratic and Linear Debond Criterion for the 3rd quadrant of the corner fiber

Fiber Spacing	Exp db Limits (deg)	Quadratic db Criterion limits (deg)	%Δ	Linear db Criterion limits (deg)	%Δ
1.57d _f	224.5	224	1.1	216	18.7
1.9d _f	212	206	10.3	219	12.1
2.0d _f	215	207	14.5	219	7.3
2.5d _f	246.5	259	53.2	247	2.1
6.0d _f	246	259	54.2	247	4.2

Finally, Table 88 lists the standard deviations of the measured debond widths and their corresponding debond limits. In addition, Table 88 also lists the predicted debond limits determined by the Quadratic and Linear Debond Criteria. From inspection of Table 88 all predicted fiber matrix debond limits from both criteria fall within the standard deviation of the experimental debond measurements except for the 1.57d_f fiber spacing group Linear Debond Criterion prediction for the southern hemisphere. However, it's predicted limit in the 3rd quadrant is only ½ degree from the experimental standard deviation.

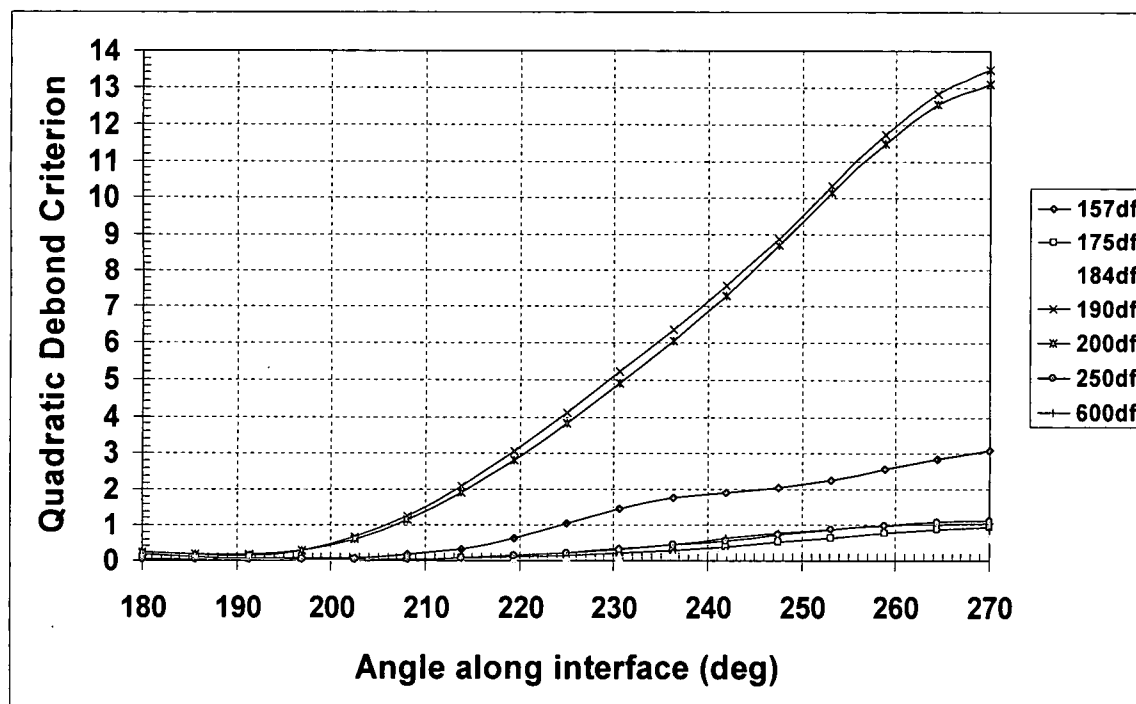


Figure 254: Quadratic Debond Criterion evaluated at the debond locations in the 3rd quadrant of the corner fiber with $A = 15.0$ and $B = 1.0$

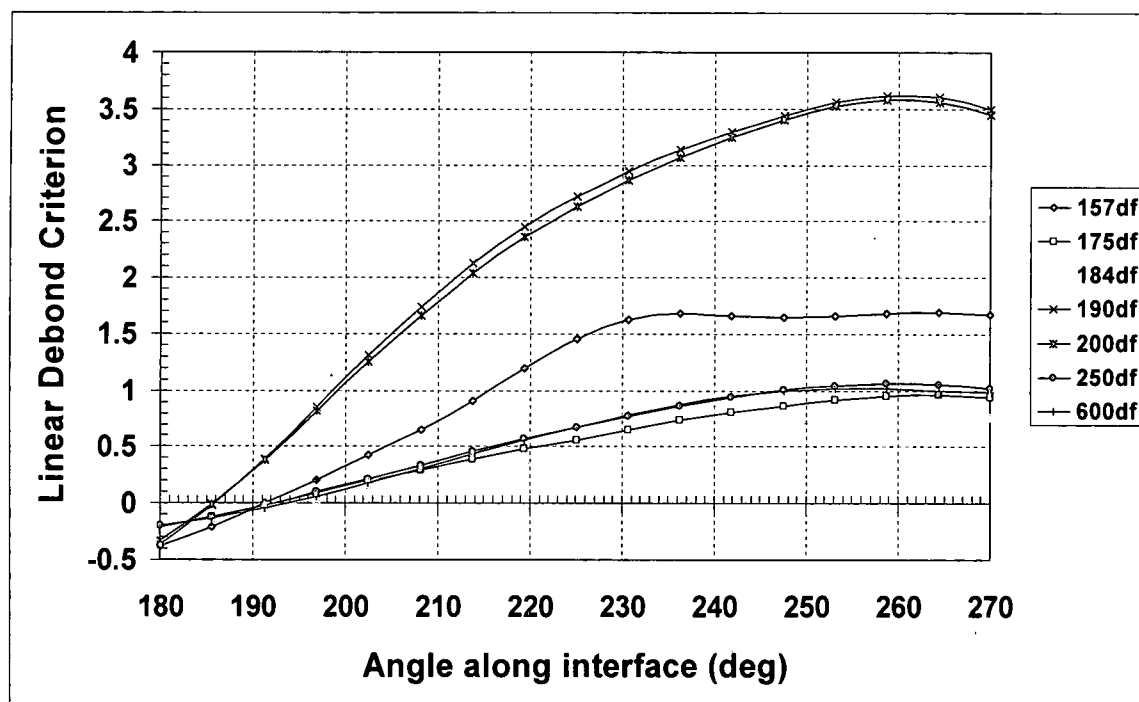


Figure 255: Linear Debond Criterion evaluated at the debond locations in the 3rd quadrant of the corner fiber with $A = 11/3$ and $B = 4/3$

Table 88: Experimental standard deviation debond limits with debond limits determined by the Quadratic and Linear Debond Criteria

Spec.	Average Debond Width, mm (Std dev)	Experimental Debond Limits	Quadratic Prediction Debond limits	Linear Prediction Debond limits
1.57d _r	0.053 (0.019)	44.5° to 135.5° NP 224.5° to 315.5° SP	51° to 132° NP 224° to 307° SP	41° to 143° NP 216° to 314° SP
	Std-dev Small	54° to 126° NP 234° to 306° SP		
	Std-dev Large	36.5° to 143.5° NP 216.5° to 323.5° SP		
1.9d _r	0.083 (0.045)	32° to 148° NP 212° to 328° SP	31° to 147° NP 206° to 326° SP	23° to 154° NP 219° to 334° SP
	Std-dev Small	52° to 128° NP 232° to 308° SP		
	Std-dev Large	16° to 164° NP 196° to 344° SP		
2.0d _r	0.075 (0.036)	35° to 145° NP 215° to 325° SP	31° to 147° NP 207° to 326° SP	24° to 154° NP 219° to 334° SP
	Std-dev Small	51° to 129° NP 231° to 309° SP		
	Std-dev Large	22° to 158° NP 202° to 338° SP		
2.5d _r	0.015 (0.004)	66.5° to 113.5° NP 246.5° to 293.5° SP	75° to 107° NP 259° to 285° SP	64° to 119° NP 247° to 295° SP
	Std-dev Small	69.5° to 110.5° NP 249.5° to 290.5° SP		
	Std-dev Large	63.5° to 116.5° NP 243.5° to 296.5° SP		
6.0d _r	0.01525 (0.0051)	66° to 114° NP 246° to 294° SP	81° to 100° NP 259° to 278° SP	68° to 113° NP 247° to 292° SP
	Std-dev Small	71° to 109° NP 251° to 289° SP		
	Std-dev Large	62° to 118° NP 242° to 298° SP		
SF	0.07 (0.033)	37° to 143° NP	34° to 146° NP	26° to 154° NP
	Std-dev Small	52° to 128° NP		
	Std-dev Large	25° to 155° NP		

Fiber-Matrix Debond Initiation Criterion - Summary

To summarize, the Quadratic Debond Criterion predicted the debonds for the majority of the fiber spacing groups, 3 out of 5, in the 2nd quadrant more accurately than the Linear Criterion.

The Linear Debond Criterion, however, predicted the majority of fiber spacing groups with the greatest accuracy in the 3rd quadrant. From a strictly scorecard perspective, the Linear Debond Criterion tied the Quadratic Debond Criterion in quadrants 2 and 3. These results coupled with those discussed in Chapter 4 lead to concluding that the Linear Debond Criterion shown in equation 3 best describes the 828/D-230 fiber matrix debond failure initiation.

$$\frac{11}{3} \left(\frac{\sigma_r}{\sigma_{yt}} \right) + \frac{4}{3} \left(\frac{\tau_{r\theta}}{\tau_y} \right) \geq 1 \quad (3)$$

Where σ_r and $\tau_{r\theta}$ are the interfacial radial and shear stress, respectively, determined from the cruciform FEA and σ_{yt} and τ_y are the tensile and shear strengths respectively, determined from the neat resin test results.

Having justified the debond criterion using the corner fiber because the majority of the debonds occurred at the corner fiber for all specimens exhibiting fiber-matrix debond as their first failure; the criterion will now be applied to the center fiber. Figure 256 is the linear debond criterion distribution at the fiber-matrix interface along the center fiber. Only one specimen in both the 6.0d_f and 2.5d_f fiber spacing groups initiated a debond at the center fiber. Two specimens each in the 1.9d_f and 2.0d_f groups initiated at the center fiber, while 3 at the 1.57d_f spacing initiated at the center fiber.

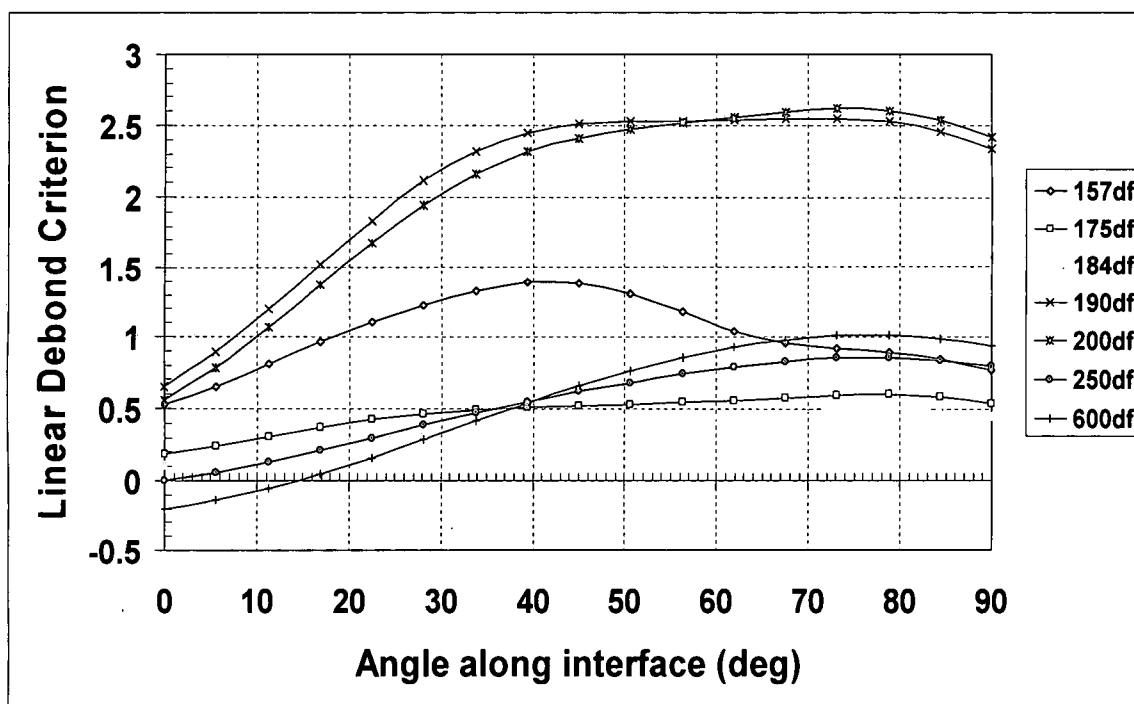


Figure 256: Linear Debond Criterion at the fiber-matrix interface of the center fiber

In accordance with Table 88 above only for the $6.0d_f$ fiber spacing group does the criterion come close to predicting the debond observed in the cruciform tests. For the lone specimen debonding it initiated at the north pole with an individual debond arc length of 48° which translates to an debond limit of 66° . From Figure 256 the criterion predicts that the debond will occur at 71° , under predicting the observed limit but coming very close. The criterion does even predict that the $2.5d_f$ fiber spacing group will develop a fiber-matrix debond on the center fiber as evidenced by a less than 1 criterion value shown in Figure 256. Furthermore, the limits predicted by the criterion are over conservative for the $1.57d_f$, $1.9d_f$ and $2.0d_f$ comparing Figure 256 to the limits listed in Table 88. Thus, it appears that the linear debond criterion is conservative for its debond predictions for the fiber spacing at $2.5d_f$ and below while very close for the $6.0d_f$ fiber spacing.

828/D-230 Matrix Failure Criterion Evaluation

In this section high stress areas in partially visible regions and beyond the visible regions of the cruciform specimen will be evaluated and discussed. In addition, the evaluation of the matrix band regions around the fibers will also be presented.

The next regions of the specimen that indicate cavitation is present in both the experimental and analytical results are the partially visible BTF and UBTF regions of the cruciform. Figure 257 shows the distribution of the Mohr-Coulomb Criterion in the YZ plane of the aforementioned regions of the FEM. Also plotted are the Mohr-Coulomb critical value plane, determined to be 36.27 MPa (see Chapter 4), and the cavitation location listed in Table 43 for the BTF region by the black vertical line. Similar to the EM and UEM regions shown in Chapter 4, the $1.75d_f$, $1.84d_f$ and the $6.0d_f$ fiber spacing groups exceed the apparent critical matrix failure criterion, while only a very small segment of the $2.5d_f$ spacing exceeds the apparent critical value. It also appears that the $1.75d_f$ and $1.84d_f$ have a larger magnitude than the $2.5d_f$ and $6.0d_f$. The plot of the Mohr-Coulomb Criterion in the YZ plane along the loading direction at $Z = 0$, shown in Figure 258, indicates that $1.84d_f$ spacing has a larger magnitude than the $6.0d_f$ although both surpass the apparent critical value. Similarly, Figure 259 is a plot of the matrix failure criterion in the XZ plane along the specimen thickness at $Z = 0$ showing the same results as those shown in Figure 258.

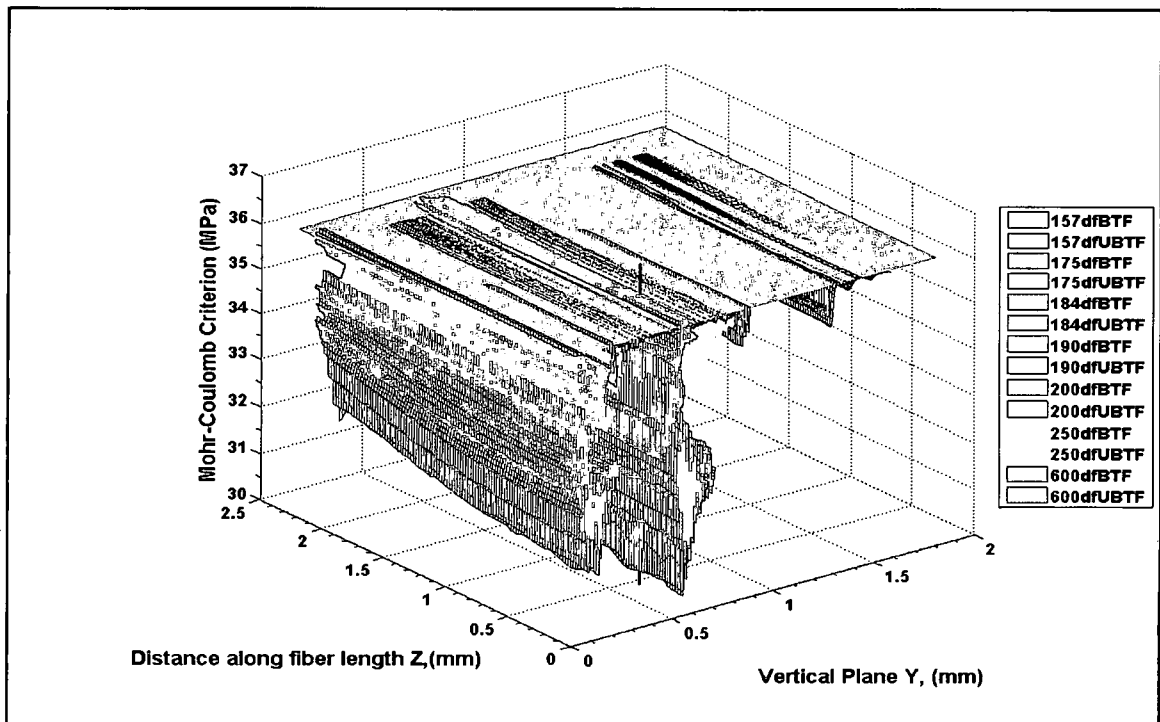


Figure 257: Mohr-Coulomb Criterion distribution in the YZ plane of the BTF and UBTF regions of the FEM

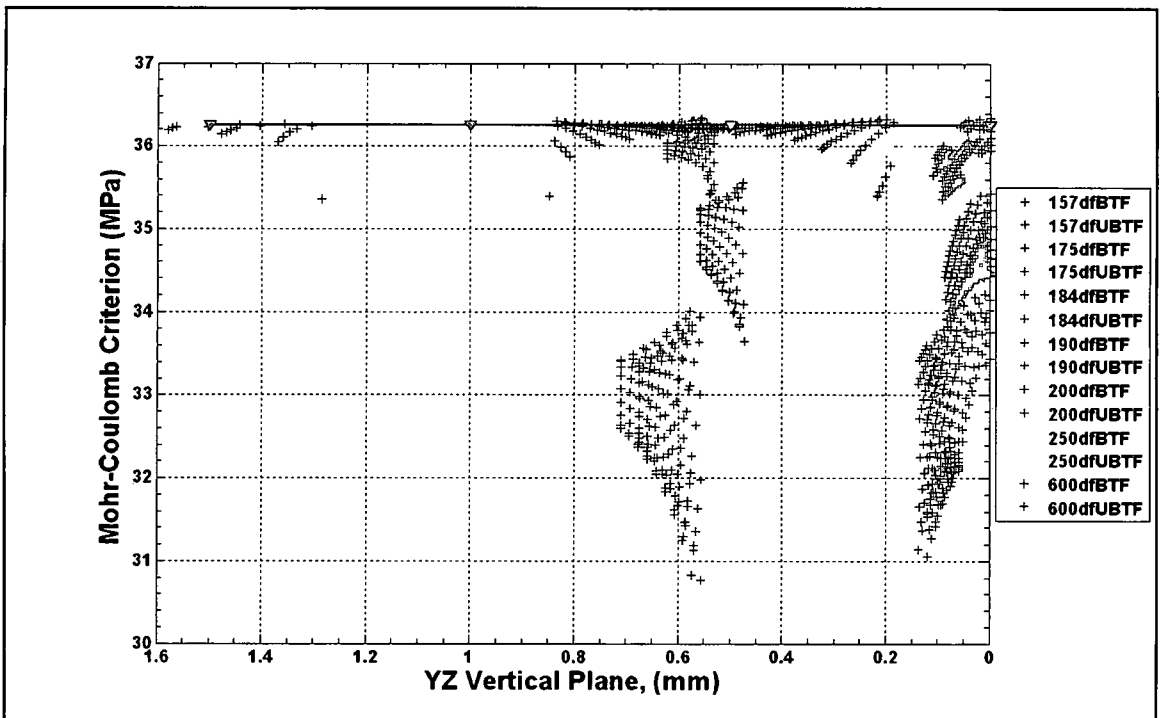


Figure 258: Mohr-Coulomb Criterion plot in the YZ plane along the vertical direction, Y, at Z=0 in the BTF and UBTF region of the FEM

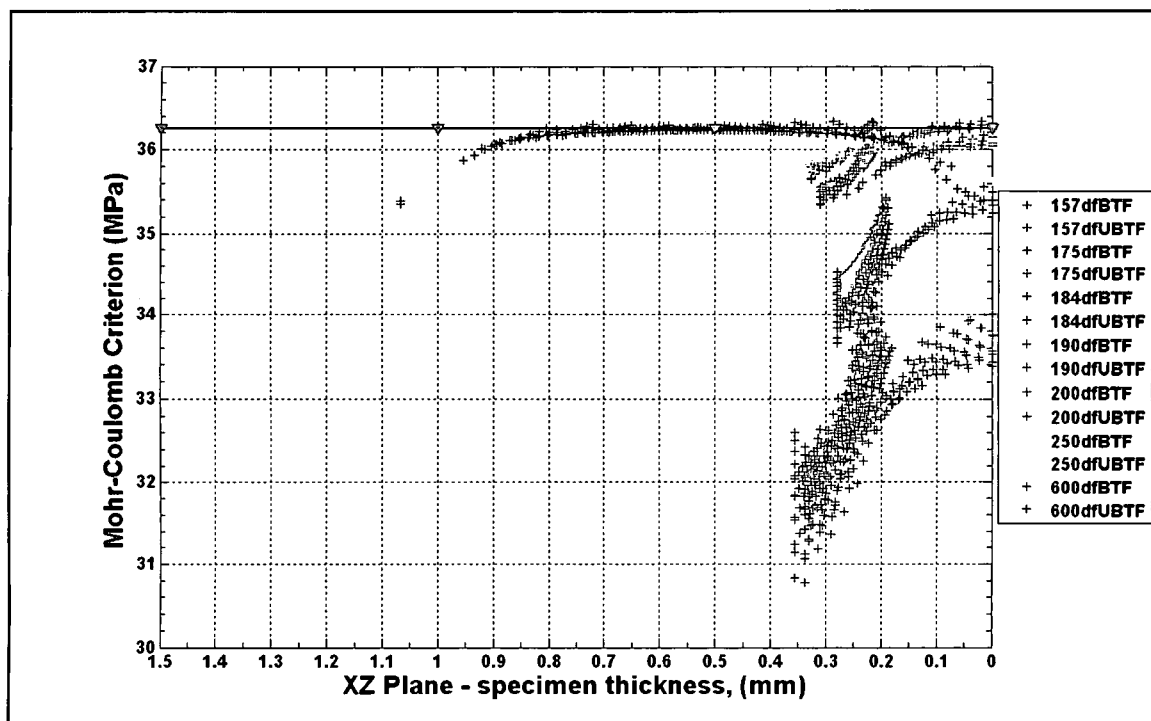


Figure 259: Mohr-Coulomb Criterion plot in the XZ plane along the specimen thickness, X, at Z=0 in the BTF and UBTF region of the FEM

Evaluating the matrix failure criterion in the center fiber matrix band region of the FEM is shown in Figures 260 through 262. Recall that the matrix band around the fibers is densely meshed into six concentric matrix rings as shown in Figure 83. Furthermore, the center fiber is partially visible centered in the specimen for all fiber spacings. For the $1.75d_f$ spacing the visible sector of the center fiber ranges from $\theta = 311^\circ$ to 360° in the 4th quadrant and from $\theta = 0^\circ$ to 49° in the 1st quadrant being a total vertical distance of 0.27 mm. This translates into a FEM visible area of $\theta = 0^\circ$ to 49° and a distance of 0.135 mm. Likewise, the $1.84d_f$ fiber spacing is visible from $\theta = 302^\circ$ to 360° in the 4th quadrant and from 0° to 58° in the 1st quadrant for a total vertical distance of 0.30 mm; thus translating into a FEM visible area of $\theta = 0^\circ$ to 58° and a distance of 0.15 mm. Figure 260 shows the analytical results of the criterion evaluation at the fiber matrix interface, i.e. at $R = 0.1778$ mm, whereas, Figure 261 is the criterion distribution at the mid-plane of the band at $R = 0.1978$ mm. Figure 262 is the Mohr-Coulomb Criterion distribution at the outer band limits where $R = 0.2178$ mm. Also plotted in all three figures is the apparent critical value for

the Mohr-Coulomb Criterion. Figure 260 indicates that there is no fiber spacing matrix failure criterion evaluation exceeding the apparent critical value. Thus the analytical results indicate that the matrix does not cavitated at the interface of the center fiber. However, Figure 261 shows that both the $1.75d_f$ and $1.84d_f$ fiber spacing groups exceed the apparent critical value in two locations, primarily around the fiber equator between $\theta = 0^\circ$ to about 12° along the entire fiber length within view and again near the north pole between approximately $\theta = 80^\circ$ to 90° near the end of the field of view. The angular position at the equator along the center fiber translates into a vertical distance of approximately 0.04 mm from the equator in the direction of loading placing the area directly in front of the center fiber. From Figure 262 the criterion evaluated for the $1.84d_f$ fiber spacing group at the outer band clearly has its magnitude of the criterion greater than the apparent critical value around its equator stretching the entire fiber length within the field of view. The location where this occurs ranges from $\theta = 0^\circ$ to approximately 12° along the interface of the center fiber making a vertical distance of about 0.045 mm from the fiber equator in the direction of the loading. Like at the mid-plane of the fiber matrix band, the cavitation area for the outer band limit is located right in front of the center fiber.

Referring to Table 43, the $1.75d_f$ and $1.84d_f$ fiber spacing groups have cavitations occurring in the EM and CNB regions of the specimen. Due to the fact that the depth of where the cavitation occurs cannot be determined with any certainty the field of view directly in front of the center fiber traverses the EM, BTF and CNB sectors of the FEM. Thus the FEM results correlate the experimental results.

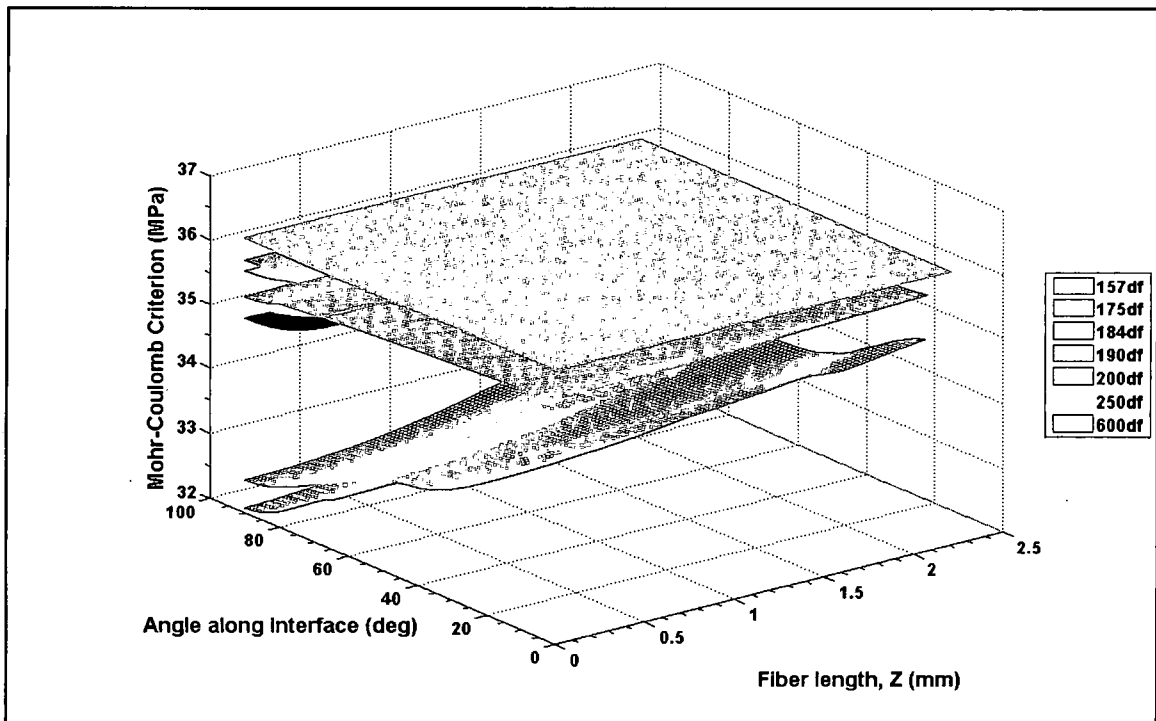


Figure 260: Mohr-Coulomb Criterion distribution in the center fiber matrix band at the fiber matrix interface

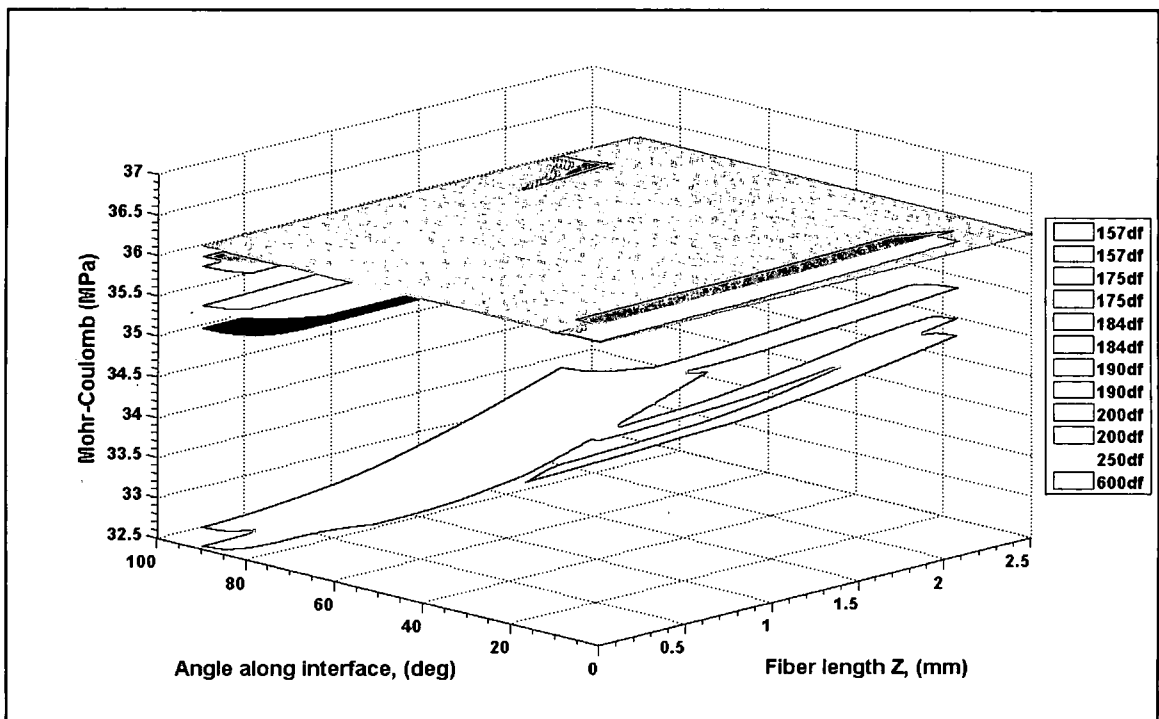


Figure 261: Mohr-Coulomb Criterion distribution in the center fiber matrix band at the mid-plane of the matrix band, $R = 0.1978$ mm

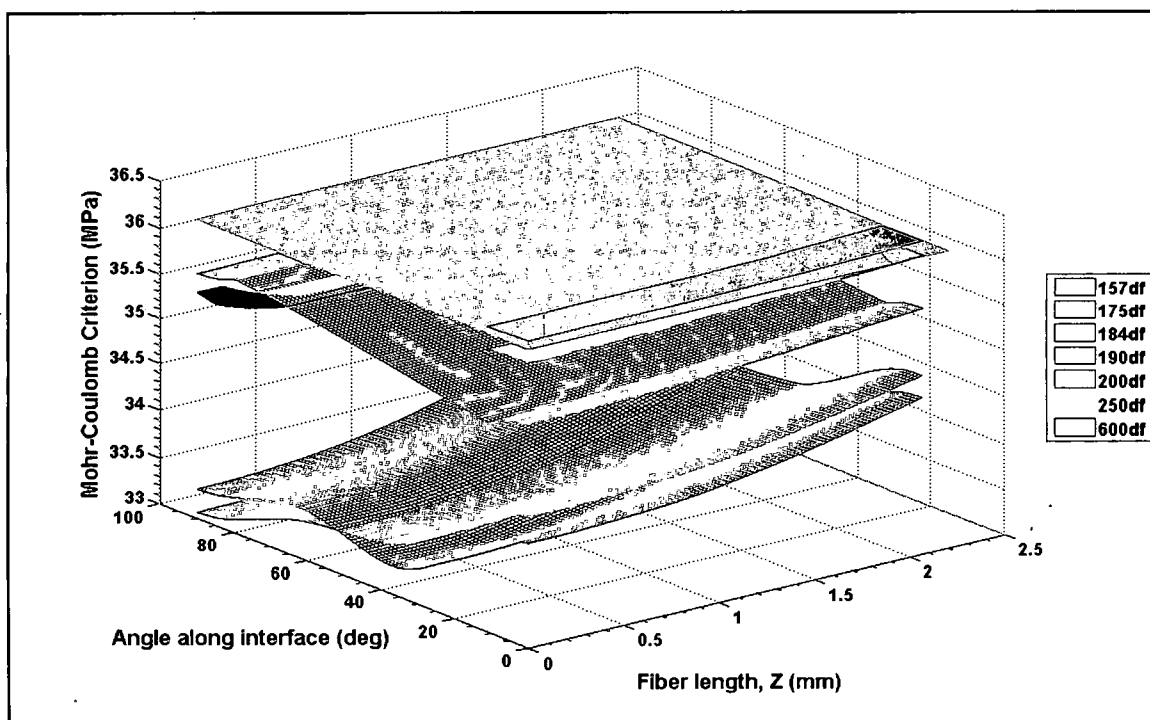


Figure 262: Mohr-Coulomb Criterion distribution in the center fiber matrix band at the outer band limits, $R = 0.2178$ mm

For the corner fiber matrix band regions, the visible sectors are the CRB090 and CRB270360 regions. Figures 263 through 265 and 266 through 268 show the Mohr-Coulomb Criterion evaluated for all fiber spacing groups at the interface, mid-plane and outer band limits along the fiber length within the viewable area in the CRB090 and CRB270360 matrix band regions respectively. Also plotted in each Figure is the apparent critical matrix failure stress. The Mohr-Coulomb Criterion distribution evaluated for each fiber spacing in the CRB090 matrix band show that no fiber spacing group exceeds the critical matrix failure stress at the interface, see Figure 263, at the mid-plane where $R = 0.1978$ mm, see Figure 264, and at the outer band limits where $R = 0.2178$ mm, shown in Figure 265.

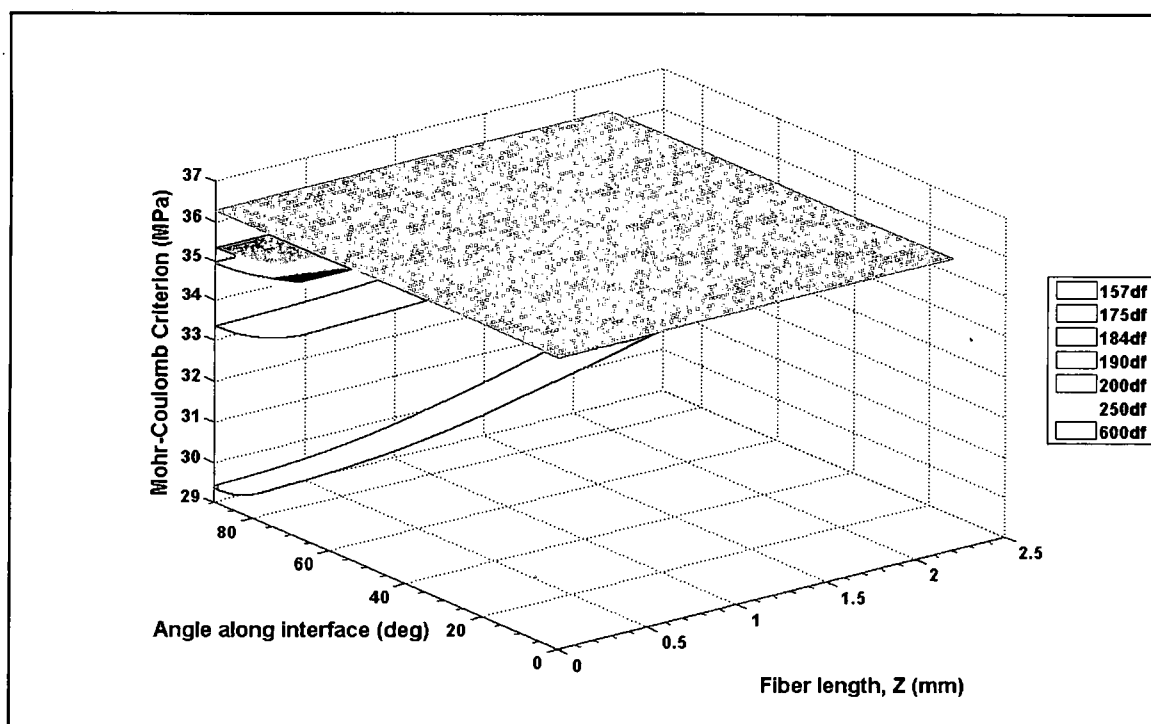


Figure 263: Mohr-Coulomb Criterion distribution in the corner fiber $0^\circ - 90^\circ$ matrix band at the fiber matrix interface

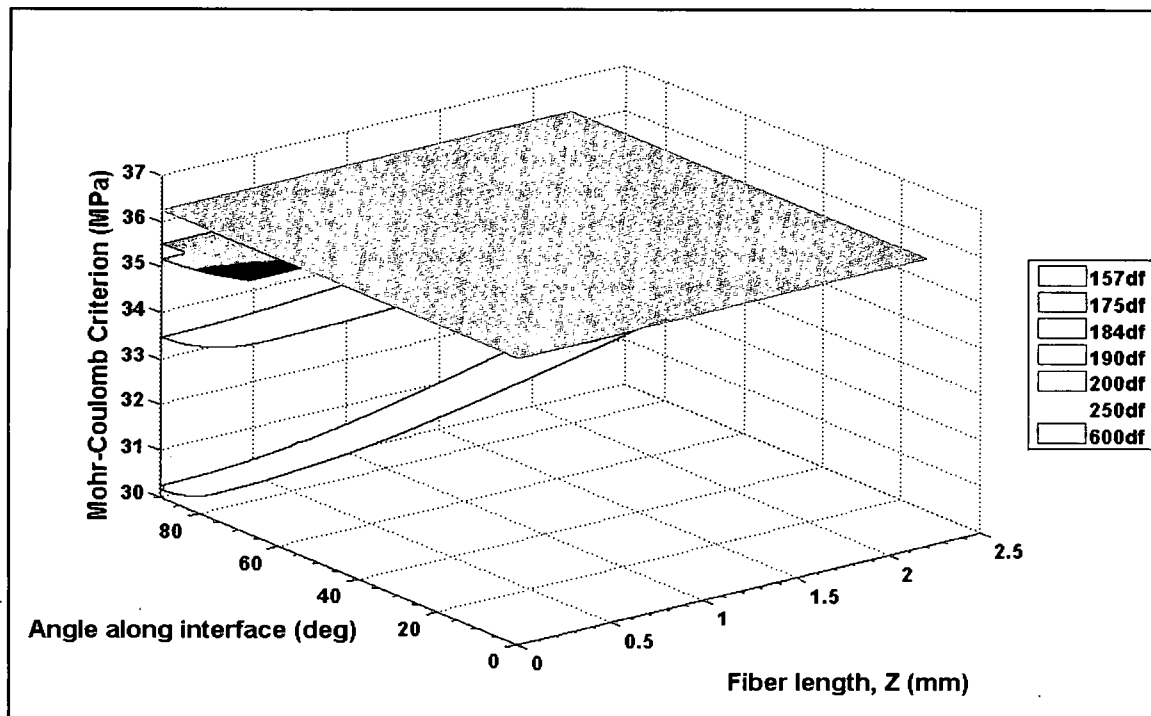


Figure 264: Mohr-Coulomb Criterion distribution in the corner fiber $0^\circ - 90^\circ$ matrix band at the mid-plane of the matrix band, $R=0.1978$ mm

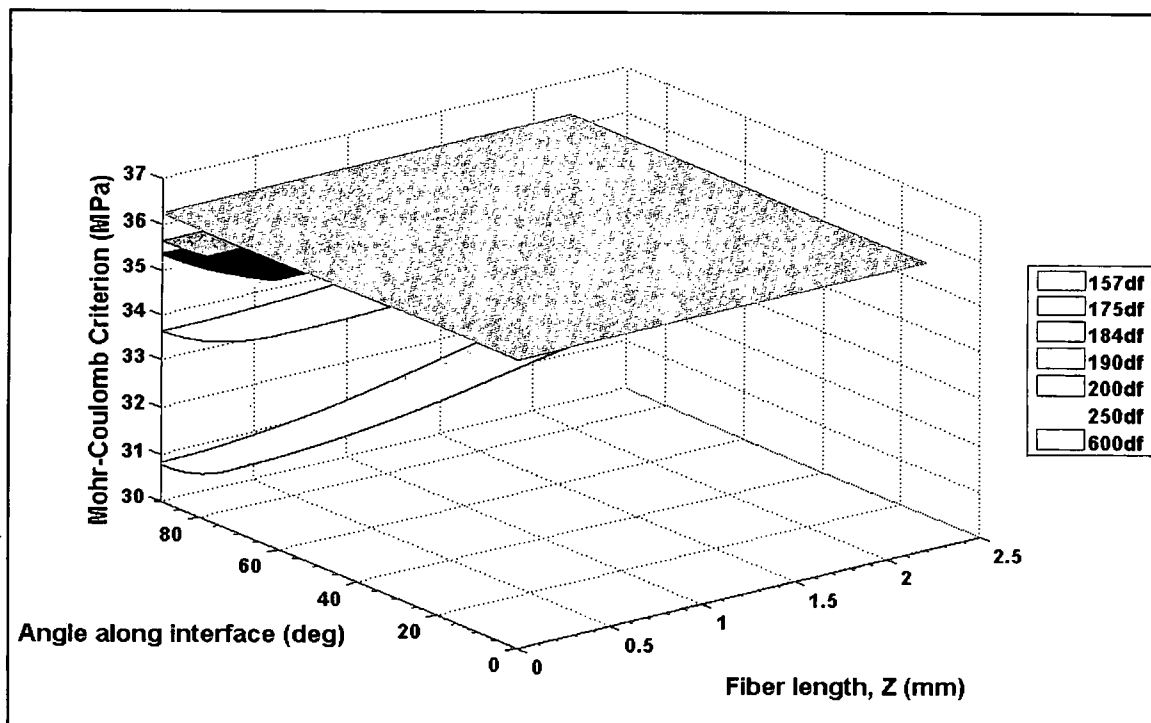


Figure 265: Mohr-Coulomb Criterion distribution in the corner fiber 0° – 90° matrix band at the outer band limits, $R=0.2178$ mm

The CRB270360 corner fiber matrix band Mohr-Coulomb Criterion evaluation for all fiber spacing groups concur with the CRB090 matrix band evaluation results; that no fiber spacing group evaluates the criterion with a greater magnitude than the critical value at the interface. The plots of the Mohr-Coulomb evaluation in the CRB270360 matrix region are shown in Figure 266 at the fiber-matrix interface; at the mid-plane of the matrix band, $R=0.1978$ mm, in Figure 267, and at the outer band limits, $R=0.2178$ mm, in Figure 268. Thus no cavitation would occur within these matrix regions of the specimen.

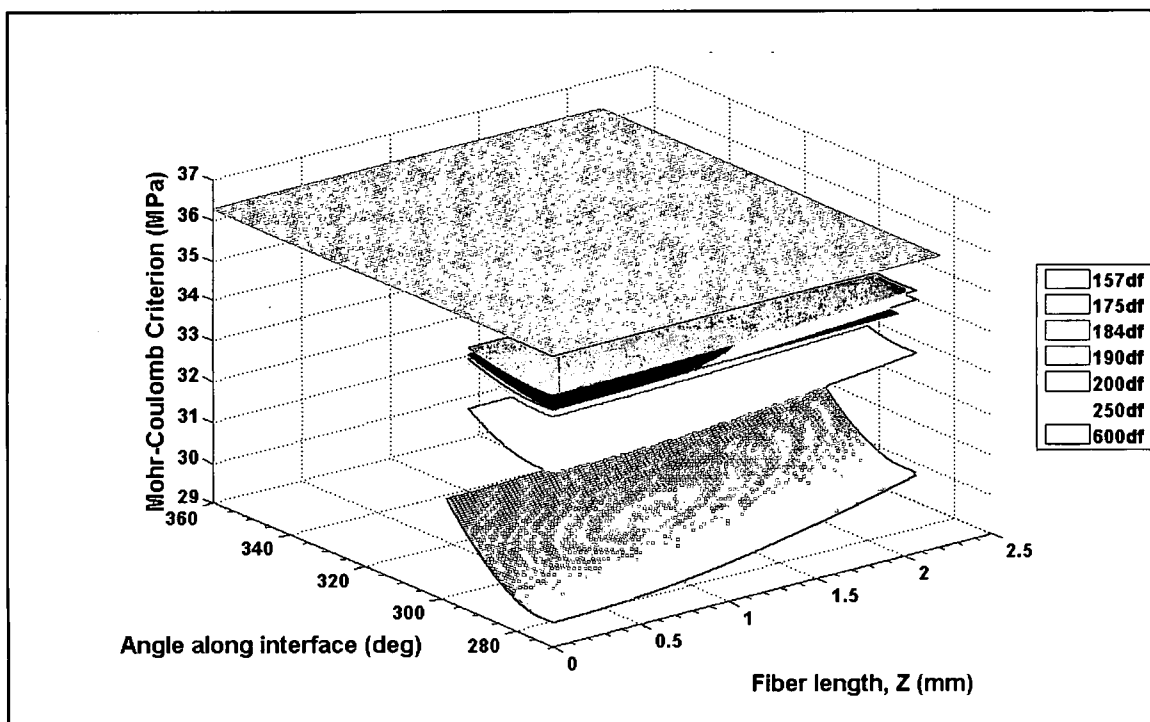


Figure 266: Mohr-Coulomb Criterion distribution in the corner fiber 270° – 360° matrix band
at the fiber matrix interface

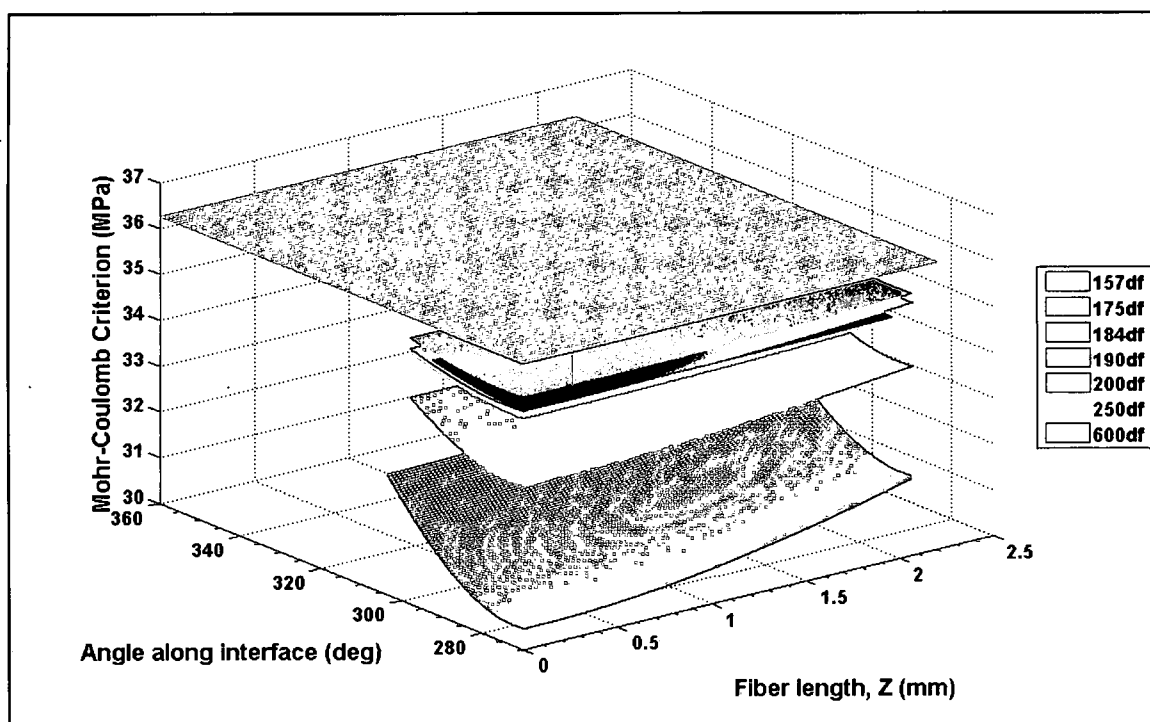


Figure 267: Mohr-Coulomb Criterion distribution in the corner fiber 270° – 360° matrix band
at the mid-plane of the matrix band, $R=0.1978$ mm

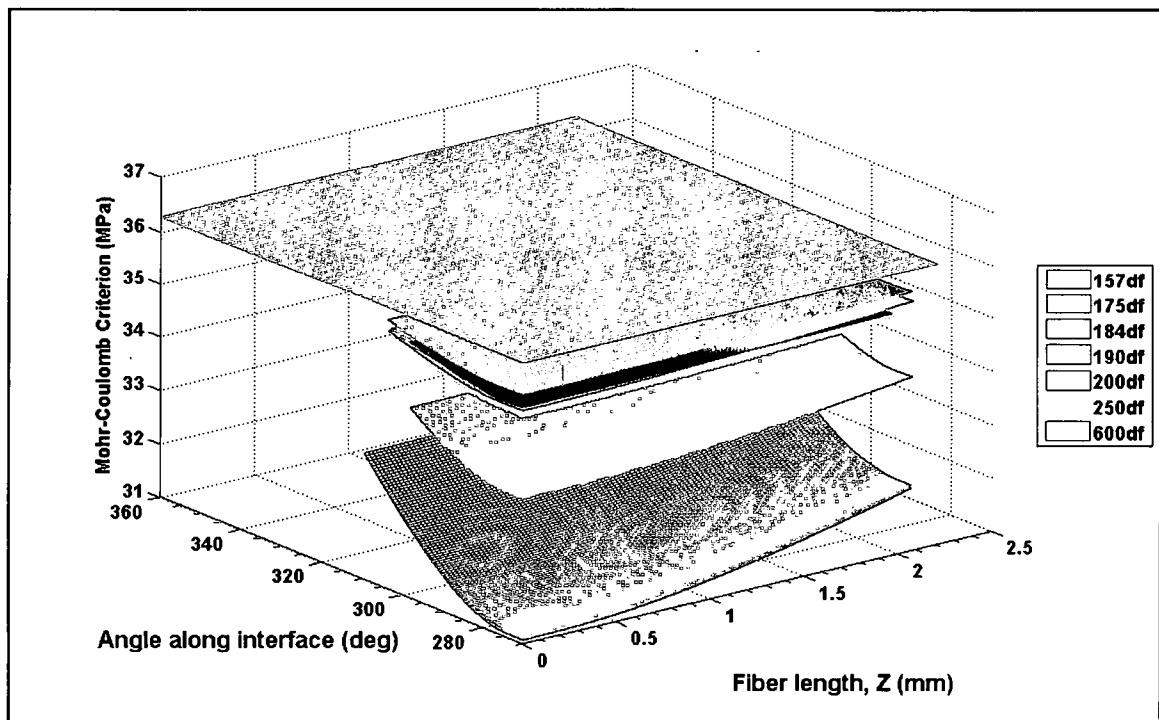


Figure 268: Mohr-Coulomb Criterion distribution in the corner fiber 270° – 360° matrix band at the outer band limits, $R=0.2178$ mm

Investigating the Mohr-Coulomb Criterion in the corner fiber sectors not visible during cruciform testing is shown in Figures 269 through 271 for the CRB90180 matrix band and in Figure 272 through 274 for the CRB180270 matrix band. In each instance the matrix failure criterion is evaluated for each fiber spacing group within the matrix band, at the interface, mid-plane and outer band limits. Not surprisingly the CRB90180 matrix failure evaluation distribution, Figures 269 through 271, is the mirror image of Figures 263 through 265 and the results of the evaluation for the CRB90180 also concur with the results of the CRB090 matrix band. Similarly, the evaluation of the Mohr-Coulomb Criterion shown in Figures 272 through 274 for the CRB180270 is the mirror image of the distribution for the CRB270360 shown in Figures 266 through 268 and their evaluation results agree with each other as well. Consequently, it appears that no matrix cavitation occurs in the corner fiber matrix bands.

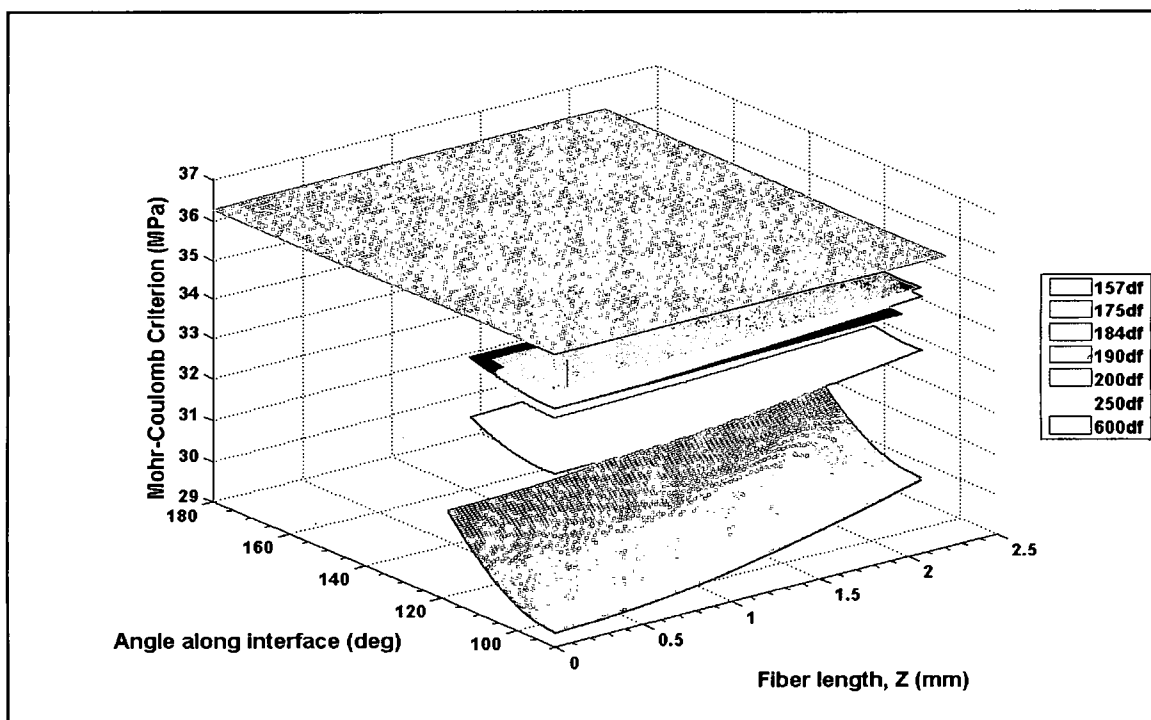


Figure 269: Mohr-Coulomb Criterion distribution in the corner fiber $90^\circ - 180^\circ$ matrix band
at the fiber matrix interface

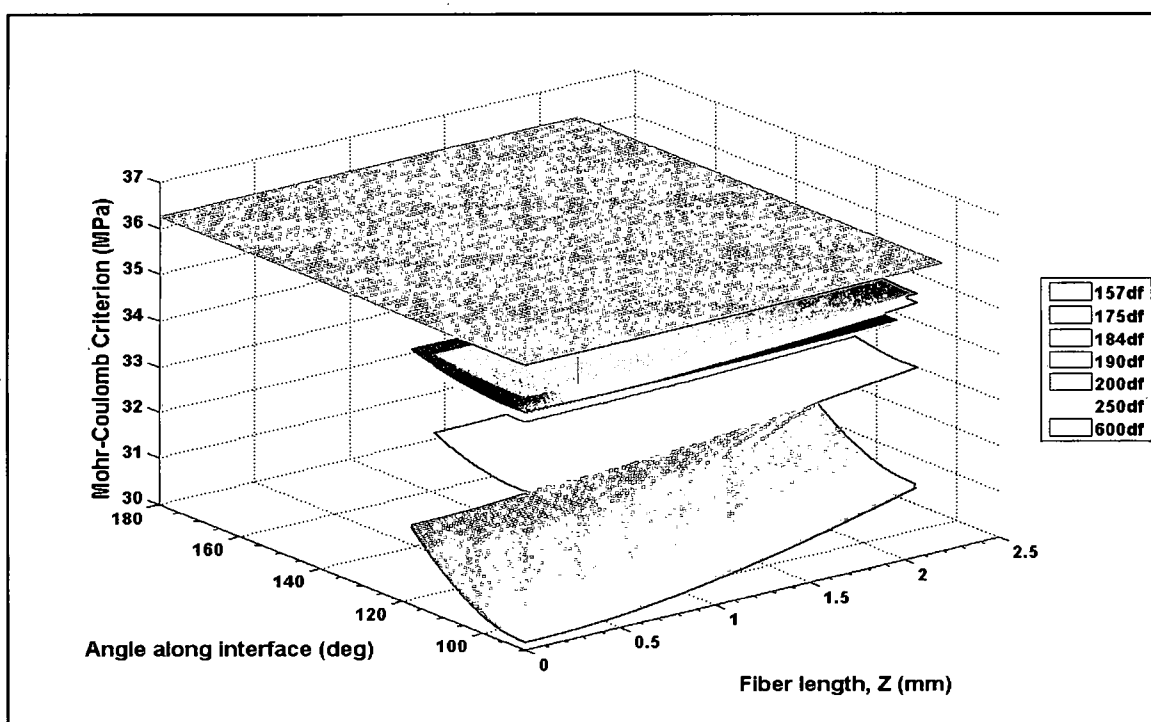


Figure 270: Mohr-Coulomb Criterion distribution in the corner fiber $90^\circ - 180^\circ$ matrix band
at the mid-plane of the matrix band, $R=0.1978$ mm

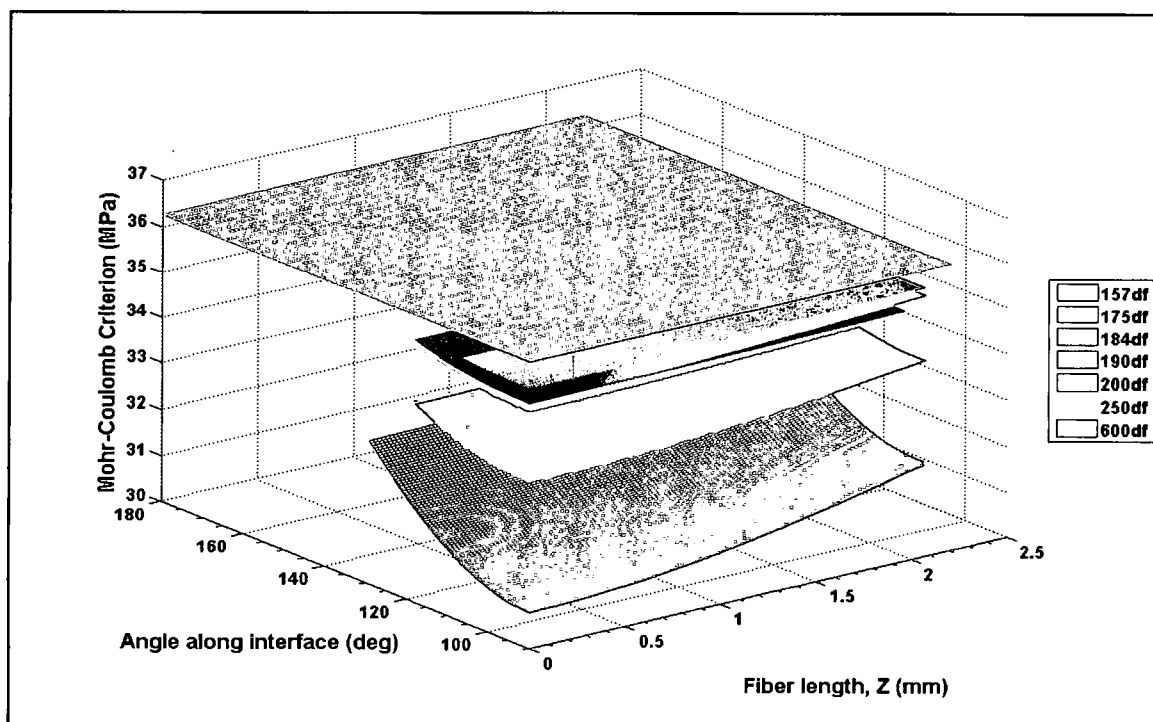


Figure 271: Mohr-Coulomb Criterion distribution in the corner fiber 90° – 180° matrix band
at the outer band limits, $R=0.2178$ mm

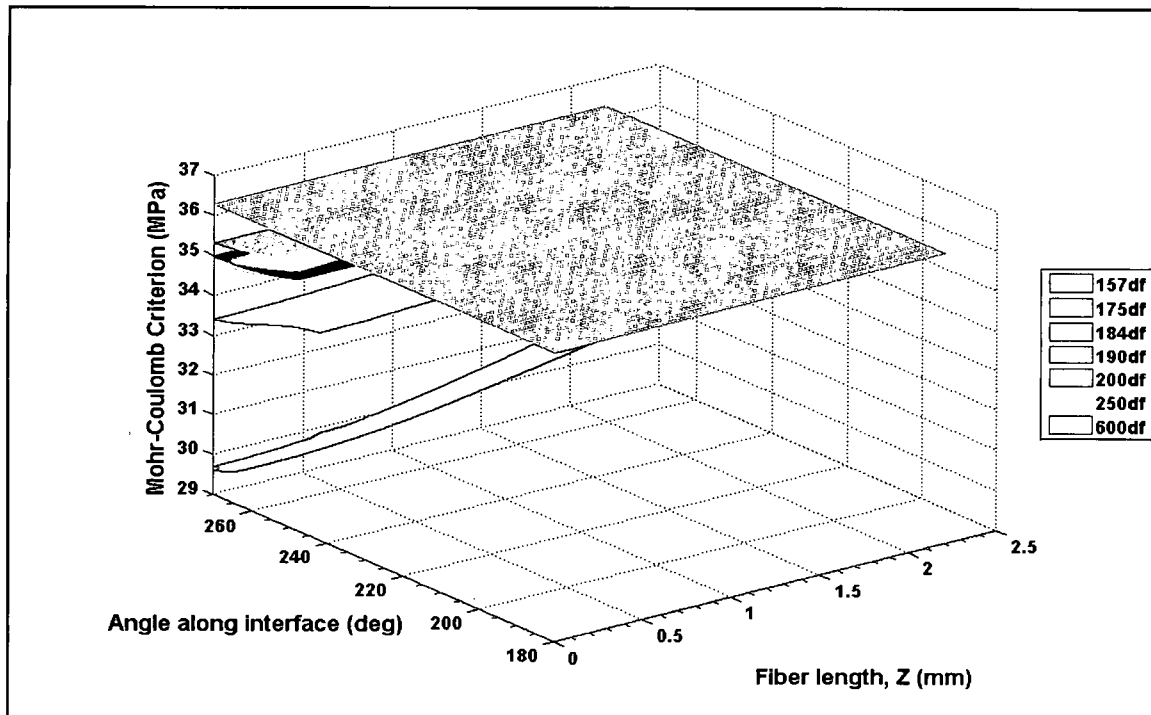


Figure 272: Mohr-Coulomb Criterion distribution in the corner fiber 180° – 270° matrix band
at the fiber matrix interface

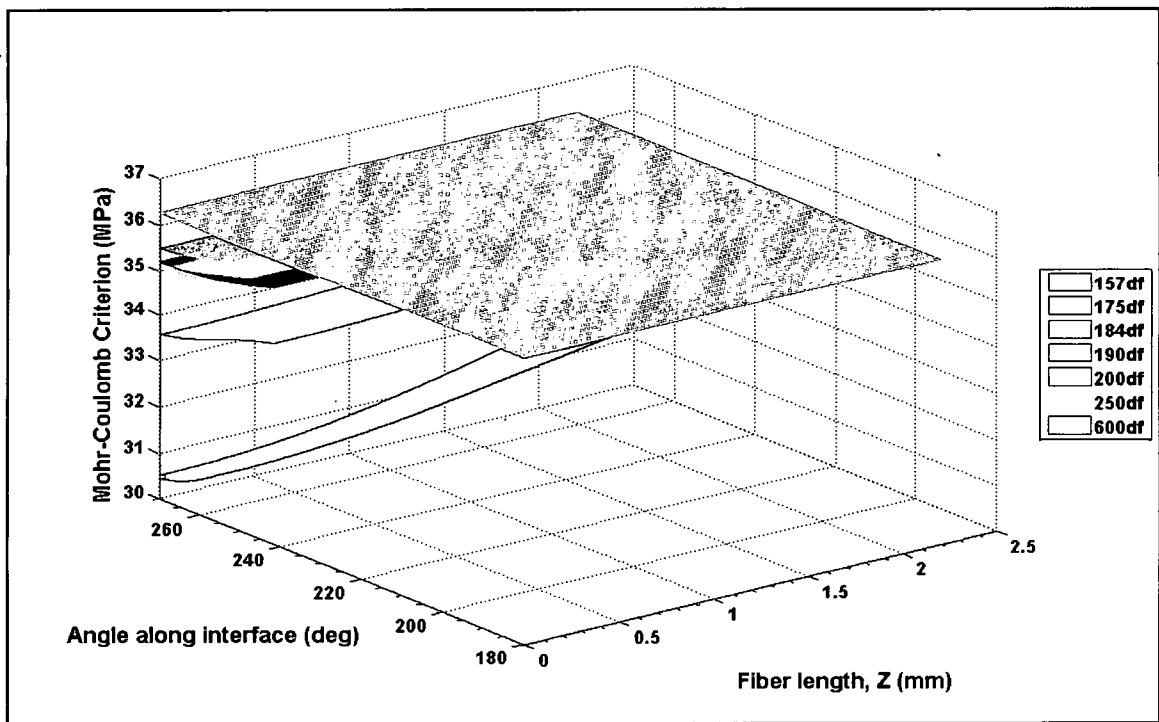


Figure 273: Mohr-Coulomb Criterion distribution in the corner fiber 180° – 270° matrix band
at the mid-plane of the matrix band, $R=0.1978$ mm

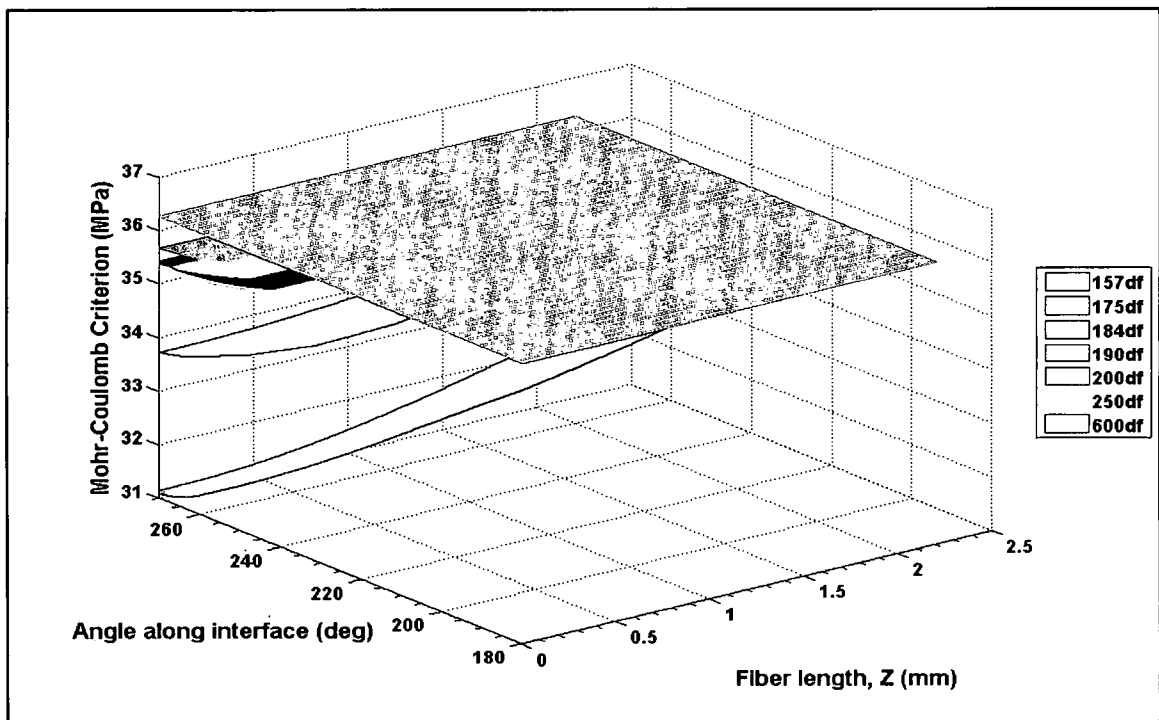


Figure 274: Mohr-Coulomb Criterion distribution in the corner fiber 180° – 270° matrix band
at the outer band limits, $R=0.2178$ mm

Matrix Failure Initiation Criterion - Summary

The experimental results show that matrix cavitation is the first failure mechanism for 1.75d_f and 1.84d_f fiber spacing groups in the 828/D-230 matrix system. Table 43 lists the location of the first cavitation observed for each specimen in these two fiber spacing groups. The Mohr-Coulomb Criterion was chosen for further evaluation as the matrix failure criterion for all fiber spacing groups based upon the fact it predicted the octahedral shear stress of the neat resin tests better than the Modified-Tresca Criterion predicted the critical shear stress of the same neat resin experiments. A critical value of the Mohr-Coulomb Criterion was obtained by FEA based upon the location of the observed cavitation occurring in the 1.75d_f and 1.84d_f fiber spacing specimens and also listed in Table 43. The criterion was then evaluated for all fiber spacing groups in each region of the FEM exhibiting a tri-axial state of stress, which included all or portions of every region of the FEM. The evaluation revealed that the 1.75d_f, 1.84d_f, 2.5d_f and the 6.0d_f fiber spacing groups had exceeded the critical criterion stress in the BTF and UBTF regions of the cruciform specimen indicating cavitation occurring. The 2.5d_f fiber spacing had exceeded the critical criterion stress in only the BTF region and only by a very small amount. However, in those regions where both the 6.0d_f and 2.5d_f also exceeded the critical criterion stress the 1.75d_f and 1.84d_f groups have larger magnitudes of the criterion. In addition, the 1.75d_f and 1.84d_f exceeded the critical value in the center fiber matrix band at the mid-plane, $R = 0.1978$ mm, and at the outer band limit, $R = 0.2178$ mm, where both the 2.5d_f and 6.0d_f groups had considerably lower magnitudes. Furthermore, the debond criterion evaluation for the 2.5d_f and 6.0d_f fiber spacing groups indicated debonds occurred, whereas for the 1.75d_f and 1.84d_f fiber spacing groups it did not. Since no cavitation was observed as occurring as the first failure mechanism for the 2.5d_f and 6.0d_f fiber spacing groups then the apparent critical value may be too low. An adjustment to the apparent critical Mohr-Coulomb criterion to 36.35 MPa, which is within the standard deviation as shown in Table 43, was done in Chapter 4. The Mohr-Coulomb plot in the EM and UEM regions shown in Chapter 4 reveal that the cavitation locations are still contained within the area exhibiting maximum Mohr-Coulomb values for the 1.75d_f and 1.84d_f while the 6.0d_f is barely exceeding the critical plane.

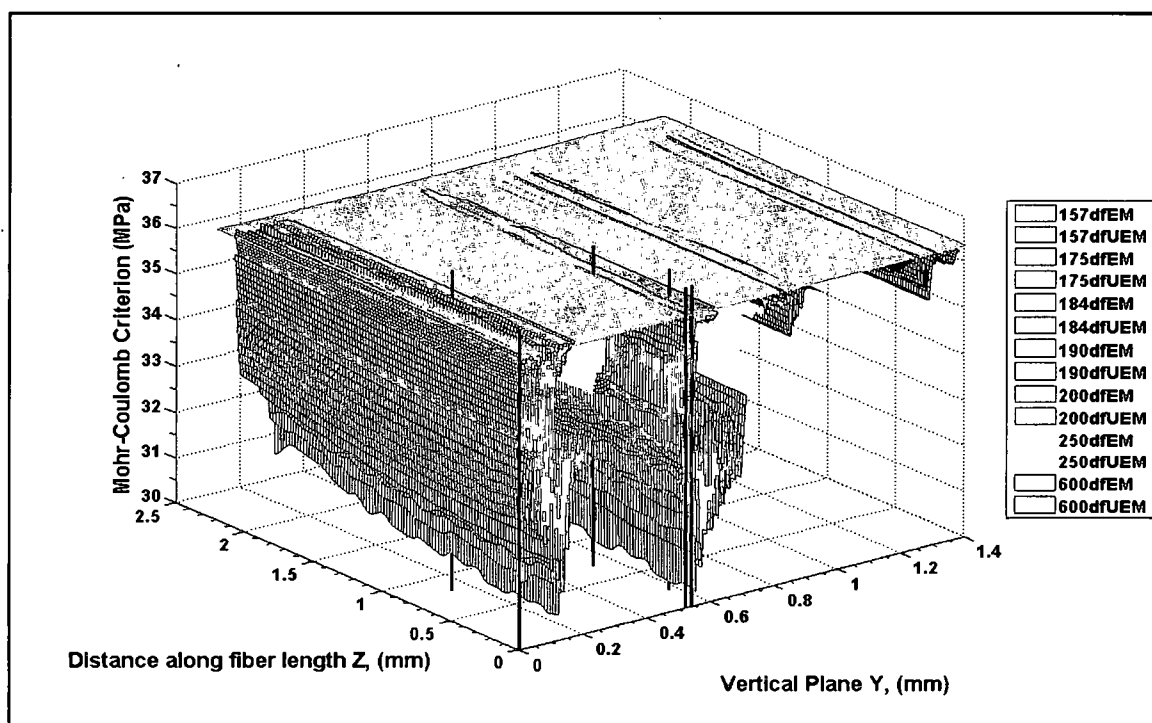


Figure 275: Mohr-Coulomb Criterion distribution in the YZ plane of the EM and UEM regions of the FEM showing the critical value plane at 36.35 MPa and cavitation locations

Figure 276 shows the Mohr-Coulomb distribution in the YZ plane of the FEM for the UM region having the apparent critical value plane adjusted in 36.35 MPa. One of the two cavitation locations is right at the boundary while the other is just outside of the boundary of 1.84d_f fiber spacing group maximum Mohr-Coulomb values. Although the 1.9d_f and 2.0d_f specimens maximum Mohr-Coulomb exceed the apparent critical value plane in one location at the edge of the field of view, no other fiber grouping exceeds the critical value. Most likely the 1.9d_f and 2.0d_f location is a consequence of the plot routine used in the Matlab® program. Figure 277 shows the UBTF region of the FEM Mohr-Coulomb distribution in the YZ plane with the apparent critical value plane and cavitation locations. The lone cavitation location is fairly close to the 1.84d_f specimen maximum Mohr-Coulomb area while the 6.0d_f specimen has barely any maximum Mohr-Coulomb values exceeding the critical value plane.

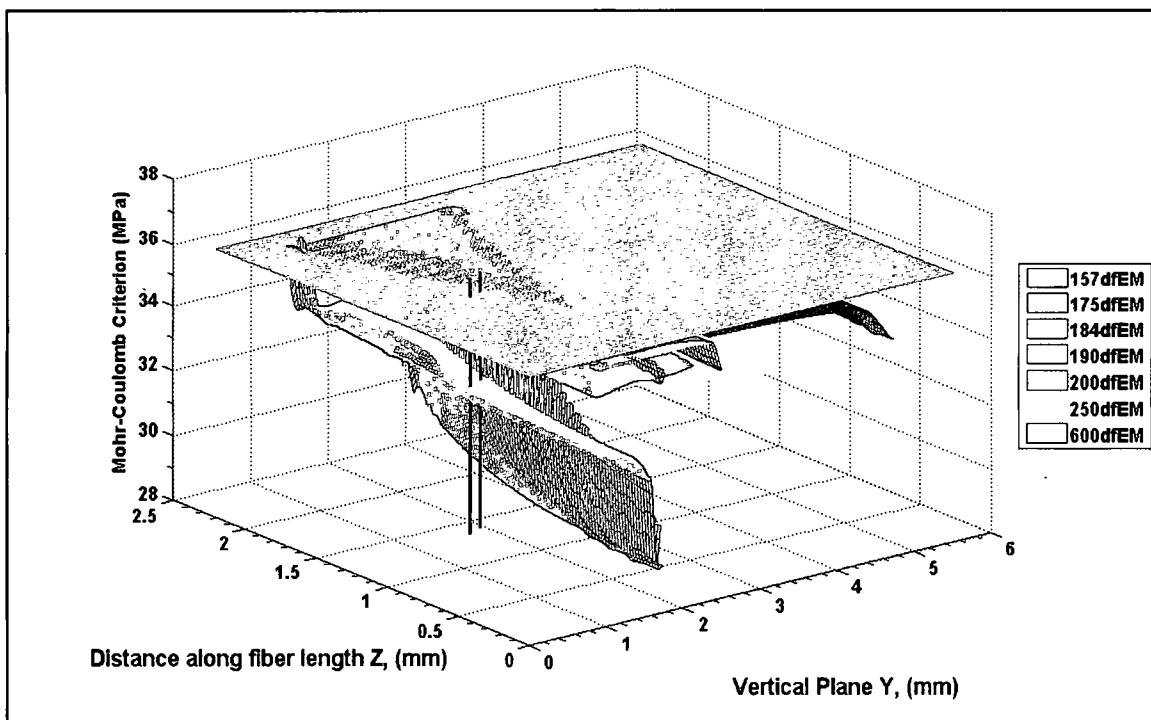


Figure 276: Mohr-Coulomb Criterion distribution in the YZ plane of the UM regions of the FEM showing the critical value plane at 36.35 MPa and cavitation locations

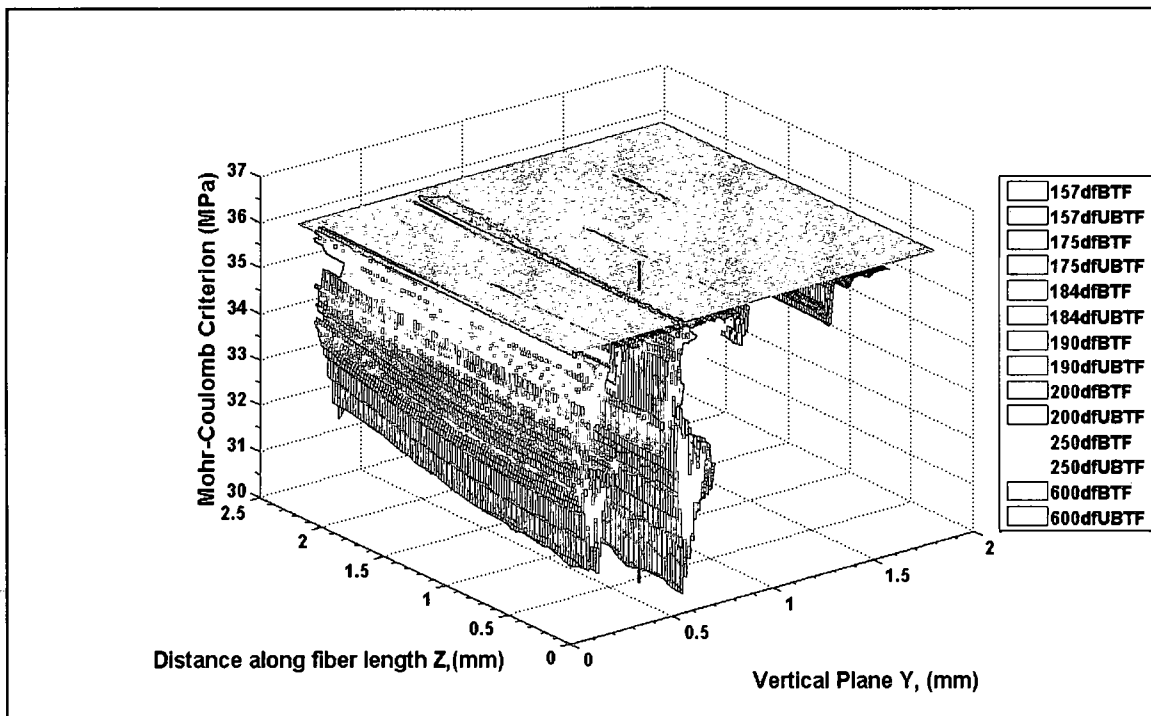


Figure 277: Mohr-Coulomb Criterion distribution in the YZ plane of the UBTF regions of the FEM showing the critical value plane at 36.35 MPa and cavitation locations

It should be noted that in each specimen where matrix cavitation was observed, it's the first instance of the damage mechanism that is recorded from which the far-field stress was determined. From Figures 276 and 277 there exist areas within the region where the maximum Mohr-Coulomb criterion exceeds the apparent critical value, when for the experiments it is at the first instance. Also, the locations of the cavitations were determined and measured with the best available tools and methodologies present. Due to the transparency of the matrix, distortion of the cavitation through the resin will cause errors in the location measurements which cannot be determined. Due to the FEM nodal solution the Mohr-Coulomb values at adjacent node will have slight variances between them having magnitudes of tenths or hundreds of an MPa. The plot routine employed in the Matlab® program interpolates between the nodal values of the Mohr-Coulomb to create the plane for the 3D plots used in this body of work. Close inspection of the plane reveals a wave or oscillation pattern. In reality these nodes or points within the continuum of the matrix would not have the oscillation but would be smooth. Most likely the plane representative of the actual value occurring in the matrix is probably somewhere between the peaks of the nodal points. Consequently, based upon the preceding discussion the Mohr-Coulomb criterion as presented by equation (6) very accurately describes the matrix cavitation occurring in the cruciform specimens have a fiber spacing at $1.75d_f$ and $1.84d_f$. The Mohr-Coulomb failure criterion critical magnitude is 36.35 MPa. Thus, when the criterion evaluates greater than 36.35 MPa matrix cavitation occurs. Due to the fact that the Mohr-Coulomb criterion best describes matrix cavitation there is strong evidence that the failure mechanism occurring in the cruciform specimens has a strong shear bias.

862/W Fiber-Matrix Debond Criterion Evaluation

Quadratic Debond Criterion

Since the linear debond criterion seems to be a better fit for predicting the debond limits in the 1st and 4th quadrants of the corner fiber, before down selecting to the

recommended criterion a comparison at the debond locations on the corner fiber is detailed below. As discussed above, the locations along the axis of the fiber where the debond initiated is measured from the center of the specimen, $Z = 0$, during the photomicrograph analysis of the failure initiation for each specimen. Figures 278 and 279 show the interfacial quadratic debond criterion distribution for the corner fiber at the location of the debond initiation in the 1st quadrant and the 4th quadrant, respectively. Similarly, Figure 280 and 281 show the linear debond criterion distribution for the corner fiber at the location of the debond initiation in the 1st quadrant and the 4th quadrant, respectively. Tables 89 and 90 lists the comparison between the quadratic and linear debond criteria obtained from Figures 278 through 281 for the 1st and 4th quadrant of the corner fiber respectively.

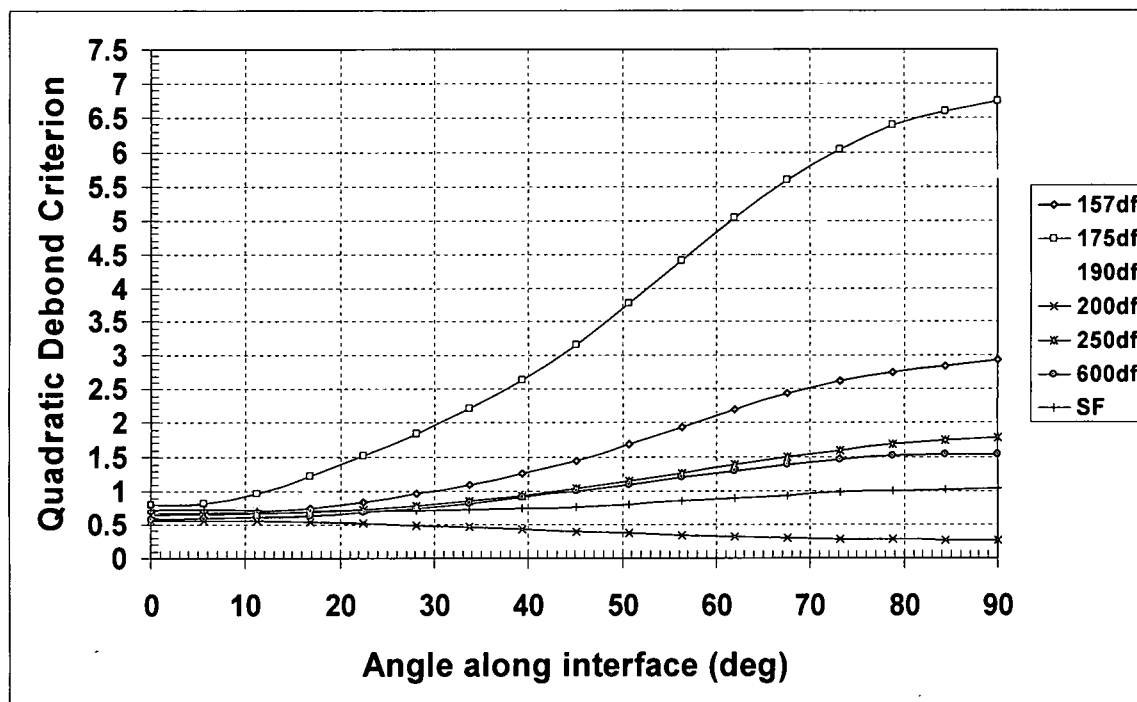


Figure 278: Quadratic Debond Criterion evaluated at the fiber matrix interface of the corner fiber at debond locations in field of view from $\theta = 0^\circ$ to 90° with $A = 21$ and $B = 14$

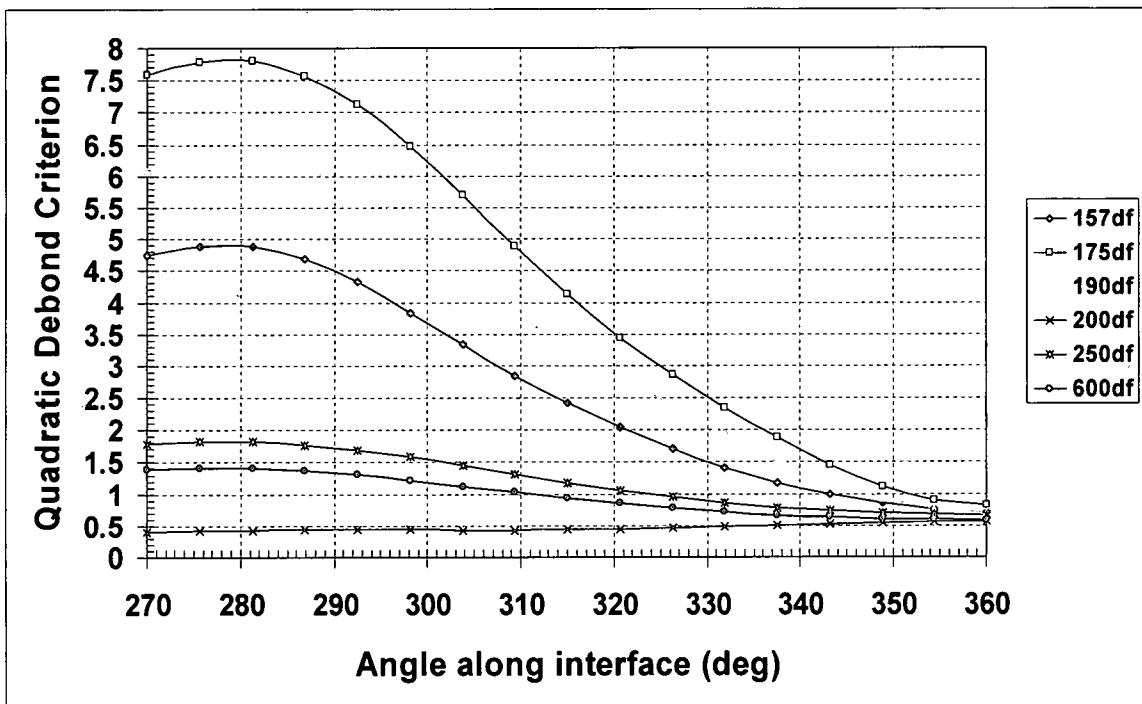


Figure 279: Quadratic Debond Criterion evaluated at the fiber matrix interface of the corner fiber at debond locations in field of view from $\theta = 270^\circ$ to 360° with $A = 21$ and $B = 14$

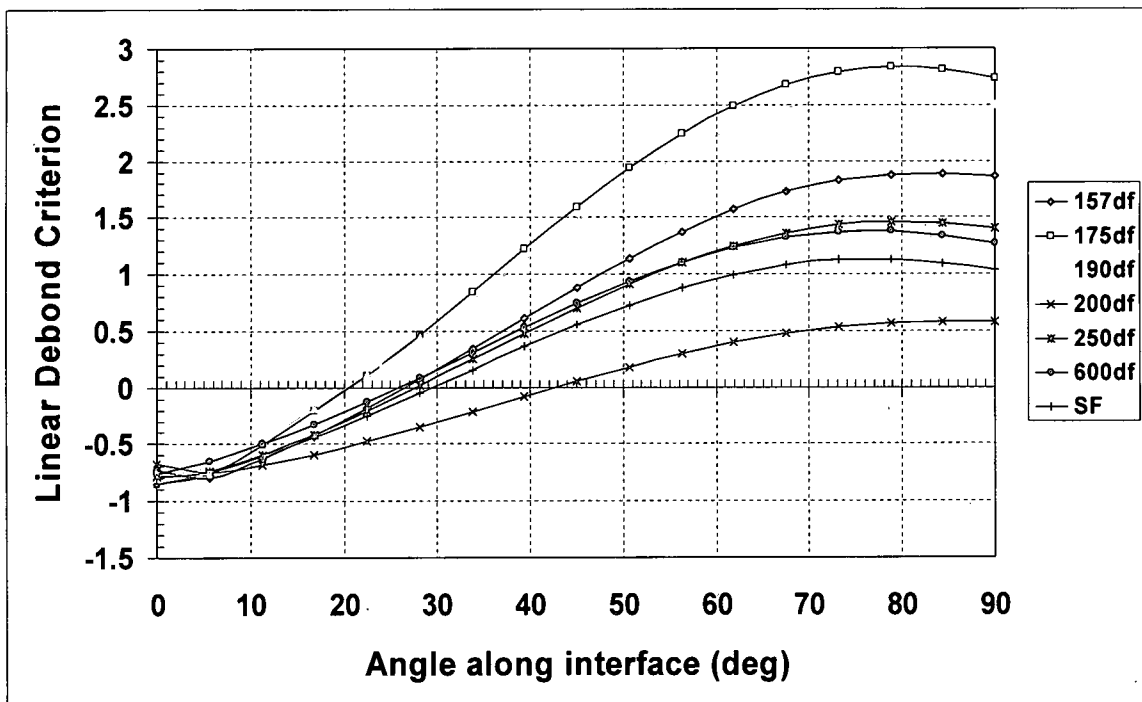


Figure 280: Linear Debond Criterion evaluated at the fiber matrix interface of the corner fiber at debond locations in field of view from $\theta = 0^\circ$ to 90° with $A = 4.62$ and $B = 1.95$

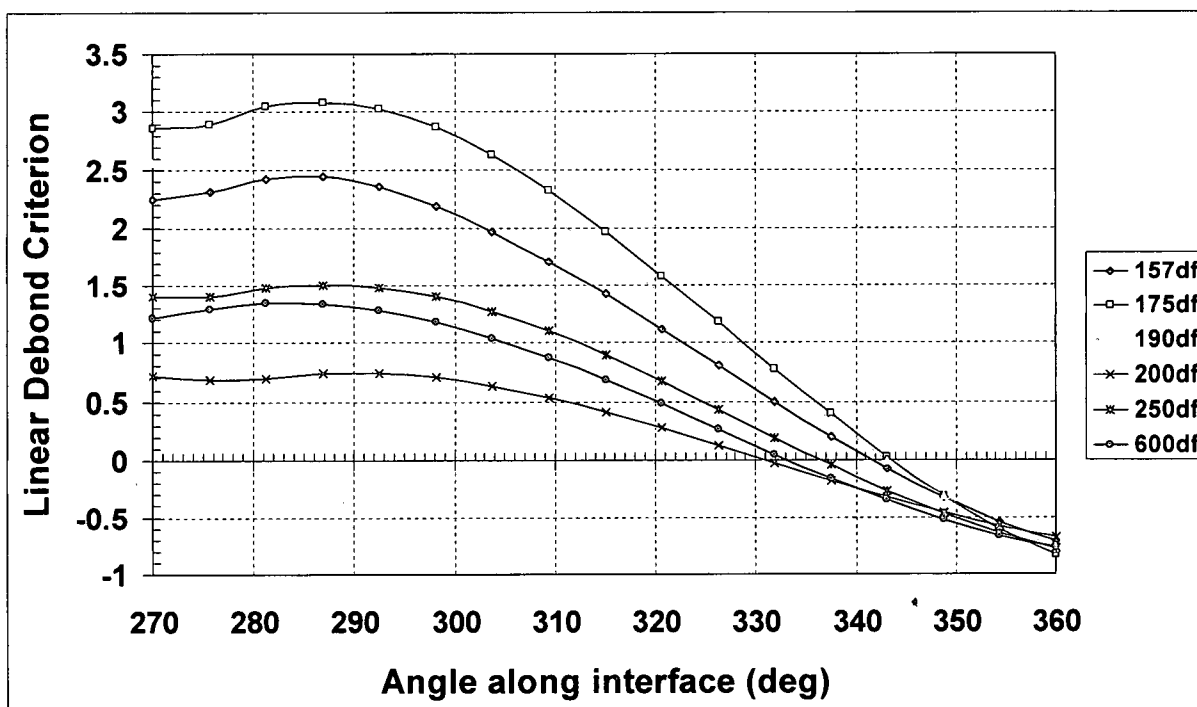


Figure 281: Linear Debond Criterion evaluated at the fiber matrix interface of the corner fiber at debond locations in field of view from $\theta = 270^\circ$ to 360° with $A = 4.62$ and $B = 1.95$

Table 89: Comparison of the fiber matrix debond limits predicted by the Quadratic and Linear Debond Criterion for the 1st quadrant of the corner fiber at debond locations on the corner fiber

Fiber Spacing	Exp db Limits (deg)	Quadratic db Criterion limits (deg)	% Δ	Linear db Criterion limits (deg)	% Δ
1.57d _f	46	30	26.7	47	2.3
1.75d _f	38	12	33.3	36	3.7
1.9d _f	50	16	45.4	37	24.5
2.5d _f	52	44	17.4	53	2.6
6.0d _f	51	44	15.2	52	2.6
SF	63	78	55.6	62	3.6

Table 90: Comparison of the fiber matrix debond limits predicted by the Quadratic and Linear Debond Criterion for the 4th quadrant of the corner fiber at debond locations on the corner fiber

Fiber Spacing	Exp db Limits (deg)	Quadratic db Criterion limits (deg)	%Δ	Linear db Criterion limits (deg)	%Δ
1.57d _f	314	343	39.7	323	17
1.75d _f	322	351	35.8	329	11.9
1.9d _f	310	347	48.1	327	29.8
2.5d _f	308	324	29.6	312	9.5
6.0d _f	309	311	4.9	305	10.3

Inspection of Tables 89 and 90 reveal that the linear debond criterion is more accurate in predicting the debond limits at the debond locations on the corner fiber than the quadratic criterion. Although, the debond limits for the 6.0d_f spacing is better represented by the quadratic criterion, the linear criterion performs consistently better for all other fiber spacing groups at the center of the specimen, i.e. at Z = 0, and at the debond locations on the corner fiber. Both criteria are for the most part conservative in the prediction of the debond limits, i.e. they predict a longer debond length than is actually observed. However, due to the large relative difference percentages shown in the evaluation of the quadratic debond criterion's prediction of the debond limits to the actual debond limits discussed above; plus the fact that the quadratic criterion does not reflect the compression stresses at the interface along the fiber equator; the linear debond criterion as shown in equation (13), and repeated below, best describes the fiber matrix debonding limits for the cruciform specimens in the 862/W matrix system.

$$4.62 \left(\frac{\sigma_r}{\sigma_{yt}} \right) + 1.95 \left(\frac{\tau_{r\theta}}{\tau_y} \right) \geq 1 \quad (13)$$

Where σ_r and $\tau_{r\theta}$ are the interfacial radial and shear stress, respectively, determined from the cruciform FEA and σ_{yt} and τ_y are the tensile and shear strengths respectively, determined from the neat resin test results.

For the areas of the cruciform specimen where the field of view is either partially or completely obstructed by other fibers, namely the 2nd and 3rd quadrants of the corner fiber and the center fiber; the discussion of the evaluation of the proposed linear debond criterion follows. Figure 282 shows the interfacial linear debond criterion distribution in the 2nd quadrant of the corner fiber at $Z = 0$ for all cruciform specimens in the 862/W matrix system. Likewise, Figure 283 shows the interfacial linear debond criterion distribution in the 3rd quadrant of the corner fiber at $Z = 0$.

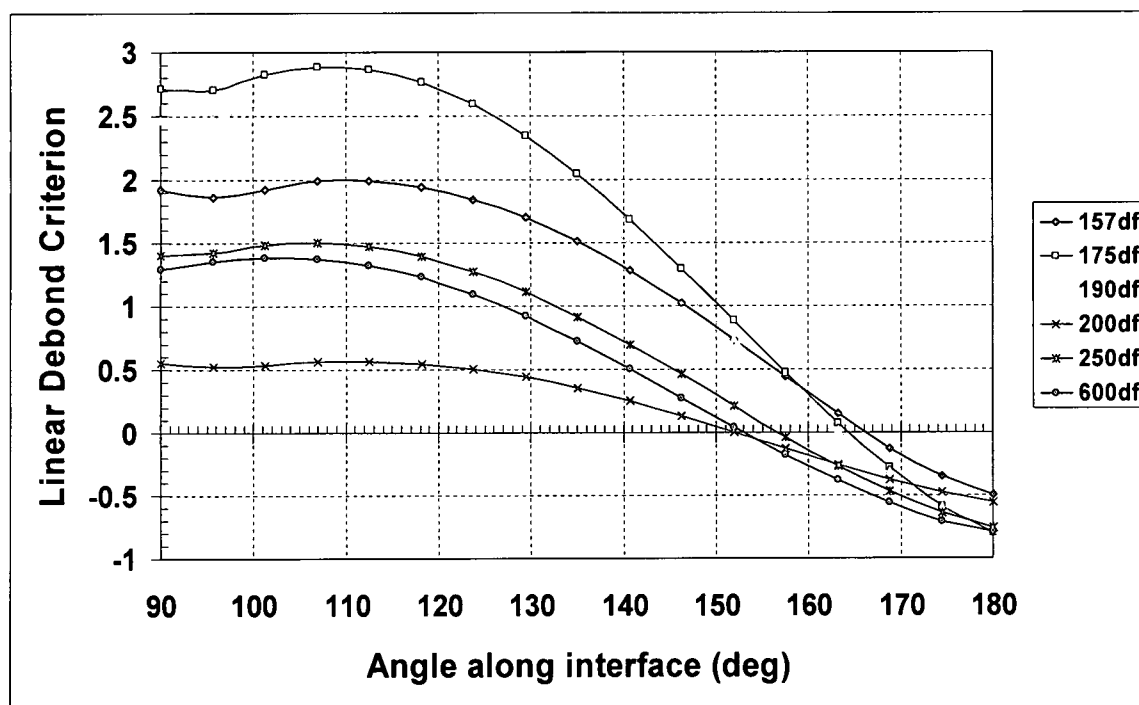


Figure 282: Linear Debond Criterion evaluated at the fiber matrix interface of the corner fiber in field of view from $\theta = 90^\circ$ to 180° at $Z = 0$ with $A = 4.62$ and $B = 1.95$

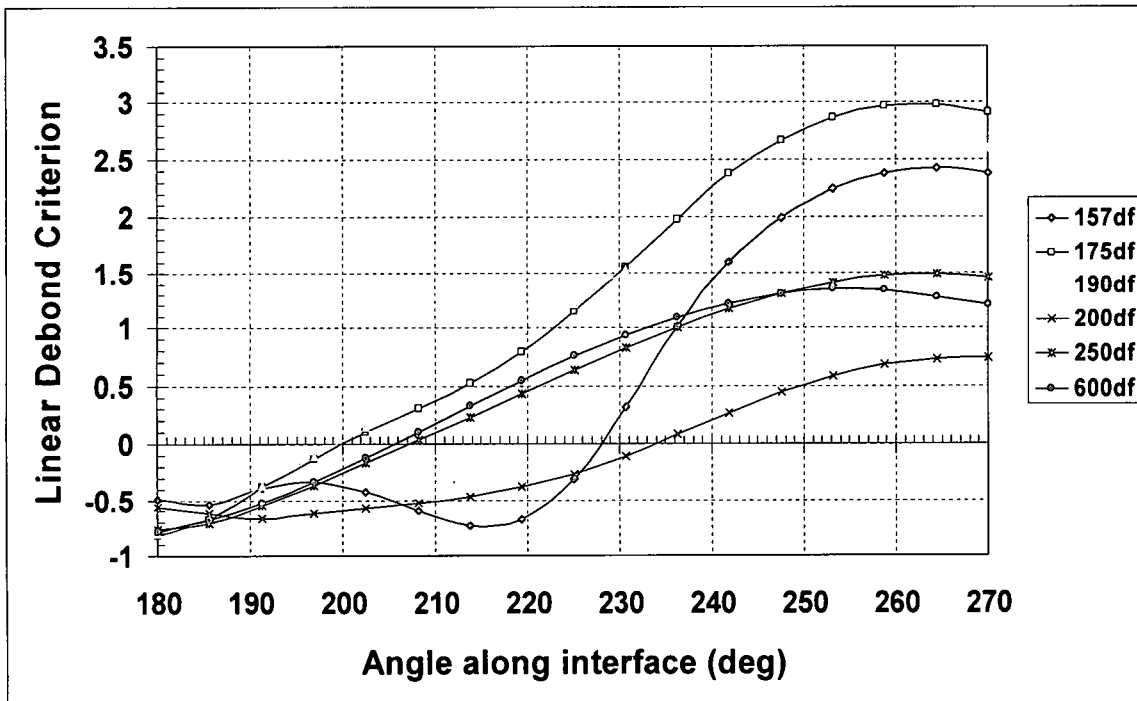


Figure 283: Linear Debond Criterion evaluated at the fiber matrix interface of the corner fiber in field of view from $\theta = 180^\circ$ to 270° at $Z = 0$ with $A = 4.62$ and $B = 1.95$

In all cases where the specimen's first failure mechanism was fiber matrix debonding, namely the 1.57d_f, 1.75d_f, 1.9d_f, 2.5d_f and the 6.0d_f groups, the linear debond criterion exceeds 1.0 indicating fiber matrix debond present at that particular fiber spacing. Furthermore, for the specimen exhibiting matrix cavitation as its first failure mechanism, the 2.0d_f spacing, the criterion is less than 1.0. Thus it appears that the linear debond criterion correlates to the observed experimental results in the 2nd and 3rd quadrants of the corner fiber. Table 91 lists the predicted debond limits by the linear debond criterion in the 2nd and 3rd quadrant of the corner fiber compared to the experimentally observed debond limits. Inspection of Table 91 shows that the linear debond criterion is pretty accurate in predicting the debond limits for the 6.0d_f fiber spacing; while fairly accurate predicting the 1.75d_f and 2.5d_f fiber spacing groups in the 2nd and 3rd quadrant. It is only moderately successful in predicting the debond limits for the 1.57d_f fiber spacing group in both quadrants. Due to reason explained above, it is hard to qualitatively

compare the analytical debond criterion results to the experimental debond measurements for the 1.9d_f fiber spacing.

Table 91: Comparison of the fiber matrix debond limits predicted by the Linear Debond Criterion for the 2nd and 3rd quadrant of the corner fiber at Z = 0

Fiber Spacing	Exp debond Limits (deg)		Linear Debond Criterion limits in 2 nd Quad (deg)	%Δ	Linear Debond Criterion limits in 3 rd Quad (deg)	%Δ
	2 nd Quad	3 rd Quad				
1.57d _f	134	226	147	22.8	236	22.7
1.75d _f	142	218	150	13.3	223	9.6
1.9d _f	130	230	148	31	221	18.4
2.5d _f	128	232	133	11.6	236	10.5
6.0d _f	129	231	127	5.1	232	2.6

The reason for the varying degree of success of the linear debond criterion can be explained in part due to the fiber configuration within the cruciform specimen that the 2nd and 3rd quadrants of the corner fiber is either partially or completely obstructed from view. Consequently, the debond limits cannot be determined by photomicrograph analysis in these quadrants. The experimentally observed debond limits are only observed in the 1st and 4th quadrant of the corner fiber. They occur predominantly in the 1st quadrant of the corner fiber and they are assumed to act equal distance centered at the fiber poles. However, based on the analytical results discussed in Chapter 3, it is known that neighboring fiber effects occur in these two quadrants to varying degrees with respect to the fiber spacing. Also shown in Chapter 3 is that the 2.5d_f and 6.0d_f fiber spacing groups behave almost as a group of isolated fibers showing minimal effects of neighboring fibers from the combined loading, as well as for the mechanical load and residual stress loading. Based upon the analysis for the 2.5d_f and 6.0d_f groups in Chapter 3 and it is shown for the SF case that the linear debond criterion predicts its debond limits pretty accurately where no neighboring fiber exist, explains why in the 2nd and 3rd quadrant the criterion predicts the 2.5d_f and 6.0d_f spacing debond limits pretty accurately.

The debond criterion over predicts the debond limit in the 2nd quadrant while under predicting the limit in the 3rd quadrant for the remaining fiber spacing groups, ignoring the 1.9d_f spacing for reasons mentioned above. Recall that over predicting the debond limit means that the

prediction has a longer length than the experimental debond length, while under predicting it means that the experimental debond length is greater. It is conceivable that the actual cruciform debonds are not symmetric about the fiber poles. Based upon the stress state at the fiber matrix interface, the debond in the 2nd quadrant could be greater than in the 1st quadrant where it is observed. On the other hand, the debond limit in the 3rd quadrant is most likely smaller. From Figure 226 the radial stress due to the combination of mechanical loading and matrix cure residual stresses has a larger interfacial circumferential length over which the maximum magnitudes are acting in the 2nd quadrant from about $\theta = 90^\circ$ to 130° (a comparable experimental debond length) compared to Figure 225 from about $\theta = 50^\circ$ to 90° . Figure 227 shows a smaller interfacial circumferential length over which the maximum magnitudes are acting in the 3rd quadrant from about $\theta = 230^\circ$ to 270° compared to Figure 228 from about $\theta = 270^\circ$ to 310° . Similarly, the magnitude of the shear stress is larger in the 2nd quadrant as shown in Figure 238 compared to Figure 237 over the same length mentioned above, while there is very little change in the 3rd quadrant comparing Figure 239 with 240 over a 20° sweep symmetrical about the pole. While the dominate stress acting in the criterion is the radial stress, the examination of the analytical results suggests that due to the stress state in the 2nd and 3rd quadrant of the corner fiber the actual debonds could be unsymmetrical about the poles. This give confidence to the concept that debonds could have a greater length in the 2nd quadrant and a shorter length in the 3rd quadrant than the assumption of symmetry about the poles based upon the observed debond length.

Table 92 list the experimentally observed debond widths along with their standard deviations and the corresponding debond limits plus the predicted debond limits determined by the Linear Debond Criteria for all fiber spacing groups in the 862/W matrix system exhibiting fiber matrix debonding as failure initiation. With the exception for the 1.9d_r fiber spacing for reason explained above, all specimens predicted debond limits fall within the standard deviations of their experimentally observed debond limits. Consequently, it can be concluded based upon the preceding discussion that the linear debond criterion as given in equation (13) adequately describes the fiber matrix debond failure initiation of the 862/W matrix system.

Table 92: Experimental standard deviation debond limits with debond limits determined by the Linear Debond Criteria

Spec.	Average Debond Width, mm (Std dev)	Experimental Debond Limits	Linear Prediction Debond limits
1.57d _f	0.049 (0.024)	46° to 134° NP 226° to 314° SP	46° to 147° NP 236° to 324° SP
	Std-dev Small	59° to 111° NP 239° to 291° SP	
	Std-dev Large	36° to 144° NP 216° to 324° SP	
1.75d _f	0.068 (0.041)	38° to 142° NP 218° to 322° SP	36° to 150° NP 223° to 329° SP
	Std-dev Small	58° to 122° NP 238° to 302° SP	
	Std-dev Large	23° to 157° NP 203° to 337° SP	
1.9d _f	0.041 (0.041)	50° to 130° NP 230° to 310° SP	37° to 148° NP 221° to 327° SP
	Std-dev Small	50° to 130° NP 230° to 310° SP	
	Std-dev Large	50° to 130° NP 230° to 310° SP	
2.5d _f	0.037 (0.021)	52° to 128° NP 232° to 308° SP	52° to 133° NP 236° to 313° SP
	Std-dev Small	66° to 114° NP 246° to 294° SP	
	Std-dev Large	42° to 138° NP 222° to 318° SP	
6.0d _f	0.039 (0.0012)	51° to 129° NP 231° to 309° SP	52° to 127° NP 232° to 306° SP
	Std-dev Small	52° to 128° NP 232° to 308° SP	
	Std-dev Large	51° to 129° NP 231° to 309° SP	
SF	0.023 (0.007)	63° to 117° NP	65° to 115° NP
	Std-dev Small	66° to 114° NP	
	Std-dev Large	56° to 124° NP	

Fiber-Matrix Debond Initiation Criterion – Summary

Due to evidence from the cruciform specimen fracture surface analysis indicating an interaction between the shear and tensile forces, discussed in Chapter 2. Then, through an

analysis of the interfacial radial and shear stresses acting over the measured debond length for each fiber spacing group; it was concluded a definite interaction exists between the radial and shear stresses acting at the fiber-matrix interface creating the debond. A quadratic and linear debond criteria were investigated to see which one better predicted the debond limits observed in the cruciform experiments exhibiting fiber-matrix debond as their failure initiation for all fiber spacing groups. A thorough comparison was made between the two forms of the debond criteria in the visible 1st and 4th quadrants of the corner fiber. From these results it was found that the linear debond criterion better predicted the debond limits for all fiber spacing groups in both quadrants except for the 6.0d_f fiber spacing group in the 4th quadrant. However, since the majority of the fiber-matrix debond occurred at the north pole of the corner fiber at the 6.0d_f fiber spacing and it was better described by the linear debond criterion in the 1st quadrant it was concluded that the linear debond criterion is the best fit for the 6.0d_f spacing. Therefore, strong evidence exists that the linear debond criterion, shown in equation (13), best predicts the fiber-matrix debonds for all fiber spacing groups based upon its performance, shown above. Furthermore, the linear debond criterion best described the interfacial stress state reflecting the compressive nature of the radial stress at the fiber equator which the quadratic criterion did not. Further tests show that the linear debond criterion adequately predicts the debond limits of the quadrants of the corner fiber obstructed from view based a symmetrical debond occurring at the fiber poles.

Having justified the debond criterion using the corner fiber because the majority of the debonds occurred at the corner fiber for all specimens exhibiting fiber-matrix debond as their first failure; the criterion will now be applied to the center fiber. Figure 284 is the linear debond criterion distribution at the fiber-matrix interface along the center fiber. Three specimens at the 6.0d_f fiber spacing group initiated a debond at the center fiber. Two specimens each in the 2.5d_f, 1.75d_f and 1.57d_f groups initiated at the center fiber.

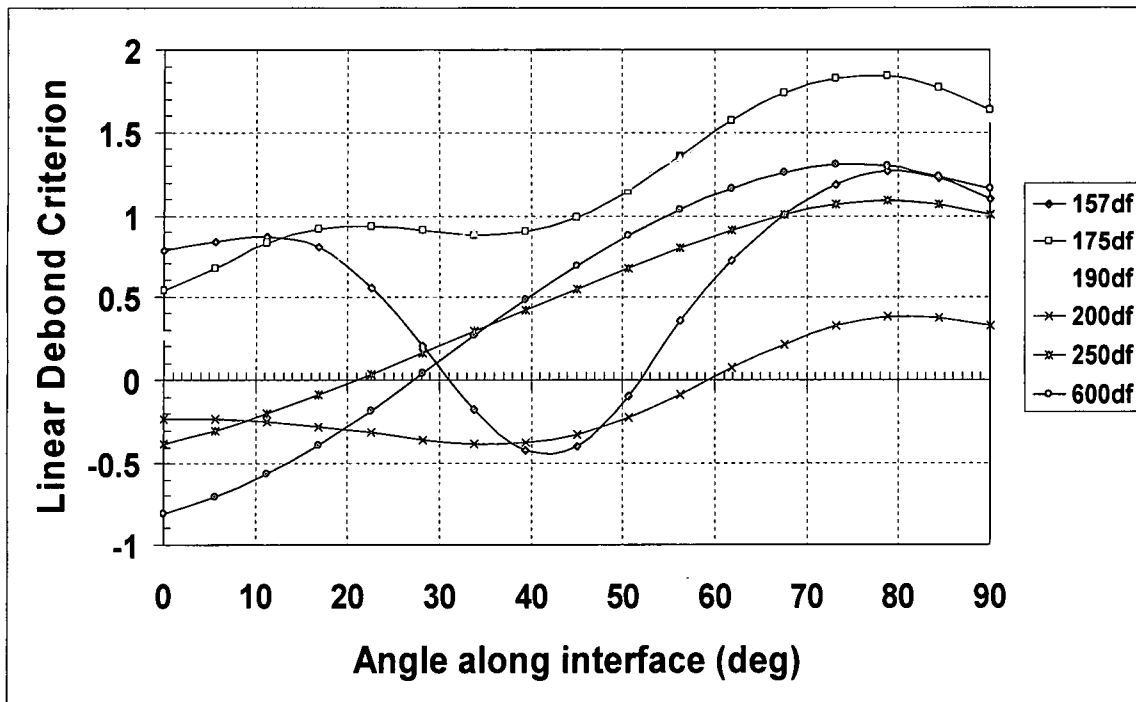


Figure 284: Linear Debond Criterion at the fiber-matrix interface of the center fiber

Unlike the 828/D-230 system where the debond criterion only predicted the $6.0d_f$ spacing fairly accurately and being overly conservative for the rest; in the 862/W matrix system the predicted limits of the debond fall within the experimentally observed limits for all fiber spacing groups except the $1.9d_f$ group. From Figure 284 and Table 92 the predicted limit for the $6.0d_f$ spacing is 55° and the observed limit is 51° . Likewise, for the $2.5d_f$ its predicted limit is 67.5° and the observed is 52° ; for the $1.75d_f$ it predicted limit is 46° and the observed is 38° and lastly for the $1.57d_f$ its predicted limit is 67.5° while its observed limit is 46° . Although the predicted limits fall within the observed limits they tend to be not conservative, in that it predicts a smaller debond that what was actually observed. It should be noted that Table 92 is using the average of all specimens that exhibited debonds at the fiber pole and the preceding discussion is applying it to the center fiber where only a few specimens actually exhibited debonds. This generalization is not totally accurate. For example at the $6.0d_f$ spacing 3 specimens debond at the center fiber, 2 exhibit a thin debond having limits of 28° to 37° and 26° to 37° respectively, and one debonds at the pole with a limit of 51° . The predicted limit at $6.0d_f$ is 55° which is close to the specimen

exhibiting debonds at the pole but not so good in predicting the thin debonds occurring for the other two specimens. However, a majority of the debonds taking place in the 862/W system occur at the fiber poles for all the fiber spacings exhibiting fiber-matrix debonding as their first failure mechanism.

Summary

A quadratic and linear interaction debond criteria were evaluated in all four quadrants of the corner fiber for both the 828/D-20 and 862/W matrix systems. The interaction criterion involved the sum of the ratios of the interfacial radial stress to the tensile strength and the interfacial shear stress to the shear strength in a quadratic and linear form. It is shown that for the 828/D-230 matrix system that the linear debond criterion expressed in equation (3) shown previously and repeated below best predicts the experimentally observed fiber-matrix debonds. The Linear Debond Criterion out-performed the Quadratic Debond Criterion in corner fiber quadrants 3 and 4, while the converse occurred in quadrant 2 and they tied in quadrant 1.

$$\frac{11}{3} \left(\frac{\sigma_r}{\sigma_{yt}} \right) + \frac{4}{3} \left(\frac{\tau_{r\theta}}{\tau_y} \right) \geq 1 \quad \text{828/D-230 Linear Debond Initiation Criterion}$$

For the 862/W matrix system the linear debond criterion, expressed in equation (13) shown previously and repeated below also best predicted the debonds than the quadratic criterion. The linear debond criterion better predicted the debond limits for all fiber spacing groups in the 1st and 4th quadrants, the field of view, except for the 6.0d_f group in the 4th quadrant. Since the majority of debond at the 6.0d_f spacing occurred at the north pole of the corner fiber and the debonds were better predicted by the linear in that quadrant it was concluded that the linear debond criterion is the best fit for the 6.0d_f spacing.

$$4.62 \left(\frac{\sigma_r}{\sigma_{yt}} \right) + 1.95 \left(\frac{\tau_{r\theta}}{\tau_y} \right) \geq 1 \quad \text{862/W Linear Debond Initiation Criterion}$$

It was determined and shown in Chapter 4 that the Mohr-Coulomb Criterion best described the matrix cavitation observed in the multi-fiber cruciform specimens for both resins systems. Here in Appendix E, the Mohr-Coulomb results for the 828/D-230 matrix is thoroughly evaluated in all quadrants of the FEM not discussed in Chapter 4. The results contained herewith show that the critical value of the Mohr-Coulomb Criterion is 36.35 MPa in all regions of the cruciform specimen exhibiting cavitation. It was also shown that matrix failure initiation does not occur around the fibers from the fiber-matrix interface to a radial distance of 0.04 mm, except at the equator of the center fiber.

R702034919